Transactions of the ASME

Technical Editor, **L. B. FREUND**

Division of Engineering
Brown University
Providence, R.I. 02912

APPLIED MECHANICS DIVISION

Chairman, **M. M. CARROLL**
Secretary, **J. R. RICE**
Associate Editors,
T. BELYTSCHKO
D. B. BOGY
R. M. CHRISTENSEN
R. J. CLIFTON
T. L. GEERS
MAURICE HOLT
THOMAS J. R. HUGHES
W. D. IWAN
W. G. KNAUSS
F. A. LECKIE
FRANCIS C. MOON
J. W. NUNZIATO
R. H. PLAUT
R. T. SHIELD
J. G. SIMMONDS
K. R. SREENIVASAN
J. S. WALKER
Z. WARHAFT
G. A. WEMPNER
L. T. WHEELER
S. E. WIDNALL

BOARD ON COMMUNICATIONS
Chairman and Vice-President
K. N. REID, JR.

Members-at-Large
W. BEGELL
J. T. COKONIS
W. G. GOTTENBERG
F. LANDIS
J. R. LLOYD
R. E. NICKELL
J. ORTLOFF
C. PHILLIPS
R. E. REDER
F. W. SCHMIDT

President, **L. S. FLETCHER**
Exec. Dir.
PAUL ALLMENDINGER
Treasurer, **ROBERT A. BENNETT**

PUBLISHING STAFF
Mng. Dir., Pub., **J. J. FREY**
Dep. Mng. Dir., Pub.
JOS. SANSONE
Managing Editor,
CORNELIA MONAHAN
Production Editor, **REMO SALTA**
Prod. Asst., **MARISOL ANDINO**

The Journal of Applied Mechanics (ISSN 0021-8936) is published quarterly for $100 per year by The American Society of Mechanical Engineers, 345 East 47th Street, New York, NY 10017. *Second class postage paid at New York, NY and additional mailing offices.* POSTMASTER: Send address changes to The Journal of Applied Mechanics, c/o THE AMERICAN SOCIETY OF MECHANICAL ENGINEERS, 22 Law Drive, Box 2300, Fairfield, NJ 07007-2300.
CHANGES OF ADDRESS must be received at Society headquarters seven weeks before they are to be effective. Please send old label and new address.

PRICES: To members, $24.00, annually; to nonmembers, $100.00.
Add $6.00 for postage to countries outside the United States and Canada.

STATEMENT from By-Laws. The Society shall not be responsible for statements or opinions advanced in papers or . . . printed in its publications (B7.1, Par. 3).

COPYRIGHT © 1985 by the American Society of Mechanical Engineers. Reprints from this publication may be made on condition that full credit be given the TRANSACTIONS OF THE ASME, JOURNAL OF APPLIED MECHANICS, and the author, and date of publication be stated.

INDEXED by the Engineering Index, Inc.

Journal of Applied Mechanics

Published Quarterly by The American Society of Mechanical Engineers

VOLUME 52 • NUMBER 3 • SEPTEMBER 1985

505 Reviewers

TECHNICAL PAPERS

507 A New Displacement Form for the Nonlinear Equations of Motion of Shells of Revolution
J. G. Simmonds

510 Analysis of Wire Ropes With Internal-Wire-Rope Cores (85-APM-36)
J. W. Phillips and G. A. Costello

517 Counterintuitive Behavior in a Problem of Elastic-Plastic Beam Dynamics (85-APM-38)
P. S. Symonds and T. X. Yu

523 Buckling of an Elastic Elliptical Ring Insde a Rigid Boundary (85-APM-26)
T. C. Soong and I. Choi

529 The Effect of Curvature and Torsion on the Temperature Distribution in a Helix
D. D. Sayers and M. C. Potter

533 A New Rate Principle Suitable for Analysis of Inelastic Deformation of Plates and Shells (85-APM-34)
S. Mukherjee and F. G. Kollmann

536 Large-Amplitude Oscillations of Unsymmetrically Laminated Anisotropic Rectangular Plates Including Shear, Rotatory Inertia, and Transverse Normal Stress
K. S. Sivakumaran and C. Y. Chia

543 Thermal Effect on the Transverse Vibration of High-Speed Rotating Anisotropic Disk
N. C. Ghosh

549 Vibration and Stability of Circular Plates Under Partially Distributed or Concentrated Inplane Loads
Y. Narita

553 Large Deflection Behavior of Simply Supported Laminated Panels Under In-Plane Loading
Y. Zhang and F. L. Matthews

559 Transient Loads Analysis by Dynamic Condensation
K. Kubomura

565 Eigenfunctions at a Singular Point in Transversely Isotropic Materials Under Axisymmetric Deformations (85-APM-22)
T. C. T. Ting, Y. Jin, and S. C. Chou

571 First-Order Variation in Elastic Fields Due to Variation in Location of a Planar Crack Front (85-APM-25)
J. R. Rice

580 Dynamic Fracture of an Idealized Fiber-Reinforced Cantilever (85-APM-35)
L. F. Mannion

585 Dynamic Fracture Under Normal Impact Loading of the Crack Faces (85-APM-27)
K.-S. Kim

593 A Continuum Model for Dynamic Tensile Microfracture and Fragmentation
L. Seaman, D. R. Curran, and W. J. Murri

601 On the Asymptotic Continuum Analysis of Quasistatic Elastic – Plastic Crack Growth and Related Problems
W. J. Drugan

606 Compressibility of an Isolated Spheroidal Cavity in an Isotropic Elastic Medium
R. W. Zimmerman

609 Influence of Cavity Shape on Damage Parameter
S. Jansson and U. Stigh

615 A Physically Based Constitutive Equation for Creep-Damaging Solids
A. J. Levy

621 Nonproportional Loading Steps in Multiaxial Creep of 2618 Aluminum (85-APM-32)
J. L. Ding and W. N. Findley

629 A Viscoplastic Theory With Anisotropic Hardening and Its Application to Pressure-Shear Plate Impact Experiments (85-APM-37)
A. Gilat

634 Optimal Cooling Paths for a Class of Thermorheologically Complex Viscoelastic Materials
B. D. Harper

639 An Incremental Constitutive Relation of Unilateral Contact Friction for Large Deformation Analysis (85-APM-24)
J.-H. Cheng and N. Kikuchi

649 On the Uniqueness of Solution of the Initial Value Problem in Softening Materials (85-APM-29)
K. C. Valanis

654 The Uniaxial Unloading Behavior of Two Engineering Alloys at Room Temperature (85-APM-31)
E. Krempl and V. V. Kallianpur

(Contents continued on Inside Back Cover)

Downloaded 04 May 2010 to 171.66.16.49. Redistribution subject to ASME license or copyright; see http://www.asme.org/terms/Terms_Use.cfm

CONTENTS (CONTINUED)

659 **Acoustoelastic Response of a Polycrystalline Aggregate With Orthotropic Texture** (85-APM-23)
G. C. Johnson

664 **Scattering of a Rayleigh Wave by an Elastic Quarter Space** (85-APM-30)
A. K. Gautesen

669 **An Experimental Study of the Reflection and Transmission of Flexural Waves at Discontinuities**
J. F. Doyle and S. Kamle

674 **Prediction of Impact Force and Duration Due to Low-Velocity Impact on Circular Composite Laminates**
K. N. Shivakumar, W. Elber, and W. Illg

681 **Asymmetric Problem of Loading Under a Smooth Punch**
V. I. Fabrikant, A. P. S. Selvadurai, and G. D. Xistris

686 **Stability of a Rigid Body With an Oscillating Particle: An Application of MACSYMA** (85-APM-28)
L. A. Month and R. H. Rand

693 **A Study of Dynamic Instability of Plates by an Extended Incremental Harmonic Balance Method** (85-APM-33)
C. Pierre and E. H. Dowell

698 **On the Recursive Determination of Body Frames for Multibody Dynamic Simulation**
R. E. Roberson

701 **Coupled Torsional and Transverse Vibration of Unbalanced Rotor**
R. Cohen and I. Porat

706 **Laminar Sart-Up Flow in a Pipe**
D. R. Otis

712 **Effect of Hinge Gap on Aerodynamics of Thin Airfoils Having an Oscillating Flap**
S. Ando and D.-H. Lee

718 **Time-Dependent Stokes Flow Induced by Instantaneous Sources**
O. O. Ajayi and A. Falade

DESIGN DATA AND METHODS

725 **Axisymmetric Postbuckling of Orthotropic Tapered Thick Annular Plates**
P. C Dumir

BRIEF NOTES

Theoretical and Experimental Analysis of Flexural Vibration of the Viscoelastic Timoshenko Beam 728
T. Nakao, T. Okano, and I. Asano

An *Action-Based Method for the Kinetic Stability of Potential* But Nonconservative Systems 731
J. G. Papastavridis

Steady-State Response of an Internally Damped Cylindrical Shell Translationally or Rotationally Driven at an Edge 733
T. Irie and Y. Kobayashi

DISCUSSION

737-738 Discussion on previously published paper by **D. C. Kammer and A. L. Schlack, Jr.**

BOOK REVIEWS

739 ***The Mechanical Behavior of Electromagnetic Solid Continuua*** edited by **G. A. Maugin** . . . Reviewed by **R. D. James**

739 ***Numerical Methods for Nonlinear Variational Problems*** by **Roland Glowinski** . . . Reviewed by **J. T. Oden**

740 ***Nonlinear Elastic Deformations*** by **R. W. Ogden** . . . Reviewed by **E. Sternberg**

741 ***Computational Techniques for Differential Equations*** edited by **John Noye** . . . Reviewed by **G. Majda**

741 ***Atmospheric Dispersion of Heavy Gases and Small Particles*** edited by **G. Ooms** and **H. Tennekes** . . . Reviewed by **R. A. Dobbins**

Books Received by the office of the Technical Editor

700, 727, 738	Worldwide Mechanics Meeting List
509, 516, 542, 548, 558, 564	Applied Mechanics Symposium Proceedings
584, 600, 605, 614, 633	Applied Mechanics Symposium Proceedings
648	IUTAM Symposia
663	A Symposium on Mixture Theory
608	Change of Address Form

Downloaded 04 May 2010 to 171.66.16.49. Redistribution subject to ASME license or copyright; see http://www.asme.org/terms/Terms_Use.cfm

A New Displacement Form for the Nonlinear Equations of Motion of Shells of Revolution[1]

J. G. Simmonds

Department of Applied Mathematics,
University of Virginia,
Charlottesville, Va. 22901
Mem. ASME

In the theory of shells of revolution undergoing torsionless, axisymmetric motion, an extensional and a bending hoop strain are introduced that are linear in the displacements, regardless of the magnitudes of the strains and the meridional rotation. The resulting equations of motion and boundary conditions are derived and some common conservative surface loads are listed along with their potentials. The governing equations appear to be the simplest possible in terms of displacements.

Introduction

To simplify terminology, I call a shell of revolution that undergoes torsionless, axisymmetric motion an *axishell*. Reissner has perfected the equations for static axishells in a sequence of papers [1–4]. In [4] there is no restriction on the size of the extensional strains and Reissner includes the nonclassical effects of transverse shear strain and a stress couple that turns about the normal to the deformed midsurface. The *primary* kinematic variables in Reissner's approach are the angle of rotation of meridional fibers and various strains that are related by compatibility conditions.

In some problems, e.g., dynamic ones, a displacement formulation may be advantageous. Unfortunately, Reissner's bending strains, while simple in terms of rotations, become somewhat unwieldy in terms of displacements. (It must be emphasized that Reissner never intended displacements to be the basic variables in his theory.) In the classical, nonlinear theory of arbitrary shells, Budiansky [5] has defined extensional strains that are quadratic in the displacements and bending strains that, in general, are cubic in the displacements but which, for axishells, are also quadratic. Out of many possibilities, Budiansky has chosen definitions such that the associated field equations, when linearized, reduce to the "best" linear shell theory [6] of Sanders [7] and Koiter [8]. However, Budiansky's strains are not the simplest possible for axishells.

A key feature of the static, linear Sanders-Koiter shell theory is that it exhibits a particularly simple static-geometry duality which can lead to significant analytic economy. However, in nonlinear problems or in dynamic linear problems, the static-geometric duality does not hold and there is no reason why it should dictate the choice of strains. The main contribution herein is the introduction of pairs of extensional and bending strains, $(\gamma_\sigma, \kappa_\sigma)$ and $(e_\theta, \kappa_\theta)$, such that while the first pair is quadratic in the displacements, the second pair is *linear*. In what follows, we develop the associated field equations and boundary conditions for a large strain, classical theory.

Analysis

Let (r, θ, z) denote circular cylindrical coordinates and $\{\mathbf{e}_r, \mathbf{e}_\theta, \mathbf{e}_z\}$ the associated standard orthonormal basis. Further, let S denote a reference surface of revolution whose meridian $\mathfrak{M}$ has the vector parametric representation

$$\xi = r(\sigma)\mathbf{e}_r(\theta) + z(\sigma)\mathbf{e}_z, \quad 0 \le \sigma \le L, \tag{1}$$

where σ is arc length along $\mathfrak{M}$. Unit tangent and normal vectors to $\mathfrak{M}$ are defined and denoted by

$$\mathbf{t} \equiv \xi' = \cos\phi\mathbf{e}_r + \sin\phi\mathbf{e}_z \tag{2}$$

$$\mathbf{n} \equiv \mathbf{t} \times \mathbf{e}_\theta = -\sin\phi\mathbf{e}_r + \cos\phi\mathbf{e}_z, \tag{3}$$

where

$$\cos\phi \equiv r'(\sigma), \quad \sin\phi \equiv z'(\sigma) \tag{4}$$

and a prime denotes partial or total differentiation with respect to σ. Denote by

$$\mathbf{y} = \bar{r}(\sigma,t)\mathbf{e}_r(\theta) + \bar{z}(\sigma,t)\mathbf{e}_z \tag{5}$$

the deformed image of ξ when the shell undergoes torsionless, axisymmetric motion.

If we denote stress resultants and couples per unit *undeformed* length along parallels and meridians of S by

$$\mathbf{N}_\sigma, N_\theta\mathbf{e}_\theta, -M_\sigma\mathbf{e}_\theta, \mathbf{M}_\theta, \tag{6}$$

then the equations of motion of an axishell take the form [9]

$$(r\mathbf{N}_\sigma)' - N_\theta\mathbf{e}_r + r\mathbf{p} = \dot{r}m\dot{\mathbf{y}} \tag{7}$$

$$(rM_\sigma)' - \mathbf{M}_\theta \cdot \mathbf{e}_r + r\mathbf{N}_\sigma \cdot \mathbf{m} + rl = rI\dot{\omega}. \tag{8}$$

In these equations,

[1]This work was supported by the National Science Foundation under grant number CEE-8117103.

Contributed by the Applied Mechanics Division for publication in the JOURNAL OF APPLIED MECHANICS.

Discussion on this paper should be addressed to the Editorial Department, ASME, United Engineering Center, 345 East 47th Street, New York, N.Y. 10017, and will be accepted until two months after final publication of the paper itself in the JOURNAL OF APPLIED MECHANICS. Manuscript received by ASME Applied Mechanics Division, July, 1984; final revision, October, 1984.

Copyright © 1985 by ASME
Downloaded 02 May 2010 to 171.66.16.54. Redistribution subject to ASME license or copyright; see http://www.asme.org/terms/Terms_Use.cfm

$$\mathbf{m} \equiv \mathbf{y}' \times \mathbf{e}_\theta, \tag{9}$$

$\mathbf{p}$, l, m, and I are, respectively, an external force and couple, a mass, and a moment of inertia per unit area of S, ω is an angular velocity, and a dot denotes differentiation with respect to time.

Let

$$\beta \equiv \int_0^t \omega(\sigma,\tau)\,d\tau. \tag{10}$$

Taking the dot product of (7) with $\delta\mathbf{y}$, a variation of $\mathbf{y}$, multiplying (8) by $\delta\beta$, a variation of β, adding the resulting expressions, integrating from $\sigma = 0$ to $\sigma = L$, and by parts to remove derivatives on $\mathbf{N}_\sigma$ and M_σ, we obtain *the virtual work identity*

$$[r(\mathbf{N}_\sigma \cdot \delta\mathbf{y} + M_\sigma \delta\beta)]_0^L + \int_0^L (\mathbf{p}\cdot\delta\mathbf{y} + l\delta\beta)\,r\,d\sigma$$

$$= \int_0^L \{m\ddot{\mathbf{y}}\cdot\delta\mathbf{y} + I\ddot{\beta}\delta\beta + [\mathbf{N}_\sigma\cdot(\delta\mathbf{y}' - \mathbf{m}\delta\beta) + N_\theta r^{-1}\mathbf{e}_r\cdot\delta\mathbf{y} + M_\sigma\delta\beta' + \mathbf{M}_\theta\cdot\mathbf{e}_r r^{-1}\delta\beta]\}\,r\,d\sigma. \tag{11}$$

It is convenient to use $\{\mathbf{y}', \mathbf{m}\}$ as a ortho*non*normal moving reference frame for the components of the stress resultants and couples. Thus we set

$$\mathbf{N}_\sigma \equiv \tilde{N}_\sigma \mathbf{y}' + \tilde{Q}\mathbf{m}, \quad \mathbf{M}_\theta \equiv \hat{M}_\theta \mathbf{y}' + \hat{M}\mathbf{m} \tag{12}$$

and, to introduce strain-displacement and rotation-displacement relations, set

$$\mathbf{u} \equiv \mathbf{y} - \xi \equiv u(\sigma,t)\mathbf{e}_r(\theta) + w(\sigma,t)\mathbf{e}_z \tag{13}$$

and

$$\mathbf{y}' \equiv \lambda_\sigma(\cos\bar{\phi}\mathbf{e}_r + \sin\bar{\phi}\mathbf{e}_z), \tag{14}$$

where λ_σ is the *principal meridional stretch*. It follows from (13) and (14) that

$$\bar{\phi} = \tan^{-1}\left(\frac{\sin\phi + w'}{\cos\phi + u'}\right) \tag{15}$$

$$\lambda_\sigma^2 = 1 + 2\gamma_\sigma, \tag{16}$$

where

$$\gamma_\sigma \equiv \mathbf{u}'\cdot\mathbf{t} + \tfrac{1}{2}\mathbf{u}'\cdot\mathbf{u}' = u'\cos\phi + w'\sin\phi + \tfrac{1}{2}(u'^2 + w'^2) \tag{17}$$

is the *Lagrangian meridional strain*.

We now define *first-approximation shell theory* by the conditions

$$\bar{\phi} = \phi + \beta \tag{18}$$

$$\hat{M} = l = I = 0. \tag{19}$$

The part of the integrand in the second line of (11) in brackets reduces to

$$\tilde{N}_\sigma\delta\gamma_\sigma + N_\theta\delta e_\theta + M_\sigma\delta\beta' + \tilde{M}_\theta r^{-1}\lambda_\sigma\delta\sin(\phi+\beta), \tag{20}$$

where

$$e_\theta \equiv u/r \tag{21}$$

is the *engineering hoop strain*.

From (15)–(18),

$$\kappa_\sigma \equiv \lambda_\sigma^2\bar{\phi}' - \phi' = (\cos\phi + u')\,w'' - (\sin\phi + w')\,u'' + (u'\cos\phi + w'\sin\phi)\,\phi'. \tag{22}$$

Hence, from (16) and (18),

$$\delta\kappa_\sigma = \lambda_\sigma^2\delta\beta' + 2(\phi+\beta)'\,\delta\gamma_\sigma. \tag{23}$$

From (13), (14), and (18),

$$\kappa_\theta \equiv \frac{\lambda_\sigma\sin(\phi+\beta) - \sin\phi}{r} = \frac{w'}{r}. \tag{24}$$

Hence,

$$\delta\kappa_\theta = r^{-1}[\lambda_\sigma\delta\sin(\phi+\beta) + \lambda_\sigma^{-1}\sin(\phi+\beta)\,\delta\gamma_\sigma]. \tag{25}$$

It now follows from (23) and (25) that if we introduce the *modified stress resultant and couple*

$$\hat{N}_\sigma \equiv \tilde{N}_\sigma - 2(\phi+\beta)'\hat{M}_\sigma - (r\lambda_\sigma)^{-1}\sin(\phi+\beta)\hat{M}_\theta \tag{26}$$

$$\hat{M}_\sigma \equiv \lambda_\sigma^{-2}M_\sigma, \tag{27}$$

equation (11) takes the form

$$[r(H\,\delta u + V\,\delta w + M_\sigma\delta\beta)]_0^L + \int_0^L (p_H\delta u + p_V\delta w)\,r\,d\sigma = \int_0^L [m(\ddot{u}\delta u + \ddot{w}\delta w) + \hat{N}_\sigma\delta\gamma_\sigma + N_\theta\delta e_\theta + \hat{M}_\sigma\delta\kappa_\sigma + \hat{M}_\theta\delta\kappa_\theta]\,r\,d\sigma, \tag{28}$$

where

$$H \equiv \mathbf{N}_\sigma\cdot\mathbf{e}_r, \quad V \equiv \mathbf{N}_\sigma\cdot\mathbf{e}_z, \quad p_H \equiv \mathbf{p}\cdot\mathbf{e}_r, \quad p_V \equiv \mathbf{p}\cdot\mathbf{e}_z, \tag{29}$$

and, from (15) and (18),

$$\beta = \tan^{-1}\left(\frac{\sin\phi + w'}{\cos\phi + u'}\right) - \phi. \tag{30}$$

The following field equations and canonical boundary conditions are implied by (17), (21), (22), (24), and (28):

$$(rH)' - N_\theta + rp_H = rm\ddot{u}, \quad (rV)' + rp_V = rm\ddot{w} \tag{31,32}$$

at $\sigma = 0, L$ prescribe u or H, w or V, β or M_σ, (33)

where

$$H = \hat{N}_\sigma(\cos\phi + u') + r^{-1}(r\hat{M}_\sigma)'(\sin\phi + w') + 2\hat{M}_\sigma(\sin\phi + w')' \tag{34}$$

$$V = \hat{N}_\sigma(\sin\phi + w') - r^{-1}(r\hat{M}_\sigma)'(\cos\phi + u') - 2\hat{M}_\sigma(\cos\phi + u')' + \hat{M}_\theta. \tag{35}$$

We call (33) canonical because they are the simplest and most common boundary conditions that appear in the literature. Obviously more general conditions, e.g., elastic restraints against displacement or rotation, could be imposed. Initial conditions are standard:

at $t = 0$ prescribe $u(\sigma,0), \dot{u}(\sigma,0), w(\sigma,0), \dot{w}(\sigma,0)$. (36)

If a strain energy density $V = V(\gamma_\sigma, e_\theta, \kappa_\sigma, \kappa_\theta; \sigma)$ exists (reckoned per unit area of S), then, by the usual arguments,

$$\hat{N}_\sigma = \frac{\partial V}{\partial\gamma_\sigma}, \; N_\theta = \frac{\partial V}{\partial e_\theta}, \; \hat{M}_\sigma = \frac{\partial V}{\partial\kappa_\sigma}, \; \hat{M}_\theta = \frac{\partial V}{\partial\kappa_\theta} \tag{37}$$

and (31)–(33) can be expressed explicitly in terms of u and w via (17), (21), (22), and (24).

Some Potential Surface Loads

To facilitate the use of the field equations (31) and (32) or the derivation of variational principles, I have listed some of the more common types of surface loads and their associated potentials (which, in the case of normal pressure, exist only for certain edge conditions). These expressions are valid for deformations of arbitrary size.

Self-Weight (Gravity Loading).

$$p_H = 0, \quad p_V = -mg \tag{38}$$

$$\int_0^L \mathbf{p}\cdot\delta\mathbf{y}\,r\,d\sigma = \delta\left[-mg\int_0^L wr\,d\sigma\right], \tag{39}$$

where g is the local gravitational constant.

Centrifugal Loads.

$$p_H = m(r+u)\Omega^2, \; p_V = 0 \tag{40}$$

$$\int_0^L \mathbf{p}\cdot\delta\mathbf{y}\,r\,d\sigma = \delta\left[m\Omega^2\int_0^L (ru + \tfrac{1}{2}u^2)\,r\,d\sigma\right], \tag{41}$$

Downloaded 02 May 2010 to 171.66.16.54. Redistribution subject to ASME license or copyright; see http://www.asme.org/terms/Terms_Use.cfm

where Ω is the constant angular velocity about the z-axis. Because Coriolis forces would tend to produce nonaxisymmetric motion, equation (40) applies only if $\dot{u}=0$.

Normal Pressure (Constant or Hydrostatic). Let $d\bar{A} \equiv \delta_\sigma \bar{r} d\sigma d\theta$ denote the deformed image of the differential element of surface area $rd\sigma d\theta$ and

$$\bar{\mathbf{n}} \equiv -\sin\bar{\phi}\mathbf{e}_r + \cos\bar{\phi}\mathbf{e}_z \tag{42}$$

denote a unit normal to the deformed image of the meridian $\mathfrak{M}$. If p is a normal pressure, i.e., a force per unit deformed area acting in the $-\bar{\mathbf{n}}$ direction, then $\mathbf{p} = -p\lambda_\sigma(\bar{r}/r)\bar{\mathbf{n}}$. From (13), (14), and (29) follows

$$p_H = p(1+u/r)(\sin\phi + w'),\ p_V = -p(1+u/r)(\cos\phi + u'). \tag{43}$$

If $p = p_0$, a constant, then

$$2\pi\int_0^L \mathbf{p}\cdot\delta\mathbf{y} r d\sigma = \delta[p_0(\bar{V}-V)] - \pi p_0 (r+u)^2 \delta w|_0^L, \tag{44}$$

where

$$\bar{V} = \pi\int_0^L \bar{r}^2\bar{z}'d\sigma = \pi\int_0^L (r+u)^2(\sin\phi + w')d\sigma \tag{45}$$

is the volume enclosed by the deformed image of S and V is the undeformed volume. Thus a pressure potential exists only if the last term on the right of (44) vanishes or can be written as a total variation. (See Bufler [10] for a general discussion of the existence of pressure potentials in large deformation problems.)

If the pressure is hydrostatic and we choose the origin so that $\bar{z} = 0$ at the top of the liquid, then

$$p = -\rho g(z+w), \tag{46}$$

where ρ is the density of the liquid. Thus

$$2\pi\int_0^L \mathbf{p}\cdot\delta\mathbf{y} r d\sigma = \delta[\rho g\pi(\bar{P}-P)] + \rho g\pi(r+u)^2(z+w)\delta w|_0, \tag{47}$$

where

$$\bar{P} \equiv -\int_0^L \bar{r}^2\bar{z}\bar{z}'d\sigma = -\int_0^L (r+u)^2(z+w)(\sin\phi + w')d\sigma \tag{48}$$

is proportional to the gravitational potential of the liquid contained by the deformed shell. As with constant pressure, we see that a hydrostatic potential exists only if an integrated term either vanishes (which it does at $\sigma = L$ because of our choice of origin) or can be written as a total variation.

References

1 Reissner, E., "On Axisymmetric Deformations of Thin Shells of Revolution," *Proc. Sym. Appl. Math.*, Vol. 3, McGraw-Hill, New York, 1950, pp. 27–52.

2 Reissner, E., "On the Equations for Finite Symmetrical Deflections of Thin Shells of Revolution," *Progress in Applied Mechanics, The Prager Anniversary Volume*, Drucker, D. C., Ed., MacMillian, New York, 1963, pp. 171–178.

3 Reissner, E., "On Finite Symmetrical Deflections of Thin Shells of Revolution," ASME JOURNAL OF APPLIED MECHANICS, Vol. 36, 1969, pp. 267–270.

4 Rissner, E., "On Finite Symmetrical Strain in Thin Shells of Revolution," ASME JOURNAL OF APPLIED MECHANICS, Vol. 39, 1972, p. 1137.

5 Budiansky, B., "Notes on Nonlinear Shell Theory," ASME JOURNAL OF APPLIED MECHANICS, Vol. 35, 1968, pp. 393–401.

6 Budiansky, B., and Sanders, J. L., Jr., "On the 'Best' First-Order Linear Shell Theory," *Progress in Applied Mechanics, The Prager Anniversary Volume*, Drucker, D. C., Ed., MacMillian, New York, 1963, pp. 129–140.

7 Sanders, J. L., Jr., "An Improved First-Approximation Theory for Thin Shells," NASA Rept. No. 24, 1959.

8 Koiter, W. T., "A Consistent First Approximation in the General Theory of Thin Elastic Shells," *The Theory of Thin Shells*, Proc., IUTAM Sym. Delft, 1959, Koiter, W. T., Ed., North-Holland, Amsterdam, 1960, pp. 12–33.

9 Libai, A., and Simmonds, J. G., "Nonlinear Elastic Shell Theory," *Advances in Applied Mechanics*, Vol. 23, Hutchinson, J. W., and Wu, T. Y., Eds., Academic Press, New York, 1983, pp. 271–371.

10 Bufler, H., "Pressure Loaded Structures Under Large Deformations," *ZAMM*, Vol. 64, 1984, pp. 287–295.

Downloaded 02 May 2010 to 171.66.16.54. Redistribution subject to ASME license or copyright; see http://www.asme.org/terms/Terms_Use.cfm

J. W. Phillips
Professor.

G. A. Costello
Professor.
Fellow ASME

Department of Theoretical
and Applied Mechanics,
University of Illinois at Urbana-Champaign,
Urbana, Ill. 61801

Analysis of Wire Ropes With Internal-Wire-Rope Cores

Stresses in the individual wires of complex wire rope are determined for rope constructions having an internal-wire-rope (IWRC). The ropes may be pulled, twisted, and bent over a sheave or drum. The effects of friction are neglected. Specific results for a 6 × 25 filler-wire IWRC rope that is prevented from twisting indicate that the maximum stresses (exclusive of contact stresses) are typically 1.5 to 3 times as large as the nominal rope stress based on rope load and total metallic area.

Introduction

Over the years, many types of wire rope have been designed and tested for various applications where a tensile load must be transmitted by a flexible member. The theoretical analysis of wire rope is inherently rather complex, as Suslov [1] points out, and it is perhaps not surprising that most of the work reported prior to about 1950 consisted of results of extensive testing programs involving both static and fatigue loading. In 1945, Drucker and Tachau [2] assessed the existing fatigue data and presented a useful design criterion for wire rope.

In the early 1950s, Hall [3] and Hruska [4-6] developed some of the first theoretical models to predict the stresses in the individual wires of a strand. Leissa [7], Starkey and Cress [8], Bert and Stein [9], Durelli and Machida [10, 11], Lutchansky [12], Knapp [13], and Huang [14] have subsequently examined the behavior of strands for particular strand geometries.

In 1973, Costello and Phillips [15] discussed the contact stresses in a strand; in their paper the six nonlinear equations of equilibrium for a thin wire were solved for the case of a wire initially in the shape of a helix. This solution led to a series of papers [16-22] on the properties of strands.

Velinsky [23] made a major contribution in 1981, when he linearized the theory developed by Costello et al. [15-22], and provided a rational procedure for treating the strands in a rope in a manner not unlike that for treating wires within a strand. In particular, Velinsky considered the Seale construction with an internal-wire-rope core (IWRC), as shown in Fig. 1. Important aspects of Velinsky's work were subsequently discussed in a paper by Velinsky, Anderson, and Costello [24]. Phillips and Fotsch [25] later presented similar results for a particular filler-wire construction that is commonly used in hoisting operations.

The purpose of this paper is to generalize the approach developed by Velinsky [23] for any kind of wire rope that contains an IWRC. Expressions for the axial, bending, torsional, and line-contact loads on individual wires and on the strands that comprise complex wire-rope constructions are developed for the common loading situation where a rope is pulled axially and simultaneously bent over a sheave or drum. Frictional effects are neglected; consequently the results are expected to apply only for rope that is well lubricated, or for rope that is loaded only in tension (without twisting or bending).

Analysis of a Straight Rope

The analysis of a rope begins with a study of the deformation of a helical wire in a straight starnd. By "piecing together" the deformations of all the wires in a given strand, one determines the axial and torsional response of that strand. Each strand in the rope is then assumed to have been bent into the shape of a helix, and, again by "piecing together" the deformations of all the strands in the rope, one determines the axial and torsional response of a straight rope.

General Relations for a Wire or Strand. The equations of equilibrium for a helical wire in a straight strand are the same as those for a helical strand in a straight rope. In either case, the relevant equations can be derived from Love's general equilibrium equations [26] for an arbitrarily shaped thin rod undergoing small extensional strain. The nontrivially satisfied equations [17] are

$$\frac{dN}{d\xi} - N'\tau + T\kappa' + X = 0, \tag{1}$$

and

$$\frac{dG}{d\xi} - G'\tau + H\kappa' - N' + K = 0, \tag{2}$$

where ξ denotes the position along the wire or strand centerline; N, N', and T denote the normal and binormal shear forces and the tensile force, respectively; G, G', and H denote the normal and binormal bending moments and the twisting moment, respectively; κ' and τ denote the binormal curvature and the twist, respectively, in the deformed state; X denotes

Contributed by the Applied Mechanics Division and presented at the 1985 Joint ASME/ASCE Applied Mechanics, Fluids Engineering, and Bioengineering Conference, Albuquerque, N. Mex., June 24-26, 1985 of The American Society of Mechanical Engineers.

Discussion on this paper should be addressed to the Editorial Department, ASME, United Engineering Center, 345 East 47th Street, New York, N.Y. 10017, and will be accepted until two months after final publication of the paper itself in the Journal of Applied Mechanics. Manuscript received by ASME Applied Mechanics Division, October, 1985; final revision, October, 1984. Paper No. 85-APM-36.

Copyright © 1985 by ASME
Downloaded 02 May 2010 to 171.66.16.54. Redistribution subject to ASME license or copyright; see http://www.asme.org/terms/Terms_Use.cfm

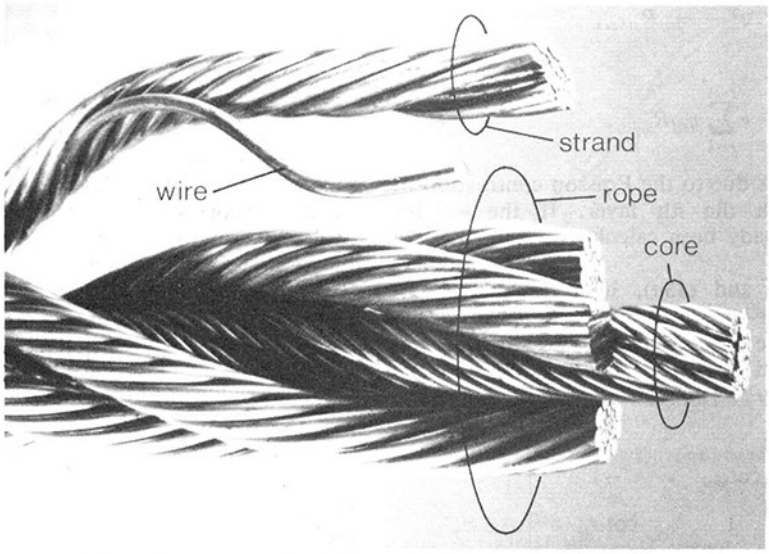

Fig. 1 Photograph of a right lay, regular lay, 6 × 19 Seale IRWC rope

the externally applied distributed force per unit length in the normal direction; and K denotes externally applied distributed moment per unit length in the normal direction. If it is assumed that the generalized forces are independent of ξ and that $K = 0$, then

$$X = N'\tau - T\kappa', \tag{3}$$

where

$$N' = -G'\tau + H\kappa'. \tag{4}$$

Strictly speaking, these equations for X and N' are nonlinear since τ and κ' refer to the deformed configuration of the wire or strand [15]; however, the changes in τ and κ' during deformation are very small, and with sufficient accuracy, the values of τ and κ' in the equilibrium equations (3) and (4) may be taken to be the initial values.

Analysis of a Wire. Consider first the deformation of a helical wire in a *straight* strand that is pulled and twisted. The strand is to be regarded as any one of the m_s strands in the sth strand layer in the rope. Within this strand there are l_s layers of helically wrapped wires; the ith layer of these wires contains m_{si} identical wires, each having the wire radius R_{si}, the helix angle α_{si} (measured counterclockwise from a plane normal to the strand centerline), and the helix radius r_{si}. In the initial configuration, the normal and binormal curvatures and twist of each wire are given by

$$\kappa_{si} = 0, \quad \kappa'_{si} = \frac{\cos^2\alpha_{si}}{r_{si}}, \quad \text{and} \quad \tau_{si} = \frac{\sin\alpha_{si}\cos\alpha_{si}}{r_{si}}, \tag{5}$$

respectively. When the strand is pulled and twisted, each wire undergoes an axial (extensional) strain ϵ_{si}, in addition to changes $\Delta\kappa'_{si}$ and $\Delta\tau_{si}$ in the binormal curvature and twist, respectively. There is no change in the normal curvature. The nonvanishing generalized strains (ϵ_{si}, $\Delta\kappa'_{si}$, $\Delta\tau_{si}$) give rise to the generalized wire loads

$$T_{si} = \pi R_{si}^2 \epsilon_{si}, \tag{6}$$

$$G'_{si} = \frac{\pi E R_{si}^4}{4}\Delta\kappa'_{si}, \tag{7}$$

and

$$H_{si} = \frac{\pi E R_{si}^4}{4(1+\nu)}\Delta\tau_{si}. \tag{8}$$

Here, E and ν denote Young's modulus and Poisson's ratio, respectively, for the wire material. Since there is no change in the normal curvature, the normal bending moment G_{si} is equal to zero.

Small changes in r_{si} and α_{si} are directly related to small changes in curvature and twist, and vice versa. It is readily shown by partial differentiation of equations (5) that

$$\frac{\Delta r_{si}}{r_{si}} = -2\tan\alpha_{si}(r_{si}\Delta\tau_{si}) + (\tan^2\alpha_{si} - 1)(r_{si}\Delta\kappa'_{si}) \tag{9a}$$

and

$$\Delta\alpha_{si} = (r_{si}\Delta\tau_{si}) - \tan\alpha_{si}(r_{si}\Delta\kappa'_{si}). \tag{9b}$$

Compatibility Conditions for Wires Within a Strand. A straight strand that is pulled and twisted undergoes an axial strain ϵ_s and a change in twist (angle of twist per unit length) $\Delta\tau_s$. The wire layers comprising the strand must deform in a manner compatible with these strand strains, and, in addition, adjacent wire layers must remain in contact with each other.

In all, three "compatibility conditions" arise for each layer of wires. The first two are found by considering the extension and the change in twist, respectively, of the strand. It is easily shown [17] that when a given wire undergoes a small extensional strain ϵ_{si} and a change in helix angle $\Delta\alpha_{si}$, the strand must undergo an axial strain ϵ_s given by

$$\epsilon_s = \epsilon_{si} + \cot\alpha_{si}\Delta\alpha_{si}. \tag{10}$$

Similarly, it may be shown [12] that the change in strand twist $\Delta\tau_s$ is given by

$$\Delta\tau_s = \frac{1}{r_{si}}\left[\cot\alpha_{si}\left(-\frac{\Delta r_{si}}{r_{si}} + \epsilon_{si}\right) - \Delta\alpha_{si}\right]. \tag{11}$$

Equations (10) and (11) provide two conditions that the values of Δr_{si} and $\Delta\alpha_{si}$ must satisfy. The necessary third condition for wires in the ith wire layer of a given strand is that they remain in contact with the wires in some other layer – usually the $(i-1)$th layer – in the same strand. If the deformations due to contact-line loads are neglected, this condition effectively prescribes the value of the helix radius r_{si} in terms of the various wire radii R_{sj} as follows:

$$r_{si} = \sum_{j=1}^{i} \eta_{sij} R_{sj}. \tag{12}$$

Here the η_{sij} are known dimensionless weighting factors of the order of unity; they are either pure constants (such as 0 or 1), or they are complicated but *extremely weak* functions of the helix angle α_{si}, in which case the functions may be approximated by constants evaluated under the assumption that the wire cross sections are circular. A change in helix radius Δr_{si} will then be attributed only to Poisson contraction of all the wires in the strand, i.e.,

Downloaded 02 May 2010 to 171.66.16.54. Redistribution subject to ASME license or copyright; see http://www.asme.org/terms/Terms_Use.cfm

$$\Delta r_{si} = \Delta r_{si}^{p} - \nu \eta_{sii} R_{si} \epsilon_{si}, \tag{13a}$$

where Δr_{si}^{p}, given by

$$\Delta r_{si}^{p} = -\nu \sum_{j=1}^{i-1} \eta_{sij} R_{sj} \epsilon_{sj}, \tag{13b}$$

is that part of Δr_{si} that is due to the Poisson contraction of wires in layers beneath the ith layer. If the ϵ_{sj} for $j = 1, \ldots, i-1$ have already been calculated, then Δr_{si}^{p} is a known quantity.

Equations (10), (11), and (13a), in conjunction with equations (9), provide the three conditions needed to determine the generalized wire strains ϵ_{si}, $\Delta\tau_{si}$, $\Delta\kappa_{si}'$ uniquely in terms of the generalized strand strains ϵ_s, $\Delta\tau_s$ and the "sublayer contraction" Δr_{si}^{p}. The relations may be put in the form

$$\begin{bmatrix} 1 & \cot\alpha_{si} & -1 \\ \cot\alpha_{si} & 1 & \cot\alpha_{si} \\ \nu\eta_{sii}(R_{si}/r_{si})\cot^2\alpha_{si} & -2\cot\alpha_{si} & (1-\cot^2\alpha_{si}) \end{bmatrix}$$

$$\begin{Bmatrix} \epsilon_{si} \\ r_{si}\Delta\tau_{si} \\ r_{si}\Delta\kappa_{si}' \end{Bmatrix} = \begin{Bmatrix} \epsilon_s \\ r_{si}\Delta\tau_s \\ (\cot^2\alpha_{si}/r_{si})\Delta r_{si}^{p} \end{Bmatrix}, \tag{14}$$

and solved by some appropriate method, such as Cramer's rule, in the general case where $\cot\alpha_{si} \neq 0$. In the often-encountered case where a wire is parallel to the strand axis, i.e. $\cot\alpha_{si} = 0$, equations (14) yield $\epsilon_{si} = \epsilon_s$, $\Delta\tau_{si} = \Delta\tau_s$, and $\Delta\kappa_{si}' = 0$.

Generalized Forces on a Strand. The resultant tensile force T_s on a strand is given by

$$T_s = \sum_{i=1}^{l_s} m_{si}(T_{si}\sin\alpha_{si} + N_{si}'\cos\alpha_{si}), \tag{15}$$

while the resultant torque H_s is given by

$$H_s = \sum_{i=1}^{l_s} m_{si}[(H_{si}\sin\alpha_{si} + G_{si}'\cos\alpha_{si}) + r_{si}(T_{si}\cos\alpha_{si} - N_{si}'\sin\alpha_{si})], \tag{16}$$

where T_{si}, G_{si}', H_{si}, and N_{si}' are computed from equations (6), (7), (8), and (4), respectively, after the values of ϵ_{si}, $\Delta\tau_{si}$, and $\Delta\kappa_{si}'$ for all the wires in the strand have been determined by solving equations (14) for $i = 1, \ldots, l_s$.

A value for the strand binormal bending moment resultant G_s' will be needed in subsequent calculations. The determination of the bending stiffness of strands is complicated by the presence of friction, and elementary formulas are available only for certain limiting conditions. McConnell and Zemke [27] conducted flexural tests on axially loaded strands and found that, even under tension, strands exhibit a flexural stiffness that is much closer to that of a collection of frictionless wires than it is to that of a "locked" set of wires in which plane strand sections remain plane. Of the two extremes, the frictionless case is taken to be the more relevant one in the present work, particularly if application is restricted to well-lubricated wire rope. Costello's recent generalization [28] of the solution for a bent helical wire (given earlier by Timoshenko [29]) then becomes applicable; it follows from [28, 29] that the bending moment G_s' needed to induce a strand-centerline curvature change $\Delta\kappa_s'$ is given by

$$G_s' = \left(\sum_{i=1}^{l_s} m_{si} \frac{\sin\alpha_{si}}{1 + \frac{1}{2}\nu\cos^2\alpha_{si}} \frac{\pi E R^4}{4} \right) \Delta\kappa_s'. \tag{17}$$

Strand Geometry. Typical IWRC ropes contain three layers of strands – two layers that comprise the IWRC and a third layer consisting of strands of a particular type, such as a Seale, Warrington, filler-wire, or flattened strand. Let R_s be the radius of a strand in the sth strand layer. If the l_s layers of wires in this strand have been ordered in such a way that the l_sth layer of wires is the outermost one, then

$$R_s = r_{si} + R_{si} \quad (i = l_s \text{ only}). \tag{18}$$

The helix radius r_s of the sth strand will be of the form

$$r_s = \sum_{t=1}^{s} \eta_{0st} R_t, \tag{19}$$

where, typically, the constants η_{0st} are integers. The rope radius R is given by

$$R = r_s + R_s \quad (s = l \text{ only}), \tag{20}$$

where l is the number of strand layers in the rope.

Each preformed strand in a rope has its own twist τ_s and curvature κ_s' given by

$$\tau_s = \frac{\sin\alpha_s\cos\alpha_s}{r_s} \quad \text{and} \quad \kappa_s' = \frac{\cos^2\alpha_s}{r_s} \tag{21a,b}$$

where α_s is the helix angle of that strand within the rope. When the rope is subjected to an axial force T and twisting moment H, each strand in the rope is subjected to an axial strain ϵ_s and changes in the strand twist and curvature, denoted by $\Delta\tau_s$ and $\Delta\kappa_s'$, respectively.

Compatibility Conditions for Strands Within a Rope. As was the case for wires within a strand, there arise three conditions governing the behavior of strands within a rope, and these three conditions lead to a set of three simultaneous equations for the generalized strand strains ϵ_s, $\Delta\tau_s$, and $\Delta\kappa_s'$. The first two conditions are similar those encountered previously for wires within a strand, and lead to expressions that resemble equations (10) and (11).

The third condition pertains to the change in strand radius. This change must occur in such a way that strands in the sth strand layer remain in contact with those in the $(s-1)$th strand layer. From equations (12) and (18) it will be seen that the change in strand radius ΔR_s, due to Poisson contraction of the wires within the strand, will satisfy the relation

$$R_s + \Delta R_s = \sum_{j=1}^{l_s} \eta_{s0j}(1 - \nu\epsilon_{sj}) R_{sj}, \tag{22}$$

where the ϵ_{sj} are the strains in the individual wires, i.e.,

$$\Delta R_s = -\nu \sum_{j=1}^{l_s} \eta_{s0j}\epsilon_{sj} R_{sj}, \tag{23}$$

and the η_{s0j} are known weighting factors. It is important to note that both the extension and the twisting of a strand give rise to strains ϵ_{sj} in the individual wires of a strand, and consequently both modes of loading must be considered when computing the change in strand radius. The fact that the twisting of a strand affects the radius of the strand is one of the features that distinguishes the behavior of a strand from that of a solid wire.

Since the ϵ_{sj} are linear functions of both ϵ_s and $\Delta\tau_s$, and since the ϵ_{sj} vanish when both ϵ_s and $\Delta\tau_s$ are equal to zero, it follows that

$$\epsilon_{sj} = \frac{\partial\epsilon_{sj}}{\partial\epsilon_s}\epsilon_s + \frac{\partial\epsilon_{sj}}{\partial\Delta\tau_s}\Delta\tau_s, \tag{24}$$

Downloaded 02 May 2010 to 171.66.16.54. Redistribution subject to ASME license or copyright; see http://www.asme.org/terms/Terms_Use.cfm

where the partial derivatives $\partial\epsilon_{sj}/\partial\epsilon_s$ and $\partial\epsilon_{sj}/\partial\Delta\tau_s$ can be computed (numerically if necessary) from the previously developed solution for wires within a loaded strand. Using equations (19), (23), and (24), one can show that the change in strand helix radius Δr_s is given by

$$\Delta r_s = \Delta r_s^p + \eta_{0ss}\frac{\partial R_s}{\partial \epsilon_s}\epsilon_s + \eta_{0ss}\frac{\partial R_s}{\partial \Delta\tau_s}\Delta\tau_s, \tag{25}$$

where Δr_s^p denotes that portion of Δr_s that is due solely to the known changes in strand radii of strands underlying the sth one:

$$\Delta r_s^p \equiv \sum_{t=1}^{s-1}\eta_{0st}\left(\frac{\partial R_t}{\partial \epsilon_t}\epsilon_t + \frac{\partial R_t}{\partial \Delta\tau_t}\Delta\tau_t\right). \tag{26}$$

Equation (25) will now be transformed by recalling a fundamental relation – similar to equation (9*a*) – that gives the change in helix radius Δr_s as a function of the change in twist $\Delta\tau_s$ and the change in curvature $\Delta\kappa_s'$. Performing this substitution, multiplying both sides of the resulting equation by $\cot^2\alpha_s/r_s$, and introducing the definitions

$$C_s^{\epsilon} \equiv \eta_{0ss}\frac{\partial R_s}{\partial \epsilon_s}, \quad C_s^{\Delta\tau} \equiv \eta_{0ss}\frac{\partial R_s}{\partial \Delta\tau_s}, \tag{27a,b}$$

one finds that

$$-\frac{\cot^2\alpha_s}{r_s}C_s^{\epsilon}\epsilon_s + \left[-2\cot\alpha_s - \frac{\cot^2\alpha_s}{r_s}C_s^{\Delta\tau}\right](r_s\Delta\tau_s)$$

$$+(1-\cot^2\alpha_s)(r_s\Delta\kappa_s') = \frac{\cot^2\alpha_s}{r_s}\Delta r_s^p. \tag{28}$$

Three equations have now been derived for the generalized strains associated with the sth strand: two equations similar to equations (10) and (11), which ensure that the strand will deform in a manner compatible with that of the rope, and equation (28), which ensures that the various layers of strand will remain in contact with each other in the deformed configuration of the rope. The three equations, when collected together, are:

$$\begin{bmatrix} 1 & \cot\alpha_s & -1 \\ \cot\alpha_s & 1 & \cot\alpha_s \\ -(\cot^2\alpha_s/r_s)C_s^{\epsilon} & -2\cot\alpha_s-(\cot^2\alpha_s/r_s)C_s^{\Delta\tau} & (1-\cot^2\alpha_s) \end{bmatrix}$$

$$\begin{Bmatrix} \epsilon_s \\ r_s\Delta\tau_s \\ r_s\Delta\kappa_s' \end{Bmatrix} = \begin{Bmatrix} \epsilon \\ r_s\Delta\tau \\ (\cot^2\alpha_s/r_s)\Delta r_s^p \end{Bmatrix}. \tag{29}$$

These equations are very similar to equations (14).

Having solved equations (29) for each strand in the rope, one can use equations (15)-(17) to determine the tensile force T_s, the twisting moment H_s, and the bending moment G_s' acting on each strand. Equilibrium equations (3), (4) can then be used to determine the shear force N_s' and the distributed normal load X_s acting on each strand. The total force T and twisting moment H sustained by the rope can be computed by resolving in the axial direction of the rope the forces and moments acting on individual strands. The process is analogous to the procedure used for each strand, in terms of the wires within the strands – see equations (15), (16) – and the results are:

$$T = \sum_{s=1}^{l} m_s(T_s\sin\alpha_s + N_s'\cos\alpha_s) \tag{30}$$

and

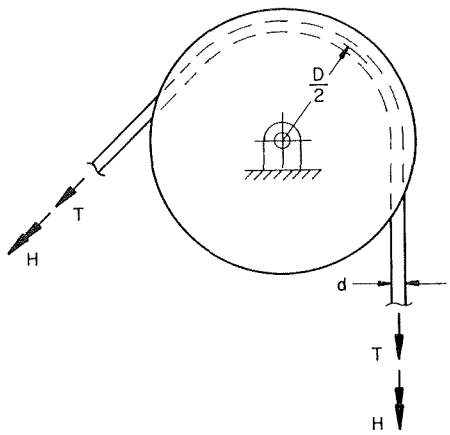

Fig. 2 Loaded rope passed over a sheave

$$H = \sum_{s=1}^{l} m_s[(H_s\sin\alpha_s + G_s'\cos\alpha_s) + r_s(T_s\cos\alpha_s - N_s'\sin\alpha_s)], \tag{31}$$

where m_s is the number of strands in the sth layer of strands, and l is the number of strand layers.

Analysis of Loaded Rope Bent Over a Sheave

IWRC ropes are typically subjected not only to axial loads but also to additional bending loads that are induced when the rope is wound around a drum or passed over a sheave, as illustrated in Fig. 2. In this paper, the assumption is made that the stresses in the individual wires of an axially loaded rope bent around a sheave consist of the stresses that would exist in the same axially loaded rope if it were straight, *plus* the bending stress that would be induced in the individual preformed wires, each in the shape of a double helix, bent elastically into the rope-centerline curvature that is imposed by the sheave. This assumption is realistic only for well-lubricated wire rope in which neighboring wires are free to slide relative to each other; as noted earlier, McConnell and Zemke's experimental results [29] on strand-bending compliance suggest that the conditions for this assumption are met approximately.

It can be shown [28] that the maximum change in normal curvature $\Delta\kappa_{si}$ in a helical wire in a straight strand that is undergoing a change in strand curvature $\Delta\kappa_s$ has a value somewhat smaller than that of $\Delta\kappa_s$, namely

$$\Delta\kappa_{si} = \frac{\sin\alpha_{si}}{1+\frac{1}{2}\nu\cos^2\alpha_{si}}\Delta\kappa_s, \tag{32}$$

where α_{si} is the helix angle of the wire within the strand. Similarly, the maximum change in strand curvature $\Delta\kappa_s$ that occurs when the axis of a straight strand is bent into the arc of a circle of radius $D/2$ is

$$\Delta\kappa_s = \frac{\sin\alpha_s}{1+\frac{1}{2}\nu_s\cos^2\alpha_s}\cdot\frac{1}{D/2}, \tag{33}$$

where α_s is the helix angle of the strand in the rope, and ν_s is a "strand Poisson's ratio." The term $\frac{1}{2}\nu_s\cos^2\alpha_s$ has a magnitude much smaller than unity and with negligible error ν_s may be set equal to the Poisson's ratio of the wire material, ν. Equations (20), (32), and (33) may now be used to predict the maximum bending stress σ_{si}^B due to sheave curvature in terms of the D/d ratio, where d is the rope diameter (equal to $2R$), as follows:

Downloaded 02 May 2010 to 171.66.16.54. Redistribution subject to ASME license or copyright; see http://www.asme.org/terms/Terms_Use.cfm

Table 1 Geometrical data

Type of rope	Strand data					Wire data							
	Layer, s	No., m_s	Angle, α_s	Factors $t=$	η_{s2s}	Layer, i	No., m_{si}	Angle, α_{si}	Radius, R_{si} (mm)	Factors, η_{sij} $(j=1,\cdots,i)$ $j=1$	$j=2$	$j=3$	$j=4$
6x25 filler-wire IWRC, left lay regular lay	1	1	90.0°	1	0	1	1	90.0°	0.343	0	–	–	–
						2	6	83.5°	0.305	1	1	–	–
	2	6	82.8°	1	1	1	1	90.0°	0.292	0	–	–	–
				2	1	2	6	84.4°	0.267	1	1	–	–
	3	6	109.7°	1	1	1	1	90.0°	0.483	0	–	–	–
				2	2	2	6	80.0°	0.445	1	1	–	–
				3	1	3	6	76.8°	0.191	$\cos(\pi/m_{32})$	η_{332}	$\cos\gamma_3$	–
						4	12	72.1°	0.406	η_{341}	η_{342}	η_{343}	$\cos\gamma_2$

$\gamma_3 = \sin^{-1}[((R_{31}+R_{32})/(R_{32}+R_{33}))\sin(\pi/m_{32})]$; $\eta_{332} = \cos(\pi/m_{32}) + \cos\gamma_3$;
$\gamma_2 = \sin^{-1}[(r_{33}/(R_{31}+R_{34}))\sin(\pi/m_{34})]$, where $r_{33} = \eta_{331}R_{31} + \eta_{332}R_{32} + \eta_{333}R_{33}$;
$\eta_{341} = \cos(\pi/m_{34})\eta_{331}$; $\eta_{342} = \cos(\pi/m_{34})\eta_{332}$; $\eta_{343} = \cos(\pi/m_{34})\eta_{333} + \cos\gamma_2$.

$$\sigma_{si}^B = ER_{si}\Delta\kappa_{si}$$

$$= E\frac{R_{si}}{R}\cdot\frac{\sin\alpha_s}{1+\frac{1}{2}\nu\cos^2\alpha_s}\cdot\frac{\sin\alpha_{si}}{1+\frac{1}{2}\nu\cos^2\alpha_{si}}\left(\frac{D}{d}\right)^{-1}. \quad (34)$$

The factors involving $\sin\alpha_s$ and $\sin\alpha_{si}$ vary between about 0.9 and 1 for typical rope constructions. The appearance of the factor R_{si}/R in equation (52) suggests that, for a given D/d ratio, the stresses due to bending over a sheave or drum can be minimized by using a rope having a large number of very fine wires, as is generally well known.

Results and Discussion

The geometrical data for a particular 12.7-mm-dia. filler-wire IWRC rope appear in Table 1.

Results for Straight Rope. For the rope described in Table 1, the generalized strains and loads in each wire and strand have been calculated for an overall rope strain ϵ of 1000 $\mu\epsilon$ and a rope twist $\Delta\tau$ of zero. The results are listed in Table 2. (Although the analysis developed in this paper allows the rope twist $\Delta\tau$ to take on nonzero values, most rope in service is prevented from rotating – at least at its ends – during use; consequently results for nonzero $\Delta\tau$ will not be reported here.) Young's modulus E for the wire material is taken as 207 GPa.

In Table 2, the column headings ϵ, $\Delta\tau$, $\Delta\kappa'$, T, etc., are understood to have the subscripts s or si when entries for strands or wires are considered. Note that the maximum axial strains ϵ_s and ϵ_{si} occur in strands and wires that are aligned with the rope axis; the axial strains in all other wires are smaller in magnitude. On the other hand, the wires that are not axially aligned within strands sustain changes in curvature and twist and are therefore subjected to bending and shear stresses that the axially aligned wires do not experience.

As it turns out, the shearing stresses due to the twisting moments H_{si} and the transverse shear forces N'_{si} are negligible, at least in the present case where $\Delta\tau = 0$. The maximum tensile stress on the cross section of a given wire, due to the axial extension of a straight rope, is given by

$$\sigma_{si}^T = \frac{1}{\pi R_{si}^2}T_{si} + \frac{R_{si}}{\pi R_{si}^4/4}|G'_{si}| + \frac{ER_{si}\sin\alpha_{si}}{1+\frac{1}{2}\nu\cos^2\alpha_{si}}|\Delta\kappa'_s|, \quad (35)$$

where the last term arises because of the bending stresses induced in strand wires when the strand undergoes a change in curvature – see equation (17). Although the binormal axis of a wire within a strand does not generally coincide with the binormal axis of the strand, these axes will coincide once within each lay length of the wire within the strand, and consequently the algebraic addition of the maximum bending stresses in equation (35) is justifiable if one is seeking only the maximum stresses in a given wire cross section.

The line loads X_s and X_{si} give rise to contact stresses that can be very large [15, 16], but no attempt is made to calculate values of the contact stresses in this paper. It should be mentioned that the X_s and X_{si} values given in Table 2 are *net* values of the distributed line loads and may be due to contact with wires or strands both in layers inside and in layers outside a given wire or strand layer.

Table 2 Summary of generalized strains and loads in wires and strands of a straight rope, for an axial rope strain of 0.001 with no rope twist

Type of rope	Strand, s	Component	ϵ (10^{-3})	$\Delta\tau$ (m^{-1})	$\Delta\kappa'$ (m^{-1})	T (kN)	G' (N·mm)	H (N·mm)	N' (N)	X (N/mm)	Rope factors z_{si}^T	z_{si}^B
6x25 filler-wire IWRC, left lay regular lay	1	Strand	1000	0	0	0.430	0	+25.1	0	0	–	–
		Wire 1	1000	0	0	0.077	0	0	0	0	1.31	0.0503
		Wire 2	983	−0.169	−0.045	0.059	−0.07	−0.18	+0.008	−1.2	1.31	0.0444
	2	Strand	980	−0.067	−0.020	0.320	−0.12	+13.7	+0.128	−2.8	–	–
		Wire 1	980	−0.067	0	0.054	0	−0.06	0	0	1.29	0.0424
		Wire 2	964	−0.232	−0.051	0.045	−0.05	−0.15	+0.005	−0.8	1.29	0.0385
	3	Strand	857	+0.048	−0.048	1.82	−4.63	+650	+15.4	−45.0	–	–
		Wire 1	857	+0.048	0	0.129	0	+0.33	0	0	1.15	0.0656
		Wire 2	831	−0.102	−0.046	0.107	−0.29	−0.50	+0.037	−3.5	1.14	0.0593
		Wire 3	812	−0.093	−0.058	0.019	−0.01	−0.01	+0.002	−0.8	1.09	0.0250
		Wire 4	777	−0.077	−0.072	0.083	−0.32	−0.26	+0.040	−4.5	1.08	0.0519
	Rope		1000†	0†	–	12.6	–	−13 600	–	–	–	–

†Prescribed deformation of rope

The data in Table 2 may be scaled for ropes of identical construction but of different rope diameter d. Force resultants vary as d^2 whereas moment resultants vary as d^3.

It is interesting to compute the values of σ_{si}^T in equation (35) and to compare them with the nominal stress σ_{nom} defined by $\sigma_{\text{nom}} \equiv T/A$, where A is the "metallic area" of the rope:

$$A = \sum_{s=1}^{l} m_s \sum_{i=1}^{l_s} m_{si}\pi R_{si}^2. \quad (36)$$

The nondimensional ratio, or "straight rope factor," $z_{si}^T \equiv \sigma_{si}^T/\sigma_{\text{nom}}$, is given in Table 2 for all the wires in the rope under consideration. Note that this ratio is always greater than or equal to unity. Actually, it suffices to compare just the term $E\epsilon_{si}$ (the leading term in equation (35)) with the term $E_{\text{eff}}\epsilon$, where E_{eff} is the effective modulus [17] of the rope, to see why this is so. The effective modulus is given by

$$E_{\text{eff}} \equiv \frac{\sigma_{\text{nom}}}{\epsilon} = \frac{T}{A\epsilon} \quad (37)$$

and turns out to have the value $0.762E$ for the rope listed in Table 2. The values of ϵ_{si} are consistently greater than $(E_{\text{eff}}/E)\epsilon$ and thus the axial wire stresses consistently exceed the nominal rope stress.

Worn-in ropes containing an IWRC are known to have an effective modulus of about one-half [30] to two-thirds of E in the "working region" of the load-deflection curve. Since the present theory does not account for the radial deformation due to the point and line loads associated with the X_s and X_{si}, the theory should be providing an upper bound on the effective modulus. This seems to be the case.

Loaded Rope Bent Over a Sheave or Drum. When a straight rope sustaining a nominal stress σ_{nom} is bent around a drum or sheave of diameter D, additional bending stresses given by equation (34) are imposed. By superposition, the maximum stress σ_{si} in an arbitrary wire may be represented in a nondimensional form as

$$\frac{\sigma_{si}}{\sigma_{\text{nom}}} = z_{si}^T + z_{si}^B\left(\frac{D}{d}\cdot\frac{\sigma_{\text{nom}}}{E}\right)^{-1}, \quad (38)$$

where, from equation (34), the "bending factor" z_{si}^B is given by

$$z_{si}^B = \frac{R_{si}}{R}\cdot\frac{\sin\alpha_s}{1+\frac{1}{2}\nu\cos^2\alpha_s}\cdot\frac{\sin\alpha_{si}}{1+\frac{1}{2}\nu\cos^2\alpha_{si}}. \quad (39)$$

Values of z_{si}^B are given in Table 2. It should be noted that both z_{si}^T and z_{si}^B are independent of E and σ_{nom}. When σ_{si} is nor-

Downloaded 02 May 2010 to 171.66.16.54. Redistribution subject to ASME license or copyright; see http://www.asme.org/terms/Terms_Use.cfm

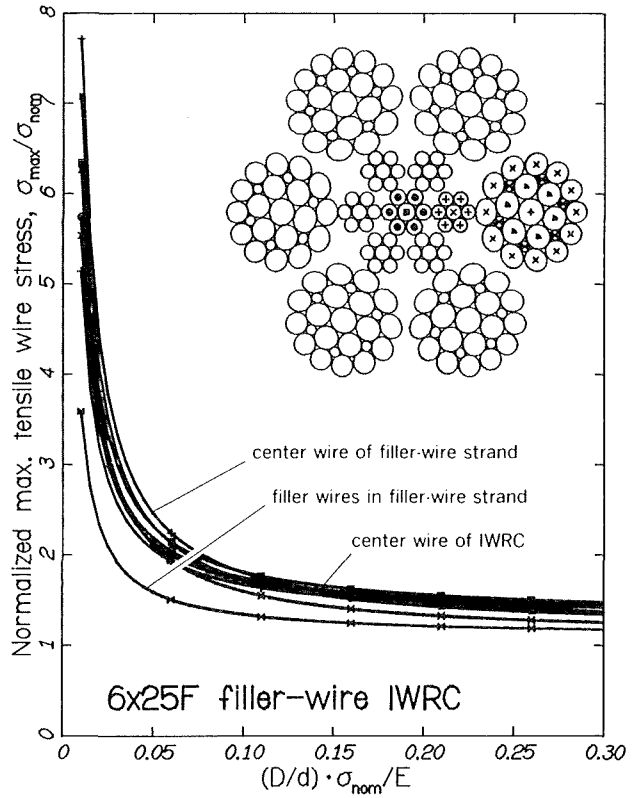

Fig. 3 Maximum tensile wire stresses in a 6 × 25 filler-wire IWRC as functions of the bending parameter $D/d\cdot\sigma_{nom}/E$.

malized with respect to σ_{nom}, the value of σ_{nom} appears in the parameter multiplying z_{si}^{B} because the bending stresses due to sheave curvature are actually independent of σ_{nom}.

Recommended values of D/d for headframe sheaves lie between about 60 and about 100, depending on the rope diameter, the rope construction, and the type of application [31], and σ_{nom} is typically of the order of $0.003E$, at least for steel rope with the usual factors of safety applied. Maximum values of the parameter $D/d\cdot\sigma_{nom}/E$ are therefore of the order of 0.3, as illustrated in Fig. 3, where the normalized maximum stresses in the 6 × 25 filler-wire IWRC are plotted in accordance with equation (58) and the appropriate values of z_{si}^{T} and z_{si}^{B} from Table 2.

Note that, for large values of $D/d\cdot\sigma_{nom}/E$, it is the centermost wire of the IWRC that is subjected to the maximum stress; this stress is approximately 1.5 σ_{nom} even for *very large* values of D/d. On the other hand, for values of $D/d\cdot\sigma_{nom}/E$ less than about 0.1, it is the center wire of the filler-wire strand that experiences the maximum stress, which becomes arbitrarily large as $D/d\rightarrow 0$; maximum-stress values of 2 or 3 times σ_{nom} would be typical for rope that is wrapped around small sheaves (as in the case of the various hoist ropes in mobile yard cranes). In filler-wire rope, the small filler wire itself is understressed throughout the loading range. All the other wires, however, are stressed in a remarkably uniform manner. It is perhaps this uniformity in stress loading that has led to the widespread use of filler-wire rope in hoisting operations.

Curves like the ones shown in Fig. 3 may also be derived for other types of rope [32]. For the 6 × 19 Seale construction, for example, the curves tend to be more spread out vertically, indicating a less-optimum distribution of stresses among the various wires.

Conclusions

Linearized equations of equilibrium for helical wires and for helical strands of wires can be satisfied, along with appropriate compatibility conditions for wires within strands and for strands within the rope, in a manner that allows the strains, stresses, the generalized forces in all the wires and strands to be computed for ropes of complex cross section, including ropes with internal-wire-rope cores. The results may be extended by superposition to include the important case of loaded ropes pulled over a sheave or bent around a drum.

In this paper, results are given for a certain filler-wire construction and results could be generated for other constructions, such as the 6 × 31 Warrington-Seale, the 6 × 43 filler-wire Seale, and the 6 × 46 Seale filler-wire [30, p. 12].

Predicted values of the "effective modulus" are slightly higher than those given in the literature for IWRC ropes. The discrepancy is probably due to the failure to take into account the contact deformations arising from the internal point and line loads, and other possible interstitial movements afforded in actual ropes. The theory given in this paper would have to be modified slightly to treat in a realistic manner the deformation of ropes that *do not* have internal-wire-rope cores; the modification would concern the change in strand radius which, in this paper, was assumed to depend solely on Poisson contraction of the given strand and all the strands beneath it.

Acknowledgments

Valuable discussions with Mr. Eugene H. Skinner and Mr. Grant L. Anderson, P. E., of the U.S. Interior Department's Bureau of Mines, Spokane, are gratefully acknowledged. Much of the work reported here may be found in a recent report [32] to the Bureau of Mines on Contract J0100011 with the University of Illinois at Urbana-Champaign.

References

1 Suslov, B. M., "On the Modulus of Elasticity of Wire Ropes," *Wire and Wire Products*, Vol. 11, 1936, pp. 176-182.

2 Drucker, D. C., and Tachau, H., "A New Design Criterion for Wire Rope," ASME JOURNAL OF APPLIED MECHANICS, Vol. 12, 1945, pp. A33-38.

3 Hall, H. M., "Stresses in Small Wire Ropes," *Wire and Wire Products*, Vol. 26, 1951, pp. 257-259.

4 Hruska, F. H., "Calculations of Stresses in Wire Rope," *Wire and Wire Products*, Vol. 26, 1951, pp. 766-767; 799-801.

5 Hruska, F. H., "Radial Forces in Wire Ropes," *Wire and Wire Products*, Vol. 27, 1952, pp. 459-463.

6 Hruska, F. H., "Tangential Forces in Wire Ropes," *Wire and Wire Products*, Vol. 28, 1953, pp. 455-460.

7 Leissa, A. W., "Contact Stresses in Wire Ropes," *Wire and Wire Products*, Vol. 34, 1959, pp. 307-314; 372-373.

8 Starkey, W. L., and Cress, H. A., "An Analysis of Critical Stresses and Mode of Failure of a Wire Rope," ASME *Journal of Engineering for Industry*, Vol. 81, 1959, pp. 307-316.

9 Bert, C. W., and Stein, R. A., "Stress Analysis of Wire Rope in Tension and Torsion," *Wire and Wire Products*, Vol. 37, 1962, pp. 769-770.

10 Machida, S., and Durelli, A. J., "Response of a Strand to Axial and Torsional Displacements," *Journal of Mechanical Engineering Science*, Vol. 15, 1973, pp. 241-251.

11 Durelli, A. J., and Machida, S., "Response of Epoxy Oversized Models of Strands to Axial and Torsional Loads," *Experimental Mechanics*, Vol. 13, 1973, pp. 313-321.

12 Lutchansky, M., "Axial Stresses in Armor Wires of Bent Submarine Cables," ASME *Journal of Engineering for Industry*, Vol. 91, 1969, pp. 687-693.

13 Knapp, R. H., "Derivation of a New Stiffness Matrix for Helically Armoured Cables Considering Tension and Torsion," *International Journal for Numerical Methods in Engineering*, Vol. 14, 1979, pp. 515-529.

14 Huang, N. C., "Finite Extension of an Elastic Strand with a Central Core," ASME JOURNAL OF APPLIED MECHANICS, Vol. 45, 1978, pp. 852-858.

15 Costello, G. A., and Phillips, J. W., "Contact Stresses in Thin Twisted Rods," ASME JOURNAL OF APPLIED MECHANICS, Vol. 40, 1973, pp. 629-630.

16 Phillips, J. W., and Costello, G. A., "Contact Stresses in Twisted Wire Cables," *Journal of the Engineering Mechanics Division*, ASCE, Vol. 100, 1974, pp. 1096-1099.

17 Costello, G. A., and Phillips, J. W., "Effective Modulus of Twisted Wire Cables," *Journal of the Engineering Mechanics Division*, ASCE, Vol. 102, 1976, pp. 171-181.

18 Phillips, J. W., and Costello, G. A., "Axial Impact of Twisted Wire Cables," ASME JOURNAL OF APPLIED MECHANICS, Vol. 44, 1977, pp. 127-131.

19 Costello, G. A., and Sinha, S. K., "Static Behavior of Wire Rope," *Journal of the Engineering Mechanics Division*, ASCE, Vol. 103, 1977, pp. 1011-1022.

Downloaded 02 May 2010 to 171.66.16.54. Redistribution subject to ASME license or copyright; see http://www.asme.org/terms/Terms_Use.cfm

20 Costello, G. A., and Miller, R. E., "Lay Effect of Wire Rope," *Journal of the Engineering Mechanics Division*, ASCE, Vol. 105, 1979, pp. 597-608.

21 Costello, G. A., and Butson, G. J., "A Simplified Bending Theory for Wire Rope," *Journal of the Engineering Mechanics Division*, ASCE, Vol. 108, 1982, pp. 219-227.

22 Costello, G. A., "Stresses in Multilayered Cables," ASME *Journal of Energy Resources Technology*, Vol. 105, 1983, pp. 337-340.

23 Velinsky, S. A., "Analysis of Wire Ropes With Complex Cross Sections," Ph.D. Thesis, University of Illinois at Urbana-Champaign, Department of Theoretical and Applied Mechanics, 1981, 87 pp.

24 Velinsky, S. A., Anderson, G. L., and Costello, G. A., "Wire Rope with Complex Cross Sections," *Journal of the Engineering Mechanics Division*, ASCE, Vol. 110, 1984, pp. 380-391.

25 Phillips, J. W., and Fotsch, P. D., "Preliminary Analysis of Filler-Wire Hoisting Rope," *Developments in Mechanics*, Vol. 12, 1983, pp. 397-400.

26 Love, A. E. H., *A Treatise on the Mathematical Theory of Elasticity*, Dover, New York, 1944, Chapters 18 and 19.

27 Timoshenko, S. P., *Strength of Materials, Part II*, 3rd ed., D. Van Nostrand, New York, 1956, pp. 295-298.

28 Costello, G. A., "Large Deflections of Helical Springs Due to Bending," *Journal of the Engineering Mechanics Division*, ASCE, Vol. 103, 1977, pp. 481-487.

29 McConnell, K. G., and Zemke, W. P., "The Measurement of Flexural Stiffness of Multistranded Electrical Conductors while Under Tension," *Experimental Mechanics*, Vol. 20, 1980, pp. 237-244.

30 *Wire Rope Users Manual*, American Iron and Steel Institute, Washington, 1979.

31 *Code of Federal Regulations*, U.S. Government Printing Office, Washington, Vol. 30 (Mineral Resources), 1980, Article 57.19-39.

32 Costello, G. A., and Phillips, J. W., "Stress Analysis of Wire Hoist Rope," Technical Report No. UILU-ENG 83-6006, Engineering Documents Center, University of Illinois at Urbana-Champaign, Urbana, Ill. Sept. 1983, 103 pp.

Downloaded 02 May 2010 to 171.66.16.54. Redistribution subject to ASME license or copyright; see http://www.asme.org/terms/Terms_Use.cfm

Counterintuitive Behavior in a Problem of Elastic-Plastic Beam Dynamics

P. S. Symonds
Division of Engineering,
Brown University,
Providence, R.I. 02912
Fellow, ASME

T. X. Yu
Department of Mechanics,
Peking University,
Beijing, Peoples Republic of China

In a particular example of short pulse loading on a pin-ended beam, the permanent deflection is predicted by a numerical solution to be in the direction opposite that of the load. Analysis of a Shanley-type model shows that this surprising behavior may occur as a consequence of plastic irreversibility combined with geometric nonlinearity, when the peak deflection produced by the pulse lies in a certain range of small magnitudes. Results from a number of well-known structural dynamics codes are shown. These exhibit a wide spread in the predicted final deflections, indicating strong sensitivities of both physical and computational nature.

1 Introduction and Problem Statement

Consider a uniform beam (Fig. 1*a*) whose ends are attached to smooth fixed pins. It is subjected to a uniformly distributed pressure applied as a rectangular pulse, with constant magnitude p_0 up to time t_0 and zero thereafter (Fig. 1*c*). The beam material is assumed to exhibit linear elastic-perfectly plastic behavior (Fig. 1*d*), the constants being typical of a structural aluminum alloy. The values in our example are listed in the caption of Fig. 1.

The counterintuitive behavior referred to in the title is observed for certain pulses that produce plastic deformations, the particular example being one with load p_0 four times the limit load for the beam if simply supported, and duration $t_0 = 0.5$ ms. It was found in a numerical solution using a finite element code[1] that after a maximum deflection (taken as positive in the direction of the loading), the beam moved backward to a deflection on the negative side; the beam then vibrated elastically with negative minimum and maximum values. The calculation did not introduce physical damping, but the final permanent deflection is presumed to be the mean deflection of the elastic vibration, and is thus predicted to be negative. In other words, a load which, if applied statically, would lead to a permanent deflection in a certain direction, when applied as a pulse results in a permanent final deflection in the opposite direction.

Figure 2 shows the midpoint deflection history computed by ABAQUS for this example. All other examples in a series

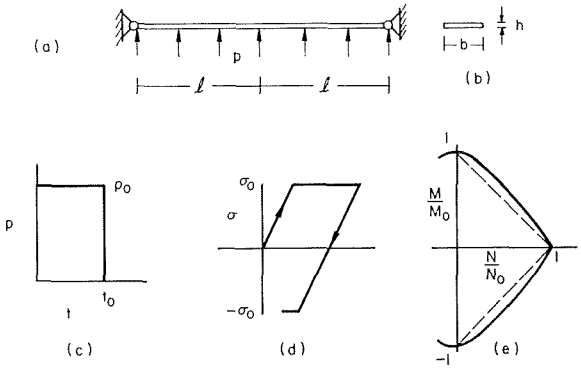

Fig. 1 A uniform beam of length $2l$ = 200 mm, width b = 20 mm, and depth 4 mm is subjected to uniformly distributed load p per unit length. The end supports are smooth fully fixed pins. The load is a rectangular pulse constant at magnitude p_0 = 19.2 N/mm for duration t_0 = 0.5 milliseconds, with $p = 0$ for $t \geq t_0$. The beam has Young's modulus $E = 80 \times 10^9$ N/m^2, yield stress $\sigma_0 = 0.3 \times 10^9$ N/m^2, and mass density $\rho = 2700$ kg/m^3. Elastic-perfectly plastic behavior as in (*d*) is assumed.

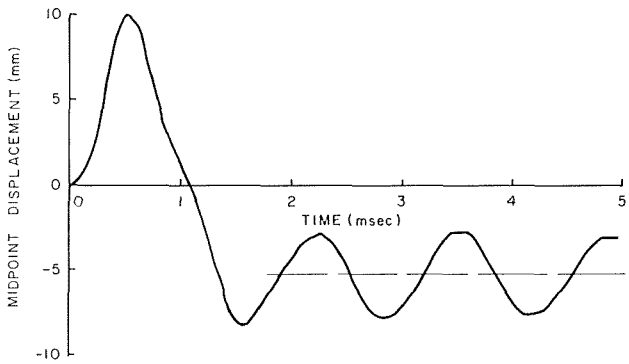

Fig. 2 Response history by finite element code ABAQUS

[1] We used the program ABAQUS which was made available for our research use by Hibbitt, Karlsson and Sorensen, Inc., 35 South Angell St., Providence, R.I. 02906. All calculations using ABAQUS reported here were made on the Brown University, Division of Engineering VAX-11/780 computer, whose acquisition was made possible by grants from the U.S. National Science Foundation (grant ENG78/9378), the General Electric Foundation, and the Digital Equipment Corporation.

Contributed by the Applied Mechanics Division and presented at the 1985 Joint ASME/ASCE Applied Mechanics, Fluids Engineering, and Bioengineering Conference, Albuquerque, N. Mex., June 24-26, 1985 of THE AMERICAN SOCIETY OF MECHANICAL ENGINEERS.

Discussion on this paper should be addressed to the Editorial Department, ASME, United Engineering Center, 345 East 47th Street, New York, N.Y. 10017, and will be accepted until two months after final publication of the paper itself in the JOURNAL OF APPLIED MECHANICS. Manuscript recevied by ASME Applied Mechanics Division, December, 1984; final revision, January, 1985. Paper No. 85-APM-38.

Copyright © 1985 by ASME
Downloaded 02 May 2010 to 171.66.16.54. Redistribution subject to ASME license or copyright; see http://www.asme.org/terms/Terms_Use.cfm

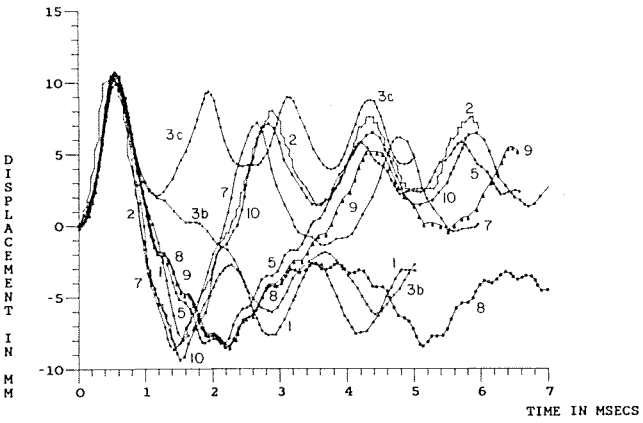

Fig. 3 Midpoint deflection—time curves according to eight codes (ABAQUS result is curve No. 1) for the problem defined in Fig. 1. Curves 3*b* and 3*c* are from the same code, the load pulses for these being taken to decrease linearly to zero in an interval 0.2 msec and 0.1 msec, respectively, with pulse area $p_0 t_0$ in both cases.

of calculations using ABAQUS exhibited the intuitively more expected behavior, with final displacement in the direction of the load. Many experiments on plastic deformations of pulse loaded beams with fully fixed ends (Symonds and Jones, 1972) have led to the same result, including some tests on beams of high yield stress and predominately elastic response (Symonds 1980a, 1980b). No tests with end conditions of smooth fixed pins are known to the authors. They are also not aware of any published numerical solutions for single pulse loading which predict permanent deflection in the opposite sense to the loading.

2 Predictions of Other Numerical Codes

To check that our use of ABAQUS was correct, independent solutions on different machines were obtained, first by staff at Hibbitt, Karlsson and Sorensen, and then by a colleague at another university using ABAQUS. Essentially indentical solutions to ours were obtained. The same colleague then attempted to run the problem using another general purpose code with nonlinear capability, available on his facility. A solution was eventually obtained which agreed with our ABAQUS solution only through the first peak displacement. It appears to predict a positive permanent displacement, but this is uncertain since the calculation was not continued long enough to show a full cycle of the rather irregular continuing elastic motion.

We then sent a statement of the problem to a number of persons known to us as developers or expert users of established codes. Solutions with midpoint deflection-time plots were received from nine codes, of which seven were of finite element and two of finite difference type. In several cases we were sent more than one solution, corresponding to different time step size and other input variables. Considering all the codes, 12 solutions may be considered strictly comparable; a thirteenth solution appears anomalous, but is of interest. The predictions are summarized as follows: (1) except for the anomalous case, all the codes predicted approximately the same peak deflection (about 10.5 mm occurring at about 0.55 msec; the anomalous code predicted a peak of about 15 mm). (2) Typically the initial positive peak was followed by a negative deflection of somewhat smaller peak magnitude, which led to a continuing vibratory motion; this had a negative mean value in four cases (including the ABAQUS solution), and a positive mean value in eight cases. (The anomalous solution also predicted a positive vibration, but of mean value—about 14 mm—much larger than any of the others). The amplitude of the continuing vibration was roughly 5 mm, whether the mean value was positive or negative. The period of this motion ranged from 1.1 msec to 2.3 msec, but in some cases the motion was irregular, with poorly defined period. (3) The multiple solutions by the same code which were sent us, corresponding to different choices of solution strategy or to changes in the load pulse input data that would seem insignificantly physically, showed that small changes in input variables could in some cases result in large changes in the predicted response.

Figure 3 shows deflection-time curves by eight of the ten codes from which we obtained solutions. The codes represented are ABAQUS, ANSYS, DYCAST, MARC, MENTOR, REPSIL, WHAMS, and WRECKER. The identification numbers in Fig. 3 have no relation to the above order. One code is represented by two curves marked 3*b* and 3*c*. The data input for these was identical except that the force pulse was terminated by ramps of 0.2 msec and 0.1 msec duration, respectively, with constant impulse. It is seen that with this change, the continuing vibration changes from a negative to a positive ("intuitive") mean value. (In an experiment, such a change would normally be negligible—apart from the impossibility of controlling the pulse shape to such a degree.) We are especially grateful to the respondent who sent us these among several other calculated responses.

The omission of two codes requries explanation. One is the code that we have mentioned as giving anomalous results. This code required more CP time (by orders of magnitude) than the others, and is evidently inappropriate for our problem. The other code omitted from Fig. 3 was represented by two solution curves, one sent by the originator of the code and the other by a "user." The former clearly predicts a negative final deflection, while the latter apparently predicts a positive one but with some uncertainty. Such differences are of practical interest and we regret the need to omit these solution curves, but they are not essential for present purposes.

In summary, 10 highly reputed codes, run by experts (but not treating the problem as a research project) have failed to establish a credible solution for the permanent deflection. This is rather worrisome, but it is obvious that the problem itself is unexpectedly tricky.

3 Solution by Simplified Eastic-Plastic Technique

Since there are large discrepancies between the predictions of numerical solutions for the final displacement, it is of special interest to apply the approximate approach of (Symonds 1980a, 1980b). This method, being directly based on intuitive hypotheses, may at least provide guidance if it furnishes unequivocal answers.

The main simplifying hypothesis is that of separating elastic from plastic responses (see also Symonds 1980c, Raphanel and Symonds 1984, Symonds and Mosquera 1984). An initial stage of elastic response is followed by a rigid-plastic one. The maximum deflection occurs at the end of the rigid-plastic stage. The stresss field at this instant is the relatively simple one of a mode form solution. It is assumed that elastic recovery then occurs, leading to elastic vibrations which are finally damped out, leaving permanent deflections and residual stresses.

The application of this approach is outlined in the Appendix. It predicts the maximum deflection for our example in good agreement with the numerical codes. However difficulties are encountered in estimating the elastic recovery by the method previously found successful. Thus the simple method does not serve to definitely pick out the "correct" one of the conflicting numerical solutions. This is a consequence of the highly unusual features of this example, as will be seen.

4 Analysis for Shanley Model

A model of the type introduced by Shanley (1947) enables much insight to be gained. This model (Fig. 4) consists of two

Downloaded 02 May 2010 to 171.66.16.54. Redistribution subject to ASME license or copyright; see http://www.asme.org/terms/Terms_Use.cfm

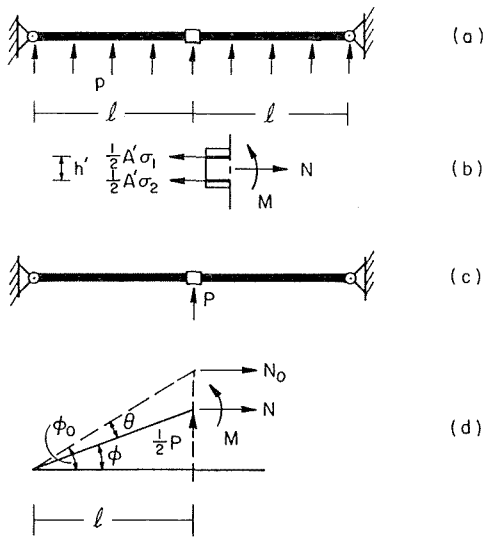

Fig. 4 *(a)* **Shanley model has rigid bars of length** *l*; *(b)* **deformable "cell" at midpoint taken as sandwich beam; (c) static loading by force** *P*; **and (***d***) notation for deflections**

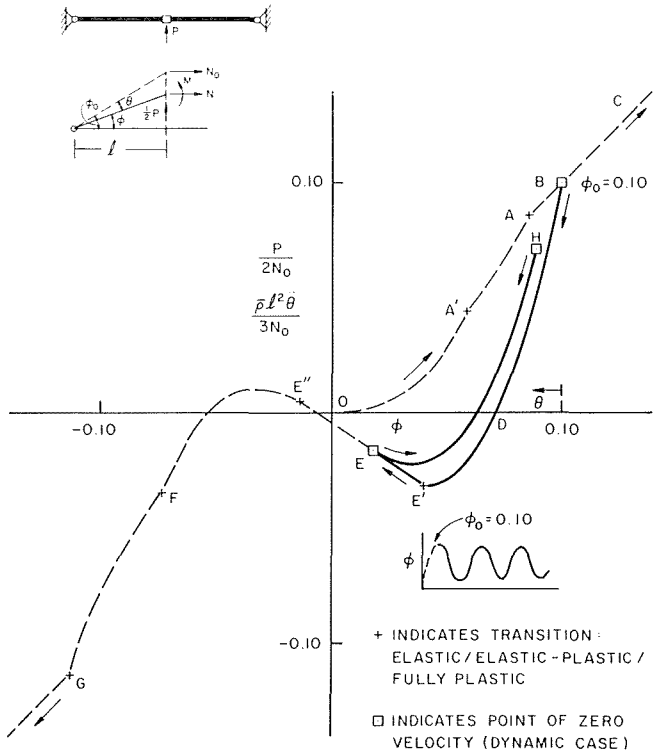

Fig. 5 Dashed line shows $P-\phi$ relation for static equilibrium; on first loading OA' is elastic, $A'A$ partially plastic, AC fully plastic. Unloading is shown from $\phi_0 = 0.10$, following curve *BDEFG*. Solid line shows accelerations in dynamic case ($P = 0$). Velocity first reaches zero at *E*. Curve *EH* indicates elastic oscillation between *E* and *H*.

rigid bars attached to smooth fixed pins. They are connected by a small "cell" where deformations of extension and flexure take place, and which is endowed with appropriate elastic-plastic constitutive relations. For simplicity we take these relations to be those of a sandwich beam (Fig. 4*b*), consisting of two bars (thin "flanges") distance h' apart, each in simple tension or compression. Each flange is assumed to have area $A'/2$ and elastic-plastic behavior (Fig. 1(*d*)) with yield stress σ_0' and Young's modulus E'. We take the elastic relation to be

$$\sigma_1 = E' e_1/l; \quad \sigma_2 = E' e_2/l \tag{1}$$

Th two rigid bars of length l are assumed to have mass per unit length $\bar{\rho}$, the same as for the uniform beam.

The angle of rotation ϕ is taken to define the displacement a; we will assume, for small magnitudes, that

$$a = l\phi \tag{2a, 2b}$$

An increment of rotation $d\phi$ requires an increment de of centerline extension, and we take de and e (by integration) to be given, for first loading, by

$$de = l\phi d\phi; \quad e = l\phi^2/2 \tag{3}$$

The equation of motion in the elastic range of the model subjected to a load p_0 per unit length is

$$\frac{1}{3}\bar{\rho} l\ddot{a} + \frac{A' h'^2 E'}{4l^3} a + \frac{A' E'}{2l^3} a^3 = \frac{1}{2} p_0 l \tag{4}$$

In the plastic range, the model is described by fully plastic force N_0' and moment M_0' given by

$$N_0' = A' \sigma_0'; \quad M_0' = A' h' \sigma_0'/2 \tag{5}$$

Interaction between N/N_0' and M/M_0' when plastic flow is occurring obeys the linear relation indicated in Fig. 1(*e*) by the dashed line.

The constants σ_0', E', A', and h' are abitrary, but need to be chosen so that results obtained for the model will be indicative of those of the prototype uniform beam, whose constants are σ_0, E, $A = bh$, and h.
We have chosen to take

$$A' = A, \quad \sigma_0' = \sigma_0, \quad E' = 3E/2, \quad h' = 0.68h \tag{6}$$

Comparing equations (3 and 4) with equations (*A*1)-(*A*3) of the Appendix, these provide agreement between small and large deflection elastic behaviors and between the large deflection plastic behaviors of the model and prototype. The small deflection plastic behavior (involving bending) is modeled more approximately, with fully plastic moment $M_0' = (0.34/0.25)\ M_0 = 1.36\ M_0$, but the model should nonetheless be valid for qualitative guidance. For non-dimensional analysis the quantities used are

$$\mu = E'/\sigma_0' = 3E/2\sigma_0 = 400; \quad \eta = h'/l = 0.68h/l = 0.0271 \tag{7}$$

taking data as given in the caption for Fig. 1.

The Shanley-type model allows complete deflection histories for any pulse loading to be worked out. However it is more instructive to begin by plotting the relation for static equilibrium between a load force P (Fig. 4(*c*)) and the deflection angle ϕ. This is shown by the dashed curves in Figs. 5 and 6. Curve $OA'ABC$ in Fig. 5 shows the relation for load steadily increasing from zero, A' being the point where plastic flow starts and A being the point where the model becomes fully plastic in tension. Curve $BDEFG$ depicts unloading from a starting angle ϕ_0, taken in the example as $\phi_0 = 0.10$, larger than the angle $\phi_0 = 0.086$ at which fully plastic yielding in tension begins. Note that this shows values of P required for static equilibrium when the angle ϕ is monotonically decreased. The significant features of this curve are its reversed—S shape and the positive force values in a negative interval of ϕ. Elastic unloading continues until point E' is reached. The top bar yields in compression between E' and E'' when it unloads, and both bars are elastic between E'' and F. Fully plastic flow in tension starts at G.

We may use this curve to examine the dynamic case. Suppose the model structure reaches the angle ϕ_0 and is then released, i.e., we then set $P = 0$. The vertical axis in Fig. 5 then represents accelerations. If θ is the angle of rotation in the reverse direction (Fig. 4(*d*)), the vertical scale represents $\bar{\rho} l^3 \ddot{\theta}/3N_0 l$. This is the same as $dK/d\theta$, where K is the kinetic energy $\bar{\rho} l^2 \dot{\theta}^2/6N_0$ in dimensionless form. Thus the area under the curve represents the gain in kinetic energy as the bar moves down, starting from the rest position at ϕ_0.

The solid curve in Fig. 5 shows the dynamic response

Downloaded 02 May 2010 to 171.66.16.54. Redistribution subject to ASME license or copyright; see http://www.asme.org/terms/Terms_Use.cfm

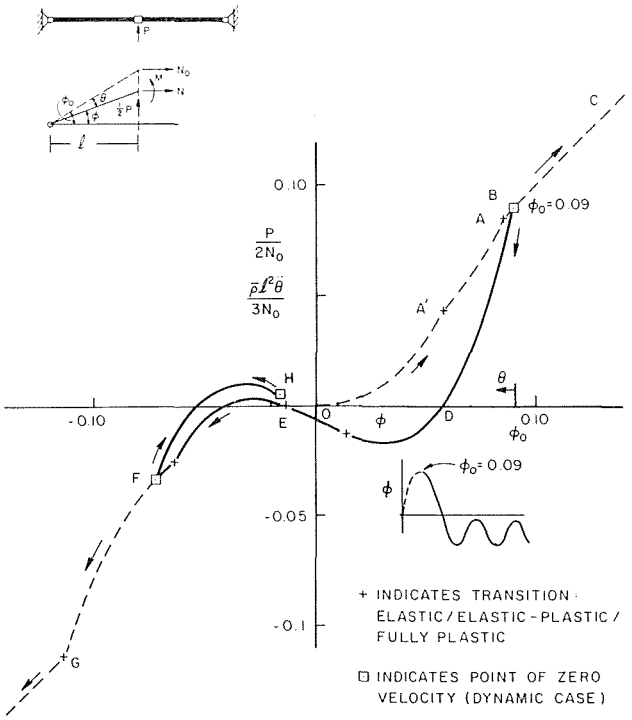

Fig. 6 $P - \phi$ curve (dashed) for first static loading $OA'AC$ same as for Fig. 6(*a*). Unloading curves now start from $\phi_0 = 0.09$. In dynamic case, ordinate shows acceleration, areas kinetic energy. Velocity first reaches zero at *F*. Curve *FH* indicates elastic oscillation between *F* and *H*.

behavior when ϕ_0 is sufficiently large. Elastic unloading takes place until point E' is reached. At point E ($\phi = 0.018$ with our numbers) the total area under the curve BDE is zero. The beam comes to rest at this point, but its acceleration is such that it then starts to move upward, both bars behaving elastically. It continues to move upward until point H is reached, when it again comes to rest, the area under the curve EH being zero. In our example $\phi = 0.089$ at H. Since only elastic behavior occurs in EH, elastic oscillations continue indefinitely between points E and H. As sketched in the inset diagram, this is the "intuitively expected" response behavior.

The heavy curve in Fig. 6 shows what happens when the starting angle ϕ_0 is smaller; the structure has been loaded only a small way into the fully plastic (membrane) phase. The unloading elastic curve is somewhat different, of course. Beyond point D where the curve crosses the axis the velocity is decreasing. However in this case, when the curve again crosses the axis at E, the structure has not come to rest. It then accelerates again, in a small interval, and reaches zero velocity finally at F. Additional plastic flow has occurred in the segment from D to F. At F there is a reversal of direction (upward motion starts), and elastic deformation occurs from F to H where the velocity again comes to zero. The continuing elastic vibration is now represented by the segment FH, the angle ϕ being negative at both F and H. This is the "counterintuitive" behavior of the original example, the curve of Fig. 2.

The response behavior depends sharply on the starting point B, i.e., on the deflection angle ϕ_0 at which unloading starts. If ϕ_0 is large, the structure presents much more resistance to the downward motion. Then it is brought to rest at a positive angle ϕ_*, so that the continuing elastic vibration lies between two positive magnitudes. For the model, the determining magnitude is the amplitude ϕ_0 at which elastic recovery starts from rest, under zero external load. It is unimportant how this value is reached, statically or dynamically.

Some further details of the dependence of the final elastic vibration on the starting point ϕ_0 are shown in Fig. 7. This shows the upper and lower limits of the elastic vibration as a function of ϕ_0. This diagram illustrates vividly the small range of ϕ_0, between approximately 0.086 and 0.092, in which the pulse loading leads to a vibration between negative extreme values.

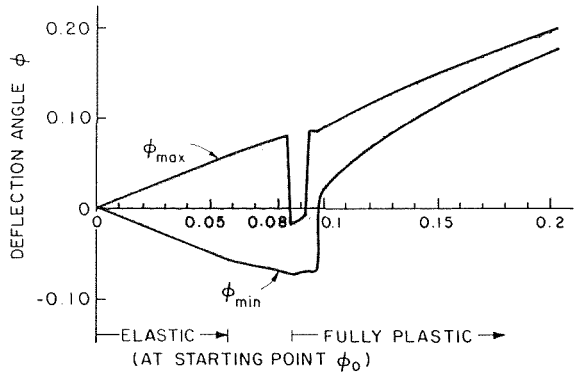

Fig. 7 Envelope curves (maximum and minimum deflection angles) of the continuing elastic vibration as function of the starting "release" angle ϕ_0. The average deflection is positive except in the range of ϕ_0 between approximately 0.086 and 0.092.

5 Discussion

The Shanley model helps to understand a phenomenon in structural dynamics that apparently has not previously been described in the literature. It shows that if the model beam is subjected to a class of short pulses acting in a direction say $+y$, there is a deflection angle magnitude ϕ_0^* such that if tne deflection reaches a peak deflection ϕ_0 greater than ϕ_0^* and the load thereafter is zero, the deflection remains on the $+y$ side; on the other hand, if ϕ_0 is in a certain range below ϕ_0^*, the final permanent deflection is on the $-y$ side. The model indicates a discontinuous behavior analogous to that seen in analyses of snap buckling, which of course is a related phenomenon.

We have no proof that the behavior predicted by the Shanley model occurs in the uniform beam of our example problem (Fig. 1), whose behavior is much more complex. However, the Shanley model has generally indicated physically realizable behaviors, and we now feel that the prediction by ABAQUS of the deflection history of Fig. 2, and the basically similar histories predicted by some other finite element codes (see Fig. 3), may well be correct in the sense that a carefully performed laboratory experiment would give close to the same result. At this point, the correct solution is unknown.

The question of why different codes predict different histories for times after the first deflection peak is an interesting one which demands further study. Evidently the class of problem illustrated by the example of Fig. 1 involves acute sensitivities to the physical parameters (loading, structure geometry, and material behavior), when these lie in certain small ranges. These effects apparently exacerbate the mathematical sensitivities normally present in computational structural mechanics, so that small changes in the solution strategy may lead to large changes in output. The present example may have future value as a test problem, when the various sensitivities are better understood and correct solutions are established. Also worth study is the question of whether the unexpected phenomena observed here, in a rather artificial problem, has counterparts in problems of more direct engineering interest.

Acknowledgments

We want to express our thanks to all those who responded with computer solutions, in particular to T. B. Griffin, N. J.

Downloaded 02 May 2010 to 171.66.16.54. Redistribution subject to ASME license or copyright; see http://www.asme.org/terms/Terms_Use.cfm

Huffington, Jr., Ted Belytschko, Joop C. Nagtegaal, Raymond D. Krieg, David M. Webb, Dana Meredith, Sing C. Tang, K. S. Yeung, K. J. Bathe, Peter C. Kohnke, Robert Winter, and Allan Pifko.

Special thanks are due to Dr. Pierre Burgers of Hibbitt, Karlsson and Sorensen, Inc., for checking our original solution; to Prof. J. F. McNamara, currently at Brown University on leave from University College, Galway, for advice and help with graphics; and to Karen Levesque for expert typing and patient retyping.

Dr. Tong-Xi Yu acknowledges the support he received from Brown University under a General Electric Foundation grant, which made possible his visit in the Division of Engineering in January and February 1984.

References

1 Den Hartog, J. P., 1928, "The Lowest Natural Frequency of Circular Arcs," *Phil. Mag.*, Series 7, Vol. 5, pp. 400-408.

2 Martin, J. B., and Symonds, P. S., 1966, "Mode Approximations for Impulsively Loaded Rigid-Plastic Structures," *J. Eng. Mech. Div., Proc. ASCE*, Vol. 92, No. EM5, pp. 43-66.

3 Mosquera, J. M., Kolsky, H., and Symonds, P. S., 1984, "Experiments, Finite Element Solutions and a Simplified Elastic-Plastic Approach to Impact of Frames," Tech. Report NR-1 of Brown University to Office of Naval Research under Contract N00014-82-K-0063 May, 1984. *Proc. ASCE J. Eng. Mech. Div.*, to be published.

4 Raphanel, J. L., and Symonds, P. S., 1984, "The Estimation of Large Deflections of a Portal Frame under Asymmetric Pulse Loading," ASME Journal of Applied Mechanics, Vol. 51, pp. 494-500.

5 Shanley, F. R., 1947, "Inelastic Column Theory," *J. Aero. Sci.*, Vol. 14, p. 261.

6 Symonds, P. S., 1980a, "Elastic, Finite Deflection and Strain Rate Effects in a Mode Approximation Technique for Plastic Deformation of Pulse Loaded Structures," *J. Mech. Eng. Sci.*, Vol. 22, pp. 189-197.

7 Symonds, P. S., 1980b, "Finite Elastic and Plastic Deformations of Pulse Loaded Structures by an Extended Mode Technique," *Int. J. Mech. Sci.*, Vol. 22, pp. 597-605.

8 Symonds, P. S., 1980c, "Elastic-Plastic Deflections due to Pulse Loading," in *Preceedings of Second Speciality Conference on Dynamic Response of Structures: Experiments, Observation, Prediction and Control*, Hart, G., ed., New York, pp. 887-901.

9 Symonds, P. S., and Jones, N., 1972, "Impulsive Loading of Fully Clamped Beams with Finite Plastic Deflections and Strain-rate Sensitivity," *Int. J. Mech. Sci.*, Vol. 14, pp. 49-69.

10 Symonds, P. S., and Mosquera, J. M., 1983, "A Simplified Approach to Elastic-Plastic Response to General Pulse Loads," Report NR-2 of Brown Univ. Division of Engineering to Office of Naval Research, under Contract N00014-82-K-0063, Dec., 1983; Journal of Applied Mechanics, in press.

11 Symonds, P. S., and Raphanel, J. L., 1979, "Large Deflections of Impulsively Loaded Plane Frames—Extensions of the Mode Approximation Technique," *Proc. Conf. on Mechanical Properties of Materials at High Rates of Strain*, Institute of Physics Conf. Ser. No. 47, Harding, J., ed., London and Bristol, pp. 277-287.

APPENDIX

Here we outline the simplest version of the simplified elastic-plastic technique, writing the equations of both the elastic and the rigid-plastic stages in single degree-of-freedom form, choosing appropriate shape functions and deriving the equations by work-energy rate equations.

For the elastic stage we assume the deflection $w(x, t)$ can be written in terms of an amplitude $a(t)$ and a shape function $\phi(x)$. These functions and the equation of motion derived are as follows

$$w(x,t) = a(t)\,\phi(x) = a(t)\,\frac{3}{2}\left(\xi - \frac{1}{3}\xi^3\right) \qquad (A1a)$$

$$\frac{17}{35}\bar{\rho}l^3\ddot{a} + \frac{3EI}{l^3}a + \frac{36}{35}\frac{AE}{l^3}a^3 = \frac{5}{8}p_0 l \qquad (A1b)$$

where $\xi = x/l$, $\bar{\rho} = \rho A$ is the mass per unit length, equal to mass density ρ times cross-sectional area $A = bh$, and $I = bh^3/12$ is the area moment of inertia; other quantities are defined in Fig 1. The natural frequency for small vibrations

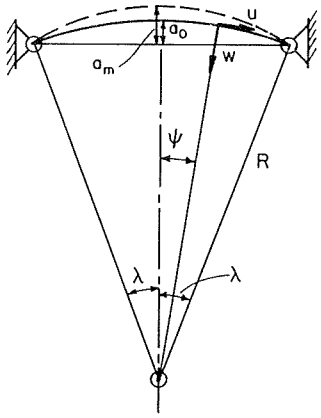

Fig. A1 Notation for circular arch

agrees to better than one percent with the fundamental frequency $(\pi^2/4)\sqrt{EI/\bar{\rho}l^4}$. The bending moment M and axial force N are derived from expressions

$$M = EI\,\kappa, \quad \kappa = \partial^2 w/\partial x^2 \qquad (A1c)$$

$$N = AE\epsilon, \quad \epsilon = (\partial w/\partial x)^2/2 \qquad (A1d)$$

Fully plastic behavior is taken to be governed by the relation

$$|M|/M_0 + N^2/N_0^2 = 1 \qquad (A2a)$$

where $M_0 = \sigma_0 bh^2/4$, $N_0 = \sigma_0 bh$ are fully plastic bending moment and axial force, respectively. This holds for the rigid-plastic motion assumed in the second stage, together with the associated flow rule. The termination of the elastic stage is always somewhat arbitrary. We here take the condition to be when equation $(A2a)$ is satisfied but with $N(x, t)$ replaced by its average $\bar{N}(t)$ over the span. For the pulse example defined in Fig. 1, the yield condition so defined is found to be satisfied at time $t_1 = 0.342$ ms with midpoint displacement $a(t_1) = a_1 = 1.52\ h = 6.1$ mm. The rigid-plastic stage in the present example does not include a phase involving the interaction relation equation $(A2a)$. This may be shown by an argument similar to that given in (Symonds 1980b), involving the flow rule and the relation between extension and rotation of the beam. Thus the rigid-plastic stage here involves only membrane action, with $N = N_0$, $M = 0$. An appropriate form of displacement and the equation of motion derived from it (by work-energy rate) are as follows:

$$w(x,t) = a(t)\,\phi(x) = a(t)\sin\pi\xi/2 \qquad (A2b)$$

$$\frac{\bar{\rho}l}{2}\ddot{a} + \frac{\pi^2 N_0}{8l}a = \frac{2}{\pi}p_0 l, \quad t \le t_0 \qquad (A2c)$$

For $t > t_0 = 0.5$ ms the right-hand side is zero. The solution to equation $(A2c)$ requires values a_2 and $\dot{a}_2$ at the start of rigid-plastic stage at time t_1. We determined these in the same way as in previous applications, namely by taking $a_2 = a_1$, and finding $\dot{a}_2$ from $\dot{a}_1$ by the "minimum Δ_0" technique (Martin and Symonds 1966): this implies a scalar momentum conservation. Omitting details, we have

$$\dot{a}_2 = 96\dot{a}_1/\pi^4 \qquad (A2d)$$

The maximum displacement a_m occurs at time t_m such that $\dot{a}(t_m) = 0$. For our example we find $a_m = 9.8$ mm and $t_m = 0.55$ ms. Thus the increment of displacement in the rigid-plastic stage is $9.8 - 6.1 = 3.7$ mm. This might be taken as a crude estimate of the final permanent displacement; this method gave satisfactory comparisons with tests in (Symonds 1980a, 1980b).

In approximate solutions it is desirable to make alternative calculations based on different points of view. Previous work

Downloaded 02 May 2010 to 171.66.16.54. Redistribution subject to ASME license or copyright; see http://www.asme.org/terms/Terms_Use.cfm

(Raphanel and Symonds 1984, Symonds and Mosquera 1984, Mosquera et al. 1984) has suggested treating the elastic recovery by assuming that an elastic strain energy is available at the end of the rigid-plastic stage, and that this energy determines the amplitude of the continuing elastic vibration. The stress state at the close of the rigid-plastic stage is relatively simple, corresponding to a mode form velocity pattern. In the present example the closing plastic stress field is one of pure tension at the yield stress σ_0. Thus the available elastic strain energy can be estimated as $2lbh\sigma_0^2/2E = V_r$. This may be equated to the strain energy of vibration of a curved beam. For simplicity we suppose the beam has the shape of a flat circular arch in its unstressed position, with height of crown a_0. We adopt the expression for strain energy due to Den Hartog (1928) to obtain the frequency of small amplitude vibrations; for the flat arch we are concerned with, a symmetric mode with non-zero middle surface strains is appropriate. The vibrations involve radial and tangential displacements w, u as shown in Fig. A1. Following Den Hartog (1928), formulas for small strain components are adopted as

$$e = \frac{w}{R} - \frac{1}{R}\frac{\partial u}{\partial \psi}; \quad \kappa = \frac{w}{R^2} + \frac{1}{R^2}\frac{\partial^2 w}{\partial \psi^2} \qquad (A3a)$$

for compressive centerline strain e and curvature κ. The displacements are taken as

$$w = D\cos\frac{\pi\psi}{2\lambda}\sin\omega t; \quad u = \left(\alpha_1 \sin\frac{\pi\psi}{\lambda} + \alpha_2 \sin\frac{3\pi\psi}{\lambda}\right)\sin\omega t \qquad (A3b)$$

where λ is the angle of the arch of radius R and ψ is measured from the middle. The coefficients α_1 and α_2 are found in terms of the amplitude D so as to minimize the strain energy, which can then be written as follows:

$$V = D^2\frac{EI\lambda}{2R^3}\left[0.8186\frac{R^2}{i^2} + \left(\frac{\pi^2}{4\lambda^2} - 1\right)^2\right] \qquad (A3c)$$

where $i = h\sqrt{12}$ is the radius of gyration; Fig. 7 shows λ and R which are readily expressed in terms of the height a_0 of the crown by

$$\lambda = 2\tan^{-1}\frac{a_0}{R}; \quad R = \frac{l}{2}\frac{1 + a_0^2/l^2}{a_0/l} \qquad (A3d)$$

We take a_0 as the height of the arch obtained from the maximum deflection a_m by assuming that the maximum length is reduced by the factor $1 - \sigma_0/E$. (This is approximately the same as reducing the average stress to zero by appropriate displacements). For our example with $a_m = 9.8$ mm, we obtain $a_0 = 6.3$ mm. Correspondingly we have $R = 799$ mm, $\lambda = 0.1254$. Equating V_r to V we obtain $D = 4.5$ mm.

This result is unsatisfactory because it implies that the elastic recovery has a maximum $6.3 + 4.5 = 10.8$ mm larger than the peak elastic-plastic deflection due to the load pulse, estimated as 9.8 mm. Moreover, the stresses computed from equations (A3a) and Hooke's law are found to exceed the yield magnitude σ_0 by amounts as large as 50 percent.

These results suggest that for this problem it may in fact not be possible to have a wholly elastic recovery. Since the "standard procedure" appears unsatisfactory, other points of view were tried. The basic problem is to show that the kinetic energy developed following the peak deflection can be absorbed by elastic strain energy. If elastic deformations following the maximum deflection are specified in terms of centerline compressive strain e and curvature κ, the kinetic energy can be computed as

$$K = RA\int_{-\lambda}^{\lambda}\left(\sigma_0 e - \frac{1}{2}Ee^2 - \frac{1}{2}Ei^2\kappa^2\right)d\psi \qquad (A3e)$$

We ask whether displacements specified in terms of amplitudes such as those written in equations (A3b), for example, can be found such that the beam is brought to rest at a new extreme position, with all stresses in the elastic range. Experimentation with various possible deflection shapes was unsuccessful. This provides further indication that the recovery may not be elastic. In any case it seems clear that the simple approximate approach that was successful in previous applications does not, in this example, provide a confident prediction for the final permanent deflections.

In conclusion, we note that the "simplified elastic-plastic" method predicts a peak displacement (9.8 mm) and time (0.55 msec) close to what almost all of the numerical codes agree on. Its failure to give an unequivocal estimate of the "elastic" recovery and the continuing vibration is an indication that elastic recovery should not here be assumed; it provides a warning that the "standard procedure" is questionable. However, the Shanley model shows that this particular example is truly exceptional; as the peak deflection due to the load is made larger or smaller than the critical range the difficulties and disagreements in both the numerical solutions and the simplified technique rapidly disappear.

Downloaded 02 May 2010 to 171.66.16.54. Redistribution subject to ASME license or copyright; see http://www.asme.org/terms/Terms_Use.cfm

T. C. Soong
Engineering Fellow.

I. Choi
Senior Engineering Specialist.

Xerox Corporation,
Rochester, N.Y. 14644

Buckling of an Elastic Elliptical Ring Inside a Rigid Boundary

The buckling of a thin, elastic ring confined in an elliptical hole whose circumference is smaller than that of the ring is studied. The effect of post-buckling slippage of the ring along the boundary with a corresponding curvature change is included. Buckling configurations with no friction that are (a) symmetric to one axis, and (b) symmetric to both axes, and (c) buckling configurations with no-slip are presented. Buckling with a strain energy consideration added as a criterion and buckling merely from compatibility alone are discussed. Results include curves for buckling loads of different ellipticities for different radius-to-thickness ratios.

Introduction

If a thin, elastic ring is compressed by being inserted into a rigid boundary whose circumference is smaller than the unstressed length of the ring, a hoop stress is created. When a critical value is exceeded, the ring may suddenly collapse along part of its circumference. This instability has been studied in relation to thermal expansion, shrink-fitting, etc. When buckling occurs, if the ring can slip freely along the boundary surface, the hoop stress will be reduced in the portion of the ring that is still in line contact with the boundary and the resulting relief in strain will make inward deflection possible. A kinematic assumption regarding buckling, which we will call compatibility, is that the unstressed length of the complete ring before and after buckling should be the same. This is different from another kind of instability where the ring is cut and a constant end load is applied, then when buckling occurs, the end load remains unchanged during the movement of the end point. An Euler column with a constant end load is an example of the latter type, while a column with a fixed distance between its two ends in thermal buckling is of the former type.

For the former type of instability, Lo, Bogdanoff, Goldberg, and Crawford [1] studied an elastic circular ring under thermal expansion by using Tsien's energy criteria [2, 3]. Hus, Elkon, and Pian [4] extended the study to a similar problem with a point obstacle on the boundary. They found that their buckling load for rings with small imperfections on the boundary was much higher than that based on energy criteria. El-Bayoumy [5] also considered the buckling of a circular ring. Employing the approximation of shallow arch theory, he reduced the boundary value problem to a solution of purely algebraic equations. The approximate formulas for a critical diametral interference in shrink buckling of thin circular rings were found by Chicurel [6].

The present analysis suggests a procedure for studying the instability of a thin, elastic ring inside a rigid, noncircular hole. An elliptical ring is used as an example. There are significant differences in the mechanics of buckling for a noncircular ring and its circular counterpart to warrant a study. Before buckling, the compressive hoop strain is prescribed. When buckling occurs, if no friction is assumed, a portion of the ring will collapse inward to form a buckle and the rest will slide forward along the boundary resulting in a reduced, post-buckling, variable hoop strain. An exact analysis is possible, which leads to a precise account of the hoop strain in the ring still contacting the boundary. Therefore, one can calculate rigorously the stress-free length of the ring before and after buckling and estabish a compatibility requirement for the instability to occur with minimum hoop compression. This is lower bound of instability. External excitation must occur to bring it about. In further analysis, a strain energy criteria is established that yields a buckling load higher than the lower, compatibility-based bound. The derivation of the equations, the numerical results, and discussions will be presented in the following sections.

Derivation

In Fig. 1, assume that buckled ring is symmetric to the vertical axis. The equation of the ellipse is

$$(x/a)^2 + (y/b)^2 = 1. \tag{1a}$$

Let α be the curvilinear coordinate of the ellipse measured along the periphery as shown. The rectangular system can be related to the curvilinear system by an implicit parameter t defined by

$$x/a = \cos t, \qquad y/b = \sin t. \tag{1b}$$

The t is the subtended angle of an arc if the ellipse is a circle.

The coordinates α and t are related by

$$\frac{d\alpha}{dt} = |\mathbf{r}'| = (a^2\sin^2 t + b^2\cos^2 t)^{1/2} \tag{2}$$

Contributed by the Applied Mechanics Division and presented at the 1985 Joint ASME/ASCE Applied Mechanics, Fluids Engineering, and Bioengineering Conference, Albuquerque, N. Mex., June 24-26, 1985 of The American Society of Mechanical Engineers.

Discussion on this paper should be addressed to the Editorial Deparment, ASME, United Engineering Center, 345 East 47th Street, New York, N.Y. 10017, and will be accepted until two months after final publication of the paper itself in the Journal of Applied Mechanics. Manuscript received by ASME Applied Mechanics Division, May, 1984; final revision, August, 1984. Paper No. 85-APM-26.

Copyright © 1985 by ASME
Downloaded 02 May 2010 to 171.66.16.54. Redistribution subject to ASME license or copyright; see http://www.asme.org/terms/Terms_Use.cfm

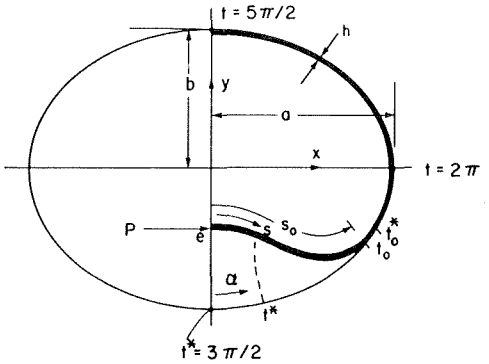

Fig. 1 An ellipse with a buckle symmetrical to the y-axis

where $\mathbf{r}$ is the vector and $(\,)'$ denotes differentiation with respect to t. The curvature of a point t along the elliptical boundary is

$$\frac{1}{R} = |\mathbf{r}' \times \mathbf{r}''| / |\mathbf{r}'|^3 = (\tilde{a}/b)(1 + k^2 \sin^2 t)^{-3/2} \tag{3}$$

where

$$\tilde{a} = a/b$$
$$k = (\tilde{a}^2 - 1)^{1/2} \tag{4}$$

The arc length of curvilinear coordinate α measured from $t = 3\pi/2$ to t is

$$\alpha = b\int_{3\pi/2}^{t} (1 + k^2 \sin^2\beta)^{1/2} d\beta. \tag{5}$$

The hoop strain before buckling is assumed to be P_0/AE where P_0 is the axial compressive force, A is the cross-sectional area, and E is the Young's modulus. This uniform compression can be brought about by a thermal expansion, a shrink-fit, or a cut in the ring compressed by an end force P_0 at the cut, assuming that there is no friction. After buckling, if there is no friction, every point in the portion of the ring that still fully contacts the elliptical boundary will slide forward, with a corresponding change of curvature, except the end point $t = 5\pi/2$. From $t = t_0$ to $t = 3\pi/2$, the ring is deflected to form an elastica. At point t_0, continuities of slope and curvature are maintained. Note, however, that since the material point at t_0 has an initial curvature different from $1/R(t_0)$, the end moment of the elastica at $s = s_0$ is not zero.

To study instability, we have to determine the post-buckling displacement of the portion of the ring that contacts the boundary. Assuming that the boundary has no friction, the equilibrium of a small curved element, as shown in Fig. 2, is governed by

$$\frac{T}{R} + \frac{dV}{d\alpha} = p \tag{6}$$

$$\frac{V}{R} - \frac{dT}{d\alpha} = 0 \tag{7}$$

where T is the axial compressive force, p is the contact pressure, and V is the transverse shear. Assume that the element at $\alpha(t)$ after buckling has a previous coordinate $\alpha^*(t^*)$ and a curvature $1/R(\alpha^*)$, then the bending moment at α required to hold the necessary curvature of $1/R(\alpha)$ is

$$M(\alpha) = \frac{EI}{R(\alpha)} - \frac{EI}{R(\alpha^*)} \tag{8}$$

where the product EI is the bending rigidity.

The transverse shear V that produced this moment is

$$\frac{V(\alpha)}{EI} = \frac{d(M/EI)}{d\alpha}$$

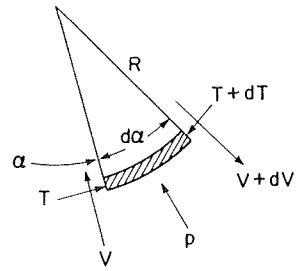

Fig. 2 Equilibrium of a curved element

$$= \frac{d}{d\alpha}\left(\frac{1}{R(\alpha)}\right) - \frac{d\alpha^*}{d\alpha} \cdot \frac{d}{d\alpha^*}\left(\frac{1}{R(\alpha^*)}\right). \tag{9}$$

Substituting equation (9) into (7) yields the axial compression

$$\frac{dT}{d\alpha} = \frac{EI}{R(\alpha)} \frac{d}{d\alpha}\left(\frac{1}{R(\alpha)}\right) - \frac{EI}{R(\alpha)} \cdot \frac{d\alpha^*}{d\alpha} \cdot \frac{d}{d\alpha^*}\left(\frac{1}{R(\alpha^*)}\right). \tag{10}$$

For nondimensionalization, let R_0 be the radius of a circle whose circumference is equal to the ellipse; then from equation (5),

$$b = \pi R_0 \Big/ \int_{3\pi/2}^{5\pi/2} (1 + k^2 \sin^2\beta)^{1/2} d\beta. \tag{11}$$

Let

$$\bar{b} = b/R_0, \quad \bar{R} = R/R_0, \quad \bar{T} = TR_0^2/EI, \tag{12}$$

then after changing variables from α and α^* to t and t^*, equation (10) can be written as

$$\frac{d\bar{T}(t)}{dt} = \frac{1}{\bar{R}(t)} \frac{d}{dt}\left(\frac{1}{\bar{R}(t)}\right) - \frac{1}{\bar{R}(t)} \cdot \frac{dt^*}{dt} \cdot \frac{d}{dt^*}\left(\frac{1}{\bar{R}(t^*)}\right). \tag{13}$$

The relationship between dt^*/dt in equation (13) can be found from considering elongation. Between $t = 5\pi/2$ and t_0, the point that is originally at t^* under compression P_0 and has a curvature $1/R(t^*)$ should have the same unstressed length after being displaced to t when both are measured from $t = t^* = 5\pi/2$. Thus

$$(1 + \bar{P}_0 C_1)\int_{t^*}^{5\pi/2} (1 + k^2 \sin^2\beta)^{1/2} d\beta = \int_{t}^{5\pi/2} (1 + \bar{T}(\beta) C_1)(1 + k^2 \sin^2\beta)^{1/2} d\beta \tag{14}$$

where

$$\bar{P}_0 = P_0 R_0^2/EI$$
$$C_1 = I/AR_0^2 = \left(\frac{\rho}{R_0}\right)^2 = \left(\frac{h/\sqrt{12}}{R_0}\right)^2 \tag{15}$$

where ρ is the radius of gyration of the section and h is the thickness.

An equivalent differential relationship can be obtained by differentiating equation (14), which yields

$$\frac{dt^*}{dt} = \frac{(1 + \bar{T}(t) C_1)(1 + k^2 \sin^2 t)^{1/2}}{(1 + \bar{P}_0 C_1)(1 + k^2 \sin^2 t^*)^{1/2}} \tag{16}$$
$$t_0 \le t \le 5\pi/2$$

with the end condition

$$t^*_{<t=5\pi/2>} = 5\pi/2. \tag{17}$$

Substituting equations (3) and (16) into equation (13) yields

Downloaded 02 May 2010 to 171.66.16.54. Redistribution subject to ASME license or copyright; see http://www.asme.org/terms/Terms_Use.cfm

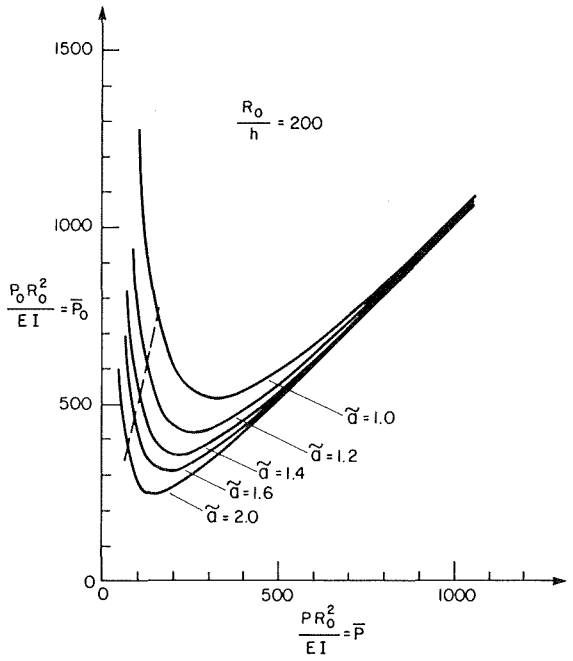

Fig. 3 Buckling symmetrical to y-axis. One buckle case. No friction.

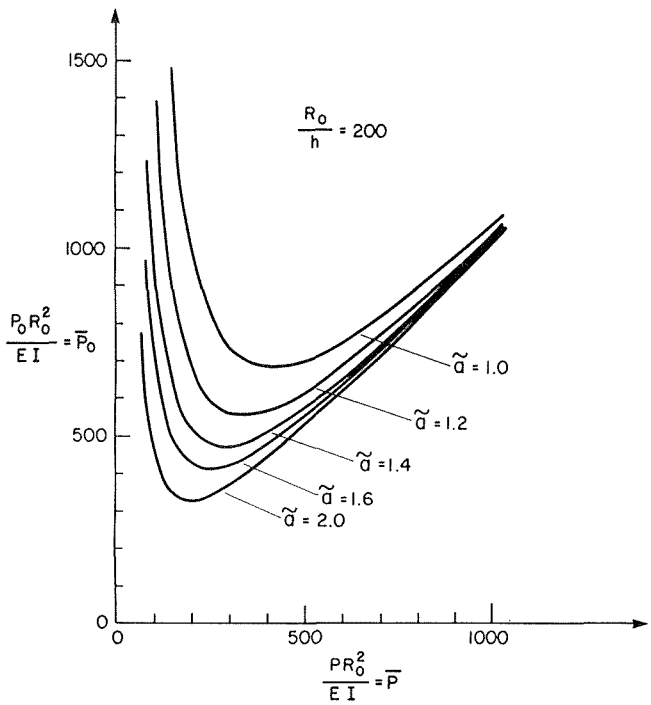

Fig. 4 Buckling symmetrical to both x and y axes. Two-buckle case. No friction.

$$\frac{d\bar{T}(t)}{dt} = -\frac{3\tilde{a}^2k^2}{\bar{b}^2}\left[\frac{\sin t\cos t}{(1+k^2\sin^2 t)^4} - \left(\frac{1+\bar{T}(t)C_1}{1+\bar{P}_0C_1}\right)\frac{\sin t^*\cos t^*}{(1+k^2\sin^2 t)\,(1+k^2\sin^2 t^*)^3}\right]$$

$$t_0 \le t \le 5\pi/2. \tag{18}$$

The starting condition at $t = t_0$ can be found from the end point of the deflected portion of the ring, that is,

$$\bar{T}_{<t=t_0>} = \bar{P}\cos\varphi(s_0) = \bar{P}\cos\left(\tan^{-1}\left(\frac{dy}{dx}\right)_{<s=s_0>}\right) = \bar{P}\cos\left(\tan^{-1}(\cot t_0/(-\tilde{a}))\right) \tag{19}$$

where the nondimensional end force $\bar{P}$ is

$$\bar{P} = PR^2{}_0/EI, \tag{20}$$

P is the compression at $s = 0$ as shown in Fig. 1, and $\varphi(s_0)$ is the slope of the deflected ring at $s = s_0$.

The unstressed length of the buckled ring from t_0 to $t = 5\pi/2$ is found

$$\bar{L}_f = L_f(\bar{P},\bar{P}_0,t_0)/R_0 = \bar{b}\int_{t_0}^{5\pi/2}(1+T(\beta)C_1)(1+k^2\sin^2\beta)^{1/2}d\beta. \tag{21}$$

This $\bar{L}_f$ is a relationship to be used in the compatibility equation, equation (30). The rest of the derivation is devoted to the deflected portion of the ring.

At a point on the elastica with coordinate $\bar{s}$, whose original undeflected position at the ellipse is t^*, the differential equation of the elastica is

$$\frac{d^2\varphi}{d\bar{s}^2} = \frac{d}{d\bar{s}}\left(\frac{1}{\bar{R}(t^*)}\right) - \bar{P}\sin\varphi \qquad 0 \le \bar{s} \le \bar{s}_0 \tag{22}$$

where φ is the slope measured from the x-axis and $\bar{s}$ is the nondimensional coordinate, defined as

$$\bar{s} = s/R_0. \tag{23}$$

Since $d(1/\bar{R}(t^*))/d\bar{s} = (dt^*/d\bar{s})\,d(1/\bar{R}(t^*))/dt^*$, we need to calculate $dt^*/d\bar{s}$. Since $t^* = 3\pi/2$ is a point of symmetry of the buckled ring, we have the following equation from a length consideration, which relates a point of coordinate $\bar{s}$ on the deflected curve to the corresponding undeflected coordinate t^*

$$\bar{b}(1+\bar{P}_0C_1)\int_{3\pi/2}^{t^*}(1+k^2\sin^2\beta)^{1/2}d\beta = \int_0^{\bar{s}}[1+\bar{P}C_1\cos\varphi(\xi)]d\xi \quad 0 \le \bar{s} \le \bar{s}_0, \quad 3\pi/2 \le t^* \le t^*{}_0 \tag{24}$$

where the material point $t^*{}_0$ moves to t_0 after buckling. Differentiation yields

$$\frac{dt^*}{d\bar{s}} = \frac{1+\bar{P}C_1\cos\varphi(\bar{s})}{\bar{b}(1+\bar{P}_0C_1)(1+k^2\sin^2 t^*)^{1/2}} \tag{25}$$

The starting value is

$$t^*{}_{<\bar{s}=0>} = 3\pi/2. \tag{26}$$

Equations (25) and (26) or equation (24) gives the coordinate relationship between the unbuckled point t^* and the deflected point $\bar{s}$; the curvature change of these two points give the moment required.

Substituting equations (25) and the differentiated expression of equation (3) into (22) yields

$$\frac{d^2\varphi}{d\bar{s}^2} = -\frac{3\tilde{a}k^2}{\bar{b}^2}\frac{\sin t^*\cos t^*}{(1+k^2\sin^2 t^*)^3}\left(\frac{1+\bar{P}C_1\cos\varphi(\bar{s})}{1+\bar{P}_0C_1}\right) - \bar{P}\sin\varphi(\bar{s}) \qquad 0 \le \bar{s} \le \bar{s}_0. \tag{27}$$

The end conditions are:

$$\varphi_{<\bar{s}=0>} = 0 \tag{28}$$

$$\varphi_{<\bar{s}=\bar{s}_0>} = \tan^{-1}(\cot t_0/(-\tilde{a})). \tag{29}$$

If the ring can slide freely on the boundary, a necessary condition for deformation to occur is that the stress-free length of the half ring before and after buckling should be the same. This necessary condition, which we call compatibility, is given in the following

$$(1+\bar{P}_0C_1)\bar{b}\int_{3\pi/2}^{5\pi/2}(1+k^2\sin^2\beta)^{1/2}d\beta$$

Downloaded 02 May 2010 to 171.66.16.54. Redistribution subject to ASME license or copyright; see http://www.asme.org/terms/Terms_Use.cfm

$$= \int_0^{\bar{s}_0} [1 + \bar{P}C_1 \cos\varphi(\bar{s})]d\bar{s} + \bar{L}_f(\bar{P}, \bar{P}_0, t_0) \quad (30)$$

where $\bar{L}_f$ is given from equation (21).

Concerning the buckled shape of the elastica, there are two constraining geometrical conditions to be satisfied: the curvature at the end of the buckle must be the same as that of the ellipse and the end of the buckle must touch the ellipse at t_0. The equations that describe these conditions are

$$\frac{d\varphi}{d\bar{s}}_{<\bar{s}=\bar{s}_0>} = \frac{1}{\bar{R}_{<t=t_0>}} = (\tilde{a}/b)(1 + k^2 \sin^2 t_0)^{-3/2} \quad (31)$$

and

$$\int_0^{\bar{s}_0} \cos\varphi(\bar{s})\, d\bar{s} = x_{<t=t_0>}/R_0 = \tilde{a}\cos t_0. \quad (32)$$

where $\tilde{a} = a/R_0$.

By substituting equation (32) into equation (30), the latter can be simplified so that the exact length of the elastica can be expressed in a closed form

$$\bar{s}_0 = (1 + \bar{P}_0 C_1)\pi - \tilde{a}\bar{P}C_1 \cos t_0 - \bar{L}_f(\bar{P}, \bar{P}_0, t_0). \quad (33)$$

If the effect on the tangential hoop force T due to curvature change during buckling is neglected in the portion of the ring that contacts the elliptical boundary, then the hoop force is uniform and is equal to the compressive force at the point t_0, which is

$$P\cos(\tan^{-1}(\cot t_0/(-\tilde{a})))$$

Equation (33) then becomes

$$\bar{s}_0 = (1 + \bar{P}_0 C_1)\pi - \tilde{a}\bar{P}C_1 \cos t_0 - \bar{b}[1 + \bar{P}C_1 \cos(\tan^{-1}(\cot t_0/(-\tilde{a})))] \times \int_{t_0}^{5\pi/2} (1 + k^2 \sin^2\beta)^{1/2} d\beta. \quad (34)$$

If equation (34) is used in the analysis, the analysis will be much simpler, because the computations from equations (6)–(21) can be bypassed.

Solution

For given values of C_1 in equation (15) and the ellipticity constant $\tilde{a}$ of equation (4), we assume that the ring is buckled as shown in Fig. 1 and that the end load is $\bar{P}$. For that $\bar{P}$, a pair of trial values of $\bar{P}_0$ and t_0 are assumed. Next, $\bar{L}_f(\bar{P}, \bar{P}_0, t_0)$ is to be found from the two first-order differential equations, equations (16) and (18), with boundary conditions given by equations (17) and (19). Then, the length of the buckled portion of the ring, $\bar{s}_0$, is obtained from equation (33).

Now, for the assumed $\bar{P}$ values, we have the corresponding, calculated $\bar{s}_0$ and $\bar{L}_f(\bar{P}, \bar{P}_0, t_0)$ values. The slope of the deflected curve $\varphi(\bar{s})$ and the variable $t(\bar{s})$ of equation (25) can be found by treating differential equations (25) and (27) as three first-order differential equations. Their boundary conditions are equations (26), (28), and (29). For the prescribed $\bar{P}$, the trial values of $\bar{P}_0$ and t_0 will be iterated to their true values, until they satisfy the two geometric constraining conditions represented by equations (31) and (32). The Newton-Raphson method can be used for the iteration. Details are omitted.

Finally, we vary $\bar{P}$ and repeat the procedure. The information from t_0 and $\bar{s}_0$ as a function of $\bar{P}$ (or $\bar{P}_0$) shows that the geometry of the buckle varies with the hoop stress. The curve in which $\bar{P}_0$ varies with $\bar{P}$ shows the hoop stress necessary to maintain the buckle.

Numerical Results

Three buckling cases are studied. In each case, the ellipse has the same length as a circle of radius R_0 and the ratio of radius-to-ring thickness h is fixed at 200.

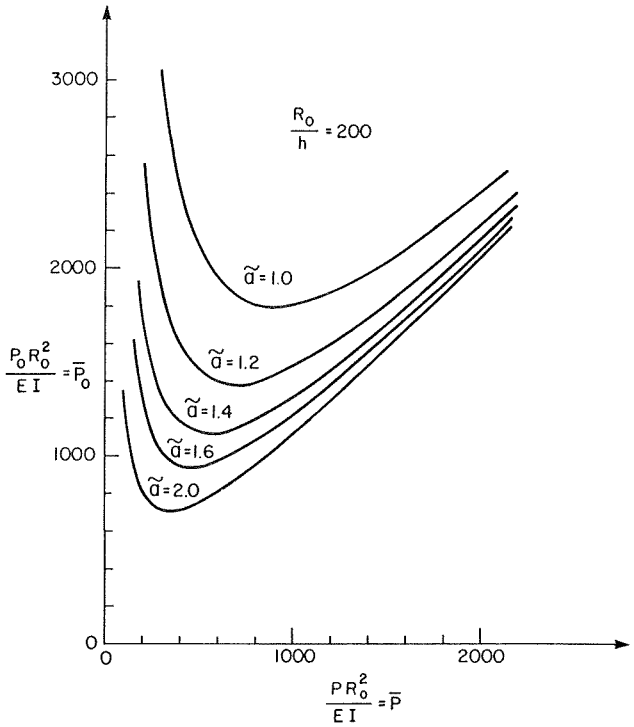

Fig. 5 Buckling with no-slip

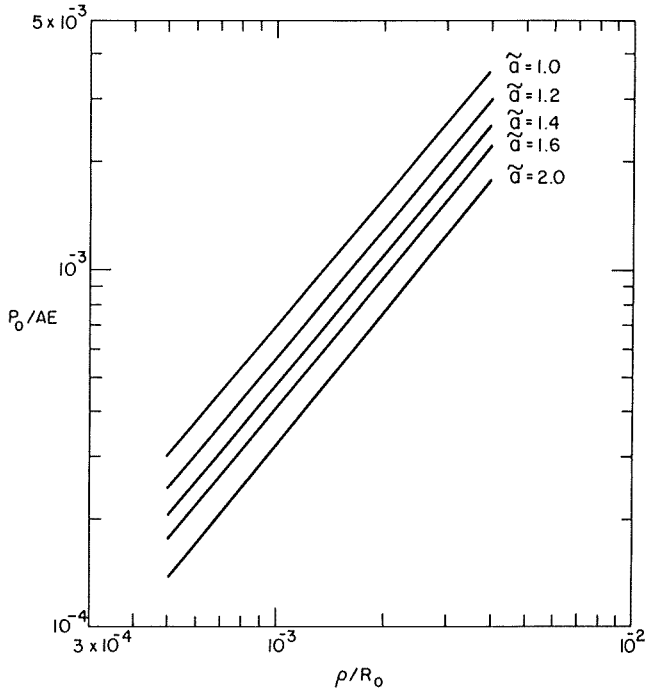

Fig. 6 Buckling load (lowest P_0 in Fig. 3 curves) versus ρ/R_0 for different ellipticities $\tilde{a}$

1. The One-Buckle Case. The geometry is shown in Fig. 1. The buckled shape is symmetric to the y-axis, but is not symmetric to the x-axis. Figure 3 shows that the buckling load P_0 varies with the buckled end load P for different ellipticities $\tilde{a}$.

2. The Two-Buckle Case. Figure 4 shows the P_0 versus P diagram corresponding to the case where the boundary has no

Downloaded 02 May 2010 to 171.66.16.54. Redistribution subject to ASME license or copyright; see http://www.asme.org/terms/Terms_Use.cfm

Table 1 Value of t_0 at the Minimum P_0

$\tilde{a}$ \ Case	One buckle	Two buckle	No-slip
1.0	4.9653	4.9328	4.8620
1.2	4.9703	4.9373	4.8691
1.4	4.9763	4.9425	4.8762
1.6	4.9826	4.9481	4.8832
2.0	4.9959	4.9598	4.8967

friction and the buckled ring is symmmetric to both the x and the y axes. It is obtained by changing the upper limit, $5\pi/2$, of the integral in equation (30) and (21) to 2π.

3. No-Slip Case. If the ring cannot slide during buckling, then in equation (30), $5\pi/2$ is changed to t_0 and $L_f(P, P_0, t_0)$ becomes zero. The result is shown in Fig. 5. This buckling load is the highest of the three cases.

Note that the $\tilde{a} = 1$ curve of Fig. 4 agrees completely with the $V/N = 0$ curve in Fig. 3 of reference [4], which describes buckling of a half circular ring confined in a circular boundary with its ends contrained.

In Figs. 3, 4, and 5, the smallest P_0 values in a curve of constant $\tilde{a}$ is a lower bound for buckling. Below that value, a buckle will snap back to its original shape after the external excitation is removed. The buckled shape simply cannot maintain equilibrium with the available length dictated from its stress-free state.

To give an idea of the buckled shape, Table 1 shows the value of t_0 at the smallest P_0 for the three cases. Note that $t^*_0 = 3\pi/2$ is the middle point with a zero arc length. Take the one-buckle, $\tilde{a} = 1$ case: $t_0 = 4.9653$. The subtended angle of half-buckle for this t_0 is 14.5 deg.

El-Bayoumy's solution for a circular ring [5], which employs shallow arch theory, was compared with the current solution. As might be expected, the mismatch between two solutions increases as the subtended angle of buckle increases. For example, at the aspect ratio of $I/AR_0^2 = 10^{-6}$, the difference in the initial compression P_0 between the two solutions is negligible when the subtended angle of half buckle is 0.4 radian, but the current method becomes 8 percent greater in P_0 than the El-Bayoumy's when the subtended angle is 0.7 radians. It should also be mentioned that a concentrated lateral force exists at the transition points between the buckled and unbuckled portions, which are necessary to enforce the required curvature rate change at that transition point. The existence of this force was shown in reference [5] and also in [7].

Strain Energy Criterion

If an external excitation occurs and is quickly removed but the compressed ring is temporarily displaced to form a buckle, then whether or not the buckle will snap back to its original state or continue to buckle to reach another equilibrium state will depend on the magnitude of the hoop compression P_0. If P_0 is less than the lower bound, as shown in Figs. 3–5, it is not possible for the ring to remain in any buckled state. However, if P_0 is higher than this lower bound value and the strain energy before buckling is equal to the strain energy stored in a post-buckling mode, then once the ring is disturbed the displaced ring could seek the second equilibrium state and remain there. This is the energy criterion and reference [1] supplies a solution for the circular ring case.

The strain energy of the complete ring after buckling, denoted by U_a, for the case of Fig. 3 is

$$\frac{U_a}{EI/R_0} = \int_0^{\bar{s}_0} \left\{ \left(\frac{d\varphi(\bar{s})}{d\bar{s}} - \frac{1}{\bar{R}(t^*)} \right)^2 + C_1 \left(\bar{P} \cos\varphi(\bar{s}) \right)^2 \right\} d\bar{s}$$

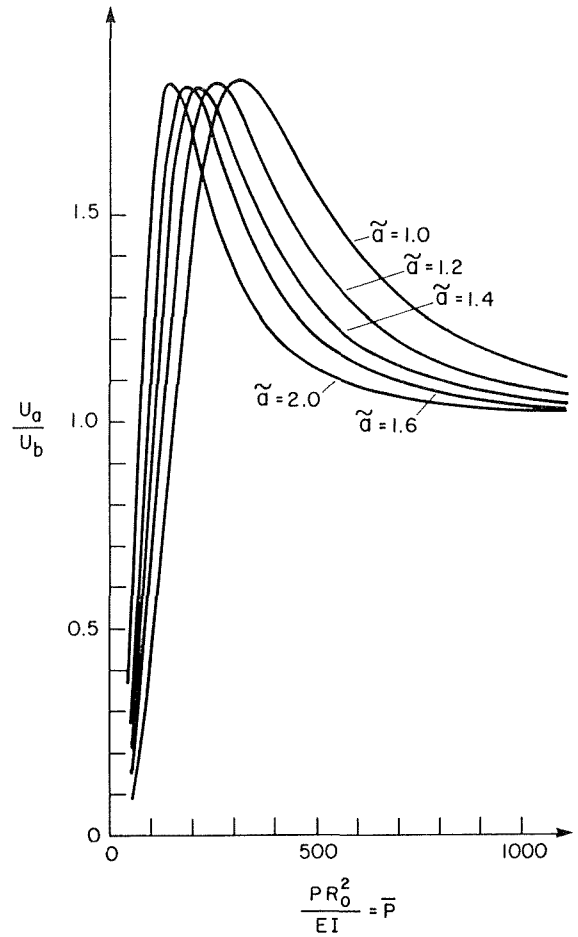

Fig. 7 Strain energy ratio versus P for different $\tilde{a}$

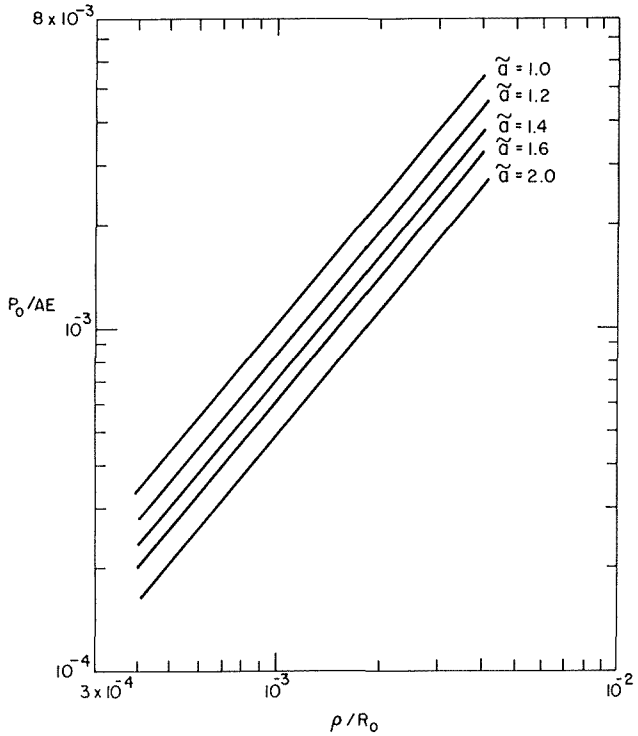

Fig. 8 Buckling load satisfies both compatibility and energy criteria. P_0/AE versus ρ/R_0 for different $\tilde{a}$.

Downloaded 02 May 2010 to 171.66.16.54. Redistribution subject to ASME license or copyright; see http://www.asme.org/terms/Terms_Use.cfm

$$+\int_{t_0}^{5\pi/2} \frac{d\bar{\alpha}}{dt}\left\{\left(\frac{1}{\bar{R}(t)}-\frac{1}{\bar{R}(t^*)}\right)^2+C_1\bar{T}^2(t)\right\}dt \qquad (35)$$

where the first integral is the bending strain energy and the axial strain energy of the deflected portion, its independent variable $\bar{s}$, runs from 0 to $\bar{s}_0$. The second integral is the portion that slides but is still in contact with the boundary, its variable t runs from t_0 to $5\pi/2$. In equation (35), $1/\bar{R}(t)$ or $1/\bar{R}(t^*)$ is from equation (3), $\varphi(\bar{s})$ and $t(\bar{s})$ are solved from equations (25) and (27). $d\bar{\alpha}/dt$ is from equation (2), $\bar{\alpha} = \alpha/R_0$, and $\bar{T}(t)$ and $t^*(t)$ are solved from equations (16) and (18).

The strain energy of the complete ring before buckling, denoted by U_b, consists of the axial compressive strain only. It is

$$\frac{U_b}{EI/R_0} = 0.5\pi C_1 P_0{}^2. \qquad (36)$$

For the one buckle case of Fig. 1, the ratio U_a/U_b is plotted against P in Fig. 7. The P_0 value at $U_a/U_b = 1.0$ is the buckling load based on length compatibility and energy criteria. It is obtained from Figs. 3 and 7. Figure 8 shows the buckling load for a wide range of ρ/R_0. The dotted line in Fig. 3 which meets the solid curves, also indicates the buckling load based on energy criterion. It is to be noted that the curve of $\tilde{a} = 1$ in Fig. 8, which depicts buckling load of a circle, is the same as the result from reference [1].

Conclusion

A procedure is suggested for analyzing buckling of a complete, thin ring confined in a noncircular hole subjected to hoop stress. An elliptical ring is studied in detail. Three buckling cases are studied: The one-buckle case, the two-buckle case with no friction, and the no-slip buckle case. The complication arising from slipping over the boundary surface is that after buckling, points on the ring that still contact the boundary will have a curvature change and, consequently, the axial compressive stress is no longer constant. For an elliptical ring, the ellipticity reduces the buckling load, because buckling occurs at the flatter part of the ring. The numerical results were obtained by an exact analysis in which the curvature change due to slipping was included. However, if the curvature change due to slipping in the contact zone is neglected and the tangential force is taken as constant with equation (34) replacing equation (33), the error is relatively insignificant for the cases studied. In the case of $\tilde{a} = 2$ and $R_0/h = 200$, the difference in buckling load was found to be less than 1 percent.

References

1 Lo, H., Bogdanoff, J. L., Goldberg, J. E., and Crawford, R. F., "A Buckling Problem of a Circular Ring," *Proceedings of the 4th U.S. National Congress of Applied Mechanics*, ASME, 1962, pp. 691-695.

2 von Karman, T., and Tsien, H. S., "The Buckling of Spherical Shells by External Pressure," *Journal of Aerospace Sciences*, Vol. 7, No. 2, Dec. 1939, pp. 43-50.

3 von Karman, T., and Tsien, H. S., "The Buckling of Thin Cylindrical Shells under Axial Compression," *Journal of Aerospace Sciences*, Vol. 8, No. 8, June, 1944, pp. 303-312.

4 Hsu, P. T., Elkon, J., and Pian, T. H. H., "Note on the Instability of Circular Rings Confined to a Rigid Boundary," ASME JOURNAL OF APPLIED MECHANICS, Vol. 31, Sept. 1964, pp. 559-562.

5 El-Bayoumy, L., "Buckling of a Circular Elastic Ring Confined to a Uniformly Contracting Circular Boundary," ASME JOURNAL OF APPLIED MECHANICS, Vol. 39, Sept. 1972, pp. 758-766.

6 Chicurel, R., "Shrink Buckling of Thin Circular Rings," ASME JOURNAL OF APPLIED MECHANICS, Vol. 35, Sept. 1968, pp. 608-610.

7 Soong, T. C., and Choi, I., "An Elastica That Involves Line Contact with the Boundary," Xerox internal report, to be published.

Downloaded 02 May 2010 to 171.66.16.54. Redistribution subject to ASME license or copyright; see http://www.asme.org/terms/Terms_Use.cfm

The Effect of Curvature and Torsion on the Temperature Distribution in a Helix

D. D. Sayers
Assoc. Mem. ASME

M. C. Potter
Mem. ASME

Department of Mechanical Engineering,
Michigan State University,
East Lansing, MI 48824

Traditional analysis treats the helix as a straight wire with the effects of nonuniform heating, torsion, and large curvature ignored. Using a helical coordinate system the governing partial differential equation including these effects is derived. The equation is then solved numerically using the finite element method. The results indicate a strong dependence of the temperature on the torsion parameter when the curvature parameter is significant. As the curvature parameter increases, the temperature distribution becomes skew-symmetric and the maximum temperature in the helix increases. Nonuniform heating influences the temperature distribution independent of the curvature and torsion.

Introduction

The temperature distribution and the maximum temperature in a helix subject to internal heat generation is the topic of this paper. Traditional analysis often treats the helix as a straight cylinder with the effects of curvature[1], torsion[2], and nonuniform heating ignored.

Jakob [1] was the first to deal with the effect of variable heat flux on the temperature distribution in a solid, straight cylinder. All effects relating to curvature and torsion were ignored because they were believed to be negligible. Jakob's solution to the governing differential equation involves a combination of zeroth-order Bessel functions resulting in the possibility of an infinite temperature at the first zero. Physically this is a consequence of heat being generated at such a rate near the center of the coil that conduction can no longer carry it away. Jakob also noted that this may occur at a surprisingly low current.

In his second work, Jakob [2] discovered that due to the increase in resistance with temperature, as much as 40 percent more heat per unit volume is generated at the warmest spot in the coil as compared to a location just below the surface. His work also showed that nonuniform generation of heat does not significantly effect the shape of the temperature profile; it does, however, effect the maximum temperature generated in the coil.

Nicholson [3] was the first to attempt a definition of a helical coordinate system. The coordinate system was erroneously thought to be orthogonal; it was first correctly defined by Wang [4], who used this coordinate system to solve for the effect of curvature and nonuniform heat generation on the temperature distribution in a helix for small curvatures. The basic solution was found using an asymptotic expansion of Bessel functions of the first kind of the zeroth order; the first and second correction terms for curvature and nonuniform heating involved Bessel functions of the first kind of zeroth, first and second order. Wang also correctly noted that torsion was insignificant for small curvatures.

This study includes the effect of torsion along with the effects of curvature and nonuniform heating (due to the change in resistance with temperature). Previously, nonuniform heating had been modeled, neglecting the effects of torsion and large curvature. When torsion is neglected and curvature is assumed small the solution to the problem can be determined analytically. When torsion and large curvature are included, as in the present study, the resulting describing equation must be solved numerically. The finite element method was selected as the method of solution.

Describing Equation

The steady-state, heat transfer equation for conduction in a solid with heat generation, expressed using helical coordinates [4], is

$$T_{rr}+\left(1-\frac{\alpha r\cos\theta}{1-\alpha\cos\theta}\right)\frac{1}{r}T_r+\left(\frac{\alpha\sin\theta}{1-\alpha r\cos\theta}\right)\left[1-\frac{\tau^2r^2}{(1-\alpha r\cos\theta)^2}\right]\frac{1}{r}T_\theta+\left[1+\frac{\tau^2r^2}{(1-\alpha r\cos\theta)^2}\right]\frac{1}{r^2}T_{\theta\theta}=\frac{-q_0}{k}\left[1+\delta(T-T_0)\right] \quad (1)$$

where q_0 represents the heat generation per unit volume, α is

[1] The radius of curvature is the minimum radius of a segment of the coil; curvature is the inverse of this radius of curvature, i.e., $\alpha=c/(b^2+c^2)$. See Fig. 1.

[2] Torsion is related to the distance between the loops measured along the axis of the coil, i.e., $\tau=b/(b^2+c^2)$. See Fig. 1.

Contributed by the Applied Mechanics Division for publication in the JOURNAL OF APPLIED MECHANICS.

Discussion on this paper should be addressed to the Editorial Department, ASME, United Engineering Center, 345 East 47th Street, New York, N.Y. 10017, and will be accepted until two months after final publication of the paper itself in the JOURNAL OF APPLIED MECHANICS. Manuscript received by ASME Applied Mechanics Division, December, 1983; final revision, August 1984.

Copyright © 1985 by ASME
Downloaded 02 May 2010 to 171.66.16.54. Redistribution subject to ASME license or copyright; see http://www.asme.org/terms/Terms_Use.cfm

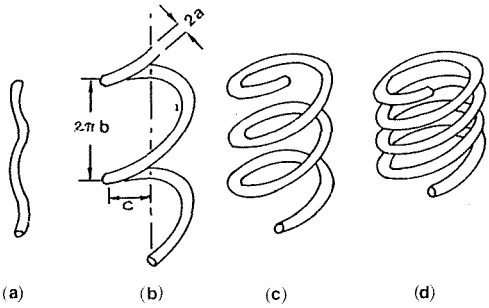

Fig. 1 Helical coils with $\epsilon = 0.1$ (*a*) $\beta = 3.0$, (*b*) $\beta = 0.5$, (*c*) $\beta = 0.2$, and (*d*) $\beta = 0.1$

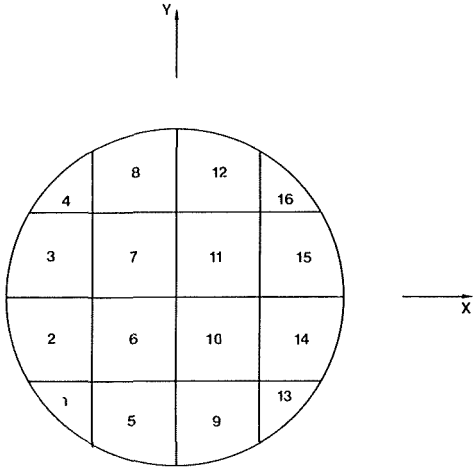

Fig. 2 The element grid configuration

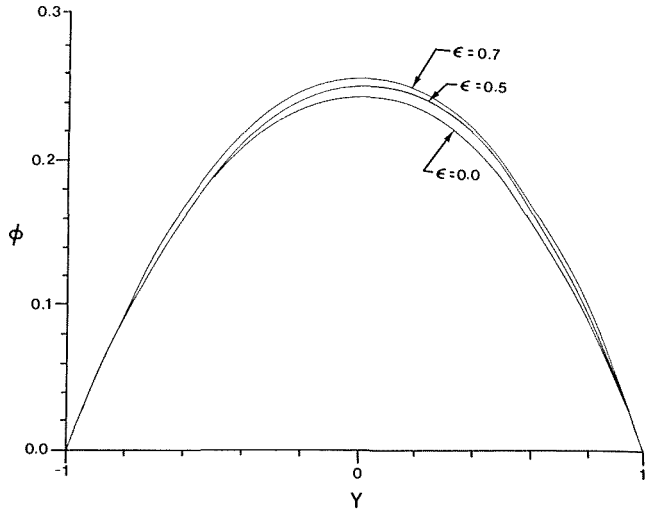

Fig. 3 Dimensionless temperature profiles for $\lambda = 0.0$, $\beta = 0.5$

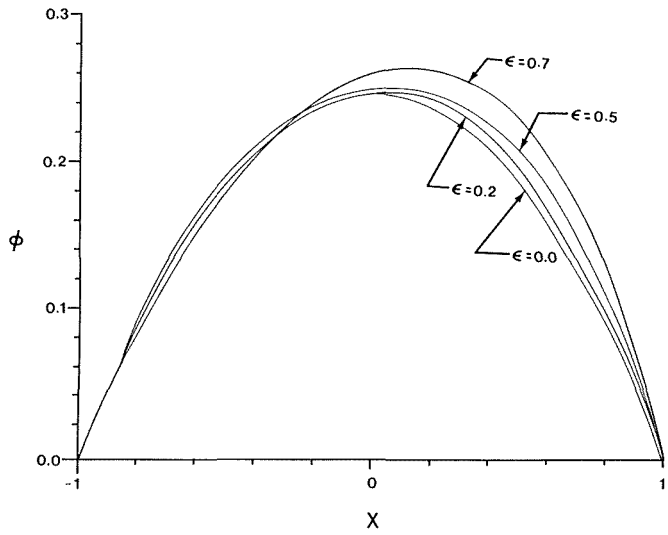

Fig. 4 Dimensionless temperature profiles for $\lambda = 0.0$, $\beta = 0.5$

the curvature, and τ is the torsion. The parameter δ is a measure of the nonuniform heating with uniform heat generation occurring when $\delta = 0$; it provides a means to account for the variation of the material resistance with temperature. As an example, copper has a value of δ equal to $0.004\,^{\circ}C^{-1}$. Equation (1) is linear, nonhomogeneous, and has variable coefficients. The boundary conditions are

$$T \quad \text{is finite at} \quad r = 0 \tag{2}$$

$$T = T_0 \quad \text{at} \quad r = a \tag{3}$$

This last condition is assumed to be maintained by forced convection. Since the rectangular coordinate system (x, y) is generally used with the finite element method, equation (1) was transformed to the rectangular coordinate system. Using

$$x = r\cos\theta \qquad y = r\sin\theta \qquad x^2 + y^2 = r^2 \tag{4}$$

equation (1) is transformed to

$$T_{xx}\left[x^2 + y^2\left(1 + \frac{\tau^2 r^2}{(1-\alpha x)^2}\right)\right] + T_{yy}\left[y^2 + x^2\left(1 + \frac{\tau^2 r^2}{(1-\alpha x)^2}\right)\right] - 2T_{xy}\frac{xy\tau^2 r^2}{(1-\alpha x)^2} + T_x\left[\frac{-\alpha x^2}{1-\alpha x} - \frac{y^2\alpha}{1-\alpha x}\left(1 - \frac{\tau^2 r^2}{(1-\alpha x)^2}\right) - \frac{x\tau^2 r^2}{(1-\alpha x)^2}\right] + T_y\left[\frac{xy\alpha}{1-\alpha x}\left(\frac{-\tau^2 r^2}{(1-\alpha x)^2}\right) - \frac{y\tau^2 r^2}{(1-\alpha x)^2}\right] = \frac{-q_0}{k}[1 + \delta(T - T_0)](x^2 + y^2) \tag{5}$$

Dimensionless Parameters

The transformed equation (5) can be placed in a more general form by introducing dimensionless parameters, using as reference quantities the wire radius (a), the thermal conductivity (k) and the heat generation per unit volume (q_0). The dimensionless variables are then

$$\epsilon = \alpha a \qquad \beta = a\,\tau/\epsilon \qquad Y = y/a \qquad X = x/a$$

$$\phi = (T - T_0)k/q_0 a^2 \qquad \lambda^2 = q_0 a^2 \delta/k$$

$$D = \epsilon^2\beta^2(X^2 + Y^2)/(1 - \epsilon X)^2 \tag{6}$$

Substituting these dimensionless groups into equation (5) the equation that will be solved is

$$\phi_{XX}[X^2 + Y^2(1+D)] + \phi_{YY}[Y^2 + X^2(1+D)] + \phi_{XY}[-2XYD] + \phi_X\left[\frac{-\epsilon X^2}{1-\epsilon X} - \frac{\epsilon Y^2}{1-\epsilon X}(1-D) - XD\right] + \phi_Y\left[\frac{-\epsilon X}{1-\epsilon X} - 1\right]YD + [1 + \lambda^2\phi](X^2 + Y^2) = 0 \tag{7}$$

with boundary conditions

$$\phi = 0 \quad \text{at} \quad X^2 + Y^2 = 1 \tag{8}$$

$$\phi \quad \text{is finite at} \quad X^2 + Y^2 = 0 \tag{9}$$

Several of the dimensionless parameters have bounds that are not apparent from their definitions. For example, $\epsilon < 1$ by the fact that loops of the helix can at most touch each other; it is not physically possible for different coil loops to occupy the

Downloaded 02 May 2010 to 171.66.16.54. Redistribution subject to ASME license or copyright; see http://www.asme.org/terms/Terms_Use.cfm

Table 1 Dimensionless temperatures for $\beta = 0.5$, $\lambda = 0.0$

X	ε=0	ε=.2	ε=.4	ε=.5	ε=.7	ε=.8	ε=.9
-1.0000	0.0000	0.0000	0.0000	0.0000	0.0000	0.0000	0.0000
-0.9375	0.0308	0.0296	0.0288	0.0285	0.0281	0.0280	0.0281
-0.8750	0.0595	0.0573	0.0559	0.0553	0.0546	0.0545	0.0546
-0.8125	0.0860	0.0830	0.0811	0.0804	0.0794	0.0793	0.0797
-0.7500	0.1103	0.1068	0.1045	0.1036	0.1026	0.1026	0.1032
-0.6875	0.1325	0.1287	0.1261	0.1252	0.1242	0.1242	0.1253
-0.6250	0.1526	0.1486	0.1459	0.1450	0.1441	0.1443	0.1458
-0.5625	0.1705	0.1665	0.1639	0.1630	0.1624	0.1628	0.1647
-0.5000	0.1862	0.1825	0.1801	0.1793	0.1790	0.1797	0.1822
-0.4375	0.2011	0.1976	0.1955	0.1949	0.1950	0.1961	0.1993
-0.3750	0.2141	0.2109	0.2091	0.2087	0.2093	0.2109	0.2151
-0.3125	0.2251	0.2224	0.2210	0.2208	0.2221	0.2242	0.2294
-0.2500	0.2341	0.2319	0.2311	0.2312	0.2333	0.2360	0.2425
-0.1875	0.2412	0.2396	0.2393	0.2400	0.2428	0.2462	0.2542
-0.1250	0.2463	0.2454	0.2459	0.2468	0.2508	0.2550	0.2645
-0.0625	0.2495	0.2493	0.2506	0.2520	0.2571	0.2623	0.2735
0.0000	0.2506	0.2513	0.2535	0.2554	0.2619	0.2680	0.2811
0.0625	0.2495	0.2510	0.2541	0.2565	0.2642	0.2711	0.2851
0.1250	0.2463	0.2486	0.2526	0.2555	0.2645	0.2721	0.2870
0.1875	0.2412	0.2442	0.2491	0.2525	0.2626	0.2711	0.2869
0.2500	0.2341	0.2378	0.2434	0.2473	0.2587	0.2680	0.2847
0.3125	0.2251	0.2293	0.2357	0.2400	0.2527	0.2629	0.2805
0.3750	0.2141	0.2189	0.2259	0.2306	0.2446	0.2557	0.2742
0.4375	0.2011	0.2063	0.2139	0.2191	0.2344	0.2465	0.2659
0.5000	0.1862	0.1918	0.1999	0.2055	0.2221	0.2352	0.2555
0.5625	0.1705	0.1765	0.1856	0.1922	0.2135	0.2338	0.2797
0.6250	0.1526	0.1587	0.1682	0.1753	0.1995	0.2243	0.2879
0.6875	0.1326	0.1384	0.1478	0.1549	0.1800	0.2069	0.2800
0.7500	0.1104	0.1157	0.1243	0.1309	0.1549	0.1815	0.2561
0.8125	0.0860	0.0905	0.0978	0.1135	0.1244	0.1481	0.2161
0.8750	0.0595	0.0628	0.0683	0.0725	0.0884	0.1067	0.1601
0.9375	0.0308	0.0326	0.0357	0.0380	0.0470	0.0573	0.0881
1.0000	0.0000	0.0000	0.0000	0.0000	0.0000	0.0000	0.0000

Table 2 Maximum dimensionless temperatures for $\beta = 0.5$

ε	λ	ϕ_{max}	X
0.0	0.0	0.2506	0.000
0.2	0.0	0.2514	0.020
0.4	0.0	0.2542	0.050
0.5	0.0	0.2565	0.065
0.7	0.0	0.2646	0.100
0.8	0.0	0.2721	0.125
0.9	0.0	0.2872	0.150
1.0	0.0	0.2968	0.500
0.0	1.0	0.3071	0.000
0.2	1.0	0.3083	0.025
0.4	1.0	0.3126	0.055
0.5	1.0	0.3163	0.070
0.7	1.0	0.3291	0.110
0.8	1.0	0.3412	0.135
0.9	1.0	0.3668	0.170
0.0	2.0	0.8581	0.000
0.2	2.0	0.8685	0.035
0.4	2.0	0.9041	0.070
0.5	2.0	0.9361	0.090
0.7	2.0	1.0611	0.140
0.8	2.0	1.2050	0.175
0.9	2.0	1.6640	0.224
0.0	2.3	3.0858	0.000
0.2	2.3	3.2184	0.040
0.4	2.3	3.7392	0.080
0.5	2.3	4.3235	0.100
0.7	2.3	9.0135	0.155

same physical space. A zero value for ϵ corresponds to a straight wire and the solution is independent of β. Conversely, if β goes to infinity, the solution also approaches the straight wire case (see Fig. 1). Also, at λ equal 2.4048, a singularity exists such that λ is limited by this value.

Finite Element Method

When Galerkin's method (a weighted residual method) is used in conjunction with finite elements the formulation of the problem, from [5], demands that

$$\int_A [N]^T \Big\{ \phi_{XX}[X^2 + Y^2(1+D)] + \phi_{YY}[Y^2 + X^2(1+D)] + \phi_{XY}[-2XYD] + \phi_X\left[\frac{-\epsilon X^2}{1-\epsilon X} - \frac{\epsilon Y^2}{1-\epsilon X}(1-D) - XD\right] + \phi_Y\left[\frac{-\epsilon X}{1-\epsilon X} - 1\right] YD + [1+\lambda^2\phi](X^2+Y^2)\Big\} dA = 0 \quad (10)$$

where the shape functions $[N]^T$ serve as weighting functions and the area A is divided into several elements. The shape functions used are linear interpolation functions over the element. The element matrices are calculated from the preceding integral formulation. Integrals involving first-order derivatives or no derivatives can be evaluated directly. Integrals involving second-order derivatives must be expressed in terms of first-order terms because the temperature equation does not have a continuous first derivative between elements. Introducing the eight nodal dimenionless temperatures $\{\phi\}$,

$$\phi = [N]\{\phi\} \quad (11)$$

equation (10) takes the form

$$\int_A \Big\{ \Big[(X^2 + Y^2(1+D))\Big(\frac{\partial N_i}{\partial X}\frac{\partial N_j}{\partial X}\Big) + (Y^2 + X^2(1+D))\Big(\frac{\partial N_i}{\partial Y}\frac{\partial N_j}{\partial Y}\Big) - XYD\Big(\frac{\partial N_i}{\partial X}\frac{\partial N_j}{\partial Y} + \frac{\partial N_i}{\partial Y}\frac{\partial N_j}{\partial X}\Big) + \Big(\frac{\epsilon X^2}{1-\epsilon X} + \frac{\epsilon Y^2}{1-\epsilon X}(1-D) + XD\Big)\cdot \Big(N_i\frac{\partial N_j}{\partial X}\Big) + YD\Big(1 + \frac{\epsilon X}{1-\epsilon X}\Big)\Big(N_i\frac{\partial N_j}{\partial Y}\Big) + \lambda^2(X^2+Y^2)N_i\Big]\{\phi\} + (X^2+Y^2)N_j\Big\} dA = 0 \quad (12)$$

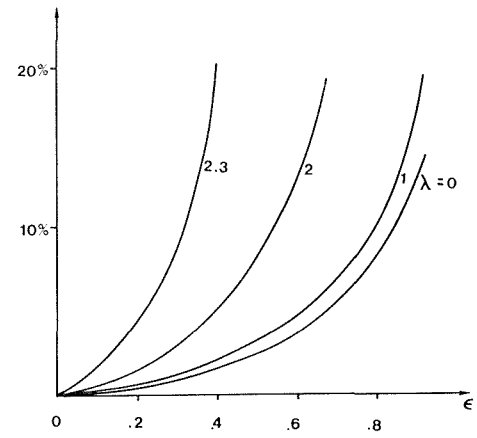

Fig. 5 Percent increase in dimensionless temperature for $\beta = 0.5$ ($\phi max/\phi max|_{\epsilon=0.0}$)

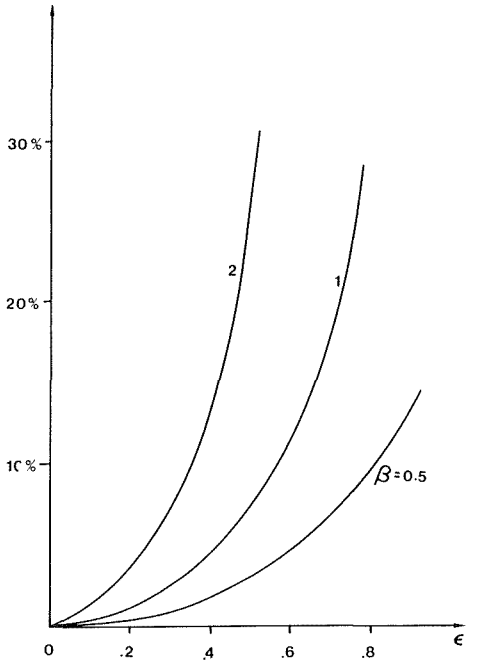

Fig. 6 Percent increase in dimensionless temperature $\lambda = 1.0$ ($\phi max/\phi max|_{\epsilon=0.0}$)

Downloaded 02 May 2010 to 171.66.16.54. Redistribution subject to ASME license or copyright; see http://www.asme.org/terms/Terms_Use.cfm

Equation (12) is integrated numerically for each element to produce the desired solution. The critical term in equation (12), when determining the order of numerical integration, is the term containing $N_i N_j$, which is sixth order in X and Y. Two-dimensional, eight-node, quadratic, quadralateral elements were used in this study. The element grid configuration consisting of 16 elements (see Fig. 2) results in nodal values that are accurate to within 0.01 percent of the analytical solution [6] for the case $\epsilon = \lambda = 0$.

Numerical Results

Temperature distributions and maximum temperatures were calculated for selected values of ϵ, β, and λ. Table 1 contains the values of the dimensionless temperature at selected positions for various values of ϵ. This is shown graphically in Figs. 3 and 4. Note that as ϵ increases, the temperature distribution is no longer symmetric with respect to the X-coordinate but remains symmetric with respect to the Y-coordinate. The maximum temperature, which occurs on the X-axis, increases whenever ϵ, β, or λ increases. Table 2 contains the value of the maximum dimensionless temperature and the location where it occurs for various values of ϵ and β.

As ϵ approaches 1, the mathematical model breaks down; this is particularly evident for data presented at λ equal 2.3. This is not unexpected since the singularity due to the first zero of the zeroth-order Bessel function at λ equal 2.4048 strongly influences the solution. Also, as ϵ approaches 1, terms involving $1/(1-\epsilon X)$ in the governing equations become very large ($1-\epsilon X$ approaches zero near $X=1$) resulting in large off-diagonal terms in the matrices.

Figures 5 and 6 show the effect of changing β and λ on the percent increase in the maximum dimensionless temperature. Increasing β or λ intensifies the effect of ϵ on the maximum temperature.

Conclusions

Based on the results obtained it can be concluded that:

1. As the curvature parameter ϵ increases, ϕ_{max} increases and ϕ_{max} occurs at an ever increasing value of X. For $\epsilon = 0$, $\phi_{max} = 0.02506$ at $X = 0$; for $\epsilon = 0.5$, $\phi_{max} = 0.2644$ at $X = 0.070$. ($\beta = 1.0$ and $\lambda = 0$).

2. As the torsion parameter β increases, ϕ_{max} increases and the effect of ϵ is amplified. For $\beta = 0.5$, $\phi_{max} = 0.3163$; for $\beta = 1.0$, $\phi_{max} = 0.3288$. ($\beta = 0.5$, $\lambda = 1.0$).

3. Increasing the nonuniformity of the internal heat generation, as measured by λ, results in an increase in ϕ_{max}. For $\lambda = 1.0$, $\phi_{max} = 0.3099$; for $\lambda = 2.0$, $\phi_{max} = 0.8824$ ($\epsilon = 0.2$, $\beta = 1.0$).

4. For small values of ϵ (less than approximately 0.2), the temperature distribution is essentially independent of β. For $\beta = 1.0$, $\phi_{max} = 0.3099$; for $\beta = 2.0$, $\phi_{max} = 0.3163$, a change of less than 2 percent ($\epsilon = 0.2$, $\lambda = 1.0$).

5. Maximum temperatures always lie on the x-axis.

6. The temperature distribution is always symmetrical about the y-axis.

It is evident from the results that the torsion parameter β cannot be neglected if $\epsilon > 0.2$. Also, when $\epsilon > 0.2$ the higher-order terms in the asymptotic expansion technique used by Wang [4] become significant and must be included. For more details see [7].

References

1 Jakob, M., *Heat Transfer*, Vol. 1, Wiley, New York, 1949, pp. 173-194.

2 Jakob, M., "Influence of Nonuniform Development of Heat Upon the Temperature Distribution in Electrical Coils and Similar Heat Sources of Simple Form," ASME JOURNAL OF APPLIED MECHANICS, Vol. 10, 1943, pp. 593-605.

3 Nicholson, J. W., "The Effective Resistance and Inductance of a Helical Coil," *Philosophical Magazine*, Vol. 19, 1910, pp. 77-91.

4 Wang, C. Y., "The Helical Coordinate System and the Temperature Distribution Inside a Helical Coil," ASME JOURNAL OF APPLIED MECHANICS, Vol. 47, 1980, pp. 951-953.

5 Zienkiewicz, O. C., *The Finite Element Method*, New York, 3rd ed., McGraw-Hill, 1977, pp. 49-58.

6 Holman, J. R., *Heat Transfer*, 4th ed., McGraw-Hill, New York, 1976, pp. 33-35.

7 Sayers, D. D., "The Effect of Curvature and Torsion on the Temperature Distribution in a Helix," M.S. thesis, Michigan State University, 1983.

Downloaded 02 May 2010 to 171.66.16.54. Redistribution subject to ASME license or copyright; see http://www.asme.org/terms/Terms_Use.cfm

S. Mukherjee
Associate Professor,
Department of Theoretical
and Applied Mechanics,
Kimball Hall,
Cornell University,
Ithaca, N.Y. 14853
Mem. ASME

F. G. Kollmann
Professor,
Maschinenelemente und Getriebe,
Technische Hochschule Darmstadt,
6100 Darmstadt,
Federal Republic of Germany
Mem. ASME

A New Rate Principle Suitable for Analysis of Inelastic Deformation of Plates and Shells

A variational principle for linear elasticity, using displacements and strains as independent functions, is presented in this paper. An extension of this principle in rate form is claimed to be extremely useful for the analysis of inelastic deformation of thin plates and shells.

Introduction

In solid mechanics, a suitably chosen variational principle is commonly introduced as a basis for an approximation using the finite element method (FEM). In linear elasticity, usually the minimum potential energy principle is used. In this principle only the displacements are dependent variables and as such subject to variation. The strains, therefore, have to be obtained by spatial differentiation of the displacements. Numerical differentiation will, of course, degrade the accuracy of the strains relative to that of the displacements. Therefore, for some more advanced applications such as plates and shells, variational principles not only containing displacements but also stresses and even strains are sometimes used. Many researchers start from the Hellinger-Reissner functional [1] which contains the displacements and stresses as dependent variables. Only recently, the more general Hu-Washizu principle has been used for a FEM-approximation for shells [2]. This functional contains, in addition, the strains.

In the theory of shells, integration of the stresses over the shell thickness leads to stress resultants (forces and couples). These stress resultants prove useful in the theory of linear-elastic shells where a linear distribution of the stresses over the shell thickness can be assumed. Here it is possible to compute the stresses from the stress resultants. But this does not hold true for the analysis of rate-dependent inelastic deformation usually involving the use of creep or viscoplastic constitutive equations such as power law creep [3] or perhaps a new generation constitutive model such as the one due to Hart [4]. In such shell theories, the distribution of the stresses over the shell thickness is not known a priori but is history-dependent and, therefore, a part of the solution. Also, in these problems, it is not possible to obtain the stress distribution through the thickness from integrated quantities like stress resultants. Inclusion of stresses or stress rates in a variational principle for inelastic shell analysis thus appears to be of dubious value. To improve any FEM-approximation for inelastic shells beyond a mere displacement formulation, it seems useful, therefore, to start from a variational principle containing displacements and strains, or their respective rates, as primary variables.

This paper begins with a brief summary of known variational principles in linear elasticity. Next, a new variational principle for linear elasticity, using displacements and strains as dependent variables, is presented. The relationship between this new and the other known variational principles is discussed. Further, an extension of this principle in rate form, suitable for the analysis of inelastic structures, is derived. Finally, the usefulness of this new rate principle for the analysis of inelastic deformation of thin plates and shells is discussed.

Equations of Linear Elasticity

Using the usual notation, the field equations and boundary conditions for linear elasticity can be written as

Equilibrium:

$$\sigma_{ij,j} + \bar{f}_i = 0 \quad \text{in} \quad B \tag{1}$$

Kinematic:

$$\epsilon_{ij} = 1/2(u_{i,j} + u_{j,i}) \quad \text{in} \quad B \tag{2}$$

Constitutive:

$$\sigma_{ij} = a_{ijkl}\epsilon_{kl} \quad \text{in} \quad B \tag{3a}$$

or

$$\epsilon_{ij} = b_{ijkl}\sigma_{kl} \quad \text{in} \quad B \tag{3b}$$

Traction boundary conditions:

$$\tau_i = \bar{\tau}_i \quad \text{on} \quad \partial B_\tau \tag{4}$$

Contributed by the Applied Mechanics Division and presented at the 1985 Joint ASME/ASCE Applied Mechanics, Fluids Engineering and Bioengineering Conference, Albuquerque, N. Mex., June 24-26, 1985 of THE AMERICAN SOCIETY OF MECHANICAL ENGINEERS.

Discussion on this paper should be addressed to the Editorial Department, ASME, United Engineering Center, 345 East 47th Street, New York, N.Y. 10017, and will be accepted until two months after final publication of the paper itself in the JOURNAL OF APPLIED MECHANICS. Manuscript received by ASME Applied Mechanics Division, May, 1984; final revision September, 1984. Paper No. 85-APM-34.

Copyright © 1985 by ASME
Downloaded 02 May 2010 to 171.66.16.54. Redistribution subject to ASME license or copyright; see http://www.asme.org/terms/Terms_Use.cfm

Displacement boundary conditions:

$$u_i = \bar{u}_i \quad \text{on} \quad \partial B_u \tag{5}$$

In the foregoing, the surface traction vector τ_i at a point on the boundary ∂B of the body is defined as

$$\tau_i = \sigma_{ij} n_j \quad \text{on} \quad \partial B \tag{6}$$

A bar above a variable denotes a prescribed quantity.

Existing Variational Principles

The variational principles presented in this section have been discovered by various researchers over the years. They are well known. The reader is referred to the excellent book by Washizu [5] for further details and proofs of existing variational principles.

It is assumed that the functions in the variational principles presented next satisfy the necessary continuity requirements [6] in B and on ∂B. Also, equation (6) is assumed to be a definition of τ_i and is therefore satisfied a priori in all cases.

The Minimum Potential Energy Principle. Consider a set of displacement fields u_i that satisfy the displacements boundary conditions (5). Let the strians and displacements be related by the kinematic equations (2) and the stresses and strains by the constitutive equations (3*a*). Of all such stress fields, the one that satisfies the equilibrium equations (1) and traction boundary conditions (4) is of interest. The correct displacement field is the one that makes the functional π_p a minimum, where

$$\pi_P = \int_B (\tfrac{1}{2} a_{ijkl} u_{i,j} u_{k,l} - \bar{f}_i u_i)\, dV - \int_{\partial B_\tau} \bar{\tau}_i u_i dS \tag{7}$$

Variations of π_P must be taken with respect to u_i only.

The Minimum Complementary Energy Principle. Consider a set of stress fields σ_{ij} that satisfy the equilibrium equations (1) and the traction boundary conditions (4). Let the strains and displacements be related by the kinematic equations (2). Of all such stresses, strains, and displacements the ones that satisfy the constitutive equations (3*b*) and displacement boundary conditions (5) are of interest. The correct stress field is the one that makes the functional π_C a minimum, where

$$\pi_C = \int_B \tfrac{1}{2} b_{ijkl} \sigma_{ij} \sigma_{kl} dV - \int_{\partial B_u} \bar{u}_i \tau_i dS \tag{8}$$

Variations of π_C must be taken with respect to σ_{ij} only.

The Hellinger-Reissner Principle. Consider sets of displacements, strain, and stress fields, u_i, ϵ_{ij}, and σ_{ij}, respectively. Let the strains and displacements be related by the kinematic equations (2). Of all such stresses, strains, and displacements the ones that satisfy the equations of equilibrium (1), the constitutive equations (3*b*), the traction boundary conditions (4), and displacement boundary conditions (5) make the functional π_R stationary, where

$$\pi_R = \int_B \{ \tfrac{1}{2} \sigma_{ij} (u_{i,j} + u_{j,i}) - \tfrac{1}{2} b_{ijkl} \sigma_{ij} \sigma_{kl} - \bar{f}_i u_i \} dV - \int_{\partial B_\tau} \bar{\tau}_i u_i dS - \int_{\partial B_u} \tau_i (u_i - \bar{u}_i)\, dS \tag{9}$$

Variations of π_R must be taken with respect to σ_{ij} and u_i.

The Hu-Washizu Principle. Consider sets of displacement, strain, and stress fields u_i, ϵ_{ij}, and σ_{ij}, respectively. Of all such stresses, strains, and displacements, the ones that satisfy all the field equations (1)–(3) and the boundary conditions (4) and (5) make the functional π_W stationary, where

$$\pi_W = \int_B \{ \tfrac{1}{2} a_{ijkl} \epsilon_{ij} \epsilon_{kl} - \sigma_{ij} (\epsilon_{ij} - \tfrac{1}{2} (u_{i,j} + u_{j,i})) - \bar{f}_i u_i \} dV - \int_{\partial B_\tau} \bar{\tau}_i u_i dS - \int_{\partial B_u} \tau_i (u_i - \bar{u}_i)\, dS \tag{10}$$

Variations of π_W must be taken with respect to σ_{ij}, ϵ_{ij}, and u_i.

A New Variational Principle

Theorem. Consider sets of displacements, strain, and stress fields u_i, ϵ_{ij}, and σ_{ij}, respectively. Let the stresses and strains be related by the constitutive equations (3*a*). Of all such stresses, strains, and displacements the ones that satisfy the equations of equilibrium (1), the kinematic equations (2), the traction boundary conditions (4), and the displacement boundary conditions (5) make the functional π_M stationary, where

$$\pi_M = \int_B \{ \tfrac{1}{2} a_{ijkl} (u_{i,j} + u_{j,i}) \epsilon_{kl} - \tfrac{1}{2} a_{ijkl} \epsilon_{ij} \epsilon_{kl} - \bar{f}_i u_i \} dV - \int_{\partial B_\tau} \bar{\tau}_i u_i dS - \int_{\partial B_u} \tau_i (u_i - \bar{u}_i)\, dS \tag{11}$$

Proof. This theorem can be proved by taking variations of π_M with respect to u_i and ϵ_{ij}. Before taking the variations, however, τ_i in the last integral must be replaced by $a_{ijkl} \epsilon_{kl} n_j$ by using equations (6) and (3*a*). After suitable applications of the divergence theorem, the result is

$$\delta\pi_M = \int_B \{ -a_{ijkl} (\epsilon_{ij} - \tfrac{1}{2} (u_{i,j} + u_{j,i})) \delta\epsilon_{kl} - ((a_{ijkl} \epsilon_{kl})_{,j} + \bar{f}_i) \delta u_i \} dV - \int_{\partial B_\tau} (\bar{\tau}_i - n_j a_{ijkl} \epsilon_{kl}) \delta u_i dS - \int_{\partial B_u} n_j a_{ijkl} (u_i - \bar{u}_i) \delta\epsilon_{kl} dS \tag{12}$$

Using the auxilliary equation (3*a*), it can be easily seen that $\delta\pi_M$ vanishes if and only if equations (1), (2), and (4), and (5) are satisfied. It must be remembered that equation (6), as mentioned before, is treated here as a definition of τ_i and is assumed to be satisfied a priori in this as well as the other variational principles mentioned earlier.

It should be mentioned here that the admissible functions in π_M have to meet the following requirements:

(*I*) u_i is an admissible displacement field i.e.,
  (1) u_i is of class C^2 in B.
  (2) u_i and $u_{i,j}$ are continuous on $\bar{B} = BU\partial B_\tau U \partial B_u$.

(*II*) ϵ_{ij} is a symmetric tensor field which is C^1-continuous on $\bar{B}$.

Relationship to Other Principles. The new variational principle can be derived from the Hu-Washizu principle by using equation (3*a*) to replace the stresses in π_W in terms of the strains, just as the Hellinger-Reissner principle can be obtained from the Hu-Washizu principle by using equation (3*b*) to replace the strains in π_W in terms of the stresses [5]. Thus, for elasticity problems, there is no significant difference in the usefulness of the Hellinger-Reissner and the new principle. The usefulness of the new principle occurs for inelasticity problems of plates and shells as will be discussed later in the paper.

It should also be mentioned that replacing the strains in π_M by the displacements gradients through equation (2) and setting $u_i = \bar{u}_i$ on ∂B_u reduces the new principle to the potential energy principle.

Extension of the New Principle to Inelasticity

Small strain inelasticity problems are considered here in which the total strain rate can be additively decomposed into an elastic and a nonelastic rate. The elastic strain rate is related to the stress rate through Hooke's law while the nonelastic strain rate $\dot{\epsilon}_{ij}^{(n)}$ must be determined from a suitable viscoplastic constitutive model. Thus, equations (3*a*) and (3*b*) are replaced here by

$$\dot{\sigma}_{ij} = a_{ijkl} (\dot{\epsilon}_{kl} - \dot{\epsilon}_{kl}^{(n)}) \tag{13a}$$

Downloaded 02 May 2010 to 171.66.16.54. Redistribution subject to ASME license or copyright; see http://www.asme.org/terms/Terms_Use.cfm

$$\dot{\epsilon}_{ij} - \dot{\epsilon}_{ij}^{(n)} = b_{ijkl}\dot{\sigma}_{kl}, \tag{13b}$$

respectively.

The other governing equations (1), (2), and (4)-(6) are replaced by the corresponding rate equations. An extension of the new variational principle to a rate principle is now given by

$$\delta\hat{\pi}_M = 0 \tag{14}$$

where

$$\hat{\pi}_M = \int_B \{ \tfrac{1}{2}a_{ijkl}(\dot{u}_{i,j} + \dot{u}_{j,i})(\dot{\epsilon}_{kl} - \dot{\epsilon}_{kl}^{(n)}) - \tfrac{1}{2}a_{ijkl}\dot{\epsilon}_{ij}\dot{\epsilon}_{kl} - \dot{\bar{f}}_i\dot{u}_i \} dV - \int_{\partial B_\tau} \dot{\bar{\tau}}_i\dot{u}_i dS - \int_{\partial B_u} \dot{\tau}_i(\dot{u}_i - \dot{\bar{u}}_i) dS$$

This principle can be proved by first setting $\dot{\tau}_i = a_{ijkl}(\dot{\epsilon}_{kl} - \dot{\epsilon}_{kl}^{(n)})n_j$ in the last integral and then taking variations of $\hat{\pi}_M$ with respect to $\dot{u}_i$ and $\dot{\epsilon}_{ij}$. The nonelastic strain rate components $\dot{\epsilon}_{ij}^{(n)}$ are treated as *prescribed quantities* and *must not be varied.* This results in

$$\delta\hat{\pi}_M = \int_B \{ -a_{ijkl}(\dot{\epsilon}_{ij} - \tfrac{1}{2}(\dot{u}_{i,j} + \dot{u}_{j,i}))\delta\dot{\epsilon}_{kl} - ((a_{ijkl}(\dot{\epsilon}_{kl} - \dot{\epsilon}_{kl}^{(n)}))_{,j} + \dot{\bar{f}}_i)\delta\dot{u}_i \} dV - \int_{\partial B_\tau} (\dot{\bar{\tau}}_i - n_j a_{ijkl}(\dot{\epsilon}_{kl} - \dot{\epsilon}_{kl}^{(n)}))\delta\dot{u}_i dS - \int_{\partial B_u} n_j a_{ijkl}(\dot{u}_i - \dot{\bar{u}}_i)\delta\dot{\epsilon}_{kl} dS \tag{15}$$

Using the auxilliary equation (13*a*), it can be easily seen that $\delta\hat{\pi}_M$ vanishes if and only if equations (1), (2), (4), and (5) are satisfied in rate form.

Usefulness of the New Rate Principle for the Analysis of Inelastic Deformation of Plates and Shells

Analysis of rate-dependent inelastic deformation usually involves the use of creep or viscoplastic constitutive equations such as power law creep (see, for example, (3)) or perhaps a new generation constitutive model such as the one due to Hart [4]. Generally, the nonelastic strain rate is a very sensitive function of stress, so that for a time-marching integration scheme to succeed, the stresses must be obtained sufficiently accurately throughout the structure at every discrete time. It has been the experience of one of the authors (Mukherjee) that an attempt to analyze inelastic deformation of plates, by a finite element method (FEM) discretization based on a rate form of the potential energy principle, failed because the calculated stresses were not sufficiently accurate. This is due to the degradation of the accuracy of the strains (and the stresses) because of numerical differentiation. Therefore, any variational principle used for this analysis should contain strain and/or stress rates, in addition to displacement rates.

Rate principles based on the Hellinger-Reissner or the Hu-Washizu principles are possible candidates. The former generally works well for inelastic analysis of bulky structures. Plates and shells, however, are structures in which one dimension is small compared with the other two and one usually makes some approximation regarding the dependence of relevant variables in the thickness direction and then integrates out this thickness dependence in order to obtain a two-dimensional theory. Kinematic assumptions regarding the thickness variation of displacements and strains are made first. Owing to the linearity of equation (3), this is tantamount, in linear elasticity, to making an assumption about the stress variation through the thickness. Such, however, is far from the case in inelasticity, where the stress is nonlinear and history-dependent, so that the stress dependence through the thickness of a plate or shell cannot be prescribed a priori, but is, in fact, a part of the solution of a problem. Thus, while kinematic assumptions regarding dependence on the thickness variable can be justified in inelastic plate or shell analysis, such initial assumptions regarding stress variation through the thickness cannot, in general, be justified.

The Hellinger-Reissner principle suffers from the fact that it contains a quadratic function of stress (see equation (9)). While this causes no problems for linear-elastic plate or shell analysis, the rate form of the principle, with a quadratic term in stress rates, requires an a priori prescription of the variation of stress rates through the thickness. This is very difficult to do for the case of inelatic analysis of plates or shells, for the reason set forth in the previous paragraph. One can, perhaps, use a set of layers in the thickness direction and make some piecewise approximation for the stress rates through the thickness, but this makes the plate or shell FEM model very close to a three-dimensional one. The Hu-Washizu rate principle avoids this difficulty since it contains stress rates in a form where suitable stress rate resultants can be defined by integrating through the thickness. This principle, however, is too elaborate in that it allows too much flexibility and leads to a very large number of variables at each mode in an FEM model [7]. Also, it carries stress rate resultants as primary variables. While stress resultants are very useful in linear-elastic analysis since stresses can be directly obtained from the resultants, such is not the case for inelastic analysis. Thus, stress rate resultants as primary variables are of dubious value for inelastic plate or shell analysis and seem to add to the computational burden without offering a sufficient reward.

The need aries, therefore, for a rate principle purely in terms of kinematic variables with full freedom of choice of the displacement and strain rates. In such a case, there is no difficulty in reducing the principle to a two-dimensional FEM model in terms of midsurface plate or shell variables. Also, such a principle is more general than the potential energy principle and should hopefully deliver both the displacement and strain rates (and therefore the stress rates through equation (13*a*)) sufficiently accurately, while not requiring any more computational effort than that required for the FEM implementation of the Hellinger-Reissner principle. The new rate principle seems to fulfill all these requirements. It has recently been reduced to a strictly-two dimensional formulation containing vector and tensor fields referred to the base vectors of the undeformed shell midsurface [8]. Work on an FEM implementation of this principle for inelastic shell analysis is currently in progress.

Acknolwedgments

Mukherjee's contribution to this research was supported by Grant No. CEE-8206344 of the U.S. National Science Foundation to Cornell University.

References

1 Wunderlich, W., "On a Consistent Shell Theory in Mixed Tensor Formulation," *Theory of Shells*, Proceedings of the Third IUTAM Symposium on Shell Theory, North-Holland, Amsterdam, New York, Oxford, 1980.

2 Wempenr, G., Talaslidis, D., and Hwang, C.-M., "A Simple and Efficient Approximation of Shells via Finite Quadrilateral Elements," ASME/Journal of Applied Mechanics, Vol. 49, No. 1, 1982, pp. 115-120.

3 Kraus, H., *Creep Analysis*, John Wiley & Sons, New York, 1980.

4 Hart, E. W., "Constitutive Relations for the Nonelastic Deformation of Metals," *ASME/Journal of Engineering Materials and Technology*, Vol. 98, No. 3, 1976, pp. 193-202.

5 Washizu, K., *Variational Methods in Elasticity and Plasticity*, 3rd ed., Pergamon Press, Oxford, 1982.

6 Gurtin, M. E., "The Linear Theory of Elasticity," *Encylcopedia of Physics*, Flügge, S., ed., Vol.. VI a/2, Springer, Berlin, Heidelberg, New York, 1972.

7 Kollman, F. G., and Mukherjee, S., *A Theory of Inleastic Thin Shells*, unpublished report, Fachgebiet Mashinenelemente und Getriebe, Technische Hochschule Darmstadt, Darmstadt FRG, 1983.

8 Kollman, F. G., and Mukherjee, S., "A General, Geomtrically Linear Theory of Inelastic Thin Shells," *Acta Mechanica*, in press.

Downloaded 02 May 2010 to 171.66.16.54. Redistribution subject to ASME license or copyright; see http://www.asme.org/terms/Terms_Use.cfm

Large-Amplitude Oscillations of Unsymmetrically Laminated Anisotropic Rectangular Plates Including Shear, Rotatory Inertia, and Transverse Normal Stress

K. S. Sivakumaran
Assistant Professor,
Department of Civil Engineering and Engineering Mechanics,
McMaster University,
Hamilton, Ontario, Canada L85 4L7

C. Y. Chia
Professor,
Department of Civil Engineering,
The University of Calgary,
Calgary, Alberta, Canada T2N 1N4

This paper is concerned with nonlinear free vibrations of generally laminated anisotropic elastic plates. Based on Reissner's variational principle a nonlinear plate theory is developed. The effects of transverse shear, rotatory inertia, transverse normal stress, and transverse normal contraction or extension are included in this theory. Using the Galerkin procedure and principle of harmonic balance, approximate solutions to governing equations of unsymmetrically laminated rectangular plates including transverse shear, rotatory inertia, and transverse normal stress are formulated for various boundary conditions. Numerical results for the ratio of nonlinear frequency to linear frequency of unsymmetric angle-ply and cross-ply laminates are presented graphically for various values of elastic properties, fiber orientation angle, number of layers, and aspect ratio and for different boundary conditions. Present results are also compared with available data.

Introduction

The dynamic von Kármán plate theory has been formulated by Herrmann [1] for isotropic plates and extended to laminated anisotropic plates by Whitney and Leissa [2]. It has been generalized to include effects of transverse shear and rotatory inertia in the theories of orthotropic plates by Medwadowski [3] and of anisotropic plates by Ebcioglu [4]. In addition to these effects Habip [5] has incorporated the effects of transverse normal stress and strain in a general nonlinear theory of elastic plates. The transverse shear and rotatory inertia effects have been also considered in some other nonlinear theories [6–8]. A solution to the foregoing nonlinear plate equations of unsymmetric laminates including these effects, however, can be rarely found in the literature. Based on Berger's approach Wu and Vinson [9, 10] have included these effects in the study of nonlinear oscillations of transversely isotropic and specially orthotropic plates. The transverse shear effect has been also discussed by Ambartsumyan [11] in nonlinear vibration and post-buckling analysis of orthotropic plates. Using Hamilton's principle, Sathyamoorthy and Chia [12, 13] have extended the dynamic von Kármán plate theory to include these effects on nonlinear vibrations of anisotropic rectangular and skew plates. The effects of transverse shear and rotatory inertia in the case of circular [14–16] and annular [17] plates have also been studied. Recently, Reddy and Chao [18] have employed a finite element formulation to study these effects on nonlinear oscillations of laminated rectangular plates.

In the formulation of the present theory Reissner's variational principle is used to derive nonlinear equations of motion, constitutive relations, and boundary conditions of a generally laminated anisotropic plate including effects of transverse shear, rotatory inertia, transverse normal stress, and transverse normal strain. In this work these effecs can be individually examined. These equations are then simplified to two coupled nonlinear equations in terms of the transverse displacement and a force function for flexural vibrations of the plate including shear deformation, rotatory inertia, and transverse normal stress which readily reduce to those obtained in a recent theory of anisotropic plates [12] and to dynamic von Kármán plate equations. Based on a single-mode analysis solutions for these effects on large-amplitude vibrations of unsymmetrically laminated angle-ply and cross-ply rectangular plates with all-simply supported edges, all-clamped edges and simply supported-clamped edges are presented by use of the Galerkin procedure and the principle of harmonic balance. The effects of transverse shear, rotatory inertia, and transverse normal stress on nonlinear vibration behavior of these laminates are examined for different values of plate parameters and boundary conditions. Excluding these effects present results are in excellent agreement with those obtained by Chia and Prabhakara [19]. Including the shear

Contributed by the Applied Mechanics Division for publicaiton in the JOURNAL OF APPLIED MECHANICS.

Discussion on this paper should be addressed to the Editorial Department, ASME, United Engineering Center, 345 East 47th Street, New York, N.Y. 10017, and will be accepted until two months after final publication of the paper itself in the JOURNAL OF APPLIED MECHANICS. Manuscript received by ASME Applied Mechanics Division, March, 1983; final revision, May, 1984.

Copyright © 1985 by ASME
Downloaded 02 May 2010 to 171.66.16.54. Redistribution subject to ASME license or copyright; see http://www.asme.org/terms/Terms_Use.cfm

deformation and rotatory inertia, present results agree well with the finite element analysis of Reddy and Chao [18] for laminated plates.

Governing Equations

Consider a plate of constant thickness constructed of an arbitrary number of homogeneous orthotropic layers perfectly bonded together. Each layer is of arbitrary thickness, elastic properties, and orientation of orthotropic axes with respect to plate axes. The elastic rectangular plate under consideration is initially flat and is referred to a right-handed Cartesian coordinates system. The reference plane $z = 0$ is located at the undeformed middle plane. The displacement components that include the effects of transverse shear deformation, rotatory inertia, transverse normal stress, and transverse normal contraction or extension may assume the following form:

$$U_i(x,y,z,t) = u_i(x,y,t) + z\alpha_i(x,y,t) \qquad i = 1, 2, 3 \tag{1}$$

in which U_i are the two inplane and transverse displacements in x, y, and z directions, respectively, and u_i are the values of U_i at the middle surface. For moderately thick plates, the Lagrangian strain components may be simplified to

$$\epsilon_{ij} = \frac{1}{2}\,(U_{i,j} + U_{j,i} + U_{3,i}U_{3,j}) \qquad i,j = 1, 2, 3 \tag{2}$$

In view of the foregoing equations, strain components can be expressed in terms of displacement functions u_i and α_i.

The generalized Hooke's law for the kth layer with respect to plate axes is obtained by use of the constitutive equation for a three-dimensional orthotropic body and of the classical transformation relations for elastic stiffnesses. The Kirchhoff stress components in the kth layer with respect to plate axes can be expressed in terms of these displacement functions. Now Reissner's variational principle [20] is used in derivation of equations of motion, constitutive relations, and six boundary conditions along each edge of the plate. These equations of motion are obtained in terms of u_i, α_i, stress resultants, and stress couples after integration across the plate thickness h. Using these constitutive relations, eliminating u_j and α_j ($j = 1, 2$) and neglecting the inplane inertia terms, a system of equations of transverse motion in terms of force function ψ, transverse displacement w ($= u_3$), and transverse normal contraction γ ($= \alpha_3$) may be obtained as follows:

$$\begin{aligned}
&\Delta(a_1\psi_{,xxxx} + a_2\psi_{,xxxy} + a_3\psi_{,xxyy} + a_4\psi_{,xyyy} + a_5\psi_{,yyyy})\\
&\quad + I_1\{S_{22}[I_{1s}(\psi)] - S_{12}[I_{2s}(\psi)]\} + I_2\{S_{11}\\
&\quad [I_{2s}(\psi)] - S_{21}[I_{1s}(\psi)]\}\\
&\quad = \Delta[w^2{}_{,xy} - w_{,xx}w_{,yy}) - N_1(\gamma,w)]\\
&\quad - I_1\{S_{22}[w_{,x} - N_{1s}(\gamma,w)] - S_{12}[w_{,y} - N_{2s}(\gamma,w)]\}\\
&\quad - I_2\{S_{11}[w_{,y} - N_{2s}(\gamma,w)] - S_{21}[w_{,x} - N_{1s}(\gamma,w]\}
\end{aligned} \tag{3}$$

$$\begin{aligned}
&\Delta\{w_{,xx}\psi_{,yy} + w_{,yy}\psi_{,xx} - 2w_{,xy}\psi_{,xy}) - I_1(\psi_{,x}) - I_2(\psi_{,y})\\
&\quad - \gamma_{,x}I_1(\psi) - \gamma_{,y}I_2(\psi) - [\gamma_{,xx}K_1(\psi) + 2\gamma_{,xy}K_3(\psi)\\
&\quad + \gamma_{,yy}K_2(\psi)]\} + I_3\{S_{22}[I_{1s}(\psi)] - S_{12}[I_{2s}(\psi)]\}\\
&\quad + I_4\{S_{11}[I_{2s}(\psi)] - S_{21}[I_{1s}(\psi)]\}\\
&\quad = \Delta[(\rho h w_{,tt} - q) - N_2(\gamma,w) - I_3\{S_{22}[w_{,x} - N_{1s}(\gamma,w)]\\
&\quad - S_{12}[w_{,y} - N_{2s}(\gamma,w)]\} - I_4\{S_{11}[w_{,y} - N_{2s}(\gamma,w)]\\
&\quad - S_{21}[w_{,x} - N_{1s}(\gamma,w)]\}
\end{aligned} \tag{4}$$

$$\begin{aligned}
&\Delta\{[F^*_{11}I_1(\psi) + F^*_{21}I_2(\psi)]_{,x} + [F^*_{12}I_1(\psi) + F^*_{22}I_2(\psi)]_{,y}\\
&\quad + L_1(\psi) - w_{,x}I_1(\psi) - w_{,y}I_2(\psi) - [w_{,xx}K_1(\psi) + 2w_{,xy}K_3(\psi)\\
&\quad + w_{,yy}K_2(\psi)\} + I_5\{S_{22}[I_{1s}(\psi)] - S_{12}[I_{21}(\psi)]\\
&\quad + I_6\{S_{11}[I_{2s}(\psi)] - S_{21}[I_{1s}(\psi)]\} = \Delta\left[q\,\frac{h}{2} - N_3(\gamma,w)\right]\\
&\quad - I_5\{S_{22}[w_{,x} - N_{1s}(\gamma,w)] - S_{12}[w_{,y} - N_{2s}(\gamma,w)]\}\\
&\quad - I_6\{S_{11}[w_{,y} - N_{2s}(\gamma,w)] - S_{21}[w_{,x} - N_{1s}(\gamma,w)]\}
\end{aligned} \tag{5}$$

In equations (3)–(5) ρ is the mass density, t is the time, q is the transverse load intensity, a_i and F^*_{ij} are constants, and Δ, I_i, I_{is}, K_i, L_i, N_i, N_{is}, and S_{ij} are differential operators. They are given in [21].

Equations (3)–(5) constitute a system of equations governing the large-amplitude flexural vibration of laminated plates including effects of transverse normal strain and stress, transverse shear, and rotatory inertia. It is to be noted that, with appropriate simplifications of these equations, the resulting equations can be used to study the individual effect on the elastic behavior of generally laminated plates with appropriate boundary conditions.

If the transverse normal contraction γ is neglected, equation (5) and the boundary condition corresponding to γ become invalid from the present variation principle. The remaining two equations reduce to

$$\begin{aligned}
&\Delta(a_1\psi_{,xxxx} + a_2\psi_{,xxxy} + a_3\psi_{,xxyy} + a_4\psi_{,xyyy} + a_5\psi_{,yyyy})\\
&\quad + I_1\{S_{22}[I_{1s}(\psi)] - S_{12}[I_{2s}(\psi)]\} + I_2\{S_{11}\\
&\quad [I_{2s}(\psi)] - S_{21}[I_{1s}(\psi)]\}\\
&\quad = \Delta(w^2{}_{,xy} - w_{,xx}w_{,yy}) - I_1[S_{22}(w_{,x}) - S_{12}(w_{,y})]\\
&\quad - I_2[S_{11}(w_{,y}) - S_{21}(w_{,x})]
\end{aligned} \tag{6}$$

$$\begin{aligned}
&\Delta\{w_{,xx}\psi_{,yy} + w_{,yy}\psi_{,xx} - 2w_{,xy}\psi_{,xy}) - I_1(\psi_{,x}) - I_2(\psi_{,y})\}\\
&\quad + I_3\{S_{22}[I_{1s}(\psi)] - S_{12}[I_{2s}(\psi)]\}\\
&\quad + I_4\{S_{11}[I_{2s}(\psi)] - S_{21}[I_{1s}(\psi)]\}\\
&\quad = \Delta(\rho h w_{,tt} - q) - I_3[S_{22}(w_{,x}) - S_{12}(w_{,y})]\\
&\quad - I_4[S_{11}(w_{,y}) - S_{21}(w_{,x})]
\end{aligned} \tag{7}$$

which require five boundary conditions along each edge.

Equations (6) and (7), which are solvable, can be written in a better form [21]. In this study the boundary conditions for a rectangular plate of length a in the x direction and width b in the y direction are considered as follows:

The out-of-plane conditions are

I. all edges simply supported (*SS*)

$$\begin{aligned}
w = M_x = M_{xy} = 0 \qquad &\text{at } x = \pm a/2\\
w = M_y = M_{xy} = 0 \qquad &\text{at } y = \pm b/2
\end{aligned} \tag{8}$$

II. two opposite edges simply supported and the other edges clamped (*SC*)

$$\begin{aligned}
w = M_x = M_{xy} = 0 \qquad &\text{at } x = \pm a/2\\
w = \alpha = \beta = 0 \qquad &\text{at } y = \pm b/2
\end{aligned} \tag{9}$$

in which $\alpha = \alpha_1$ and $\beta = \alpha_2$.

III. all edges clamped (*CC*)

$$\begin{aligned}
w = \alpha = \beta = 0 \qquad &\text{at } x = \pm a/2\\
w = \alpha = \beta = 0 \qquad &\text{at } y = \pm b/2
\end{aligned} \tag{10}$$

and the inplane conditions are all edges free from stresses

$$\begin{aligned}
\psi_{,yy} = \psi_{,xy} = 0 \qquad &\text{at } x = \pm a/2\\
\psi_{,xx} = \psi_{,xy} = 0 \qquad &\text{at } y = \pm b/2
\end{aligned} \tag{11}$$

Equations (6) and (7) thus are to be solved in conjunction with these three sets of boundary conditions.

Method of Solution

In view of the nonlinear nature of governing equations (6) and (7), only approximate solutions are attempted herein for the three sets of boundary conditions (8)–(11). In this work a single-mode analysis is carried out and hence the transverse displacement satisfying appropriate boundary conditions is taken to be

Downloaded 02 May 2010 to 171.66.16.54. Redistribution subject to ASME license or copyright; see http://www.asme.org/terms/Terms_Use.cfm

$$SS: \frac{w}{h} = f_s(t)\text{Cos}\frac{\pi x}{a}\text{Cos}\frac{\pi y}{b} \tag{12}$$

$$SC: \frac{w}{h} = \frac{f_m(t)}{2}\text{Cos}\frac{\pi x}{a}\left(1+\text{Cos}\frac{2\pi y}{b}\right) \tag{13}$$

$$CC: \frac{w}{h} = \frac{f_c(t)}{4}\left(1+\text{Cos}\frac{2\pi x}{a}\right)\left(1+\text{Cos}\frac{2\pi y}{b}\right) \tag{14}$$

in which f's are functions of time to be determined later.

In view of equations (6) and (12)-(14) the inplane stress function is of the form,

$$\psi = \psi_1(x,y)f(t) + \psi_2(x,y)f^2(t) \tag{15}$$

where $f(t)$ takes a subscript s, m, and c for all-edges simply supported, two opposite edges simply supported, and the other edges clamped, and all-edges clamped, respectively. In this equation functions ψ_1 and ψ_2 are represented by modified double Fourier series as

$$\frac{\psi_1}{h} = \sum_{p=1}^{\infty}\sum_{q=1}^{\infty}\lambda_{pq}r_p(x)s_q(y) \tag{16}$$

$$\frac{\psi_2}{h} = \sum_{p=1}^{\infty}\sum_{q=1}^{\infty}\mu_{pq}r_p(x)s_q(y) \tag{17}$$

where λ_{pq} and μ_{pq} are constant coefficients to be determined and where

$$\begin{aligned} r_p(x) &= \left[(-1)^{p+1} + \text{Cos}\frac{2p\pi x}{a}\right] \\ s_q(y) &= \left[(-1)^{q+1} + \text{Cos}\frac{2q\pi y}{b}\right] \end{aligned} \tag{18}$$

It is evident that the force function given by equation (15) satisfies all inplane boundary conditions (11). Each of these assumed transverse displacement (12)-(14), and force function (15) are substituted into equation (6). The resulting equation is multiplied by $r_m(x)\, s_n(y)$ and integrated from $-a/2$ to $a/2$ with respect to x and from $-b/2$ to $b/2$ with respect to y. By use of orthogonality relations the following differential equations are obtained for three sets of boundary conditions:

$$\begin{aligned} &\lambda_{pq}^s\left[H_1^{pq}f_s(t) + H_2^{pq}R_i\frac{d^2f_s(t)}{dt^2} + H_3^{pq}R_i\frac{d^4f_s(t)}{dt^4}\right] \\ &+ \mu_{pq}^s\left[H_1^{pq}f_s^2(t) + H_2^{pq}R_i\frac{d^2f_s^2(t)}{dt^2} + H_3^{pq}R_i\frac{d^4f_s^2(t)}{dt^4}\right] \\ &= X_1^{pq}f_s(t) + X_2^{pq}R_i\frac{d^2f_s(t)}{dt^2} + X_3^{pq}f_s^2(t) + X_4^{pq}R_i\frac{d^2f_s^2(t)}{dt^2} \\ &+ X_5^{pq}R_i\frac{d^4f_s^2(t)}{dt^4} \qquad p,q = 1, 2, 3\ldots \qquad (SS) \end{aligned} \tag{19}$$

$$\begin{aligned} &= Y_1^{pq}f_m(t) + Y_2^{pq}R_i\frac{d^2f_m(t)}{dt^2} + Y_3^{pq}f_m^2(t) + Y_4^{pq}R_i\frac{d^2f_m^2(t)}{dt^2} \\ &+ Y_5^{pq}R_i\frac{d^4f_m^2(t)}{dt^4} \qquad p,q = 1,2,3\ldots \qquad (SC) \end{aligned} \tag{20}$$

$$\begin{aligned} &= Z_1^{pq}f_c(t) + Z_2^{pq}R_i\frac{d^2f_c(t)}{dt^2} + Z_3^{pq}f_c^2(t) + Z_4^{pq}R_i\frac{d^2f_c^2(t)}{dt^2} \\ &+ Z_5^{pq}R_i\frac{d^4f_c^2(t)}{dt^4} \qquad p,q = 1, 2, 3\ldots \qquad (CC) \end{aligned} \tag{21}$$

In these equations H, X, Y, and Z are constant coefficients given in [21] and R_i is the tracing constant that represents the effect of rotatory inertia when $R_i = 1$ and the effect is neglected when $R_i = 0$. It should be observed that the left-hand side of equations (19)-(21) are the same, irrespective of boundary conditions.

Each of the assumed transverse displacements (12)-(14) and the force function (15) generally do not satisfy equation (7) of the transverse motion of the plate. Thus the Galerkin procedure is used to minimize the error produced by trial functions (12)-(14) for w and furnishes a differential equation for the time function. In the case of all-simply supported (SS) edges the time equation is given by

$$\begin{aligned} &X_1\frac{d^6f_s(t)}{dt^6} + X_2\frac{d^4f_s(t)}{dt^4} + X_3\frac{d^2f_s(t)}{dt^2} + X_4f_s(t) \\ &= \sum_{p=1}^{\infty}\sum_{q=1}^{\infty}\left\{\lambda_{pq}^s\left[X_6^{pq}f_s(t) + X_7^{pq}R_i\frac{d^2f_s(t)}{dt^2} + X_8^{pq}R_i\frac{d^4f_s(t)}{dt^4}\right]\right. \\ &+ \mu_{pq}^s\left[X_6^{pq}f_s^2(t) + X_7^{pq}R_i\frac{d^2f_s^2(t)}{dt^2} + X_8^{pq}R_i\frac{d^4f_s^2(t)}{dt^4}\right] \\ &+ \lambda_{pq}^s\left[X_9^{pq}f_s^2(t) + X_{10}^{pq}R_i\frac{d^2f_s^2(t)}{dt^2} + X_{11}^{pq}R_i\frac{d^4f_s^2(t)}{dt^4}\right] \\ &\left.+ \mu_{pq}^s\left[X_9^{pq}f_s^3(t) + X_{10}^{pq}R_i\frac{d^2f_s^3(t)}{dt^2} + X_{11}^{pq}R_i\frac{d^4f_s^3(t)}{dt^4}\right]\right\} \end{aligned} \tag{22}$$

in which constant coefficients X's, are presented in [21]. The time equations for SC and CC edges are of the same form as equation (22). Each of equations (19)-(21) consists of an infinite set of differential equations. Each set, however, can be truncated to any desired degree of accuracy. For given values of p and q each of these equations gives the same number of equations in λ_{pq} and μ_{pq}. The method of harmonic balance is used in obtaining solutions of these equations. Each time function $f(t)$ is expanded into Fourier cosine series as

$$f(t) = \sum_{k=0}^{\infty}c_k\cos k\omega t \tag{23}$$

where ω is the frequency of vibration and c_k are Fourier coefficients. Substituting the assumed solution (23) in equations (19)-(21), respectively, and equating coefficients of like terms, the values of coefficients λ_{pq} and μ_{pq} for the kth harmonic are obtained. In the case of the SS edges these coefficients are

$$\begin{aligned} \lambda_{pq}^{sk} &= \frac{X_1^{pq} - R_ik^2\omega_s^2X_2^{pq}}{H_1^{pq} - R_ik^2\omega_s^2H_2^{pq} + R_ik^4\omega_s^4H_3^{pq}} \\ \mu_{pq}^{sk} &= \frac{X_3^{pq} - R_ik^2\omega_s^2X_4^{pq} + R_ik^4\omega_s^4X_5^{pq}}{H_1^{pq} - R_ik^2\omega_s^2H_2^{pq} + R_ik^4\omega_s^4H_3^{pq}} \end{aligned} \qquad p,q = 1, 2, 3, \ldots \tag{24}$$

In the cases of the SC and CC edges, coefficients λ's and μ's are of the same form as equations (24).

Similarly, substituting the time series (23) in equation (22) and equating coefficients of like cosine terms result in a set of simultaneous algebraic equations. However, due to the complexity of numerical calculations the first eight terms in series (23) are considered in this analysis. Neglecting the higher harmonics the resulting eight equations for the SS edges are

$$K_{k1}c_k + K_{k2}\bar{c}_k + K_{k3}\bar{\bar{c}}_k = 0 \qquad (k = 0, 1, 2, \ldots, 7) \tag{25}$$

in which $\bar{c}_k$ and $\bar{\bar{c}}_k$ containing quadratic and cubic terms of c_k are presented in [21] and in which

Downloaded 02 May 2010 to 171.66.16.54. Redistribution subject to ASME license or copyright; see http://www.asme.org/terms/Terms_Use.cfm

Table 1 Numerical values of elastic constants

	Graphite-epoxy	Boron-epoxy	Glass-epoxy
E_1/E_2	40	10	3
E_4/E_2	1	1	1
G_{12}/E_2	0.5	0.33	0.5
$\nu_{12}, \nu_{14}, \nu_{24}$	0.25	0.22	0.25
G_{14}/E_2	0.5	0.33	0.5
G_{24}/E_2	0.33	0.2	0.33
ρ/E_2	0.2×10^{-10}	0.2×10^{-10}	0.2×10^{-10}

Table 2 Effect of number of terms in time series (23) on amplitude w/h of a two-layer unsymmetric cross-ply GR square plate having $a = 10\,h$ and $\omega = 1.30\,\omega_0$

No. of terms	*SS*	*SC*	*CC*
4	2.628453	2.768521	2.297782
6	2.629637	2.769626	2.298868
8	2.629662	2.769649	2.298893

$$K_{k1} = (-k^6\omega_s^6 X_1 + k^4\omega_s^4 X_2 - k^2\omega_s^2 X_3 + X_4 - \sum_{p=1}^{\infty}\sum_{q=1}^{\infty}(X_6^{pq} - R_i k^2\omega_s^2 X_7^{pq} + R_i k^4\omega_s^4 X_8^{pq})\lambda_{pq}^{sk}$$

$$K_{k2} = -\sum_{p=1}^{\infty}\sum_{q=1}^{\infty}\left[(X_9^{pq} - R_i k^2\omega_s^2 X_{10}^{pq} + R_i k^4\omega_s^4 X_{11}^{pq})\lambda_{pq}^{sk} + (X_6^{pq} - R_i k^2\omega_s^2 X_7^{pq} + R_i k^4\omega_s^4 X_8^{pq})\mu_{pq}^{sk}\right] \quad (26)$$

$$K_{k3} = -\sum_{p=1}^{\infty}\sum_{q=1}^{\infty}(X_9^{pq} - R_i k^2\omega_s^2 X_{10}^{pq} + R_i k^4\omega_s^4 X_{11}^{pq})\mu_{pq}^{sk}$$

In the cases of *SC* and *CC* edges algebraic equations similar to equation (25) can be obtained.

Numerical Results and Discussion

Numerical results are presented for unsymmetrically laminated angle-ply and cross-ply rectangular plates. Unless otherwise stated the materials of these plates under consideration are glass-epoxy (GL), boron-epoxy (BO), and graphite-epoxy (GR) composites. The values of elastic constants typical of these materials are given in Table 1.

The effect of number of terms in the time series (23) on a typical amplitude-frequency response of an unsymmetric cross-ply plate is given in Table 2 where ω is the nonlinear frequency including the effects of transverse shear and rotatory inertia and ω_0 is the corresponding linear frequency of a classical plate. The result indicates that this series converges rapidly. The use of the first four terms in each time series should be adequate in engineering calculations but eight terms are considered in this study.

The amplitude-period response of an anisotropic rectangular plate obtained in the present analysis is compared in Fig. 1 with that given by Sathyamoorthy and Chia [12]. Both results include the effects of transverse shear and rotatory inertia. The difference between these two sets of values arises from the inplane boundary conditions. The plate edges in the present analysis are free from stresses and those in [12] are the vanishing of total inplane force along each edge. In the figure θ is the fiber orientation angle with the longitudinal sides of the plate and T/T_0 is the ratio of the nonlinear period T of vibration, including effects of transverse shear deformation and rotatory inertia, to the corresponding linear period T_0 of a classical plate, excluding these effects. These effects at zero deflection do not depend on the inplane boundary conditions [12, 13, 18]. This phenomena is verified again in this work.

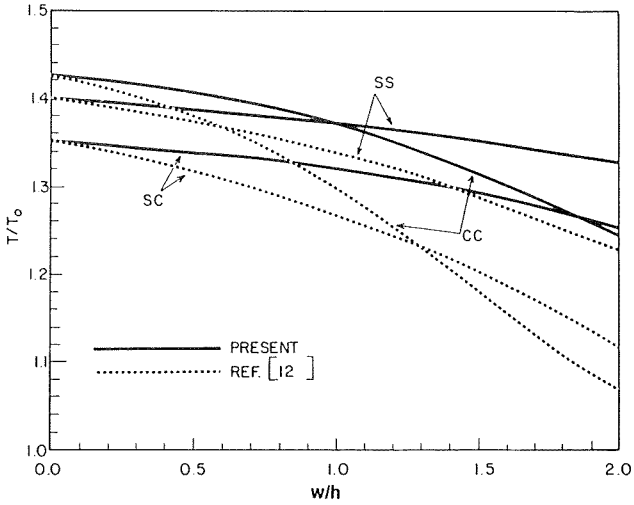

Fig. 1 Comparison of amplitude-period response curves for anisotropic rectangular plate with material properties being E_1/E_2 = 17.66, ν_{12} = 0.256, $G_{12}/E_2 = G_{14}/E_2$ = 0.349, and G_{24}/E_2 = 0.196 ($R_s = R_i$ = 1, a/b = 1.5, θ = 30 deg, a/h = 10)

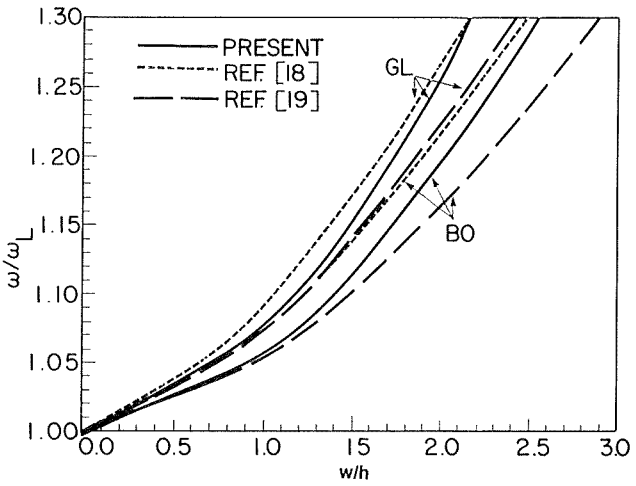

Fig. 2 Comparison of amplitude-frequency response curves for square simply supported two-layer ±45 deg angle-ply plate (a = 1000 h)

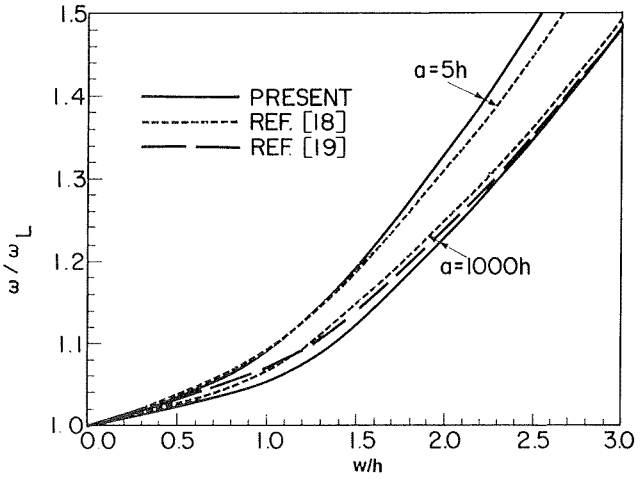

Fig. 3 Comparison of amplitude-frequency response curves for square simply supported two-layer graphite-epoxy cross-ply plate

Figure 1 also shows that the hardening effect on stress-free edges is considerably less than zero inplane stress-resultant edges at large amplitudes of vibration. In Figs. 2 and 3 present results are compared with those obtained by Reddy and Chao

Downloaded 02 May 2010 to 171.66.16.54. Redistribution subject to ASME license or copyright; see http://www.asme.org/terms/Terms_Use.cfm

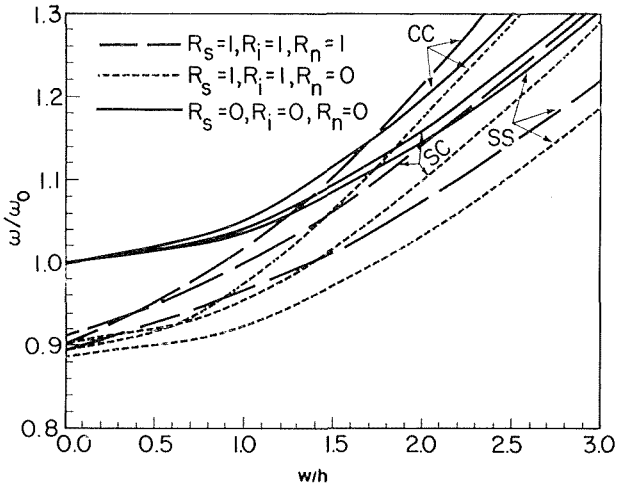

Fig. 4 Effects of transverse normal stress, shear, and rotatory inertia on frequency of square two-layer graphite-epoxy ±45 deg angle-ply plate (a = 10 h) for different edge conditions

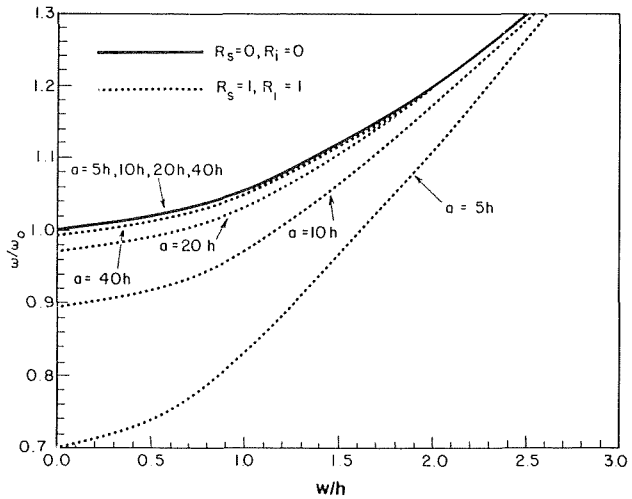

Fig. 6 Effect of thickness-to-span ratio on frequency of square clamped two-layer graphite-epoxy ±45 deg angle-ply plate

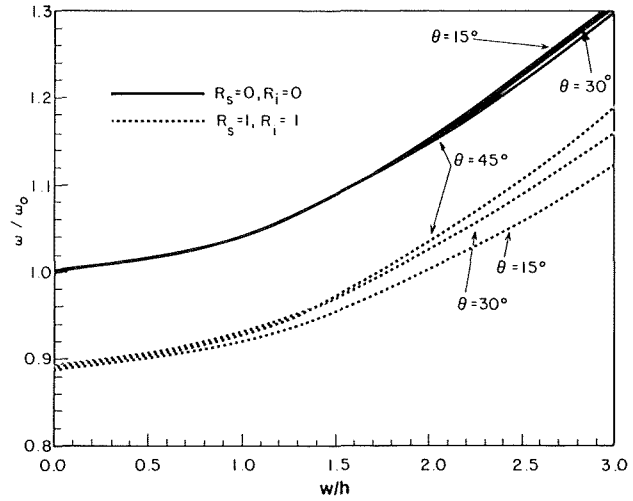

Fig. 5 Effect of orientation angle on frequency of square simply supported two-layer graphite-epoxy angle-ply plate (a = 10 h)

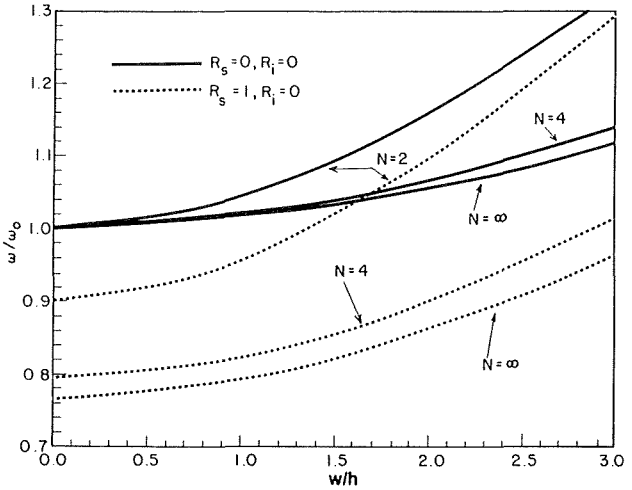

Fig. 7 Effect of number of layers on frequency of square simply supported-clamped graphite epoxy ±45 deg angle-ply plate (a = 10 h)

[18]. The frequency ratio (ω/ω_L), in these figures is the ratio of nonlinear frequency ω to the corresponding linear frequency ω_L, where both include effects of transverse shear deformation and rotatory inertia. Figure 2 shows the amplitude-frequency response of square simply supported two-layer ±45 deg angle-ply boron-epoxy and glass-epoxy plates (a = 1000 h). Since these plates are very thin, the effects of transverse shear deformation and rotatory inertia should be negligible. The results given by Chia and Prabhakara [19] using a multimode solution to the dynamic von Kármán-type equations are applicable to the present case. It is seen from Fig. 2 that the present results are closer to those obtained from the multimode analysis than the finite element analysis [18], especially for the values of w less than 1.5 h. Figure 3 shows the effect of the span-to-thickness ratio on the vibration of a square simply supported two-layer graphite-epoxy cross-ply plate. The present solution agrees well with the finite-element solution [18] for two different ratios of the span to thickness. In the case when a = 1000 h the results given in [19] are also shown for comparison.

In Figs. 4–10 R_s is the tracing constant that represents the effect of transverse shear when R_s = 1 and this effect is neglected when R_s = 0. The tracing constants R_i and R_n representing the effects of rotatory inertia and transverse normal stress, respectively, are similarly defined. The amplitude-frequency response of a square two-layer graphite-epoxy ±45 deg angle-ply plate is shown in Fig. 4 for different boundary conditions. The fundamental linear frequency parameter $\Omega_0 = \omega_0 b^2(\rho/E_2h^2)^{1/2}$ is 14.6353, 19.9960, and 24.5430 for plate with *SS*, *SC*, and *CC* boundary conditions, respectively. Evidently the frequency ratio is lower for the *SS* and *SC* plates than for the *CC* plate. The transverse normal stress always reduces the amplitude or increases the frequency of vibration. For these three sets of boundary conditions the maximum effect of this stress on the frequency is nearly 1 percent at infinitesimally small amplitudes and less than 3 percent at large amplitudes. The effects of transverse shear and rotatory inertia in a *SS* plate which are more significant than the *SC* and *CC* plates reduce the frequency by approximately 11 percent at infinitesimally small amplitudes. In the case of a *CC* plate these effects decrease more rapidly with increasing the amplitude of vibration.

For simplicity the effect of the transverse normal stress on the vibration of composite plates is neglected in the following graphical results. The linear frequency parameter Ω_0 in Fig. 5 is 13.2429, 13.9252, and 14.6353 for the orientation angle θ = 15 deg, 30 deg and 45 deg, respectively. The value of Ω_0 in Fig. 6 is 24.5430 for any thickness-to-span ratio. Figure 5 shows that the effects of transverse shear and rotatory inertia on the dynamic behavior of a simply supported angle-ply plate decreases as the orientation angle θ of filaments in-

Downloaded 02 May 2010 to 171.66.16.54. Redistribution subject to ASME license or copyright; see http://www.asme.org/terms/Terms_Use.cfm

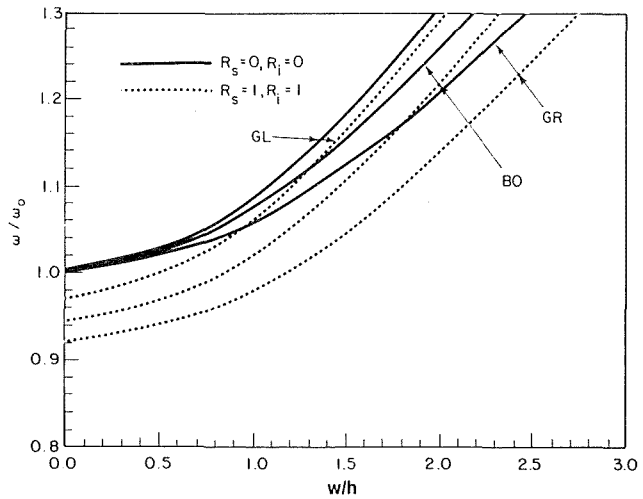

Fig. 8 Effect of elastic properties on frequency of square clamped two-layer cross-ply plate ($a = 10\,h$)

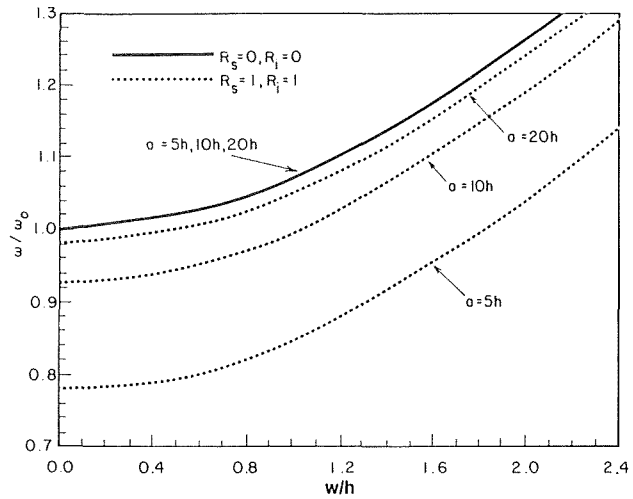

Fig. 10 Effect of thickness to span ratio on frequency of square simply supported two-layer graphite-epoxy cross-ply plate

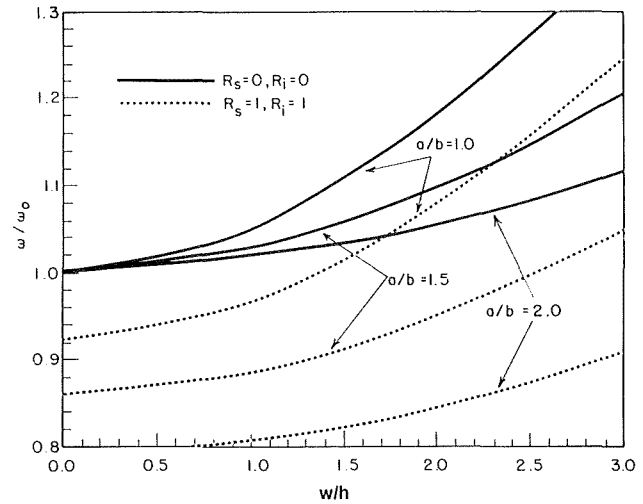

Fig. 9 Effect of aspect ratio on frequency of simply supported-clamped two-layer graphite-epoxy cross-ply plate ($a = 10\,h$)

creases. In Fig. 6 the effect of the plate thickness on the vibration of a clamped angle-ply plate is illustrated. As expected these effects are quite significant in thick plates. However it is seen that for a thin plate ($a = 20\,h$), the dynamic von Kármán-type nonlinear theory can predict the fundamental frequency with only 3 percent difference from the correct solution. In thick plates ($a = 5\,h$) these effects reduce the frequency by approximately 30 percent at infinitesimally small amplitudes and this reduction decreases with increasing the amplitude. The effect of number of layers, N, on the amplitude-frequency response of an SC graphite-epoxy angle-ply plate is shown in Fig. 7 in which the values of Ω_0 are 19.9960 for $N = 2$, 31.7766 for $N = 4$, 34.8243 for $N = \infty$. The effects of transverse shear and rotatory inertia increase with increasing N. The plate with a large number of layers mechanically behaves as a specially orthotropic plate ($N = \infty$).

Figures 8–10 show the amplitude-frequency response of a two-layer cross-ply plate with different material properties, aspect ratios, and thickness-to-span ratios. The linear frequency parameter Ω_0 in Fig. 8 is 24.5430 for a GR plate, 16.1341 for a BO plate, and 13.3415 for a GL plate. The values of Ω_0 in Fig. 9 are 19.0401, 17.5089, and 17.1692 for the aspect ratio $a/b = 1.0$, 1.5, and 2.0, respectively. The value of Ω_0 in Fig. 10 is 19.0401 for any thickness-to-span ratio. Figure 8 indicates that the effects of transverse shear and rotatory inertia are more significant for a high-modulus material than for a low-modulus material. From Fig. 9 it may be stated that the higher the aspect ratio, the higher the reduction in the frequency ratio due to these effects. This reduction decreases slightly at large amplitudes of vibration. In the case when $a/b = 2.0$ the reduction of the frequency ratio is approximately 20 percent at infinitesimally small amplitudes. Figure 10 shows the effect of the thickness-to-span ratio on the frequency-amplitude relations. Evidently the dynamic von Kármán-type nonlinear theory cannot take the variations of the thickness-to-span ratio into account. In the present case the transverse shear and rotatory inertia effects reduce the frequency of thick plates ($a = 5\,h$) by approximately 22 percent and this reduction is less than 2 percent in the case of thin plates ($a = 20\,h$). Finally, it should be stated that the effect of the rotatory inertia on plate vibrations is found to be much less significant than the shear effect.

Conclusions

A theory is established for the nonlinear flexural free vibration of unsymmetrically laminated rectangular plates including the effects of transverse shear, rotatory inertia, transverse normal stress, and transverse normal contraction or extension. The resulting equations of motion readily reduce to the existing nonlinear equations for anisotropic plates including the effects of transverse shear and rotatory inertia and dynamic von Kármán-type equations of generally laminated plates. Based on a single-mode analysis numerical results are presented for unsymmetric angle-ply and cross-ply plates with different material properties and boundary conditions and are in good agreement with available data.

From the present results some concluding remarks may be drawn.

1. The transverse normal stress increases the frequency of vibration at any amplitude of moderately thick plates. The effect of this stress on the frequency is not significant at small amplitudes but becomes somewhat significant at large amplitudes.

2. The transverse shear and rotatory inertia decrease the frequency at any amplitude of vibration. These effects decrease with increasing the amplitude and with decreasing the thickness-to-span ratio. In general these effects are not significant for the plate span greater than 20 times the thickness.

Downloaded 02 May 2010 to 171.66.16.54. Redistribution subject to ASME license or copyright; see http://www.asme.org/terms/Terms_Use.cfm

3. The higher the number of layers of plate, the higher the transverse shear and rotatory inertia effects. However, these effects increase very slowly for plates of more than four layers. At large amplitudes of vibration these effects generally are more significant for all-simply supported plates than for all-clamped plates. In addition these effects increase with increasing the tensile modulus and aspect ratio but with decreasing the orientation angle of filaments. Therefore, the vibration behavior of laminated plates are not easily predictable as homogeneous plates.

Acknowledgment

The results presented in this paper were obtained in the course of research sponsored by the Natural Sciences and Engineering Research Council of Canada and Killam Trust in Canada.

References

1 Herrmann, G., "Influence of Large Amplitudes on Flexural Motions of Elastic Plates," National Advisory Committee for Aeronautics, Technical Note 3578, Washington, D.C., May 1955.

2 Whitney, J. M., and Leissa, A. W., "Analysis of Heterogeneous Anisotropic Plates," ASME JOURNAL OF APPLIED MECHANICS, Vol. 36, 1969, pp. 261-266.

3 Medwadowski, S. J., "A Refined Theory of Elastic, Orthotropic Plates," ASME JOURNAL OF APPLIED MECHANICS, Vol. 25, 1958, pp. 437-443.

4 Ebcioglu, I. K., "A Large Deflection Theory of Anisotropic Plates," *Ingenieur-Archiv*, Vol. 33, 1964, pp. 396-403.

5 Habip, L. M., "Theory of Elastic Plates in the Reference State," *International Journal of Solids and Structures*, Vol. 2, 1966, pp. 157-166.

6 Kaul, R. K., "Finite Thermal Oscillations of Thin Plates," *International Journal of Solids and Structures*, Vol. 2, 1966, pp. 337-350.

7 Chia, C. Y., "Nonlinear Theory of Heterogeneous and Anisotropic Plates," *Proceedings of the 3rd Australasian Conference on the Mechanics of Structures and Materials*, Vol. II, Session B2-Plate Theory, University of Auckland, 1971, pp. 1-25.

8 Schmidt, R., "A Refined Nonlinear Theory of Plates With Transverse Shear Deformation," *Journal of Industrial Mathematics Society*, Vol. 27, 1977, pp. 23-37.

9 Wu, C. I., and Vinson, J. R., "Influence of Large Amplitudes, Transverse Shear Deformation, and Rotatory Inertia on Lateral Vibrations of Transversely Isotropic Plates," ASME JOURNAL OF APPLIED MECHANICS, Vol. 36, 1969, pp. 254-460.

10 Wu, C. I., and Vinson, J. R., "On the Nonlinear Oscillations of Plates Composed of Composite Materials," *Journal of Composite Materials*, Vol. 3, 1969, pp. 548-561.

11 Ambartsumyan, S. A., *Theory of Anisotropic Plates*, Technomic Publishing, 1970.

12 Sathyamoorthy, M., and Chia, C. Y., "Nonlinear Vibration of Anisotropic Rectangular Plates Including Shear and Rotatory Inertia," *Fibre Science and Technology*, Vol. 13, 1980, pp. 337-361.

13 Sathyamoorthy, M., and Chia, C. Y., "Effect of Transverse Shear and Rotatory Inertia on Large Amplitude of Anisotropic Skew Plates, Part 1—Theory, Part 2—Numerical Results," ASME JOURNAL OF APPLIED MECHANICS, Vol. 47, 1980, pp. 128-138.

14 Kanaka Raju, K., and Venkateswara Rao, G., "Axisymmetric Vibrations of Circular Plates Including the Effects of Geometric Non-Linearity, Shear Deformation and Rotatory Inertia," *Journal of Sound and Vibration*, Vol. 47, 1976, pp. 179-184.

15 Chia, C. Y., and Sathyamoorthy, M., "NonLinear Vibration of Circular Plates with Transverse Shear and Rotatory Inertia," *Journal of Sound and Vibration*, Vol. 78, 1981, pp. 131-137.

16 Sathyamoorthy, M., and Chia, C. Y., "Nonlinear Flexural Vibration of Moderately Thick Orthotropic Circular Plates," *Ingenieur-Archiv.*, Vol. 52, 1982, pp. 237-243.

17 Reddy, J. N., and Huang, C. L., "Nonlinear Axisymmetric Bending of Annular Plates With Varying Thickness," *International Journal of Solids and Structures*, Vol. 17, 1981, pp. 811-825.

18 Reddy, J. N., and Chao, W. C., "Nonlinear Oscillations of Laminated, Anisotropic, Rectangular Plates," ASME JOURNAL OF APPLIED MECHANICS, Vol. 49, 1982, pp. 396-402.

19 Chia, C. Y., and Prabhakara, M. K., "A General Mode Approach to Nonlinear Flexural Vibration of Laminated Rectangular Plates," ASME JOURNAL OF APPLIED MECHANICS, Vol. 45, 1978, pp. 623-628.

20 Reissner, E., "On the Variational Theorem for Finite Elastic Deformations," *Journal of Mathematical Physics*, Vol. 31, 1953, pp. 129-135.

21 Sivakumaran, K. S., "A Refined Theory of Generally Laminated Plates," Thesis submitted to the Faculty of Graduate Studies, The University of Calgary, in partial fulfillment of the requirements for the degree of Doctor of Philosophy, Jan. 1983.

Downloaded 02 May 2010 to 171.66.16.54. Redistribution subject to ASME license or copyright; see http://www.asme.org/terms/Terms_Use.cfm

Thermal Effect on the Transverse Vibration of High-Speed Rotating Anisotropic Disk

N. C. Ghosh
Research Associate,
Department of Mathematics,
Jadavpur University,
Calcutta, India 700 032

An attempt has been made to consider the thermal effect on the transverse vibration of a high-speed rotating disk in a steady-state heat conduction. The material of the disk, in this case, is assumed to be thermomechanically anisotropic. The present attempt is made with an objective to provide some theoretical studies on the problem that may serve as a base from which more detailed investigations with regard to the usage of composite material may be attempted to gain new and needed design information regarding turbine disks and thereby to reduce the chances of turbine failure. In this connection a new critical speed of disk rotation has been obtained and consequently this critical speed is found to depend on central temperature, thermomechanical anisotropy, and so forth.

Introduction

Due to recent aerospace and commercial applications (space shuttle, advanced air crafts, turbine structures etc.) laminated composite media are effectively utilized in high temperature environments. Now it is found that a coating in thick laminated form is capable of absorbing and thereby of reducing vibration level to a great extent. Thus study of composite media has now become essential for their possible applications in engineering systems.

In this paper, an attempt has been made to account for thermal effect on the transverse vibration of composite disk spinning with a high speed. In this study, the main emphasis is on thermomechanical anisotropy of composite media.

In recent papers [1, 2] it has been shown that flexural vibration of a spinning disk is strongly affected by the heat flow across the disk and specially by the parabolic type of temperature distribution (in fact most common temperature distributions could be approximated to a parabolic type [3]). In this connection, a more recent work [4] has become worth mentioning where the transverse vibration of a disk has been considered under possible transition of an isotropic material to anisotropic one owing to the existence of high temperature and pressure around the disk for long duration.

In this paper the topic has been divided into two parts, the first of which is confined to the evaluation of thermoelastic stresses in the rotating disk according to some recent works [4–13] in this field, while the second contains the solution and necessary discussions for thermoelastic vibration of the disk.

Contributed by the Applied Mechanics Division for publication in the JOURNAL OF APPLIED MECHANICS.
Discussion on this paper should be addressed to the Editorial Department, ASME, United Engineering Center, 345 East 47th Street, New York, N.Y. 10017, and will be accepted until two months after final publication of the paper itself in the JOURNAL OF APPLIED MECHANICS. Manuscript received by ASME Applied Mechanics Division, October, 1981; final revision, October, 1983.

Part 1: Determination of Stresses of an Anisotropic Rotating Disk in Steady-State Heat Flow

Statement of the Problem

A thin anisotropic elastic disk of radius a is assumed to be spinning uniformly about its polar axis with an angular velocity ω in a steady-state heat flow, governed by the following heat conduction equation in cylindrical coordinates (r,θ,z):

$$k_{11}\left(\frac{\partial^2 T}{\partial r^2}+\frac{1}{r}\frac{\partial T}{\partial r}\right)+k_{22}\frac{1}{r^2}\frac{\partial^2 T}{\partial \theta^2}+k_{33}\frac{\partial^2 T}{\partial z^2}=0 \tag{1}$$

where k_{11}, k_{22}, k_{33}, and T are, respectively, coefficients of thermal conductivities in radial, tangential, and thickness directions and difference of temperature.

Solution

In this problem, it is assumed that the disk is made of a material that is mechanically and thermally anisotropic. For such a disk, following stress-strain relations may be taken as a starting point:

$$\left.\begin{aligned}\sigma_r &= c_{11}\epsilon_r + c_{12}\epsilon_\theta - (c_{11}\alpha_{11}+c_{12}\alpha_{22})T\\ \sigma_\theta &= c_{12}\epsilon_r + c_{22}\epsilon_\theta - (c_{12}\alpha_{11}+c_{22}\alpha_{22})T\\ \tau_{r\theta} &= 0\end{aligned}\right\} \tag{2}$$

where

σ_r = radial stress component
σ_θ = hoop stress (tangential stress component)
c_{11}, c_{12}, c_{22} = elastic constants
ϵ_r = strain in radial direction
ϵ_θ = strain in tangential direction
α_{11} = thermal expansion coefficient in radial direction
α_{22} = thermal expansion coefficient in tangential direction

Copyright © 1985 by ASME
Downloaded 02 May 2010 to 171.66.16.54. Redistribution subject to ASME license or copyright; see http://www.asme.org/terms/Terms_Use.cfm

Following Boley and Weiner [14], it becomes very convenient for this problem to deal with average stresses P & Q where

$$P=\frac{1}{2h}\int_{-h}^{+h}\sigma_r\,dz$$
$$Q=\frac{1}{2h}\int_{-h}^{+h}\sigma_\theta\,dz \tag{3}$$

and

$2h$ = thickness of the disk

Again for a circular disk, we get from Love [15]

$$\left.\begin{aligned}\epsilon_r&=\frac{\partial u}{\partial r}-z\frac{\partial^2 w'}{\partial r^2}\\ \epsilon_\theta&=\frac{u}{r}-z\left(\frac{1}{r}\frac{\partial w'}{\partial r}+\frac{1}{r^2}\frac{\partial^2 w'}{\partial\theta^2}\right)\end{aligned}\right\} \tag{4}$$

where u, w' are components of displacement along r and z directions, respectively. Here it is to be noted that u represents a middle-surface displacement.

Now combining (2), (3), and (4) we get P and Q for a thin circular disk as:

$$\left.\begin{aligned}P&=c_{11}\frac{du}{dr}+c_{12}\frac{u}{r}-\frac{(c_{11}\alpha_{11}+c_{12}\alpha_{22})}{2h}\int_{-h}^{+h}T\,dz\\ Q&=c_{12}\frac{du}{dr}+c_{22}\frac{u}{r}-\frac{(c_{12}\alpha_{11}+c_{22}\alpha_{22})}{2h}\int_{-h}^{+h}T\,dz\end{aligned}\right\} \tag{5}$$

It can be observed from (3) that P and Q are independent of z and have to satisfy only one equation of equilibrium, namely,

$$\frac{dP}{dr}+\frac{P-Q}{r}=-\rho\omega^2 r$$

which takes the following form after elimination of P and Q.

$$c_{11}\frac{d^2u}{dr^2}+\frac{c_{11}}{r}\frac{du}{dr}-c_{22}\frac{u}{r^2}-\frac{(c_{11}\alpha_{11}+c_{12}\alpha_{22})}{2h}$$
$$\frac{d}{dr}\left[\int_{-h}^{+h}T\,dz\right]-\frac{\{(c_{11}-c_{12})\alpha_{11}+(c_{12}-c_{22})\alpha_{22}\}}{2h}$$
$$\frac{1}{r}\left[\int_{-h}^{+h}T\,dz\right]=-\rho\omega^2 r \tag{6}$$

According to Stavsky [5], here also, it may be assumed that the thermal field is independent of θ and so, the third term viz. $\partial^2 T/\partial\theta^2$ in equation (1) may be omitted in this problem. Hence T becomes a function of r and z. Under this assumption, heat conduction equation (1) reduces to the form:

$$k_{11}\left(\frac{\partial^2 T}{\partial r^2}+\frac{1}{r}\frac{\partial T}{\partial r}\right)+k_{33}\frac{\partial^2 T}{\partial z^2}=0 \tag{7}$$

Let $T=\phi\psi$ as the solution to equation (7), where ϕ and ψ are two different functions of r and z. Hence, it follows from (7)

$$\frac{1}{\phi}\left(\frac{d^2\phi}{dr^2}+\frac{1}{r}\frac{d\phi}{dr}\right)=-\frac{k_{33}}{k_{11}}\frac{1}{\psi}\frac{d^2\psi}{dz^2}=-k^2$$

where k is a real constant. Hence, we get two ordinary differential equations from the foregoing, namely;

$$\frac{d^2\phi}{dr^2}+\frac{1}{r}\frac{d\phi}{dr}+k^2\phi=0 \tag{8}$$

and

$$\frac{d^2\psi}{dz^2}-\frac{k_{11}\cdot k^2}{k_{33}}\psi=0 \tag{9}$$

It must be noted here that the equation (8) is a Bessel's equation of order zero and thereby its solution follows immediately as

$$\phi=A\,J_0(kr)+BI_0(kr)$$

where A and B are two unknown constants of integrations,

$$J_0(kr)=1-\frac{(kr)^2}{2^2}+\frac{(kr)^4}{2^2\cdot4^2}-\frac{(kr)^6}{2^2\cdot4^2\cdot6^2}$$
$$+-\ldots\ldots\ldots\ldots\ldots\ldots\ldots\ldots \tag{10}$$

and

$$I_0(kr)=J_0(kr)\log(r)+\frac{(kr)^2}{2^2}-\frac{(kr)^4}{2^2\cdot4^2}\left(1+\frac{1}{2}\right)$$
$$+\frac{(kr)^6}{2^2\cdot4^2\cdot6^2}\left(1+\frac{1}{2}+\frac{1}{3}\right)-+\ldots\ldots\ldots \tag{11}$$

It is observed from the expression (11) that $I_0(kr)$ becomes undefined at the center, i.e., at $r=0$, and so, $I_0(kr)$ should be omitted for a complete disk which can be done by equating unknown constant B to zero. Hence, the solution to equation (8), for a complete disk, is

$$\phi=A\,J_0(kr) \tag{12}$$

On the other hand, equation (9) admits of an easy solution as

$$\psi=ce^{k\sqrt{\frac{k_{11}}{k_{33}}}z}+De^{-k\sqrt{\frac{k_{11}}{k_{33}}}z} \tag{13}$$

where c and D are unknown constants of integrations. Thus, solution of heat conduction equation (7) follows from (12) and (13) as

$$T=A\left(ce^{k\sqrt{\frac{k_{11}}{k_{33}}}\cdot z}+De^{-k\sqrt{\frac{k_{11}}{k_{33}}}\cdot z}\right)J_0(kr)$$

Boundary conditions for the problem may be assumed as:

$$\frac{1}{2h}\int_{-h}^{+h}T\,dz=T_0 \qquad \text{when} \quad r=0$$
$$\frac{1}{2h}\int_{-h}^{+h}T\,dz=0 \qquad \text{when} \quad r=a$$
$$\frac{\partial}{\partial z}\left[\frac{1}{2h}\int_{-h}^{+h}T\,dz\right]=0 \qquad \text{when} \quad z=\pm h$$

Of the preceding three boundary conditions, the third one is satisfied automatically by

$$\left[\frac{1}{2h}\int_{-h}^{+h}T\,dz\right]$$

which is a function of r only. Now applying the first and second boundary conditions, we get

$$\frac{1}{2h}\int_{-h}^{+h}T\,dz=T_0\,J_0(kr) \tag{14}$$

and

$$J_0(ka)=0 \tag{15}$$

which is possible in this problem when $k=2.4/a$ (Mclachlan [19]). Therefore, we can approximate $J_0(kr)$ in the interval $0\le kr\le 2.4$ by the relation

$$J_0(kr)\cong 1-\left(\frac{r}{a}\right)^2 \tag{16}$$

Hence, we obtain from the relations (14), (15) and (16),

$$\frac{1}{2h}\int_{-h}^{+h}T\,dz=T_0\left(1-\frac{r^2}{a^2}\right) \tag{17}$$

Downloaded 02 May 2010 to 171.66.16.54. Redistribution subject to ASME license or copyright; see http://www.asme.org/terms/Terms_Use.cfm

which satisfies Leopold's [3] expression for temperature gradient curves. Now using the relation (17), we get from (6)

$$c_{11}r^2\frac{d^2u}{dr^2}+c_{11}r\frac{du}{dr}-c_{22}u+\left[\frac{T_0}{a^2}\{(3c_{11}-c_{12})\alpha_{11}+(3c_{12}-c_{22})\alpha_{22}\}+\rho\omega^2\right]r^3T_0\{(c_{11}-c_{12})\alpha_{11}+(c_{12}-c_{22})\alpha_{22}\}r=0 \tag{18}$$

For a complete disk, the solution to equation (18) will take the form:

$$u=Rr\sqrt{\frac{c_{22}}{c_{11}}}-T_0\left\{\frac{(c_{11}-c_{12})\alpha_{11}+(c_{12}-c_{22})\alpha_{22}}{c_{11}-c_{22}}\right\}r-\frac{T_0\{(3c_{11}-c_{12})\alpha_{11}+(3c_{12}-c_{22})\alpha_{22}\}+\rho\omega^2a^2}{a^2(9c_{11}-c_{22})}r^3 \tag{19}$$

where R is a constant to be determined.

Now eliminating u and T from the relations given in (5), by their respective expressions (19) and (17), we get

$$P=R(\sqrt{c_{11}c_{22}}+c_{12})r\sqrt{\frac{c_{22}}{c_{11}}}^{-1}-\frac{T_0(c_{12}^2-c_{11}c_{22})(\alpha_{22}-\alpha_{11})}{c_{11}-c_{22}}-\left\{\frac{T_0(c_{12}^2-c_{11}c_{22})(3\alpha_{22}-\alpha_{11})}{9c_{11}-c_{22}}+\frac{3c_{11}+c_{12}}{9c_{11}-c_{22}}\rho\omega^2a^2\right\}\frac{r^2}{a^2}$$

and

$$Q=R\sqrt{\frac{c_{22}}{c_{11}}}(\sqrt{c_{11}c_{22}}+c_{12})r^{\frac{c_{22}}{c_{11}}-1}+\frac{T_0(c_{12}^2-c_{11}c_{22})(\alpha_{22}-\alpha_{11})}{c_{11}-c_{22}}-\left\{\frac{3T_0(c_{12}^2-c_{11}c_{22})(3\alpha_{22}-\alpha_{11})}{9c_{11}-c_{22}}+\frac{3c_{12}+c_{22}}{9c_{11}-c_{22}}\rho\omega^2a^2\right\}\frac{r^2}{a^2} \tag{20}$$

Linking the problem with stress-free boundary condition (i.e., $P=0$, when $r=a$), we find from equation (20)

$$\left(a\sqrt{\frac{c_{22}}{c_{11}}}^{-1}\right)R=\frac{2T_0(c_{12}^2-c_{11}c_{22})(4c_{11}\alpha_{11}-3c_{11}\alpha_{22}-c_{22}\alpha_{22})(9c_{11}-c_{22})+(3c_{11}+c_{12})\rho\omega^2a^2}{(9c_{11}-c_{22})(\sqrt{c_{11}c_{22}}+c_{12})} \tag{21}$$

Substituting the foregoing value of R, the expressions for P and Q given in (20), are modified as:

$$\left.\begin{aligned}P&=\beta\left(\frac{r}{a}\right)^{\lambda-1}-\mu_1\left(\frac{r}{a}\right)^2+n\\Q&=\beta\lambda\left(\frac{r}{a}\right)^{\lambda-1}-\mu_2\left(\frac{r}{a}\right)^2+n\end{aligned}\right\} \tag{22}$$

where

$$\beta=\frac{2T_0(c_{12}^2-c_{11}c_{22})(4c_{11}\alpha_{11}-3c_{11}\alpha_{22}-c_{22}\alpha_{22})}{(9c_{11}-c_{22})(c_{11}-c_{22})}$$

$$+\frac{3c_{11}+c_{12}}{9c_{11}-c_{22}}\rho\omega^2a^2 \tag{22a}$$

$$\lambda=\sqrt{\frac{c_{22}}{c_{11}}} \tag{22b}$$

$$\mu_1=\frac{T_0(c_{12}^2-c_{11}c_{22})(3\alpha_{22}-\alpha_{11})}{9c_{11}-c_{22}}+\frac{(3c_{11}+c_{12})\rho\omega^2a^2}{9c_{11}-c_{22}} \tag{22c}$$

$$\mu_2=\frac{3T_0(c_{12}^2-c_{11}c_{22})(3\alpha_{22}-\alpha_{11})}{9c_{11}-c_{22}}+\frac{(3c_{12}+c_{22})\rho\omega^2a^2}{9c_{11}-c_{22}} \tag{22d}$$

$$\eta=\frac{T_0(c_{12}^2-c_{11}c_{22})(\alpha_{22}-\alpha_{11})}{c_{11}-c_{22}} \tag{22e}$$

Part 2: Transverse Vibration of High-Speed Rotating Disk

Here also P and Q will represent mean radial and tangential stresses which obviously remain unaffected for a small transversal deflection w normal to undisturbed central plane of the disk. The equation of transverse motion of any elementary mass $2hpr\delta\theta\delta r$ of the thin disk, possessing negligibly small flexural rigidity, will take the form [1]:

$$\rho\frac{\partial^2w}{\partial t^2}=\frac{1}{r}\frac{\partial}{\partial r}\left(Pr\frac{\partial w}{\partial r}\right)+\frac{Q}{r^2}\frac{\partial^2w}{\partial\theta^2} \tag{23}$$

where t = time variable.

Solution

Considering w in the form

$$w=W\,\mathrm{Cos}S\theta\mathrm{Cos}pt \tag{24}$$

and eliminating P and Q from (23) by their expressions given in (22), we find that the equation of motion (23) is modified as:

$$\left(x^{\lambda+1}-\frac{\mu_1}{\beta}x^4+\frac{\eta}{\beta}x^2\right)\frac{d^2W}{dx^2}+\left(\lambda x^\lambda-\frac{3\mu_1}{\beta}x^3+\frac{\eta}{\beta}x\right)\frac{dW}{dx}-\left(\lambda S^2x^{\lambda-1}-\frac{\mu_2S^2+\rho p^2a^2}{\beta}x^2+\frac{\eta}{\beta}S^2\right)W=0 \tag{25}$$

where W is a function of r only, and $x=r/a$. Here it is important as well as interesting to note that it appears from the expressions (22a) and (22e) that η/β becomes very very small for a high-speed rotating disk. As such we may neglect η/β from equation (25) for its negligible contribution.

Hence the preceding equation can be rewritten as:

$$\left(x^{\lambda-1}-\frac{\mu_1}{\beta}x^2\right)\frac{d^2W}{dx^2}+\left(\lambda x^{\lambda-2}-\frac{3\mu_1}{\beta}x\right)\frac{dW}{dx}-\left(\lambda S^2x^{\lambda-3}-\frac{\mu_2S^2+\rho p^2a^2}{\beta}\right)W=0 \tag{26}$$

The solution to the foregoing equation can be obtained as a series of the form:

Downloaded 02 May 2010 to 171.66.16.54. Redistribution subject to ASME license or copyright; see http://www.asme.org/terms/Terms_Use.cfm

$$W=\sum_{\nu=0}^{m} C_{\delta-\nu\alpha}x^{\delta-\nu\alpha} \tag{27}$$

where

$$\alpha=\lambda-3<0 \tag{27a}$$

δ is the lowest degree of x in the series and $C_{\delta-\nu\alpha}$ are constants to be determined.

Inserting this expression for W in equation (26), we get

$$\sum_{\nu=0}^{m}\{(\delta-\nu\alpha)(\delta-\nu\alpha+\alpha+2)-\lambda S^2\}C_{\delta-\nu\alpha}x^{\delta-\nu\alpha+\alpha}$$

$$-\left\{\frac{\mu_1}{\beta}(\delta-\nu\alpha)(\delta-\nu\alpha+2)-\frac{\mu_2 S^2+\rho p^2a^2}{\beta}\right\}C_{\delta-\nu\alpha}x^{\delta-\nu\alpha}=0 \tag{28}$$

Remembering (27*a*), we know α is negative and $(\delta-\nu\alpha+\alpha)$ will, therefore, be always less than $\delta-\nu\alpha$. Now equating the coefficient of $x^{\delta-\nu\alpha+\alpha}$ to zero, we get

$$\frac{C_{\delta-\nu\alpha}}{C_{\delta}-\nu\alpha+\alpha}=\frac{\mu_1(\delta-\nu\alpha+\alpha)(\delta-\nu\alpha+\alpha+2)-(\mu_2 S^2+\rho p^2a^2)}{\beta\{(\delta-\nu\alpha)(\delta-\nu\alpha+\alpha+2)-\lambda S^2\}} \tag{29}$$

Since δ is the lowest degree in the series (27), $C_{\delta+\alpha}$ must be zero.

Therefore it follows from (29)

$$\delta^2+(\alpha+2)\delta-\lambda S^2=0$$

which gives

$$\delta=\frac{-(\alpha+2)+\sqrt{(\alpha+2)^2+4\lambda S^2}}{2} \tag{29a}$$

Now it should be noted that the other value of δ viz.

$$\frac{-(\alpha-2)-\sqrt{(\alpha+2)^2+4\lambda s^2}}{2}$$

(which is a negative quantity) renders infinite deflection to the center of the disk during vibration and so, this value of δ has been ignored in the present problem. Henceforth, by δ, we shall mean its positive value given in (29*a*).

With the help of (29*a*), we can now write recurrence relation (29) in more compact form as:

$$\frac{C_{\delta-\nu\alpha}}{C_{\delta-\nu\alpha+\alpha}}=-\frac{\mu_1(\delta-\nu\alpha+\alpha)(\delta-\nu\alpha+\alpha+2)-(\mu_2 S^2+\rho p^2a^2)}{\nu\alpha\beta(2\delta-\nu\alpha+\alpha+2)} \tag{29b}$$

$$\mu_1(\delta-m\alpha)(\delta-m\alpha)(\delta-m\alpha+2)-(\mu_2 S^2+\rho p^2a^2)=0$$

or

$$p^2=\frac{\mu_1(\delta-m\alpha)(\delta-m\alpha+2)-\mu_2 S^2}{\rho a^2} \tag{30}$$

The foregoing relation (30) has a special significance relating to the present problem. This equation will help us to determine the frequency of vibration when number of terms of the series (27) will be known. As such the relation is better to be known as "frequency equation." However, we can write this recurrence relation (29*b*) in the following form, introducing the expression for p^2 in (29*b*).

$$\frac{C_{\delta-\nu\alpha}}{C_{\delta-\nu\alpha+\alpha}}=-\frac{\mu_1(m-\nu+1)\{2\delta+2-(m+\nu-1)\alpha\}}{\nu\beta\{2\delta+2-(\nu-1)\alpha\}} \tag{31}$$

Here it can be proved very easily that the factor

$$\frac{2\delta+2-(m+\nu-1)\alpha}{2\delta+2-(\nu-1)\alpha}$$

will remain positive for all possible values of ν in this problem. Hence the exact solution to the equation of motion (23) will be

$$w=C_{\delta}x^{\delta}\left\{1-\frac{\mu_1}{\beta}\frac{m(2\delta+2-m\alpha)}{1\cdot(2\delta+2)}x^{-\alpha}\right.$$

$$+\frac{\mu_1^2}{\beta^2}\frac{m(m-1)\{2\delta+2-m\alpha\}\{2\delta+2-(m+1)\alpha\}}{1\cdot2\cdot(2\delta+2)(2\delta+2-\alpha)}x^{-2\alpha}$$

$$\left.-+\ldots\ldots\ldots\ldots\right\}\mathrm{Cos}S\theta\mathrm{Cos}pt \tag{32}$$

Following a similar method, the solution of equation of motion may be constructed for positive α. The case $\alpha=0$ is not valid here as the case leads $(9c_{11}-c_{22})$, denominator of so many expressions, to vanish.

Discussion

It becomes interesting to note that the factor μ_1/β reduces to unity if we do not consider the thermal influence. Consequently the expression (32) for w makes an exact tally with the expression for deflection obtained in the previous paper [4] relating to the transverse vibration of spinning aeolotropic disk.

It is important here to remember that the series contains only $(m+1)$ terms which are alternately positive and negative due to the factor

$$\frac{2\delta+2-(m+\nu-1)\alpha}{2\delta+2-(\nu-1)\alpha}$$

which always remains positive for all possible ν in this problem. In this connection it must be noted that these $(m+1)$ terms lead w to vanish over the circumferences of m different concentric circles and thereby introduce m nodal circles. On the other hand, $\mathrm{Cos}S\theta$ produce S equidistant nodal diameters. Consequently these nodal lines represent different modes of vibrations and thereby become very significant for determining deflections of the disk and frequencies of vibrations. To illustrate and explain the importance and utility of these lines, we may take the following special modes of vibrations.

For the first instance, let us suppose that the mode of vibration consists of only one nodal diameter and of no-nodal circle, i.e., $S=1$, and $m=0$.

In this case, it follows from (27) and (29*a*), $\delta=1$ and consequently it also follows from (30) and (32).

$$p=\omega$$

and

$$w=c_1\frac{r}{a}\mathrm{Cos}\theta\mathrm{Cos}\omega t$$

Here it is very easy to observe that under this mode of vibration, frequency and deflection remain free from the thermal and anisotropic effect. This has happened here due to thermomechanical independence of the factor $(3\mu_1-\mu_2)$. Consequently the foregoing results make a good tally with the results obtained in connection with "thermal effect on the transverse vibration of isotropic rotating disk," [1, 2] and "transverse vibration of rotating aeolotropic disk" [4].

Let us consider another example where mode of vibration having one nodal circle and no nodal diameter. In this case we obtain from (29*a*), (30), and (32) through very easy calculations, $\delta=0$,

$$\text{radius of nodal circle} = a\left\{\frac{\mu_1}{\beta}\cdot\frac{2-\alpha}{2}\right\}^{1/\alpha},$$

$$p=\left\{\frac{\mu_1\alpha(\alpha-2)}{\rho\beta a^2}\right\}^{1/2},$$

and

$$w=C_0\left\{1-\frac{\mu_1}{\beta}\cdot\frac{(2-\alpha)}{2}\left(\frac{r}{a}\right)^{-\alpha}\right\}\mathrm{Cos}pt.$$

Thus it appears from the foregoing that due to the existence of

Downloaded 02 May 2010 to 171.66.16.54. Redistribution subject to ASME license or copyright; see http://www.asme.org/terms/Terms_Use.cfm

the factor μ_1/β (which can be expressed in terms c_{11}, c_{12}, c_{22} and T_0), nodal circle, frequency and deflection suffer considerable thermal affect on them.

Besides these nodal lines, the frequency equation (30) has some more significant features in this problem. This frequency equation leads to some interesting results when we write the equation in an alternative form as below:

$$p^2 = f^2 - \Delta(f^2 - S^2\omega^2) \tag{33}$$

where

$$f^2 = \left\{ \frac{3c_{11}+c_{12}}{9c_{11}-c_{22}} (\delta - m\alpha)(\delta - m\alpha + 2) - \frac{3c_{12}+c_{22}}{9c_{11}-c_{22}} S^2 \right\} \omega^2 \tag{34}$$

and

$$\Delta = \frac{T_0(c_{11}c_{22} - c_{12}^2)(3\alpha_{22} - \alpha_{11})}{(3c_{11}+c_{12})\rho\omega^2 a^2} \tag{35}$$

Here, f specifies the period of lateral vibration of an anisotropic rotating disk ignoring thermal influence on the disk. Consequently f makes an exact tally with result of paper [4] previously obtained under the same condition. Moreover, the factor Δ indicates the thermal effect on the frequency of vibration. It is very clear that for positive $(f^2 - S^2\omega^2)$, p will be less than f due to thermal influence. Hence we can conclude that the square of the natural frequency will be reduced by the factor $\Delta(f^2 - S^2\omega^2)$ when thermal distribution is considered.

Another interesting case arises while we consider w to vary as $\mathrm{Cos}(S\theta \pm pt)$ instead of $\mathrm{Cos}S\theta\mathrm{Cos}pt$. The factor $\mathrm{Cos}(S\theta \pm pt)$ does not change our previous results but produces two trends of traveling waves carried around the disk; one with backward angular speed $-p/S$ and other with forward angular speed p/S. The existence of these two traveling waves were experimentally observed by Campbell [16]. It was also observed there, while these backward traveling waves coincide with the forward speed of the disk, a standing wave is formed that ultimately causes failure of the turbine disk. Hence we may write down the condition for the formation of standing waves as

$$\omega = p/s \tag{36}$$

Thus it follows from (33)

$$(\Delta - 1)(f^2 - S^2\omega^2) = 0$$

which gives us two conditions, viz.

$$f^2 - S^2\omega^2 = 0$$

and

$$\Delta = 1$$

Of the preceding two conditions the first one, viz. $f^2 - S^2\omega^2 = 0$ corresponds to the condition of disk failure in absence of heating effect and consequently is quite in agreement with Campbell's condition [16]. On the other hand, the second condition, i.e. $\Delta = 1$ leads us to an important and interesting feature of the present discussion.

If we, now, expand Δ in terms of c_{11}, c_{12}, c_{22}, α_{11}, α_{22} etc., we get from (35) that

$$\omega^2 = \frac{T_0(c_{11}c_{22} - c_{12}^2)(3\alpha_{22} - \alpha_{11})}{(3c_{11}+c_{12})\rho a^2} \tag{37}$$

Thus we see that this value of ω^2 gives us one more condition of disk failure owing to thermal effect under consideration. Hence, it may be logical to interpret this particular value of ω as a critical speed of the disk that leads to a failure and so, we wish to denote, henceforth, this critical speed by ω_c. Moreover, it is quite easy to observe the dependence of ω_c on the thermomechanical anisotropy of the disk material, size of the disk, and temperature at center of the disk. Hence to avoid such a critical condition, selection of material and size of the disk become important for design consideration. Thus inclusion of some examples may be significant for the present discussion. Before going to include examples it is better to make some conversions as below:

$$\frac{c_{22}}{c_{11}c_{22} - c_{12}^2} = \frac{1}{E_1}$$

$$\frac{c_{11}}{c_{11}c_{22} - c_{12}^2} = \frac{1}{E_2}$$

$$\sigma_{12} = \frac{c_{12}}{c_{11}}$$

$$\sigma_{21} = \frac{c_{12}}{c_{22}}$$

where

E_1 = Young's modulus in radial direction
E_2 = Young's modulus in tangential direction
σ_{12} = Poisson's ratio for radial strain
σ_{21} = Poisson's ratio for tangential strain

Hence the critical speed, ω_c, can be written as

$$\omega_c = \left\{ \frac{T_0 E_2(3\alpha_{22} - \alpha_{11})}{(3+\sigma_{12})\rho a^2} \right\} \tag{37a}$$

By means of following conversions, we can find ω_c for isotropic case:

$$E_1 = E_2$$

$$\sigma_{12} = \sigma_{21}$$

$$\alpha_{11} = \alpha_{22}$$

and thereby

$$\omega_c = \left\{ \frac{2T_0 E_1 \alpha_{11}}{(3+\sigma_{12})\rho a^2} \right\}^{1/2} \tag{37b}$$

Now if we consider such a thermal situation that rate of generation of heat is fixed amount Q per unit volume, then

$$\frac{d}{dr}\left[\frac{1}{2h} \int_{-h}^{+h} T\, dz \right] = -\frac{Q}{2k^*}$$

where k^* is the thermal conductivity.

Hence

$$\frac{2T_0}{a^2} = \frac{Q}{2k^*}$$

Substituting this value in (37b), we get

$$\omega_c = \left\{ \frac{E_1 \alpha_{11} Q}{2k^* \rho(3+\sigma_{12})} \right\}^{1/2}$$

which makes a tally with the result previously obtained by the author [1,2] for isotropic disks.

Acknowledgment

The author would like to convey his sincere thanks and gratitude to Dr. B. B. Chatterjee, Head, Department of Mathematics, Jadavpur University, Calcutta, India 700032, for his inspiration and interest during the progress of the work. This work has been performed under the research project sponsored by the Council of Scientific and Industrial Research, India.

References

1 Ghosh, N. C., "Thermal Effect on the Transverse Vibration of Spinning Disk," *Indian Journal of Pure and Applied Mathematics*, Vol. 5, No. 2, 1974, pp. 137-146.

2 Ghosh, N. C., "Thermal Effect on the Transverse Vibration of Spin-

Downloaded 02 May 2010 to 171.66.16.54. Redistribution subject to ASME license or copyright; see http://www.asme.org/terms/Terms_Use.cfm

ning Disk of Variable Thickness," ASME JOURNAL OF APPLIED MECHANICS, Vol. 42, 1975, pp. 358-362.

3 Leopold, W. R., "Centrifugal and Thermal Stresses in Rotating Disks," ASME JOURNAL OF APPLIED MECHANICS, Vol. 15, Dec. 1948, pp. 322-326.

4 Ghosh, N. C., "The Transverse Vibration of Spinning Aeolotropic Disk," *Czechoslovak Journal of Physics*, Vol. *B* 23, 1973, pp. 506-511.

5 Stavsky, Y., "Thermoelastic Stability of Laminated Orthotropic Circular Plates," *Acta Mechanica*, Vol. 22, 1975, pp. 32-51.

6 Tauchert, T. R., and Aköz, A. Y., "Stationary Temperature and Stress Fields in an Anisotropic Elastic Slab," ASME JOURNAL OF APPLIED MECHANICS, Vol. 42, 1975, pp. 647-650.

7 Tauchert, T. R., and Aköz, A. Y., "Thermal Stresses in an Orthotropic Elastic Slab Due to Prescribed Surface Temperatures," ASME JOURNAL OF APPLIED MECHANICS, Vol. 41, 1974, pp. 222-228.

8 Clements, D. L., "Thermal Stresses in an Anisotropic Elastic Half Space," SIAM *Journal of Applied Mathematics*, Vol. 24, No. 3, 1973, pp. 332-337.

9 Padovan, J., "Thermoelasticity of Cylindrically Anisotropic Generally Laminated Cylinders," ASME JOURNAL OF APPLIED MECHANICS, Vol. 43, 1976, pp. 124-130.

10 Bufler, H., "Theory of Elasticity of a Multilayered Medium," *Journal of Elasticity*, Vol. 1, 1971, pp. 125-130.

11 Ryabov, A. F., "Thermoelastic Problem of Multilayer Plates," *Prikladnaya, Mekhanika*, Vol. 3, 1967, p. 16.

12 Padovan, J., "Thermoelasticity of Anisotropic Generally Laminated Slabs Subject to Spatially Periodic Thermal Loads," ASME JOURNAL OF APPLIED MECHANICS, Vol. 42, 1975, pp. 341-346.

13 Pell, W. H., "Thermal Deflections of Anisotropic Thin Plates," *Quart. Appl. Math.*, Vol. 4, Apr. 1946, pp. 27-44.

14 Boley, B. A., and Weiner, J. H., *Theory of Thermal Stresses*, 2nd Ed., Wiley, New York, 1962.

15 Love, A. E. H., *A Treatise on the Mathematical Theory, of Elasticity*, 4th Ed., Dover, 1927.

16 Campbell, W., "The Protection of Steam Turbine Disk Wheels from Axial Vibrations," Trans. ASME, Vol. 46, 1924, pp. 31-160.

17 Ashton, J. E., Halpin, J. C., and Petit, P. H., *Primer on Composite Materials: Analysis*," Technomic Publishing Co., Westport, Conn., 1969.

18 "Plastics for Aerospace Vehicles, Part I, Reinforced Plastics," Military Hand Book 17A, Jan. 1971.

19 Mclachlan, N. W., *Bessel Function for Engineers*, Oxford, 1934.

Downloaded 02 May 2010 to 171.66.16.54. Redistribution subject to ASME license or copyright; see http://www.asme.org/terms/Terms_Use.cfm

Vibration and Stability of Circular Plates Under Partially Distributed or Concentrated Inplane Loads

Y. Narita
Lecturer,
Computer Center,
Hokkaido Institute of Technology,
Teine Maeda 419-2,
Sapporo, Japan 061-24

A method is presented for analyzing the free transverse vibration and elastic stability of circular plates under nonuniform distribution of the inplane stresses. A general solution procedure is developed, and a frequency equation is derived for the case when a pair of loads are locally distributed in the plane along the edge. Numerical results are presented for natural frequencies and buckling loads of the plates, and the effect of the partial inplane loading is discussed. A limiting case for a concentrated inplane load is also considered.

Introduction

The transverse vibration and stability problem of plate elements has been of considerable importance in engineering, and a great number of publications have resulted [1]. For problems of solid circular plates, an analytical solution was presented by Wah [2], and the Ritz and Galerkin solutions have been obtained by Laura and his co-workers [3–5] to calculate fundamental frequencies and buckling loads. Pardoen [6, 7] dealt with the problem by the finite element approach. Jain [8] and Gupta and Lal [9] analyzed circular plates of variable thickness by a Frobenius' method, and this problem was also solved by the Ritz method [10]. Recently, Celep [11, 12] studied dynamic stability of free circular plates under nonconservative loading. These papers are all concerned with circular plates subjected to *uniform* inplane loads.

In practical applications, structural elements are supported by the surrounding structure and undergo complicated actions of inplane loads. Therefore, such effects of nonuniform inplane forces should be included in the analysis to yield more meaningful results. There are, however, only a limited number of papers that deal with the problem with consideration of nonuniform loading. In 1957, a buckling problem of a circular plate subjected to a pair of local inplane forces was studied by Yamaki [13]. Recent related publications are that of Zajaczkowski [14] for a circular plate subjected to a tangent uniform or concentrated forces, and that of Srinivasan and Ramamurti [15] which treats inplane response of an annular disk under concentrated loads. Virtually, no papers are found that propose a method of analysis that takes into account arbitrary distribution of the inplane forces.

In the paper presented here, an attempt was made to develop a general solution procedure for the vibration and stability analysis under arbitrary distribution of the inplane forces. For this purpose, a Galerkin method was applied to the governing differential equation of motion, wherein an exact solution of a circular plate without inplane loading is used as an admissible function for deflection of the plate. Nonuniform load distribution along the boundary was accommodated by expanding it into Fourier series, and the stresses were determined by making use of Airy stress function. By substituting the inplane stresses thus obtained into the Galerkin integral, a frequency equation was derived for the plates considered. Numerical results are presented for natural frequencies and buckling loads of circular plates subjected to constant inplane loads added along two opposite parts of the edge. As a special case, an interesting problem of the circular plate undergoing concentrated loading is considered.

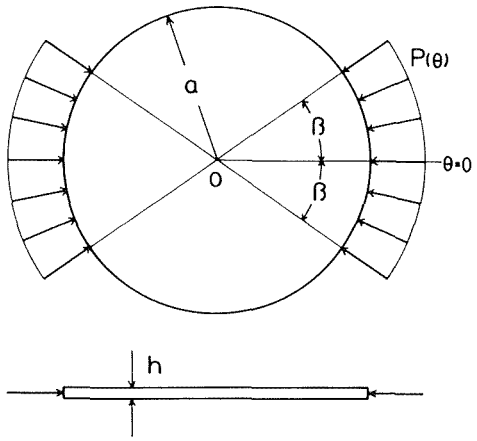

Fig. 1 Circular plate under nonuniform inplane loads

Equation of Motion

Consider a thin homogeneous solid circular plate of radius a, as shown in Fig. 1, under normal inplane forces $N_r(r, \theta)$, $N_\theta(r, \theta)$ and a shear force $N_{r\theta}(r, \theta)$. The governing differential equation of motion is given in nondimensional form by

Contributed by the Applied Mechanics Division for publication in the JOURNAL OF APPLIED MECHANICS.
Discussion on this paper should be addressed to the Editorial Department, ASME, United Engineering Center, 345 East 47th Street, New York, NY. 10017, and will be accepted until two months after final publication of the paper itself in the JOURNAL OF APPLIED MECHANICS. Manuscript received by ASME Applied Mechanics Division, June, 1984.

Copyright © 1985 by ASME
Downloaded 02 May 2010 to 171.66.16.54. Redistribution subject to ASME license or copyright; see http://www.asme.org/terms/Terms_Use.cfm

$$L(w)=(\bar{\nabla}^4-\Omega^4)W-\bar{N}_\eta\frac{\partial^2 W}{\partial\eta^2}-\bar{N}_\theta\left(\frac{1}{\eta}\frac{\partial W}{\partial\eta}+\frac{1}{\eta^2}\frac{\partial^2 W}{\partial\theta^2}\right)$$

$$-2\bar{N}_{\eta\theta}\frac{\partial}{\partial\eta}\left(\frac{1}{\eta}\frac{\partial W}{\partial\theta}\right)=0 \tag{1}$$

($\eta = r/a$), where $W(\eta, \theta)$ is deflection of the plate; $\bar{\nabla}^4$ is the biharmonic operator (i.e., $\bar{\nabla}^4 = \bar{\nabla}^2\bar{\nabla}^2, \bar{\nabla}^2 = \partial^2/\partial\eta^2 + (1/\eta)\partial/\partial\eta + (1/\eta^2)\partial^2/\partial\theta^2$); $\Omega^4 = \omega^2 a^4\rho h/D$ is a frequency parameter with ω being the radian frequency of free vibration, ρ being mass per unit volume and h being the uniform plate thickness; and $D = Eh^3/12(1-\nu^2)$ is the flexural ridigity given in terms of Young's modulus E, Poisson's ratio ν, and the thickness. The nondimensional inplane forces $\bar{N}_\eta$, $\bar{N}_\theta$ and $\bar{N}_{\eta\theta}$ are obtained by multiplying (a^2/D) to dimensional quantities N_r, N_θ, and $N_{r\theta}$, respectively. The overall operators in equation (1) are defined by L.

Since a general exact solution to equation (1) hardly appears possible, a Galerkin method is applied here to the equation of motion. An admissible function for the deflection of plate is expressed as

$$W_{mn}(\eta,\theta)=\sum_{m=0}^{M}\sum_{n=0}^{N}(A_{mn}F_{mn}(\eta)\cos n\theta+A^*_{mn}F_{mn}(\eta)\sin n\theta) \tag{2}$$

where A_{mn}, A^*_{mn} are undetermined coefficients. Equation (2) is assumed to be an exact solution for a solid circular plate with no inplane loads, and therefore $F_{mn}(\eta)$ takes the form of

$$F_{mn}(\eta)=J_n(\lambda_{mn}\eta)+C_nI_n(\lambda_{mn}\eta) \tag{3}$$

where J_n and I_n are regular and modified Bessel functions of the first kind, respectively. An unknown coefficient C_n and eigenvalue λ_{mn} are determined from the boundary conditions in terms of deflection W. For plates elastically constrained by rotational and translational springs with spring constants K and $\bar{K}$, respectively, the boundary conditions are given by

$$M_\eta-(K/a)\partial w/\partial\eta=0,\quad V_\eta+\bar{K}w=0 \tag{4}$$

where M_η and V_η are bending moment and Kirchhoff shear force, respectively, in radial direction. When one considers symmetric and antisymmetric deflections with regard to $\theta = 0$ in case of the symmetric inplane loading, the terms of $\cos n\theta$ and $\sin n\theta$ in equation (2) can be treated separately.

By use of equations (1) and (2), the Galerkin integral is expressed by

$$\int_0^1\int_0^{2\pi}L(W_{mn})W_{kl}\eta\,d\theta\,d\eta=0 \tag{5}$$

$$(k=0,1,\ldots,M;l=0.1,\ldots,N)$$

where $L(W_{mn})$ is a residual caused by substituting an approximate solution W_{mn} into equation (1), and W_{kl} is a weighting function. Since W_{mn} is the exact solution of equation $(\bar{\nabla}^4-\lambda^4_{mn})W=0$, the first term $(\bar{\nabla}^4-\Omega^4)W_{mn}$ in $L(W_{mn})$ is replaced by $(\lambda^4_{mn}-\Omega^4)W_{mn}$. This process of replacing $\bar{\nabla}^4$ (nine operators in polar coordinates) by constants (eigenvalues) reduces significantly the amount of analytical and computational procedures.

Determination of the Inplane Forces

The two-dimensional stress distribution is determined by obtaining a solution to equation $\nabla^4\phi(r,\theta)=0$ expressed in terms of Airy stress function ϕ, which is related to the stresses by

$$\sigma_r(r,\theta)=\frac{1}{r}\frac{\partial\phi}{\partial r}+\frac{1}{r^2}\frac{\partial^2\phi}{\partial\theta^2},\quad \sigma_\theta(r,\theta)=\frac{\partial^2\phi}{\partial r^2}$$

$$\tau_{r\theta}(r,\theta)=-\frac{\partial}{\partial r}\left(\frac{1}{r}\frac{\partial\phi}{\partial\theta}\right) \tag{6}$$

The inplane normal load distributed symmetrically about $\theta = 0$ is expanded into the Fourier series as

Table 1 Convergence of frequency parameters for a simply supported circular plate under partial inplane loading; $\nu = 0.3$

(a) $\beta/\pi = 0.25$, $\gamma = 4$ Number of i	SS − 1	SS-2	SS-3
5	3.571	24.21	28.97
10	3.572	24.22	28.96
15	3.572	24.22	28.96
	[a](3.572)	(24.22)	(28.96)
	[b](3.572)	(24.22)	(28.96)
20	3.572	24.22	28.96
(b) $\beta/\pi = 1/90$, $\gamma = 100$ Number of i	SS-1	SS-2	SS-3
5	3.225	19.82	31.55
10	3.232	18.25	32.04
15	3.274	17.65	32.18
	[a](3.269)	(17.46)	(32.16)
20	3.306	17.39	32.23
25	3.412	17.25	32.25
30	3.415	17.19	32.26

[a]( ): 16 × 16 matrix
[b]( ): 16 points integration

Table 2 Comparison of fundamental frequency parameters for simply supported and clamped circular plates under uniform loading: $\nu = 0.3$, $\beta/\pi = 0.5$

	Simply supported circular plate		Clamped circular plate	
γ	Present	Laura [4]	Present	Laura [4]
−20	11.843	11.842	15.495	15.491
−10	9.073	9.073	13.147	13.146
0	4.935	4.935	10.216	10.217
2	3.571	3.571	9.512	9.512
4	1.072	1.071	8.746	8.747

$$P(\theta)=p_0\left(L_0+\sum_{i=1}^{\infty}L_i\cos i\theta\right) \tag{7}$$

where p_0 is a load constant, and L_0 and L_i are Fourier coefficients. When one considers only normal loading to the edge, the boundary conditions become

$$\sigma_r(a,\theta)=-P(\theta),\quad \tau_{r\theta}(a,\theta)=0 \tag{8}$$

For problems of a single-connected body, like a solid circular plate here, the stresses are uniquely determined only by use of boundary conditions related to stresses. A general solution having only relevant terms [16] is substituted into equations (6), and with use of the boundary conditions in equations (8), nondimensional inplane forces through the plate thickness are determined as follows.

$$\bar{N}_\eta(\eta,\theta)=-\gamma\left[L_0+\sum_{i=1}^{\infty}\frac{L_i}{2}\{i\eta^{i-2}-(i-2)\eta^i\}\cos i\theta\right]$$

$$\bar{N}_\theta(\eta,\theta)=-\gamma\left[L_0-\sum_{i=1}^{\infty}\frac{L_i}{2}\{i\eta^{i-2}-(i+2)\eta^i\}\cos i\theta\right] \tag{9}$$

$$\bar{N}_{\eta\theta}(\eta,\theta)=\gamma\sum_{i=1}^{\infty}\frac{L_i}{2}i(\eta^{i-2}-\eta^i)\sin i\theta$$

with $\gamma = p_0 ha^2/D$.

Frequency Equation of the Problem

The frequency equation is derived, by substituting the inplane forces (9) into equation (5), as

$$\sum_{m=0}^{M}\sum_{n=0}^{N}\left((\lambda^4_{mn}-\Omega^4)\int_1^{(0)}\delta_{nl}+\gamma\left[L_0\int_1^{*(0)}\delta_{nl}+\sum_{i=1}^{\infty}\frac{L_i}{4}\left[\left\{i\int_{i-1}^{(2)}\right.\right.\right.$$

$$\left.\left.\left.-(i-2)\int_{i+1}^{(2)}-i\int_{i-2}^{(1)}+(i+2)\int_i^{(1)}\right\}g_c\right.\right.$$

Downloaded 02 May 2010 to 171.66.16.54. Redistribution subject to ASME license or copyright; see http://www.asme.org/terms/Terms_Use.cfm

$$+n^2\left\{i\oint_{i-3}^{(0)}-(i+2)\oint_{i-1}^{(0)}\right\}g_c$$

$$-2ni\left\{\oint_{i-3}^{(0)}-\oint_{i-1}^{(0)}-\oint_{i-2}^{(1)}+\oint_{i}^{(1)}\right\}g_s\Big]\Big]\Big)_{,mnkl}A_{mn}=0 \quad (10)$$

$$(k=0,1,\ldots,M;l=0,1,\ldots,\mathcal{N})$$

where

$$\oint_{t,mnkl}^{(q)}=\int_0^1\eta^t\frac{d^{(q)}}{d\eta^{(q)}}F_{mn}(\eta)\cdot F_{kl}(\eta)d\eta \quad (11)$$

In particular, $\oint_1^{*(0)}$ is a simplified expression given by

$$\oint_{1,mnkl}^{*(0)}=\int_0^1\eta(\bar{\nabla}^2F_{mn}(\eta))\cdot F_{kl}(\eta)d\eta$$

$$=-\lambda_{mn}^2\int_0^1\eta\bar{F}_{mn}(\eta)\cdot F_{kl}(\eta)d\eta \quad (12)$$

where $\bar{F}_{mn}(\eta)$ is an equation in which C_n is replaced by $-C_n$ in $F_{mn}(\eta)$; and g_c and g_s are given as

$$\begin{aligned}g_c &= \pm\delta_{(n+l)i}+\delta_{(n-l)i}+\delta_{(l-n)i}\\ g_s &= \pm\delta_{(n+l)i}+\delta_{(n-l)i}-\delta_{(l-n)i}\end{aligned} \quad (13)$$

with δ being Kronecker's delta, and the signs take (+) for symmetric ($\cos n\theta$) mode and (−) for antisymmetric ($\sin n\theta$) mode. The definite integrals in equations (11) and (12) are calculated numerically by the Gauss-Legendre quadrature, and the differentials therein are evaluated by the well-known formulas of Bessel functions. The determination of the eigenvalues in equation (10) is the standard eigenvalue problem, since $\oint_1^{(0)}$ multiplied to the eigenvalue Ω^4 is zero for $m \neq k$ due to the normalized relation.

Numerical Results

Numerical results are presented for the circular plates where the deflection is rigidly constrained but the rotation is elastically constrained with a spring constant $\kappa = K(a/D)$, and the constant inplane loads are distributed along two opposite parts ($-\beta < \theta < \beta$, $\pi-\beta < \theta < \pi+\beta$) of the edge, as shown in Fig. 1. In this case, Fourier coefficients used in equation (7) are given by $L_0 = 2\beta/\pi$, and $L_i = (4/i\pi)\sin i\beta$ for $i = 2, 4, \ldots$ and $L_i = 0$ for $i = 1,3, \ldots$. Mode shapes fall into either symmetric or antisymmetric mode with regard to the two axes of $\theta = 0$ and $\theta = \pi/2$, thereby resulting in four classes of symmetry. In the frequency equation, one must take $\cos n\theta$ ($n = 0,2, \ldots$) for the SS mode, $\cos n\theta$ ($n = 1,3, \ldots$) for the SA mode, $\sin n\theta$ ($n = 1,3 \ldots$) for the AS mode, and $\sin n\theta$ ($n = 2,4, \ldots$) for the AA mode. Poisson's ratio ν is taken as 0.3 throughout in the paper.

Table 1 presents a convergence study of frequency parameters Ω^2 as the number of term i in equation (7) is increased for the fixed number of terms $m \times n = 3 \times 3$ (9×9 matrix) with the 10-points numerical integration. Case (*a*) deals with that of the compression load ($\gamma = 4$) distributed along half of the edge, and the frequencies calculated for SS modes present excellent convergence characteristics. The values in (*a*)( ) and (*b*)( ) are results obtained by use of $m \times n = 4 \times 4$ (16×16 matrix) and numerical integration of 16 points, respectively, and the identical values are found in all trials. In case (*b*), the large compression load ($\gamma = 100$) acting along very small portions of the edge ($\beta/\pi = 1/90 = 2$ degree) is considered to represent approximately the concentrated load. Because of its singularity, the convergence is found to be relatively slow. By taking more number of terms in i, however, reasonable accuracy is attained. This result clearly shows that the present method is applicable to a problem of concentrated loads with good accuracy. From the convergence study, the following numerical calculations are carried out by using $i = 15$, $m \times n = 3 \times 3$ and the 10-points integration.

Table 2 presents a comparison of frequencies for simply supported and clamped circular plates under uniform inplane

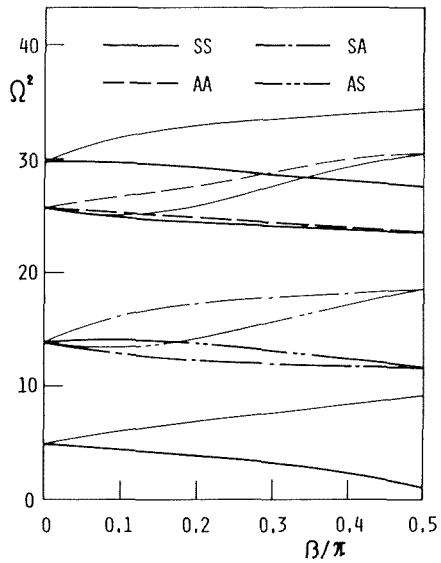

Fig. 2 Variations of frequencies for a simply supported circular plate versus load distribution angle (thick line —: compression ($\gamma = 4$), thin line —: tension ($\gamma = -10$))

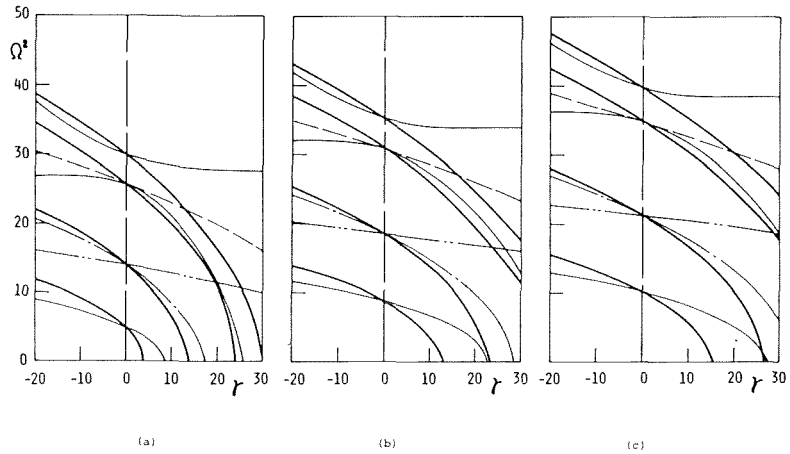

Fig. 3 Frequency parameters of circular plates subjected to uniform and partial inplane loads (thick line —: uniform load, thin line —: partial load ($\beta/\pi = 0.25$)). (*a*) simply supported plate ($\kappa = 0$); (*b*) elastically constrained plate ($\kappa = 10$), and (c) clamped plate ($\kappa = \infty$).

Downloaded 02 May 2010 to 171.66.16.54. Redistribution subject to ASME license or copyright; see http://www.asme.org/terms/Terms_Use.cfm

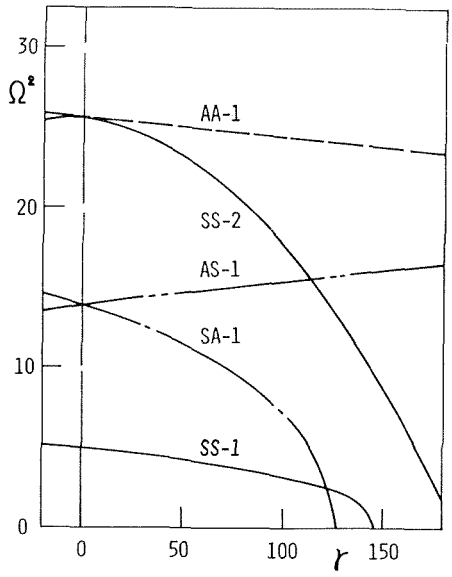

Fig. 4 Frequency parameters of a simply supported circular plate subjected to concentrated inplane loads

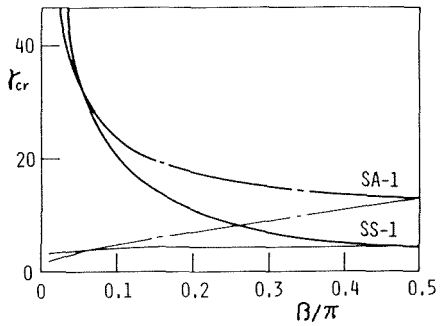

Fig. 5 Buckling coefficients γ_{cr} of a simply supported circular plate subjected to partial inplane loads

loads. The present values agree well with those of Laura et al. [4] for ranges between $\gamma = -20$ (tension) and 4 (compression).

Figure 2 shows behavior of frequencies for a compression load ($\gamma = 4$: denoted by thick lines) and a tension load ($\gamma = -10$: thin lines) as the angle of load distribution is increased. Frequency parameters generally tend to decrease in compression and increase in tension, since the total amount of loads added becomes large as the angle is increased.

Figure 3 shows variations of frequencies for the loads varying from tension to compression, for circular plates with inplane loads along the entire ($\beta/\pi = 0.5$: thick lines) and half edge ($\beta/\pi = 0.25$: thin lines), thereby in latter case giving half of the total load as in former case. Figure 3(a)-(c) show results for nondimensional spring rigidity $\kappa = 0$ (simple support), 10, ∞ (clamp), respectively. As expected, the frequencies decrease monotonously with increase of the loads. It is also seen that a case of the uniform load (thick line) exhibits tendency of frequencies changing parallel each other. However, the behaviors of the partial loading case vary individually depending upon modes, and one knows here that the effects of the nonuniform force distribution considerably depend upon mode shapes.

Figure 4 illustrates variations of frequencies for a simply supported plate with loads distributed along very small portion of the edge ($\beta/\pi = 1/90 = 2$ deg), in order to examine an effect of the concentrated inplane loading. As γ is increased, the AS-1 mode shows an exceptional behavior of increasing its value, in spite that other frequencies monotonically become small. To clarify this rather strange behavior, the inplane stress distribution was plotted for various value of β, and it turned out that for small β the tensional stress regions exist around $\theta = \pi/2$ and $3\pi/2$ even for the compression load. (On the contrary, the compression region exists for the tension load.) Since the effect of inplane forces is dependent on the curvature and the AS-1 mode has large curvatures in the regions, it was known that the AS-1 mode exhibits the behavior of increasing the frequency even when the compression is added.

The critical buckling load γ_{cr} is shown in Fig. 5 for a change of the load distribution angle. The values are denoted by thick lines for the SS-1 and SA-1 modes. It is interesting here that the buckling load of the SA-1 mode becomes smaller than that of the SS-1 mode for $\beta/\pi < 0.05$. Furthermore, the buckling loads are converted into $\gamma_{cr}(2\beta/\pi)$ (denoted by thin lines) to have the same total load and to indicate effects of changing only β. It is known from the slopes of both straight lines that the locally distributed loads has more explicit effect in the SA-1 mode than in the SS-1 mode. This seems to agree with our physical intuition.

Concluding Remarks

A solution procedure has been demonstrated for a previously unsolved problem of the vibration and stability of circular plates under arbitrarily nonuniform inplane loads. This analytical approach was applied to a case when a circular plate is subjected to a pair of partial inplane loadings along opposite parts of the edge, and the effect of such nonuniformness in stress was discussed on the vibration and buckling characteristics. As a special case of partial loading, the concentrated load was considered, and through numerical examples interesting behaviors of natural frequencies and critical buckling loads were found.

References

1 Leissa, A. W., "Vibration of Plates," NASA SP-160, U.S. Govt. Printing Office, 1969.

2 Wah, T., "Vibration of Circular Plates," *Journal of the Acoustical Society of America*, Vol. 34, No., 1962, pp. 275-281.

3 Laura, P. A. A., Paloto, J. C., and Santos, R. D., "A Note on the Vibration and Stability of a Circular Plate Elastically Restrained against Rotation," *Journal of Sound and Vibration*, Vol. 41, No. 2, 1975, pp. 177-180.

4 Laura, P. A. A., Arias, A., and Luisoni, L. E., "Fundamental Frequency of Vibration of a Circular Plate Elastically Restrained against Rotation and Carrying a Concentrated Mass," *Journal of Sound and Vibration*, Vol. 45, No. 2, 1976, pp. 298-301.

5 Laura, P. A. A., Luisoni, L. E., and Arias, A., "Antisymmetric Modes of Vibration of a Circular Plate Elastically Restrained Against Rotation and Subjected to a Hydrostatic State of In-Plane Stress," *Journal of Sound and Vibration*, Vol. 47, No. 3. 1976, pp. 433-437.

6 Pardoen, G. C., "Static, Vibration and Buckling Analysis of Axisymmetric Circular Plates Using Finite Elements," *Computer and Structures*, Vol. 3, 1973, pp. 355-375.

7 Pardoen, G. C., "Asymmetric Vibration and Stability of Circular Plates," *Computer and Structures*, Vol. 9, 1978, pp. 89-95.

8 Jain, R. K., "Vibrations of Circular Plates of Variable Thickness under an Inplane Force," *Journal of Sound and Vibration*, Vol. 23, No. 4, 1972, pp. 407-414.

9 Gupta, U. S., and Lal, R., "Buckling and Vibrations of Circular Plates of Variable Thickness," *Journal of Sound and Vibration*, Vol. 58, No. 4, 1978, pp. 501-507.

10 Valerga de Greco, B., and Laura, P. A. A., "Vibration and Buckling of Circular Plates of Variable Thickness," *Journal of the Acoustical Society of America*, Vol. 72, No. 3, 1982, pp. 856-858.

11 Celep, Z., "Axially Symmetric Stability of a Completely Free Circular Plate Subjected to a Nonconservative Edge Load," *Journal of Sound and Vibration*, Vol. 65, No. 4, 1979, pp. 549-556.

12 Celep, Z., "Vibration and Stability of a Free Circular Plate Subjected to Nonconservative Loading," *Journal of Sound and Vibration*, Vol. 80, No. 3, 1982, pp. 421-432.

13 Yamaki, N., "Buckling of a Circular Plate Under Locally Distributed Forces," Report of the Institute of High Speed Mechanics, Tohoku University, Vol. 8, 1957, pp. 13-24.

14 Zajaczkowski, J., "Stability of Transverse Vibration of a Circular Plate Subjected to a Periodically Varying Torque," *Journal of Sound and Vibration*, Vol. 89, No. 2, 1983, pp. 273-286.

15 Srinivasan, V., and Ramamurti, V., "Dynamic Response of an Annular Disk to a Moving Concentrated, In-Plane Edge Load," *Journal of Sound and Vibration*, Vol. 72, No. 2, pp. 251-262.

16 Timoshenko, S. P., and Goodier, J. N., *Theory of Elasticity*, 3rd ed., McGraw-Hill, New York.

Downloaded 02 May 2010 to 171.66.16.54. Redistribution subject to ASME license or copyright; see http://www.asme.org/terms/Terms_Use.cfm

Large Deflection Behavior of Simply Supported Laminated Panels Under In-Plane Loading

Y. Zhang[1]
Structural Analyst Engineer,
Shenyang Aircraft Company,
China

F. L. Matthews
Senior Lecturer,
Aeronautics Department,
Imperial College,
London, England SW72BY

An analysis is presented for nonbifurcational behavior of flat and curved panels of unsymmetrically laminated composite materials under in-plane loading, either compression or shear. A pair of governing equations in the von Karman sense are solved in conjunction with simply supported boundaries. A series of computations is carried out for panels having different curvatures, different lay-ups, and different materials. The results show that during loading, lateral deflection is involved in panels with unsymmetric cross-ply layers under compression or in those with unsymmetric angle-ply layers under shear. This effect increases deflection of the flat plates under loading and reduces resistance of curved panels against collapse.

Introduction

The increasing use of high-performance composite materials has intensified the demand for the development of analytical methods for anisotropic structures. Since Stavsky and Reissner [1] revealed the bending-stretching coupling effect in laminated composite plates, a considerable amount of work has been done on the linear and nonlinear analyses of such plates. For compendiums, see references [2–4].

In general, laminated composite plates consist of a number of layers of orthotropic material with the orthotropic axes of each layer oriented at an arbitrary angle to the plate axes. It is well known that in these plates lamination asymmetry results in a coupling between bending or twisting and extension or shearing. Two types of unsymmetric arrangements are asymmetric cross-ply and angle-ply laminates. The analytical investigation for the behavior of such laminates are often found in the open literature. Buckling and postbuckling studies have been done by a few investigators such as Whitney and Leissa [5], Jones [6], Turvey and Wittrick [7], Chia and Prabhakara [8], etc. In these works the bifurcational type of buckling or postbuckling behavior of such plates under in-plane loading was analyzed and extensive results were obtained.

But in unsymmetrically laminated plates, lateral deflection, i.e., plate bending, may be involved immediately when the load is applied, even though only in-plane loading exists. Research work done in this area is sparse. In 1976, Prabhakara [9] carried out a study for flat plates with unsymmetric cross-ply arrangements under compressive loading. It is found that the loading-transverse deflection behavior of such plates is no longer bifurcational; because of the coupling terms B_{11}^* and B_{22}^* the plates start bending from the beginning of the loading process. In such cases, the approximate analysis in which the B_{ij}^* terms are deleted is not acceptable at all. To-date the bending effect of in-plane shear loading on unsymmetric laminates appears not to have been considered.

It is well known from investigations of isotropic structures that curved structural members are, in general, very sensitive to all kinds of imperfection, either of geometry or loading. So it could be of great interest to know how curved panels with unsymmetric lay-ups behave under in-plane loading.

The current work discusses the nonbifurcational behavior of cylindrically curved panels with unsymmetric lay-ups under both compressive and shear loading. This work is developed on the basis of the authors' previous papers [10, 11], where the bifurcational behavior of curved laminates is studied. The governing equations are obtained from the virtual displacement and virtual force principles. The effect of boundary moments are included in the pair of coupled nonlinear differential equations. This set of equations is solved in conjunction with simply supported boundary conditions. The transverse deflection and stress function in the equations are expressed as infinite series. Both double sine terms and double sine-squared terms are used for the deflection function, while appropriate characteristic beam function terms are used for the stress function. The computation results are presented graphically for panels with different curvatures, different stacking sequences and different composite materials.

Governing System

Consider a cylindrically curved panel with midsurface radius R and thickness h, having length a and arc b (see Fig. 1). The panel is assumed to consist of composite layers with

[1]Academic Visitor, Aeronautics Department, Imperial College, London, England, 1980–82.

Contributed by the Applied Mechanics Division for publication in the JOURNAL OF APPLIED MECHANICS.

Discussion on this paper should be addressed to the Editorial Department, ASME, United Engineering Center, 345 East 47th Street, New York, N.Y. 10017, and will be accepted until two months after final publication of the paper itself in the JOURNAL OF APPLIED MECHANICS. Manuscript received by ASME Applied Mechanics Division, July, 1982; final revision, August, 1984.

Copyright © 1985 by ASME
Downloaded 02 May 2010 to 171.66.16.54. Redistribution subject to ASME license or copyright; see http://www.asme.org/terms/Terms_Use.cfm

elastic properties and arbitrary orientations of orthotropic axes with respect to the generators of the panel. It is also assumed that the panel is thin and the geometry is perfect.

The constitutive relations of the panel may be obtained on the basis of the Kirchhoff hypothesis. The partial inverted form of these relations may be written, i.e.,

$$\begin{Bmatrix} \boldsymbol{\epsilon}^\circ \\ \mathbf{M} \end{Bmatrix} = \begin{bmatrix} \mathbf{A}^* & \mathbf{B}^* \\ (-\mathbf{B}^*)^t & \mathbf{D}^* \end{bmatrix} \begin{Bmatrix} \mathbf{N} \\ \mathbf{k} \end{Bmatrix} \tag{1}$$

where

$$\begin{aligned} \boldsymbol{\epsilon}^\circ &= [\epsilon_x^\circ \epsilon_y^\circ \gamma_{xy}^\circ]^t \\ \mathbf{N} &= [N_x N_y N_{xy}]^t \\ \mathbf{M} &= [M_x M_y M_{xy}]^t \\ \mathbf{k} &= [k_x k_y k_{xy}]^t \\ &= -\left[\frac{\partial^2 w_0}{\partial x^2} \frac{\partial^2 w_0}{\partial y^2} 2\frac{\partial^2 w_0}{\partial x \partial y}\right]^t \end{aligned} \tag{2}$$

and

$$\begin{aligned} \epsilon_x^\circ &= \frac{\partial u_0}{\partial x} + \frac{1}{2}\left(\frac{\partial w_0}{\partial x}\right)^2 \\ \epsilon_y^\circ &= \frac{\partial v_0}{\partial y} + \frac{1}{2}\left(\frac{\partial w_0}{\partial y}\right)^2 - \frac{w_0}{R} \\ \gamma_{xy}^\circ &= \frac{\partial u_0}{\partial y} + \frac{\partial v_0}{\partial x} + \left(\frac{\partial w_0}{\partial x}\right)\left(\frac{\partial w_0}{\partial y}\right) \end{aligned} \tag{3}$$

in which N_x, N_y, N_{xy} are membrane forces; M_x, M_y, M_{xy} bending moments and torque; ϵ_x°, ϵ_y°, γ_{xy}° midsurface strains; k_x, k_y, k_{xy} flexural curvatures; and u_0, v_0, w_0 midsurface displacements. Note that w_0 is positive in the positive z-direction (Fig. 1). $\mathbf{A}^*$, $\mathbf{B}^*$, $\mathbf{D}^*$ are all 3×3 square matrices. The components of these matrices are the reduced stiffness coefficients.

The governing equations including the effect of boundary moments are obtained from the virtual displacement and virtual force principles in the previous work [11], i.e.

$$\begin{aligned} &\int_0^a \int_0^b \left\{ \frac{\partial^2 M_x}{\partial x^2} + \frac{\partial^2 M_y}{\partial y^2} + 2\frac{\partial^2 M_{xy}}{\partial x \partial y} + \frac{N_y}{R} \right. \\ &\left. + N_x \frac{\partial^2 w_0}{\partial x^2} + N_y \frac{\partial^2 w_0}{\partial y^2} + 2N_{xy} \frac{\partial^2 w_0}{\partial x \partial y} \right\} \delta w_0 \, dx dy \\ &+ \int_0^b \left[M_x \delta\left(\frac{\partial w_0}{\partial x}\right) \right] \Big|_{x=0}^{x=a} dy \\ &+ \int_0^a \left[M_y \delta\left(\frac{\partial w_0}{\partial y}\right) \right] \Big|_{y=0}^{y=b} dx = 0 \end{aligned} \tag{4}$$

$$\begin{aligned} &\int_0^a \int_0^b \left\{ \frac{\partial^2 \epsilon_x^\circ}{\partial y^2} + \frac{\partial^2 \epsilon_y^\circ}{\partial x^2} - \frac{\partial^2 \gamma_{xy}^\circ}{\partial x \partial y} - \left(\frac{\partial^2 w_0}{\partial x \partial y}\right)^2 \right. \\ &\left. + \frac{\partial^2 w_0}{\partial x^2} \frac{\partial^2 w_0}{\partial y^2} + \frac{1}{R} \frac{\partial^2 w_0}{\partial x^2} \right\} \delta\phi \, dx dy = 0 \end{aligned} \tag{5}$$

where ϕ is the stress function defined by

$$N_x = \frac{\partial^2 \phi}{\partial y^2}, \qquad N_y \frac{\partial^2 \phi}{\partial x^2}, \qquad N_{xy} = -\frac{\partial^2 \phi}{\partial x \partial y} \tag{6}$$

Setting (1)–(3) into equations (4) and (5) the governing system in nondimensional form may be obtained by using the following, and other, nondimensional parameters

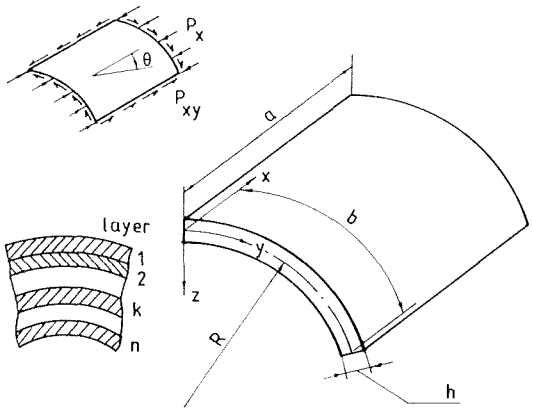

Fig. 1 Definition of geometry and external forces

$$\xi = \frac{x}{a}, \qquad \eta = \frac{y}{b}, \qquad \beta = \frac{a}{b}, \tag{7}$$

$$w = \frac{w_0}{h}, \qquad F = \frac{\phi}{A_{22}h^2}, \qquad K_R = \frac{b^2}{Rh}$$

The membrane forces and moments may also be expressed in nondimensional form as follows:

$$\begin{Bmatrix} N_\xi \\ N_\eta \\ N_{\xi\eta} \end{Bmatrix} = \frac{b^2}{A_{22}h^2} \begin{Bmatrix} N_x \\ N_y \\ N_{xy} \end{Bmatrix}$$

$$= \begin{bmatrix} 1 & 0 & 0 \\ 0 & 1/\beta^2 & 0 \\ 0 & 0 & 1/\beta \end{bmatrix} \begin{Bmatrix} \partial^2 F/\partial\eta^2 \\ \partial^2 F/\partial\xi^2 \\ -\partial^2 F/\partial\xi\partial\eta \end{Bmatrix} \tag{8}$$

$$\begin{Bmatrix} M_\xi \\ M_\eta \\ M_{\xi\eta} \end{Bmatrix} = \frac{b^2}{A_{22}h^2} \begin{Bmatrix} M_x \\ M_y \\ M_{xy} \end{Bmatrix}$$

$$= -\begin{bmatrix} B_{11}^* & B_{21}^* & B_{61}^* \\ B_{12}^* & B_{22}^* & B_{62}^* \\ B_{16}^* & B_{26}^* & B_{66}^* \end{bmatrix} \begin{bmatrix} 1 & 0 & 0 \\ 0 & 1/\beta^2 & 0 \\ 0 & 0 & 1/\beta \end{bmatrix} \begin{Bmatrix} \partial^2 F/\partial\eta^2 \\ \partial^2 F/\partial\xi^2 \\ -\partial^2 F/\partial\xi\partial\eta \end{Bmatrix}$$

$$- \begin{bmatrix} D_{11}^* & D_{12}^* & D_{16}^* \\ D_{21}^* & D_{22}^* & D_{26}^* \\ D_{61}^* & D_{62}^* & D_{66}^* \end{bmatrix} \begin{bmatrix} 1/\beta^2 & 0 & 0 \\ 0 & 1 & 0 \\ 0 & 0 & 1/\beta \end{bmatrix} \begin{Bmatrix} \partial^2 w/\partial\xi^2 \\ \partial^2 w/\partial\eta^2 \\ 2\partial^2 w/\partial\xi\partial\eta \end{Bmatrix} \tag{9}$$

Solutions

The plate under consideration is subjected to uniform edge compression P_x and shear P_{xy}, per unit width. The simply supported boundary conditions may be written in nondimensional form as follows:

$$\begin{aligned} &w = 0, \quad M_\xi = 0, \quad \frac{\partial^2 F}{\partial\eta^2} = -\bar{N}_x, \quad \frac{\partial^2 F}{\partial\xi\partial\eta} = -\beta\bar{N}_{xy} \quad \text{at } \xi = 0,1 \\ &w = 0, \quad M_\eta = 0, \quad \frac{\partial^2 F}{\partial\xi^2} = 0, \quad \frac{\partial^2 F}{\partial\xi\partial\eta} = -\beta\bar{N}_{xy} \quad \text{at } \eta = 0,1 \end{aligned} \tag{10}$$

Downloaded 02 May 2010 to 171.66.16.54. Redistribution subject to ASME license or copyright; see http://www.asme.org/terms/Terms_Use.cfm

where $\bar{N}_x = P_x b^2/A_{22}h^2$ and $\bar{N}_{xy} = P_{xy}b^2/A_{22}h^2$ are the nondimensional edge compressive and shear load.

The assumed functions for the nondimensional deflection w and stress function F take the form:

$$F = -\bar{N}_x\eta^2/2 - \beta\bar{N}_{xy}\xi\eta + \sum_{m=1}^{\infty}\sum_{n=1}^{\infty} F_{mn}X_m(\xi)Y_n(\eta) \tag{11}$$

$$w = \sum_{p=1}^{\infty}\sum_{q=1}^{\infty}[w_{pq}^{(1)}\sin p\pi\xi\sin q\pi\eta + w_{pq}^{(2)}\sin^2 p\pi\xi\sin^2 q\pi\eta]$$

in which the characteristic beam functions $X_i(\xi)$ and $Y_i(\eta)$ are defined by

$$\begin{aligned} X_i(\xi) &= \cosh\alpha_i\xi - \cos\alpha_i\xi - \gamma_i(\sinh\alpha_i\xi - \sin\alpha_i\xi) \\ Y_i(\eta) &= \cosh\alpha_i\eta - \cos\alpha_i\eta - \gamma_i(\sinh\alpha_i\eta - \sin\alpha_i\eta) \end{aligned} \tag{12}$$

where α_i and γ_i are constants which with 15 significant digits may be found in the authors' previous work [10]. The functions $X_i(\xi)$ and $Y_i(\eta)$ are orthogonal functions. Their properties are also discussed in detail in reference [10].

It is found that the function F satisfies the boundary conditions (10), but the deflection function w satisfies only the zero deflection conditions. Fortunately, however, the effect of unbalanced moments on the boundaries has been considered in equation (4). So we simply set the solution (11) into the non-dimensional governing equations.

After much tedious algebraic manipulation, details of which are given in reference [12], a set of equations containing an infinite number of terms is obtained. It is obvious that in practice only a finite number of terms in the functions F and w of (11) need to be used to obtain numerical results. If the first M^2 terms in the first expression in (11) and $2M^2$ in the second are taken, after eliminating the F_{ij} terms from the resultant algebraic equations we eventually obtain a set of matrix equations containing a total of $2M^2$ algebraic cubic equations:

$$\begin{aligned} &[[B^{(1)}] + K[B^{(2)}]]\{w^{(1)}\} + [[B^{(3)}] + K[B^{(4)}]]\{w^{(2)}\} \\ &\qquad = K[\mu_x\{A^{(1)}\} + \mu_s\{A^{(2)}\}] \\ &[[C^{(1)}] + K[C^{(2)}]]\{w^{(1)}\} + [[C^{(3)}] + K[C^{(4)}]]\{w^{(2)}\} = 0 \end{aligned} \tag{13}$$

The variables in (13) are $w_{pq}^{(1)}$, $w_{pq}^{(2)}$ and the loading parameter K, defined as follows:

$$\mu_x K = \frac{P_x b^2}{E_{22}h^3}, \quad \mu_s K = \frac{P_{xy}b^2}{E_{22}h^3} \tag{14}$$

With the loading ratios μ_x and μ_s properly selected one may have any specified loading ratio between compression and shear. For instance, $\mu_x = 1$, $\mu_s = 0$ represents pure compression; $\mu_x = 0$, $\mu_s = 1$ corresponds to pure shear, and so on.

The elements of column matrices $[A^{(1)}]$ and $[A^{(2)}]$ are given in the following:

$$\begin{aligned} A_j^{(1)} &= (b_1 L_0^i T_1^j + b_2 L_0^i T_1^i)\frac{E_{22}h}{A_{22}} \\ A_j^{(2)} &= (b_3 L_0^i L_0^i T_1^j + b_4 L_0^i T_1^i)\frac{E_{22}h}{A_{22}} \end{aligned} \tag{15}$$

L_0^i and T_1^i in expression (15) are constants only, which are given in reference [12].

Computation

As the preceding analytical procedure does not include any limitation on lay-ups, the resultant equations (13) may be used for laminated panels with arbitrary lay-ups. We need to examine the right-hand side of the first equation in equations (13). It is seen that the term $K[\mu_x\{A^{(1)}\} + \mu_s\{A^{(2)}\}]$ involves neither the deflection function w nor the stress function F, and is clearly proportional to the in-plane loading parameter K. It may, therefore, be expected that when in-plane load is applied to the panel, the deflection w occurs immediately if $\{A^{(1)}\}$ and $\{A^{(2)}\}$ are not all zero.

As seen from (15) the values of $A_j^{(1)}$ and $A_j^{(2)}$ depend on the coefficients b_1, b_2, b_3, and b_4. These coefficients may be written as follows

$$\begin{aligned} b_1 &= \beta^2 B_{11}^*(A_{22}h^2/D_{11}^*) \\ b_2 &= \beta^4 B_{12}^*(A_{22}h^2/D_{11}^*) \\ b_3 &= -\beta B_{61}^*(A_{22}h^2/D_{11}^*) \\ b_4 &= -\beta^3 B_{62}^*(A_{22}h^2/D_{11}^*) \end{aligned} \tag{16}$$

Now it can be concluded that if the stretching-bending coupling terms B_{11}^* and B_{12}^* of the panel are not equal to zero, deflection will occur when axial compression is applied on the panel. Likewise, if the coupling terms B_{61}^* and B_{62}^* are not equal to zero, deflection of the panel will also occur when in-plane shear loading is applied. In those cases, the behavior of the panels under in-plane loading is no longer of the bifurcational type, and the load-deflection relations are curved directly from the origin.

As is very well known, B_{11}^* is not zero for panels with antisymmetrical cross-ply lay-ups. Therefore bending is involved when the panels are subjected to axial compression. In the current work the behavior of such panels is investigated. General cross-ply situations are discussed in the examples as well. In this case B_{11}^* and B_{12}^* are both nonzero. It is also known that for panels with antisymmetric angle-ply layers B_{61}^* and B_{62}^* are not zero. In examples, the lateral deflection of such panels under shear loading are also investigated.

To solve the nonlinear algebraic equation set of (13) an iterative procedure, based on the modified Newton method, is used. As described in reference [11] the prescribed component of the deflection must be selected properly at the beginning of computation because the load-deflection curves resulting from the bending effect are, in many cases, steep at the beginning of the loading process. Too large a step length may cause the iterative scheme to fail and too small a step length results in high computing cost. The step lengths used in the examples vary from panel to panel and may also vary on different parts of the behavior path of one panel.

Computation is carried out for typical unidirectional boron/epoxy and carbon/epoxy composites. The properties of the materials used for the calculations are listed in Table 1. The panels are assumed to have length a and arc b both equal to 250 mm. The total thickness of the panels are kept equal to 2.5 mm, no matter how many layers are in the panels.

In the computations, a four-term approximation for the stress function F and an eight-term approximation for the deflection function w are used. Because there is no term involving the coupling stiffnesses D_{16} and D_{26} in the examples, such approximations for F and w are adequate to show the effects of panel bending, while keeping the computing cost within reasonable limits.

The computing program has been verified for panels having bifurcational behavior. In those cases the comparison between the results of the current computation and previous work, [2] and [8], gives good agreement. Details may be found in references [10, 11].

Table 1 Elastic constants of composites

Materials	E_{11}(GN/m^2)	E_{22}(GN/m^2)	ν_{12}	G_{12}(GN/m^2)
Boron/Epoxy	206.9	20.7	0.3	5.2
Carbon/Epoxy	206.9	5.2	0.25	2.6

Downloaded 02 May 2010 to 171.66.16.54. Redistribution subject to ASME license or copyright; see http://www.asme.org/terms/Terms_Use.cfm

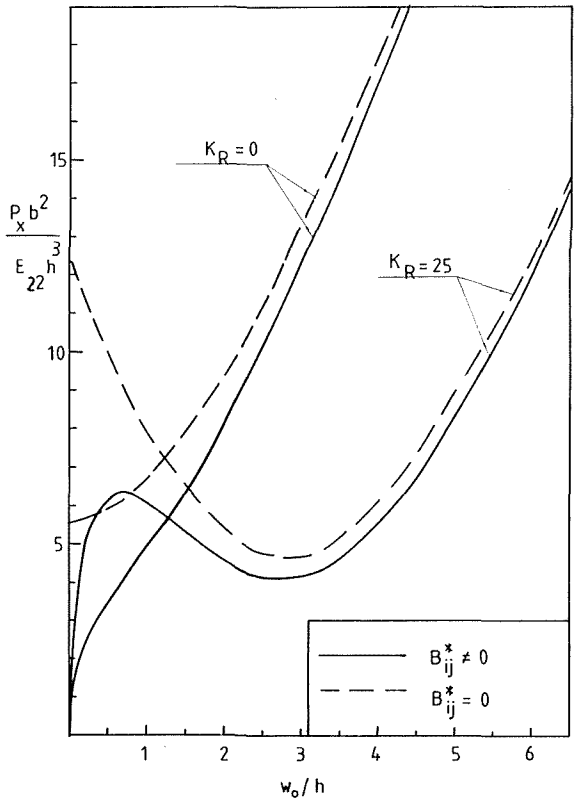

Fig. 2 Variation of central deflection with axial compression of boron/epoxy panels; (90 deg, 0 deg) lay-up, different curvatures

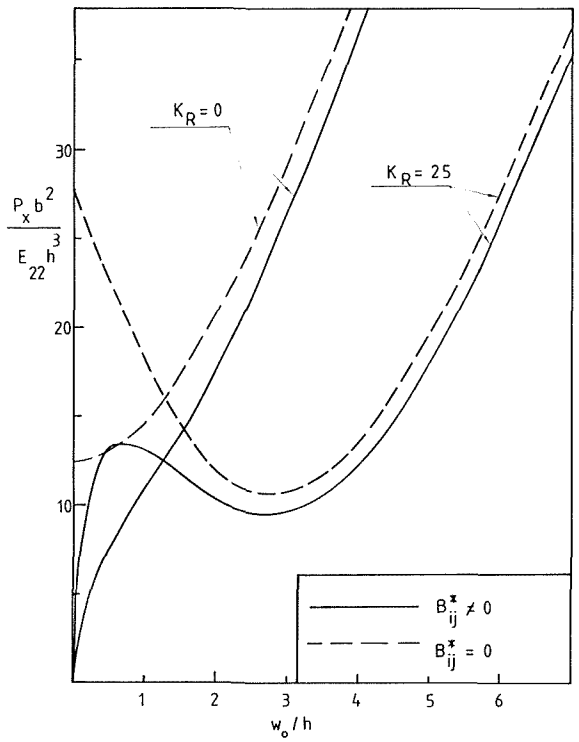

Fig. 3 Variation of central deflection with axial compression of carbon/epoxy panels; (90 deg, 0 deg) lay-up, different curvatures

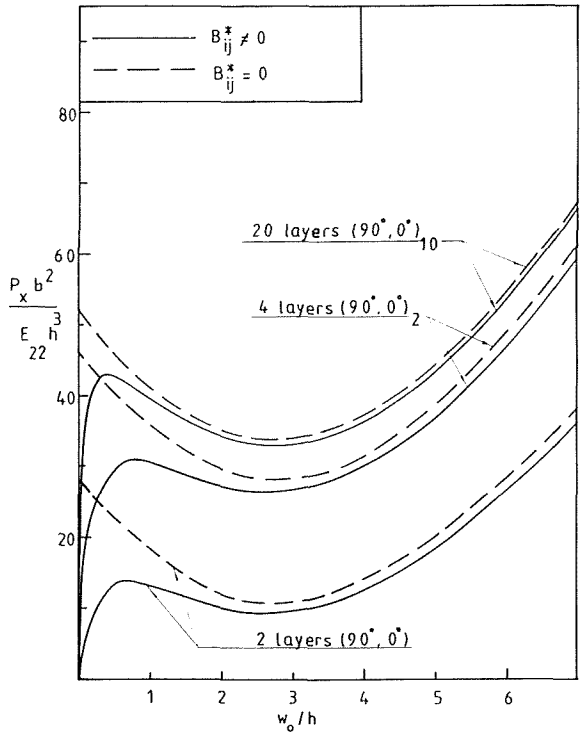

Fig. 4 Variation of central deflection with axial compression of boron/epoxy panels; antisymmetric cross-ply lay-ups, $K_R = 25$

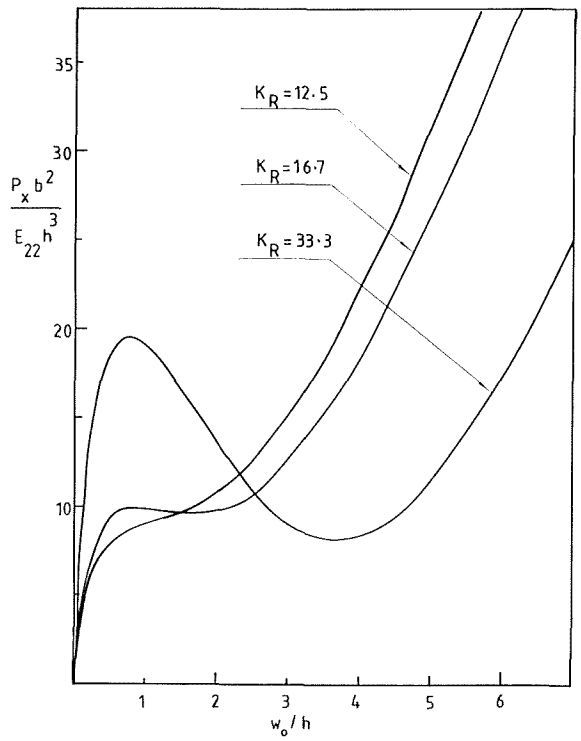

Fig. 5 Variation of central deflection with axial compression of carbon/epoxy panels; (90 deg, 0 deg) lay-up, different curvatures

Results

The results of the computations are summarized in Figs. 2–7. In all these figures the influence of the B^*_{ij} terms can be seen. The dashed curves marked $B^*_{ij} = 0$ represent approximate results obtained by deleting B^*_{ij} terms from the analysis. As is well known such an approach has been suggested [13] although these terms may not be zero in realistic panels. In the current investigation big differences have been found for the behavior of the panels with or without such terms.

Downloaded 02 May 2010 to 171.66.16.54. Redistribution subject to ASME license or copyright; see http://www.asme.org/terms/Terms_Use.cfm

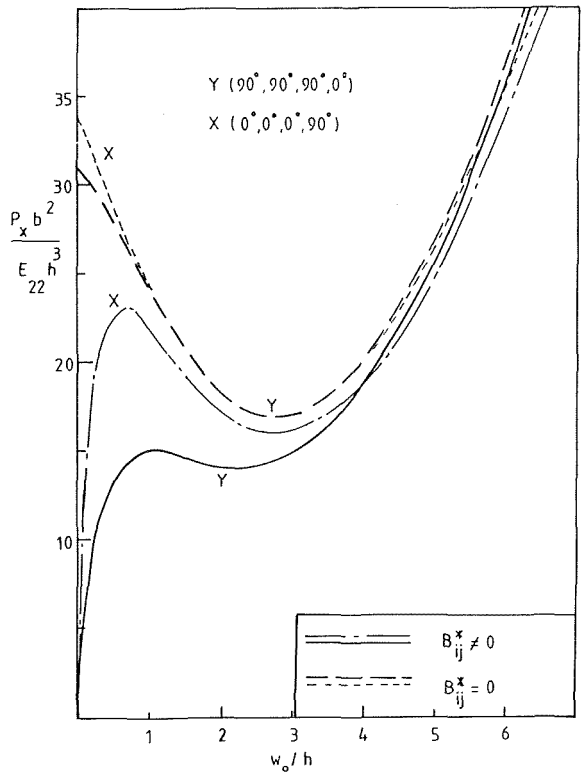

Fig. 6 Variation of central deflection with axial compression of carbon/epoxy panels; nonsymmetric lay-ups, $K_R = 25$

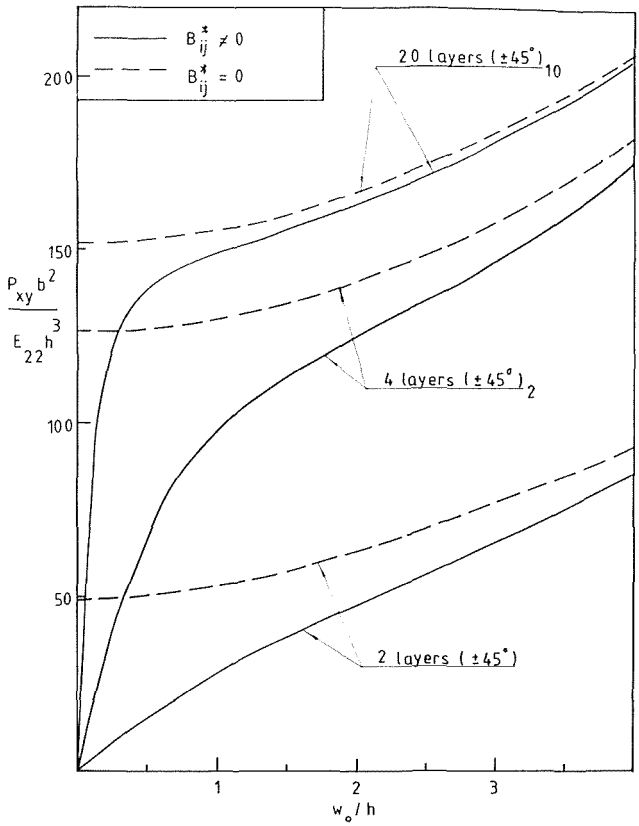

Fig. 7 Variation of central deflection with shear of carbon/epoxy flat plates; antisymmetric angle-ply lay-ups

Figure 2 is obtained for panels with two layers, (90 deg, 0 deg), of boron/epoxy composite under compression. The load-central deflection results of flat plates and curved panels are shown. It can be clearly seen that the inclusion of the coupling terms B^*_{ij} causes differences in behavior of laminated panels under in-plane loading; bending exists from the beginning of the loading process. For a flat plate ($K = 0$) with such a lay-up the deflection increases monotonically with increasing load, the curve being tangential to the vertical axis (zero slope) at zero load. This means that for such a plate under axial compression lateral deflection (i.e., bending) occurs instead of buckling. For a curved panel ($K = 25$) the initial slope is not zero and a snap-through may occur when the applied compression reaches a certain level. It is worth pointing out, however, that the maximum load for snap-through is much lower than the bifurcation load because the B^*_{ij} terms greatly reduce the resistance of the panel against collapse.

Figures 3–6 are all obtained for carbon/epoxy panels under axial compression. The load-central deflection relations are shown on the figures. Figure 3 repeats Fig. 2 except for a different composite material. The same phenomena are seen as in Fig. 2, although the absolute values of load and deflection are different in both cases.

Figure 4 shows the effect of the number of layers in panels with $K = 25$, having antisymmetric cross-ply lay-ups. It is found that the bending effect decreases with increasing number of layers. That is, the more alternate layers there are in the panel the higher is the performance of the panel and the smaller is the influence of the coupling terms.

Figure 5 shows the influence of panel curvature. This figure is obtained for two-layer (90 deg, 0 deg) panels. It is seen that the maximum snap-through load decreases as the panel becomes less curved and no snap-through load is found when the panel becomes very flat, say $K = 12.5$.

Figure 6 is obtained for four-layer panels having general cross-ply arrangements. It can be seen that for such panels, the coupling terms B^*_{ij} also have significant influence. The bending of such panels can be even more severe than for antisymmetric cross-ply arrangements as shown in Fig. 4.

Figure 7 is obtained for flat plates with antisymmetric angle-ply arrangements of carbon/epoxy composites. The effect of increasing the number of alternate layers on the behavior of the plates under shear is demonstrated. The load-central deflection curves indicate that for plates with such lay-ups, bending occurs immediately when in-plane shear loading is applied. The effect is most severe for the two-layer plate and decreases as the number of alternate layers increases.

Conclusions

From the preceding examples conclusions may be summarized:

1. Owing to the coupling terms B^*_{ij}, there is bending of laminated composite panels with unsymmetric cross-ply lay-ups even if only in-plane compression is applied. This is true both for flat plates and curved panels.

2. Because of such bending effects the behavior of unsymmetric laminated composite panels is no longer of the bifurcational type.

3. These effects increase the deflection of flat plates under an identical level of loading and reduce the resistance of curved panels against collapse, compared to an approximate analysis in which coupling terms are ignored.

4. A bending effect is also found to exist under shear loading for panels having antisymmetric angle-ply lay-ups.

5. This bending behavior may be reduced by increasing the number of alternate layers in the panel, whilst keeping constant thickness. The two-layer asymmetric lay-up results in the lowest performance of the panel.

Downloaded 02 May 2010 to 171.66.16.54. Redistribution subject to ASME license or copyright; see http://www.asme.org/terms/Terms_Use.cfm

References

1 Reissner, E., Stavsky, Y., "Bending and Stretching of Certain Types of Heterogeneous Aeolotropic Elastic Plates," ASME JOURNAL OF APPLIED MECHANICS, Vol. 28, 1961, pp. 402-408.

2 Ashton, J. E., and Whitney, J. M., *Theory of Laminated Plates*, Technomic Publishing Co., 1970.

3 Chia, C. Y., *Nonlinear Analysis of Plates*, McGraw-Hill, New York, 1980.

4 Leissa, A. W., "Advances in Vibration, Buckling, and Postbuckling Studies on Composite Plates," *Proc. Int. Conf. On Composite Structures*, Applied Science, Paisley, Scotland, 1981, pp. 312-334.

5 Whitney, J. M., and Leissa, A. W., "Analysis of Simply Supported Laminated Anisotropic Rectangular Plates," *AIAA J.*, Vol. 8, Jan. 1970, pp. 28-33.

6 Jones, R. M., "Buckling and Vibration of Unsymmetrically Laminated Cross-ply Rectangular Plates," *AIAA J.*, Vol. 11, Dec. 1973, pp. 1626-1632.

7 Turvey, G. J., and Wittrick, W. H., "The Large Deflection and Post-Buckling Behavior of Some Laminated Plates," *Aero. Quart.*, Vol. 24, May 1973, pp. 77-86.

8 Chia, C. Y., and Prabhakara, M. K., "Postbuckling Behavior of Unsymmetrically Layered Anisotropic Rectangular Plates," ASME JOURNAL OF APPLIED MECHANICS, Vol. 41, 1974, pp. 155-162.

9 Prabhakara, M. K., "Postbuckling Behavior of Simply Supported Cross-ply Rectangular Plates," *Aero. Quart.*, Vol. 27, Nov. 1976, pp. 309-316.

10 Zhang, Y., and Matthews, F. L., "Initial Buckling of Curved Panels of Generally Layered Composite Materials," *Int. J. of Composite Structures*, Vol. 1, No. 1, 1983, pp. 3-30.

11 Zhang, Y., and Matthews, F. L., "Postbuckling Behavior of Curved Panels of Generally Layered Composite Materials," *Int. J. of Composite Structures*, Vol. 1, No. 2, 1983, pp. 115-136. Also presented at Ninth U.S. Congress of Applied Mechanics, Ithaca, N.Y., June 1982.

12 Zhang, Y., "Buckling and Postbuckling Studies of Flat and Curved Unstiffened Panels of Generally Laminated Composite Materials," Ph.D Thesis, Imperial College, University of London, Oct. 1982.

13 Ashton, J. E., "Approximate Solutions for Unsymmetrical Laminated Plates," *J. Composite Materials*, Vol. 3, 1969, p. 189.

Downloaded 02 May 2010 to 171.66.16.54. Redistribution subject to ASME license or copyright; see http://www.asme.org/terms/Terms_Use.cfm

Transient Loads Analysis by Dynamic Condensation

K. Kubomura[1]
Beloit Manhattan,
Clarks Summit, Pa 18411

This paper investigates an alternative finite-difference time-integration procedure in structural dynamics. The integral form of the equation of motion, instead of the differential form, is used to develop the finite-difference time-integration method. An expression called dynamic condensation is presented to relate the dynamic response and unknown force at a limited number of degrees of freedom. A stable and accurate method of analysis is derived to determine the transient loads of structural components in a structural system without constructing the system equation of motion.

Introduction

Structural dynamics problems are described by the second-order finite element differential equations of motion. For time integration of the equations of motion, various finite-difference equations, which relate unknown displacements to prescribe applied forces, have been developed. The time integration involve progressively solving unknown displacements in the finite-difference equation.

There are structural dynamic problems that necessitate solving unknown forces subjected to prescribed compatibilities. Some examples of these problems include the sudden adherence of several structures that vibrate independently, the change of state from sliding contact to adhesion of structures that are vibrating with friction forces present, and the calculation of applied forces given the corresponding measured response. In this paper, finite-difference equations subjected to compatibility conditions are developed to solve unknown forces.

Time differentiations in the differential form of the equations of motion operate on displacements. The velocities and accelerations are considered to be interpolated from the instantaneous values of the displacements. The interpolations are introduced into the equations and the resulting equations are evaluated at a specified time. Thus, finite-difference equations are derived and relate the unknown instantaneous displacements to prescribed forces. Various interpolations of displacements, velocities, and accelerations lead to developing different finite-difference time integration methods such as the central difference [1], Houbolt [2], and Newmark [3] methods. The stability and accuracy of the methods are strongly dependent on how the instantaneous values of displacements, velocities, accelerations, and time increments are expressed.

The equations of motion can also be expressed in integral form (the Duhamel integral), in which integration is performed on the forces. Finite-difference time integration methods can also be developed based on the integral form of the equations of motion. This is done by interpolating forces from instantaneous values and evaluating the integral equations at a specified time. Thus derived, finite-difference equations relate instantaneous values of unknwon forces to those of known quantities. The derived finite-difference equations are considered to fit the solution of problems in which compatibility conditions are given, or the structural response, such as displacements, velocities, and accelerations, are prescribed. In many cases, the number of unknwon forces and the prescribed response or compatibility conditions are limited; therefore, the finite-difference equations are presented as they relate the limited number of instantaneous value of unknown forces to prescribed response (dynamic condensation). It appears that how compatibilities are assessed, how unknown forces are interpolated, and how the size of the time increment control the stability and accuracy of the methods.

An example problem, which deals with the modal transient load analysis of a system's substructure without substructural coupling, will be considered to investigate the stability and accuracy of this approach. In the conventional transient load analysis, each substructure's stiffness and mass matrices are reduced in size by modal synthesis and coupled to construct reduced system equations of motion [4–7]. The system equations of motion are decoupled by an eigenanalysis and truncated. Next, the modal force-time histories are calculated and the modal coordinates time-integrated.

In the transient load analysis of the Space Transportation System (STS) payload [8], the major substructures and forcing functions are not changed from flight to flight. Whenever payload structures are changed, the conventional aforementioned coupled load analysis requires repeating costly calculations of system modes and modal force history. In the past, several investigations were conducted on cost and time-saving alternative transient load analysis methods [9–14], and it appears that no one method can accommodate the needs for the STS payload analysis [15].

The example problem presented here is representative of

[1]Formerly with Rockwell International.

Contributed by the Applied Mechanics Division for publication in the JOURNAL OF APPLIED MECHANICS.

Discussion on this paper should be addressed to the Editorial Department, ASME, United Engineering Center, 345 East 47th Street, New York, N.Y. 10017, and will be accepted until two months after final publication of the paper itself in the JOURNAL OF APPLIED MECHANICS. Manuscript received by ASME Applied Mechanics Division, December, 1983; final revision December, 1984.

Copyright © 1985 by ASME
Downloaded 02 May 2010 to 171.66.16.54. Redistribution subject to ASME license or copyright; see http://www.asme.org/terms/Terms_Use.cfm

launch vehicle and payload system structures. It does not include costly substructure coupling, system eigenanalysis, and associated model-force calculation. In the proposed method, finite-difference equations for the reaction forces are developed by dynamic condensation, and then, through the equilibrium and compatibility conditions at the interface, a recurrence equation for unknown reaction forces is developed. By simultaneously solving the recurrence equation, the finite difference equations of motion for each substructure are progressively time-integrated.

In this paper, finite-difference equations are developed based on the integral form of the equations of motion, solution procedures are developed for the example problem, and then, the results of the numerical studies are presented. Next, the accuracy and stability of the methods are investigated and the appropriate assessment of compatibility and interpolation of forces are discussed.

Dynamic Condensation

For a vibrating linear structure, the response vector, $\mathbf{g}(t)$ (i.e., displacements, velocities, and accelerations) may be expressed as the sum of forced and free vibration responses

$$\mathbf{g}(t) = \int_0^t \mathbf{H}(t-z)\mathbf{F}(z)\,dz + {}^f\mathbf{g}(t) \tag{1}$$

Here, the convolution integration respresents the forced vibration response. The matrix $\mathbf{H}(z)$ is the response of the structure at time z subjected to the unit impulse at time 0 with the initial conditions set equal to zero. In equation (1), the second term represents the free vibration response from time 0 with nonzero initial conditions. When the time-integration interval is sufficiently short, the force vector $\mathbf{F}(z)$ can be adequately interpolated by a simple function. For example, the forces may be written using values $\mathbf{F}^0$ and $\mathbf{F}^t$ at the beginning and end of the interval, respectively, i.e.,

$$F(z) = \mathbf{L}^0(z)\mathbf{F}^0 + \mathbf{L}^t(z)\mathbf{F}^t \tag{2}$$

Introducing equation (2) into equation (1) and arranging the resulting equation, produces

$$\mathbf{g}(t) = \mathbf{G}^0\mathbf{F}^0 + \mathbf{G}^t\mathbf{F}^t + {}^f\mathbf{g}(t) \tag{3}$$

where

$$\mathbf{G}^0 = \int_0^t \mathbf{H}(t-z)\mathbf{L}^0(z)\,dz$$

$$\mathbf{G}^t = \int_0^t \mathbf{H}(t-z)\mathbf{L}^t(z)\,dz$$

For many static structutal problems, a large number of degrees of freedom are involved in a finite element equation. This equation relates the displacements and applied forces (including zero forces) at all degrees of freedom. Static condensation [16] converts the original large finite element equation to a small equation. This reduced equation relates the displacements and applied forces for a limited number of degrees of freedom. This technique has been extensively applied to static problems of complex structures consisting of several substructures. Also, this technique can be applied to problems in which it is required to repeat calculation of displacements and forces for a limited number of degrees of freedom (e.g., quasistatic friction problem).

There are dynamic problems that necessitate repeated calculation of the response (displacements, velocities, and accelerations) and unknown forces for a limited number of degrees of freedom. Equation (3) is partitioned at these degrees of freedom with the understanding that the unknown forces are acting on the degrees of freedom indicated by subscript b and the response is prescribed at the degrees of freedom indicated by r. Thus, the equation is rewritten in the partitioned form

$$\mathbf{g}_b(t) = \mathbf{G}^0_{br}\mathbf{F}^0_r + \mathbf{G}^t_{br}\mathbf{F}^t_r + {}^f\mathbf{g}^{(t)}_b \tag{4}$$

where subscripts b and r indicate that vectors and matrices are partitioned at these degrees of freedom. If the response and forces at $t = 0$ are known, equation (4) represents the relationship between the response and the unknown forces at time t. In the case that the unknown forces are nonlinearly dependent on the response $\mathbf{g}_b(t)$, the nonlinear forces may be calculated by iterating the reduced equation (4). Analogous to the static condensation expression, equation (4) can be called dynamic condensation.

Matrices $\mathbf{G}^0$ and $\mathbf{G}^t$, and vector ${}^f\mathbf{g}(t)$ in equation (4) can be evaluated from the eigenvectors and eigenvalues of the structure, which are calculated primarily for the purpose of decoupling the equations of motion in the transient load analysis. A solution for a decoupled equation is given by

$${}^m a^t = \int_0^t {}^m h(t-z)\,{}^m q(z)\,dz + {}^m d\,{}^m a^0 + {}^m e\,{}^m \dot{a}^0 \tag{5}$$

$${}^m h(z) = \frac{{}^m w}{\sqrt{1-\zeta^2}}\, e^{-\zeta\,{}^m wz} \sin({}^m w\sqrt{1-\zeta^2}\,z) \tag{6}$$

$${}^m d = e^{-\zeta\,{}^m wz}\left\{ \frac{\zeta}{\sqrt{1-\zeta^2}} \sin({}^m w\sqrt{1-\zeta^2}\,z) + \cos({}^m w\sqrt{1-\zeta^2}\,z)\right\} \tag{7}$$

$${}^m e = e^{-\zeta\,{}^m wz}\,\frac{1}{{}^m w\sqrt{1-\zeta^2}} \sin({}^m w\sqrt{1-\zeta^2}) \tag{8}$$

where ${}^m a^t$ is a modal coordinate with ${}^m(\ )$, indicating the association with the mth natural mode. This mode is assumed to be normalized with respect to the mass matrix. ${}^m a^0$ and ${}^m \dot{a}^0$ are the initial modal displacement and velocity, respectively, and ${}^m w$ and ζ are the frequency and damping coefficient, respectively. The associated modal force ${}^m q(z)$ is interpolated by using the values of ${}^m q^0$ and ${}^m q^t$ at time 0 and t, respectively. Hence, using interpolation functions $l^0(z)$ and $l^t(z)$, we obtain

$$\begin{aligned} {}^m q(z) &= l^0(z)\,{}^m q^0 + l^t(z)\,{}^m q^0 \\ &= l^0(z)\,{}^m \mathbf{P}^T\mathbf{F}^0 + \mathbf{l}^t(z)\,{}^m P^T\mathbf{F}^t \end{aligned} \tag{9}$$

where ${}^m \mathbf{P}^T$ is the transpose of the mth mode vector, and vectors $\mathbf{F}^0$ and $\mathbf{F}^t$ are forces at time 0 and time t. If the interpolated modal force is substituted into equation (5) and the resulting equation is premultiplied by the mth mode vector ${}^m\mathbf{P}$, a summation over all modes will result in equation

$$\mathbf{U}^t = \mathbf{A}\mathbf{F}^0 + \mathbf{B}\mathbf{F}^t + \mathbf{D}\mathbf{a}^0 + \mathbf{E}\mathbf{a}^0 \tag{10}$$

It is understood that the displacement vector $\mathbf{U}^t$ at time t is expressed as the linear combination of all natural modes with the linear coefficients representing the modal coordinates. In equation (10), the following relations are used where M number of modes are considered.

$$\mathbf{A} = \sum_{m=1}^{M} {}^m i\,{}^m\mathbf{P}\,{}^m\mathbf{P}^T \tag{11}$$

$$\mathbf{B} = \sum_{m=1}^{M} {}^m j\,{}^m\mathbf{P}\,{}^m\mathbf{P}^T \tag{12}$$

$$\mathbf{D} = [{}^1 d\,{}^1\mathbf{P},\ {}^2 d\,{}^2\mathbf{P},\ \ldots,\ {}^M d\,{}^M\mathbf{P}] \tag{13}$$

$$\mathbf{E} = [{}^1 e\,{}^1\mathbf{P},\ {}^2 e\,{}^2\mathbf{P},\ \ldots,\ {}^M e\,{}^M\mathbf{P}] \tag{14}$$

Downloaded 02 May 2010 to 171.66.16.54. Redistribution subject to ASME license or copyright; see http://www.asme.org/terms/Terms_Use.cfm

$$ {}^{m}i = \int_0^t {}^{m}h(t-z)\,I^0(z)\,dz \tag{15} $$

$$ {}^{m}j = \int_0^t {}^{m}h(t-z)\,I^t(z)\,dz \tag{16} $$

Equation (10) is partitioned at degrees of freedom b and r. The result is:

$$ \mathbf{U}_b^t = \mathbf{A}_{br}\mathbf{F}_r^0 + \mathbf{B}_{br}\mathbf{F}_r^t + \mathbf{D}_b\mathbf{a}^0 + \mathbf{E}_b\dot{a}^0 \tag{17} $$

This equation relates displacements $\mathbf{U}_b^t$ at time t to forces $\mathbf{F}^t$ at time t by using quantities at time 0. $\mathbf{a}^0$ and $\dot{\mathbf{a}}^0$ are vectors with their components being ${}^{m}a^0$ and ${}^{m}\dot{a}^0$, respectively. If the first or second derivatives of equations (6)-(8) are used in equation (5), expressions similar to that of equation (17) can be derived for velocity vector $\dot{\mathbf{U}}^t$:

$$ \dot{\mathbf{U}}_b^t = \dot{\mathbf{A}}_{br}\mathbf{F}_r^0 + \dot{\mathbf{B}}_{br}\mathbf{F}_r^t + \dot{\mathbf{D}}_b\mathbf{a}^0 + \dot{\mathbf{E}}_b\dot{\mathbf{a}}^0 \tag{18} $$

and for acceleration vector U^t:

$$ \ddot{\mathbf{U}}_b^t = \ddot{\mathbf{A}}_{br}\mathbf{F}_r^0 + \ddot{\mathbf{B}}_{br}\mathbf{F}_r^t + \ddot{\mathbf{D}}_b\mathbf{a}^0 + \ddot{\mathbf{E}}_b\dot{\mathbf{a}}^0 \tag{19} $$

Here, matrices $\dot{\mathbf{A}}_{br}$, $\dot{\mathbf{B}}_{br}$, $\dot{\mathbf{D}}_b$, $\dot{\mathbf{E}}_b$ and $\ddot{\mathbf{A}}_{br}$, $\ddot{\mathbf{B}}_{br}$, $\ddot{\mathbf{D}}_b$, and $\ddot{\mathbf{E}}_b$ are derived by replacing ${}^{m}d$, ${}^{m}e$, and ${}^{m}h$ of equations (13)-(16), respectively, with their first and second time derivatives.

Formulation of Transient Load Analysis Method

Conventionally, several substructures are coupled to form a system equation of motion for a linear transient loads analysis. The system equation is decoupled through an eigenanalysis and then time-integrated. The example problem investigated here does not couple substructures to form the system equation of motion. Instead, the reaction force at each substructure interface is treated as an unknown applied forces. This requires the simultaneous calculation of the substructure equations of motion and the reaction forces. In this section, recurrence equations will be developed for calculating the unknown reaction forces. First, both the reaction and applied forces during each small time interval are interpolated from the instantaneous values. Then, the finite-difference equations are derived using dynamic condensation. In the equations, the interface displacements, velocities, and accelerations associated with the applied forces are grouped together. Since the response associated with applied forces in this problem can be considered as known values, they are replaced by known values. Then, by assessing the equilibrium and compatibility conditions at the interface, the recurrence equations for the unknown reaction force calculation are derived. Several different reaction force interpolations and compatibility assessments are discussed in the following.

The reaction force vector $\mathbf{R}(z)$ during the small time interval t and $t+dt$ can be interpolated with known values $\mathbf{R}^t$ at the beginning of the interval and unknown values $\mathbf{R}^{t+dt}$ at the end of the interval,

$$ \mathbf{R}(z) = \left(1 - \frac{z}{dt}\right)\mathbf{R}^t + \frac{z}{dt}\mathbf{R}^{t+dt} \tag{20} $$

Using this reaction force interpolation in deriving equations (17)-(19) and replacing superscripts 0 and t with t and $t+dt$, respectively, the interface displacement vector $\mathbf{U}_b^{t+dt}$ at time $t+dt$ are expressed by

$$ \mathbf{U}_b^{t+dt} = \mathbf{A}_{bb}\mathbf{R}^t + \mathbf{B}_{bb}\mathbf{R}^{t+dt} + {}^{A}\mathbf{U}_b^{t+dt} + {}^{f}\mathbf{U}_b^{t+dt} \tag{21} $$

where ${}^{A}\mathbf{U}_b^{t+dt}$ is a vector of the interface displacements at time $t+dt$ due to the applied forces, and ${}^{f}\mathbf{U}_b^{t+dt}$ is a vector of the free vibration displacements due to the reaction forces. Similarly, the expressions for interface velocity and acceleration vectors $\dot{\mathbf{U}}_b^{t+dt}$ and $\ddot{\mathbf{U}}_b^{t+dt}$, respectively, are derived as follows:

$$ \dot{\mathbf{U}}_b^{t+dt} = \dot{\mathbf{A}}_{bb}\mathbf{R}^t + \dot{\mathbf{B}}_{bb}\mathbf{R}^{t+dt} + {}^{A}\dot{\mathbf{U}}_b^{t+dt} + {}^{f}\dot{\mathbf{U}}_b^{t+dt} \tag{22} $$

$$ \ddot{\mathbf{U}}_b^{t+dt} = \ddot{\mathbf{A}}_{bb}\mathbf{R}^t + \ddot{\mathbf{B}}_{bb}\mathbf{R}^{t+dt} + {}^{A}\ddot{\mathbf{U}}_b^{t+dt} + {}^{f}\ddot{\mathbf{U}}_b^{t+dt} \tag{23} $$

where vectors ${}^{A}\dot{\mathbf{U}}_b^{t+dt}$ and ${}^{A}\ddot{\mathbf{U}}_b^{t+dt}$ are the velocities and accelerations associated with the applied forces, and vectors ${}^{f}\dot{\mathbf{U}}_b^{t+dt}$ and ${}^{f}\ddot{\mathbf{U}}_b^{t+dt}$ are the free vibration velocities and accelerations associated with the reaction forces.

Let the system structure consist of two substructures, O and P. At the interface, the accelerations of substructures O and P are continuous and the reaction forces are the same in magnitude and opposite in direction. Assigning superscripts o and p to equation (21), equating the interface displacements and realizing ${}^{o}\mathbf{R}^{t+dt} = {}^{p}\mathbf{R}^{t+dt} = -\mathbf{R}^{t+dt}$, the unknown reaction forces $\mathbf{R}^{t+dt}$ at time $t+dt$ may be expressed by

$$ \mathbf{X}\mathbf{R}^{t+dt} = \mathbf{Y}^{t+dt} \tag{24} $$

where

$$ \begin{aligned} \mathbf{X} &= ({}^{p}\mathbf{B}_{bb} + {}^{o}\mathbf{B}_{bb}) \\ \mathbf{Y}^{t+dt} &= ({}^{p}\mathbf{A}_{bb} + {}^{o}\mathbf{A}_{bb})R^t + {}^{o}({}^{A}\mathbf{U}_b^{t+dt}) \\ &\quad - {}^{p}({}^{A}\mathbf{U}_b^{t+dt}) + {}^{o}({}^{f}\mathbf{U}_b^{t+dt}) + {}^{p}({}^{f}\mathbf{U}_b^{t+dt}) \end{aligned} \tag{25} $$

with superscripts o and p indicating the quantities that pertain to substructures O and P, respectively. The displacements ${}^{o}({}^{A}\mathbf{U}_b^{t+dt})$ and ${}^{p}({}^{A}\mathbf{U}_b^{t+dt})$, which are associated with the applied forces, are calculated independently for substructures O and P, and are treated as the known displacements. When the forces are applied only to substructure O and once these displacements are calculated, the calculation of modal forces and the response associated with the applied forces does not have to be repeated, even for the frequent structural change of substructure P. The reaction forces $\mathbf{R}^t$ at time t are known from the previous time interval and the free vibration displacements ${}^{o}({}^{f}\mathbf{U}_b^{t+dt})$ and ${}^{p}({}^{f}\mathbf{U}_b^{t+dt})$ are calculated using the displacements and velocities at time t, which are calculated from the previous time interval. Thus, the reaction forces at time $t+dt$ can be calculated from this equation. By calculating reaction forces, the equations of motion for each substructure are progressively integrated. Also, expressions similar to equation (24) are obtained by equating the interface velocities or accelerations.

Displacements, velocities, and accelerations are all continuous at the substructure interfaces. At the interface, assuming the compatibility of either the displacements, velocities, or accelerations, does not guarantee the compatibility of the remaining two variables. There is one unknown reaction force at each interface degree of freedom and there are three variables to be constrained; therefore, compatibility is enforced by a least squares method. In the present formulation, two variables are chosen to be constrained, and in the case of displacement and velocity compatibility assessment, the problem is to seek the reaction forces $\mathbf{R}^{t+dt}$ that minimize a function W, which is defined by

$$ W = ({}^{o}\mathbf{U}_b^{t+dt} - {}^{p}\mathbf{U}_b^{t+dt})^2 + ({}^{o}\dot{\mathbf{U}}^{t+dt} - {}^{p}\dot{\mathbf{U}}_b^{t+dt})^2 \tag{26} $$

where superscripts o and p are used with the same meaning as in the displacement compatibility. Introducing equations (21) and (22) into equation (26), taking the derivatives of W with respect to $\mathbf{R}^{t+dt}$, equating the resulting equations to zero, and rearranging the terms, results in

$$ \bar{\mathbf{X}}\mathbf{R}^{t+dt} = \bar{\mathbf{Y}}^{t+dt} \tag{27} $$

where

$$ \begin{aligned} \bar{\mathbf{X}} &= ({}^{p}\mathbf{B}_{bb} + {}^{o}\mathbf{B}_{bb})^T({}^{p}\mathbf{B}_{bb} + {}^{o}\mathbf{B}_{bb}) + ({}^{p}\dot{\mathbf{B}}_{bb} + {}^{o}\dot{\mathbf{B}}_{bb})^T \\ &\quad ({}^{p}\dot{\mathbf{B}}_{bb} + {}^{o}\dot{\mathbf{B}}_{bb}) \\ Y^{t+dt} &= ({}^{p}B_{bb} + {}^{o}B_{bb})^T\{({}^{p}A_{bb} + {}^{o}A_{bb})R^t + {}^{o}({}^{f}U_b^{t+dt}) \end{aligned} \tag{28} $$

Downloaded 02 May 2010 to 171.66.16.54. Redistribution subject to ASME license or copyright; see http://www.asme.org/terms/Terms_Use.cfm

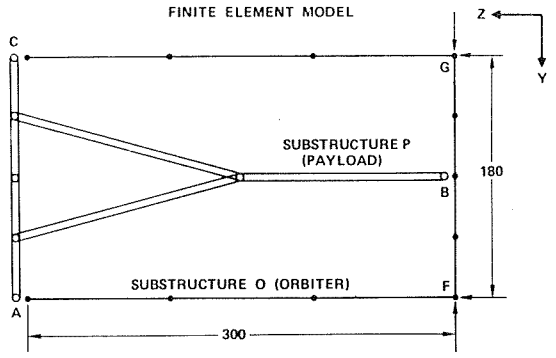

APPLIED FORCE

LOCATION	FORCE TIME HISTORY
Y-DOF AT F	+SIN (5t) –COS (400t) +COS (750t) –SIN (1,500t)
Z-DOF AT F	–SIN (10t) +COS (200t) –COS (750t) +SIN (1,500t)
Y-DOF AT G	+SIN (30t) –COS (100t) +COS (750t) –SIN (1,500t)
Z-DOF AT G	–SIN (50t) +COS (80t) –COS (750t) +SIN (1,500t)

MATERIAL AND GEOMETRICAL PROPERTIES

ELEMENT	YOUNG'S MODULUS	POISSON'S RATIO	MASS DENSITY	CROSS-SECTIONAL AREA	MOMENT OF INERTIA
	10 E+6	0.3	0.003	5.0	20
	10 E+6	0.3	0.003	2.5	10

Fig. 1 Model structure (unit = in. sec, lb)

$$-{}^{p}({}^{f}U_b^{t+dt})$$
$$+{}^{o}({}^{A}U_b^{t+dt})-{}^{p}({}^{A}U_b^{t+dt})\}+({}^{p}\dot{B}_{bb}+{}^{o}\dot{B}_{bb})\{({}^{p}\dot{A}_{bb}$$
$$+{}^{o}\dot{A}_{bb})R^{t}$$
$$+{}^{o}({}^{f}\dot{U}_b^{t+dt})-{}^{p}({}^{f}\dot{U}_b^{t+dt})+{}^{o}({}^{A}\dot{U}_b^{t+dt})-{}^{p}({}^{A}\dot{U}_b^{t+dt})\} \quad (29)$$

In many cases, the initial values for a modal transient load analysis are expressed as zero velocity, zero rigid body modal displacement, zero elastic mode acceleration, nonzero elastic mode displacement, and nonzero rigid body acceleration. This is to describe a steady-state deformation of a structure subjected to corresponding initial values of the applied forces. As the applied forces change, the structure undergoes a transient vibration. A starting procedure of analysis was developed to simulate this situation. To calculate reaction forces at the beginning of the analysis, the interface displacements and accelerations of the independent substructures are needed.

Numerical Investigation

The proposed methods were investigated using the example problem shown in Fig. 1. The system structure consists of two substructures, O and P, which are composed of truss elements. Each element has bending and extensional stiffness and distribution mass (properties are shown in the figure). Respectively, substructures O and P consist of 22 and 14 degrees of freedom after reducing the rotational degrees of freedom about the X-axis with Guyan's method [17]. Stiffness and mass matrices were calculated using NASTRAN version 17.5 [18]. The system structure was subjected to the applied forces at points F and G in the figure. Also shown in Fig. 1 are the applied force time histories along with their locations of application.

The example problem was first solved with the conventional transient load analysis method so that the solution could be used as a reference. The substructure O and P were coupled through Y and Z degrees of freedom at points A, B, and C (as shown in Fig. 1), which results in the 30 structural system degrees of freedom. From the coupled system

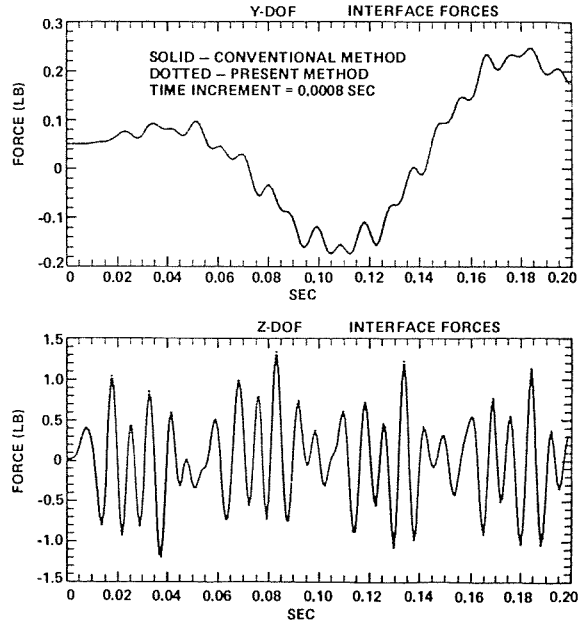

Fig. 2 Interface forces at point C (0.0008 sec)

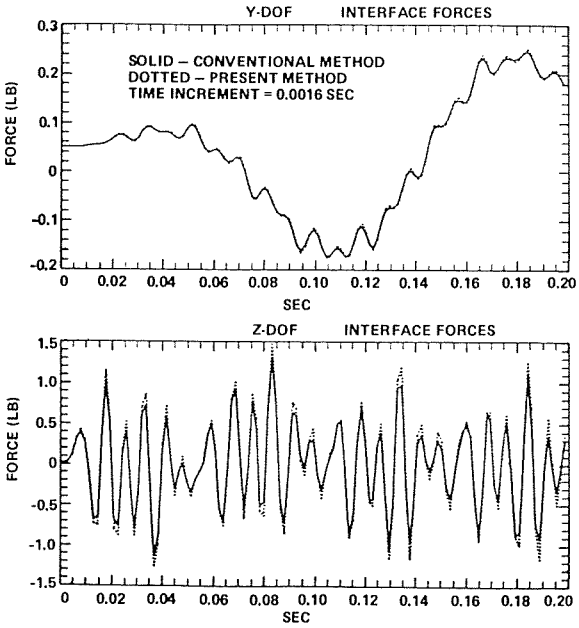

Fig. 3 Interface forces at point C (0.0016 sec)

structure, the eigenvalues (up to frequencies of 346.72 Hz) and eigenvectors were calculated by the NASTRAN version 17.5 READ module in which the Given eigensolution routine was used. Then, the system equation of motion was transformed to modal coordinates and time integrated. A value of 0.0002 second was used for the time integration step. In Figs. 2 and 3, the Y and Z-direction reaction forces between substructures O and P at point C in Fig. 1 are plotted using solid curves. No damping was included in the analysis.

Next, the interface response of substructure O was calculated as the input response to the recurrence equations for the reaction force calculation in the proposed method. It corresponds to interface vectors ${}^{o}({}^{A}\mathbf{U}_b^{t+dt})$, ${}^{o}({}^{A}\dot{\mathbf{U}}_b^{t+dt})$, and ${}^{o}({}^{A}\ddot{\mathbf{U}}_b^{t+dt})$. Since the forces are not applied to the substructure P, ${}^{p}({}^{A}\mathbf{U}_b^{t+dt})$, ${}^{p}({}^{A}\dot{\mathbf{U}}_b^{t+dt})$, and ${}^{p}({}^{A}\ddot{\mathbf{U}}_b^{t+dt})$ are zero vectors. The eigenvalues and eigenvectors of substructures O (up to 383.38 Hz) and P (up to 330.88 Hz) were independently

Downloaded 02 May 2010 to 171.66.16.54. Redistribution subject to ASME license or copyright; see http://www.asme.org/terms/Terms_Use.cfm

calculated. Then, the modal equations of motion for substructure O were time integrated by subjecting the substructure to the same forces as those applied to the system structure at points F and G. Again, the value of the time-integration step size was 0.0002 and no damping was included in the analysis. From the integrated modal time histories, the displacements, velocities, and accelerations at Y and Z degrees of freedom at points A, B, and C were recovered as the input response.

For analysis by the proposed method, three different interface reaction interpolations, fifteen different time increments, and five different interface compatibility assessments were implemented in developing the equations. First, using all of the free-free modes from each substructure, the proposed finite-difference equations of motion were developed independently for each substructure. In the development, the reaction forces were interpolated with functions that are constant within the time interval, linear within the interval, and continuous across the interval or continuous up to the first-time derivatives across the interval. In each equation, the time increments used were 0.0001, 0.0002, 0.0004, 0.0006, 0.0008, 0.001, 0.0012, 0.0014, 0.0016, 0.0018, 0.002, 0.004, 0.006, 0.008, or 0.01 second. No damping was included in the calculation. Then, at the interface of substructures O and P, the interface compatibility was assessed to formulate the recurrence equations for the interface reaction force calculation. In the formulation, the compatibility of either the interface displacements, velocities, or accelerations were assessed. Also, the compatibility of both displacements and velocities or both velocities and accelerations were assessed using the least squares method. Thus developed methods were numerically examined for accuracy and stability.

The reaction forces calculated with the method based on the compatibility of both displacements and velocities and linear continuous reaction force interpolation are plotted in Figs. 2 and 3 with dotted curves. For those plotted, the time increments are 0.0008 and 0.0016 second, as indicated. Examination of these figures shows that for time increments smaller than about one-fourth (0.0026) of the highest structure frequency, the differences between the reaction forces calculated by the conventionally coupled transient loads analysis method (solid curves in the figures) and the proposed method (dotted curves in the same figures) are negligible. It can be seen that when the time increment equals about one-half of the period of the highest frequency, there are notable differences in the reaction forces.

The reaction forces that were calculated based on velocity and acceleration compatibility, and velocity or acceleration compatibility with the linear interpolation of reaction forces were also compared to the reference solution. Though plots were not included, they showed the same degree of accuracy and frequency dependence when the time increment was small. When the time increment became greater or close to the period of the highest substructure frequency, the solutions by these three compatibility assessments displayed instability; however, the solutions by the method based on the displacement and velocity compatibility are stable for all 15 values of the time increment examined.

The methods using interpolations with reaction forces constant during the time interval and with reaction forces continuous across the interval up to the first time derivatives were also numerically examined. Two different time increments were used in the analyses. The reaction forces calculated with the methods using these two interpolations diverged for time increments of 0.0001 to 0.001 regardless of compatibility assessments. Also, the reaction forces calculated from the method with displacement compatibility diverged regardless of interpolation function tried. In conclusion, among these methods investigated, the linear reaction force interpolation and displacement and velocity compatibility assessment best fits the example problem.

Discussion and Concluding Remarks

Finite-difference time-integration equations have been developed based on the integral form equation of motion for linear structure vibration problems. Using the developed equations, alternative time-integration methods have been investigated for the transient load analysis of a system structure without substructure coupling. Among several methods investigated, a stable and accurate one has been found. In this method, the unknown reaction forces during a small time interval are linearly interpolated and the displacement and velocity compatibility is enforced. An accurate solution can be obtained by using the time increment and is less than a period of the highest frequency.

The transient load analysis of several minor substructures in a complex large system structure is considered to best fit the proposed method. To analyze the minor structures, this method requires certain information from the major substructure, including the modal displacements for interface degrees of freedom, associated eigenvalues, modal damping, and the interface responses caused by applied forces. Once this information is obtained, the proposed method does not require these data to be recalculated to analyze different minor structures. Therefore, this method has potential advantages over the conventional linear transient load analysis when the number of interface degrees of freedom between the major and minor substructures is small compared with that of the system structure, and the analysis involves frequent structural changes of minor substructures while the major substructure remains unchanged. This is the case for the transient load analysis of a launch vehicle and payload structural system with the launch vehicle being considered the major substructure, and the payloads, the minor substructures.

When the higher modes are truncated out in both the conventional and present transient load analysis methods, the reaction forces transmitted through the substructure interfaces are the linear combination of the forces associated with the retained lower frequency modes. It can be understood that the truncated substructure modes can only approximate the system mode. Thus, a reaction force calculated by the present method is an approximation of the one calculated by the conventional method; therefore, when the coupling of the substructure equations of motion is foregone, this approximation seems to be associated with any type of transient load analysis in which the substructure and system modes are truncated. In reality, the number of substructural degrees of freedom is usually large and the substructure modes are truncated in order to minimize the computation time required. This is also the case for the STS payload transient load analysis [14]. As shown in reference [15], these truncation effects have been investigated for the STS seventh flight payload analysis. It reports that approximately a 10 percent difference between the solutions by the both methods was attained.

It is possible to obtain the reduced equations that relate the limited number of applied forces and responses from the finite difference equations developed based on the differential form of the equation of motion. These reduced equations do not include the force-time dependence; therefore, they may lack the flexibility to accommodate different force-time dependences that seem so important to obtain an accurate and stable finite difference method. The linear continuous reaction force interpolation with displacement and velocity compatibility assessment is adequate for an accurate and stable solution for the present problem. However, the present interpolation and compatibility assessment is adequate only

Downloaded 02 May 2010 to 171.66.16.54. Redistribution subject to ASME license or copyright; see http://www.asme.org/terms/Terms_Use.cfm

for the present problem and may not be appropriate for different dynamic problems. A different problem may require a different compatibility assessment and interpolation of forces. It should be noted that the expression of dynamic conditions is also a very efficient tool for evaluating nonlinear forces when the nonlinearity is localized in a large complex structure.

References

1 Crandall, S. H., *Engineering Analysis*, McGraw-Hill, New York, 1956.

2 Houbolt, J. H., "A Recurrence Matric Solution for the Dynamic Response of Elastic Aircraft," *Journal of Aeronautical Science*, Vol. 17, 1950, pp. 540-550.

3 Newmark, N. M., "A Method of Computation for Structural Dynamics," *ASCE, Journal of Engineering Mechanics Division*, Vol. 85, 1959, pp. 67-94.

4 Kubomura, K., "A Theory of Substructure Model Synthesis," ASME JOURNAL OF APPLIED MECHANICS, Vol. 49, 1982, pp. 903-909.

5 Craig, R. R., and Bampton, M. C., "Coupling of Substructures for Dynamic Analysis," *AIAA Journal*, Vol. 7, July, 1968, pp. 1313-1319.

6 MacNeal, R. H., "A Hybrid Method of Component Mode Synthesis," *Computer and Structures*, Vol. 1, Dec. 1971, pp. 581-601.

7 Rubin, S., "Improved Component-Mode Representation for Structural Dynamic Analysis," *AIAA Journal*, Vol. 13, No. 8, Aug. 1975, pp. 995-1006.

8 Chao, R. S., Leang, J. L., Fan, H. S., and Yahata, S. J., "Load Data Book for STS-7 Verification Loads Analysis," Rockwell International, Space Operation/Integration and Satellite Systems Division, STS 82-0782, Nov. 1982.

9 Chen, J. C., and Wada, B. K., "Matrix Perturbation for Structural Dynamic Analysis," *AIAA Journal*, Aug. 1977, pp. 1095-1100.

10 Payne, K. R., "An Impedance Technique for Determining Low Frequency Payload Environments," *The Shock and Vibration Bulletin*, No. 49, Part II, Sept. 1979, pp. 1-4.

11 Trubert, M., and Salama, M., "Generalized Shock Spectra Method for Spacecraft Loads Analysis," *AIAA Journal*, Vol. 18, No. 8, Aug. 1980, pp. 988-994.

12 Engles, R. C., Harcrow, H. W., and Shanahan, T. G., "An Integration Scheme to Determine the Dynamic Response of a Launch Vehicle With Several Payloads," *AIAA/ASME/ASCE/AMS*, 23rd Structural Dynamics Material Convergence Paper No. 82-0632, Apr. 1, 1982.

13 Chen, J. G., Garba, J. A., and Wada, B. K., "Estimation of Payload Loads Using Rigid-Body Interface Accelerations," *Journal of Spacecraft and Rockets*, Vol. 16, No. 2, 1979, pp. 74-80.

14 Chen, J. C., Garba, J. A., Salama, M., and Trubert, N., "A Survey of Load Methodologies for Shuttle Orbiter Payloads," Jet Propulsion Laboratory, 80-37, June 15, 1980.

15 Kubomura, K., "The Space Shuttle Payload Transient Load Analysis by the Flex-Base Drive Method," *AIAA/ASME/ASCE/AMS* 25th Structural Dynamics and Material Conference, Paper No. 84-0947, May 14, 1984.

16 Wilson, E. L., "The Static Condensation Algorithm," *International Journal for Numerical Methods in Engineering*, Vol. 8, June 15, 1980, pp. 199-203.

17 Guyan, R. J., "Reduction of Stiffness and Mass Matrices," *AIAA Journal*, Vol. 3, No. 2, Feb. 1965.

18 "Rockwell NASTRAN Programmer's Manual Level 17.5," Rockwell International Space Operation/Integration and Satellite Systems Division, Sept. 1979.

Downloaded 02 May 2010 to 171.66.16.54. Redistribution subject to ASME license or copyright; see http://www.asme.org/terms/Terms_Use.cfm

T. C. T. Ting
Professor.

Yijian Jin
Graduate Student.

Department of Civil Engineering,
Mechanics and Metallurgy,
University of Illinois at Chicago,
P.O. Box 4348,
Chicago, Ill. 60680

S. C. Chou
U.S. Army Materials and
Mechanics Research Center,
Watertown, Mass. 02172

Eigenfunctions at a Singular Point in Transversely Isotropic Materials Under Axisymmetric Deformations

When a two-dimensional elastic body that contains a notch or a crack is under a plane stress or plane strain deformation, the asymptotic solution of the stress near the apex of the notch or crack is simply a series of eigenfunctions of the form $\rho^{\delta} f(\psi,\delta)$ *in which* (ρ,ψ) *is the polar coordinate with origin at the apex and* δ *is the eigenvalue. If the body is a three-dimensional elastic solid that contains axisymmetric notches or cracks and subjected to an axisymmetric deformation, the eigenfunctions associated with an eigenvalue contains not only the* ρ^{δ} *term, but also the* $\rho^{\delta+1}$, $\rho^{\delta+2}$ *. . . terms. Therefore, the second and higher-order terms of the asymptotic solution are not simply the second and subsequent eigenfunctions. We present the eigenfunctions for transversely isotropic materials under an axisymmetric deformation. The degenerate case in which the eigenvalues* p_1 *and* p_2 *of the elasticity constants are identical is also considered. The latter includes the isotropic material as a special case.*

1 Introduction

It is well-known that the stress distribution near the apex of an isotropic elastic wedge or a notch under a plane-stress or plane-strain deformation can be expressed in terms of a series of eigenfunctions of the form $\rho^{\delta} f(\psi,\delta)$ where ρ is the radial distance from the apex and f is a function of the polar angle ψ and the eigenvalue δ, [1, 2]. For given wedge angle and homogeneous boundary conditions at the sides of the wedge, there are in general infinitely many eigenvalues δ and the associated eigenfunctions $\rho^{\delta} f(\psi,\delta)$. Particularly important in applications is when one or more of the δ's is negative and the stress is singular at the apex. For instance, if the specimen shown in Fig. 1 represents a two-dimensional body under an external loading, $\delta = -1/2$ at the crack tip Q. At points R, N, and M, it can be shown [3] that there are two negative δ's. Hence the stress is singular at points Q, R, N, and M. In solving stress distribution in the entire specimen numerically by a finite element scheme, one may use regular finite elements everywhere except at the singular points Q, R, N, and M. At these singular points, a special element is used in which the singular nature of the stress is given by the analytical expression $\rho^{\delta} f(\psi,\delta)$. It may be sufficient to consider only the first term (or terms) for which δ is negative in the special element. In many cases, however, more terms including those associated with positive δ are required [4, 5].

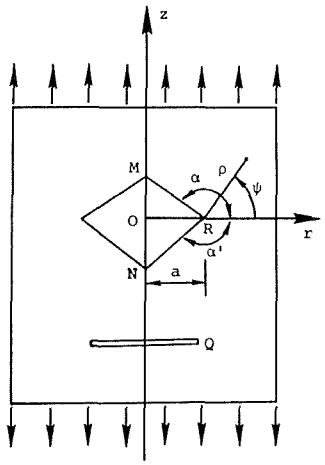

Fig. 1 Cross section of an axisymmetric body that contains a crack and notches

In this paper, we consider the case in which the specimen shown in Fig. 1 is a cross section of an axisymmetric body under an axisymmetric deformation. The material is assumed to be transversely isotropic with the z-axis being the axis of symmetry. The associated problem for isotropic materials was investigated by Delale and Erdogan [6] and Delale, Kishore, and Wang [7]. However, their objectives are different from ours and hence their series solution is different from the one presented here. After presenting the basic equations for transversely isotropic materials under an axisymmetric deformation in Section 2, we present in Section 3 a general solution in the form of a power series in ρ. Application of the stress-free conditions at the sides of the wedge leads to equations for the eigenvalue δ and the coefficients in the power series. This is presented in Section 4. It is seen that the

Contributed by the Applied Mechanics Division and presented at the 1985 Joint ASME/ASCE Applied Mechanics, Fluids Engineering, and Bioengineering Conference, Albuquerque, N. Mex., June 24-26, 1985 of THE AMERICAN SOCIETY OF MECHANICAL ENGINEERS.

Discussion on this paper should be addressed to the Editorial Department, ASME, United Engineering Center, 345 East 47th Street, New York, N.Y. 10017, and will be accepted until two months after final publication of the paper itself in the JOURNAL OF APPLIED MECHANICS. Manuscript received by ASME Applied Mechanics Division, April, 1984. Paper No. 85-APM-22.

Copyright © 1985 by ASME
Downloaded 02 May 2010 to 171.66.16.54. Redistribution subject to ASME license or copyright; see http://www.asme.org/terms/Terms_Use.cfm

eigenfunction associated with an eigenvalue δ no longer contains a single term $\rho^{\delta} f(\psi,\delta)$. It also has the terms $\rho^{\delta+1} f_1(\psi,\delta)$, $\rho^{\delta+2} f_2(\psi,\delta)$ . . . . Therfore, the inclusion of the second and higher-order terms in the special element is not simply the inclusion of the eigenfunctions associated with the subsequent smallest eigenvalues δ. A similar situation occurs in wedges with curved sides under a two-dimensional deformation [8]. The derivations presented in Sections 3 and 4 are for the general case in which the two eigenvalues p_1, p_2 of the elasticity constants are distinct. The degenerate case in which $p_1 = p_2$ (of which the isotropic material is a special case) is discussed in Section 5. For two-dimensional deformations, the displacement of the singular point R (Fig. 1) does not produce stresses and hence can be ignored. For axisymmetric deformations, a displacement in the r-direction does produce nonzero stresses. A particular solution associated with the displacement of the singular point is presented in Section 6.

2 Mathematical Formulation

We choose a cylindrical coordinate system (r,θ,z) in the transversely isotropic medium such that the z-axis is the axis of material symmetry. Let (u_r,u_θ,u_z) be the displacement components. We assume that the deformation is axisymmetric in which $u_\theta = 0$ while u_r and u_z are functions of r and z only. Introducing the displacement potential $\phi(r,z)$ from which u_r and u_z are given by [9-11]

$$u_r = \frac{\partial \phi}{\partial r}, \quad u_z = m\frac{\partial \phi}{\partial z}, \tag{1}$$

where m is a constant to be determined, the stresses have the expressions

$$\left.\begin{aligned}
\sigma_r &= c_{11}\frac{\partial^2\phi}{\partial r^2} + c_{12}\frac{\partial\phi}{r\partial r} + c_{13}m\frac{\partial^2\phi}{\partial z^2},\\
\sigma_\theta &= c_{12}\frac{\partial^2\phi}{\partial r^2} + c_{11}\frac{\partial\phi}{r\partial r} + c_{13}m\frac{\partial^2\phi}{\partial z^2},\\
\sigma_z &= c_{13}\frac{\partial^2\phi}{\partial r^2} + c_{13}\frac{\partial\phi}{r\partial r} + c_{33}m\frac{\partial^2\phi}{\partial z^2},\\
\sigma_{rz} &= c_{44}(1+m)\frac{\partial^2\phi}{\partial r\partial z},
\end{aligned}\right\} \tag{2}$$

in which c_{ij} are the elasticity constants. The equations of equilibrium are satisfied if

$$\frac{\partial^2\phi}{\partial r^2} + \frac{\partial\phi}{r\partial r} - \frac{1}{p^2}\frac{\partial^2\phi}{\partial z^2} = 0, \tag{3}$$

where

$$p^2 = \frac{-c_{11}}{c_{13}m + (1+m)c_{44}} = \frac{c_{13}+(1+m)c_{44}}{-c_{33}m}, \tag{4a}$$

or

$$-m = \frac{c_{11}+c_{44}p^2}{(c_{13}+c_{44})p^2} = \frac{c_{13}+c_{44}}{c_{44}+c_{33}p^2}. \tag{4b}$$

The second equality of equations (4a) and (4b) yield, respectively,

$$m^2 - 2\left[\frac{c_{11}c_{33}-c_{13}^2}{2c_{44}(c_{13}+c_{44})} - 1\right]m + 1 = 0, \tag{5a}$$

$$p^4 + 2\left[\frac{c_{11}c_{33}-c_{13}^2-2c_{13}c_{44}}{2c_{33}c_{44}}\right]p^2 + \frac{c_{11}}{c_{33}} = 0, \tag{5b}$$

It can be shown [12] that p cannot be real if the strain energy is positive-definite. We therefore have two pairs of complex conjugates for p denoted by p_1, p_2, and $\bar{p}_1, \bar{p}_2$ where an overbar denotes the complex conjugate. The associated m are denoted by m_1, m_2, and $\bar{m}_1$, and $\bar{m}_2$. We see from equation (5a) that

$$m_1 m_2 = 1. \tag{5c}$$

Since equation (5b) is a quadric in p^2 with real coefficients, if p_1 is purely imaginary so is p_2. In this case m_1, m_2 are real and $m_1 = \bar{m}_1$, $m_2 = \bar{m}_2$. If p_1 and p_2 are not purely imaginary, we may choose

$$p_1 = u + iv, \quad p_2 = -u + iv = -\bar{p}_1, \tag{6}$$

where u, v are real. In this case m_1, m_2 are complex and $m_1 = \bar{m}_2$. In view of the fact that the equations are linear, the general solution for ϕ is obtained by superimposing ϕ's associated with $p = p_1, p_2$, and $\bar{p}_1$, $\bar{p}_2$. We will assume that $p_1 \neq p_2$. The degenerate case $p_1 = p_2$ will be discussed in Section 5.

3 Eigenfunctions for Small ρ

Let $(r,z) = (a,0)$ be a singular point which may be the apex of a wedge, notch, or crack. In this paper, we consider the cases in which $a \neq 0$. The case in which $a = 0$ (such as the point M and N in Fig. 1) is studied in [13]. Using the singular point as the origin, we define

$$x = r - a = \rho\cos\psi, \quad z = \rho\sin\psi. \tag{7}$$

We assume that $\psi = \alpha$ and $\psi = \alpha'$ are the free surfaces. To find the eigenfunction for ϕ that is valid for small ρ, we rewrite equation (3) as

$$\frac{\partial^2\phi}{\partial x^2} - \frac{1}{p^2}\frac{\partial^2\phi}{\partial z^2} = -\frac{1}{a+x}\frac{\partial\phi}{\partial x} = -\frac{1}{a}\frac{\partial\phi}{\partial x}\sum_{s=0}^{\infty}\left(\frac{-x}{a}\right)^s. \tag{8}$$

Let

$$\phi = \phi^{(0)} - \frac{1}{a}\phi^{(1)} + \frac{1}{a^2}\phi^{(2)} - \ldots = \sum_{k=0}^{\infty}\left(\frac{-1}{a}\right)^k \phi^{(k)}, \tag{9a}$$

$$\phi^{(k)} = \sum_{t=0}^{k} A_t^{(k)} x^t Z^{\delta+k-t+2}/(\delta+k-t+2)(\delta+k-t+1), \tag{9b}$$

$$Z = x + pz, \tag{10}$$

where δ is the eigenvalue and $A_t^{(k)}$ are constants to be determined. Using equation (7), we have

$$x^t Z^{\delta+k-t+2} = \rho^{\delta+k+2}(\cos\psi)^t \zeta^{\delta+k-t+2}, \tag{11}$$

$$\zeta = \cos\psi + p\sin\psi. \tag{12}$$

Hence $\phi^{(k)}$ is of order $\rho^{\delta+k+2}$. By substituting equations (9) into (8) and equating the coefficients of $x^t Z^{\delta+k-t+2}$, it can be shown that (see Appendix)

$$A_k^{(k)} = \frac{2k-1}{2k}A_{k-1}^{(k-1)}, \quad (k \geq 1), \tag{13a}$$

$$A_t^{(k)} = \frac{2t-1}{2t}A_{t-1}^{(k-1)} + \frac{1}{2(\delta+k-t)}\left[tA_t^{(k-1)} - (t+1)A_{t+1}^{(k)}\right], \quad (t = k-1, k-2, \ldots 1;\ k \geq 2). \tag{13b}$$

Hence the only unknowns are $A_0^{(k)}$, $(k = 0,1,2, \ldots)$ which will be determined from the boundary conditions at $\psi = \alpha$ and α'.

We will let the solutions given by equations (9)-(13) apply to $p = p_1$. For $p = p_2$, $\bar{p}_1$, and $\bar{p}_2$ we will use the same expressions except that $A_t^{(k)}$ is replaced by $B_t^{(k)}$, $C_t^{(k)}$, and $D_t^{(k)}$, respectively. Thus the general solution for $\phi^{(k)}$ is

$$\phi^{(k)} = \sum_{t=0}^{k}\left\{A_t^{(k)} x^t Z_1^{\delta+k-t+2} + B_t^{(k)} x^t Z_2^{\delta+k-t+2}\right.$$

Downloaded 02 May 2010 to 171.66.16.54. Redistribution subject to ASME license or copyright; see http://www.asme.org/terms/Terms_Use.cfm

$$+ C_t^{(k)} x^t \bar{Z}_1^{\delta+k-t+2} + D_t^{(k)} x^t \bar{Z}_2^{\delta+k-t+2} \Big\} \Big/ (\delta+k-t+2)(\delta+k-t+1), \tag{14a}$$

$$Z_s = x + p_s z, \quad (s=1,2), \tag{14b}$$

Substituting (14) into (1), we obtain

$$u_r^{(k)} = \Big\{ \sum_{t=0}^{k} A_t^{(k)} + \sum_{t=0}^{k-1} A_{t+1}^{(k)} (t+1)/(\delta+k-t) \Big\} x^t Z_1^{\delta+k-t+1}/(\delta+k-t+1)$$

$$+ \Big\{ \sum_{t=0}^{k} B_t^{(k)} + \sum_{t=0}^{k-1} B_{t+1}^{(k)} (t+1)/(\delta+k-t) \Big\} x^t Z_2^{\delta+k-t+1}/(\delta+k-t+1)$$

$$+ \Big\{ \sum_{t=0}^{k} C_t^{(k)} + \sum_{t=0}^{k-1} C_{t+1}^{(k)} (t+1)/(\delta+k-t) \Big\} x^t \bar{Z}_1^{\delta+k-t+1}/(\delta+k-t+1)$$

$$+ \Big\{ \sum_{t=0}^{k} D_t^{(k)} + \sum_{t=0}^{k-1} D_{t+1}^{(k)} (t+1)/(\delta+k-t) \Big\} x^t \bar{Z}_2^{\delta+k-t+1}/(\delta+k-t+1) \tag{15}$$

To simplify the expression, we will let

$$A_t^{(k)} = B_t^{(k)} = C_t^{(k)} = D_t^{(k)} = 0, \quad \text{if} \quad t>k, \tag{16}$$

and rewrite equation (15) as

$$u_r^{(k)} = \sum_{t=0}^{k} \Big[A_t^{(k)} + A_{t+1}^{(k)} (t+1)/(\delta+k-t) \Big] x^t Z_1^{\delta+k-t+1}/(\delta+k-t+1) + \ldots \tag{17a}$$

where the dots stand for the similar expressions associated with $p=p_2$, $\bar{p}_1$, and $\bar{p}_2$. Likewise, we have

$$u_z^{(k)} = \sum_{t=0}^{k} A_t^{(k)} m_1 p_1 x^t Z_1^{\delta+k-t+1}/(\delta+k-t+1) + \ldots \tag{17b}$$

In substituting equation (14) into (2), we first replace the terms $\partial\phi/(r\partial r)$ in (2) by $\partial^2\phi/\partial x^2$ and $\partial\phi^2/\partial z^2$ using equation (3). We then have

$$\sigma_r^{(k)} = \sum_{t=0}^{k} \Big[-A_t^{(k)} c_{44}(1+m_1)p_1^2 + A_{t+1}^{(k)} 2(c_{11} - c_{12})(t+1)/(\delta+k-t) + A_{t+2}^{(k)} (c_{11}-c_{12})(t+2)(t+1)/(\delta+k-t)(\delta+k-t-1) \Big] x^t Z_1^{\delta+k-t} + \ldots \tag{18a}$$

$$\sigma_\theta^{(k)} = \sum_{t=0}^{k} \Big[A_t^{(k)} (c_{12} + c_{13} m_1 p_1^2) - A_{t+1}^{(k)} 2(c_{11} - c_{12})(t+1)/(\delta+k-t) - A_{t+2}^{(k)} (c_{11}-c_{12})(t+2)(t+1)/(\delta+k-t)(\delta+k-t-1) \Big] x^t Z_1^{\delta+k-t} + \ldots \tag{18b}$$

$$\sigma_z^{(k)} = \sum_{t=0}^{k} -A_t^{(k)} c_{44}(1+m_1) x^t Z_1^{\delta+k-t} + \ldots \tag{18c}$$

$$\sigma_{rz}^{(k)} = \sum_{t=0}^{k} \Big[A_t^{(k)} + A_{t+1}^{(k)} (t+1)/(\delta+k-t) \Big] c_{44}(1 + m_1) p_1 x^t Z_1^{\delta+k-t} + \ldots \tag{18d}$$

In (18*a*) and (18*c*), the following identities which are obtained from equation (4*a*) have been used:

$$\left.\begin{aligned} c_{11} + c_{13} m p^2 &= -c_{44}(1+m)p^2, \\ c_{13} + c_{33} m p^2 &= -c_{44}(1+m). \end{aligned}\right\} \tag{19}$$

4 Determination of $A_0^{(k)}$, $B_0^{(k)}$, $C_0^{(k)}$, $D_0^{(k)}$, and δ

The problem reduces to the determination of $A_0^{(k)}$, $B_0^{(k)}$, $C_0^{(k)}$, $D_0^{(k)}$, and δ. The stress-free boundary conditions at $\psi=\alpha$ and α' are

$$\left.\begin{aligned} \sigma_r \sin\psi - \sigma_{rz}\cos\psi = 0, \\ \sigma_{rz}\sin\psi - \sigma_z \cos\psi = 0, \end{aligned}\right\} \tag{20a}$$

or in matrix notations

$$\mathbf{N}\sigma = \mathbf{0}, \qquad (\psi = \alpha, \alpha'), \tag{20b}$$

where

$$\mathbf{N}(\psi) = \begin{bmatrix} \sin\psi & -\cos\psi & 0 \\ 0 & \sin\psi & -\cos\psi \end{bmatrix}, \tag{21}$$

$$\sigma = \sum_{k=0}^{\infty} \sigma^{(k)}, \qquad \sigma^{(k)} = \begin{bmatrix} \sigma_r^{(k)} \\ \sigma_{rz}^{(k)} \\ \sigma_z^{(k)} \end{bmatrix}. \tag{22}$$

From equations (18), we may write $\sigma^{(k)}$ as, using equation (11),

$$\sigma^{(k)} = \rho^{\delta+k} \sum_{t=0}^{k} \Big\{ \mathbf{S}_t(\psi, \delta+k)\mathbf{q}_t^{(k)} + \mathbf{T}_t(\psi,\delta+k)\mathbf{q}_{t+1}^{(k)} + \mathbf{U}_t(\psi,\delta+k)\mathbf{q}_{t+2}^{(k)} \Big\}, \tag{23}$$

in which

$$\mathbf{q}_t^{(k)} = \begin{bmatrix} A_t^{(k)} \\ B_t^{(k)} \\ C_t^{(k)} \\ D_t^{(k)} \end{bmatrix}, \tag{24}$$

$$\mathbf{S}_t(\psi,\delta) = c_{44} \begin{bmatrix} -(1+m_1)p_1^2 & * & * & * \\ (1+m_1)p_1 & * & * & * \\ -(1+m_1) & * & * & * \end{bmatrix} \mathbf{Q}_t(\psi,\delta), \tag{25a}$$

$$\mathbf{T}_t(\psi,\delta) = \frac{t+1}{\delta-t} \begin{bmatrix} 2(c_{11}-c_{12}) & * & * & * \\ c_{44}(1+m_1)p_1 & * & * & * \\ 0 & 0 & 0 & 0 \end{bmatrix} \mathbf{Q}_t(\psi,\delta), \tag{25b}$$

$$\mathbf{U}_t(\psi,\delta) = \frac{(t+2)(t+1)(c_{11}-c_{12})}{(\delta-t)(\delta-t-1)} \begin{bmatrix} 1 & 1 & 1 & 1 \\ 0 & 0 & 0 & 0 \\ 0 & 0 & 0 & 0 \end{bmatrix} \mathbf{Q}_t(\psi,\delta). \tag{25c}$$

In equations (25), the second column of the matrix is obtained from the first column by replacing p_1 by p_2 (and of course m_1 by m_2). The third and fourth columns are, respectively, the complex conjugate of the first and second columns. $\mathbf{Q}_t(\psi,\delta)$ is a diagonal matrix given by

$$\mathbf{Q}_t(\psi,\delta) = (\cos\psi)^t \mathrm{diag}\Big[\xi_1^{\delta-t}, \xi_2^{\delta-t}, (\bar{\xi}_1)^{\delta-t}, (\bar{\xi}_2)^{\delta-t} \Big]. \tag{26}$$

$\mathbf{q}_t^{(k)}$ of equation (24) are related to $\mathbf{q}_t^{(k-1)}$ by using equations (13*a*) and (13*b*). Notice that equation (13*a*) can be regarded as

Downloaded 02 May 2010 to 171.66.16.54. Redistribution subject to ASME license or copyright; see http://www.asme.org/terms/Terms_Use.cfm

a special case of equation (13*b*) if we use equation (16) and allow $t=k$ in (13*b*). Thus we have, for $k\geq 1$,

$$\mathbf{q}_t^{(k)}=\frac{2t-1}{2t}\mathbf{q}_{t-1}^{(k-1)}+\frac{1}{2(\delta+k-t)}\Big[t\mathbf{q}_t^{(k-1)}-(t+1)\mathbf{q}_{t+1}^{(k)}\Big],\qquad t=k,k-1,\ldots,1, \tag{27a}$$

$$\mathbf{q}_t^{(k)}=\mathbf{0},\qquad \text{if}\quad t>k, \tag{27b}$$

Hence the only unknowns are $\mathbf{q}_0^{(k)}$ $(k=0,1,2\ldots)$.

Before we substitute (21)–(23) into (20*b*), we rewrite (23) as, making use of (27*b*)

$$\sigma^{(k)}=\rho^{\delta+k}\Big\{\mathbf{S}_0(\psi,\delta+k)\mathbf{q}_0^{(k)}+\sum_{t=1}^{k}\Big[\mathbf{S}_t(\psi,\delta+k)+\mathbf{T}_{t-1}(\psi,\delta+k)+\mathbf{U}_{t-2}(\psi,\delta+k)\Big]\mathbf{q}_t^{(k)}\Big\}, \tag{28a}$$

where we have assumed

$$\mathbf{U}_t(\psi,\delta+k)\equiv 0,\qquad \text{if}\quad t<0. \tag{28b}$$

Now substitution of (21), (22), and (28*a*) into (20*b*) for $\psi=\alpha$ and α' yields the following equations for $\mathbf{q}_0^{(k)}$, $(k=0,1,2\ldots)$:

$$\mathbf{K}(\delta)\mathbf{q}_0^{(0)}=\mathbf{0}, \tag{29a}$$

$$\mathbf{K}(\delta+k)\mathbf{q}_0^{(k)}=-\sum_{t=1}^{k}\mathbf{W}_t(\delta+k)\mathbf{q}_t^{(k)},\qquad k\geq 1, \tag{29b}$$

in which

$$\mathbf{K}(\delta)=\begin{bmatrix}\mathbf{N}(\alpha)\mathbf{S}_0(\alpha,\delta)\\ \mathbf{N}(\alpha')\mathbf{S}_0(\alpha',\delta)\end{bmatrix} \tag{30a}$$

$$\mathbf{W}_t(\delta)=\begin{bmatrix}\mathbf{N}(\alpha)[\mathbf{S}_t(\alpha,\delta)+\mathbf{T}_{t-1}(\alpha,\delta)+\mathbf{U}_{t-2}(\alpha,\delta)]\\ \mathbf{N}(\alpha')[\mathbf{S}_t(\alpha',\delta)+\mathbf{T}_{t-1}(\alpha',\delta)+\mathbf{U}_{t-2}(\alpha',\delta)]\end{bmatrix}. \tag{30b}$$

For a nontrivial solution of $\mathbf{q}_0^{(0)}$, we see from (29*a*) that

$$\|\mathbf{K}(\delta)\|=0, \tag{31}$$

Thus δ is the eigenvalue of the matrix $\mathbf{K}$ and $\mathbf{q}_0^{(0)}$ is the associated eigenvector. With δ and $\mathbf{q}_0^{(0)}$ obtained from (31) and (29*a*), (29*b*) provides $\mathbf{q}_0^{(k)}$ for $k\geq 1$ and (27*a*) gives $\mathbf{q}_t^{(k)}$ for $1\leq t\leq k$.

If $(\delta+k)$ is also an eigenvalue of $\mathbf{K}$, we see from (29*b*) that a solution for $\mathbf{q}_0^{(k)}$ exists if and only if [14]

$$\mathbf{l}^T\sum_{t=1}^{k}\mathbf{W}_t(\delta+k)\mathbf{q}_t^{(k)}=0, \tag{32a}$$

where $\mathbf{l}$ is the left eigenvector of $\mathbf{K}(\delta+k)$:

$$\mathbf{l}^T\mathbf{K}(\delta+k)=\mathbf{0}. \tag{32b}$$

If (32*a*) holds, $\mathbf{q}_0^{(k)}$ exists but is not unique. However, the nonunique portion of $\mathbf{q}_0^{(k)}$ can be ignored because that portion is represented by the eigenfunction associated with the eigenvalue $\delta+k$. An example of this case in a related problem can be found in [8].

If $(\delta+k)$ is an eigenvalue of $\mathbf{K}$ and (32*a*) does not hold, a solution for $\mathbf{q}_0^{(k)}$ does not exist. In this case, the solution for $\phi^{(k)}$ cannot be given by equation (9*b*). Instead, we use the following modified solution:

$$\phi^{(k)}=\frac{d}{d\delta}\sum_{t=0}^{k-1}A_t^{(k)}x^tZ^{\delta+2+k-t}/(\delta+2+k-t)(\delta+1+k-t)+[A_k^{(k)}Z^{\delta+2}/(\delta+2)(\delta+1)], \tag{33}$$

in which $A_0^{(k)}$ is now assumed to depend on δ. In other words, the terms associated with $A_0^{(k)}$ and hence with $\mathbf{q}_0^{(k)}$ have to be modified. We may also have to modify terms associated with $A_t^{(k+s)}$, $(0<t\leq s)$. Examples of this case in other related problems can be found in [15–17].

We see from equations (22) and (28) that for each eigenvalue δ, the stress σ has the terms $\rho^{\delta}f(\psi,\delta)$, $\rho^{\delta+1}f_1(\psi,\delta)$, $\rho^{\delta+2}f_2(\psi,\delta)\ldots$ Thus the eigenfunction associated with an eigenvalue has infinite terms for axisymmetric deformations.

5 Degenerate Case: $m_1=m_2=1$

When $p_1=p_2$, p must be purely imaginary. This follows from equation (5*b*) and the fact that p cannot be real. By equations (4*b*) and (5*c*), we have $m_1=m_2=1$. We cannot have $m_1=m_2=-1$ because this would make p real. By setting $m=1$, the second equality of equation (4*a*) yields

$$(c_{13}+2c_{44})^2=c_{11}c_{33}. \tag{34}$$

Hence when equation (34) is satisfied, $p_2=p_1$ and we have a degenerate case. The five material constants are now reduced to four by equation (34). Introducing the new material constants ν, μ, γ, and β, we let

$$\left.\begin{aligned}c_{11}&=(\lambda+2\mu)\beta^2\\ c_{33}&=(\lambda+2\mu)/\beta^2\\ c_{44}&=\mu\\ c_{13}&=\lambda\\ c_{11}-c_{12}&=2\gamma\mu\end{aligned}\right\} \tag{35a}$$

in which

$$\lambda=2\mu\nu/(1-2\nu). \tag{35b}$$

Equations (35*a*) satisfy (34). With (35*a*), equations (5) give

$$p=\beta i,\qquad m=1. \tag{36}$$

For isotropic materials, we have $\beta=\gamma=1$ and ν and μ are the Poisson's ratio and shear modulus, respectively.

In a degenerate case $p_1=p_2$, the terms associated with $B_t^{(k)}$ and $D_t^{(k)}$ are identical, respectively, to the terms associated with $A_t^{(k)}$ and $C_t^{(k)}$. We therefore need a new solution for $B_t^{(t)}$ and $D_t^{(k)}$. This can be accomplished by replacing the coefficients of $B_t^{(k)}$ and $D_t^{(k)}$ by their derivatives with respect to p_2 and $\bar{p}_2$ [18, 19]. Thus, for instance, equation (14*a*) becomes

$$\phi^{(k)}=\sum_{t=0}^{k}\Big\{A_t^{(k)}x^tZ^{\delta+k-t+2}+C_t^{(k)}x^t\bar{Z}^{\delta+k-t+2}\Big\}\Big/(\delta+k-t+2)(\delta+k-t+1)+\sum_{t=0}^{k}\Big\{B_t^{(k)}zx^tZ^{\delta+k-t+1}+D_t^{(k)}zx^t\bar{Z}^{\delta+k-t+1}\Big\}\Big/(\delta+k-t+1), \tag{37}$$

where we have omitted the subscripts 1 and 2 for Z and $\bar{Z}$. Similarly, equations (17) and (18) are replaced by (noting that m in the $B_t^{(k)}$ and $D_t^{(k)}$ terms must also be differentiated with respect to p by using equation (4*b*)).

$$u_r^{(k)}=\sum_{t=0}^{k}\Big[A_t^{(k)}+A_{t+1}^{(k)}(t+1)/(\delta+k-t)\Big]x^tZ^{\delta+k-t+1}\Big/(\delta+k-t+1)+\sum_{t=0}^{k}\Big[B_t^{(k)}+B_{t+1}^{(k)}(t+1)/(\delta+k-t)\Big]x^tzZ^{\delta+k-t}+\ldots \tag{38a}$$

$$u_z^{(k)}=\sum_{t=0}^{k}\Big[A_t^{(k)}\beta i-B_t^{(k)}(3-4\nu)\Big]x^tZ^{\delta+k-t+1}\Big/$$

Downloaded 02 May 2010 to 171.66.16.54. Redistribution subject to ASME license or copyright; see http://www.asme.org/terms/Terms_Use.cfm

$$(\delta+k-t+1)+\sum_{t=0}^{k} B_t^{(k)}\beta i x^t z Z^{\delta+k-t}+\ \ldots \qquad (38b)$$

$$\frac{1}{2\mu}\sigma_r^{(k)}=\sum_{t=0}^{k}\Big[\Big(A_t^{(k)}\beta^2-B_t^{(k)}2\nu\beta i\Big)+A_{t+1}^{(k)}2\gamma(t+1)/(\delta+k-t)$$

$$+A_{t+2}^{(k)}\gamma(t+2)(t+1)/(\delta+k-t)\,(\delta+k-t-1)\Big]x^t Z^{\delta+k-t}$$

$$+\sum_{t=0}^{k}\Big[B_t^{(k)}\beta^2(\delta+k-t)+B_{t+1}^{(k)}2\gamma(t+1)$$

$$+B_{t+2}^{(k)}\gamma(t+2)(t+1)/(\delta+k-t-1)\Big]zx^t Z^{\delta+k-t-1}$$

$$+\ \ldots \qquad (39a)$$

$$\frac{1}{2\mu}\sigma_\theta^{(k)}=\sum_{t=0}^{k}\Big\{\Big[A_t^{(k)}(\beta^2-\gamma)-B_t^{(k)}2\nu\beta i\Big]$$

$$-A_{t+1}^{(k)}2\gamma(t+1)/(\delta+k-t)-A_{t+2}^{(k)}\gamma(t+2)(t+1)/$$

$$(\delta+k-t)\,(\delta+k-t-1)\Big\}x^t Z^{\delta+k-t}+\sum_{t=0}^{k}\Big[B_t^{(k)}(\beta^2$$

$$-\gamma)(\delta+k-t)-B_{t+1}^{(k)}2\gamma(t+1)-B_{t+2}^{(k)}\gamma(t+2)(t+1)/$$

$$(\delta+k-t-1)\Big]zx^t Z^{\delta+k-t-1}+\ \ldots \qquad (39b)$$

$$\frac{1}{2\mu}\sigma_z^{(k)}=\sum_{t=0}^{k}-\Big[A_t^{(k)}+B_t^{(k)}2(1-\nu)i\beta^{-1}\Big]x^t Z^{\delta+k-t}$$

$$-\sum_{t=0}^{k}B_t^{(k)}(\delta+k-t)zx^t Z^{\delta+k-t-1}+\ \ldots \qquad (39c)$$

$$\frac{1}{2\mu}\sigma_{rz}^{(k)}=\sum_{t=0}^{k}\Big\{\Big[A_t^{(k)}\beta i-B_t^{(k)}(1-2\nu)\Big]+\Big[A_{t+1}^{(k)}\beta i$$

$$-B_{t+1}^{(k)}(1-2\nu)\Big](t+1)/(\delta+k-t)\Big\}x^t Z^{\delta+k-t}$$

$$+\sum_{t=0}^{k}\Big[B_t^{(k)}(\delta+k-t)+B_{t+1}^{(k)}(t+1)\Big]\beta i z x^t Z^{\delta+k-t-1}$$

$$+\ \ldots \qquad (39d)$$

In equations (38) and (39), the dots stand for the $C_t^{(k)}$ and $D_t^{(k)}$ terms that are obtained from the $A_t^{(k)}$ and $B_t^{(k)}$ terms by replacing βi and Z by $-\beta i$ and $\bar{Z}$ respectively. Equations (20)–(32) remain valid except (25), which are replaced by

$$\mathbf{S}_t(\psi,\delta)$$

$$=2\mu\begin{bmatrix}\beta^2, & [-2\nu\beta i+\beta^2(\delta-t)\zeta^{-1}\sin\psi] & * & *\\ \beta i, & [-(1-2\nu)+(\delta-t)\beta i\zeta^{-1}\sin\psi] & * & *\\ -1, & -[2(1-\nu)i\beta^{-1}+(\delta-t)\zeta^{-1}\sin\psi] & * & *\end{bmatrix}\mathbf{Q}_t(\psi,\delta), \qquad (40a)$$

$$\mathbf{T}_t(\psi,\delta)$$

$$=\frac{2\mu(t+1)}{\delta-t}\begin{bmatrix}2\gamma, & 2\gamma(\delta-t)\zeta^{-1}\sin\psi & * & *\\ \beta i, & [-(1-2\nu)+(\delta-t)\beta i\zeta^{-1}\sin\psi] & * & *\\ 0, & 0 & 0 & 0\end{bmatrix}\mathbf{Q}_t(\psi,\delta), \qquad (40b)$$

$$\mathbf{U}_t(\psi,\delta)$$

$$=\frac{2\mu\gamma(t+2)(t+1)}{(\delta-t)(\delta-t-1)}\begin{bmatrix}1, & (\delta-t)\zeta^{-1}\sin\psi & * & *\\ 0 & 0 & 0 & 0\\ 0 & 0 & 0 & 0\end{bmatrix}\mathbf{Q}_t(\psi,\delta) \qquad (40c)$$

$\mathbf{Q}_t(\psi,\delta)$ is defined in (26) with $\zeta_1=\zeta_2=\zeta$. As in equation (25), the third and fourth columns of equations (40) are, respectively, the complex conjugate of the first and second columns.

6 Particular Solution for the Displacement of the Singular Point

Let $(u_r, u_\theta)=(u_0,0)$ at the singular point $(r,z)=(a,0)$ where u_0 is a constant. A particular solution that yields this displacement is

$$u_r=u_0 r/a,\quad u_z=0, \qquad (41a)$$

$$\left.\begin{aligned}&\sigma_r=\sigma_\Theta=u_0(c_{11}+c_{12})/a,\\ &\sigma_z=2u_0c_{13}/a,\\ &\sigma_{rz}=0.\end{aligned}\right\} \qquad (41b)$$

Let

$$\sigma_0=\frac{u_0}{a}\begin{bmatrix}c_{11}+c_{12}\\ 0\\ 2c_{13}\end{bmatrix}. \qquad (42)$$

To satisfy the stress-free boundary conditions, equation (20*b*), we superimpose equation (42) to (23) with $\delta=0$ and write the stress σ as

$$\sigma=\sigma_0+\sum_{k=0}^{\infty}\rho^k\sum_{t=0}^{k}\Big[\mathbf{S}_t(\psi,k)\mathbf{q}_t^{(k)}+\mathbf{T}_t(\psi,k)\mathbf{q}_{t+1}^{(k)}$$

$$+\mathbf{U}_t(\psi,k)\mathbf{q}_{t+2}^{(k)}\Big]. \qquad (43)$$

Equation (20*b*) now provides the following equations for $\mathbf{q}_0^{(k)}$

$$\mathbf{K}(k)\,\mathbf{q}_0^{(k)}=\mathbf{b}^{(k)},\qquad (k=0,1,2,\ \ldots), \qquad (44)$$

in which

$$\mathbf{b}^{(0)}=-\begin{bmatrix}\mathbf{N}(\alpha)\\ \mathbf{N}(\alpha')\end{bmatrix}\sigma_0, \qquad (45a)$$

$$\mathbf{b}^{(k)}=-\sum_{t=1}^{k}\mathbf{W}_t(k)\,\mathbf{q}_t^{(k)},\quad k\geq 1 \qquad (45b)$$

and $\mathbf{W}_t(k)$ is defined in equation (30*b*). Equation (44) has a unique solution for $\mathbf{q}_0^{(k)}$ if k is not an eigenvalue of $\mathbf{K}$. If k is, then the discussions presented near the end of Section 4 apply here also.

Acknowledgments

The work presented here is supported by the U.S. Army Materials and Mechanics Research Center under Contract DAAG 46-83-K-0159 to the University of Illinois at Chicago.

References

1 Knien, M., "Zur Theorie des Druckversuchs," Zeit. Ang. Math. Mech., Vol. 6, 1926, pp. 414–416.

Downloaded 02 May 2010 to 171.66.16.54. Redistribution subject to ASME license or copyright; see http://www.asme.org/terms/Terms_Use.cfm

2 Williams, M. L., "Stress Singularities Resulting From Various Boundary Conditions in Angular Corners of Plates in Extension," ASME JOURNAL OF APPLIED MECHANICS, Vol. 19, 1952, pp. 526-528.

3 Ting, T. C. T., "The Wedge Subjected to Tractions: A Paradox Re-Examined," *J. Elasticity*, Vol. 14, No. 3, 1984, pp. 235-247.

4 Tong, P., Pian, T. H. H., and Lasry, S. J., "A Hybrid-Element Approach to Crack Problems in Plane Elasticity," *Int. J. Numerical Meth. in Eng.*, Vol. 7, 1973, pp. 297-308.

5 Lin, K. Y., and Mar, J. W., "Finite Element Analysis of Stress Intensity Factors for Cracks at a Bimaterial Interface," *Int. J. Fracture*, Vol. 12, 1976, pp. 521-531.

6 Delale, F., and Erdogan, F., "The Axisymmetric Elasticity Problem for a Laminated Plate Containing a Circular Hole," Lehigh University Report, July 1981.

7 Delale, F., Kishore, N. N., and Wang, A. S. D., "Stress Analysis of a Composite Plate With Circular Hole Under Axisymmetric Bending," *J. Composite Materials*, Vol. 18, 1984, pp. 420-433.

8 Ting, T. C. T., "Asymptotic Solution Near the Apex of an Elastic Wedge With Curved Boundaries," *Q. Appl. Math*, Vol. 42, No. 4, 1985.

9 Elliott, H. A., "Three-Dimensional Stress Distributions in Hexagonal Aeolotropic Crystals," *Proc. Cambridge Phil. Soc.*, Vol. 44, 1948, pp. 522-533.

10 Green, A. E., and Zerna, W., *Theoretical Elasticity*, Oxford University Press, Oxford, 1954.

11 Kassir, M. K., and Sih, G. C., "Three-Dimensional Crack Problems," in: *Mechanics of Fracture*, Vol. 2, Noordhoff, 1975, pp. 336-342.

12 Eshelby, J. D., Read, W. T., and Shockley, W., "Anisotropic Elasticity With Applications to Dislocation Theory," *Act. Met.*, Vol. 1, 1953, pp. 251-259.

13 Somaratna, Nihal, and Ting, T. C. T., "Three-Dimensional Stress Singularities at Conical Notches and Inclusions in Transversely Isotropic Materials," ASME JOURNAL OF APPLIED MECHANICS. To appear.

14 Hilderbrand, F. B., *Methods of Applied Mathematics*, Prentice-Hall, Englewood Cliffs, N.J., 1954.

15 Dempsey, J. P., "The Wedge Subjected to Tractions: A Paradox Resolved," *J. Elasticity*, Vol. 11, 1981, pp. 1-10.

16 Zwiers, R., Ting, T. C. T., and Spilker, R. L., "On the Logarithmic Singularity of Free-Edge Stress in Laminated Composite Under Uniform Extension," ASME JOURNAL OF APPLIED MECHANICS, Vol. 49, 1982, pp. 561-569.

17 Ting, T. C. T., and Chou, S. C., "Logarithmic Singularity of an Elastic Composite Wedge Subjected to Out-of-the-Plane Extensional Strain," *Theoretical and Applied Fractural Mechanics*, to appear in Vol. 4, No. 3.

18 Ting, T. C. T., and Chou, S. C., "Edge Singularities in Anisotropic Composites," *Int. J. Solids Structures*, Vol. 17, 1981, pp. 1057-1068.

19 Ting, T. C. T., "Effects of Change of Reference Coordinates on the Stress Analysis of Anisotropic Elastic Materials," *Int. J. Solids Structures*, Vol. 18, 1982, pp. 139-152.

APPENDIX

Derivation of Equations (13)

Substitution of equation (9*a*) into (8) and noticing that $\phi^{(k)}$ is of order $\rho^{\delta+k+2}$, we see that equation (8) is satisfied if

$$\frac{\partial^2\phi^{(0)}}{\partial x^2}-\frac{1}{p^2}\frac{\partial^2\phi^{(0)}}{\partial z^2}=0, \tag{A1}$$

$$\frac{\partial^2\phi^{(k)}}{\partial x^2}-\frac{1}{p^2}\frac{\partial^2\phi^{(k)}}{\partial z^2}=\sum_{m=0}^{k-1}x^{k-1-m}\frac{\partial\phi^{(m)}}{\partial x},\quad k\geq 1 \tag{A2}$$

Thus each term in equation (*A*2) is of order $\rho^{\delta+k}$. Using equation (9*b*) in (*A*2), we obtain

$$\sum_{t=1}^{k-1}A_{t+1}^{(k)}t(t+1)x^{t-1}Z^{(\delta+k-t+1)}/(\delta+k-t+1)(\delta+k-t)$$

$$+\sum_{t=1}^{k}A_t^{(k)}2tx^{t-1}Z^{(\delta+k-t+1)}/(\delta+k-t+1)=I_1+I_2 \tag{A3}$$

where

$$I_1=\sum_{m=1}^{k-1}x^{k-1-m}\sum_{s=0}^{m-1}A_{s+1}^{(m)}(s+1)x^sZ^{(\delta+m-s+1)}\Big/(\delta+m-s+1)(\delta+m-s) \tag{A4}$$

$$I_2=\sum_{m=0}^{k-1}x^{k-1-m}\sum_{s=0}^{m}A_s^{(m)}x^sZ^{(\delta+m-s+1)}\Big/(\delta+m-s+1) \tag{A5}$$

By letting $s=t+m-k$ and interchanging the summations, we have

$$I_1=\sum_{t=1}^{k-1}\left\{\sum_{m=k-t}^{k-1}(t-k+m+1)A_{t-k+m+1}^{(m)}\right\}x^{t-1}Z^{(\delta+k-t+1)}\Big/(\delta+k-t+1)(\delta+k-t) \tag{A6}$$

$$I_2=\sum_{t=1}^{k}\left\{\sum_{m=k-t}^{k-1}A_{t-k+m}^{(m)}\right\}x^{t-1}Z^{(\delta+k-t+1)}\Big/(\delta+k-t+1) \tag{A7}$$

It follows from equations (*A*3), (*A*6), and (*A*7) that for $t=k$,

$$2kA_k^{(k)}=\sum_{m=0}^{k-1}A_m^{(m)} \tag{A8}$$

and for $t\leq k-1$,

$$t(t+1)A_{t+1}^{(k)}+2t(\delta+k-t)A_t^{(k)}$$

$$=\sum_{m=k-t}^{k-1}\left\{(t-k+m+1)A_{t-k+m+1}^{(m)}+(\delta+k-t)A_{t-k+m}^{(m)}\right\} \tag{A9}$$

Equation (*A*9) can be rewritten as, by letting $m=s+k-t-1$,

$$t(t+1)A_{t+1}^{(k)}+2t(\delta+k-t)A_t^{(k)}$$

$$=\sum_{s=1}^{t}\left\{sA_s^{(s+k-t-1)}+(\delta+k-t)A_{s-1}^{(s+k-t-1)}\right\},$$

$$\text{for } t\leq k-1 \tag{A10}$$

To express equation (*A*8) in the form of equation (13*a*), we replace k by $k-1$ in (*A*8) to obtain

$$2(k-1)A_{k-1}^{(k-1)}=\sum_{m=0}^{k-2}A_m^{(m)} \tag{A11}$$

Subtract equation (*A*11) from (*A*8), we have

$$2kA_k^{(k)}-2(k-1)A_{k-1}^{(k-1)}=A_{k-1}^{(k-1)} \tag{A12}$$

which is identical to equation (13*a*). Similarly, we replace k and t by $k-1$ and $t-1$, respectively, in equation (*A*10):

$$(t-1)tA_t^{(k-1)}+2(t-1)(\delta+k-t)A_{t-1}^{(k-1)}$$

$$=\sum_{s=1}^{t-1}\left\{sA_s^{(s+k-t-1)}+(\delta+k-t)A_{s-1}^{(s+k-t-1)}\right\} \tag{A13}$$

Equation (13*b*) is obtained when (*A*13) is subtracted from (*A*10).

Downloaded 02 May 2010 to 171.66.16.54. Redistribution subject to ASME license or copyright; see http://www.asme.org/terms/Terms_Use.cfm

First-Order Variation in Elastic Fields Due to Variation in Location of a Planar Crack Front

J. R. Rice
Division of Applied Sciences,
Harvard University,
Cambridge, Mass. 02138

The problem explained in the title is formulated generally and given an explicit solution for tensile loadings opening a half-plane crack in an infinite body. For the half-plane crack, changes in the opening displacement between the crack surfaces and in the stress-intensity factor distribution along the crack front are calculated to first order in an arbitrary deviation of the crack-front position from a reference straight line. The deviations considered lie in the original crack plane. The results suggest that in the presence of loadings that would induce uniform conditions along the crack front, if it were straignt, small initial deviations from straightness should reduce in size during quasistatic crack growth if of small enough spatial wavelength but possibly enlarge in size if of longer wavelength. The solution methods rely on elastic reciprocity, in terms of a three-dimensional version of weight function theory for tensile cracks, and on direct solution of elastic crack problems. The weight function is derived for the half-plane crack by solving for the first-order variation in the elastic displacement field associated with arbitrary variations of the crack front from a straight reference line. Also, a new three-dimensional weight function theory is developed for planar cracks under general mixed-mode loading involving tension and shears relative to the crack, the connection between weight functions and the Green's function for crack problems is shown, and some results are given for the half-plane crack on the variations of elastic fields for variation of crack-front location in the presence of general loadings including shear.

Theory for Tensile Cracks

A three-dimensional elastic solid contains a planar crack with smooth bounding contour C along the crack front. For the present we assume that the solid is homogeneous, isotropic, symmetric about the crack plane, and subjected to an "original" load system consisting of some distribution of fixed forces and/or imposed boundary displacements that induce "mode 1" tension along the crack front. A cartesian x,y,z coordinate system is attached so that the crack plane lies on $y=0$ (Fig. 1). In addition to the original load system described, a pair of concentrated forces $\pm P$ wedges open the crack at locations $x,0^+,z$ and $x,0^-,z$ on its surfaces. Let $\Delta u(x,z)$ be the opening gap between the crack surfaces at the load location. (So that Δu is bounded when $P\neq 0$, it is convenient at this stage in the development to regard the forces $\pm P$ as being distributed uniformly over a disk of arbitrary small radius ϵ centered on x,z. Then $\Delta u(x,z)$ is understood as the average opening over the same disk, so that $P\delta(\Delta u)$ is the work done by the forces. Later we will be interested in the case $P=0$ and can let $\epsilon\to 0$ with impunity.)

Suppose that while the combined load system (original plus forces $\pm P$ on crack surfaces) is acting, the crack front C is advanced normal to itself on the $y=0$ plane by some variable distance $\delta a(s)$ as in Fig. 1; s is the measure of arc length along C. Thus, treating $\delta a(s)$ as infinitesimal, the change in strain energy U plus potential energy V_0 of the fixed forces of the original load system is

$$\delta(U+V_0)=P\delta[\Delta u(x,z)]-\int_C G(s)\,\delta a(s)\,ds \qquad (1)$$

where G is the energy release per unit crack area of elastic fracture mechanics. G is related to the crack tip stress intensity factor $K[=K(s)]$ by the Irwin relation

$$G=(1-\nu^2)K^2/E \qquad (2)$$

(E = Young tensile modulus, ν = Poisson ratio), whereas K itself appears in expressions for the tensile stress σ across the plane $y=0$ at small distance r ahead of the crack tip and for the opening gap Δu at small distance r behind the tip through the asymptotic forms

$$\sigma\sim K/(2\pi r)^{1/2}, \qquad \Delta u\sim 8(1-\nu^2)(K/E)\,(r/2\pi)^{1/2}. \qquad (3)$$

It is evident that such quantities as U and V_0 can depend only on the magnitude of P or Δu and on the location of the crack front, and thus that the right side of equation (1) is a

Contributed by the Applied Mechanics Division and presented at the 1985 Joint ASME/ASCE Applied Mechanics, Fluids Engineering, and Bioengineering Conference, Albuquerque, N. Mex., June 24-26, 1985 of The American Society of Mechanical Engineers.

Discussion on this paper should be addressed to the Editorial Department, ASME, United Engineering Center, 345 East 47th Street, New York, N.Y. 10017, and will be accepted until two months after final publication of the paper itself in the Journal of Applied Mechanics. Manuscript received by ASME Applied Mechanics Division, October, 1984. Paper No. 85-APM-25.

Copyright © 1985 by ASME
Downloaded 02 May 2010 to 171.66.16.54. Redistribution subject to ASME license or copyright; see http://www.asme.org/terms/Terms_Use.cfm

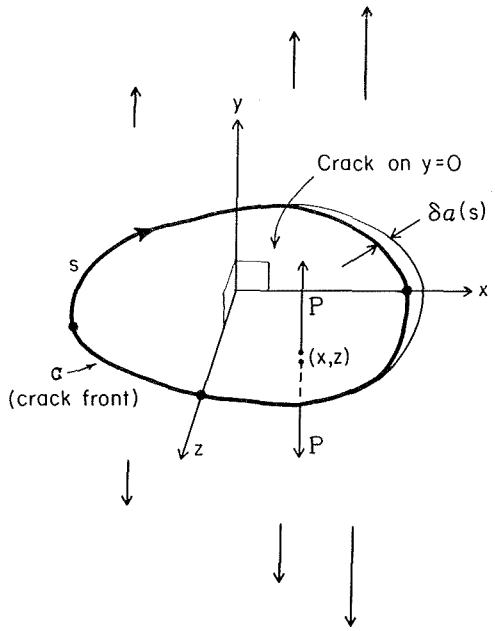

Fig. 1 A planar crack on $y=0$ with front along the arc C. Forces $\pm P$ applied to the upper and lower crack faces at position (x,z). The crack front is advanced normal to itself, in the plane $y=0$, by amount $\delta a(s)$, where s denotes arc length along C.

perfect differential. It then follows (next paragraph) that, to first order in $\delta a(s)$, the variation in opening displacement $\Delta u(x,z)$ when the crack front location is altered while P and the original load system are held fixed is

$$\delta[\Delta u(x,z)] = \int_C \frac{\partial G(s)}{\partial P}\,\delta a(s)\,ds$$

$$= \frac{2(1-\nu^2)}{E}\int_C K(s)\,\frac{\partial K(s)}{\partial P}\,\delta a(s)\,ds, \qquad (4)$$

where the derivatives with respect to P are evaluated with the crack front fixed in position along arc C.

To prove this result, introduce an arbitrary function $g(s)$ along C that describes the shape of a crack-front alteration and a quantity A that describes the amplitude of that alteration, such that

$$\delta a(s) = g(s)\,\delta A. \qquad (5)$$

Then after a Legendre transformation of equation (1) one has

$$\delta[P(\Delta u) - U - V_0] = (\Delta u)\,\delta P + \left(\int_C Gg\,ds\right)\delta A. \qquad (6)$$

Since for any given $g(s)$, the quantities in brackets on the left can all be regarded as functions of P and A, the right side is a perfect differential. Hence the coefficients of δP and δA, regarded as functions of P and A, must satisfy the reciprocal relation

$$\partial(\Delta u)/\partial A = \partial\left(\int_C Gg\,ds\right)/\partial P = \int_C (\partial G/\partial P)g\,ds. \qquad (7)$$

Upon multiplying this last equation through by δA and recognizing that $g(s)\delta A$ represents an arbitrary distribution of crack advance $\delta a(s)$, one verifies equation (4).

In fact, equation (4) must hold no matter what the magnitude of P and, in particular, it must hold when $P=0$ so that no wedging forces are present at all (we may then let $\epsilon \to 0$). It is evident that in the case $P=0$ we may write for insertion in equation (4) that

$$K(s) = K^\circ(s), \qquad \partial K(s)/\partial P = k(s;x,z), \qquad (8)$$

where $K^\circ(s)$ is the intensity factor distribution induced along the crack front by the original load system and $k(s;x,z)$ is defined such that $Pk(s;x,z)$ is the intensity factor at position s along the crack front due to wedge forces $\pm P$ opening the crack at location x,z. Hence, the variation in crack-opening displacement at location x,z when the crack-front position is altered by $\delta a(s)$ in presence of (only) the original load system is

$$\delta[\Delta u(x,z)] = \frac{2(1-\nu^2)}{E}\int_C K^\circ(s)\,k(s;x,z)\,\delta a(s)\,ds \qquad (9)$$

to first order in $\delta a(s)$.

It may be noticed that the original load system enters into this result only through the distribution $K^\circ(s)$ of intensity factor that it causes but not otherwise. Thus two "original" load systems that induce identical K° distributions will induce identical first-order alterations in crack opening for a given advance $\delta a(s)$. The derivation of equation (9) follows essentially the author's (Rice, 1972) formulation of the theory of Bueckner's (1970) "weight functions" for two-dimensional elastic crack mechanics, and particularly parallels the Appendix of Rice (1972) in which three-dimensional weight function theory is introduced; equation (9) may be recognized as a special case of equation (*A*7) in that work. Bueckner (1972) gave an equivalent three-dimensional extension of his weight function theory based on "fundamental fields" that satisfy the equations of elasticity but have normally inadmissable singularities of arbitrarily prescribed strength around the crack rim. In fact, Bueckner's (1972) fundamental fields have displacements that may be regarded as specific realizations of $\delta(\Delta u)$ in the foregoing and his strength measure may be regarded as being proportional to the product $K^\circ(s)\,\delta a(s)$. The significance of that product or of the related product $K^\circ(s)g(s)$ will be clear from several subsequent expressions.

Equation (9) may be put to use in two ways. First, in a manner paralleling the typical two-dimensional applications of weight function theory, suppose $\delta(\Delta u)$ can be calculated to first order for arbitrary $\delta a(s)$ in presence of the original load system. Then equation (9) evidently enables one to infer the expression for the unknown function $k(s;x,z)$, namely, the intensity factor at s per unit wedging forces applied to the crack faces at x,z. This is easy to use in two dimensions because then δa has no dependence on distance s along the crack front and we have only to calculate $\partial(\Delta u)/\partial a$ to extract the desired function $k(x)$. Analogous three-dimensional applications have not been much considered, apparently because it always seemed impossible to solve the three-dimensional elasticity equations in enough generality to calculate $\delta(\Delta u)$ for arbitrary $\delta a(s)$. It will be shown here a few sections later, however, that such a solution can be constructed for the simple geometry of a half-plane crack in an infinite body. Also, Parks and Kamenetzky (1979) have outlined a numerical implementation of three-dimensional weight function theory in a finite element procedure and Bueckner (1972) has pointed out that, effectively, the solution to $\delta(\Delta u)$ for simpler $\delta a(s)$ amounting, say, to expansion in radius or translation in center location for a three-dimensional crack, allows certain weighted averages of k around the crack rim to be obtained. The latter idea was also developed by Besuner (1974).

For the second use of equation (9), suppose that we know from some other source the function $k(s;x,z)$ for a given crack geometry. Then equation (9) lets us construct the first-order variation $\delta[\Delta u(x,z)]$ for arbitrary variation $\delta a(s)$ from the given crack geometry. The equation is applied in that way in the next section. As will be seen, such an application enables one to calculate the corresponding variation $\delta K(s)$ in intensity factor along the crack front to first order in $\delta a(s)$, as considered recently by Meade and Keer (1984*b*), and the calculations allow study of the configurational stability of a three-dimensional crack front.

Downloaded 02 May 2010 to 171.66.16.54. Redistribution subject to ASME license or copyright; see http://www.asme.org/terms/Terms_Use.cfm

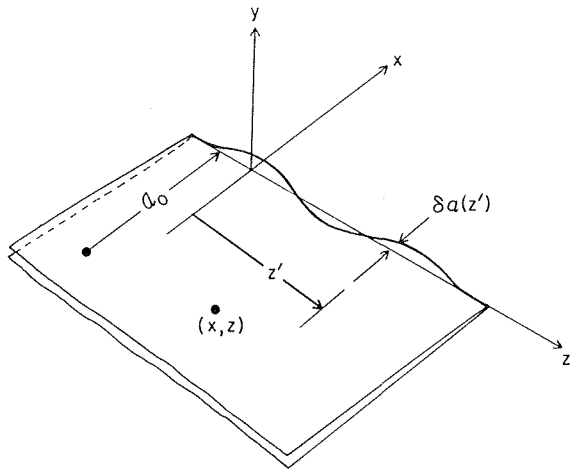

Fig. 2 Half-plane crack on $y = 0$ in an infinite body. Reference straight crack front along z axis; z' denotes location along front and $\delta a(z')$ denotes advance of crack front; a is distance from some fixed point on a crack surface to reference straight crack front and $a = a_0$ when front lies along z axis as shown.

Before turning to the applications, we note the following extensions of equation (9). Suppose, for example, that we wish to know the variation of a certain weighted average of the crack opening when the crack front is advanced. Thus for weighting with some function $p(x,z)$

$$\delta\left[\int\int p(x,z)\,\Delta u(x,z)\;dx\;dz\right]$$

$$= \frac{2(1-\nu^2)}{E}\int_C K^\circ(s)\,\bar{k}(s)\,\delta a(s)\;ds \tag{10}$$

to first order in δa where evidently

$$\bar{k}(s) = \int\int p(x,z)\,k(s;x,z)\;dx\;dz, \tag{11}$$

and hence $\bar{k}(s)$ is the stress-intensity factor distribution due to a "loading" $p(x,y)$ considered as a pressure distribution on the crack faces. A similar expression is obtained for other deformation measures than crack-opening displacement. For example, if Q measures the intensity of some arbitrary additional force distribution acting symmetrically about the crack plane, and if q is the conjugate deformation quantity (i.e., defined so that $Q\delta q$ is a work increment of that additional force distribution) then

$$\delta q = 2\frac{1-\nu^2}{E}\int_C K^\circ(s)\,\bar{k}(s)\,\delta a(s)\;ds \tag{12}$$

is the change in q to first order when the crack is advanced in presence of the original load system but with $Q=0$. Here $\bar{k}(s)$ is the intensity factor induced by unit Q.

Variation of Front of a Half-Plane Crack in an Infinite Body

Suppose that the crack front C, or at least the segment of interest whose location is to be perturbed, is initially straight. Provided that we are interested only in the opening displacements in the vicinity of this straight front, at points x,z that are much closer to it than to external boundaries of the cracked body or to other segments of the crack front, it will suffice to use in equation (9) the result for $k(s;x,z)$ for an infinite body containing a half-plane crack. In particular, the crack front C is chosen to coincide with the z axis and the crack plane with the plane $y=0$, $x<0$ as in Fig. 2. Now we let z', which runs along the z axis, replace s and rewrite equation (9) as

$$\delta[\Delta u(x,z)]$$

$$= \frac{2(1-\nu^2)}{E}\int_{-\infty}^{+\infty} K^\circ(z')\,k(z';x,z)\,\delta a(z')\;dz'. \tag{13}$$

The formulation is complete once we have a formula for $k(z';x,z)$, which can depend on only $z'-z$ and x, and this can be taken from published work. The stress intensity factors for arbitrary point forces on a semi-infinite crack face are given in the handbook by Tada et al. (1973) and referenced to prior elasticity analyses by Uflyand (1965), Sih and Liebowitz (1968), and Kassir and Sih (1973). The problem has recently been given a convenient reformulation by Meade and Keer (1984*a*). The result for the mode I stress intensity at z' along the crack tip due to unit opening forces applied on the crack faces at $x(<0),z$ is

$$k(z';x,z) = (-2x/\pi^3)^{1/2}/[x^2+(z'-z)^2], \tag{14}$$

where positive square root is implied, and thus the alteration of the opening displacement of the crack faces is

$$\delta[\Delta u(x,z)]$$

$$= \frac{8(1-\nu^2)}{E}\left(\frac{-x}{2\pi}\right)^{1/2}\left[\frac{1}{2\pi}\int_{-\infty}^{+\infty}\frac{K^\circ(z')\,\delta a(z')dz'}{x^2+(z-z')^2}\right]. \tag{15}$$

At this point it is useful to recall, as suggested by equation (3), that the opening displacement very near a point along the (altered) crack tip will have the form

$$\Delta u(x,z) = \frac{8(1-\nu^2)}{E}\left(\frac{\delta a - x}{2\pi}\right)^{1/2} K + O(\delta a - x)^{3/2} \tag{16}$$

where K is the stress intensity factor at that point. If we now let $x\to 0^-$ in equation (15) at a location z where $\delta a(z) \neq 0$, it is easy to show that the bracketed term becomes infinite as

$$[\ \ldots\ ] \sim K^\circ(z)\,\delta a(z)/(-2x), \tag{17}$$

and thus equation (15) predicts that $\delta[\Delta u]$ behaves as

$$\delta[\Delta u(x,z)] \sim \frac{4(1-\nu^2)}{E}\,\frac{\delta a(z)}{(-2\pi x)^{1/2}}\,K^\circ(z). \tag{18}$$

This is an obviously correct asymptotic form as $x\to 0^-$, as we can check from equation (16); it corresponds to evaluating $d(\Delta u)/d(\delta a)$ at $\delta a = 0$ from that equation and then multiplying the result by δa to give the first-order result.

Suppose now that at a particular value of z, $\delta a(z) = 0$. Assuming that $d[\delta a(z)]/dz$ exists at that point, one may show that the bracketed term in equation (15) has a well-defined limit as $x\to 0$ and that this limit is

$$\lim_{x\to 0}\ [\ \ldots\ ] = \frac{1}{2\pi}PV\int_{-\infty}^{+\infty}\frac{K^\circ(z')\delta a(z')}{(z'-z)^2}\,dz' \tag{19}$$

where PV in front of the improper integral denotes the principal value. (To prove this, break the integral on z' up into one over $z-\eta$ to $z+\eta$ and another over the rest of the axis. One shows that the limit as $x\to 0$ of the integral from $z-\eta$ to $z+\eta$ vanishes when one takes the subsequent limit $\eta\to 0$, and the limit $\eta\to 0$ of the integral over the rest of the axis with $x=0$ defines the PV.) However, if we compare equation (15) to equation (16) at a point z where $\delta a(z) = 0$, it is evident that the then well-defined value of the bracketed term of equation (19) can be interpreted as the variation of intensity factor K at z due to some or all of the rest of the crack front being altered in position. Hence to first order in δa,

$$\delta K(z) = \frac{1}{2\pi}PV\int_{-\infty}^{+\infty}\frac{K^\circ(z')\,\delta a(z')}{(z'-z)^2}\,dx' \tag{20}$$

is the variation in stress-intensity factor at a location z where $\delta a(z) = 0$ but $d[\delta a(z)]/dz$ exists, and the total stress intensity factor $K(z)$ at that location is

$$K(z) = K^\circ(z) + \delta K(z). \tag{21}$$

To find K at some location z where $\delta a(z) \neq 0$ we simply

Downloaded 02 May 2010 to 171.66.16.54. Redistribution subject to ASME license or copyright; see http://www.asme.org/terms/Terms_Use.cfm

relocate the reference straight crack front by moving it along the x direction an amount $\delta a(z)$ and then apply the formulas just derived. To express this in an equation, a variable a is introduced to measure the distance of the reference straight crack front from some given point of the body on one of the crack surfaces (a has the value a_0 shown in Fig. 2 when the reference straight crack front coincides with the z axis). Further, to emphasize dependence on a, the intensity distribution $K^\circ(z)$ induced along a straight crack front by the original loadings is written henceforth as $K^\circ(z;a)$. Evidently, to calculate the stress-intensity factor at location z, we want to move the reference straight crack front to $a = a_0 + \delta a(z)$, and then use equation (20) to account for the nonstraightness of the crack with $\delta a(z')$ replaced with $\delta a(z') - \delta a(z)$. It is convenient to write the result using the notation

$$a(z) = a_0 + \delta a(z), \tag{22}$$

and the stress-intensity factor at location z is therefore

$$K(z) = K^\circ[z;a(z)] + \frac{1}{2\pi} PV \int_{-\infty}^{+\infty} \frac{K^\circ[z';a(z)][a(z') - a(z)]}{(z'-z)^2} dz'. \tag{23}$$

This formula is accurate to first order in $a(z) - a(z')$.

The result just obtained appears not to be consistent with one presented by Meade and Kerr (1984*b*) for a half-plane crack in an infinite body with a wavy crack front in the form

$$a(z) = a_0 - A[1 - \cos(2\pi z/\lambda)]. \tag{24}$$

Here A is a small parameter. They consider opening loadings applied to the crack faces as uniform line loads, applied along lines parallel to z on the crack faces at distances a_0 from the tip. For their method of loading, $K^\circ = K^\circ(a)$, independent of z (and $K^\circ = 2^{1/2} P_0/\pi^{1/2} a^{1/2}$, where P_0 is the intensity of their line loading). They propose in their equation (110) that

$$K(z) = K^\circ[a(z)] + O(A^2/\lambda^2), \tag{25}$$

and this is at conflict with equation (23) in the foregoing, where the PV integral contributes an effect of first order in A. This particular case is discussed further in the next section. Also, in the section after that the convenient formulation presented by Meade and Keer (1984*a*,*b*) for three-dimensional problems of plane cracks in infinite elastic bodies is used to give an alternative derivation of equation (15) in the foregoing which is the basis of equation (23) for $K(z)$, and also to discuss an apparent inconsistency of the solution to the elastic field equations for a wavy crack front proposed by Meade and Keer (1984*b*). As a bonus, that alternate derivation leads to a new derivation of the intensity factor distribution of equation (14), and also to the general three-dimensional weight function for a half-plane tensile crack in an infinite body.

A similar approach to that leading to equation (23) from (20) is useful for rewriting the result for the crack-surface opening displacement. As it stands, equation (15) for $\delta(\Delta u)$ is rigorously correct to first order in $\delta a(z)$ but, because of the effect of transport of the crack tip singularity in changing the $(-x)^{1/2}$ of equation (16) to $(-x)^{-1/2}$ where indicated in equation (15) is not very useful near the tip of a crack at a location where $\delta a(z) \neq 0$. Indeed, the first order expression for $\delta(\Delta u)$ becomes highly inaccurate when $(-x)$ is of the same order or smaller than $\delta a(z)$. By moving the reference crack tip to $a = a_0 + \delta a(z)$ we eliminate this problem.

Thus, we introduce the notation $\Delta u^\circ(x,z;a)$ for the distribution of opening displacement when the crack front is straight and at distance a from the fixed point on the crack surface. One notes incidently from equation (15) with δa uniform in z that the a dependence of this opening distribution must satisfy

$$\frac{\partial \Delta u^\circ(x,z;a)}{\partial a} = \frac{8(1-\nu^2)}{E} \left(\frac{a - a_0 - x}{2\pi}\right)^{1/2} \times \left[\frac{1}{2\pi} \int_{-\infty}^{+\infty} \frac{K^\circ(z';a)\,dz'}{(a-a_0-x)^2 + (z-z')^2}\right]; \tag{26}$$

here $-x$ has been replaced by $a - a_0 - x$ to accommodate general location of the crack front, and the derivative on the left is calculated as the limit of $\delta(\Delta u)/\delta a$. When K° is uniform in z, this reduces to

$$\frac{\partial \Delta u^\circ(x;a)}{\partial a} = \frac{4(1-\nu^2)}{E} \frac{K^\circ(a)}{[2\pi(a - a_0 - x)]^{1/2}}, \tag{27}$$

which is essentially K° times the two-dimensional Bueckner weight function for the semi-infinite crack in an infinite body.

Now, the total crack-opening displacement $\Delta u(x,z)$ along the crack faces at a given location z can be obtained by adding Δu° when $a = a_0 + \delta a(z)$ to $\delta(\Delta u)$ as calculated from equation (15) with $\delta a(z')$ replaced with $a(z') - a(z)$. Thus there results

$$\Delta u(x,z) = \Delta u^\circ[x,z;a(z)] + \frac{8(1-\nu^2)}{E} \left[\frac{a(z) - a_0 - x}{2\pi}\right]^{1/2} \times \left\{\frac{1}{2\pi} \int_{-\infty}^{+\infty} \frac{K^\circ[z';a(z)][a(z') - a(z)]}{[a(z) - a_0 - x]^2 + (z-z')^2}\, dz'\right\} \tag{28}$$

which is accurate to first order in $a(z') - a(z)$ and remains well defined as x approaches the crack tip at $a(z) - a_0$.

Wavy Crack Front and Stability

Consider the crack profile

$$a(z) = a_0 + A \cos(2\pi z/\lambda), \tag{29}$$

$\lambda > 0$, and suppose that the cracked body is loaded such that the intensity factor is uniform along the crack front when the front is straight, i.e., that $K^\circ(z;a) = K^\circ(a)$. Then insertion of the preceding $a(z)$ in equation (23) and calculation of the integral shows that

$$K(z) = K^\circ[a_0 + A \cos(2\pi z/\lambda)]\{1 - \pi(A/\lambda) \cos(2\pi z/\lambda)\} \tag{30}$$

to first-order accuracy in A. If we rewrite the equation to exhibit only those terms that are of zeroth and first order in A, then

$$K(z) = K^\circ(a_0) + [dK^\circ(a_0)/da_0 - \pi K^\circ(a_0)/\lambda] A \cos(2\pi z/\lambda). \tag{31}$$

This solution enables one to address the following stability problem. Suppose a small deviation from straightness in the form of equation (29) exists along a uniformly stressed crack front, that is, along one that would be uniformly stressed if it were straight. Will the deviation grow or decay as cracking advances quasistatically by, say, fatigue or corrosion? It seems reasonable to conclude that the deviation will grow if K is higher at the most advanced parts of the crack front ($z = 0, \pm\lambda, \pm 2\lambda$, etc.) than at the most retarded ($z = \pm\lambda/2, \pm 3\lambda/2$, etc.), and that the deviation will decay if the opposite is true. Thus the sign of the bracket governs and decay will occur, i.e., deviations from straightness will be smoothed out, if the bracket is negative. We conclude that the straight crack-front configuration is stable to small-amplitude perturbations of wavelength satisfying

$$\lambda dK^\circ(a_0)/da_0 < \pi K^\circ(a_0). \tag{32}$$

Further, if $dK^\circ/da_0 < 0$, as is the case, e.g., with localized wedging forces applied on or near the crack surfaces, then the straight configuration is stable to perturbations of all wavelengths. On the other hand, if $dK^\circ/da_0 > 0$ as is normally the case when loads are applied remotely from the crack tip, then there exists a critical wavelength $\lambda_c = \pi K^\circ/(dK^\circ/da_0)$ above which perturbations will tend to grow.

As a practical matter, λ_c as just defined will typically be of

Downloaded 02 May 2010 to 171.66.16.54. Redistribution subject to ASME license or copyright; see http://www.asme.org/terms/Terms_Use.cfm

the order of the crack length itself for disk-like or tunnel cracks, and hence conditions may not generally be met to consider perturbations on the scale of λ_c by use of the model of a half-plane crack in an infinite body, i.e., by neglect of proximity of the perturbed region to boundaries or to other differently oriented segments of crack front. For $\lambda << \lambda_c$ such is not a concern, and in that case the term involving λ in equation (31) dominates the first order effect. Thus K is decreased by $\pi K^\circ A/\lambda$ at the most advanced penetrations, and increased by the same amount at the most retarded locations. This increase may be taken to describe the stress intensification at microscale heterogeneities when a crack tip begins to advance by and surround a fracture-resistant zone of material.

We may also consider the perturbation of equation (24) considered by Meade and Keer (1984*b*). In this case equation (23) implies that

$$K(z) = K^\circ(a_0) + [dK^\circ(a_0)/da_0]A[\cos(2\pi z/\lambda) - 1] - \pi K^\circ(a_0)(A/\lambda)\cos(2\pi z/\lambda). \quad (33)$$

when only zeroth and first orders in A are retained. By contrast, the solution proposed by Meade and Keer (1984*b*) when expanded to the same order is

$$K(z) = K^\circ(a_0) + [dK^\circ(a_0)/da_0]A[\cos(2\pi z/\lambda) - 1]. \quad (34)$$

This is missing the last term of equation (33), which is the result of the principal value integral in equation (23). Given the form of perturbation from straightness in equation (24), it would seem evident that K at $z = 0$ should indeed decrease with increasing A. This is because more of the crack surfaces are attached back together when $A > 0$, compared to the situation when $A = 0$, and the most advanced parts of the crack front ($z = 0, \pm\lambda, \pm 2\lambda$, etc.) are then shielded by the rejoined elements of material to their sides. This effect of decrease of K at $z = 0$ with increase of A is predicted by equations (23) and (33) but not (at least to first order) by equations (25) and (34).

Direct Solution for Half-Plane Crack in Infinite Body

Since there is disagreement with other work, it seems appropriate to reexamine the problem of a wavy half-plane crack in a full space here by directly solving the Navier equations of elasticity. Meade and Kerr (1984*a*,*b*) show, following Sections 5.8 of Green and Zerna (1954), that these equations are satisfied in a manner compatible with tensile loading that is symmetric relative to the crack plane if displacement components are written as

$$u_y = -2[(1-\nu^2)/E]Y + [(1+\nu)/E]y\,\partial Y/\partial y$$
$$u_x = [(1+\nu)/E]\partial(F + yY)/\partial x$$
$$u_z = [(1+\nu)/E]\partial(F + yY)/\partial z \quad (35)$$

where F and Y are harmonic functions related by $\partial F/\partial y = (1-2\nu)Y$. In addition, the stress components that enter crack-surface boundary conditions are calculated from the stress-strain relations as

$$\sigma_{yy} = -\partial Y/\partial y + y\partial^2 Y/\partial y^2$$
$$\sigma_{yx} = y\partial^2 Y/\partial y \partial x, \qquad \sigma_{yz} = y\partial^2 Y/\partial y \partial z \quad (36)$$

and cause no shear traction on $y = 0$. Thus the problem of loading on the crack face is one of finding a function Y satisfying $\nabla^2 Y = 0$, having vanishing derivatives at infinity, and generating stress σ and opening gap Δu on $y = 0$ given by

$$\sigma = -\partial Y/\partial y\Big|_{y=0} \quad \text{and} \quad \Delta u = -[4(1-\nu^2)/E]Y\Big|_{y=0^+} \quad (37)$$

respectively, such that boundary conditions are satisfied. If the crack tip lies along

$$x = Ag(z), \quad (38)$$

where $g(z)$ is some arbitrary function of z, and the crack faces are loaded by normal pressure $p(x,z)$ $[= -\sigma(x,z)]$, these conditions are

$$\partial Y/\partial y\Big|_{y=0} = p(x,z) \qquad \text{for} \qquad x < Ag(z),$$

and

$$Y\Big|_{y=0} = 0 \qquad \text{for} \qquad x > Ag(z) \quad (39)$$

as discussed by Meade and Keer (1984*b*) for their particular case. The problem cannot be solved explicitly in this generality but it is known that solutions to it, when restricted to have bounded energy in any finite region about the crack tip, exhibit characteristic inverse square root stress singularities whose nature is indicated in such equations as (3) and (16). The harmonic function Y generating such a singularity necessarily has the form

$$Y \sim -2K(r/2\pi)^{1/2}\sin(\theta/2) \quad (40)$$

(plus another part generating finite ∇Y) near the tip, where r and θ are polar coordinates in planes locally perpendicular to the tip; $\theta = \pm\pi$ on the crack surfaces.

Let the solution of the boundary value problem as formulated be $Y(x,y,z;A)$. We now turn to calculation of the function

$$W(x,y,z) = [\partial Y(x,y,z;A)/\partial A]\Big|_{A=0}. \quad (41)$$

It is evident that $\nabla^2 W = 0$ and, since the crack-face loading has no dependence on A,

$$\partial W/\partial y\Big|_{y=0} = 0 \qquad \text{for} \qquad x < 0,$$

$$W\Big|_{y=0} = 0 \qquad \text{for} \qquad x > 0. \quad (42)$$

This apparently homogeneous boundary value problem for W would have only the solution $W = 0$ if restricted to the bounded energy class in the same way as for conventional elastic solutions. However, W has a stronger singularity along the crack front than normally allowed. We can calculate this by calculating $\partial r/\partial A$ and $\partial\theta/\partial A$, corresponding to fixed x,y,z, in equation (40) at $A = 0$ so as to calculate $\partial Y/\partial A$. Of course, K at any particular z also varies with A but this does not affect the most strongly singular term. The result of a straightforward calculation is that

$$W \sim -K^\circ(z)g(z)(2\pi r)^{-1/2}\sin(\theta/2) \quad (43)$$

where, in this limit, the crack front is straight and coincident with the z axis, and $K^\circ(z)$ is the K distribution induced by the given loadings $p(x,z)$ for that straight configuration. Note that the nature of the original loading and shape g of the incipient growth appear only in the product $K^\circ(z)g(z)$.

To obtain a solution of $\nabla^2 W = 0$ with the singular form indicated, introduce the Fourier representation

$$K^\circ(z)g(z) = \frac{1}{2\pi}\int_{-\infty}^{+\infty}\alpha(\omega)e^{i\omega z}d\omega. \quad (44)$$

Evidently, we wish to seek solutions of $\nabla^2 W = 0$ with a z dependence of form $e^{i\omega z}$, and to meet the homogeneous boundary conditions of equations (42) on the crack faces one begins by looking for harmonic functions in the form

$$f(r)\sin(m\theta/2)e^{i\omega z} \quad (45)$$

with $m = 1, 3, 5, \ldots$. As it happens, all conditions on the problem can be met with $m = 1$. In that case it is easy to show that the possible forms for $f(r)$ are

$$f(r) = r^{-1/2}e^{\pm|\omega|r}, \quad (46)$$

and obviously the + sign must be rejected in the present case. Thus we see that

Downloaded 02 May 2010 to 171.66.16.54. Redistribution subject to ASME license or copyright; see http://www.asme.org/terms/Terms_Use.cfm

$$r^{-1/2}e^{-|\omega|r}\sin(\theta/2)e^{i\omega z} \tag{47}$$

is harmonic, and this has precisely the singular structure as $r\to 0$ required in equation (43). Therefore the solution is

$$W=-(1/2\pi)(2\pi r)^{-1/2}\sin(\theta/2)\int_{-\infty}^{+\infty}\alpha(\omega)e^{-|\omega|r}e^{i\omega z}d\omega \tag{48}$$

since, by equation (44), this reduces to equation (43) when $r\to 0$.

To complete the solution, we write by Fourier inversion of equation (44) that

$$\alpha(\omega)=\int_{-\infty}^{+\infty}K^{\circ}(z')g(z')e^{-i\omega z'}dz', \tag{49}$$

insert this into equation (48), change the order of integration, and note that

$$\int_{-\infty}^{+\infty}e^{-i\omega z'}e^{-|\omega|r}e^{i\omega z}d\omega=2r/[r^2+(z-z')^2]. \tag{50}$$

The result for W is therefore that

$$W(r,\theta,z)$$

$$=-(1/\pi)(r/2\pi)^{1/2}\sin(\theta/2)\int_{-\infty}^{+\infty}\frac{K^{\circ}(z')g(z')dz'}{r^2+(z-z')^2}. \tag{51}$$

Remembering that W is $\partial Y/\partial A$ at $A=0$ and that the opening gap Δu is related to Y as in equation (37) on $\theta=0,\pi$, we have therefore derived that

$$\left.\frac{\partial\Delta u(x,z,A)}{\partial A}\right|_{A=0}$$

$$=\frac{8(1-\nu^2)}{E}\left(\frac{-x}{2\pi}\right)^{1/2}\left[\frac{1}{2\pi}\int_{-\infty}^{+\infty}\frac{K^{\circ}(z')g(z')}{x^2+(z-z')^2}dz'\right]. \tag{52}$$

Here θ has been set equal to π and thus r to $-x$. This last equation is precisely the same as equation (15); $\delta a(z)$ is just $\delta A g(z)$. Thus an independent derivation of equation (15) is now at hand, and the result given earlier in equation (23) for K along a nonstraight crack tip follows from there.

Now, in what amounts to an application of weight function ideas of the first type described in the opening section, let us note that equation (52), just independently derived, and equation (13) must be consistent with one another for arbitrary $\delta a(z)$. Their consistency requires that $k(z';x,z)$ have a certain definite form, which is exactly that given in equation (14). Thus the solution derived in this section together with the fundamental equation (13) of weight function theory gives the solution for the stress intensity distribution k along the crack front due to unit concentrated forces opening the crack faces.

It has been shown (Rice, 1972, equations (A8) to (A11) put in the notation for the present problem) that if the displacement vector variation is expressed as

$$\delta\mathbf{u}(x,y,z)=\int_{-\infty}^{+\infty}\mathbf{U}^{\circ}(x,y,z;z')\delta a(z')dz' \tag{53}$$

to first order in $\delta a(z)$ for a crack under some "original" tensile loading, then

$$\mathbf{h}(x,y,z;z')=E\mathbf{U}^{\circ}(x,y,z;z')/2(1-\nu^2)K^{\circ}(z') \tag{54}$$

is the three-dimensional weight function. This is unique within rigid motions, is independent of the nature of the original loading system, and has the property that for arbitrary distributions of body force $\mathbf{f}(x,y,z)$ compatible with tensile loadings, the stress intensity factor induced along the crack front is

$$K(z')=\int\mathbf{f}(x,y,z)\cdot\mathbf{h}(x,y,z;z')\,dxdydz. \tag{55}$$

The integral extends over all locations where the body force acts and loads on the crack faces can, of course, be included as concentrations of body force.

By substituting from equation (54) in (53), we may write the latter in a manner to show that the weight function can be read off when we have obtained a representation for $\delta\mathbf{u}$ in the form

$$\delta\mathbf{u}(x,y,z)$$

$$=\frac{2(1-\nu^2)}{E}\int_{-\infty}^{+\infty}\mathbf{h}(x,y,z;z')K^{\circ}(z')\delta a(z')dz'. \tag{56}$$

But $\delta\mathbf{u}$ can be written from equations (35) as a linear operation on δY, the same operation that forms $\mathbf{u}$ from Y. Also, recognizing that δY is just $W\delta A$ with the product $g(z')\delta A$ written as $\delta a(z')$, we may write from equation (51) that

$$\delta Y(x,y,z)=-\int_{-\infty}^{+\infty}H(x,y,z;z')K^{\circ}(z')\delta a(z')dz' \tag{57}$$

with

$$H(x,y,z;z')=(r/2\pi^3)^{1/2}\sin(\theta/2)/[r^2+(z-z')^2]. \tag{58}$$

Thus recognizing that $\delta\mathbf{u}$ of equation (56) is formed from δY of (57) by the linear operation (35), we conclude that $2(1-\nu^2)\mathbf{h}/E$ is formed from $-H$ by the same linear operation. Thus the components of the weight function are

$$\begin{aligned}h_y&=H-[1/2(1-\nu)]y\,\partial H/\partial y\\ h_x&=-[1/2(1-\nu)]\partial(L+yH)/\partial x\\ h_z&=-[1/2(1-\nu)]\partial(L+yH)/\partial z\end{aligned} \tag{59}$$

where

$$L(x,y,z;z')=-(1-2\nu)\int_{y}^{\infty}H(x,\bar{y},z;z')d\bar{y}. \tag{60}$$

This seems to be the first case for which a three-dimensional weight function has been determined. Regrettably, since the integral defining L cannot be reduced to a simple form, the x and z components of the weight function are not in a very convenient form for applications. However, h_y has no similar difficulties and it is all that is needed when loads act in directions perpendicular to the crack plane. As a check, letting $y\to 0^+$ or 0^-, one observes that

$$h_y(x,\pm 0,z;z')=H(x,\pm 0,z;z')=\pm(1/2)k(z';x,z) \tag{61}$$

as expected, where k is the intensity factor of equation (14).

Mead and Keer (1984*b*) attempt to directly calculate the function Y defined by equations (39), for their particular shape function

$$g(z)=-[1-\cos(2\pi z/\lambda)], \tag{62}$$

and for loading of the crack faces by line loads of intensity P_0 at distance a_0 from the tip as described earlier. Shortly after their equation (47), they propose that the solution for Y (in present notation) is

$$Y=-\frac{P_0}{2\pi}\log\left\{\frac{r+a_0+Ag(z)+2[ra_0+rAg(z)]^{1/2}\sin(\theta/2)}{r+a_0+Ag(z)-2[ra_0+rAg(z)]^{1/2}\sin(\theta/2)}\right\}+O(A^2/\lambda^2) \tag{63}$$

where

$$r^2=[x-Ag(z)]^2+y^2,\qquad \tan\theta=y/[x-Ag(z)]. \tag{64}$$

The difficulty is that when this solution is used to calculate $\partial Y(x,y,z,A)/\partial A$ at $A=0$, it does not give a result that coincides with the exact solution derived here. In particular, when the $g(z)$ of equation (62) is used and we use $K^{\circ}(a)=2^{1/2}P_0/\pi^{1/2}a^{1/2}$ as appropriate for the line-load problem, there results from the solution in equation (51) for W that

$$W\equiv\left.\partial Y/\partial A\right|_{A=0}=(P_0/\pi)(a_0r)^{-1/2}\sin(\theta/2)[1$$

Downloaded 02 May 2010 to 171.66.16.54. Redistribution subject to ASME license or copyright; see http://www.asme.org/terms/Terms_Use.cfm

$$-\cos(2\pi z/\lambda)e^{-2\pi r/|\lambda|}]. \quad (65)$$

By contrast, the corresponding quantity calculated from equation (63) for Y as proposed by Meade and Keer does not show the exponential decay of the effect of the $\cos(2\pi z/\lambda)$ wiggle in crack-front position at large distances r, nor does it show a dependence on a_0 only in the form of a factor. Meade and Kerr develop their analysis by asymptotic methods based in part on multiple (double) scaling in the z direction, one length scale being based on A and the other on λ. Equation (65) together with the fix-up of type in going from equation (15)-(28), based on placing the reference straight crack front at $a(z)$, i.e., at $x = Ag(z)$, suggest that there may not in fact be a double scale of the type they assumed for the z dependence of the solution, but that instead such occurs for the x and y dependence.

Cracks Under General Mixed Mode Conditions

As a generalization, we can consider a possibly anisotropic body of arbitrary shape containing a planar crack on $y=0$ and suppose that the original loading system induces opening as well as shear displacements in the x and z directions on the crack faces. In this case there are three stress-intensity factors, given subscripts 1,2,3 where 1 refers to tension, 2 to in-plane shear, and 3 to antiplane shear relative to a plane locally perpendicular to the crack front. Thus in the plane $y=0$ at distance r ahead of the tip there is the asymptotic stress distribution

$$(\sigma_{yy},\sigma_{yn},\sigma_{ys}) \sim (K_1,K_2,K_3)/(2\pi r)^{1/2}, \quad (66)$$

where n and s denote directions in the plane $y=0$ that are, respectively, normal and tangential to the crack front C. The Irwin relation for the energy release per unit area of crack extension is

$$G = \Lambda_{\alpha\beta}K_\alpha K_\beta \quad (67)$$

where α,β range over 1,2,3 with summation on repeated indices, where $\Lambda_{\alpha\beta} = \Lambda_{\beta\alpha}$, and for an isotropic material

$$\Lambda_{11} = \Lambda_{22} = (1-\nu^2)/E, \qquad \Lambda_{33} = (1+\nu)/E,$$
$$\text{other} \qquad \Lambda_{\alpha\beta} = 0. \quad (68)$$

For anisotropic solids the calculation of $\Lambda_{\alpha\beta}$ is discussed by Stroh (1958) and Barnett and Asaro (1972); $\Lambda_{\alpha\beta}$ can be expressed as a numerical factor times the inverse of a matrix appearing in the prelogarithmic energy factor of dislocation theory. In general, the $\Lambda_{\alpha\beta}$ will depend on the local tangent direction to the crack front.

Suppose that in addition to the original loading system, a distribution of forces with intensity proportional to Q acts, as in the discussion preceding equation (12), and that q is the conjugate deformation quantity. Then with the original load system fixed, one has

$$Q\delta q - \int_C \Lambda_{\alpha\beta}(s)K_\alpha(s)K_\beta(s)\delta a(s)\, ds = \delta(U+V_0), \quad (69)$$

as in equation (1), and from this we infer analogously to equations (9) and (12) that the variation in q when the crack is advanced in presence of only the original loading system ($Q=0$) is

$$\delta q = \int_C 2\Lambda_{\alpha\beta}(s)\tilde{k}_\alpha(s)K^\circ_\beta(s)\delta a(s)\, ds \quad (70)$$

to first order in $\delta a(s)$. Here K°_α are the intensity factors induced by the original loading and $\tilde{k}_\alpha$ the intensity factors induced by unit value of Q. As before, if the $\tilde{k}_\alpha$ are known, one can calculate δq, whereas if δq is known for arbitrary "source" terms $K^\circ_\alpha \delta a$ along C, one can calculate the $\tilde{k}_\alpha$.

To proceed to a three-dimensional weight function formulation appropriate for arbitrary mixed mode conditions, consider the problem of calculating the first-order variation $\delta\mathbf{u}$ in the elastic displacement field at a general position $\mathbf{r} = (x,y,z)$ when the crack advances in presence of the original loading. It is clear that $\delta\mathbf{u}$ satisfies the equations of elasticity in presence of zero body force, zero boundary traction on the crack faces and wherever else tractions were prescribed in the original loading, and zero boundary displacement where displacements were prescribed. Despite the apparent homogeneity of the problem, $\delta\mathbf{u}$ is nonzero because its three components have prescribed singularities of strengths that are linear in the three terms of form $K^\circ_\beta(s)\delta a(s)$ along the crack front. Each such source term can be regarded as generating a vector displacement field at $\mathbf{r}$ which is conveniently written as $2\Lambda_{\alpha\beta}\mathbf{h}_\alpha(\mathbf{r},s)$ weighted with the source strength $K^\circ_\beta(s)\delta a(s)$ along C. Thus

$$\delta\mathbf{u}(\mathbf{r}) = \int_C 2\Lambda_{\alpha\beta}(s)\mathbf{h}_\alpha(\mathbf{r},s)K^\circ_\beta(s)\delta a(s)\, ds. \quad (71)$$

Note that the vector functions $\mathbf{h}_\alpha$ thus defined are universal in that they have no dependence on the nature of the original loading system, other than depending on which portions of the external boundary had tractions versus displacements prescribed. Of course, the functions also depend on the shape and location of the crack. The vector functions $\mathbf{h}_\alpha(\mathbf{r},s)$ defined by equation (71) are sensibly called "weight functions." To see why, denote the components of $\mathbf{h}_\alpha$ as $h_{\alpha j}$ where $j = x, y$, or z, and observe that $\delta u_j(\mathbf{r})$ is generated by $h_{\alpha j}(\mathbf{r},s)$. But δu_j is just δq when Q measures the intensity of a concentrated force in the j direction at $\mathbf{r}$, and hence $h_{\alpha j}(\mathbf{r},s)$ must equal $\tilde{k}_\alpha(s)$ of equation (70) where the $\tilde{k}_\alpha$ are then the intensity factors induced by a unit point force in the j direction at $\mathbf{r}$. Thus for an arbitrary distribution of body force $\mathbf{f}(\mathbf{r})$, the intensity factors induced at location s along the crack front are

$$K_\alpha(s) = \int \mathbf{f}(\mathbf{r})\cdot\mathbf{h}_\alpha(\mathbf{r},s)d^3\mathbf{r} \quad (72)$$

integrated over the region of loading, confirming the weight function interpretation of the $\mathbf{h}_\alpha$. Paris et al. (1976) and Bortman and Banks-Sills (1983) introduced two-dimensional weight functions for shear modes in isotropic solids.

To summarize, if we know from some other work the stress intensity factors induced by concentrated forces at $\mathbf{r}$, then from equation (72) it is clear that we know the $\mathbf{h}_\alpha(\mathbf{r},s)$. We can then use these $\mathbf{h}_\alpha$ in equation (71) to calculate $\delta\mathbf{u}(\mathbf{r})$ and, from it, variations in stress intensity factors K_α along the crack front to first order in $\delta a(s)$. This is what was done for the half-plane tensile crack in the second section of this paper. On the other hand, if we can calculate directly $\delta\mathbf{u}(\mathbf{r})$ for arbitrary source terms $K^\circ_\beta(s)\delta a(s)$ along the crack front, as done for the half-plane tensile crack in the preceding section, then we have a more basic result. That calculation, when put in the form of equation (71), amounts to fundamental calculation of the weight functions $\mathbf{h}_\alpha(\mathbf{r},s)$. I leave for future work the full exploration of these ideas for the half-plane crack in an infinite isotropic body, under general tensile and shear loadings, and discuss here only some aspects of that case.

Specifically, let us develop the expression for general mixed-mode loading that is analogous to equations (13) and (15) for the tensile crack problem. Suppose that the faces of the half-plane crack are loaded by concentrated forces P_j at $x,0^+,z$ and $-P_j$ at $x,0^-,z$, with $j = x,y$, or z. The stress-intensity factors $k_{\alpha j} = k_{\alpha j}(z';x,z)$ induced at z' by unit P_j are (Tada et al., 1973; Meade and Keer, 1984*a*)

$$k_{1x} = k_{1z} = k_{2y} = k_{3y} = 0$$
$$k_{1y} = k$$
$$k_{2x} = \left[1 + \frac{2\nu}{2-\nu}\,\frac{x^2-(z'-z)^2}{x^2+(z'-z)^2}\right]k$$

Downloaded 02 May 2010 to 171.66.16.54. Redistribution subject to ASME license or copyright; see http://www.asme.org/terms/Terms_Use.cfm

$$k_{3z} = \left[1 - \frac{2\nu}{2-\nu}\frac{x^2-(z'-z)^2}{x^2+(z'-z)^2}\right]k$$

$$k_{2z} = k_{3x} = -\frac{4\nu}{2-\nu}\frac{x(z'-z)}{x^2+(z'-z)^2}k \tag{73}$$

where $k = k(z';x,z)$ is given by equation (14). Of course the $k_{\alpha j}(z';x,z)$ are functions only of x and $z-z'$. Evidently, the $k_{\alpha j}$ must be related to the weight functions defined in the foregoing by

$$k_{\alpha j}(z';x,z) = h_{\alpha j}(x,0^+,z;z') - h_{\alpha j}(x,0^-,z;z'). \tag{74}$$

Thus the previous formulas, written out fully for the isotropic case, imply that

$$\delta[\Delta u_j(x,z)] = \int_{-\infty}^{+\infty}\left\{\frac{2(1-\nu^2)}{E}[k_{1j}(z';x,z)K_1^\circ(z') + k_{2j}(z';x,z)K_2^\circ(z')] + \frac{2(1+\nu)}{E}k_{3j}(z';x,z)K_3^\circ(z')\right\}\delta a(z')\,dz' \tag{75}$$

is the first-order variation in j component of the relative displacement $\Delta\mathbf{u}$ of the crack faces at x,z when the crack front advances by $\delta a(z')$ in presence of (only) the original loadings, which have induced intensity factors $K_\alpha^\circ(z')$ along the reference straight crack front.

Let us note the relation between the weight functions and Green's function (i.e., the dyadic $\mathbf{G}(\mathbf{r},\tilde{\mathbf{r}})$ giving, by $\mathbf{u} = \mathbf{G}\cdot\mathbf{P}$, the displacement $\mathbf{u}$ at $\mathbf{r}$ induced by concentrated force $\mathbf{P}$ at $\tilde{\mathbf{r}}$) for a cracked body. Suppose that the "original loading" is just the concentrated force described, with null body forces and boundary tractions or displacements elsewhere. Then equation (72) requires

$$K_\beta^\circ(s) = \mathbf{h}_\beta(\tilde{\mathbf{r}},s)\cdot\mathbf{P}, \tag{76}$$

and hence equation (71) reads that

$$\delta\mathbf{u}(\mathbf{r}) = \left[\int_C 2\Lambda_{\alpha\beta}(s)\mathbf{h}_\alpha(\mathbf{r},s)\mathbf{h}_\beta(\tilde{\mathbf{r}},s)\delta a(s)\,ds\right]\cdot\mathbf{P}. \tag{77}$$

Since $\mathbf{u} = \mathbf{G}\cdot\mathbf{P}$, this shows that the bracketed term is the variation $\delta\mathbf{G}(\mathbf{r},\tilde{\mathbf{r}})$ to first order in $\delta a(s)$.

For the half-plane crack in an infinite body, this expression leads to a formula for the Green's function in terms of the weight functions. Note that if a denotes the x coordinate of the straight crack front parallel to the z axis (this means $a_0 = 0$ in Fig. 2) then, representing s by z' as before, one must have

$$\mathbf{h}_\alpha(\mathbf{r},z') = \mathbf{h}_\alpha(x-a,y,z-z'). \tag{78}$$

The Green's function must depend parametrically on a, and if we let δa denote a uniform $\delta a(z)$ along the crack front and divide by δa in equation (77), one has that

$$\frac{\partial\mathbf{G}(\mathbf{r},\mathbf{r};a)}{\partial a} = 2\Lambda_{\alpha\beta}\int_{-\infty}^{+\infty}\mathbf{h}_\alpha(x-a,y,z-z')\mathbf{h}_\beta(\tilde{x}-a,\tilde{y},\tilde{z}-z')\,dz'. \tag{79}$$

But when $a = -\infty$, $\mathbf{G}$ reduces to the function $\mathbf{G}(\mathbf{r},\tilde{\mathbf{r}};-\infty)$ obtained from the Kelvin-type solution for a point force in an infinite uncracked body. This depends only on $\mathbf{r}-\tilde{\mathbf{r}}$. Thus the Green's function when the crack tip lies along the z axis ($a=0$) is

$$\mathbf{G}(\mathbf{r},\tilde{\mathbf{r}}) = \mathbf{G}^{\text{Kelv.}}(\mathbf{r}-\tilde{\mathbf{r}}) + 2\Lambda_{\alpha\beta}\int_{-\infty}^{0}\int_{-\infty}^{+\infty}\mathbf{h}_\alpha(x-a,y,z-\tilde{z}+t)\mathbf{h}_\beta(\tilde{x}-a,\tilde{y},t)\,dt\,da. \tag{80}$$

For the half-plane crack in an infinite isotropic body, perhaps the simplest way of solving for the weight functions will be to solve the Navier elasticity equations directly for $\delta\mathbf{u}(\mathbf{r})$, with arbitrary $\delta a(z')$, putting the result in the form of equation (71) so that the $\mathbf{h}_\alpha$ can be read off. However, we can also make use of what is now available in the literature to derive an integral representation for the $\mathbf{h}_\alpha$ as follows. First note that from details of the point force solution given by Love (1927, articles 130, 131, and 141), the components of the Kelvin Green's function for the isotropic solid are

$$G_{ij}^{\text{Kelv.}}(\mathbf{r}-\tilde{\mathbf{r}}) = \frac{(\lambda+3\mu)\delta_{ij} + (\lambda+\mu)X_iX_j/R^2}{8\pi\mu(\lambda+2\mu)R} \tag{81}$$

and if $\Sigma_{pqj}^{\text{Kelv.}}$ denotes the associated stress components, i.e., stresses σ_{pq} at $\mathbf{r}$ due to unit concentrated force in the j direction at $\tilde{\mathbf{r}}$, then

$$\Sigma_{pqj}^{\text{Kelv.}}(\mathbf{r}-\tilde{\mathbf{r}}) = \frac{1}{4\pi(\lambda+2\mu)R^3}[\mu(\delta_{pq}X_j - \delta_{pj}X_q - \delta_{qj}X_p) - 3(\lambda+\mu)(X_pX_q/R^2)X_j]. \tag{82}$$

Here p,q,i,j range over x,y, and z, δ_{pq} is the Kronecker symbol,

$$X_x = x-\tilde{x}, \qquad X_y = y-\tilde{y}, \qquad X_z = z-\tilde{z}, \tag{83}$$

and $R^2 = X_pX_p$. We wish to solve for the weight functions $h_{\alpha j}(\tilde{\mathbf{r}},z')$, which can be interpreted as the stress intensities K_α at z' generated by a unit point force in the j direction at $\tilde{\mathbf{r}}$. If there were no crack, this loading would cause traction stresses σ_{yq} (i.e., σ_{yx}, σ_{yy}, σ_{yz}) on the plane $y = 0$ given as

$$\Sigma_{yqj}^{\text{Kelv.}}(x-\tilde{x},-\tilde{y},z-\tilde{z}). \tag{84}$$

To represent the effect of the crack, we must remove these tractions. This can be done by regarding $\mp\Sigma_{yqj}^{\text{Kelv.}}\,dxdy$ as concentrated forces applied to the upper and lower crack surfaces, and superposing all such forces as weighted by $k_{\alpha q}(z';x,z)$ of equations (73) to calculate K_α. Thus, using the notations $h_{\alpha j}(\tilde{\mathbf{r}},z') = h_{\alpha j}(\tilde{x},\tilde{y},\tilde{z}-z')$ and $k_{\alpha q}(z';x,z) = k_{\alpha q}(x,z-z')$ appropriate to the present case, we have

$$h_{\alpha j}(\tilde{x},\tilde{y},\tilde{z}) = -\int_{-\infty}^{0}\int_{-\infty}^{+\infty}\Sigma_{yqj}^{\text{Kelv.}}(x-\tilde{x},-\tilde{y},z-\tilde{z})k_{\alpha q}(x,z)\,dz\,dx. \tag{85}$$

The integrations implied are somewhat formidable and the further development of this topic is left to future work. However, apart from the inconvenient form of the $h_{\alpha j}$, the way is now available for the half-plane crack under general loadings to find stress intensities from equation (72), to find first-order changes in the displacement field for arbitrary deviations of the tip from straightness by equation (71), and to use the simpler equations (73) and (75) as a starting point in finding associated first-order changes in the stress-intensity factors along the crack front.

Discussion

Regarding possible applications for calculations of the type given here for tensile cracks or as outlined in the last section for general loadings, the following might be mentioned:

1. At a crustal tectonic scale it seems appropriate in some circumstances to regard the shallow seismogenic crust along plate margins as locked between great earthquakes while, in accommodation of plate motion, creep slippage occurs continuously below on the downward extension of the margin into the lower crust and mantle (e.g., see Li and Rice, 1983*a*,*b*, and references therein). Roughly speaking this geometry describes a shear crack which, late in the earthquake cycle, may show some preinstability advance into the locked shallow crust. Thus one would like to know what deformation at the Earth's surface would be associated with such crack advance and how measurements of surface deformation could constrain its form. Equation (71), with the mode 1 part

Downloaded 02 May 2010 to 171.66.16.54. Redistribution subject to ASME license or copyright; see http://www.asme.org/terms/Terms_Use.cfm

deleted for slipping cracks, provides a manner of addressing such issues. Clearly, the shear loaded half-plane crack, for which specific solutions are discussed here, should be modified to have a traction-free surface along, e.g., a plane of form x = constant to represent more accurately the Earth's surface above a strike-slip margin. Such questions are conventionally addressed in geodetic modeling by assuming a distribution of sub-surface slip rather than by assuming alteration of the boundary between a locked and slipping region, although calculations of the latter type have recently been done by Tse et al. (1984) based on approximate "line spring" modeling.

2. As suggested to the author in different contexts by B. Budiansky and E. Vanmarcke, an important problem in fracture theory is that of how a crack advances through a material with randomly variable fracture resistance. The problem arises for both tensile and tectonic shear cracking. To the extent that such crack advance can be modeled as the elastic-brittle growth of a planar crack whose front is only slightly deviated from straightness by the random highs and lows of fracture resistance, the techniques discussed here for relating local K to crack front location may be applied as a basis for analyzing growth. The problem would seem to have attributes similar to that of the failure of a long earth embankment of randomly variable properties as treated by Vanmarcke (1977). A localized weak spot may engender a local, short wavelength advance of the crack, but such will not necessarily go very far because the K at the advanced tip will generally be reduced according to the analysis here. On the other hand, long wavelength advances of the crack may correspond to effectively sampling the fracture resistance over a wide zone and are not sensitive to locally weakened zones. Thus, as is the case in Vanmarcke's (1977) analysis of embankment failure, one expects an intermediate wavelength to be most critical. There is also the prospect in such studies of quantifying the random small ruptures which precede overall failure.

3. As emphasized by Meade and Keer (1984*b*), crack-front segmentation is observed in laboratory study of brittle materials under mode 3 or combined mode 1 and mode 3 loading. They observe that modes 2 and 3 are coupled in the sense that when the crack front protrudes ahead locally in the plane $y=0$ a mode 2 intensity is induced which has different signs on opposite sides of the localized protrusion. They suggest that the induced mode 2 causes deviations from planarity of opposite sense (up versus down in y direction) on the two sides of the protrusion during tensile crack advance, leading to nonplanar segmentation. The revised basis for calculating stress intensities along a nonstraight crack front set out here may allow further evaluation of the proposed mechanism.

4. An approach to assessing whether a given solid will fail by atomistically brittle versus ductile mechanisms is based on addressing the following question (Rice and Thomson, 1974; Mason, 1979): As loading is applied to an initially sharp crack will one first reach conditions for tensile separation of lattice planes or, instead, will dislocation lines first be nucleated from the tip and blunt-out the stress concentration? Thus far the dislocation nucleation problem has been addressed beginning with an exact elastic analysis for the "image force" pulling a straight dislocation line, lying parallel to the tip, back into the tip (Rice and Thomson, 1974; Asaro, 1975; Rice, 1984). Then the analysis is adapted in a more-or-less ad hoc manner to deal with discrete atomistic and three-dimensional aspects of the problem (e.g., the dislocation line is expected to nucleate as a loop). However, the elastic field of an arbitrary three-dimensional dislocation loop can be represented in terms of the Green's function for the dislocated body. Since the Green's function for the half-plane crack is given here, it is possible in principle to represent the elastic field of a dislocation loop near a crack tip in terms of the present results, although it is far from clear that it will be feasible to carry through the calculations implied. Ideally, one would like to calculate the loop shape allowing easiest nucleation.

Acknowledgment

I am grateful for discussions on the topic of this paper with B. Budiansky, H. J. Gao, J. W. Hutchinson, L. M. Keer, P. Matagna, D. M. Parks, and E. Vanmarcke. Work in this area is supported by the NSF Materials Research Laboratory at Harvard, by the NSF Division of Earth Sciences, and the USGS Earthquake Hazards Reduction Program.

References

Asaro, R. J., 1975, "An Image Force Theorem for a Dislocation Near a Crack in an Anisotropic Elastic Material," *Journal of Physics, F: Metal Physics*, Vol. 5, pp. 2249-2255.

Barnett, D. M., and Asaro, R. J., 1972, "The Fracture Mechanics of Slit Cracks in Anisotropic Elastic Media," *Journal of the Mechanics and Physics of Solids*, Vol. 20, pp. 353-366.

Besuner, P. M., 1974, "Residual Life Estimates for Structures With Partial Thickness Cracks," *Mechanics of Crack Growth*, STP 590, ASTM, Philadelphia, pp. 403-419.

Bortman, Y., and Banks-Sills, L., 1983, "An Extended Weight Function Method for Mixed-Mode Elastic Crack Analysis," ASME JOURNAL OF APPLIED MECHANICS, Vol. 50, pp. 907-909.

Bueckner, H. F., 1970, "A Novel Principle for the Computation of Stress Intensity Factors," *Zeitschrift fur angewandte Mathematik und Mechanik*, Vol. 50, pp. 529-546.

Bueckner, H. F., 1972, "Field Singularities and Related Integral Representations," *Mechanics of Fracture 1: Methods of Analysis and Solution of Crack Problems*, Sih, G. C., ed., Noordhoff, Leyden, pp. 239-314.

Green, A. E., and Zerna, W., 1954, *Theoretical Elasticity*, Oxford University Press.

Kassir, M. K., and Sih, G. C., 1973, "Application of Papkovich-Neuber Potentials to a Crack Problem," *International Journal of Solids and Structures*, Vol. 9, pp. 643-654.

Li, V. C., and Rice, J. R., 1983*a*, "Preseismic Rupture Progression and Great Earthquake Instabilities at Plate Boundaries," *Journal of Geophysical Research*, Vol. 88, pp. 4231-4246.

Li, V. C., and Rice, J. R., 1983*b*, "Precursory Surface Deformation in Great Plate Boundary Earthquake Sequences," *Bulletin of the Seismological Society of America*, Vol. 73, pp. 1415-1434.

Love, A. E. H., 1927, *The Mathematical Theory of Elasticity*, Cambridge University Press.

Mason, D. D., 1979, "Segregation-Induced Embrittlement of Grain Boundaries," *Philosophical Magazine*, Vol. 39, pp. 445-468.

Meade, K. P., and Keer, L. M., 1984*a*, "On the Problem of a Pair of Point Forces Applied to the Faces of a Semi-Infinite Plane Crack," *Journal of Elasticity*, Vol. 14, pp. 3-14.

Meade, K. P., and Keer, L. M., 1984*b*, "Stress Intensity Factors for Semi-Infinite Plane Crack With a Wavy Front," *Journal of Elasticity*, Vol. 14, pp. 79-92.

Paris, P. C., McMeeking, R. M., and Tada, H., 1976, "The Weight Function Method for Determining Stress Intensity Factors," *Cracks and Fracture*, STP 601, ASTM, Philadelphia, pp. 471-489.

Parks, D. M., and Kamenetzky, E. A., 1979, "Weight Functions From Virtual Crack Extension," *International Journal of Numerical Methods in Engineering*, Vol. 14, pp. 1693-1706.

Rice, J. R., 1972, "Some Remarks on Elastic Crack Tip Stress Fields," *International Journal of Solids and Structures*, Vol. 8, pp. 751-758.

Rice, J. R., 1984, "Conserved Integrals and Energetic Forces," in: *Fundamentals of Deformation and Fracture (J.D. Eshelby Memorial Volume)*, Miller, K. J., et al., eds., Cambridge Univ. Press, in press.

Rice, J. R., and Thomson, R., 1974, "Ductile Versus Brittle Behavior of Crystals," *Philosophical Magazine*, Vol. 29, pp. 73-97.

Sih, G. C., and Liebowitz, H., 1968, "Mathematical Theories of Brittle Fracture," *Fracture, An Advanced Treatise: Vol. 2, Mathematical Fundamentals*, Liebowitz, H., ed., Academic Press, New York, pp. 67-190.

Stroh, A. N., 1958, "Dislocations and Cracks in Anisotropic Elasticity," *Philosophical Magazine*, Vol. 3, pp. 625-646.

Tada, H., Paris, P. C., and Irwin, G. R., 1973, *The Stress Analysis of Cracks Handbook*, Del Research Corp., Hellertown, Pa.

Tse, S. T., Dmowska, R., and Rice, J. R., 1984, "Stressing of Locked Zones Along a Creeping Fault," *Bulletin of the Seismological Society of America*, in press.

Uflyand, Y. S., 1965, *Survey of Articles on the Application of Integral Transforms to the Theory of Elasticity*, North Carolina State University, Department of Applied Mathematics Research Group, File No. PSR-24/6.

Vanmarcke, E. H., 1977, "Reliability of Earth Slopes," *Proceedings of ASCE, Journal of the Geotechnical Engineering Division*, Vol. 103, pp. 1247-1265.

Downloaded 02 May 2010 to 171.66.16.54. Redistribution subject to ASME license or copyright; see http://www.asme.org/terms/Terms_Use.cfm

Dynamic Fracture of an Idealized Fiber-Reinforced Cantilever

L. F. Mannion
Department of Mathematics and Computer Science, St. John's University, Jamaica, N.Y. 11439

The dynamic fracture of a double cantilever beam of fiber-reinforced material is discussed. The material is modeled by assuming that the fibers are inextensible and continuously distributed. The examples considered reduce to the solution of the wave equation on a time-dependent interval; the method of characteristics is used. Two fracture criteria are used to calculate the crack speed. One of these criteria is the energy release rate commonly used in elastic fracture mechanics. In the present model some fibers can carry a finite force; the second criterion is based on the force in the fiber through the crack tip. Three simple examples are given to illustrate the model.

1 Introduction

This paper concerns the propagation of a straight crack in a double cantilever beam of fiber-reinforced material. The model is based on the assumptions that the fibers are inextensible and continuously distributed; it was introduced by Mulhern, Rogers, and Spencer [1] to analyze rigid-plastic deformation of fiber-reinforced cylinders but it has been developed mainly in the context of elastic problems.

We consider plane problems with small deformations. The material is composed of two orthogonal families of straight, parallel fibers embedded in a weaker matrix. The axes of a system of Cartesian coordinates x, y are chosen to coincide with the fiber directions. If u and v are the displacement components parallel to these axes, the inextensibility constraints imply that

$$u=u(y,t), \quad v=v(x,t). \tag{1}$$

The shearing response is assumed to be linearly elastic, so that the shear stress σ_{xy} is

$$\sigma_{xy}=\mu(u_{,y}+v_{,x}), \tag{2}$$

where μ is the shear modulus. (Here and in what follows, a comma followed by a subscript denotes a partial derivative.)

The normal stresses σ_{xx} and σ_{yy} cannot be obtained from stress-strain equations since they are reactions to the inextensibility constraints. For example, for displacement in the y-direction the momentum equation is

$$\sigma_{xy,x}+\sigma_{yy,y}=\rho v_{,tt}, \tag{3}$$

where ρ is the density of the material. The stress σ_{yy} cannot be eliminated from (3) before the deformation is known; the equation of motion for v must be found by applying momentum balance directly to the beam.

The presence of constraints also affects the choice of boundary conditions. For example, displacements cannot be independently specified at more than one point on any fiber. In a body with no moving cracks the solution of a displacement boundary-value problem may be found by using the kinematic constraints, with the stresses being calculated subsequently from equations such as (2) and (3). In problems involving prescribed surface tractions, the boundary conditions appear directly in the equations of motion; this is described in [2].

The solution of a boundary-value problem in this model usually contains one or more fibers across which σ_{xy} is discontinuous; this arises since the deformation is so restricted by the kinematic constraints. These fibers are called singular fibers and they carry a finite force to balance the jump in the shearing stress.

The occurrence of singular fibers has been explained through comparison with more accurate models. Everstine and Pipkin [3] examined some solutions of corresponding problems in the idealized theory and in anisotropic elasticity. In the elastic solutions, for the limiting case of small extensibility in the preferred directions, thin layers of high normal stress appear at the locations of singular fibers in the idealized solutions. In addition to prediction of the location of these stress concentration layers, the force in a singular fiber predicts the level of stress in the corresponding layer. The correspondence holds in particular for singular fibers through crack tips [4]. These results are collected in the review by Pipkin [5]. While [3]–[5] concern static equilibrium, the same correspondence should hold in dynamic problems; this provides the motivation for the present work.

In the following sections, the model is applied to the dynamic fracture of a double cantilever beam, described in Section 2. The examples involve only one nonzero displacement component; the equation of motion is derived in Section 3. Since the equation must be solved on an interval that is unknown in advance, it is cast in characteristic form in Section 4.

Contributed by the Applied Mechanics Division and presented at the 1985 Joint ASME/ASCE Applied Mechanics, Fluids Engineering, and Bioengineering Conference, Albuquerque, N. Mex., June 24-26, 1985 of THE AMERICAN SOCIETY OF MECHANICAL ENGINEERS.

Discussion on this paper should be addressed to the Editorial Department, ASME, United Engineering Center, 345 East 47th Street, New York, N.Y. 10017, and will be accepted until two months after final publication of the paper in the JOURNAL OF APPLIED MECHANICS. Manuscript received by ASME Applied Mechanics Division, August, 1983; final revision, June, 1984. Paper No. 85-APM-35.

Copyright © 1985 by ASME
Downloaded 02 May 2010 to 171.66.16.54. Redistribution subject to ASME license or copyright; see http://www.asme.org/terms/Terms_Use.cfm

To complete the setting of a problem in fracture mechanics, a fracture criterion must be specified. The criterion most commonly used involves energy flux into the crack tip during crack propagation. In the idealized theory, a plausible criterion is that fracture continues while the force in the singular fiber at the crack tip remains at a critical level. In an experimental study based on this model, Sun, Kolsky, and Pipkin [6] found that the force criterion gave better qualitative predictions than the energy criterion. Both criteria are formulated in Section 5.

Solutions with constant crack speed are discussed in Section 6. The changes in crack speed due to point forces on the edge of the beam are discussed in Section 7, while Section 8 concerns changes in speed due to a step in the height of the beam. The results are discussed in Section 9. Two equations involved in the fracture criteria are derived in the Appendix.

2 Beam Geometry

A beam of length L and height $2h$ contains a crack of length $l(t)$ along its center line. The origin of the coordinate system is symmetrically placed at the left end of the beam so that the crack advances along the positive x-axis (Fig. 1). The beam has straight sides except possibly for a discontinuity in height at $x = a$. The beam is clamped at $x = L$ and the beam arms are given equal and opposite displacements at $x = 0$; symmetry allows us to concentrate on the upper half of the beam.

Since the end $x = L$ is fixed, inextensibility implies that u and v vanish ahead of the crack tip. In this paper, only cases in which the crack remains straight are considered; the only nonzero displacement is therefore $v(x, t)$ in $0 < x < l(t)$.

3 Momentum Balance

The equation governing $v(x, t)$ must be derived by using momentum balance. Consider momentum balance for the part of the beam in $(x, x + \Delta x)$, with $0 < x < l(t)$; assuming that the edge $y = h$ is traction free, the tractions acting on this material are the shear stresses on the vertical faces. The resultant of these tractions is found by using (2) with $u = 0$ and integrating from $y = 0$ to $y = h$. Equating rate of momentum change with resultant force yields

$$\rho h\int_x^{x+\Delta x} v_{,tt}(\xi,t)\,d\xi = \mu h[v_{,x}(x+\Delta x,t) - v_{,x}(x,t)]. \tag{4}$$

Dividing by $\mu h\Delta x$ and letting $\Delta x \to 0$, we obtain the wave equation:

$$v_{,xx} - (1/c^2)v_{,tt} = 0, \quad 0 < x < l(t). \tag{5}$$

In (5), $c = (\mu/\rho)^{1/2}$ is the speed of shear waves. At the crack tip,

$$v(l(t),t) = 0. \tag{6}$$

The boundary condition for v at $x = 0$ will be specified in Section 7; the initial conditions are

$$v(x,0) = v_{,t}(x,0) = 0, \quad 0 < x < L. \tag{7}$$

Equation (5) must be supplemented by jump conditions in two cases. If the beam height is discontinuous at $x = a$ as shown in Fig. 1, the condition is

$$h_1 v_{,x}(a+,t) = h v_{,x}(a-,t). \tag{8}$$

If the beam height is continuous but a point force of magnitude $P(t)$ in the y-direction is applied at (a, h), an additional term appears in (4) which leads to the jump condition

$$\mu h[v_{,x}(a+,t) - v_{,x}(a-,t)] = -P(t). \tag{9}$$

4 Characteristics

We will use the method of characteristics to solve (5). Using the notation

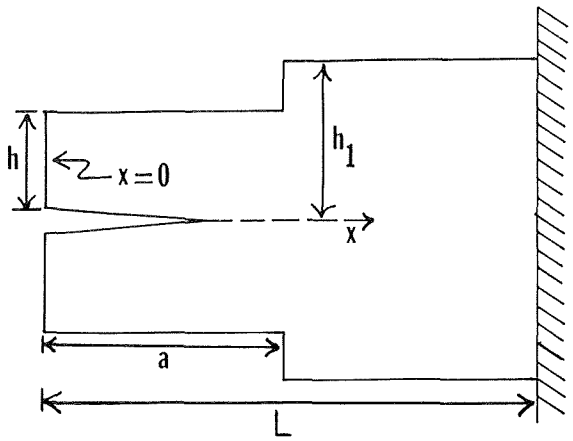

Fig. 1 Double cantilever beam

$$q(x,t) = v_{,x}(x,t), \quad s(x,t) = v_{,t}(x,t). \tag{10}$$

equation (5) is replaced by the system

$$c^2 q_{,x} - s_{,t} = 0, \tag{11}$$

$$q_{,t} - s_{,x} = 0. \tag{12}$$

Combining (11) and (12) we find

$$\frac{d}{dt}(cq - s) = 0 \quad \text{on} \quad \frac{dx}{dt} = c, \tag{13}$$

$$\frac{d}{dt}(cq + s) = 0 \quad \text{on} \quad \frac{dx}{dt} = -c. \tag{14}$$

When (6) is differentiated with respect to t, in the present notation we find

$$s(l(t),t) = -q(l(t),t)\dot{l}(t), \tag{15}$$

so that, at $x = l(t)$,

$$cq - s = (c + \dot{l})q, \quad cq + s = (c - \dot{l})q. \tag{16}$$

(A superimposed dot denotes a time-derivative.)

5 Fracture Criteria

The equation of motion and the boundary conditions are not sufficient to calculate the crack speed. The conditions under which a crack will begin and continue to move involve an assumption about the material; this assumption takes the form of a fracture criterion, which specifies the manner in which the crack motion is coupled with the deformation. Two such criteria are described in this section.

The first criterion is based on the energy release rate which is commonly used in elastic fracture mechanics. According to this criterion, a crack will continue to move while the energy release rate remains at a critical level. The energy release rate $\mathcal{G}$ may be calculated using the general expression in equation (13) of Freund [7]; in the present case we find that

$$\mathcal{G} = \mu h(1 - \dot{l}^2/c^2)[q(l,t)]^2; \tag{17}$$

this expression for $\mathcal{G}$ is also derived in the Appendix. In (17), $\mathcal{G}$ is the energy released in unit crack extension. If the critical value of $\mathcal{G}$ is denoted by $\mathcal{G}_c$, crack motion occurs as long as

$$\mathcal{G} = \mathcal{G}_c. \tag{18}$$

Combining (17) and (18), the condition for propagation may be written as

$$c^2\mathcal{G}_c/\mu h = (c^2 - \dot{l}^2)[q(l,t)]^2. \tag{19}$$

The second criterion is based on the force at the crack tip in the singular fiber $x = l(t)$; this fiber is singular because $v_{,x} = 0$ at $x = l(t)+$, while $v_{,x} \neq 0$ at $x = l(t)-$. Under this criterion, crack motion occurs while this force is maintained

Downloaded 02 May 2010 to 171.66.16.54. Redistribution subject to ASME license or copyright; see http://www.asme.org/terms/Terms_Use.cfm

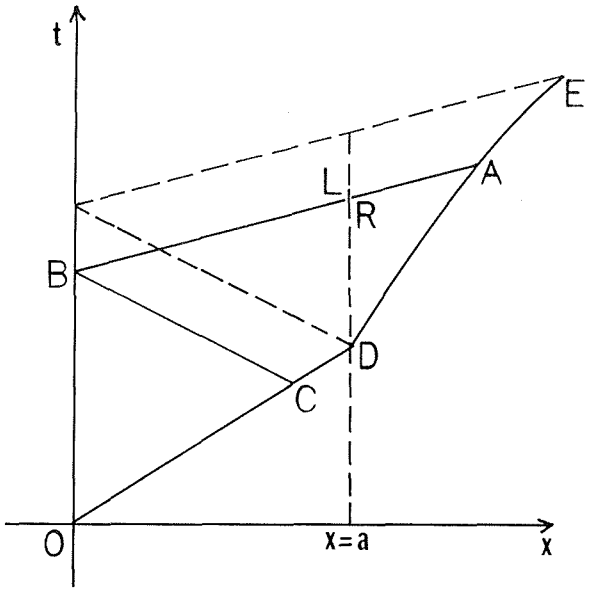

Fig. 2 Change in crack speed due to boundary discontinuities

at a critical level. The fiber force at the tip is given in this case by $G(t)$, where

$$G(t) = -\mu h(1-\dot{l}^2/c^2)q(l,t). \tag{20}$$

Equation (20) for $G(t)$ is derived in [2]; for completeness, a derivation is also given in the Appendix. If the level of force required for crack advance is G_c, (20) gives the propagation condition

$$c^2 G_c/\mu h = (\dot{l}^2 - c^2)q(l,t). \tag{21}$$

6 Constant Speed Cracks

In this section, the fracture criteria of Section 5 are used to find the crack speed when a crack starts to run from the end of the beam at $x = 0$. The ends of the beam are moved apart at a constant speed v_0, so that

$$v(0,t) = v_0 t. \tag{22}$$

The displacement

$$v(x,t) = v_0(t - x/U_0) \tag{23}$$

satisfies (5) and (22) for any constant U_0; it corresponds to a crack moving wth speed U_0 since $v(U_0 t, t) = 0$.

The value of U_0 is determined by a fracture criterion. The fracture conditions (19) and (21) use the slope at the crack tip; from (23),

$$q(U_0 t, t) = -v_0/U_0. \tag{24}$$

With the force criterion, the value of q from (24) is used in (21). We find a quadratic equation for U_0; the positive root is

$$U_0 = (c^2 G_c/2\mu v_0 h)[\{1 + (2\mu v_0 h/cG_c)^2\}^{1/2} - 1]. \tag{25}$$

For cracking under the energy criterion, (23) and (24) may be used on replacing U_0 by a different constant V_0. The propagation condition (19) gives

$$c^2 \mathcal{G}_c/\mu h = (c^2 - V_0^2)(v_0^2/V_0^2). \tag{26}$$

Solving (26) gives the speed V_0 as

$$V_0 = c(1 + c^2 \mathcal{G}_c/\mu v_0^2 h)^{-1/2}. \tag{27}$$

7 Change in Crack Speed Due to Applied Point Forces

This section concerns the change in crack speed that occurs when the tip crosses a fiber at the ends of which point forces are applied. A point force $P(t)$ in the y-direction is applied at (a, h), while an equal and opposite force is applied at $(a, -h)$; the beam height is continuous at $x = a$. We note that the time at which these forces are applied does not affect the motion, provided that they are applied while $l(t) < a$; this follows from fiber inextensibility.

The boundary condition (22) holds and the crack begins to run from $x = 0$. The applied forces have no effect on the constant speed solutions of Section 6 until $l(t) = a$. Therefore, under the tip force and energy criteria the crack speed is given, respectively, by (25) for $t < U_0/a$ and by (27) for $t < V_0/a$.

Figure 2 is used to find the change in crack speed. The portion OD of the tip path in the $x-t$ plane represents the constant speed solution. The next phase of the motion corresponds to DE; at the time t_E the first shear wave generated by the point force overtakes the tip after reflection at $x = 0$. The paths AB and BC are arbitrary characteristics for this part of the motion. Separate points L and R are necessary on AB to allow for the limiting values of the discontinuous beam slope at $x = a$.

We now find the speed along DE. Equations (13) and (14) hold on parts of characteristics that do not cross $x = a$. Applying (13) on AR and BL and using $(16)_1$ at A, we have

$$(cq - s)_R = (c + \dot{l}_A)q_A, \tag{28}$$

$$(cq - s)_L = cq_B - v_0. \tag{29}$$

We use (9) and the continuity condition

$$s_R = s_L \tag{30}$$

to combine (28) and (29). This gives

$$(c + \dot{l}_A)q_A = cq_B - v_0 - (c/\mu h)P(t_R). \tag{31}$$

Using (14) on BC yields

$$cq_B = (c - \dot{l}_C)q_C - v_0. \tag{32}$$

When (32) is used to eliminate q_B from (31) we get

$$(c + \dot{l}_A)q_A = (c - \dot{l}_C)q_C - 2v_0 - (c/\mu h)P(t_R). \tag{33}$$

With the force criterion $\dot{l}_C = U_0$ and $q_C = -v_0/U_0$ so that (33) gives

$$(c + \dot{l}_A)q_A = -v_0(1 + c/U_0) - (c/\mu h)P(t_R). \tag{34}$$

Substituting for q_A in (34) from (21) and solving for $\dot{l}_A$, we have

$$\dot{l}_A = c - (c^2 G_c/\mu h)[v_0(1 + c/U_0) + (c/\mu h)P(t_R)]^{-1}. \tag{35}$$

Equation (35) holds on DE as long as it yields a positive speed.

We consider the cases in which

$$P(t) = \pm P_0, P_0 > 0; \tag{36}$$

these forces are applied when $t = 0$. Taking the positive sign in (36), equation (35) gives a new constant crack speed U_1 on DE, where

$$U_1 = c - (c^2 G_c/\mu h)[v_0(1 + c/U_0) + (c/\mu h)P_0]^{-1}. \tag{37}$$

The change in crack speed is given by

$$U_1 - U_0 = (c - U_0)[1 + (\mu v_0 h/P_0 U_0)(1 + U_0/c)]^{-1}. \tag{38}$$

Since $U_0 < c$ we have $U_1 > U_0$, i.e., a tensile force increases the crack speed.

When the force is compressive, corresponding to the negative sign in (36), the new speed is given by

$$U_2 = c - (c^2 G_c/\mu h)[v_0(1 + c/U_0) - (c/\mu h)P_0]^{-1}. \tag{39}$$

The expression in (39) for U_2 may be used to examine the possibility that a sufficiently large compressive force will stop the crack. Crack motion beyond $x = a$ requires that U_2 be positive. From (39) we find that

$$U_2 > 0 \Longleftrightarrow P_0 < [(1 - U_0/c)^{-1} - 1]G_c. \tag{40}$$

If (40) does not hold, (39) does not apply; however, (40) may be interpreted to give the force required for crack arrest as P_0^* where

Downloaded 02 May 2010 to 171.66.16.54. Redistribution subject to ASME license or copyright; see http://www.asme.org/terms/Terms_Use.cfm

$$P_0^* = [(1 - U_0/c)^{-1} - 1]G_c. \quad (41)$$

The changes in crack speed under the energy criterion may be treated in the same way. The starting point is (34) with U_0 replaced by V_0; we retain (36) for $P(t)$. Squaring both sides of (34) and eliminating q_A^2 using the fracture condition (19) gives

$$c^2 \mathcal{G}_c/\mu h = [v_0(1 + c/V_0) \pm (cP_0/\mu h)]^2 (c - \dot{l}_A)(c + \dot{l}_A)^{-1}. \quad (42)$$

Equation (42) yields a new constant speed V_1, where

$$V_1 = c(\mu h K^2 - c^2 \mathcal{G}_c)/(\mu h K^2 + c^2 \mathcal{G}_c). \quad (43)$$

In (43),

$$K = v_0(1 + c/V_0) \pm cP_0/\mu h; \quad (44)$$

the signs in (42) and (44) correspond to those in (36).

From (43) and (44) the condition for V_1 to be positive is

$$v_0(1 + c/V_0) \pm cP_0/\mu h > c(\mathcal{G}_c/\mu h)^{1/2}. \quad (45)$$

From (26),

$$(\mathcal{G}_c/\mu h)^{1/2} < (v_0/V_0)(1 + V_0/c). \quad (46)$$

Choosing the positive sign in (45) and using (46), (45) reduces to $P_0 > 0$, given in (36). This means that the crack continues to move past any tensile force.

Using the negative sign in (45) and rejecting negative crack speeds, the compressive force for crack arrest in this case is found to be

$$P_0^{**} = (\mu h/c)[v_0(1 + c/V_0) - c(\mathcal{G}_c/\mu h)^{1/2}]. \quad (47)$$

We have examined the crack speed only on the portion DE of its path. In cases where the crack is arrested by the point force, we have only shown that it remains at rest until t_E—the time of arrival at $x = a$ of the first shear wave generated by the crack arrest at D and reflected from $x = 0$. However, the method of characteristics may be used to calculate the motion during any number of such reflections; similar remarks also apply to the next section.

8 Change in Crack Speed due to Discontinuous Beam Height

This section concerns the case where the beam height is discontinuous, as described in Fig. 1. As in the previous section, until the tip crosses $x = a$ the motion is a constant speed solution from Section 6; the initial speed is U_0 or V_0, depending on the fracture criterion. Figure 2 is also used in this case.

If the crack passes $x = a$ the jump condition (8) applies; in the notation of Fig. 2,

$$h\, q_L = h_1 q_R. \quad (48)$$

Using (13) on BL and (30), (48) at $x = a$ gives

$$c(h_1/h) q_R - s_R = c q_B - v_0. \quad (49)$$

We seek solutions with constant crack speed on DE.

Under the energy criterion $q_B = -v_0/V_0$, so that (49) gives

$$c(h_1/h) q_R - s_R = -v_0(1 + c/V_0). \quad (50)$$

Applying (13) on AR gives

$$(cq - s)_R = (c + V_2) q_A, \quad (51)$$

where V_2 is the new crack speed. A constant crack speed is accompanied by a constant slope on $(a, l(t))$; using $q_A = q_R$ in (51) gives

$$s_R = -V_2 q_A, \quad (52)$$

while (50) and (52) together give

$$(V_2 + cr) q_A = -v_0(1 + c/V_0), \quad (53)$$

where $r = h_1/h$.

For crack propagation through the new height h_1, replace h by h_1 in (19); the resulting equation is used to substitute for q_A^2 after squaring both sides in (53). We obtain

$$v_0^2(1 + c/V_0)^2 = (c^2 \mathcal{G}_c/\mu h_1)(V_2 + cr)^2 (c^2 - V_2^2)^{-1}. \quad (54)$$

Equation (26) yields

$$v_0^2(1 + c/V_0)^2 = (c^2 \mathcal{G}_c/\mu h)(c + V_0)(c - V_0)^{-1}. \quad (55)$$

Combining the last two equations gives

$$(V_2 + cr)^2 (c^2 - V_2^2)^{-1} = k^{-1}, \quad (56)$$

where

$$k = h(c - V_0)/h_1(c + V_0). \quad (57)$$

From (56) we obtain a quadratic for V_2:

$$(1 + k) V_2^2 + (2kcr) V_2 - c^2(1 - kr^2) = 0. \quad (58)$$

A real positive root of (58) exists only if $1 - kr^2 > 0$; by (57) this is equivalent to

$$h_1 < (c + V_0)h/(c - V_0). \quad (59)$$

The condition (59) is that required for crack motion beyond the step in the height of the beam.

To find the new speed under the force criterion, we return to (53); if U_3 is the new crack speed and V_0 is replaced by U_0, (53) gives

$$(U_3 + cr) q_A = -v_0(1 + c/U_0). \quad (60)$$

In the fracture condition (21), h is replaced by h_1; the result is used to eliminate q_A from (60). We find the following quadratic for U_3 after combining (21) and (24):

$$U_3^2 + [(c - U_0)/r] U_3 - cU_0 = 0. \quad (61)$$

In (61) a real, positive solution for U_3 exists for all values of r; according to this criterion the crack continues to move regardless of the change in thickness.

9 Conclusions

We have discussed a highly simplified model for dynamic fracture of a fiber-reinforced beam. The idealized theory may be regarded as an asymptotic approximation to anisotropic elasticity; it may be expected to provide the main features of anisotropic solutions (including conditions for crack arrest) without all the analytical difficulties. The model also suggests that the energy release rate criterion may not always be the most appropriate criterion for highly anisotropic materials; this is borne out by the experimental results in [6].

A limitation of the model in the present case is that it cannot account for any bending of the cracked beam; bending would absorb part of the energy supplied by the boundary conditions and this would affect the crack speed. The approach taken here may be contrasted with that in [8], where Timoshenko beam theory is used.

References

1 Mulhern, J. F., Rogers, T. G., and Spencer, A. J. M., "A Continuum Model for Fiber-Reinforced Plastic Materials," *Proceedings of the Royal Society of London*, Series A, Vol. 301, 1967, pp. 473-492.

2 Mannion, L. F., and Pipkin, A. C., "Dynamic Fracture of Idealized Fiber-Reinforced Materials," *Journal of Elasticity*, Vol. 13, 1983, pp. 395-409.

3 Everstine, G. C., and Pipkin, A. C., "Boundary Layers in Fiber-Reinforced Materials," ASME Journal of Applied Mechanics, Vol. 40, 1973, pp. 518-522.

4 Sanchez, V. M., and Pipkin, A. C., "Crack-Tip Analysis for Elastic Materials Reinforced With Strong Fibers," *Quarterly Journal of Mechanics and Applied Mathematics*, Vol. 31, 1978, pp. 349-362.

5 Pipkin, A. C., "Stress Analysis for Fiber-Reinforced Materials," *Advances in Applied Mechanics*, Vol. 19, Academic Press, 1979, pp. 1-51.

6 Sun, G., Kolsky, H., and Pipkin, A. C., "An Experimental and Theoretical Study of Crack Propagation in Crossply Fiber Composites," *Engineering Fracture Mechanics*, Vol. 17, 1983, pp. 349-360.

7 Freund, L. B., "Energy Flux Into the Tip of an Extending Crack in an Elastic Solid," *Journal of Elasticity*, Vol. 2, 1972, pp. 341-349.

Downloaded 02 May 2010 to 171.66.16.54. Redistribution subject to ASME license or copyright; see http://www.asme.org/terms/Terms_Use.cfm

8 Williams, J. H., Lee, S. S., and Kousiounelos, P. N., "Dynamic Crack Propagation and Arrest in Orthotropic DCB Fiber Composite Specimens," *Engineering Fracture Mechanics*, Vol. 14, 1981, pp. 427-438.
9 Freund, L. B., "A One-Dimensional Crack Propagation Model," in *Fracture Mechanics*, SIAM-AMS Proceedings, Vol. XII, American Mathematical Society, Providence, R.I., 1979, pp. 21-37.

APPENDIX

In this Appendix the expressions (17) for the energy release rate and (20) for the fiber force $G(t)$ are derived. We begin by deriving (17).

While the deformation of one arm of the beam is discussed in the body of the paper, both halves of the beam must be included in the energy balance. Letting T and W be the kinetic and strain energies of the whole beam, respectively, we can write

$$T=\rho h\int_0^{l(t)} s^2(x,t)\,dx, \qquad W=\mu h\int_0^{l(t)} q^2(x,t)\,dx. \tag{62}$$

Denote by P the rate of work done by the external tractions on both arms at $x = 0$; then

$$P=-2\mu hq(0,t)s(0,t). \tag{63}$$

Let $\mathfrak{F}$ be the energy flux into the crack tip during crack propagation; energy balance gives

$$P=\dot{T}+\dot{W}+\mathfrak{F}. \tag{64}$$

Since $\mathfrak{F}$ is the time rate of energy flow and $\mathcal{G}$ is energy released per unit crack extension, we have

$$\mathfrak{F}=\mathcal{G}\dot{l}. \tag{65}$$

Differentiation of the integrals in (62) gives

$$\dot{T}+\dot{W}=h\dot{l}[\mu q^2(l(t),t)+\rho s^2(l(t),t)] + 2h\int_0^{l(t)} (\mu qq_{,t}+\rho ss_{,t})\,dx. \tag{66}$$

Using (15) in the first term and (11), (12) in the integrand, (66) may be written as

$$\dot{T}+\dot{W}=\mu h\dot{l}(1+\dot{l}^2/c^2)q^2(l(t),t) + 2\mu h\int_0^{l(t)} (qs)_{,x}\,dx. \tag{67}$$

Performing the integration and using (15) again, we find

$$\dot{T}+\dot{W}=\mu h\dot{l}(\dot{l}^2/c^2-1)q^2(l(t),t)-2\mu hq(0,t)s(0,t). \tag{68}$$

Equations (63) and (68) are used to solve for $\mathfrak{F}$ in (64); when the result is compared with (65) it yields equation (17) for $\mathcal{G}$. This derivation of $\mathcal{G}$ is essentially that of Freund [9], in a different context.

Momentum balance is now used to derive (20). In a time interval $(t_1, t_1 + \Delta t)$, with $\dot{l}(t_1) > 0$, the tip fiber in $y > 0$ passes through a material element of approximate area $h\dot{l}(t_1)\,\Delta t$. This material was at rest for $t < t_1$ so the momentum change is given to first order in Δt by $\rho h\dot{l}(t_1)s(l(t_1), t_1 + \Delta t)\,\Delta t$. The external tractions on this material are the shear tractions on the vertical sides at $x = l(t_1)$ and $x = l(t)$; the resultant of the former is $-\mu hq(l(t_1), t)$ and of the latter, the force $G(t)$. Equating rate of momentum change with the resultant tractions gives

$$\rho h\dot{l}(t_1)s(l(t_1),t_1+\Delta t)=-\mu hq(l(t_1),t)+G(t)+o(\Delta t). \tag{69}$$

Letting $\Delta t \to 0$ in (6) and dropping the subscript on t, the expression (20) is found on using (15) to eliminate $s(l(t), t)$.

Downloaded 02 May 2010 to 171.66.16.54. Redistribution subject to ASME license or copyright; see http://www.asme.org/terms/Terms_Use.cfm

Dynamic Fracture Under Normal Impact Loading of the Crack Faces

K.-S. Kim
Assistant Professor,
Department of Theoretical and Applied Mechanics,
University of Illinois at Urbana-Champaign,
Urbana, Ill. 61801
Assoc. Mem. ASME

Results of experiments on crack-face impact are presented. The transient stress-intensity factor variation of a crack has been traced by the Stress-Intensity Factor Tracer (SIFT) [1] under time-stepwise uniform pressure loading of the crack faces. To see the effects of various waves generated by the loading, part of the crack faces was left free of traction within the distance l_0 from the crack tip. The crack-face impact loading was produced by an electromagnetic force induced by a square pulse of an electric current flowing through a copper strip inserted in the saw-cut crack of a Homalite 100 plate specimen. The current flowed in opposite directions in the two portions of the copper strip, between the crack faces, causing them to repel each other. The short-time and the long-time behavior of the transient stress-intensity factor variation under the impact loading have been carefully investigated. Brittle dynamic initiation of crack extension and the stress-intensity variation of a running crack have been also examined. The experimental results have been compared with theoretical predictions based on Freund's crack-face concentrated load solution [2]. The agreement between the theory and the experiment is excellent. In this study, the various waves generated by the loading are shown to play different roles in transmitting the load to the crack tip. In addition, confirmation is given that the SIFT is excellent in tracing the stress-intensity factor regardless of the crack-tip motion.

Introduction

The behavior of a cracked body under dynamic loading has long been of interest to the fracture mechanics community. In brittle fracture the measurement of the stress-intensity factor and the observation of the motion of the crack under dynamic loading have been the major concern. The stress-intensity factor represents the crack-tip loading state and the motion of the crack is the consequence of crack-tip loading, so that the measurement and observation can provide the fracture characteristics of the solid. The characteristics of interest have been the loading rate-dependent fracture initiation toughness, the crack-speed dependent dynamic fracture toughness, the arrest, and branching toughnesses of structural materials. The directional fracture initiation toughness under time-dependent mixed-mode loading is also of recent interest [3]. Evaluating the fracture characteristics requires not only a proper loading device but also accurate and adequate measurement techniques for the variation of the stress-intensity factor. For measurement with a typical laboratory specimen, a relatively long time period for observation (of the order of 10 μsec to a few msec) is necessary and submicrosecond time resolution is also required. For the dynamic fracture experiment, high-speed photography has been widely employed with some classical optical measurement techniques such as photoelasticity or shadowgraphy (or the method of caustics). In conventional measurement techniques, the limited number (10 ~ 100) of frames, the poor time resolution (1 ~ 10 μsec), the high cost of measurement, and the painstaking data reduction procedures have been the major obstacles to further progress in dynamic fracture experiment. However, recently the author developed a new optical method, the Stress-Intensity Factor Tracer (SIFT) [1], which allows the variation in stress-intensity factor to be measured with satisfactory submicrosecond time resolution and with enough long time period for observation. Furthermore, the SIFT is an inexpensive measurement technique that displays the analog signal of the stress-intensity factor (to 4/3 power) directly on the oscilloscope screen regardless of the crack-tip motion. SIFT is as applicable to an opaque material with reflecting surfaces as to a transparent material.

Since Yoffe [4] mathematically determined the stress field around the tip of a steadily moving crack of constant length, considerable progress has been made in the areas of theoretical and numerical stress analysis for dynamic brittle fracture. The uniqueness of the near-tip stress field of a running crack was proved by Freund and Clifton [5]. Thus the study justified the single parameter – stress-intensity factor –

Contributed by the Applied Mechanics Division and presented at the 1985 Joint ASME/ASCE Applied Mechanics, Fluids Engineering, and Bioengineering Conference, Albuquerque, N. Mex., June 24-26, 1985 of THE AMERICAN SOCIETY OF MECHANICAL ENGINEERS.

Discussion on this paper should be addressed to the Editorial Department, ASME, United Engineering Center, 345 East 47th Street, New York, N.Y. 10017, and will be accepted until two months after final publication of the paper itself in the JOURNAL OF APPLIED MECHANICS. Manuscript recieved by ASME Applied Mechanics Division, August, 1984. Paper No. 85-APM-27.

Copyright © 1985 by ASME
Downloaded 02 May 2010 to 171.66.16.54. Redistribution subject to ASME license or copyright; see http://www.asme.org/terms/Terms_Use.cfm

characterization of the near-tip stress state of a crack running in the opening mode with a given speed. Furthermore Freund, in his series of papers [6–9], established the universal analytic methods for evaluation of the transient stress-intensity factor of a crack in a two-dimensional geometric configuration under dynamic loading. One of his major conclusions was that the stress-intensity factor of a half-plane running crack is given by the product of the universal function of crack-tip velocity and the stress-intensity factor for an equivalent stationary crack [8]. He also provided analytic methods for evaluating the stress-intensity factor of the equivalent stationary crack, either by his fundamental solution [2] of point loading on the crack faces or by the dynamic weight function method [10]. For evaluating the stress-intensity factor, many of dynamic loading configurations of a cracked body can be converted into the equivalent problems of crack-face loading with the superposition method. In crack-face loading, the effect of the loading is transferred to the crack tip by various stress waves. The compressive, shear, and Rayleigh waves generated by the loading play different roles in transmitting the load to the crack tip.

In this paper, crack-face impact experiments are used to examine the roles of the various waves on stress-intensity factor variation and the experimental results are compared with theoretical predictions based on Freund's point-load solution [2]. Crack-face impact loading has been made by repelling electromagnetic forces induced by electric current flowing in opposite directions through a folded copper strip that is inserted into the preexisting saw-cut crack of a Homalite 100 specimen. The loading was a time-stepwise uniform pressure applied on part of the crack faces. The rest of the crack faces were left free of traction within the distance of l_0 from the crack tip. Then the transient stress-intensity factor variation was traced by the SIFT. Comparing the time scale with the travel time of the Rayleigh wave for the distance l_0, the long and the short-time variations of the stress-intensity factor after the impact loading was applied have been carefully examined for a stationary crack. The long-time observation reveals that the existence of the small traction-free area of the crack face considerably reduces the transient stress-intensity factor. The short-time observation shows that the impact loading causes the crack initially to close before the Rayleigh wave arrives. Complete closure of an initially open crack has been observed for 2 μsec during an experiment. The dynamic initiation of crack extension and the stress-intensity variation of a running crack up to the point of dynamic crack branching are also examined.

In addition, the SIFT promises to be useful for a number of other applications in which the accurate time tracing of the stress-intensity factor is required. The SIFT gives excellent results in tracing the stress-intensity factor for the stationary and running crack.

Analysis of Stress-Intensity Factor for Crack-Face Impact Loading

(i) Stationary Crack. In a two-dimensional, unbounded elastic medium coordinated by Cartesian x_1, x_2, axes, a stationary semi-infinite crack along the x_1 axis for $x_1 < 0$ is subjected to normal pressure loading, $P(x_1, t)$, on the crack faces from time $t = 0$. Then the problem can be considered as an elastodynamic problem of elastic half-space ($x_2 > 0$) with the boundary conditions,

$$\sigma_{22}(x_1, 0, t) = -P(x_1, t) \quad \text{for} \quad x_1 < 0, \tag{1}$$

$$\sigma_{12}(x_1, 0, t) = 0 \quad \text{for} \quad -\infty < x_1 < \infty, \tag{2}$$

and

$$u_2(x_1, 0, t) = 0 \quad \text{for} \quad x_1 \geq 0 \tag{3}$$

and with the initial conditions,

$$u_\alpha(x_1, x_2, 0) = \dot{u}_\alpha(x_1, x_2, 0) = 0, \quad \alpha = 1,2 \tag{4}$$

where $\sigma_{\alpha\beta}$, u_α, and $\dot{u}_\alpha$ (for α, β = 1 or 2) represent the components of the stress, displacement, and velocity. In this case whenever we are interested in the stress-intensity factor, $K_I(t)$, we can apply the dynamic weight function method [11] with the weight function [10] from the known solution of de Hoop [12] for the case of $P(x_1,t) = H(-x_1)H(t)$, where H indicates the unit step function. However, the stress-intensity factor, $K_I^C(t;l)$, for the concentrated loading of $P(x_1,t) = F\delta(x_1 + l)H(t)$, which was first solved by Freund [2], gives a more explicit expression of the stress-intensity factor for general loading by simple superposition as

$$K_I(t) = \frac{1}{F}\int_0^t \int_0^\infty K_I^C(t-\tau;l)\frac{\partial P(-l,\tau)}{\partial \tau} dl\, d\tau \tag{5}$$

where δ indicates Dirac delta function. The concentrated loading solution, $K_I^C(t;l)$ is given, in a normalized form, as [2]

$$k_I(t/al) \equiv \frac{K_I^C(t;l)}{F}\left(\frac{\pi l}{2}\right)^{1/2}$$

$$= \frac{1}{\pi}\int_1^{t/al} Im\left[\frac{(1-\zeta)^{1/2}}{(t/al-\zeta)^{1/2}S_-(a\zeta)(c/a-\zeta)}\right]d\zeta \tag{6}$$

where $Im[\ ]$ indicates the imaginary part of the function in the bracket,

$$S_\pm(\lambda) = \exp\left\{-\frac{1}{\pi}\int_a^b \tan^{-1}\left[\frac{4z^2\,|(a^2-z^2)^{1/2}|\cdot|(b^2-z^2)^{1/2}|}{(2z^2-b^2)^2}\right]\frac{dz}{z\pm\lambda}\right\}, \tag{7}$$

and a, b, and c represent the slowness of the dilatational (or plate), shear, and Rayleigh (or edge) waves.

Besides the concentrated loading, another simple impact loading on the crack faces is the partial step loading of $P(x_1,t) = P_0\,H(-x_1 - l_0)H(t)$. This loading is used in the experiments described in the next section. This type of time-stepwise uniform pressure loading, leaving the near-tip crack faces of length l_0 traction-free, can be more easily simulated in experiments than can concentrated loading. In addition, the stress-intensity factor variation under the loading can still show the effects of various waves generated from the applied loading. The expression of the pressure distribution and equations (5) and (6) give the stress-intensity factor variation, $K_I^P(t)$, under the pressure loading, in a normalized form, as

$$k_I^P(\eta) \equiv \frac{K_I^P(t)}{P_0}\left\{\frac{\pi}{2l_0}\right\}^{1/2} = \sqrt{\eta}\int_1^\eta \{k_I(\xi)/\xi^{3/2}\}d\xi \tag{8}$$

where $\eta(=t/al_0)$ is a nondimensionalized time. When the integral in equation (6) is evaluated with equation (7) on the complex ζ plane, we can get $k_I(\eta)$ and consequently $k_I^P(\eta)$ from equation (8) in more explicit forms, as in the following, where $p = b/a$, $q = c/a$.

For $\eta \leq 1$,

$$k_I(\eta) = 0 \tag{9}$$

and

$$k_I^P(\eta) = 0. \tag{10}$$

For $1 < \eta \leq p$,

$$k_I(\eta) = \frac{-2}{\pi}\int_1^\eta \frac{(\xi-1)^{1/2}(p^2-1)(q+\xi)(2\xi^2-p^2)^2 S_+(a\xi)\,d\xi}{(\eta-\xi)^{1/2}\{16\xi^4(\xi^2-1)(p^2-\xi^2)+(2\xi^2-p^2)^4\}} \tag{11}$$

and

$$k_I^P(\eta) = \sqrt{\eta}\int_1^\eta \{k_I(\xi)/\xi^{3/2}\}\,d\xi. \tag{12}$$

Downloaded 02 May 2010 to 171.66.16.54. Redistribution subject to ASME license or copyright; see http://www.asme.org/terms/Terms_Use.cfm

Table 1 Properties of Homalite 100 plate

Static Young's modulus (E_s); 4550 MN/m^2
Dynamic Young's modulus (E_d); 4820 MN/m^2
Poisson's ratio (ν); 0.31
Mass density (ρ); 1230 kg/m^3
Plane stress plate wave speed (C_p); 2.082 km/sec
Shear wave speed (C_s); 1.223 km/sec
Plane stress Rayleigh wave speed (C_R); 1.122 km/sec

For $p < \eta \leq q$,

$$k_I(\eta) = 1 - \frac{(q-1)^{1/2}}{(q-\eta)^{1/2} S_-(c)} \tag{13}$$

and

$$k_I^P(\eta) = \{k_I^P(p) + 2\}\sqrt{\eta/p} - 2 + \frac{2\sqrt{q-1}}{qS_-(c)}\{\sqrt{q-\eta} - \sqrt{\eta(q/p-1)}\}. \tag{14}$$

For $q < \eta$,

$$k_I(\eta) = 1 \tag{15}$$

and

$$k_I^P(\eta) = \{k_I^P(q) + 2\}\sqrt{\eta/q} - 2 = 2[\sqrt{\eta}/\{qS_-(0)\} - 1]. \tag{16}$$

***(ii)* Running Crack.** Under the time-stepwise uniform pressure loading on the crack faces, the stress-intensity factor of the stationary crack tip increases monotonically and indefinitely after the arrival of the Rayleigh wave front. However, the material cannot sustain the infinite stress-intensity factor so that at some finite time after the arrival of the Rayleigh wave front, the stress-intensity factor reaches a critical value and the crack begins to extend. For the moving crack, we can apply Freund's conclusion [8] that the stress-intensity factor for mode *I* extension of a half-plane crack is given by the universal function of crack-tip velocity, $k(v)$ [8], times the stress-intensity factor appropriate for a crack of fixed length, equal to the instantaneous length, subjected to the given applied loading. The use of the instantaneous crack length for equation (16), and the application of the universal function $k(v)$, after appropriate nondimensionalization, give the relation

$$k_I^P(\eta) = k(v)\left[\{k_I^P(q) + 2\}\sqrt{\eta/q} - 2\left\{1 + a\int_{\eta_0}^{\eta} v(al_0\xi)d\xi\right\}^{1/2}\right]; \quad \eta > \eta_0 \tag{17}$$

where $\eta_0 (= t_0/al_0)$ is the nondimensionalized initiation time of the crack extension and $v(t)$ is the instantaneous crack propagation speed. The rate of crack extension is often observed as constant in experiments on dynamic fracture of certain polymeric materials, e.g., Homalite, 100, under such crack-face impact loading [14, 15]. Then the term involving the integral in equation (17) is simply $av_0(\eta - \eta_0)$, where v_0 is the constant speed of the crack extension.

The results of the analysis, $k_I(\eta)$ and $k_I^P(\eta)$, for a Homalite 100 plate are presented in Fig. 1. The integrals in equations (11) and (12) are evaluated numerically. The mechanical properties and various wave speeds in plane stress approximation for the plate specimen are given in Table 1. The nondimensionalized stress intensity factor variation, $k_I(\eta)$, under concentrated time-step loading is shown in Fig. 1(*a*). The shape of the function is the same as reported by Freund [2] for a plane strain problem. Figure 1(*b*) shows the nondimensionalized stress intensity factor, $k_I^P(\eta)$, of the time-stepwise uniform partial pressure loading. In this solution the crack faces can interpenetrate. An interesting feature of the analysis is that the stress-intensity factor, $k_I^P(\eta)$, of the pressure loading decreases monotonically from the time the pressure (or plate) wave generated at the loading edge arrives at the crack tip until the Rayleigh (or edge) wave arrives. After the Rayleigh wave arrives, the stress-intensity factor increases monotonically until the crack begins to extend. The initial negative stress-intensity factor is because the surface displacement, on the traction-free surface, made by the time-stepwise uniform pressure loading bulges out and the propagating bulge tends to close the crack when it arrives at the crack tip. This explanation is strictly analogous to the explanation of the negative stress-intensity factor caused by concentrated loading, given by Freund [2] with the surface displacement of Lamb's problem [13]. After the running crack is initiated, the stress-intensity factor variation of the crack running with the constant speed, $v_0/C_R = 0.35$ is shown in Fig. 1(*b*), where C_R is the Rayleigh wave speed. The inertia effect of the running crack and the effect of crack extension away from the loading edge reduce the stress-intensity factor substantially, compared with the stress-intensity factor of the otherwise stationary crack tip. The initial drop, shown by the dashed line, on the initiation of the running crack is caused by the inertia effect. The rest of the slow incremental rate of the stress-intensity factor for the running part is caused by the effect of crack extension because the pressure loading does not follow the extending crack tip.

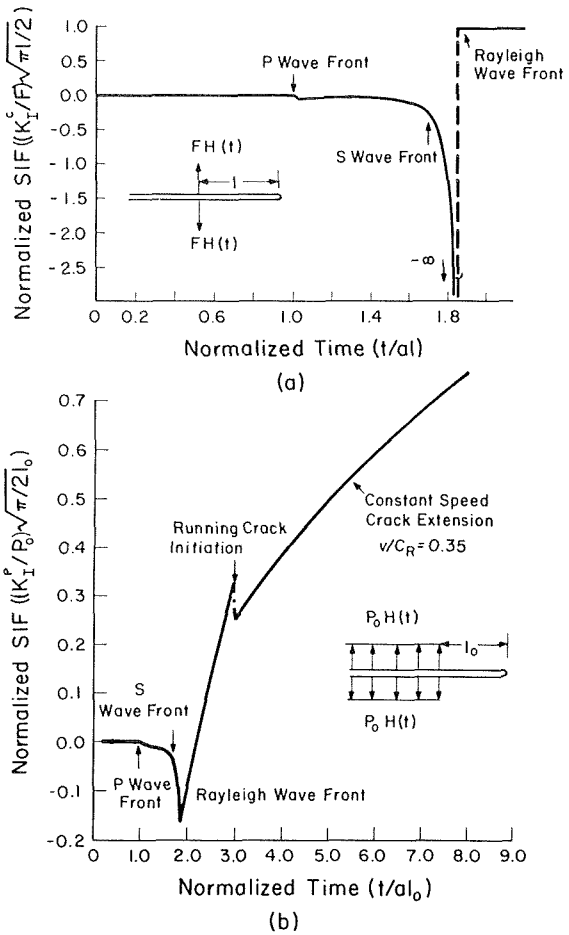

Fig. 1 Theoretical prediction of stress-intensity factor variation caused by (*a*) concentrated and (*b*) uniform partial pressure impact loading on the crack faces

Crack-Face Impact Experiment

Experiments of the time-stepwise uniform pressure crack-face impact were carried out with Homalite 100 plate specimens. The schematic of the experiment is shown in Fig.

Downloaded 02 May 2010 to 171.66.16.54. Redistribution subject to ASME license or copyright; see http://www.asme.org/terms/Terms_Use.cfm

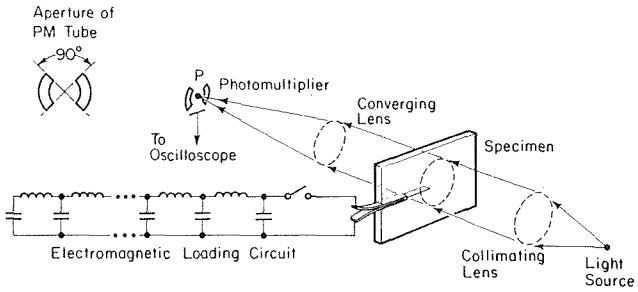

Fig. 2 Schematic of crack-face impact experiment with SIFT system

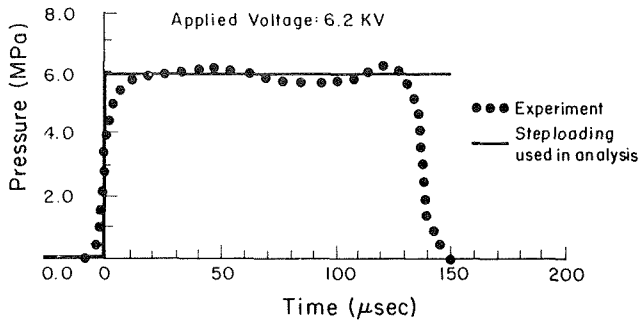

Fig. 3 Time history of pressure level on the crack faces

2. To compare the experimental result with a simple analytic solution for an infinite medium, the variation of the stress-intensity factor was measured within the time interval, approximately 130–140 μsec, after the loading began amd before any reflected waves arrived from the specimen boundaries.

The specimen was 559-mm long, 279-mm wide, and 4.76-mm thick with a single edge notch 1.18-mm thick and 300-mm long. From the notch root a sharp crack of 1–2-mm length was extended by tapping it with a razor blade. Then a 0.48-mm thick, 4.76-mm wide, and 1.2-m long copper strip was folded in half, and the 300-mm length of the folded end of the strip was inserted into the crack and bonded with epoxy to the notch faces. The legs of the folded strip in the notch were separated by an insulating mylar strip, 125-μm thick. The ends of the legs of the strip were then connected to the electrodes of a loading capacitor bank.

The capacitor bank was composed of twelve 20 KV, 25 μF capacitors arranged with 11 inductors, as shown in Fig. 2. The capacitor-inductor circuit was designed to control the time history of the electric current, i.e., to control the pressure pulse shape. The capacitors, charged to the desired voltage level (i.e., for the desired pressure level), were discharged by a thyratron-ignitron firing system to generate a square pulse of 160 μsec duration with a rise time of 20 μsec. The current flux in the copper strip was measured by a toroidal Rogovski coil and integrated by a passive RC integrator to yield the instantaneous current level. The current level was then calibrated to the pressure level applied. The pressure level is proportional to the square of the current level. A recorded typical time history of the pressure level is given in Fig 3. Details of the loading device and the calibration procedure are described by Ravichandar [15].

In the experiments on a stationary crack (tests 83KS1-3), the initial 1–2-mm sharp cracks extending from the notch root were left free of traction. For the rest of the experiments on dynamic crack extension (tests 83KS4-10), the traction-free initial cracks were extended 15–55 mm further by applying a low pressure loading pulse of 0.179 MPa pressure and 160–480 μsec duration. Those initial sharp cracks had nonzero stress-intensity factors because of the crack opening made by the inserted copper strip assemblies. The initial static stress-intensity factors were measured by optical caustics [16] before the main pressure pulse loading was applied.

For the SIFT, the illumination area was a circle with a 75-mm diameter, centered directly ahead of the crack tip. The illumination zone was arranged to include only a few mm length of the initial static sharp crack. A laser beam of a few hundred mW and a 514.5-nm wave length from a 5W argon ion laser was used for the SIFT. The laser beam was expanded by a beam expander and was collimated by a convex lens for the illumination. Because the collimated beam has Guassian distribution of light intensity, an aperture was arranged to pass only the central portion of the beam so that the uniformity of the light intensity in the illumination zone was within ±3–5 percent variation. For tests 83KS1-6, converging beams from the collimating lens were used to give an effective focal length (distance between the specimen and the focal plane) of 2.90–3.00 m. For the rest of the experiments the collimated parallel beams were transmitted through the specimen and the transmitted beam was focused by concave Schlieren mirror with a 150-mm diameter and a focal length of 3 m.

Two different light collecting apertures of the SIFT [1] were used throughout the experiment. The first aperture used in test 83KS1-6 was for the high gain of light intensity from a relatively low-level stress intensity factor. The aperture was made on the annulus with a 1.5-mm inner radius and 3.0-mm outer radius around the focal point. On the focal plane, the two ±15 deg sectors of the annulus along the direction perpendicular to the crack line were masked to block light that might possibly be diffracted by the crack. The aperture used for the rest of the tests had openings on the annulus of 2.5-mm inner radius and 5.0-mm outer radius, masked for the ±45 deg sectors along the perpendicular direction to the crack line as shown in Fig. 2. This aperture was used for the near-tip field measurement of the stress intensity factor although it gave a low gain of light intensity.

The intensity of the light collected through the aperture was measured by either a photomultiplier tube or a high-speed photodiode. Then the signal picked up by the photosensor was monitored by a high-frequency oscilloscope. An RCA photomultiplier was used for most of the tests, except for tests 83KS9 and 83KS10 for which the Spectra Physics model 403B ultra-high-speed photodiode was employed. For tests 83KS1-5, a Tektronix model 564B storage scope was used to record the signal. In the rest of the tests, the signal was recorded on a channel of a digital disk-drive Nicolet memory oscilloscope while the Rogovski coil output of loading pulse current was recorded on another channel of the scope.

The recorded light intensity signal was then converted to stress-intensity factor by the formula [1] $K_I(t) = [I(t)/B]^{3/4}$, where B is the product of several experimental quantities including a shape factor of the light-collecting aperture. In actual experiments the evaluation of the stress-intensity factor from the recorded signal was made in a simpler way. Since the vertical deflection, $V(t)$, of the signal on the oscilloscope screen is assumed to be linear to the light intensity, the stress-intensity factor is proportional to $[V(t) - V_0]^{3/4}$. V_0 is the vertical position of the signal for the zero stress-intensity factor. Then two sets of $[K_I^i, V^i]$, $i = 1, 2$, calibrated before the test can give the proportionality constant and V_0. One set of $[K_I^i, V^i]$ was the initial static stress-intensity factor recorded by the method of optical caustics and the corresponding vertical position of the signal on the scope. The other set could be easily obtained by applying some additional static load to get another static stress intensity and the corresponding vertical deflection. However, in many of the high-pressure loading experiments, V_0 could be obtained directly from the long-time trace of the SIFT signal. Especially when the initial open crack is completely closed before the Rayleigh wave

Downloaded 02 May 2010 to 171.66.16.54. Redistribution subject to ASME license or copyright; see http://www.asme.org/terms/Terms_Use.cfm

Table 2 Summary of crack-face impact experiments

Test no. (83KS-)	Pressure level P_0(MPa)	Traction-free crack-length l_0(mm)	Initial K_I (MPa$\sqrt{m}$)	Laser power (mW)	Photo-detector	Remarks on the SIFT signal and test results
1	0.13 5.85	1.5 & 85.5	0.035 0.20	150	PM tube	Excellent static trace Noise in dynamic trace
2	0.13	2.0	~0.005	150	PM tube	Excellent trace
3	0.13 2.44	1.0 41.5	0.055 ~0.005	150	PM tube	No dynamic trace
4	5.50	57.0	0.084	100	PM tube	Excellent full trace for running crack on Tektronix scope
5	7.49	29.5	–	100	PM tube	No trace due to early triggering
6	5.85	32.5	0.170	100	PM tube	Excellent full trace for running crack on Nicholet scope
7	5.85	28.5	0.092	200	PM tube	Excellent trace on Nicholet scope
8	5.50	42.0	0.140	200	PM tube	PM tube noise 165 μsec after triggering
9	5.85	25.5	–	1500	Photo Diode	Poor trace due to optical misalignment
10	5.50	16.0	–	1500	Photo Diode	Poor trace due to PD saturation

arrives, as observed in test 83KS7, V_0 is automatically determined.

Experimental Results

A summary of the tests is given in Table 2. Tests 83KS1-3 were conducted to observe relatively long-time behavior of the stress-intensity factor of a stationary crack under low-pressure impact. Tests 83KS4-6 were carried out to study the stress-intensity factor variation of a running crack under high-pressure loading. Tests 83KS7 and 83KS8 were designed to investigate the short-time behavior of the stress-intensity factor variation and the dynamic initiation of crack extension. Two additional tests, 83KS9 and 83KS10, were made to see whether as ultra-high-speed photodiode worked better for the SIFT than the photomultiplier.

(i) Stationary Crack. The typical long-time ($\eta >> 1$) behavior of the stress-intensity factor variation of a stationary crack caused by the time-stepwise uniform partial pressure loading is given in Fig. 4 from the result of experiment 83KS2. The insert in the figure shows the oscilloscope trace of the SIFT. In this experiment, approximately 2-mm length of the crack face was left traction-free (i.e., $l_0 = 2$ mm), so that the nondimensionalized unit time corresponded to approximately 1 μsec of real time ($al_0 = 1$ μsec). The applied pressure, P_0, of the loading was 0.13 MPa. The experimental stress-intensity factor variation measured by the SIFT is compared with the analytic result (the dashed line in Fig. 4), of equation (19). Except for the high-frequency noise, theory and experiment show good agreement until the wave reflected from the boundary of the specimen arrives at the crack tip. The first arrival time of the wave reflected from the side boundary of the specimen, parallel to the crack plane, was approximately 130 μsec after the step loading began and is shown as A in Fig 4.

For this low-pressure loading test, the current in the copper strip rang back and forth until the mercury ignition switch disconnected the circuit 480 μsec after the loading began. The ringing current makes pulse loadings of 160 μsec duration three times. Because of the rise time of each current pulse,

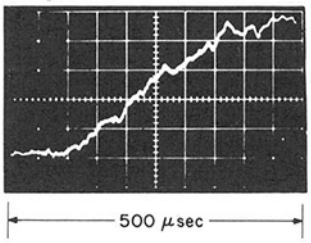

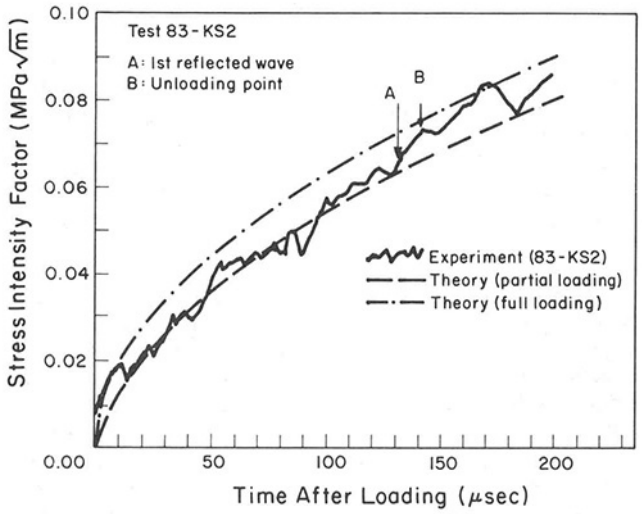

Fig. 4 Long-time behavior of the transient stress-intensity factor variation

unloading dips occurred between the pressure pulses. The first unloading is shown as B on the figure. Besides the unloading dips, many of the reflected waves from the front and back side of the specimen boundary, perpendicular to the crack plane, are also believed to cause fluctuation in the stress-intensity factor after time A. Because this test was for a low-

Downloaded 02 May 2010 to 171.66.16.54. Redistribution subject to ASME license or copyright; see http://www.asme.org/terms/Terms_Use.cfm

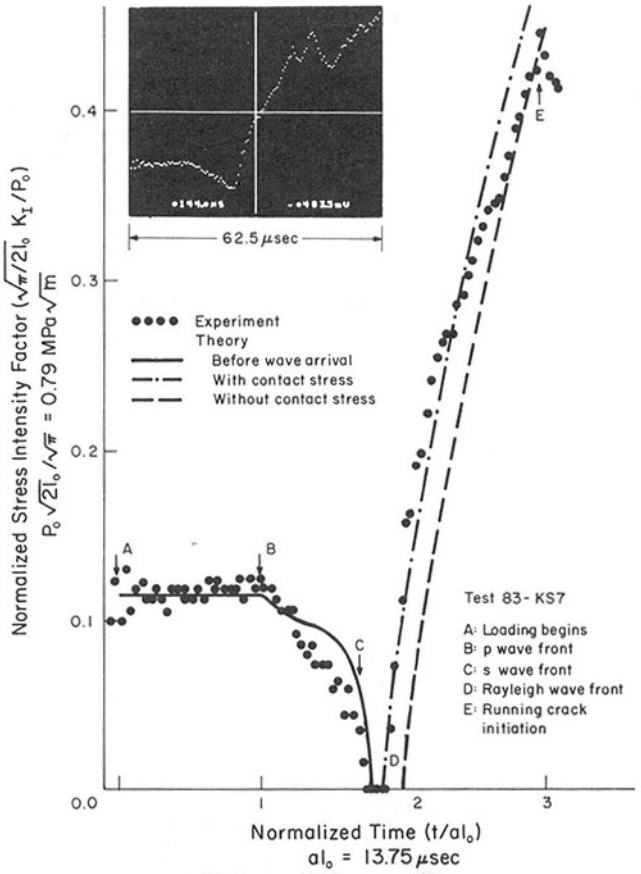

Fig. 5 Short-time behavior of the transient stress-intensity factor variation

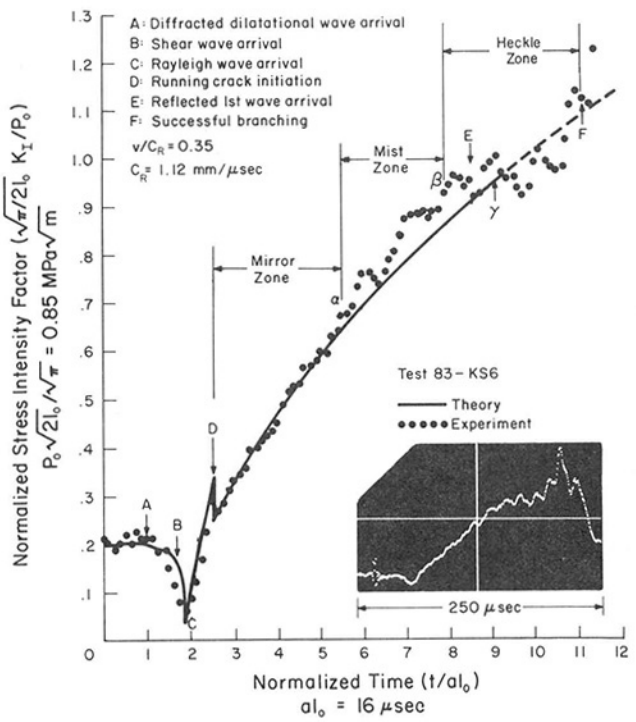

Fig. 6 Stress-intensity factor variation of a running crack tip, including the variation before the initiation of crack extension

level stress-intensity factor, the corresponding light intensity of SIFT was also very low so that high gain of the electronic system was necessary to make an oscilloscope sensitive enough to pick up some high-frequency electric and optical noise. However, many of the relatively big bumps on the oscilloscope were reproducible in the repeated tests.

The solution of de Hoop [12] is also compared with the experimental result. The solution is for a pressure loading applied on the entire crack face without leaving any portion traction-free. The solution of de Hoop is represented by the chained line in Fig. 4. Surprisingly, the small area of traction-free crack faces between the loading edge and the crack tip, a 2-mm gap in this experiment, causes a considerable reduction in the stress-intensity factor for a relatively long transient period.

In a much longer time trace of the SIFT for low-pressure loading, the transient variation of stress-intensity factor, including the variation caused by multiple stress wave reflections from the specimen boundaries, was observed to completely die out 2 msec after the loading began. After the 2-msec interval, a periodic variation of the stress-intensity factor was developed, with an approximate period of 3.5 msec, caused by a vibrational mode of the specimen that was excited by the loading. Damping of the periodic stress-intensity factor variation was also noticed. In addition, the SIFT trace was observed to be reproducible in a series of repeated tests.

Shown in Fig. 5 is a typical short-time ($\eta \sim 1$) stress-intensity factor variation of the crack-face impact experiment. The result is from test 83KS7. For the tests of short-time observation a large aperture, as described in the preceding section, was used to minimize the rise time of the SIFT system. The major contribution in the rise time of the SIFT system is believed to be the development time of the stress field around the crack tip when a stress wave strikes the crack tip. The closer the light collecting area is to the crack tip, the shorter is the development time of the crack-tip stress field. For test 83KS7, the SIFT measured the stress-intensity factor with the deformation field within the distance of 1.6 mm from the crack tip.

The length of the initial traction-free crack, l_0, for the test was 28.5 mm, so that the unit normal time, al_0, was 13.8 μsec. The initial static stress intensity was 0.092 MPa$\sqrt{m}$. The pressure level applied on the crack face was estimated to be 5.85 MPa.

Shown in the insert of the figure is the oscilloscope trace of the SIFT for 62.5 μsec. The time interval between each dot of the picture corresponds to 0.5 μsec. The trace of the SIFT is converted to the stress-intensity factor scale and is compared with the theoretical predictions in the drawing. As shown in the figure, after the loading began at *A*, the stress-intensity factor remains constant before the compressive wave front hits the crack tip at the time shown as *B* on the figure. After the compressive wave front arrives at the crack tip, the stress-intensity factor gradually decreases until the shear wave front arrives. However, comparing the theory and the experiment shows that the experimental value of the stress-intensity factor decreases more steeply than the theoretical one in this time interval. After the shear wave front strikes at *C*, the stress-intensity factor decreases more abruptly. In this test the initial static stress-intensity factor was low so that the crack was completely closed by the compressive and shear waves from the crack opening impact loading. It was closed for 2 μsec until the Rayleigh wave signal reopened the crack at *D*. After the Rayleigh wave arrived, the stress-intensity factor increased until the dynamic crack extension started at *E*. If the crack faces penetrate each other without crack closing contact stress for a mathematical solution, the theoretical prediction should follow the dashed line. On the other hand, if the negative stress-intensity factor of the no-contact stress solution is brought up to zero by simple superposition of constant stress-intensity factor after *D*, the solution would

Downloaded 02 May 2010 to 171.66.16.54. Redistribution subject to ASME license or copyright; see http://www.asme.org/terms/Terms_Use.cfm

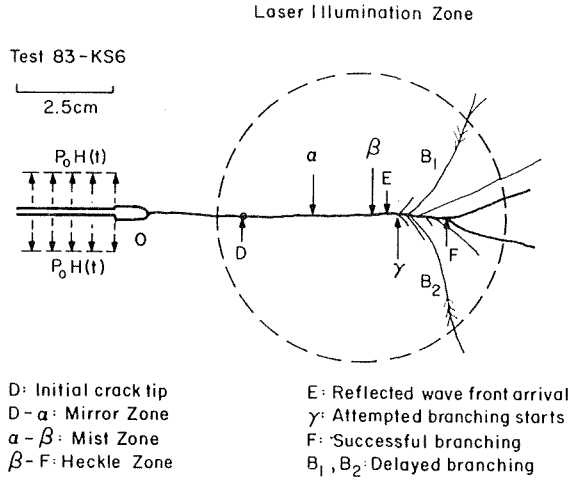

Fig. 7 Crack path in the laser illumination zone

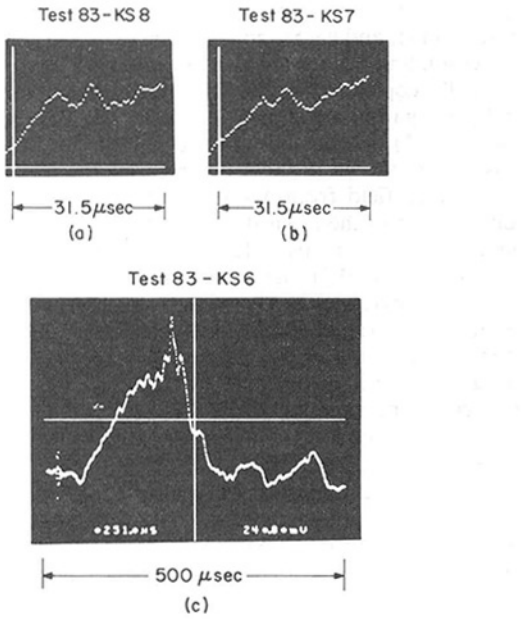

Fig. 8 (*a*) and (*b*): SIFT signal of dynamic initiation of crack extension. (*c*) Long-time trace of SIFT signal.

follow the chained line. However the experimental value makes the transition from the later chained curve to the dashed curve of the former solution in 8–10 μsec. The experimental result shows that the effect of the crack closing contact of 2 μsec lasts 8–10 μsec. After this period the stress-intensity factor varies as if no dynamic crack closure occurred. For a further extension of this study, a theoretical analysis of dynamic crack closure and its influence on the stress-intensity factor variation is suggested.

The stress-intensity factor drops at the dynamic initiation of crack extension at E. In 2–12 μsec after the dynamic crack initiation, a bumpy signal appears on the SIFT trace. This bump is not believed to be caused by actual stress intensity factor variation. Details of dynamic initiation of crack extension and of the bump signal will be discussed later (see Fig. 8(*a*) and (*b*)).

(*ii*) **Running Crack.** In Fig. 6, a typical time trace is shown of the stress-intensity factor for a dynamic crack propagation. The experimental result (test 83KS6) is plotted with dots and compared with the theoretical prediction—the solid line on the figure. The insert in the figure is the oscilloscope trace of the SIFT on a digital Nicolet scope. The dots are plotted on the figure using every fourth data points of the digital oscilloscope signal.

In this figure the stress-intensity factor variation up to $t/al_0 = 2.5$ (or $t = 40$ μsec) is for the stationary crack tip before the dynamic crack extension begins at D. For the experiment, the traction-free crack length, l_0, was 32.5 mm. Therefore, the corresponding nondimensionalized unit time, al_0, is approximately 16 μsec. The stress-intensity factor variation to the onset of dynamic crack extension shows all the effects of the different waves, as discussed earlier. The arrival times of the different wave fronts are shown as A, B, and C.

After the crack extension is initiated, the SIFT signal still shows excellent continuous traces of the stress-intensity factor variation for the running crack. The SIFT signal of the running crack was reduced to stress-intensity factor scale by applying dynamic shape factor [1] in the light-intensity–stress-intensity factor relation. The experimental evaluation of the stress-intensity factor variation was then compared with the theoretical prediction. However, the comparison is only valid until the first reflected wave arrives at the running crack tip from the specimen boundary. This is because the theoretical prediction is for an unbounded medium. The first arrival time of the reflected wave was 136 μsec after the loading began. It is represented by E on the figure.

The speed of the crack tip was estimated as approximately 0.39 mm/μsec by dividing the running distance by the running time. The running distance of the crack tip in the illumination zone was estimated from the postmortem picture of the specimen (see Fig. 7). The distance was approximately 70 mm for the main crack. The running time of the tip for the distance is estimated to be approximately 180 μsec. The running time was obtained from the long-time trace of the SIFT signal (see Fig. 8(*c*)); when the crack tip is running out of the illumination zone, the intensity of the SIFT signal drops. In this estimate, the speed of the crack was assumed to be constant during crack propagation in the illumination zone. The assumption is reasonable because the constant speed of the crack with a large variation of stress-intensity factor was observed in a similar experiment with Homalite 100 [14, 15]. Also, the continuous time trace of the crack speed variation, if necessary, can be obtained using a modified SIFT. This technique was discussed briefly in reference [17]. The theoretical prediction, based on the constant crack speed, agrees very well with the experimental values of the stress-intensity factor variation, as shown in the figure.

The first major fluctuation of the SIFT signal for the running crack, between α and β on the figure, is believed to be caused by a reflected Rayleigh wave. The wave was generated by the dynamic initiation of the crack extension and then partly reflected from the end of the copper strip. The travel time of the Rayleigh wave from the initial crack-tip position to the running crack tip, via the end of the loading strip, matches the time of the signal fluctuation. Further fluctuation of the signal, between β and F on the figure, is considered to be caused by attempted branching and many reflected waves from the specimen boundary. The attempted branching cracks were all partial cracks. These attempted branchings are believed to reduce the intensity of the SIFT signal. However, the detailed analysis of the SIFT for the attempted branching is beyond the scope of this paper.

The crack paths in the light illumination zone of the SIFT system are shown in Fig 7. The initial crack tip was located at D. The path of the main crack is indicated with a thick line and the paths of attempted branching are drawn with thin lines. Although all the attempted branching cracks are partial cracks of the plate, branches B_1 and B_2 become major cracks by reflected waves. Long featherlike fracture surface marking of branches B_1 and B_2 indicates that they were originally

Downloaded 02 May 2010 to 171.66.16.54. Redistribution subject to ASME license or copyright; see http://www.asme.org/terms/Terms_Use.cfm

partial cracks. The fracture surface of the main crack shows mirror, mist, and hackle zones, as indicated in the figure. The corresponding regions are also indicated in Fig. 6.

Oscilloscope traces of the SIFT for dynamic crack initiation and propagation are shown in Fig. 8. The first peaks in Fig. 8(*a*) and (*b*) are the initiation point of dynamic crack extension. As shown in these two figures, the transition of the K_I singular field from a static to a dynamic field causes a sudden drop in the intensity of the SIFT signal. The drop of the acutal stress-intensity factor at this point is greater than the drop of the SIFT signal, because a dynamic shape factor has to be applied for the $I(t) - K_I(t)$ relation after the crack extension is initiated. The second peak that is always observed after the initiation of dynamic crack extension is believed to be caused by the disturbance of the stress field in the finite light-collecting zone [1] of the SIFT system. The disturbance is because of the stress waves generated by the initiation of crack extension.

The dynamic initiation toughness of Homalite 100 was measured as 0.36 and 0.30 MPa$\sqrt{\text{m}}$ in tests 83KS7 and 83KS8. However, test 83KS6 gave the toughness as low as 0.26 MPa$\sqrt{\text{m}}$. It is speculated, with a limited number of observations, that the initial high-static stress intensity seems to reduce the dynamic initiation toughness of polymeric materials.

Figure 8(*c*) shows a long-time trace of the SIFT signal for propagating cracks. The first pulselike signal, apporoximately 200 μsec, is the major signal of the SIFT system. This signal was made by the main crack tip while the crack was running in the region of light illumination. The rest of the small-amplitude signals following the major signal are believed to be caused by attempted branching crack tips that were arrested in the illumination zone. The arrested crack tips were reloaded by traveling stress waves and the reloading produced the signals. As shown in this figure, the simple SIFT system is excellent for running cracks. It gives a *continuous* time trace of stress-intensity factor variation *regardless of the crack-tip motion*. In addition, the signal can be recorded by a modern digital wave-form recorder (or a digital memory scope). Over several thousand data points may be available, and the data can be processed by microcomputer for the final desired stress intensity factor levels.

Concluding Remarks

The SIFT system has been successfully used in studying dynamic fracture caused by normal impact loading on crack faces. The SIFT system provides a fine continuous time trace of stress intensity factor variation. Therefore detailed study of the role of different stress waves, generated by the impact loading, on the development of stress intensity factor variation was possible. The theoretical analysis of the stress intensity factor variation, based on Freund's concentrated time-step loading solution [2], agrees very well with the experimental observations. The study was not only for the effect of loading on a stationary crack but also for dynamic initiation of crack extension and the stress intensity factor variation of a running crack. The agreement between the stress-intensity factor variation of a running crack measured by the SIFT system and the theoretical prediction is excellent. The SIFT is shown here to provide a *continuous* time trace of the stress-intensity factor of a crack tip *regardless of the crack-tip motion*, as long as the crack tip is running in the uniform illumination zone of the SIFT system.

As an extension of this study it should be possible to apply the SIFT system for measuring various dynamic fracture toughnesses of metallic specimens. In this case reflected light form the polished surface of the specimen has to be used for the SIFT system. The SIFT system is expected to be useful particularly for studying dynamic crack initiation, propagation, and arrest with a finite-size laboratory specimen. The SIFT system might also be useful in studying fatigue crack growth for which a fine continuous time trace of stress-intensity factor is required.

Acknowledgment

The author thanks Mr. R. Paff for his assistance in carrying out the experiments, and Professor W. C. Knauss for his support with the NSF Grant, MEA-8215438 during the author's summer visit at Caltech in 1983. The author also thanks Professors R. J. Clifton and L. B. Freund of Brown University for their helpful discussions. This project was supported by the Research Board and the Department of Theoretical and Applied Mechanics, University of Illinois at Urbana-Champaign.

References

1 Kim, K. S., "A Stress Intensity Factor Tracer," ASME JOURNAL OF APPLIED MECHANCIS, accepted for publication, 1984.

2 Freund, L. B., "The Stress Intensity Factor Due to Normal Impact Loading of the Faces of a Crack," *International Journal of Engineering Science*, Vol. 12, 1974, pp. 179–189.

3 Achenbach, J. D., and Kuo, M. K., "Mode III and Mixed Mode I-II Crack Kinking Under Stress-Wave Loading," *International Journal of Solids and Structures*, to be published.

4 Yoffe, E. H., "The Moving Griffith Crack," *Philosophical Magazine*, Vol. 42, 1951, pp. 739–750.

5 Freund, L. B., and Clifton, R. J., "On the Uniqueness of Elastodynamic Solutions for Running Cracks," *Journal of Elasticity*, Vol. 4, 1974, pp. 293–299.

6 Freund, L. B., "Crack Propagation in an Elastic Solid Subjected to General Loading—I. Constant Rate of Extension," *Journal of the Mechanics and Physics of Solids*, Vol. 20, 1972, pp. 129–140.

7 Freund, L. B., "Crack Propagation in an Elastic Solid Subjected to General Loading—II. Nonuniform Rate of Extension," *Journal of the Mechanics and Physics of Solids*, Vol. 20, 1972, pp. 141–152.

8 Freund, L. B., "Crack Propagation in an Elastic Solid Subjected to General Loading—III. Stress Wave Loading," *Journal of the Mechanics and Physics of Solids*, Vol. 21, 1973, pp. 47–61.

9 Freund, L. B., "Crack Propagation in an Elastic Solid Subjected to General Loading—IV. Obliquely Incident Stress Pulse," *Journal of the Mechanics and Physics of Solids*, Vol. 22, 1974, pp. 137–146.

10 Freund, L. B., and Rice, J. R., "On the Determination of Elastodynamic Crack Tip Stress Fields," *International Journal of Solids and Structures*, Vol. 10, 1974, pp. 411–417.

11 Freund, L. B., "The Analysis of Elastodynamic Crack Tip Stress Fields," *Mechanics Today*, Vol. 3, 1976, pp. 55–91.

12 de Hoop, A. T., "Representation Theorems for the Displacement in an Elastic Solid and Their Applications to Elastodynamic Diffraction Theory," Doctoral Dissertation, Technische Hogeschool, Delft, 1958.

13 Lamb, H., Philosophical Transactions, *Royal Society of London*, Series A203, Vol. 1, 1904.

14 Kim, K. S., Dickerson, K. L., and Knauss, W. G., "Viscoelastic Effect on Dynamic Fracture, in Homalite 100," *Workshop on Dynamic Fracture*, California Institute of Technology, Pasadena, 1983, pp. 205–225.

15 Ravi Chandar, K., "An Experimental Investigation into the Mechanics of Dynamic Fracture," Ph.D. Thesis, California Institute of Technology, Pasadena, 1982.

16 Beinert, J., and Kalthoff, J. F., "Experimental Determination of Dynamic Stress Intensity Factors by the Method of Shadow Patterns," Chapter in *Mechanics of Fracture*, Vol. 7, Sih, G. C., ed., 1981.

17 Kim, K. S., and Phillips, J. W., "Focal-Plane Analysis of the Optical Pattern Produced by Mode-I Crack," *Proc. Society of Engineering Science*, Vol. 18, 1981, p. 173.

Downloaded 02 May 2010 to 171.66.16.54. Redistribution subject to ASME license or copyright; see http://www.asme.org/terms/Terms_Use.cfm

L. Seaman
Senior Research Engineer.

D. R. Curran
Department Manager.

W. J. Murri[1]
Physicist.

Poulter Laboratory,
SRI International,
Menlo Park, Calif. 94025

A Continuum Model for Dynamic Tensile Microfracture and Fragmentation

A continuum model for dynamic tensile cleavage fracture and fragmentation has been developed for detailed simulation of brittle fracture processes in elastoplastic materials. The model includes processes for nucleation of microcracks, stress-dependent growth, coalescence and fragmentation, and stress relaxation caused by the developing damage. Fracturing is characterized by a crack density with a distribution of sizes at each material point. The model extends previous work by treating more completely full material separation and stress-free volume growth, as well as multiple loadings, unloadings, and recompaction, and by describing the damage in greater microscopic detail.

Introduction

An improved continuum model for dynamic tensile fracture and fragmentation BFRACT3 has been developed for the detailed simulation and study of brittle fracture processes in elastoplastic materials. "Brittle" fracture is defined here as fracture occurring on the microlevel with a cleavage morphology rather than with a ductile void morphology. Included in the model are a threshold for the initiation of damage, a nucleation process for forming microcracks under tension, growth processes that are dependent on the tensile stress, a coalescence and fragmentation process with the resulting fragment size distribution, and stress relaxation associated with the developing damage. Cracks occur in a range of sizes at nucleation and throughout the calculation. At each material point in the current model, these cracks can have only one orientation. The orientation is fixed by the stress state that exists when the stress first exceeds the initiation criterion at that point. The present study extends previous work at SRI [1-7] by treating full separation in detail, and by describing the damage by a discrete size distribution rather than in the single analytic form used previously.

Many researchers are currently developing similar microfracture models for special applications. Davison, Stevens, and Kipp [8] derived a general approach to such models. Margolin [9] is developing a model for an elastic material with distributions of cracks in arbitrary orientations. He provides for both tensile opening and shear slip on the circular cracks. For his case in which there is no nucleation and growth occurs at a constant velocity, the stress state can be computed explicitly at any time. A similar elastic-brittle model has been derived by Krajcinovic and Fonseka [10] for application to concrete fracture. Grady and coworkers [11, 12] are developing a brittle fracture model that has some micromechanical features. With their model, they have been able to show that the fracture strength is proportional to the one-third power of strain rate (as observed experimentally) and to reproduce the measured change of fragment size with strain rate. It is expected that all the preceding models can represent these two phenomena.

Evans, Ito, and Rosenblatt [13] have given an example of a detailed study of crack formation in ceramic under impact using a combination of analytical and experimental efforts. A similar study was undertaken by Kumano and Goldsmith [15] who also derived a model to represent their findings. Several Russian investigators (see, for example, Dremin and Molodets [14]) are developing microfracture models, but they do not treat the cracks in detail.

Recently, Meyers and Aimone [16] have reviewed fracture models for spalling in metals. The present model BFRACT3 fits into this category because it treats tensile opening (no shear slip) and permits yielding of the matrix material. The nucleation and growth functions are appropriate for high-rate loading and have not been tested on quasistatic problems.

Any computational model must be validated by comparison with experimental data. Unfortunately, the interactions between nucleation, growth, and stress relaxation are generally too complex to permit direct comparison of any of these individual processes with experimental data. However, comparison of the inherently "integrated" experimental data with the model results can be used to guide modifications of the functions or parameters of the individual model processes, and to iterate to a final model that is believable if not demonstrably unique. The processes in the present model have represented, with reasonable fidelity, high-rate fracture processes in beryllium [1, 2], Armco iron [1, 2], polycarbonate [5], oil shale [6], and novaculite quartz [7]. By "represent" we mean that computations with the model are

[1] Now with Hercules, Inc., Magna, Utah 84044.

Contributed by the Applied Mechanics Division for publication in the JOURNAL OF APPLIED MECHANICS.

Discussion on this paper should be addressed to the Editorial Department, ASME, United Engineering Center, 345 East 47th Street, New York, N.Y. 10017, and will be accepted until two months after final publication of the paper itself in the JOURNAL OF APPLIED MECHANICS. Manuscript received by ASME Applied Mechanics Division, April, 1983; final revision, April, 1984.

Copyright © 1985 by ASME
Downloaded 02 May 2010 to 171.66.16.54. Redistribution subject to ASME license or copyright; see http://www.asme.org/terms/Terms_Use.cfm

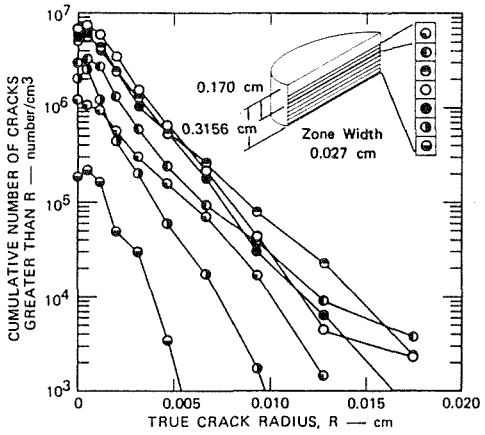

Fig. 1 Crack size distributions in zones near the spall plane in ARMCO iron: Shot S25

able to satisfactorily match measured stress or velocity histories obtained during impacts and to match the measured numbers and sizes of cracks observed throughout the specimen after the impact.

In this paper, the analytical basis and some experimental bases for the major equations of the model are presented. These equations are used in a subroutine BFRACT3, which has been used with several wave propagation computer programs to simulate fracture processes. BFRACT3 acts as a stress-strain relation in such programs.

Microcrack Kinetics in the Model

The model for tensile microfracture is designed to represent observations [1-7] from dynamic experiments in which fracture damage occurred. The fracture observations were used to distinguish and quantify the following series of processes in the model:

Initiation of fracture—when the tensile stress normal to the crack plane exceeds a critical level, fracture begins.

Nucleation of cracks—cracks are nucleated with a range of sizes and as a function of the tensile stress level.

Growth of cracks—two types of growth laws are provided, depending on the ductility of the material.

Coalescence and fragmentation—as the number and sizes of cracks increase, fragments form until the entire material disintegrates into fragments.

Each of these processes is explored in the following paragraphs. The effects of the growing damage on the stress-strain relations are then examined.

Cracks and Crack Size Distribution. The microcracks in the model are penny-shaped: circular and flat. This shape was actually observed in polycarbonate [5], which is transparent. Because a great number of cracks occur (usually 10^4 to $10^8/\text{cm}^3$), they are treated statistically, rather than individually. An indication of the form of a representative crack size distribution is shown in Fig. 1 for a disk-shaped sample of Armco iron impacted by a flat plate to a shock stress of 4 GPa. The cracks observed in this sample varied in orientation as well as length, but the angular variation is suppressed in this plot. The several distributions shown represent different stages of growth (those further to the right have grown longer). To represent the observed crack sizes, the size distribution is usually given in the analytical form:

$$N_g = N_0 \exp(-R/R_1) \tag{1}$$

where N_0 and N_g are the total number of cracks per unit volume and the number per unit volume with a radius greater than R, and R_1 is the shape parameter for the distribution. For computations, the distributions are represented by a series of line segments in the N-R plane.

The statistical nature of the crack distribution is indicated by the fact that N is a crack density (number per unit volume). Thus, the model assigns a crack density to each point in the material. The model is a continuum model, and the crack distribution acts as an internal state variable (i.e., it is an additional property of the continuum). This statistical approach is especially appropriate for finite-difference or finite-element calculations in which the material is represented by a number of small cells. The crack density is independent of cell size, whereas the common treatment of individual cracks is highly dependent on cell size.

In the model the cracks are presumed to open elastically under a tensile stress σ_n normal to the crack plane (see Sneddon and Lowengrub [17]):

$$\delta = \frac{4(1-\nu^2)}{\pi E} R\sigma_n \tag{2}$$

where δ is one-half the maximum separation of the crack faces and E and ν are Young's modulus and Poisson's ratio. This elastic opening process only approximates real material behavior in which cracks in fact open with a finite velocity and may remain open when the load is removed. The crack faces form an ellipsoid with three semiaxes, δ, R, and R. Thus, the volume of a crack is

$$V_{1c} = \frac{4\pi R^2 \delta}{3} = \frac{16(1-\nu^2)R^3\sigma_n}{3E} \tag{3}$$

The volume of the entire crack size distribution can be obtained by combining equations (1) and (3) into the following integral:

$$V_c = \int_{R_a}^{R_b} V_{1C} dN = \frac{16(1-\nu^2)\sigma_n}{3E} \int_{R_a}^{R_b} R^3 dN \tag{4}$$

$$= \frac{16(1-\nu^2)}{3E} \sigma_n \tau_z = \epsilon_n^c$$

where R_a and R_b are minimum and maximum radii in the distribution. The quantity τ_z is introduced to represent the effect of the total crack distribution. The strain ϵ_n^c represents an average elongation strain normal to the crack plane.

In the current model, all cracks in the distribution in a given material cell lie in a single plane, although they may be considered to represent some range of orientation angles (in spherical coordinates) in the actual material. For each material point, the crack orientation is fixed normal to the maximum tensile stress at the time that any stress first exceeds the initiation stress criterion for nucleation.

Nucleation and Growth Processes. Two alternative types of nucleation and growth processes are provided in the model. Their characteristics are:

1. A constant threshold stress σ_{g0} for growth. All sizes of cracks are nucleated and all grow when this tensile stress is exceeded. This process is appropriate for crack growth in ductile materials, in which considerable plastic flow accompanies cracking [1, 2].

2. A fracture mechanics threshold for growth. Only cracks above a stress-determined size can nucleate and grow. This threshold seems to fit more brittle materials such as oil shale [6] and novaculite [7].

In our model, therefore, somewhat different nucleation and crack growth relations are provided for each type of growth threshold.

Downloaded 02 May 2010 to 171.66.16.54. Redistribution subject to ASME license or copyright; see http://www.asme.org/terms/Terms_Use.cfm

Nucleation in the model occurs as the new cracks are added to the existing set. These new cracks occur in a range of sizes with the size distribution given by equation (1). At nucleation, the parameter R_1 equals R_n, a material constant indicating the inherent flaw size. The rate at which cracks are nucleated is governed by the following function:

$$\frac{dN}{dt} = \dot{N}_0 \left[\exp \frac{\sigma_n - \sigma_{n0}}{\sigma_{ns}} - 1 \right], \quad \sigma_n \geq \sigma_{n0} \qquad (5)$$
$$= 0, \quad \sigma_n < \sigma_{n0}$$

where dN/dt refers to the rate of increase of N_0, the total number of cracks per unit volume; $\dot{N}_0$ and σ_{ns} are material quantities with the dimensions of number/m^3/sec and Pa; and $\bar{\sigma}_n$ is the average stress during the time interval Δt. For the constant threshold stress, the size distribution nucleated at any time extends from $R = 0$ to $R = R_{mx}$, which is the maximum nucleated crack size (a material parameter). For the fracture mechanics threshold, the size distribution nucleated in a time increment extends only from $R = R_c$, which is a critical size defined below, to $R = R_{mx}$.

The crack growth law derived from our experimental data on cleavage crack growth in Armco iron (Seaman, et al. [18]) and beryllium (Shockey et al. [19]) is

$$\frac{dR}{dt} = \left(\frac{\sigma_n - \sigma_{g0}}{4\eta} \right) R \qquad (6)$$

where η is a growth factor with the dimensions of viscosity, and σ_{g0} is a growth threshold stress. For σ_n less tensile than σ_{g0}, no growth occurs. In our model, the crack velocity is not allowed to exceed the Rayleigh wave velocity in intact material. This growth law has been derived theoretically [20] for the expansion of spherical voids in a viscous fluid and hence may be termed a viscous growth law. Its observed occurrence for cleavage cracks in Armco iron and beryllium suggests that significant plastic flow at the microcrack tips may control growth.

When an exponential distribution of flaws, represented by equation (1), grows according to this law, the distribution remains exponential. Thus, in any material in which the crack size distribution is observed to remain exponential for a range in levels of damage, a viscous growth law is indicated. For fairly ductile materials such as Armco iron, in which considerable plastic flow accompanies growth, σ_{g0} is observed to be a material constant; i.e., alternative (1) in the foregoing is taken.

Growth with the constant threshold stress law is obtained by integrating equation (6) and treating σ_n as the time average of the solid stress normal to the crack plane:

$$R_{m+1} = R_m \exp \left[\frac{\sigma_n - \sigma_{g0}}{4\eta} \Delta t \right], \qquad \sigma_n \geq \sigma_{g0} \qquad (7)$$
$$= R_m, \qquad \sigma_n < \sigma_{g0}$$

where Δt is the time increment and R_m and R_{m+1} are radii at the beginning and end of the increment. This expression shows that every radius in the distribution increases by the same ratio. Therefore, the new distribution obtained after growth is still an exponential, with the new value of the size parameter R_1 obtained from the old one by equation (7). The crack size distributions have been observed to remain essentially exponential throughout their growth history (see Fig. 1).

For more brittle materials, such as rock, σ_{g0} is the critical stress for crack growth according to linear elastic fracture mechanics, as in alternative (2) in the foregoing:

$$\sigma_{g0} = \sqrt{\frac{\pi}{4R}} K_{1c} \qquad (8)$$

where K_{1c} is the fracture toughness, a material constant. With equation (8) in the growth law, no growth occurs for cracks with a radius smaller than R_c.

$$R_c = \frac{\pi K_{1c}^2}{4\sigma_n^2} \qquad (9)$$

When the fracture mechanics form of the growth law (6) is integrated, accounting for the variation in σ_{g0} according to equation (8), we obtain

$$\sqrt{R_{m+1}} = \left(\sqrt{R_m} - \sqrt{\frac{\pi}{4}} \frac{K_{1c}}{\sigma_n} \right) \exp \left(\frac{\sigma_n \Delta t}{8\eta} \right) + \sqrt{\frac{\pi}{4}} \frac{K_{1c}}{\sigma_n} \qquad (10)$$

where R_{m+1} and R_m are values of R at the end and beginning of the time increment Δt. Here the final size R_{m+1} is related in a complex way to R_m, so that the final distribution is not an exponential. To provide fidelity to the growth process in the model, we have represented the size distribution by a series of exponential segments. Then the growth of the R values at the ends of the segments is computed by equation (10).

After nucleation and growth during a time increment, the nucleated crack size distribution is added to the growing distribution to form a single distribution representing the current state of damage in the material. This combined distribution may grow during the next time increment.

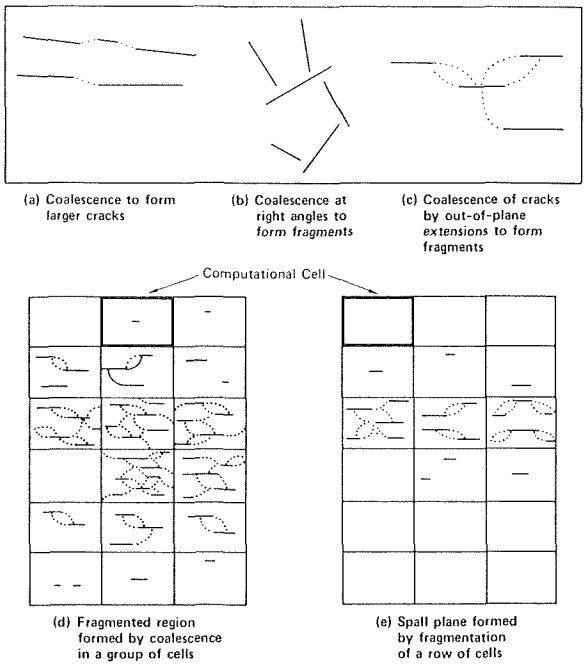

Fig. 2 Coalescence and fragmentation processes envisioned for the model

Coalescence and Fragmentation. The model coalescence processes were developed to represent observations in novaculite quartz [7]. There the resulting fragments occurred in a range of sizes from 35 μm to 5 mm, and all sizes had approximately the same aspect ratio.

The physical process of coalescence occurs when the cracks become so large that they begin to intersect other cracks. They may intersect in the same plane, thus forming larger cracks, and they may intersect at right angles, forming corners of fragments. Also, cracks in the same orientation, but on different planes, may coalesce by developing crack extensions out of the plane to join nearby cracks. Thus a family of cracks in one orientation can coalesce and form a rough, multifaceted spall plane. These three coalescence possibilities are illustrated in Fig. 2(*a-c*). Because cracks in only one orientation are permitted in the current version of the model, only coalescence of the first and third types are possible.

Downloaded 02 May 2010 to 171.66.16.54. Redistribution subject to ASME license or copyright; see http://www.asme.org/terms/Terms_Use.cfm

Presently, we are considering only the third type of coalescence. In this coalescence pattern, we obtain fragments in each cell that fully fractures. If cells above and below also fragment, as in Fig. 2(*d*), we have a region of rubble. If only a horizontal line or plane of cells fragments, as in Fig. 2(*e*), we have essentially a spall plane, with some loose chunks on the plane.

The physical processes of these crack intersections are not considered explicitly in the model; rather, the model provides only for a gradual transition from undamaged to fully fragmented material and an accounting of the fragment size distribution to the end. Let us consider the fully fragmented state first.

The fragments occur in a size distribution that we presume is related to the crack size distribution. Furthermore, we assume that for each size range, there is a constant ratio β between the number of cracks and the number of fragments:

$$\beta = \frac{N_0^f}{N_0} \tag{11}$$

where N_0^f is the total number of fragments per unit volume. Thus, we expect small cracks to coalesce with small cracks to form small fragments, and large cracks to form large fragments. Chunky fragments are usually formed by a crack face above and below and by crack extensions on the vertical sides. Because each crack forms a side of two fragments and each fragment requires two crack faces, one crack is associated with each fragment; therefore β is approximately one. Similarly, the fragment sizes are related to the crack sizes by a factor γ:

$$\gamma = \frac{R^f}{R} \tag{12}$$

where R^f is the radius of the top or bottom of the fragments. The cracks forming the fragment top and bottom have about the same area as these fragment surfaces, so γ is about 1.

To determine the fragment volume, we need some further information about the fragment shape. If we take the top and bottom of the fragment as roughly circular, then the area is $\pi(R^f)^2$. The thickness of the fragment is related to the radius R^f by the proportionality factor α such that thickness = αR^f. The fragment volume is then V_1^f

$$V_1^f = \alpha\pi(R^f)^3 = T_F(R^f)^3 \tag{13}$$

Here the coefficients in the volume expression have been combined into a single constant T_F, which characterizes the aspect ratio of the fragments. Our experimental measurements indicate that T_F should be between 1 and 3. The relative volume, τ_f, is obtained by integration over N^f.

$$\tau_f = T_F\int_{R_a}^{R_b}(R^f)^3 dN^f = T_F\,\beta\gamma^3\int_{R_a}^{R_b}R^3 dN = T_F\,\beta\gamma^3\tau_z \tag{14}$$

Thus, the fragment volume τ_f is closely related to the crack volume V_c as expressed in equation (4) and derived from the crack size distribution. When $\tau_f = 1$, the entire volume is full of fragments.

The process of gradual coalescence and fragmentation is treated in the model by requiring that τ_f always represent the portion of the material element that has fragmented.

Stress Calculations Coupled With Damage

The stress calculations for intact material are conducted until the stresses exceed a threshold level and damage is initiated. At that time the plane of fracture is determined, as discussed later. For damaged material, the following sequence of calculations is required:

Transform the average stresses in the external X, Y coordinate system to stresses in the solid material in directions normal and tangential to the fracture plane.

Compute the stresses in the solid intact material, accounting for the stress relaxation (material softening) due to the nucleation, growth, and opening of cracks.

Transform the stresses back to the external coordinate system, accounting for the reduction in area of intact material.

Each of these steps is outlined in the following sections, and a special calculation is provided for the case of full fragmentation resulting in a spall plane.

Stress-Strain Relations. The stress-strain (constitutive) relations include the usual elastic-plastic relations for intact material, plus a method to account for the effect of the developing damage on the stresses. We first present the stress-strain relations for undamaged material, and then proceed to those for damaged material.

The pressure P_s or average stress in the solid material is given by a Mie-Grüneisen relation that provides for linear thermoelastic behavior,

$$P_s = K\left(\frac{\rho_s}{\rho_{s0}} - 1\right) + \rho_s\Gamma E \tag{15}$$

where K and Γ are the bulk modulus and Grüneisen's ratio, ρ_s and ρ_{s0} are current and initial solid density, and E is the internal energy.

The deviator stress-strain relation is based on elasticity and perfect plasticity.

For calculating stress-strain relations modified by damage, the damaged material is taken as a composite of intact material with some separated fragments and material with reduced strength near cracks. Two sets of stresses are considered: solid and continuum. The solid stresses are the average of those stresses appearing in the intact material; continuum stresses are the average stresses on a cross section of a combination of intact and fractured material. Continuum stresses are transmitted out of the subroutine to the calling program because they represent the stresses acting between computational cells.

The stresses are computed in two steps, and each step is affected by the amount of damage. In the first step, the imposed strain is separated into a portion ϵ^s taken by the intact material and a portion ϵ^c representing the crack opening. The separation of the total strains into solid and crack opening components is very important for small amounts of damage. From ϵ^s the solid stresses are computed. The gross stresses are then computed from the solid stresses, using the fraction of intact material as a reduction factor. This transformation from solid to gross stresses dominates near the point of fragmentation or complete separation.

For the first step of calculating the stress in the solid material, the gross strain increments are separated into three portions following a suggestion of Herrmann [21]:

$$\Delta\epsilon_{ij} = \Delta\epsilon_{ij}^s + \Delta\epsilon_{ij}^c + \Delta\epsilon_{ij}^{op} \tag{16}$$

where superscripts indicate strains taken by the solid material (*s*), the crack opening (*c*), and the strain associated with the spall opening (*op*) that occurs in full separation. $\Delta\epsilon_{ij}^s$ is used in the elastic-plastic constitutive equations for the solid. The crack-opening strain increment is computed as the change in crack volume from equation (4). The third term is simply the separation of the broken material, calculated on a true strain basis. Note that these are continuum strain increments—averages over the material in the cell—not strains defined at a point.

As tensile loading occurs, ϵ_{ij}^s initially increases (in tensile magnitude). After cracks begin to nucleate and grow, ϵ_{ij}^c increases. With continued tensile straining, larger portions of the strain $\Delta\epsilon_{ij}$ are taken in crack opening $\Delta\epsilon_{ij}^c$. As the damage

Downloaded 02 May 2010 to 171.66.16.54. Redistribution subject to ASME license or copyright; see http://www.asme.org/terms/Terms_Use.cfm

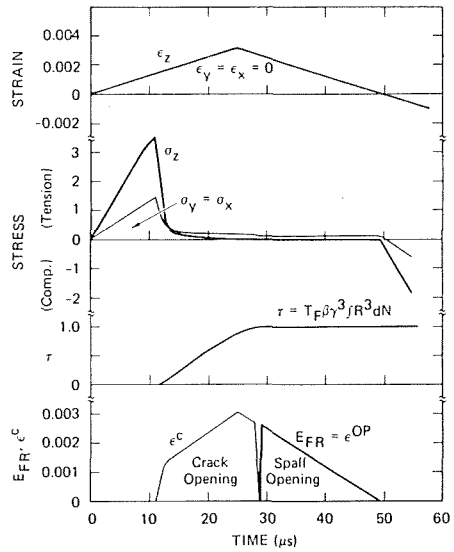

Fig. 3 Results of a subroutine test with a one-dimensional strain history

increases, the tensile solid strain ϵ_{ij}^s reaches a maximum and then begins to decrease. When separation occurs, the cracks close, so that ϵ_{ij}^c becomes zero. Simultaneously, ϵ_{ij}^{op} increases to fulfill equation (16).

The second step, the transformation from solid to continuum stresses, is accomplished using the damage quantity τ_f from equation (14):

$$\sigma_k^g = \sigma_k (1 - \tau_f) \tag{17}$$

where σ_k^g and σ_k are continuum and solid normal stresses on the kth plane, the plane of fracture. (No other stresses are modified to account for damage.) This relationship between the solid and continuum stress is borrowed from the analysis of Carroll and Holt [22] for a porous material:

$$P_g = \frac{\rho}{\rho_s} P_s \tag{18}$$

where P_g and P_s are continuum and solid pressures, and ρ and ρ_s are continuum and solid densities.

The apparent secant modulus for the cracked material can be derived from the preceding stress-strain relations and definitions of damage. By combining equations (4), (16), and (17) we can derive an elastic modulus for tensile strain normal to the crack plane. The ratio m of this apparent modulus to the modulus (M) of the intact material is

$$m = \frac{1 - \tau_f}{1 + \dfrac{16(1 - \nu^2)\tau_z M}{3E}}$$

This expression is identical to equation (6.1) of Margolin [9], except for the $1 - \tau_f$ factor introduced here to force the modulus to reduce to zero at full fragmentation under tension. This modulus expression is actually never used in calculations because tensile opening is usually accompanied by nucleation, growth, coalescence, and yielding.

Spallation. When large amounts of damage occur, the fractures are assumed to coalesce and form a local spall plane within the computational cell. Specifically, the criterion is that spall occurs when $\tau_f \geq 1.0$, where τ_f is the fragmented fraction from equation (14). Then the state of stress at the spall plane is taken to be one of plane stress, with zero stress normal to the spall plane. The spalled state route in the model contains the calculations of the stresses, plus an incrementing of the spall opening strain ϵ_n^{op}. The stress state is obtained from the usual elastic relations for the case of a free boundary. If yielding occurs, the stresses are computed using Mises plasticity and a normality rule.

Solution Procedure and Tests of the Model Results

To provide stress-strain relations that are sensitive to the growing damage, a method is required for determining the stress tensor for an imposed strain increment while accounting for the nucleation, growth, and coalescence processes. The governing equations that must be solved to determine the stresses are:

Growth law, equation (6)

Nucleation rate law, equation (5)

Crack opening relation, equation (4)

Stress-strain relation for intact material, equation (15)

Strain decomposition, equation (16)

The solution method is essentially an integration of the nucleation and growth rate laws, combined with the auxiliary algebraic equations giving the stress-strain relations.

Because of the complexity of the stress-strain and damage relations, a direct solution for the stresses is not possible in general. Therefore, an approximate procedure combining both subcycling and iteration is used. Subcycling (dividing the imposed time and strain increments into smaller units) is used to require that the stress-strain path be followed with small enough strain steps to define the process accurately. At each strain step, a combined Newton-Raphson and regula falsi solution technique (multiple trials of sets of stresses) is used to obtain sufficient accuracy for the stresses.

Calculations of Hypothetical Cases. After constructing the subroutine, we made several test calculations to eliminate bugs and examine the convergence characteristics. First tests were made with a small program that repeatedly calls the subroutine and imposes increments of strain at each call. An example of such a test is shown in Fig. 3.

For the test illustrated in Fig. 3, a strain was imposed only in the z direction. As shown, the tensile strain was increased gradually for 25 μsec and then decreased through zero to consolidation and compression. The stress histories show that all three principal stresses decrease rapidly after about 12 μsec, when the damage begins to increase rapidly (as indicated by the graph of τ_f). The crack opening rises to follow the applied strain until separation (spall) occurs at about 29 μsec. Then the crack opening vanishes, and the spall opening suddenly appears and follows the imposed strain.

Comparison of Model Results With Experimental Data

The present model, which is especially appropriate for fracturing in one plane, has been applied to impacts on disks of a propellant. Four planar gas-gun (one-dimensional) impacts were conducted on a prototype propellant with projectile velocities from 44 to 191 m/s (computed impact stresses from 0.08 to 0.37 GPa). No fracture occurred in the lowest velocity impact, but various levels of spall and fragmentation took place in the other three. Unfortunately, no low-damage results were obtained, although such data are essential for an accurate, or even unique, determination of the nucleation and growth parameters. The equation-of-state data in Table 1 were obtained from several impacts, ultrasonic tests, and other measurements (see Appendix). The fracture parameters were obtained from iterated simulations of the four experiments; these parameters are given in Table 2. Note that the brittle nature of this material under dynamic loading

Downloaded 02 May 2010 to 171.66.16.54. Redistribution subject to ASME license or copyright; see http://www.asme.org/terms/Terms_Use.cfm

caused us to select the fracture mechanics growth threshold option, alternative (2) in the foregoing. The damage computed with these parameters generally agrees well with the observed damage, as detailed in the following paragraphs.

The first shot, No. 1420, showed no damage in experiment or simulation.

In the second impact, No. 1458, a tapered flyer (projectile of varying thickness) produced a spalled portion of varying thicknesses, as shown in Fig. 4. The figure shows good agreement between computed and observed spall locations and widths of the spalled region. The location of the spall plane is readily predicted by most dynamic fracture models because it corresponds to the plane of first tension, which can be identified even without a fracture model. The thickness of the fractured region producing the separation, however, depends on the damage-induced stress-relaxation processes in the model, and is therefore a better discriminator between models.

In the third impact, No. 1460, a double spall was seen in the cross-section of the target, as shown in Fig. 5. The computations showed that a large region of material was damaged and the uppermost spall separation was formed during the first period of tensile stresses following impact. The subsequent reflections led eventually to a later spall plane, closer to the impact plane. The correspondence between computed and observed regions of damage is good enough to suggest that the computed sequence may truly represent the actual sequence.

Table 1 Values of equation-of-state parameters used in computations on propellant

Description	Values
Density, Mg/m^3	1.85
Yield stress, MPa	50.
Shear modulus, GPa	1.244
Bulk modulus, GPa	5.666
Pressure-compression relation, $P = C\mu + D\mu^2 + S\mu^3$	
μ	$\rho/\rho_0 - 1$
C, GPa	5.666
D, GPa	39.13
S, GPa	181.7

The fourth experiment, No. 1462, exhibited complete fragmentation. Figure 6 shows the cumulative fragment size distributions; the radius shown is the radius of a spherical fragment of the same mass. Both the computed and observed distributions show a change of slope around 0.1 to 0.2 cm;

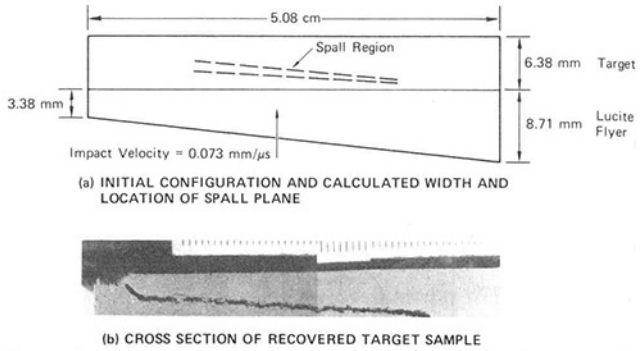

(a) INITIAL CONFIGURATION AND CALCULATED WIDTH AND LOCATION OF SPALL PLANE

(b) CROSS SECTION OF RECOVERED TARGET SAMPLE

Fig. 4 Comparison of computed and observed spall plane locations in Experiment 1458 in Propellant A

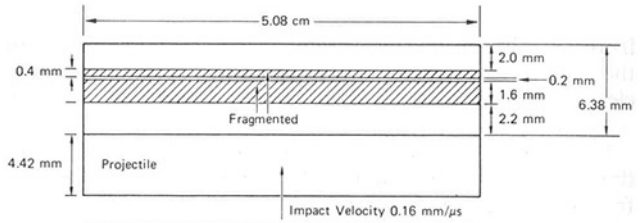

(a) CONFIGURATION AND COMPUTED RESULTS SHOWING TWO FRAGMENTED REGIONS

(b) CROSS SECTION OF SPECIMEN RECOVERED FROM EXPERIMENT 1460 SHOWING "DOUBLE" SPALL

Fig. 5 Comparison of computed and observed fragmented regions in Experiment 1460 on Propellant A

Table 2 Propellant fracture parameters BFR(M, I) used in the BFRACT3 subroutine

	Description	Value	Method for Obtaining
I = 1	Crack growth coefficient = $1/(4\eta)$ $(Pa\text{-}s)^{-1}$	− 0.15	Measured crack growth velocities at several stress levels, from impact data.
2	Dynamic fracture toughness, K_{1d} (MPa-$m^{1/2}$)	1.28	Computed from size of smallest growing cracks in impacts.
3	Size parameter of the nucleated distribution, R_n (cm)	0.0052	Measured from inclusions of virgin material, or from crack distributions under low-damage impacts.
4	Nucleation rate coefficient, $\dot{N}_0$(no./m^3/s)(T_4)	6.0×10^{13}	Computed from observed rate of appearance of crack at stresses near the threshold for damage.
5	Threshold stress for nucleation, σ_{n0}(MPa)($= T_5$)	− 50	Computed from impact conditions near the damage threshold.
6	Denominator of exponential nucleation function, $\sigma_1 = T_6$ (MPa)	− 10	Computed from nucleation rate measured in impacts at several stress levels.
7	Maximum crack size of nucleated distribution, R_{mx}(cm)($= T_7$)	0.02	Measured maximum grain, inclusion, or flaw size of the virgin material.
8	Number of size intervals for size distribution	10	Chosen for fidelity to shape of the size distribution.
9	Ratio of number of fragments to number of cracks, β	0.33	Observations of number of facets of fragments.
10	Ratio of fragment radius to crack radius, γ	1.0	Observation of shape of fragments.
11	Coefficient of fragment volume, $= V^F/R_f^3$ (T_F)	4.0	Observations of shape of fragments. Irregular fragments with mean dimensions of $a = R_f = \gamma R$, b, c have $F = 4bc/a^2$.

Downloaded 02 May 2010 to 171.66.16.54. Redistribution subject to ASME license or copyright; see http://www.asme.org/terms/Terms_Use.cfm

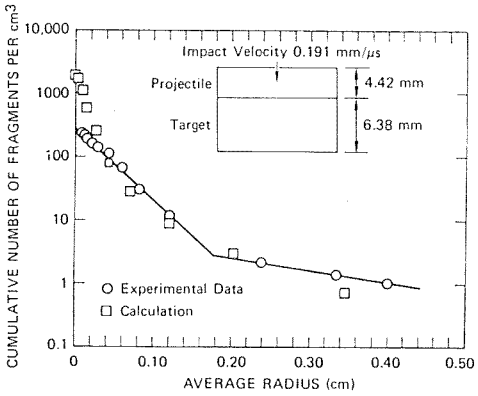

Fig. 6 Comparisons of computed and experimental fragment size distributions for Experiment 1462

this effect is probably associated with the fracture mechanics concept that allows only cracks larger than a critical size to grow.

Discussion of Results. The observed results of the four experiments ranged from no fracture to spallation to fragmentation. All three levels of damage were well represented by the model simulations, which used a single set of fracture parameters. Unfortunately, no low-damage impacts were available; hence, the nucleation and growth parameters for the model cannot be considered unique. However, because the model features were derived from a large amount of low-damage data on other materials, those aspects of the model are strongest. Although the model now includes complete separation and fragmentation, the basis for these model processes is more intuitive than experimental.

We hoped that the simulations would represent two critical features of the experimental data—double spall and the fragment size distribution. The double spall was considered critical because we felt that the location and occurrence of the second spall would depend strongly on the damage-caused stress-relaxation process in the model.

The fragment size distribution exhibited a nonexponential form, a shape that arises often in brittle materials. The curve shape is a function of the initial or nucleation size distribution, the microscopic fracture toughness, and the crack growth parameter. Hence, the observed match of experimental and computed results (Fig. 6) suggests that these three model features are reasonably accurate.

Examination of these experimental data and comparison of the model's results indicated two problem areas:

Results for low and intermediate damage are needed to determine the nucleation and growth parameters more accurately.

A more physically descriptive model fragmentation process must be developed and verified. The current process, although it represents the fragmentation data quite well, includes no detailed steps from the cracked state to the fragmented state.

Summary of Model Capabilities

A basic model for representing the complete brittle microfracturing and fragmentation processes under high-rate loading has been developed. It contains nucleation, growth, fragmentation, damage-caused stress-relaxation processes, and a stress solution procedure suited to highly nonlinear behavior. The model handles multiple loadings, unloadings, and reconsolidation. The model has been used to represent brittle fracture in a wide range of materials. However, it is not expected to match all materials. The current model is an extension of earlier models into the high-damage range where full separation and fragmentation occur. It is expected that this basic model would be used initially to represent fracture in any new material. The initial attempts to match experimental data would indicate any needed modifications in the processes. These processes, which are isolated in the model so that each can be altered independently of the others, would be changed in the computational model and the experiments would be resimulated until a satisfactory match was obtained. Thus, the model is one element in a flexible experimental-computational approach to fracture problems.

References

1 Barbee, T. W., Jr., Seaman, L., Crewdson, R. C., and Curran, D. R., "Dynamic Fracture Criteria for Ductile and Brittle Metals," *J. Materials*, JMLSA, Vol. 7, 1972, pp. 393-401.

2 Seaman, L., Curran, D. R., and Shockey, D. A., "Computational Models for Ductile and Brittle Fracture," *J. Appl. Phys.*, Vol. 47, 1976, pp. 4814-4826.

3 Shockey, D. A., Seaman, L., and Curran, D. R., "Microfracture Models and Their Applications to Nonlinear Dynamic Fracture Problems," *Nonlinear and Dynamic Fracture Mechanics*, ASME, AMD-Vol. 35, 1979, p. 79.

4 Shockey, D. A., Seaman, L., Dao, K. C., and Curran, D. R., "Kinetics of Void Development in Fracturing A533B Tensile Bars," ASME *Journal of Pressure Vessel Technology*, Vol. 102, 1980, pp. 14-21.

5 Curran, D. R., Shockey, D. A., and Seaman, L., "Dynamic Fracture Criteria for a Polycarbonate," *J. Appl. Phys.*, Vol. 44, 1973, p. 4025.

6 Murri, W. J., Young, C., Shockey, D. A., Tokheim, R. E., and Curran, D. R., "Determination of Dynamic Fracture Parameters for Oil Shale," SRI International, Final Report to Sandia Laboratories, Albuquerque, N.M., 1977.

7 Shockey, D. A., Curran, D. R., Seaman, L., Rosenberg, J. T., and Peterson, C. F., "Failure of Rock Under High Tensile Loads," *Int. J. Rock Mech. Sci. Geomech. Abstr.*, Vol. 11, 1974, pp. 303-317.

8 Davison, Lee, Stevens, A. L., and Kipp, M. E., "Theory of Spall Damage Accumulation in Ductile Metals," *J. Mech. Phys. Solids*, Vol. 25, No. 1, Feb. 1977, pp. 11-28.

9 Margolin, L. G., "Elastic Moduli of a Cracked Body," *Int. Journ. of Fracture*, Vol. 22, 1983, pp. 65-79.

10 Krajcinovic, D., and Fonseka, G. U., "The Continuous Damage Theory of Brittle Materials, Part 1: General Theory," ASME JOURNAL OF APPLIED MECHANICS, Vol. 48, 1981, pp. 809-815.

11 Kipp, M. E., Grady, D. E., and Chen, E. P., "Strain-Rate Dependent Fracture Initiation," *Int. J. of Fracture*, Vol. 16, 1980, pp. 471-478.

12 Grady, D. E., "Local Inertial Effects in Dynamic Fragmentation," *J. Appl. Phys.*, Vol. 53, No. 1, 1982, pp. 322-325.

13 Evans, A. G., Ito, Y. M., and Rosenblatt, M., "Impact Damage Thresholds in Brittle Materials Impacted by Water Drops," *J. Appl. Phys.*, Vol. 51, No. 5, 1980, pp. 2473-2482.

14 Dremin, A. N., and Molodets, A. M., "Kinetic Characteristics of Spall Fracture," *J. of Appl. Mech. and Tech. Phys.*, Vol. 21, #6, Nov.-Dec. 1980, p. 806 in Translation.

15 Kumano, A., and Goldsmith, W., "Analytical and Experimental Investigation of the Effect of Impact on Coarse Granular Rocks," *Rock Mechanics*, Vol. 15, No. 2, Aug. 1982.

16 Meyers, M. A., and Aimone, C. T., "Dynamic Fracture (Spalling) of Metals," *Progress in Materials Science*, Vol. 28, 1983, pp. 1-96.

17 Sneddon, I. N., and Lowengrub, M., *Crack Problems in the Classical Theory of Elasticity*, John Wiley & Sons, New York, 1969.

18 Seaman, L., Shockey, D. A., and Curran, D. R., "The Growth Law for Crack Propagation under Shock Conditions," *Proceedings of Conference on Dynamic Crack Propagation*, George C. Sih, Ed., Noordhoff, 1972, p. 629.

19 Shockey, D. A., Seaman, L., and Curran, D. R., "Dynamic Fracture of Beryllium Under Plate Impact and Correlation with Electron Beam and Underground Test Results," SRI International, Final Report for Kirtland Air Force Base, Albuquerque, N.M., 1973.

20 Poritsky, H., "The Collapse or Growth of a Spherical Bubble or Cavity in a Viscous Fluid," *Proceedings of the First U.S. National Congress of Applied Mechanics*, ASME, 1952, p. 813.

21 Herrmann, Walter, "Constitutive Equations for Compaction of Porous Materials," Symposium on Applied Mechanics Aspects of Nuclear Effects in Materials, ASME Winter Annual Meeting, Washington, D.C., Nov. 28-Dec. 3, 1971.

22 Carroll, M. M., and Holt, A. C., "Suggested Modification of the P-α Model for Porous Materials," *J. Appl. Phys.*, Vol. 42, 1972, p. 759.

23 Tarver, C., Lawrence Livermore National Laboratory, personal communication, March, 1980.

APPENDIX

Constitutive Relations for Propellant

Material constitutive relations for propellant were required at strain rates appropriate to the impacts causing fracture.

Downloaded 02 May 2010 to 171.66.16.54. Redistribution subject to ASME license or copyright; see http://www.asme.org/terms/Terms_Use.cfm

Table 3 SRI gas-gun impacts on propellant

Shot	Peak stress MP_a	Particle velocity m/s	Shock velocity km/s	Relief velocity km/s
23	149	42	1.92	2.13
24	329	85	2.09	2.44

Table 4 LLL ultrasonic measurements on propellant

Specimen	Longitudinal velocity km/s
1	1.995
2	2.008
3	1.974
average	1.992

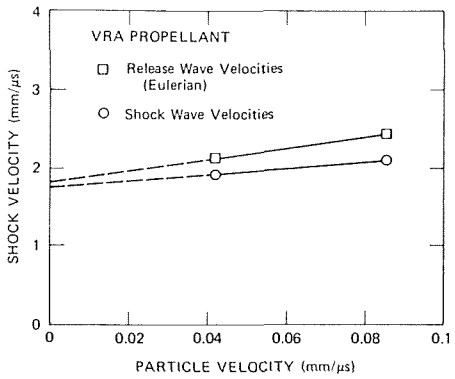

Fig. 7 Shock velocity versus particle velocity from multiple-embedded particle velocity gage experiments

Material property parameters defining dynamic stress-strain relations for propellant were obtained at strain rates appropriate to the impacts of interest. There were insufficient data to specify a rate-dependent model for this material, although its properties (especially shear modulus) change significantly from the quasistatic to dynamic loading rates. Therefore the properties developed here treat the material as rate-independent.

We used measurements from two light gas-gun impacts and ultrasonic measurements from Craig Tarver of Lawrence Livermore National Laboratory [23]. These data are shown in Tables 3 and 4. The impact data are exhibited together in Fig. 7. The conflict of these two sets of data at zero stress suggests that the ultrasonic velocity represents a longitudinal modulus, whereas the impacts exhibit only a bulk modulus. With this assumption, we computed the shear wave velocity from the relationship between longitudinal, bulk, and shear velocities

$$C_L^2 = C_B^2 + \frac{4}{3} C_S^2$$

Using C_L = 1.992 km/sec and C_B = 1.75 km/sec (the zero stress intercept), we obtained a shear wave velocity of 0.82 km/sec.

With the measured initial density of 1.85 g/cm^3 and the preceding bulk and shear velocities, we computed the following moduli: Bulk = 5.66 GPa and Shear = 1.24 GPa.

The higher order terms for bulk modulus were determined from the shock velocity versus particle velocity data in Fig. 7. They have the form

$$U_s = C_B + \lambda U_p.$$

Here U_s and U_p are shock and particle velocity and λ is the slope of the line. With the aid of the Hugoniot jump conditions, the U_s-U_p data can be transformed to a pressure-density relation that is convenient for computer simulations

$$P = C\mu + D\mu^2 + S\mu^3$$

where $\mu = \rho/\rho_0 - 1$, ρ and ρ_0 are present and initial density, and C, D, and S are material constants. The transformation gives the constants listed in Table 1 in the text.

Downloaded 02 May 2010 to 171.66.16.54. Redistribution subject to ASME license or copyright; see http://www.asme.org/terms/Terms_Use.cfm

On the Asymptotic Continuum Analysis of Quasistatic Elastic-Plastic Crack Growth and Related Problems

W. J. Drugan
Department of Engineering Mechanics,
University of Wisconsin,
Madison, Wisc. 53706
Assoc. Mem. ASME

The present work provides rigorous substantiation of certain crucial asymptotic expressions which constitute the basis of a number of previous near-tip analyses of quasistatic elastic-plastic crack growth. This is accomplished as part of an investigation of the general features of two-dimensional near-tip continuum fields for quasistatic elastic-plastic crack growth, under general unsteady conditions, for a broad class of constitutive behavior and crack loading conditions. The approach employed and results obtained are also applicable to a number of geometrically similar problems, such as the plane strain analysis of the continuum fields near the leading and trailing edges of a quasistatically moving distributed surface load.

1 Introduction

The complete elastic-plastic analysis of the stress and deformation fields in a body containing a quasistatically growing crack is of sufficient mathematical complexity to prohibit (thus far) closed-form solutions. To make these problems analytically tractable, attention is focused on the region very close to the moving crack tip, where the general continuum mechanical governing equations can be approximated by simplified asymptotic forms. Another reason for focusing on the near-tip fields is that they would be expected, on physical grounds, to play a crucial role in the behavior of a cracked solid.

In view of the complexity of the general (nonlinear) elastic-plastic continuum governing equations, it is important to ensure that their reduced forms, which are employed in asymptotic analyses, are correct. A principal goal of the present paper is to attempt to provide a rigorous basis for the asymptotic forms employed in the growing crack analyses of Rice et al. [1], Rice [2], Drugan et al. [3], and other researchers (whose work is reviewed in [2, 3]). In addition, I will sharpen the asymptotic expressions used in these studies, as well as demonstrate their validity for a wider class of problems than those thus far analyzed.

The results presented herein have already facilitated a higher-order analysis (Drugan, [4]) of the plane-strain crack growth problem studied by Drugan et al. [3], this higher-order analysis differing from typical perturbation analyses in that the higher-order structure of the continuum fields is derived rather than assumed. Furthermore, I anticipate that the present results may be suggestive, if not directly applicable, in the analysis of a number of yet unsolved problems (e.g., crack growth for more general constitutive models).

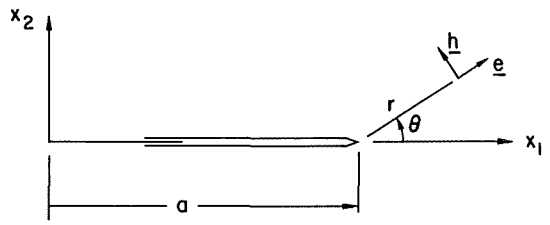

Fig. 1 Cartesian coordinates x_1, x_2, x_3 are fixed in the body; polar coordinates r, θ are centered at the tip and move with it through the material as the crack grows

The geometry of the crack problems considered is as depicted in Fig. 1: a Cartesian coordinate system x_1, x_2, x_3 is fixed in the body, with x_1 pointing in the direction of crack growth, a being the measure of crack length, and x_3 lying parallel to the crack front (which is presumed to be straight). A polar coordinate system r, θ lies in the x_1, x_2 plane, is centered at the crack tip, and moves with it through the material as the crack grows; θ is measured from the line ahead of the crack. The unit vectors **e** and **h** correspond to the radial and angular directions, respectively, of this translating polar coordinate system. Therefore

$$\partial r/\partial x_i = e_i, \quad \partial\theta/\partial x_i = h_i/r \tag{1.1}$$

where

$$e_1 = h_2 = \cos\theta, \quad e_2 = -h_1 = \sin\theta, \quad e_3 = h_3 = 0. \tag{1.2}$$

Here and throughout the paper, Latin indices i, j, k, and l have range 1, 2, 3, obey the Einstein summation convention, and indicate Cartesian components of tensors.

The two order symbols $0[w(r)]$ and $o[w(r)]$ will be used, where here $w(r)$ is an arbitrary gauge function chosen for purposes of illustration. A function $d(r)$ can be characterized as

Contributed by the Applied Mechanics Division for publication in the JOURNAL OF APPLIED MECHANICS.

Discussion on this paper should be addressed to the Editorial Department, ASME, United Engineering Center, 345 East 47th Street, New York, N.Y. 10017, and will be accepted until two months after final publication of the paper itself in the JOURNAL OF APPLIED MECHANICS. Manuscript received by ASME Applied Mechanics Division, February, 1984; final revision, September, 1984.

Copyright © 1985 by ASME
Downloaded 02 May 2010 to 171.66.16.54. Redistribution subject to ASME license or copyright; see http://www.asme.org/terms/Terms_Use.cfm

$$d(r) = 0[w(r)] \quad \text{as } r \to 0$$

if

$$\lim_{r \to 0} \left| \frac{d(r)}{w(r)} \right| < \infty;$$

$d(r)$ can be characterized as

$$d(r) = o[w(r)] \quad \text{as } r \to 0$$

if

$$\lim_{r \to 0} \left| \frac{d(r)}{w(r)} \right| = 0.$$

A clear discussion of the use of order symbols and gauge functions is given by Van Dyke [5].

2 Assumptions

2.1 Geometry. The analysis to follow will treat two-dimensional crack problems. In particular, the crack front is assumed to be straight and, with reference to Fig. 1, the continuum fields of stress, strain, body force, etc., are assumed independent of x_3. Thus, the stress field near an advancing crack tip will be regarded as

$$\sigma_{ij} = \sigma_{ij}(r,\theta,t). \tag{2.1}$$

In addition, I will neglect the effects of geometry changes due to ongoing deformation on the formulation of stresses and stress rates, and on the form of the equilibrium equations. This is equivalent to the usual "small strain" (i.e., small displacement gradient) assumption.

2.2 Material. The principal constitutive restrictions on the class of solids considered are that *deviatoric* components of stress are assumed to be bounded, that the elastic part of total strain is linearly related (although with arbitrary anisotropy) to the stress state, that stress is derivable from a positive-definite elastic strain energy function, and that inelastic deformation proceeds in accordance with the principle of maximum plastic resistance (discussed in the following). The latter three constitutive assumptions, together with the requirements of equilibrium and a continuous displacement field, are sufficient to prove that the stress field near a quasistatically growing crack tip must be *fully continuous* (Drugan and Rice, [6]). This property of the stress field renders more plausible the assumption, employed throughout the present paper, that $\sigma_{ij}(r,\theta,t)$ are differentiable with respect to each independent variable for small $r > 0$. Since the study of Drugan and Rice [6] assumes continuity of all displacement components, their proof of full stress continuity does not apply for the special case of plane stress, where the thickness direction displacement component need not be continuous (Hill, [7]). Thus the derivations to follow are valid for the cases of plane strain, antiplane strain, and general combinations of these two. The special case of plane stress is discussed separately in Section 6.

The principle of maximum plastic resistance may be stated as

$$(\sigma_{ij} - \sigma_{ij}^0) d\epsilon_{ij}^p \geq 0 \tag{2.2}$$

where σ_{ij} is the stress state (at yield) corresponding to the plastic strain increment $d\epsilon_{ij}^p$, and σ_{ij}^0 is any other stress state that is at or below yield. As discussed by Rice [8, 9], this principle, especially in its small strain form as employed here, results from a number of different viewpoints and is thus believed to be a sensible characterizer of metal plasticity.

Note that the constitutive assumptions delineated in the foregoing, and hence the resulting requirement of full stress continuity near a quasistatically advancing crack tip, restrict but do not exclude inelastic behavior characterized by strain hardening, as well as inelastic behavior that is time-dependent. The latter is true since, as shown by Rice [8], the principle of maximum plastic resistance is also a sensible restriction for time-*dependent* inelastic deformation in metals if the concept of the yield surface is replaced by that of the inelastic flow potential surface. This means that inequality (2.2) applies if σ_{ij}^0 is understood to represent a stress state lying within or on the current flow potential surface. Drugan and Rice [6] point out that their proof of stress continuity is valid for isotropically hardening solids, and also for a large class of anisotropically hardening solids defined by the requirement that the current yield locus at any step of the deformation incorporate all prior yield loci. I emphasize that time-dependent and strain-hardening material behaviors are included in the present treatment provided that the material model employed disallows unbounded *deviatoric* stresses. Since many established models of time-dependent or strain-hardening behavior permit unbounded derivatoric stresses, the primary application of the results derived here is to solids which are elastic-ideally plastic, but in the generalized sense that some rate sensitivity or strain hardening is permitted before deviatoric stresses saturate to finite levels.

2.3 Equilibrium. This study treats problems of the quasistatic type, meaning that the inertia terms in the equations of motion are negligible. Such processes are governed by the equilibrium

$$\partial \sigma_{ij} / \partial x_j + f_i = 0 \tag{2.3}$$

where $\sigma_{ij} = \sigma_{ji}$ are components of the stress tensor, and f_i are components of the body force vector which are also assumed to be bounded. These equations may be rephrased in terms of the translating polar coordinate system by regarding $\sigma_{ij} = \sigma_{ij}(r,\theta,t)$ in light of the assumptions of Section 2.1, and by using (1.1):

$$(\partial \sigma_{ij} / \partial \theta)(h_j / r) + (\partial \sigma_{ij} / \partial r) e_j + f_i = 0. \tag{2.4}$$

In terms of polar components of stress, these equations are

$$\frac{\partial \sigma_{rr}}{\partial r} + \frac{1}{r} \frac{\partial \sigma_{r\theta}}{\partial \theta} + \frac{\sigma_{rr} - \sigma_{\theta\theta}}{r} + f_r = 0 \tag{2.5a}$$

$$\frac{\partial \sigma_{r\theta}}{\partial r} + \frac{1}{r} \frac{\partial \sigma_{\theta\theta}}{\partial \theta} + \frac{2\sigma_{r\theta}}{r} + f_\theta = 0 \tag{2.5b}$$

$$\frac{\partial \sigma_{rz}}{\partial r} + \frac{1}{r} \frac{\partial \sigma_{\theta z}}{\partial \theta} + \frac{\sigma_{rz}}{r} + f_z = 0 \tag{2.5c}$$

where $z \equiv x_3$.

3 Asymptotic Structure of the Stress Field

Since a principal goal of the study is rigorous derivations of asymptotic forms of general continuum expressions and governing equations, and since these involve first partial derivatives of stress with respect to the independent variables in (2.1), it is necessary to establish the asymptotic order of such first partial derivatives. This will be accomplished by employing the assumptions of Section 2.

3.1 Radial Derivative of Stress Components. To establish the asymptotic order of the terms $\partial \sigma_{ij} / \partial r$, we begin by considering the equilibrium equations (2.5) when multiplied by r. In this form they suggest the plausibility of the assumption that

$$r \partial \sigma_{ij} / \partial r \quad \textit{exist} \text{ in the limit as } r \to 0, \tag{3.1}$$

in light of the boundedness assumptions on f_i and deviatoric stress components. On the basis of (3.1) we may write

$$\lim_{r \to 0} \left[r \partial \sigma_{ij} / \partial r \right] = A_{ij}(\theta,t) \tag{3.2}$$

where $A_{ij}(\theta,t)$ are as yet unknown. It follows that

$$\partial \sigma_{ij} / \partial r = A_{ij}(\theta,t)/r + o(1/r) \quad \text{as} \quad r \to 0. \tag{3.3}$$

Integrate this with respect to r for r small to obtain

$$\sigma_{ij} = -A_{ij}(\theta,t) ln(R/r) + o[ln(R/r)] \quad \text{as } r \to 0, \tag{3.4}$$

Downloaded 02 May 2010 to 171.66.16.54. Redistribution subject to ASME license or copyright; see http://www.asme.org/terms/Terms_Use.cfm

where R is an undetermined constant having length dimensions. Divide this equation by $[ln(R/r)]$:

$$\sigma_{ij}/[ln(R/r)] = -A_{ij}(\theta,t) + o(1) \quad \text{as } r \to 0. \tag{3.5}$$

In terms of deviatoric stress components $s_{ij}(\equiv \sigma_{ij} - 1/3\ \delta_{ij}\sigma_{kk})$, (3.5) is

$$s_{ij}/[ln(R/r)] = -A_{ij} + \frac{1}{3}\delta_{ij}A_{kk} + o(1) \quad \text{as} \quad r \to 0. \tag{3.6}$$

Now, take the limit of (3.6) as $r \to 0$, invoking the boundedness of s_{ij} to obtain

$$A_{ij}(\theta,t) - \frac{1}{3}\delta_{ij}A_{kk}(\theta,t) \equiv 0. \tag{3.7}$$

This shows, via (3.2), that

$$\lim_{r \to 0} \left[r\partial s_{ij}/\partial r \right] = 0, \tag{3.8}$$

which now may be employed to elucidate the asymptotic structure of the hydrostatic stress component $\sigma_{kk}/3$.

Asymptotic Boundedness of Hydrostatic Stress Component. To prove that hydrostatic stress is bounded as $r \to 0$, we enforce circumferential equilibrium, equation (2.5*b*), in the rearranged form

$$\partial\sigma_{\theta\theta}/\partial\theta = -2\sigma_{r\theta} - r\partial\sigma_{r\theta}/\partial r - rf_{\theta}. \tag{3.9}$$

Integrating (3.9) with respect to θ at fixed $r \neq 0$ and t gives

$$\sigma_{\theta\theta} = -2\int_{-\pi}^{\theta} \sigma_{r\theta}d\phi - \int_{-\pi}^{\theta} (r\partial\sigma_{r\theta}/\partial r)d\phi - \int_{-\pi}^{\theta} rf_{\theta}d\phi, \tag{3.10}$$

assuming traction-free crack faces; if the crack faces were subject to a traction of finite magnitude, (3.10) would contain an additional bounded term which would not affect the proof. Now making use of the bounded body force assumption and the result (3.8), we examine (3.10) as $r \to 0$ to find

$$\sigma_{\theta\theta} = -2\int_{-\pi}^{\theta} \sigma_{r\theta}d\phi + o(1) \quad \text{as} \quad r \to 0, \tag{3.11}$$

which shows that $\sigma_{\theta\theta}$ is bounded as $r \to 0$ since $\sigma_{r\theta}$ is by assumption (Section 2). Thus, coupling (3.11) with the assumption that all *deviatoric* stress components are bounded proves that *the hydrostatic component of stress is bounded in the limit of* $r \to 0$, and therefore that *all* components of stress are bounded in that limit. Applying this result to (3.5) in the limit as $r \to 0$ now shows

$$A_{ij}(\theta,t) \equiv 0 \tag{3.12}$$

so that from (3.2) we obtain the important conclusion

$$\partial\sigma_{ij}/\partial r = o(1/r) \quad \text{as } r \to 0. \tag{3.13}$$

Since many previous studies of near-tip fields depend on the veracity of (3.13), I next provide an alternate proof to the one in the foregoing. Here, instead of (3.1), I assume that *for sufficiently small* $r_o > 0$:

(*i*) $\partial\sigma_{ij}/\partial r$ are defined on the *open* interval $0 < r < r_o$ for each fixed θ,t, and

(*ii*) $|\partial\sigma_{ij}/\partial r|$ are monotonic in r on $0 < r < r_o$.

First, if $|\partial\sigma_{ij}/\partial r|$ are nonincreasing as $r \to 0$, then obviously $r|\partial\sigma_{ij}/\partial r| \to 0$ as $r \to 0$, so we need only consider the case of *increasing* $|\partial\sigma_{ij}/\partial r|$ as $r \to 0$. The stress continuity proof of Drugan and Rice [6] when applied to the radial behavior of σ_{ij} holds for $r > 0$, but since all *deviatoric* components of stress s_{ij} are assumed bounded (Section 2), they are continuous on the *closed* interval $[0,r_o]$. Then for $0 < r < r_o$

$$|s_{ij}(r,\theta,t) - s_{ij}(0,\theta,t)|$$

$$= |r\partial s_{ij}(\xi,\theta,t)/\partial r| \geq |r\partial s_{ij}(r,\theta,t)/\partial r|, \tag{3.14}$$

where the equality is the mean value theorem, with ξ lying somewhere in the *open* interval $(0,r)$ and since therefore $\xi < r$, the inequality in (3.14) follows from Assumption (*ii*) in the foregoing. Since the first term of (3.14) vanishes as $r \to 0$ due to continuity of s_{ij}, so too does the last term, thus proving (3.8). Result (3.8) then permits use of circumferential equilibrium to prove boundedness of hydrostatic stress as $r \to 0$, as in the preceding equations (3.9)-(3.11). This means that hydrostatic stress must also be continuous on the *closed* interval $[0,r_o]$, so that (3.14) may now be written for the hydrostatic stress component, and this combines with the foregoing proof of (3.8) to prove (3.13).

Results that are more strict than (3.13) are obtained by reapplying part of the first proof of (3.13); in particular, the slightly stronger requirement that

$$\partial\sigma_{ij}/\partial r = o\left[\frac{1}{r ln(R/r)}\right] \quad \text{as } r \to 0 \tag{3.15}$$

is a crucial result (e.g., see Drugan, [4]). To prove (3.15), we strengthen (3.1), on the basis of result (3.13), to the assumption that

$$r[ln(R/r)]\partial\sigma_{ij}/\partial r \quad \textit{exist} \text{ in the limit as } r \to 0, \tag{3.16}$$

and hence write

$$\lim_{r \to 0} \{ r[ln(R/r)]\partial\sigma_{ij}/\partial r \} = B_{ij}(\theta,t) \tag{3.17}$$

where $B_{ij}(\theta,t)$ are initially unknown. Now, following steps similar to those from (3.2-3.5), we find that (3.17) leads to

$$\sigma_{ij}/ln[ln(R/r)] = -B_{ij}(\theta,t) + o(1) \quad \text{as } r \to 0. \tag{3.18}$$

Taking the limit of this as $r \to 0$, enforcing the boundedness of σ_{ij}, shows $B_{ij}(\theta,t) \equiv 0$, which via (3.17) demonstrates (3.15).

3.2 Circumferential and Time Derivatives of Stress Components. If in addition to the assumptions of Section 2 I assume that $\partial\sigma_{ij}/\partial\theta$ and $\partial\sigma_{ij}/\partial t$ admit the following asymptotic representations (where here no summation is implied by repeated indices)

$$\partial\sigma_{ij}/\partial\theta = a_{ij}(r)C_{ij}(\theta,t) + o[a_{ij}(r)] \quad \text{as } r \to 0 \tag{3.19}$$

$$\partial\sigma_{ij}/\partial t = b_{ij}(r)D_{ij}(\theta,t) + o[b_{ij}(r)] \quad \text{as } r \to 0 \tag{3.20}$$

where the functions a_{ij}, b_{ij}, C_{ij}, and D_{ij} are initially unspecified except that C_{ij} and D_{ij} are bounded but not identically zero, then the maximum asymptotic orders of these quantities must be

$$\partial\sigma_{ij}/\partial\theta = 0(1) \quad \text{as } r \to 0 \tag{3.21}$$

$$\partial\sigma_{ij}/\partial t = 0(1) \quad \text{as } r \to 0. \tag{3.22}$$

I will prove (3.21) and (3.22) by contradiction. Beginning with (3.22), only the (11) component will be treated since the proof for any other component is identical. Suppose

$$|\partial\sigma_{11}/\partial t| \to \infty \quad \text{as} \quad r \to 0. \tag{3.23}$$

From assumption (3.20),

$$\partial\sigma_{11}/\partial t = b_{11}(r)D_{11}(\theta,t) + o[b_{11}(r)] \quad \text{as} \quad r \to 0, \tag{3.24}$$

which can be integrated with respect to time at fixed r, θ to give

$$\sigma_{11} = b_{11}(r)\int^{t} D_{11}(\theta,\tau)d\tau + F(r,\theta) + o[b_{11}(r)] \quad \text{as } r \to 0, \tag{3.25}$$

where $F(r,\theta)$ is a function of integration. Expression (3.25) could meet the boundedness requirement on σ_{11} in the limit of $r \to 0$ only if $F(r,\theta)$ were to cancel the singularity of the $b_{11}(r)$ term as $r \to 0$, but this is not possible for general t since $b_{11}(r)$ is multiplied by a function of t (which cannot be identically zero since $D_{11}(\theta,t) \not\equiv 0$). Thus (3.25) requires $b_{11}(r)$ to be

Downloaded 02 May 2010 to 171.66.16.54. Redistribution subject to ASME license or copyright; see http://www.asme.org/terms/Terms_Use.cfm

bounded as $r \to 0$, which via (3.24) contradicts our supposition (3.23).

The proof of (3.21) is identical to that given for (3.22) if the roles of θ and t are interchanged and assumption (3.19) is employed in place of (3.20).

4 Asymptotic Form of Equilibrium Equations

The asymptotic bounds on stress derivatives proved in Section 3 will now be applied to show how the general equilibrium equations and other important expressions simplify for small r. In the case of the equilibrium equations, the results (3.15) and (3.21) are employed, showing that equilibrium requires (via(2.4))

$$(\partial \sigma_{ij}/\partial \theta)h_j + o\{[ln(R/r)]^{-1}\} = 0 \quad \text{as } r \to 0 \tag{4.1}$$

or (via (2.5))

$$\partial \sigma_{r\theta}/\partial \theta + \sigma_{rr} - \sigma_{\theta\theta} + o\{[ln(R/r)]^{-1}\} = 0 \quad \text{as } r \to 0 \tag{4.2a}$$

$$\partial \sigma_{\theta\theta}/\partial \theta + 2\sigma_{r\theta} + o\{[ln(R/r)]^{-1}\} = 0 \quad \text{as } r \to 0 \tag{4.2b}$$

$$\partial \sigma_{\theta z}/\partial \theta + \sigma_{rz} + o\{[ln(R/r)]^{-1}\} = 0 \quad \text{as } r \to 0. \tag{4.2c}$$

5 Asymptotic Forms of Stress Rate

Constitutive laws for the types of inelastic materials considered here usually involve the stress rate at a material point, $\dot{\sigma}_{ij}$. Following Rice [2], a convenient expression for this quantity results from applying the chain rule to (2.1):

$$\dot{\sigma}_{ij} = (\partial \sigma_{ij}/\partial \theta)\dot{\theta} + (\partial \sigma_{ij}/\partial r)\dot{r} + \partial \sigma_{ij}/\partial t$$

$$= (\partial \sigma_{ij}/\partial \theta)\dot{a}\sin\theta/r - (\partial \sigma_{ij}/\partial r)\dot{a}\cos\theta + \partial \sigma_{ij}/\partial t \tag{5.1}$$

where a superposed dot denotes time rate at a material point, and we have employed $\dot{\theta} = \dot{a}\sin\theta/r$ and $\dot{r} = -\dot{a}\cos\theta$, which result from the translation of the crack tip polar coordinate system with the growing crack.

Application of the results (3.15), (3.21), and (3.22) to expression (5.1) yield the two useful asymptotic forms

$$\dot{\sigma}_{ij} = (\partial \sigma_{ij}/\partial \theta)\dot{a}\sin\theta/r - (\partial \sigma_{ij}/\partial r)\dot{a}\cos\theta + 0(1) \quad \text{as } r \to 0 \tag{5.2}$$

$$\dot{\sigma}_{ij} = (\partial \sigma_{ij}/\partial \theta)\dot{a}\sin\theta/r + o\{[rln(R/r)]^{-1}\} \quad \text{as } r \to 0. \tag{5.3}$$

Previous analyses of lowest-order *growing* crack-tip fields by Rice et al. [1], Rice [2], and Drugan et al. [3] are based on the asymptotic results (4.2) and (5.3) (although in the weaker forms obtained by using (3.13) instead of (3.15)), which were *assumed* by those authors to be valid on the basis of the stress boundedness requirement of their elastic-ideally plastic constitutive models. A principal objective of this paper was to prove these pivotal hypotheses, while at the same time strengthening them and demonstrating that their applicability extends to the more general material class delineated in Section 2.

6 Applicability to Plane Stress

All preceding results are valid for the general class of materials specified in Section 2.2, where it was mentioned that the derivations of Sections 3–5 exclude the special case of plane stress, to which the Drugan and Rice [6] proof of continuity of all stress components does not apply. However, Pan [10] has proved that the stress field near a *growing plane stress* crack must be fully continuous for an isotropic elastic-ideally plastic material which obeys the Prandtl-Reuss flow rule and Huber-Mises yield condition. Thus, for this specific material type at least, the principal results (3.15), (3.21), (3.22), (4.1), (4.2), (5.2), and (5.3) also apply to the plane stress case.

7 Results for Stationary Crack Tip Analysis

The derivations in Sections 3–5 are valid for the stress and stress rate fields near a quasistatically *growing* crack tip. Their extension to the case of a stationary crack is not automatic, since those results rely on the continuity of the stress field, which is necessary near a growing crack for the constitutive assumptions discussed (Drugan and Rice [6], Pan [10]), but not required near a stationary crack. However, some conclusions relevant to stationary crack tip analysis are still possible from the perspective of the preceding sections. In particular, (3.15) and hence (4.1) and (4.2) must hold if the dependence of σ_{ij} on r is continuous, which would seem to be a reasonable assumption in the limit as the crack tip is approached (since if a stress discontinuity surface were to exist, one would anticipate it to emanate from the tip, and hence to affect only the θ-dependence of σ_{ij} in the limit as $r \to 0$). This supports the assumption made by Rice and Tracey [11] in their analysis of the fields near a stationary crack tip in an isotropic elastic-ideally plastic Prandtl-Reuss-Mises solid, namely that $r\partial \sigma_{ij}/\partial r \to 0$ as $r \to 0$, and hence that the first term of (2.4) is asymptotically dominant.

If the loading applied to a cracked solid changes quasistatically while the crack remains stationary, a plausible assumption for many materials is that the near-tip stress field changes *continuously* with time. Whenever this is true, assumption (3.20) leads as before to (3.22), and since $\dot{a} = 0$ for a stationary crack (5.2) reduces to

$$\dot{\sigma}_{ij} = 0(1) \quad \text{as } r \to 0. \tag{7.1}$$

For materials that exhibit a linear relationship between the stress state and the elastic part of total strain, (7.1) implies that all *elastic* strain rate components must be bounded at a stationary crack tip given the assumptions stated above.

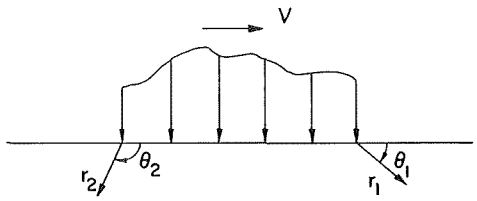

Fig. 2 Distributed load moving quasistatically, with velocity V, across the surface of an elastic-plastic body under plane strain conditions

8 Application to Related Problems

The derivations of Sections 3–5 are applicable to many problems which share a similar feature with the crack growth problems that motivated this work; in particular, problems that involve the quasistatic motion of certain geometric or load inhomogeneities through, or across the surface of, an elastic-plastic body. Just as for the crack problems, these results help elucidate the structure of the stress and stress-rate fields in the neighborhood of such a moving geometric or load inhomogeneity.

I mention just one example that will hopefully be sufficiently suggestive of the nature of related problems for which the results of this work can prove useful. Consider the plane strain problem of the quasistatic motion of a distributed load across the surface of an elastic-plastic body, as illustrated in Fig. 2. For any elastic-plastic material within the class described in Section 2, the structure of the stress and stress-rate fields in the vicinity of the leading and trailing edges of the distributed loading is delineated by the results of Sections 3–5; i.e., the asymptotic equations and expressions derived in those sections apply for r_1, θ_1 and r_2, θ_2 of Fig. 2.

Acknowledgments

Support of this work by the U.S. National Science Foundation, Solid Mechanics Program, under Grant MEA-

Downloaded 02 May 2010 to 171.66.16.54. Redistribution subject to ASME license or copyright; see http://www.asme.org/terms/Terms_Use.cfm

8312348, and by the Department of Engineering Mechanics, University of Wisconsin, is gratefully acknowledged. I am indebted to Professors R. D. James, A. C. Pipkin, and J. R. Rice for interesting and valuable discussions.

References

1 Rice, J. R., Drugan, W. J., and Sham, T-L., "Elastic-Plastic Analysis of Growing Cracks," in *Fracture Mechanics: Twelfth Conference*, ASTM STP 700, American Society for Testing and Materials, 1980, pp. 189–221.

2 Rice, J. R., "Elastic-Plastic Crack Growth," in *Mechanics of Solids: The R. Hill 60th Anniversary Volume*, Hopkins, H. G., and Sewell, M. J., eds., Pergamon Press, 1982, pp. 539–562.

3 Drugan, W. J., Rice, J. R., and Sham, T-L., "Asymptotic Analysis of Growing Plane Strain Tensile Cracks in Elastic-Ideally Plastic Solids," *Journal of the Mechanics and Physics of Solids*, Vol. 30, 1982, pp. 447–473; also Vol. 31, 1983, p. 191.

4 Drugan, W. J., "Radial Dependence of Near-Tip Continuum Fields for Plane Strain Tensile Crack Growth in Elastic-Ideally Plastic Solids," to be published.

5 Van Dyke, M., *Perturbation Methods in Fluid Mechanics*, The Parabolic Press, Stanford, Calif., 1975.

6 Drugan, W. J., and Rice, J. R., "Restrictions on Quasi-Statically Moving Surfaces of Strong Discontinuity in Elastic-Plastic Solids," in *Mechanics of Material Behavior: The D. C. Drucker Anniversary Volume*, Dvorak, G. J., and Shield, R. T., eds., Elsevier, Amsterdam, 1984, pp. 59–73.

7 Hill, R., *The Mathematical Theory of Plasticity*, Clarendon Press, Oxford, 1950; paperback, 1983.

8 Rice, J. R., "On the Structure of Stress-Strain Relations for Time-Dependent Plastic Deformation in Metals," ASME JOURNAL OF APPLIED MECHANICS, Vol. 37, 1970, pp. 728–737.

9 Rice, J. R., "Inelastic Constitutive Relations for Solids: An Internal Variable Theory and Its Application to Metal Plasticity," *Journal of the Mechanics and Physics of Solids*, Vol. 19, 1971, pp. 433–455.

10 Pan, H., "Some Discussion on Moving Strong Discontinuity Under Plane Stress Conditions," *Mechanics of Materials*, Vol. 1, 1982, pp. 325–329.

11 Rice, J. R., and Tracey, D. M., "Computational Fracture Mechanics," in *Numerical and Computer Methods in Structural Mechanics*, Fenves, S. J., et al., eds., Academic Press, 1973, pp. 585–623.

Downloaded 02 May 2010 to 171.66.16.54. Redistribution subject to ASME license or copyright; see http://www.asme.org/terms/Terms_Use.cfm

R. W. Zimmerman
Department of Mechanical Engineering,
University of California,
Berkeley, Calif. 94720

Compressibility of an Isolated Spheroidal Cavity in an Isotropic Elastic Medium

Introduction

A spheroidal cavity in an infinite, isotropic, elastic medium provides a useful model for the voids that are often present in rocks, ceramics, and porous metals. In its limiting forms, the spheroid can represent a sphere, an infinitely long cylinder, or a flat, "penny-shaped" crack. An important property of such a void is its "pore compressibility," denoted here by C_{pp}, and defined as the fractional change in the volume of the cavity resulting from the application to its surface of a hydrostatic pressure of unit magnitude. Although the problem of the elastic field around a spheroidal cavity has been examined in the past [1-3], the focus of these studies has usually been on stress concentrations. Consequently, there are certain features applicable to pore compressibility that seem to have escaped notice. One is that the pore compressibility of a *prolate* spheroid, whose shape can range from a sphere to a cylinder, is for all intents and purposes a function only of the shear modulus, and nearly independent of the compressibility of the matrix material. Also, the asymptotic expression for the pore compressibility of an *oblate* spheroid of vanishingly small aspect ratio (the usual model for the penny-shaped crack) is actually highly accurate over nearly the entire range of oblate spheroid aspect ratios.

Formulation and Solution of Problem

The problem of a pressurized, isolated, prolate spheroidal cavity in an infinite, isotropic elastic medium will be examined first. (In passing, we note that a simple change of variables renders the solution applicable to oblate spheroids.) A rectangular Cartesian coordinate system is established, with its origin at the center of the spheroidal cavity, and the coordinate axes aligned with the spheroid's axes of symmetry. The z-axis is arbitrarily chosen to coincide with the one axis of unequal length. The transformation to prolate spheroidal coordinates is accomplished by the following relations:

$$x = \sinh\alpha \sin\beta \cos\gamma,$$
$$y = \sinh\alpha \sin\beta \sin\gamma,$$
and
$$z = \cosh\alpha \cos\beta \tag{1}$$

To cover the entire three-dimensional space, α must assume values from 0 to ∞, β from 0 to π, and γ from 0 to 2π. The surfaces corresponding to constant values of α are prolate spheroids, those corresponding to constant values of β are hyperboloids, and those corresponding to constant values of γ are planes passing through the z-axis. The surface of the cavity itself corresponds to the particular value $\alpha = \alpha_o$, in which case the two equal axes have length $\sinh\alpha_o$, the unequal axis has length $\cosh\alpha_o$, and the aspect ratio (ρ) equals $\coth\alpha_o$.

It is convenient to introduce new variables defined by

$$p = \cos\beta \quad \bar{p} = \sin\beta$$
$$q = \cosh\alpha \quad \bar{q} = \sinh\alpha. \tag{2}$$

The region outside of cavity is now covered by the values $\cosh\alpha_o = q_o \le q \le \infty$, and $-1 \le p \le +1$. As this is an orthogonal system, the differential of arc-length ds has the form

$$(ds)^2 = \left(\frac{d\alpha}{h_\alpha}\right)^2 + \left(\frac{d\beta}{h_\beta}\right)^2 + \left(\frac{d\gamma}{h_\gamma}\right)^2, \tag{3}$$

where the metric coefficients h_i are given by

$$\left(\frac{1}{h_\alpha}\right)^2 = \left(\frac{1}{h_\beta}\right)^2 = q^2 - p^2,$$
$$\left(\frac{1}{h_\gamma}\right) = \bar{q}\bar{p}. \tag{4}$$

Since the cavity surface is under uniform normal pressure of magnitude P, and all stresses must vanish at an infinite distance from the cavity, the boundary conditions for the problem are:

$$\text{at } q = q_o: \quad \tau_{\alpha\alpha} = -P, \ \tau_{\alpha\beta} = \tau_{\alpha\gamma} = 0;$$
$$\text{as } q \to \infty: \quad \text{all } \tau_{ij} \to 0. \tag{5}$$

The Boussinesq three-function method, as developed in [4] (in which the case of a prolate spheroidal cavity subject to biaxial tension in the $\{x,y\}$ plane was investigated), will be used to solve the problem at hand. This method was chosen over the widely used method of Eshelby [2], primarily because it avoids the somewhat subtle energy considerations used in that approach. Furthermore, the Eshelby method is restricted to inclusions of ellipsoidal shape, while "stress-function" approaches have a wider applicability (particularly for two-dimensional problems). In the Boussinesq approach, the displacement vector $(u_x, u_y, u_z) \equiv (u, v, w)$ is derived from three harmonic functions $\{\phi, \theta, \lambda\}$ as follows:

Contributed by the Applied Mechanics Division for publication in the JOURNAL OF APPLIED MECHANICS.
Discussion on this paper should be addressed to the Editorial Department, ASME, United Engineering Center, 345 East 47th Street, New York, N.Y. 10017, and will be accepted until two months after final publication of the paper itself in the JOURNAL OF APPLIED MECHANICS. Manuscript received by ASME Applied Mechanics Division, August 1984; Final revision, January, 1985.

Copyright © 1985 by ASME
Downloaded 02 May 2010 to 171.66.16.54. Redistribution subject to ASME license or copyright; see http://www.asme.org/terms/Terms_Use.cfm

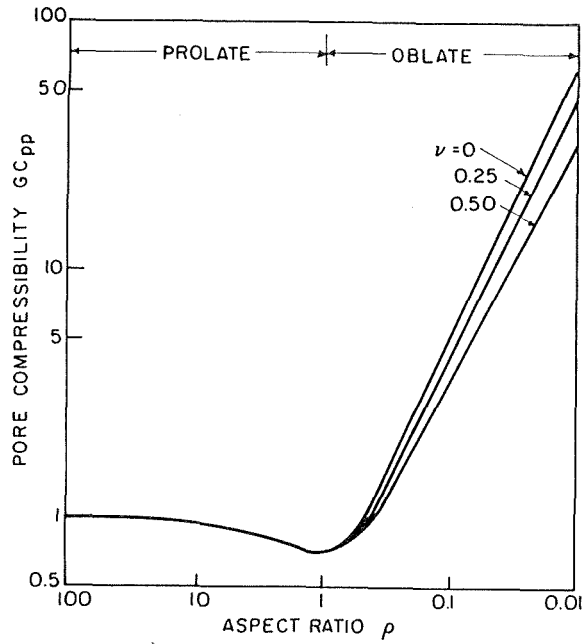

Fig. 1 Pore compressibility of a spheroidal cavity

$$2G(u,v,w) = \text{grad}\phi + 2\text{curl}(0,0,\theta) + z\text{grad}\lambda - (0,0,[3-4\nu]\lambda), \tag{6}$$

where G is the shear modulus and ν is Poisson's ratio. As long as the potentials $\{\phi,\theta,\lambda\}$ are harmonic, these displacements, and the stresses derived from them using Hooke's law, automatically satisfy the equations of static equilibrium and compatibility. Solutions to specific problems are obtained by satisfying the boundary conditions.

Following [1], in which the more general problem of a spheroidal elastic inclusion was solved, potentials of the specific form

$$\phi = A_0 S_0(q)F_0(p) + A_2 S_2(q)F_2(p),$$
$$\lambda = A_1 S_1(q)F_1(p), \tag{7}$$

are assumed, where $\{F_n, S_n\}$ are the ordinary Legendre functions of the first and second kind, and the A_n are constants to be determined from the boundary conditions at $q=q_0$. The boundary conditions at ∞ are satisfied identically by this choice (7) of stress potentials. If the stresses associated with these potentials (see [1]) are evaluated at $q=q_0$, and the boundary conditions (5) used, it is found that the constants must be:

$$A_0 = q_o\tilde{q}_o^2[2(1-2\nu)(1+2R)+3q_o^2(1+3R)]P/3D,$$
$$A_1 = -q_o\tilde{q}_o^2(1+3R)P/3D,$$
$$A_2 = -2q_o\tilde{q}_o^2[(1-2\nu)(1+2R)]P/3D,$$

where

$$R = \tilde{q}_o^2 Q_o,$$
$$Q_o = 1 + \frac{q_o}{2}\ln\frac{q_o-1}{q_o+1},$$

and

$$D = 2(1+3R)q_o^2 - 2(1+R)(\nu+R+\nu R). \tag{8}$$

The resulting volume increase of the cavity is found by integrating the normal component of the displacement (in this case, u_α) over the cavity surface. Denoting the displacement u_α due to the potential function $S_n(q)F_n(p)$ by U_n, the total displacement will be $U = A_0U_0 + A_1U_1 + A_2U_2$, and the "pore volume" increase is:

$$\Delta V_p = \int U dA = \int \Sigma A_n U_n dA = \Sigma A_n \int U_n dA. \tag{9}$$

On the cavity surface, the differential of area dA is given by

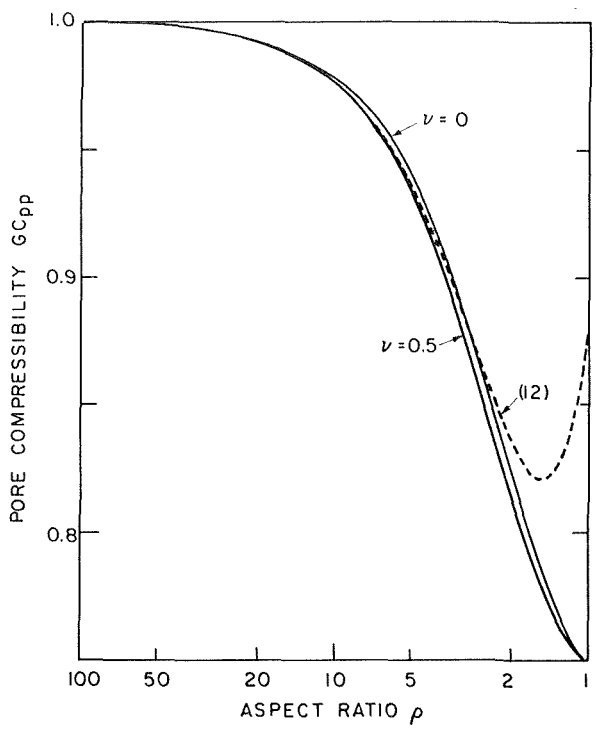

Fig. 2 Pore compressibility of a prolate spheroidal cavity

$(d\beta/h_\beta)(d\gamma/h_\gamma)$, and the surface is covered as β ranges from 0 to π, and γ ranges from 0 to 2π. The displacements U_n derived from these three potentials are given in [1], and the integrals can be evaluated as follows:

$$\int U_0 dA = \int_0^{2\pi}\int_0^{\pi} \frac{h_\beta}{2G\tilde{q}}\frac{d\beta}{h_\beta}\tilde{q}\tilde{p}d\gamma = \frac{1}{2G}\int_0^{2\pi} d\gamma \int_0^{\pi}\sin\beta d\beta = \frac{2\pi}{G};$$

$$\int U_1 dA = \int_0^{2\pi}\int_0^{\pi} \frac{h_\beta p^2[1-2(1-2\nu)R]}{2G\tilde{q}}\frac{d\beta}{h_\beta}\tilde{q}\tilde{p}d\gamma = \frac{1}{2G}\int_0^{2\pi} d\gamma\int_0^{\pi}[1-2(1-2\nu)R]\cos^2\beta\sin\beta d\beta = \frac{2\pi[1-2(1-2\nu)R]}{3G};$$

$$\int U_2 dA = \int_0^{2\pi}\int_0^{\pi} \frac{h_\beta(3p^2-1)(1+3R)}{4G\tilde{q}}\frac{d\beta}{h_\beta}\tilde{q}\tilde{p}d\gamma = \frac{(1+3R)}{4G}\times \int_0^{\pi}(3p^2-1)\tilde{p}d\beta\int_0^{2\pi} d\gamma = \frac{2(1+3R)\pi}{4G}\times \int_0^{\pi}(3\cos^2\beta-1)\sin\beta d\beta = 0. \tag{10}$$

Since the magnitude of the applied "pore pressure" is P, the pore compressibility C_{pp} is by definition equal to $\Delta V_p/V_p'P$. Use of (8), (9), and (10), along with the fact that the initial pore volume is given by $V_p' = (4\pi q_0\tilde{q}_o^2)/3$, leads to the final expression for C_{pp}:

$$C_{pp} = \frac{2(1-2\nu)(1+2R)-(1+3R)[1-2(1-2\nu)R-3q_o^2]}{4G[(1+3R)q_o^2-(1+R)(\nu+\nu R+R)]}. \tag{11}$$

This expression can be evaluated as a function of the aspect ratio ρ by using the relation $q_o^2 = \rho^2/(\rho^2-1)$, which follows from $\rho = q_o/\tilde{q}_o$ and $q_o^2 - \tilde{q}_o^2 = 1$.

The result for prolate spheroids can, through a slight

Downloaded 02 May 2010 to 171.66.16.54. Redistribution subject to ASME license or copyright; see http://www.asme.org/terms/Terms_Use.cfm

change of variables, be rendered applicable to oblate spheroids, for which the two equal axes are *longer* than the third axis. This entails replacing q with $i\bar{q}$, and $\bar{q}$ with iq, which causes the change $Q \rightarrow 1 - \bar{q}\ \text{arccot}\bar{q}$. The ensuing expression is so similar formally to that given for prolate spheroids in (11) that it need not be written out explicitly.

Results and Discussion

The resulting pore compressibilities for both prolate and oblate spheroids are plotted in Fig. 1, normalized against G. For prolate spheroids, the curves for different values of ν all coalesce at $\rho = 1$ (sphere) and $\rho = \infty$ (cylinder). For intermediate aspect ratios, the curves always lie within ± 1 percent of the $\nu = 0.25$ curve, indicating that it is the shear modulus, rather than the bulk modulus, which affects the compressibility of a prolate spheroidal pore. (For the scale used in Fig. 1, the GC_{pp} curves for different values of ν are indistinguishable for aspect ratios of one or larger). This may have useful implications for the study of the compaction of porous materials; see, in this regard, [5]. This insensitivity to Poisson's ratio also makes it possible to develop a relatively simple approximate expression for the pore compressibility of a prolate spheroidal pore which will be accurate for all values of ν, and for aspect ratios ranging from ∞ down to about 2. If the value $\nu = 0.50$ is inserted into (11), many of the terms drop out, while the term $(1 + 3R)$ cancels out of the numerator and denominator. Retaining only the leading term in the asymptotic expansion of Q_o for large values of ρ leads to the following expression for C_{pp} (see Fig. 2):

$$GC_{pp} \approx \frac{2\rho^2 + 1}{2\rho^2 + \ln 4\rho^2} \quad as \quad \rho \rightarrow \infty. \tag{12}$$

An approximate expression for the asymptotic case of very thin penny-shaped cracks can be found by starting with the first two terms of the Taylor series expansion for R about $\rho = 0$: $R \approx (\bar{q}_o/2) - 1$. Insertion of this approximation into the expression for C_{pp} leads, after some manipulation, to:

$$GC_{pp} = \frac{2(1-\nu)}{\pi\rho} + \text{terms that are finite as } \rho \rightarrow 0. \tag{13}$$

This agrees with the result that can be inferred from, for example, [6], where the limit of $\rho \rightarrow 0$ was taken *before* the equations of elasticity were solved. The most surprising feature of this asymptotic result is its range of accuracy, which extends far beyond what are usually thought of as "thin" cracks. This can be seen in Fig. 1 by the rapidity with which the curves approach the asymptotes, which appear as straight lines of unit slope on the log-log plot. In fact, for the low values of ν which are characteristic of quartzitic sandstones, for example, the simple asymptotic expression (13) could conceivably be used for the entire range of aspect ratios. This would greatly simplify the process of determining aspect ratio distributions, which are obtained by inverting sonic velocity data (see, for example, [7]).

References

1 Edwards, R. H., "Stress Concentrations Around Spheroidal Inclusions and Cavities," ASME JOURNAL OF APPLIED MECHANICS, Vol. 18, No. 1, 1951, pp. 19-27.

2 Eshelby, J. D., "The Determination of the Elastic Field of an Ellipsoidal Inclusion, and Related Problems," *Proceedings of the Royal Society of London*, Series *A*, Vol. 241, 1957, pp. 376-396.

3 Mura, T., *Micromechanics of Defects in Solids*, Martinus Nijhoff, The Hague, 1982.

4 Sadowsky, M. A., and Sternberg, E., "Stress Concentration Around an Ellipsoidal Cavity in an Infinite Body Under Arbitrary Plane Stress Perpendicular to the Axis of Revolution of Cavity," ASME JOURNAL OF APPLIED MECHANICS, Vol. 14, No. 3, 1947, pp. A191-201.

5 Bhatt, J. J., Carroll, M. M., and Schatz, J. F., "A Spherical Model Calculation for Volumetric Response of Porous Rocks," ASME JOURNAL OF APPLIED MECHANICS, Vol. 42, No. 2, 1975, pp. 363-368.

6 Sack, R. A., "Extension of Griffith's Theory of Rupture to Three Dimensions," *Proceedings of the Physical Society of London*, Vol. 58, No. 330, 1946, pp. 729-736.

7 Cheng, C. H., and Toksöz, M. N., "Inversion of Seismic Velocities for the Pore Aspect Ratio Spectrum of a Rock," *Journal of Geophysical Research*, Vol. 84, No. B13, 1979, pp. 7533-7543.

Downloaded 02 May 2010 to 171.66.16.54. Redistribution subject to ASME license or copyright; see http://www.asme.org/terms/Terms_Use.cfm

Influence of Cavity Shape on Damage Parameter

S. Jansson

U. Stigh

Division of Solid Mechanics,
Chalmers University of Technology,
S-412 96 Göteborg, Sweden

The relation between cavity shape and damage parameter is analyzed for a cavitated material. The matrix consists of isotropic, incompressible power law creeping material. The cavities are assumed to be either cylindrical or spheroidal in shape and to be well separated. Damage is defined here from the creep rate equation postulated by Rabotnov. The result shows that the damage parameter is virtually independent of the creep exponent for penny-shaped cracks and for spherical cavities. It is also observed for elongated cavities aligned to the tensile direction, that the damage parameter approaches the Kachanov-Rabotnov damage measure, equal to the area fraction of cavities in a section of a specimen. However, for all other cases the Kachanov-Rabotnov damage measure underestimates the effect of cavities on strain rate. For a plane stress or strain problem with elliptical cavities, the effect of cavity orientation on the damage parameter is shown to be severe. This indicates the need for taking cavity orientation into account when formulating creep laws for multiaxial stress states.

Introduction

The damage concept has found increasing use in applied mechanics, cf. Krajcinovic (1984). Its purpose is to describe, in continuum mechanical terms, the material deterioration that occurs in certain materials under stress, notably at high temperature and after extended time. The idea was originated by Kachanov (1958) who introduced a field variable ψ, denoted "continuity" or "soundness," in order to model brittle creep rupture. Kachanov postulated the evolution law for ψ

$$\dot{\psi} = -C(\sigma/\psi)^{\nu} \tag{1}$$

where σ denotes tensile stress, and C and ν are material constants. According to equation (1) the continuity ψ will decrease with time from an initial value ψ_0 to the final value zero at fracture. With σ = constant equation (1) shows that $\psi \to 0$ and hence $d\psi/dt \to -\infty$ after a finite time

$$t_R = \sigma^{-\nu} \frac{{\psi_0}^{\nu+1}}{C(\nu+1)} \tag{2}$$

Kachanov interpreted t_R as the brittle creep rupture time. The linear relationship between log t_R and log σ given by (2) coincides with experimental results from brittle creep rupture tests, cf. e.g., Garofalo (1965). The initial value ψ_0 may arbitrarily be taken as unity. The complementary quantity

$$\omega = 1 - \psi \tag{3}$$

will then increase with time from the initial value zero to the final value unity, which indicates rupture. It is often referred to as a damage parameter. With (3) the evolution law (1) takes the form

$$\dot{\omega} = C\left(\frac{\sigma}{1-\omega}\right)^{\nu} \tag{4}$$

Here the expression

$$\sigma_n = \frac{\sigma}{1-\omega} \tag{5}$$

may be interpreted as an "effective" or a "net" stress, which governs the damage growth rate. Rabotnov (1969) assumed that the creep rate was also governed by this net stress and postulated the creep law

$$\dot{\epsilon} = B\left(\frac{\sigma}{1-\omega}\right)^{n} \tag{6}$$

With ω increasing from zero, this predicts an increasing creep rate as manifested during the tertiary creep period. Very few successful attempts have been made to relate ω to actually occurring deterioration of the material. Various kinds of material deterioration have been observed in tests, cf. e.g., Leckie and Hayhurst (1974). Most important in this context is the formation of cavities, notably on grain boundaries in polycrystalline materials. These cavities are usually observed to be uniformly distributed (in a macroscopical sense) throughout homogeneously stressed regions, and most often to be located on grain boundaries perpendicular to the main tensile direction. Rabotnov (1969) suggested that the area fraction of cavities found in the sectioned surface of a specimen be identified as ω. This area fraction will be denoted ω_{KR} in the sequel (KR for Kachanov-Rabotnov). Although this interpretation of ω gives a good visualization of damage it implies some counterintuitive features. Since the volume fraction of cavities in a specimen is equal to the area fraction of cavities, cf. Underwood (1970), very flat cavities, i.e.,

Contributed by the Applied Mechanics Division for publication in the JOURNAL OF APPLIED MECHANICS.

Discussion on this paper should be addressed to the Editorial Department, ASME, United Engineering Center, 345 East 47th Street, New York, N.Y. 10017, and will be accepted until two months after final publication of the paper itself in the JOURNAL OF APPLIED MECHANICS. Manuscript received by ASME Applied Mechanics Division, September, 1984.

Copyright © 1985 by ASME
Downloaded 02 May 2010 to 171.66.16.54. Redistribution subject to ASME license or copyright; see http://www.asme.org/terms/Terms_Use.cfm

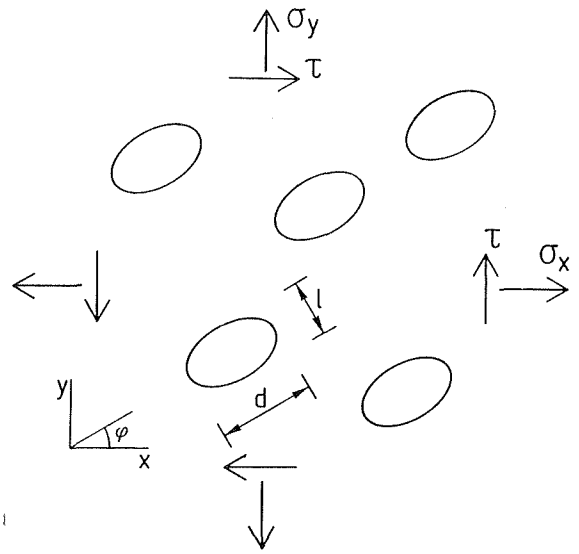

Fig. 1 Orientation and geometry of cylindrical cavities

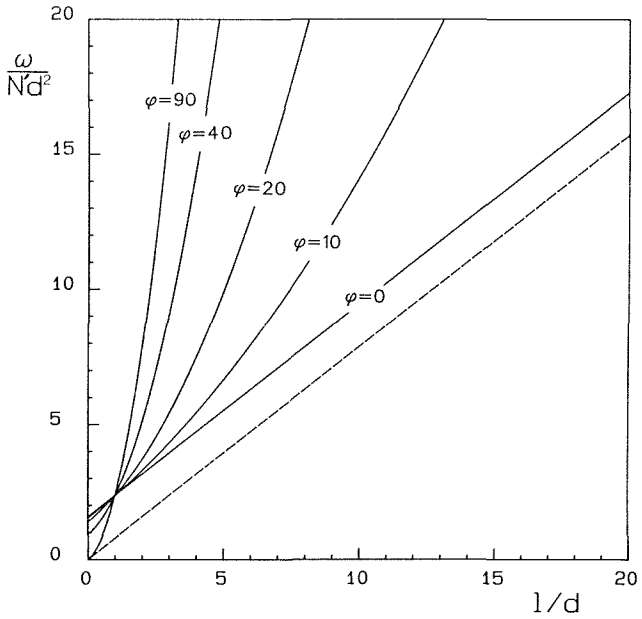

Fig. 2 Relation between damage parameters, cavity shape, and cavity orientation for cylindrical cavities. Solid lines: equation (24); dashed line: equation (7).

cracks, with average volume fraction zero, should not influence the strain rate according to Rabotnov. A means to describe the case of thin sharp cracks has been proposed by Davison and Stevens (1973). Each crack is represented by a vector normal to the crack face and with magnitude equal to the crack-face area. Karjcinovic and Ilankamban (1984) have recently suggested that each crack should be associated with an influence region of limited extent on both sides of it. This implies a nonzero area fraction even for this case and would therefore correspond to a finite value of ω_{KR} according to Rabotnov. Another characteristic of the Kachanov-Rabotnov model is that the cavity orientation does not enter the damage expression. Obviously cavities must have different influence on bulk mechanical properties at different orientation. For instance, an elongated cavity perpendicular to the load direction does have a stronger influence than one that is parallel to the load direction.

An alternative definition of ω is suggested here. It is based on equation (6). Comparison of equation (6) with micromechanical analysis of a cavitated material leads to a specific value of ω.

It is the purpose of this paper to analyze the relation between ω, as defined by (6), and cavity geometry. Two main types of cavity geometry will be considered, cylindrical and spheroidal in shape. In both cases all cavities are assumed to be equal in shape and orientation. The cavities are assumed to be randomly distributed in an incompressible, isotropic power law matrix material and to be so small in size in relation to their spacing that no interaction occurs. Only such loads will be considered where no closing of the cavities occurs. Closing and frictional sliding would complicate the analysis considerably. Such problems have been treated by Horii and Nemat-Nasser (1983) for randomly oriented sharp cracks in linearly elastic material by the self-consistent method.

Cylindrical Cavities

Parallel cylindrical cavities with elliptic cross section (principal axes d and l), extending through a plate (plane stress or plane strain) and equally oriented as shown in Fig. 1 are considered. The limiting case $l/d \to 0$ corresponds to sharp cracks of width d, and $l/d = 1$ corresponds to circular cylindrical holes. The plate is loaded in its own plane by prescribed remote stresses. The average area fraction of cavities in planes perpendicular to the x-y-plane is equal to the volume fraction of cavities, cf., Underwood (1970). Hence with N' denoting the number of cavities per unit area in the x-y-plane the Kachanov-Rabotnov damage or the area fraction is $\omega_{KR} = N' \pi l d/4$. For later interpretation this will be written in the form

$$\frac{\omega_{KR}}{N' d^2} = \frac{\pi}{4} \frac{l}{d} \tag{7}$$

shown as the dashed line in Fig. 2. This implies that sharp cracks perpendicular to the tensile direction do not influence the bulk mechanical properties, which has rightly been taken as a main argument against the soundness of the original Kachanov-Rabotnov concept. If however, crack opening is considered, then equation (7) would give nonzero damage. This would mean that damage not only measures the state of deterioration of the material but also the stress state. Such cases of load-dependent damage will however not be discussed here since this would severely limit the clearness of the damage concept. The present analysis does not consider finite deformation, i.e., the cavity shape is assumed to remain constant during load application.

Equation (7) will now be compared with the damage ω defined by equation (6). For small values of ω, corresponding to a dilute concentration of cavities, the first term in a series expansion of equation (6) gives

$$\dot{\epsilon} = B\sigma^n(1 + n\omega) \tag{8}$$

For a linearly viscous material a continuum mechanical analysis of the strain field in the plate may be performed. The method is to use the averaging procedure applied by Duva and Hutchinson (1983) and the strain energy calculation for an elliptic cavity in an infinite sheet due to Sih and Liebowitz (1967). A short recapitulation of the averaging procedure will be given for the general nonlinear case. The matrix material is characterized by a stress-potential, $\Phi(\sigma_{ij})$, such that the strain rate is given as

$$\dot{\epsilon}_{ij} = \frac{\partial \Phi}{\partial \sigma_{ij}} \tag{9}$$

A characterizing volume V of the material consists of one region occupied by the matrix material V^M and one region by the cavities V^C. The symbol $<X>$ will be used to denote the global average of the variable X. The material is then

Downloaded 02 May 2010 to 171.66.16.54. Redistribution subject to ASME license or copyright; see http://www.asme.org/terms/Terms_Use.cfm

characterized by a global stress-potential, $<\Phi(<\sigma_{ij}>)>$, such that

$$<\dot{\epsilon}_{ij}> = \frac{\partial <\Phi>}{\partial <\sigma_{ij}>} \tag{10}$$

The global potential could then be calculated from the local potential as

$$<\Phi> = \frac{1}{V}\int_{VM} \Phi \, dV \tag{11}$$

Here it has been assumed that the voids are traction-free. The global potential is then written in the form

$$<\Phi> = \Phi(<\sigma_{ij}>) + N\Phi^c \tag{12}$$

with N denoting the number of cavities per unit volume and Φ^c/V the change of global potential due to one cavity. From (11) and (12) follows

$$\Phi^c = \int_{VM} [\Phi(\sigma_{ij}) - \Phi(<\sigma_{ij}>)]dV - \Phi(<\sigma_{ij}>)V^c \tag{13}$$

which reduces to

$$\Phi^c = 2\int_0^a C^*(a)\,da \tag{14}$$

for a plane crack (with two crack tips), the crack length $2a$ being the only length parameter in the problem. Here C^* denotes the creep equivalent to the J-integral. For an elliptical cavity Φ^c is given by Sih and Liebowitz (1967) for the case of a *linear material* under plane loading conditions. It is stated here for plane stress and an incompressible matrix material with the notation of Fig. 1 and with $\varphi = 0$ in the figure.

$$\Phi^c = B\frac{\pi}{16}[(<\sigma_y> - <\sigma_x>)^2(d+l)^2 + 2(<\sigma_y>^2 - <\sigma_x>^2)(d^2 - l^2) + (<\sigma_y> + <\sigma_x>)^2(d^2+l^2) + 16<\tau>^2(d+l)^2] \tag{15}$$

Here the standard notation from linear elasticity has also been changed to conform with the previous notation for material constants. The global potential without cavities is given as

$$\Phi = \frac{B}{2}(<\sigma_x>^2 + <\sigma_y>^2 - <\sigma_x><\sigma_y> + 3<\tau>^2) \tag{16}$$

for a linear material under plane stress conditions. From (10) applied to (12) then follows, considering (15) and (16) and with $N = N'$

$$<\dot{\epsilon}_x> = B(1+\omega_x)<\sigma_x> - \frac{1}{2}B(1+\omega_{xy})<\sigma_y> \tag{17a}$$

$$<\dot{\epsilon}_y> = B(1+\omega_y)<\sigma_y> - \frac{1}{2}B(1+\omega_{xy})<\sigma_x> \tag{17b}$$

$$<\dot{\gamma}> = 3B(1+\omega_\tau)<\tau> \tag{17c}$$

Here the influence of cavities is given by

$$\omega_x = N'\frac{\pi}{2}(l^2 + ld/2) \tag{18a}$$

$$\omega_y = N'\frac{\pi}{2}(d^2 + ld/2) \tag{18b}$$

$$\omega_{xy} = N'\frac{\pi}{2}ld \tag{18c}$$

$$\omega_\tau = N'\frac{\pi}{6}(l+d)^2 \tag{18d}$$

The designations ω_x etc. have been chosen to obtain conformity with equation (8). The transformation rule for (17) to a coordinate system of different orientation is given explicitly by Lekhnitskii (1967). By means of this the case $\varphi \neq 0$ in Fig. 1 may be obtained. For this transformation (17), (18c), and (18d) remain unchanged but (18a) and (18b) change to

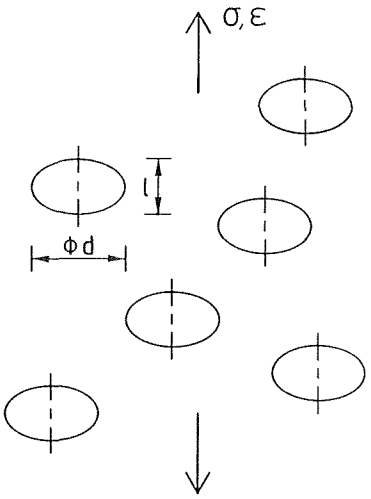

Fig. 3 Orientation and geometry of spheroidal cavities

$$\omega_x = N'\frac{\pi}{2}(l^2\cos^2\varphi + ld/2 + d^2\sin^2\varphi) \tag{19a}$$

$$\omega_y = N'\frac{\pi}{2}(l^2\sin^2\varphi + ld/2 + d^2\cos^2\varphi) \tag{19b}$$

It should be noted that the damage measures are interrelated through

$$\omega_{xy} = 3\omega_\tau - \omega_x - \omega_y \tag{20}$$

A similar calculation for plane strain yields

$$<\dot{\epsilon}_x> = \frac{3}{4}B(1+\omega_x)<\sigma_x> - \frac{3}{4}B(1+\omega_{xy})<\sigma_y> \tag{21a}$$

$$<\dot{\epsilon}_y> = \frac{3}{4}B(1+\omega_y)<\sigma_y> - \frac{3}{4}B(1+\omega_{xy})<\sigma_x> \tag{21b}$$

$$<\dot{\gamma}> = 3B(1+\omega_\tau)<\tau> \tag{21c}$$

with

$$\omega_x = N'\frac{\pi}{2}(l^2\cos^2\varphi + ld/2 + d^2\sin^2\varphi) \tag{22a}$$

$$\omega_y = N'\frac{\pi}{2}(l^2\sin^2\varphi + ld/2 + d^2\cos^2\varphi) \tag{22b}$$

$$\omega_{xy} = N'\frac{\pi}{4}ld \tag{22c}$$

$$\omega_\tau = N'\frac{\pi}{8}(d+l)^2 \tag{22d}$$

where

$$2\omega_{xy} = 4\omega_\tau - \omega_x - \omega_y \tag{23}$$

It follows that a complete characterization of the damage requires three parameters as to be expected. The equations (18), (19), and (22) show that the damage could be split up in three parts corresponding to two perpendicular cracks with length l and d and one volumetric part proportional to ld. The damage must have a volumetric part to influence the relation between a perpendicular stress and strain rate. For comparison with the Kachanov-Rabotnov result (uniaxial stress) we write (19b) or the identical (22b) in the form

Downloaded 02 May 2010 to 171.66.16.54. Redistribution subject to ASME license or copyright; see http://www.asme.org/terms/Terms_Use.cfm

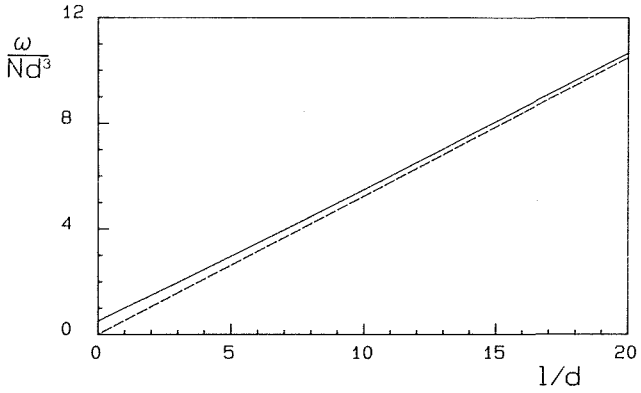

Fig. 4 Relation between damage parameters and cavity shape for spheroidal cavities. Solid line: Eshelby's solution, equations (33) and (34); dashed line: equation (25).

$$\frac{\omega}{N'd^2} = \frac{\pi}{4}[2 + l/d - 2(1-(l/d)^2)\sin^2\varphi] \tag{24}$$

The quantities ω and ω_{KR} are shown as functions of l/d and φ in Fig. 2.

The anisotropy effect is seen to be large (except, of course, for $l/d=1$). For large l/d and $\varphi=0$ we have $\omega/\omega_{KR}\to 1$ as should be expected since this is the case of slots parallel to the tensile direction, where no stress concentration exists. Hence the Kachanov-Rabotnov concept applies. For other l/d and φ the quantity ω_{KR} underestimates the damage effect.

The result applies also in the case of cavities of different size, but still of the same shape and orientation, simply by replacing $N'd^2$ with $(1/A)\,\Sigma d_i^2$ in equation (24), where the summation extends over all cavities in the loaded area A.

Spheroidal Cavities

Spheroidal cavities (principal axes d, d and l) are considered, cf. Fig. 3. The limiting case $l/d\to 0$ corresponds to penny-shaped cracks, $l/d=1$ corresponds to spherical holes, and $l/d\to\infty$ corresponds to parallel "needles" with maximum diameter d. Uniaxial stress σ is applied parallel to the rotational symmetry axis of the cavities. The average area fraction of cavities in planes perpendicular to σ (being equal to the volume fraction of cavities, cf. Underwood (1970)) is determined as for cylindrical cavities, from which

$$\frac{\omega_{KR}}{Nd^3} = \frac{\pi}{6}\frac{l}{d} \tag{25}$$

where N denotes the number of cavities per unit volume. Equation (25) is represented by the dashed straight line in Fig. 4.

The overall response of a *linearly viscous solid*, $n=1$, containing spheroidal cavities has been obtained from Eshelby's solution (1957), as outlined by Russel (1973). Here we will give a brief description of the method used by Russel to calculate the effective moduli of a composite material. Start with a large homogeneous body with the isotropic stress-strain relation $\sigma_{ij}=C_{ijkl}\epsilon_{kl}$ not varying with position. An ellipsoidal part centered in the body is then cut out and its shape is changed, giving it a homogeneous strain ϵ_{ij}^T and no stress. As shown by Eshelby (1957) the strain ϵ_{ij}^c inside the ellipsoid remains homogeneous after it has been put back into the body. The constrained strain ϵ_{ij}^c is given by

$$\epsilon_{ij}^c = S_{ijkl}\epsilon_{kl}^T \tag{26}$$

where S_{ijkl} depends on the geometry of the ellipsoid and Poisson's ratio ν. Then apply a homogeneous strain ϵ_{ij}^A to the body. The volume average of stress is

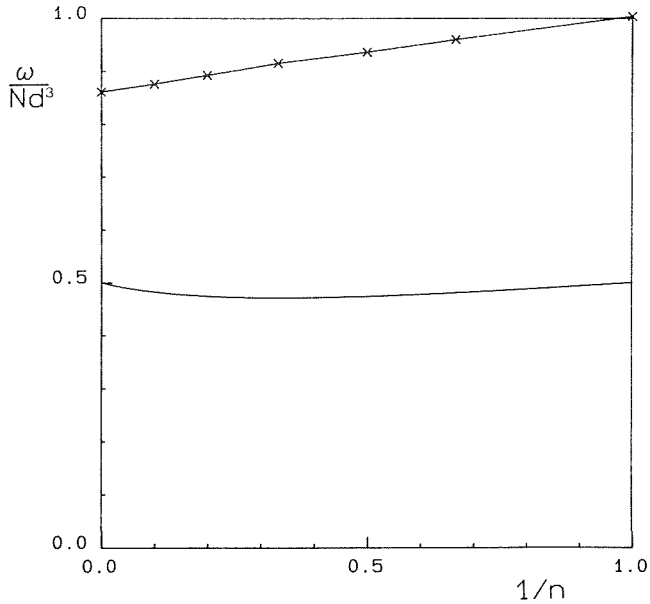

Fig. 5 Variation of damage parameter with creep exponent. Upper line: spherical cavities; lower line: penny-shaped cracks.

$$<\sigma_{ij}> \equiv \frac{1}{V}\int_V \sigma_{ij}dV = \frac{1}{V}\left[\int_V C_{ijkl}\epsilon_{kl}dV + \int_{V^c}(\sigma_{ij} - C_{ijkl}\epsilon_{kl})dV\right] = C_{ijkl}<\epsilon_{kl}> + \frac{V^c}{V}(\sigma_{ij} - C_{ijkl}\epsilon_{kl}) \tag{27}$$

The last equality follows from the fact that σ_{ij} and ϵ_{ij} are constant inside the ellipsoid with volume V^c. The stress and strain inside the ellipsoid are given by

$$\sigma_{ij} = C_{ijkl}(\epsilon_{kl}^A + \epsilon_{kl}^c - \epsilon_{kl}^T) \tag{28}$$

$$\epsilon_{ij} = \epsilon_{ij}^A + \epsilon_{ij}^c \tag{29}$$

Now rewrite equation (27) with equations (28) and (29)

$$<\sigma_{ij}> = C_{ijkl}<\epsilon_{kl}> - \frac{V^c}{V}C_{ijkl}\epsilon_{kl}^T \tag{30}$$

Consider next the special case of a spheroidal cavity with symmetry axis parallel to the x_3-axis. The effective longitudinal Young's modulus E_l is found by choosing $\epsilon_{11}^A=\epsilon_{22}^A=\epsilon_{rr}^A$ and ϵ_{33}^A as the only nonzero components of ϵ_{ij}^A. Determine ϵ_{ij}^T from equation (28) to give zero stress inside the spheroid. The solution to this equation is written by Russel as

$$\epsilon_{ij}^T = A_{ijkl}\epsilon_{kl}^A \tag{31}$$

Determine ϵ_{rr}^A so that $<\sigma_{11}> = <\sigma_{22}> = 0$ and $<\sigma_{33}> \neq 0$. The longitudinal modulus E_l is then found to be

$$E_l = \frac{<\sigma_{33}>}{<\epsilon_{33}>} = E\left\{1 - \frac{V^c}{V}[A_{3333} - \nu(A_{3311} + A_{3322})]\right\} \tag{32}$$

where ν is set equal to 1/2 giving an incompressible matrix material. There results after identification with equation (8) and use of the elastic analogy a closed form expression giving ω as a function of Nd^3 and l/d.

$$\frac{\omega}{Nd^3} = \frac{\pi}{24}\frac{\left(6-\frac{3}{2}\frac{l}{d}I\right)\left(1-\left(\frac{l}{d}\right)^2\right)+3-\frac{9}{4}\frac{l}{d}I}{\frac{3}{8}I\left(2-\frac{3}{2}\frac{l}{d}I\right)\left(1-\left(\frac{l}{d}\right)^2\right)+\left(3-\frac{9}{4}\frac{l}{d}I\right)\frac{l}{d}} \tag{33}$$

where

Downloaded 02 May 2010 to 171.66.16.54. Redistribution subject to ASME license or copyright; see http://www.asme.org/terms/Terms_Use.cfm

$$I=\begin{cases}2\left[\arccos\frac{l}{d}-\frac{l}{d}\left(1-\left(\frac{l}{d}\right)^2\right)^{1/2}\right]\Big/\left(1-\left(\frac{l}{d}\right)^2\right)^{3/2}, & \frac{l}{d}<1\\ 2\left[\frac{l}{d}\left(\left(\frac{l}{d}\right)^2-1\right)^{1/2}-\operatorname{arccosh}\frac{l}{d}\right]\Big/\left(\left(\frac{l}{d}\right)^2-1\right)^{3/2}, & \frac{l}{d}>1\end{cases} \tag{34}$$

The result is plotted in Fig. 4. For very elongated cavities, $l/d\to\infty$, ω approaches ω_{KR}. In this extreme case of parallel needle shaped cavities the stress field will be uniform throughout, and hence the Kachanov-Rabotnov concept applies. But for the more interesting case of oblate cavities, as observed late in the creep rupture process, ω_{KR} is seen severely to underestimate the influence of cavities on strain rate.

For a linearly elastic solid with aligned elliptical, as opposed to penny-shaped cracks loaded perpendicular to the crack face, Budiansky and O'Connell (1976) have given the change in strain energy due to the introduction of a crack as

$$\Phi^C=B\frac{\pi}{8}\frac{<\sigma>^2 d_1 d_2^2}{E'(d_2/d_1)} \tag{35}$$

Here d_1 and d_2 are the major and minor axes of the elliptical crack, and E' the associated complete elliptic integral of the second kind. With the averaging procedure, equations (9) to (13), there follows

$$<\dot\epsilon>=B<\sigma>\left(1+N\frac{\pi}{4}\frac{d_1 d_2^2}{E'(d_2/d_1)}\right) \tag{36}$$

Identification of ω with equation (8) gives

$$\omega=\frac{\pi}{4}\frac{N}{E'(d_2/d_1)}d_1 d_2^2 \tag{37}$$

Normalization gives

$$\frac{\omega}{N(d_1 d_2)^{3/2}}=\frac{\pi}{4}\frac{(d_2/d_1)^{1/2}}{E'(d_2/d_1)} \tag{38}$$

where the right-hand side is quite insensitive to variations in d_2/d_1. For $0.8\le d_2/d_1\le 1$ the error introduced by taking the right-hand side equal to 1/2 is less than 1 percent. This means that for nearly circulary shaped elliptical cracks d should be replaced by $\sqrt{d_1 d_2}$. For $d_2/d_1\to 0$ this approximation degenerates and equation (38) has to be used.

For a *power law* viscous material ($1<n<\infty$) the influence of a dilute concentration of penny-shaped cracks or spherical cavities on the overall strain rate is given by Duva and Hutchinson (1984). They used the concepts of equations (9) to (13) and solutions from He and Hutchinson (1981) and Budiansky, Hutchinson and Slutsky (1982). Identification of ω using equation (8), gives for penny-shaped cracks

$$\frac{\omega}{Nd^3}=\frac{1}{2}(1+1/n)(1+3/n)^{-1/2} \tag{39}$$

and for spherical cavities

$$\frac{\omega}{Nd^3}=\frac{\pi}{6}(1+1/n)(f^*+\kappa/18) \tag{40}$$

where f^* and κ are tabulated functions of n given by Duva and Hutchinson (1984). The variation of ω with the inverse of the creep exponent is given in Fig. 5. The figure shows that the influence of the creep exponent is very small for cracks (less than 6 percent) and somewhat larger for spheres (less than 15 percent). For $l/d\to\infty$ the influence of the creep exponent will vanish since the stress state is then uniaxial, and the Kachanov-Rabotnov concept applies again.

The result is again readily extended to cases with cavities of different size (but still of the same shape and orientation). Expressions Nd^3 will then be replaced by $(1/V)\Sigma d_i^3$ where the summation extends over all cavities in the loaded volume V.

Conclusions and Discussion

The present analysis, which includes stress concentration effects, shows that the Kachanov-Rabotnov creep damage measure ω_{KR}, equal to the relative area of cavities in a section of a specimen, underestimates the effect of cavities upon strain rate.

For dilute concentrations of cavities, the damage parameter ω, defined by the influence of cavities on strain rate, is shown to be virtually independent of the power law creep exponent for the cases of penny-shaped cracks and spherical cavities. It is given by

$$\omega\approx 0.5Nd^3 \tag{41}$$

for penny-shaped cracks, and

$$\omega\approx Nd^3 \tag{42}$$

for spherical cavities. For elongated cavities (no stress concentration) ω approaches ω_{KR}. As could be expected, it has thus been shown that the effect of cavity shape is substantial. For the same number of cavities per unit volume spherical cavities have approximately twice as large influence on the damage parameter as cracks with equal diameter.

An extension to nonuniform size distribution of cavities is easily performed.

The anisotropy effect is large for material with oriented oblate cavities and has to be taken in consideration when formulating multiaxial creep-laws for such materials.

It seems promising that the influence of cavities calculated from the linear solutions could be generalized, with some effort, to power-law creep due to the net stress concept.

A comparison with the numerical results presented by Iwakuma and Nemat-Nasser (1983) for high concentrations of spherical cavities arranged in a cubic array in a linear-elastic solid shows that the strain rate will be overestimated by equation (42). That is, the cavitated material will be stiffer than predicted by the dilute concentration calculation. The results presented were however calculated with Poisson's ratio equal to 0.3 for a cubic array of spherical cavities. They should therefore be used with care since Poisson's ratio and the cavity arrangement both have strong influence.

It is important to realize that for a full description of the creep damage and rupture process, several different mechanisms must be included into the analysis, c.f. Cocks and Ashby (1982). As an example could be mentioned viscous change of cavity shape and size due to stress state and time. For a recent treatment of this particular problem see Budiansky, Hutchinson, and Slutsky (1982), where references are also given to previous work.

Acknowledgment

We wish to express our gratitude to Professor Jan Hult for fruitful discussions during the work.

References

Budiansky, B., Hutchinson, J. W., and Slutsky, S., 1982, "Void Growth and Collapse in Viscous Solids," *Mechanics of Solids, the Rodney Hill 60th Anniversary Volume*, Hopkins, H. G., and Sewell, M. J., eds., Pergamon Press, Oxford, pp. 13-45.

Budiansky, B., and O'Connell, R. J., 1976, "Elastic Moduli of a Cracked Solid," *International Journal of Solids and Structures*, Vol. 12, pp. 81-97.

Cocks, A. C. F., and Ashby, M. F., 1982 "On Creep Fracture by Void Growth," *Progress in Materials Science*, Vol. 27, pp. 189-244.

Downloaded 02 May 2010 to 171.66.16.54. Redistribution subject to ASME license or copyright; see http://www.asme.org/terms/Terms_Use.cfm

Davison, L., and Stevens, A. L., 1973, "Thermomechanical Constitution of Spalling Elastic Bodies," *Journal of Applied Physics*, Vol. 44, pp. 668-674.

Duva, J. M., and Hutchinson, J. W., 1983, "Constitutive Potentials for Dilutely Voided Nonlinear Materials," *Mechanics of Materials*, Vol. 3, pp. 41-54.

Eshelby, J. D., 1957, "The Determination of the Elastic Field of an Ellipsoidal Inclusion, and Related Problems," *Proceedings of the Royal Society*, of London, Series *A*, Vol. 241, pp. 376-396.

Garofalo, F., 1965, *Fundamentals of Creep and Creep-Rupture in Metals*, Macmillan Series in Materials Science, New York.

He, M. Y., and Hutchinson, J. W., 1981, "The Penny-Shaped Crack and the Plane Strain Crack in an Infinite Body of Power-Law Material," ASME JOURNAL OF APPLIED MECHANICS, Vol. 48, pp. 830-840.

Horii, H., and Nemat-Nasser, S., 1983, "Overall Moduli of Solids With Microcracks: Load-Induced Anisotropy," *Journal of the Mechanics and Physics of Solids*, Vol. 31, pp. 155-171.

Iwakuma, T., and Nemat-Nasser, S., 1983, "Composites With Periodic Microstructure," *Computers and Structures*, Vol. 16, pp. 13-19.

Kachanov, L. M., 1958, "On the Time to Failure Under Creep Conditions," *Izv. Akad. Nauk SSSR, Otd. tekhn. n.*, No. 8, pp. 26-31.

Krajcinovic, D., 1984, "Continuum Damage Mechanics," *Applied Mechanics Reviews*, Vol. 37, pp. 1-6.

Krajcinovic, D., and Ilankamban, R., 1984, "Continuous Damage Mechanics of Rock Materials," Presented at the *Sixteenth International Congress of Theoretical and Applied Mechanics*, August 19-25, Lyngby, Denmark.

Leckie, F. A., and Hayhurst, D. R., 1974, "Creep Rupture of Structures," *Proceedings of the Royal Society London,* Series *A*, Vol. 340, pp. 323-347.

Lekhnitskii, S. G., 1968, *Anisotropic Plates*, Gordon and Breach Science Publishers, New York, pp. 37-41.

Rabotnov, Y. N., 1969, "Creep Rupture," *Proceedings of the Twelfth International Congress of Applied Mechanics*, Hetényi, M., and Vincenti, W. G., eds., Springer-Verlag, Berlin, pp. 342-349.

Russel, W. B., 1973, "On the Effective Moduli of Composite Materials: Effect of Fiber Length and Geometry at Dilute Concentrations," *Journal of Applied Mathematics and Physics (ZAMP)*, Vol. 24, pp. 581-600.

Sih, G. C., and Liebowitz, H., 1967, "On the Griffith Energy Criterion for Brittle Fracture," *International Journal of Solids and Structures*, Vol. 3, pp. 1-22.

Underwood, E. E., 1970, *Quantitative Stereology*, Addison-Wesley, Reading, Massachusetts, pp. 25-27.

Downloaded 02 May 2010 to 171.66.16.54. Redistribution subject to ASME license or copyright; see http://www.asme.org/terms/Terms_Use.cfm

A Physically Based Constitutive Equation for Creep-Damaging Solids

A. J. Levy
Department of Mechanical and Aerospace Engineering
Syracuse University,
Syracuse, N.Y. 13210
Assoc. Mem. ASME

Uniaxial and multiaxial forms of a constitutive equation, characterizing the creep-damaging behavior of metals at elevated temperatures, are developed based on Dyson's constrained cavity growth mechanism. The model employs a single scalar internal variable which can be identified with the area fraction of cavitated boundaries. This variable, together with the power law creep model is capable of describing steady creep, tertiary creep, and dilatation arising from the nucleation and growth of grain boundary cavities.

1 Introduction

It is well known that cavitation in polycrystalline metals, i.e., the nucleation and growth of cavities on grain boundaries approximately normal to the maximum tensile axis may occur when these materials are subjected to creep. The phenomenon of an accelerated strain rate (tertiary creep), commonly observed in tensile tests prior to failure, can be attributed to cavitation provided the applied load is a constant stress. Indeed recent work ([1-3]) has suggested that cavitation may be responsible for an enhanced secondary creep rate as well. The experiments of Dyson et al. [1], as well as those of Needham and Greenwood [4], have indicated that in metals where cavitation is present the strain rate is influenced by the entire state of stress. This result is in direct opposition to classical plasticity theory which assumes that the strain rate is proportional to the stress deviator and, the effective strain is a function of effective stress. The same experiments have also indicated that there is dilation in creep, a result also at odds with classical plasticity theory. In Dyson's work, experiments were performed on two sets of specimens, one set having undergone a special treatment designed to "dope" the grain boundaries with cavities. Treated and untreated specimens were deformed under identical conditions and the difference in axial strain was manifested in an enhanced secondary creep rate (but no tertiary creep) for the treated specimen. Since the untreated specimens were found to have a "near zero" damage rate it can be assumed that cavity growth (that is, the growth of the artificially induced cavities) in the treated specimens dominated the cavitation process as opposed to nucleation. Furthermore the experiments of Needham and Greenwood have indicated that the effect of pressure does not influence the creep rate through its effect on the fractional change in volume. From these results it can be inferred that tertiary creep under a constant applied stress is a consequence of the nucleation of cavities but not necessarily their growth. This aspect of the behavior, along with the others just noted, should be accounted for in a realistic theory of tertiary creep.

The purpose of this paper is to develop a physically based creep-damage constitutive equation for use in multiaxial stress analyses. The present work is concerned with steady creep and tertiary creep arising from grain boundary cavitation. Transient as well as elastic effects have been ignored however these can be included in the model without much difficulty (see for example [5, 6]). In the following two sections the basic model is described and equations for the strain rate and dilatation rate, under conditions of uniaxial tension, are presented. The strain rate equation, which resembles the power law for steady creep, involves an empirical function of the applied stress that can be identified with the nucleation rate. Next, the uniaxial equation for the strain rate is integrated and the creep strain and dilatation are determined as functions of time. Approximate values for times to fracture are determined as functions of the material parameters and applied stress and the behavior of the model is compared with experiment. The paper concludes with a generalization of the uniaxial equations to multiaxial form which is valid for complex states of stress.

2 The Strain Rate Equation

The strain rate equation presented here is based on a model developed by Dyson et al. [1] for metals with a constant, initially fixed cavity density, i.e., nucleation effects and hence tertiary creep were not considered. In that work volume changes due to cavitation are not accounted for. The current effort is aimed at the development of a concise uniaxial model that accounts for tertiary creep as well as dilatational effects.

The basis for the model presented here is the constrained cavity growth mechanism [7]. The idea is that a polycrystalline metal under typical creep conditions i.e., high temperatures and low to moderate stresses may contain, at any stage in its deformation history, many uncavitated grain boundaries. In fact, this will generally be the case since nucleation is a continuous process occurring throughout the

Contributed by the Applied Mechanics Division for publication in the JOURNAL OF APPLIED MECHANICS.
Discussion on this paper should be addressed to the Editorial Department, ASME, United Engineering Center, 345 East 47th Street, New York, N.Y. 10017, and will be accepted until two months after final publication of the paper itself in the JOURNAL OF APPLIED MECHANICS. Manuscript received by ASME Applied Mechanics Division, April, 1984; final revision, November, 1984.

Copyright © 1985 by ASME
Downloaded 02 May 2010 to 171.66.16.54. Redistribution subject to ASME license or copyright; see http://www.asme.org/terms/Terms_Use.cfm

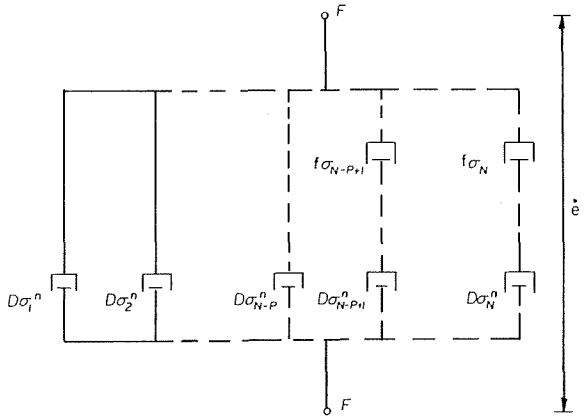

Fig. 1 Mechanical dashpot representation of a creep-cavitating body

deformation. A cavitated grain will generally deform due to power law creep (dislocation creep) within the grain and also, due to the diffusional growth of cavities in the grain boundary.[1] Under the stated conditions of stress and temperature, the deformation rate due to cavity growth will exceed that due to creep within the cavitated grain [7]. As a result its deformation will be limited (constrained) by the adjacent uncavitated grains deforming solely by power law creep. Hence the local stress in the cavited grain will fall off while the overall rate of deformation of the grain will be enhanced.

This concept can be best illustrated by the following simple mechanical analogue. Consider the system of one and two-dashpot elements shown in Fig. 1. The one-dashpot elements model grains deforming solely by power law creep while the two-dashpot elements correspond to grains deforming by both power law creep and grain boundary cavitation. Let there be a total of N elements with the strain rate in the one-dashpot elements (uncavitated grains) given by

$$\dot{e}_i = D(\sigma_i)^n, \quad i = 1,2,\ldots,N-P \tag{1}$$

where σ_i is the stress in the ith element and D and n are material parameters. At some instant during the deformation let there be P two-dashpot elements (cavitated grains) with strain rate given by

$$\dot{e}_i = D(\sigma_i)^n + f_i\sigma_i, \quad i = N-P+1,\ldots N \tag{2}$$

where the last term represents the contribution of cavitation to the strain rate while f_i will generally depend on the cavity volume and density. Since the elements are connected in parallel, the strain rates in the two-dashpot elements are constrained to equal the rates in the one-dashpot elements, thus

$$\dot{e} \equiv \dot{e}_1 = \dot{e}_2 = \ldots = \dot{e}_{N-P} = \dot{e}_{N-P+1} = \ldots = \dot{e}_N \tag{3}$$

For the range of stresses and temperatures considered here the strain rate due to cavitation will exceed that due to dislocation creep[1] and

$$f_i\sigma_i >> D(\sigma_i)^n \quad i = N-P+1, \ldots, N \tag{4}$$

which implies that the stresses in the two-dashpot elements must be very small. Equilibrium of forces acting on the system of dashpots results in the equation

$$N\sigma = \sum_{i=1}^{N-P} \sigma_i + \sum_{i=N-P+1}^{N} \sigma_i$$

and if we assume that the stresses in the two-dashpot elements are so small as to be neglected, then

$$N\sigma = \sum_{i=1}^{N-P} \sigma_i \tag{5}$$

Furthermore, by combining (1), (3), and (5) the following equations are obtained

$$\sigma_i = \sigma/(1-P/N) \quad i = 1,2, \ldots, N-P \tag{6}$$

and

$$\dot{e} = D[\sigma/(1-P/N)]^n \tag{7}$$

The quantity P/N can be identified as the number fraction, or the area fraction of cavitated grain boundaries since it has been implicitly assumed that the area of all the grain boundaries are equal. This assumption effectively uncouples the strain rate from the cavity volume. It is reasonable for many materials where the area of the cavities in the boundary is small compared to the grain boundary area. In the present theory P/N is not constant but is an increasing function of either strain or time and will be denoted by the continuous variable ω. In this physically based theory it will be advantageous to have an expression governing the evolution of the area fraction of cavitated boundaries ω that, in some sense, characterizes the actual cavity nucleation process. To this end, we now consider the nucleation of cavities and its effect on the strain rate.

It is generally believed that for many materials under typical creep conditions of stress and temperature considered here, cavity nucleation on grain boundaries is a continuous process occurring throughout the deformation of a material. Experimental evidence ([10, 11]) also tends to indicate that the nucleation of cavities is strain dependent and not time dependent and that, at least initially, this dependence is linear. Although there is still some doubt as to the basic mechanism of grain boundary nucleation a number of micromechanical models have been proposed ([11, 12]). These models assume that cavities form on boundaries subject to unusually high tensile stresses or stress concentrations which can arise by either the sliding of grain boundaries containing rigid particles or possibly localized grain deformation which can be caused by the intersection of slip bands and grain boundary particles. Since nucleation occurs continuously, local grain boundary sliding (or local grain deformation), and hence cavity formation, must be a random process occurring throughout the creep life of the material.

The use of the models noted in the foregoing in determining an equation governing the evolution of the area fraction can be circumvented by taking the number of cavities in the grain boundary $A_b\rho$, where A_b is the grain boundary area and ρ the cavity density, to be a Poisson random process with the strain as parameter (recall that due to the constraint mechanism the local grain strain is equal to the axial strain). This assumption necessarily implies that (1) the formation of cavities is independent of previous formations, (2) the probability of formation of a cavity in a strain interval is equal to the probability of formation in any other interval, and (3) the probability that two or more cavities will form in a strain interval is negligible. The probability that the number of cavities on a boundary will be a certain value k in a strain interval $[0, e]$ is then given by

$$P[A_b\rho(e) = k] = [(\lambda e)^k/k!]\exp(-\lambda e) \tag{8}$$

and the expected value of the number of cavities formed on a boundary in $[0, e]$ is simply

$$E[A_b\rho(e)] = \lambda e, \quad \lambda > 0$$

where λ is the rate of formation of cavities or nucleation rate, which is independent of strain but will generally depend on the applied stress i.e.,

$$\rho(e) = [\lambda(\sigma)/A_b]e \tag{9}$$

Equation (9) is a semi-empirical equation since the exact role

[1] Studies [8, 9] on the diffusional growth of cavities in polycrystalline metals have indicated that the growth rate of an individual cavity arising from this mechanism is proportional to the first power of the local stress, i.e., the stress acting directly on the grain boundary.

Downloaded 02 May 2010 to 171.66.16.54. Redistribution subject to ASME license or copyright; see http://www.asme.org/terms/Terms_Use.cfm

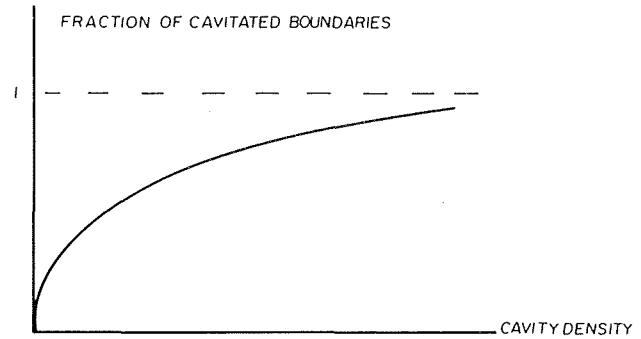

Fig. 2 Functional relationship between area fraction and cavity density

that the applied stress plays in the nucleation process is not considered. The function λ, which may now be considered as the average over all the boundaries, must be determined from experimental curves of cavity density versus strain at different applied stresses. It should be noted that the argument just given assumes no statistical dependence among the cavity densities on the individual grain boundaries. Although strictly speaking this cannot be true the difference in cavity densities on the boundaries, which probably arise from the orientation of adjacent grains and the density of grain boundary particles, are accounted for since the nucleation rates on the boundaries can differ. The average nucleation rate will inevitably be obtained from macroscopic creep fracture data. Therefore the exact nature of the relationship between the cavity density and the structure is, for this model unecessary. Although this is an oversimplification it does lead to an equation for the cavity density which is consistent with experiment i.e., a linear relationship between the cavity density and the strain.

The equation just developed is a relationship between the number of cavities per unit area of grain boundary and the strain. We have seen however that the quantity directly affecting the strain rate is the area fraction of cavitated boundaries and not the cavity density. A simple relationship between these two variables can be obtained in the following manner. Let $\mathfrak{N}(e)$ be the total number of cavities that exist at strain e on all boundaries normal to the tensile axis with area A_b,

$$\mathfrak{N}(e) = NA_b\rho(e)$$

also, the total number of cavities formed in an interval Δe is

$$\dot{\mathfrak{N}}(e)\Delta e = NA_b\dot{\rho}(e)\Delta e \tag{10}$$

Since the cavities nucleate independently of each other in the interval Δe it is reasonable to assume that the number of cavities formed on boundaries, that at strain e were uncavitated, is simply $f\dot{\mathfrak{N}}(e)\Delta e$ with $0 < f \le 1$. The quantity f can be identified with the probability that one cavity will form in Δe on a boundary which at strain e was uncavitated. Generally, f will not be constant but will depend on either the strain or the time. A little reflection should indicate that f depends critically on the number of uncavitated boundaries. In fact, f can be identified with the fraction of uncavitated boundaries and hence

$$f(e) = 1 - \omega(e), \quad 0 < f \le 1$$

Therefore the number of cavities appearing in Δe on boundaries that at strain e were uncavitated is simply $[1 - \omega(e)]\dot{\mathfrak{N}}(e)\Delta e$. Moreover, it is reasonable to assume that, in the interval Δe, the probability of two or more cavities forming on a single boundary, which at strain e was uncavited, will be small. The following approximate relationship may then be obtained

$$(1 - \omega)\dot{\mathfrak{N}}\Delta e = \dot{P}\Delta e \tag{11a}$$

which states that the number of cavities formed in Δe on previously uncavitated boundaries is approximately equal to the number of newly cavitated boundaries formed in Δe. This equation together with (10) can be combined to form the following relationship between the cavity density and the area fraction of cavitated boundaries

$$A_b\, d\rho = d\omega/(1 - \omega), \quad 0 \le \omega < 1, \ \rho \ge 0 \tag{11b}$$

The solution to this equation is immediately seen to be

$$\omega = 1 - \exp(-A_b\rho) \tag{12}$$

where we have made use of the fact that the initial density must be zero when the initial area fraction is zero. The simple functional relationship given by (12) is depicted in Fig. 2. As more and more cavities are nucleated an increasingly greater percentage of these form on already cavitated boundaries. The area fraction of cavitated boundaries must then increase but with decreasing slope which asymptotically approaches zero as the cavity density approaches infinity. Of course the specimen will fail due to the coalescense of cavities and the formation of cracks well before that point is reached.

To determine the relationship between the area fraction ω and the strain we employ (12) and (8). Then the expected value of ω is

$$\omega(e) = E\{1 - \exp[-A_b\rho(e)]\} \tag{13}$$

where the probability distribution for $A_b\rho$ is given by (8). But the expectation of a function of a random variable is just

$$E[f(X)] = \sum_X f(x)p(x)$$

where $p(x)$ is the probability density function. An application of this formula to (13) yields the following

$$\omega(e) = 1 - \exp(-\bar{\lambda}e) \tag{14}$$

where $\bar{\lambda}$ is given by

$$\bar{\lambda} = 0.632\lambda$$

Equation (14) is the desired expression describing the evolution of the area fraction of cavitated boundaries with strain. When combined with (7) there results a differential equation for the determiniation of the creep strain provided the applied stress is specified,

$$\dot{e} = D\sigma^n \exp[n\bar{\lambda}(\sigma)e] \tag{15}$$

For the model just described, it was assumed that prior to application of the load there were no cavities present in the material. In practice, this may not be the case and it is desirable to have the preceding equation modified to incorporate an initial cavity density. Assuming that when the strain is zero the cavity density is ρ_0, (9), (14), and (15) become

$$\rho(e) = [\lambda(\sigma)/A_b]e + \rho_0$$
$$\omega(e) = 1 - \exp[-\bar{\lambda}e - A_b\rho_0]$$
$$\dot{e} = D\sigma^n \exp[n(\bar{\lambda}(\sigma)e + A_b\rho_0)]$$

or, if ω_0 is defined to be $\omega(e=0)$ the initial area fraction of cavitated boundaries, then

$$\dot{e} = D\left(\frac{\sigma}{1 - \omega_0}\right)^n \exp[n\bar{\lambda}(\sigma)e]$$

This equation or equation (15) can now be integrated directly but before we do this, we will consider the effect of cavitation on the dilatation rate.

3 The Dilatation Rate Equation

Due to the nucleation and growth of grain boundary cavities a body will have a net dilatation rate. A complete description of the uniaxial deformation of a creep-cavitating body must therefore include an expression for the dilatation rate in terms of the applied stress and micromechanical

Downloaded 02 May 2010 to 171.66.16.54. Redistribution subject to ASME license or copyright; see http://www.asme.org/terms/Terms_Use.cfm

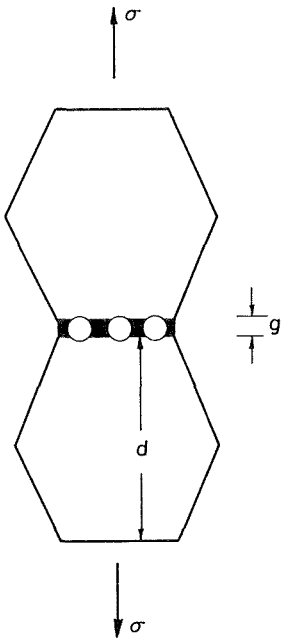

Fig. 3 Strain arising from cavitation on the boundary between two grains

variables characterizing the nucleation and growth processes. In this section such a relationship will be developed while the role of volume in the theory will be made explicit.

In Fig. 3 the boundary between two grains is depicted. The strain rate due to grain boundary cavitation is given by $\dot{g}/d$ where g is the thickness of the deposited layer of atoms arising from vacancy diffusion and d characterizes the size of the grain as shown in Fig. 3. In what follows, we will assume that a cavity nucleates and practically instantaneously becomes constrained. This assumption is reasonable since studies on unconstrained cavity growth indicate that a constant growth rate is preceded by a short transient period with a larger rate [10]. The strain rate in the cavitated grains can then be written as

$$\dot{e} = \dot{g}/d \tag{16}$$

where use has been made of (3).

The quantity $\dot{g}$ can be related to the rate of change of volume of the cavities on a single grain boundary by performing a mass balance between atoms leaving the surfaces of the cavities and depositing themselves on the grain boundary. Thus in time interval $\Delta\tau$,

$$\Delta v = A_b \Delta g$$

which implies that

$$\dot{v} = A_b \dot{g}$$

where v is the volume of cavities on a single grain boundary. The foregoing equation, when taken together with (16) yields

$$\dot{v} = A_b d\dot{e} \tag{17}$$

An expression for the total volume growth rate can be obtained by assuming that once a boundary becomes cavitated its rate of increase of volume is equal to that of the other cavitated boundaries. This assumption is justified since a cavity nucleates and practically instantaneously grows to catch up with other cavities [13] while the local strain in a grain is just the axial strain after constraint. Then we can write

$$\dot{V} = P\dot{v} \tag{18}$$

where V is the total volume of all the cavities and P, as previously defined, is the number of cavitated boundaries. The dilatation, or volume strain, is defined for an element of solid by the following

$$\Delta = (dV - dV_0)/dV_0$$

where dV_0, dV are, respectively, the volume of the element before and after deformation. For our problem the dilatation is given by

$$\Delta = V/(NA_b\ d)$$

and its rate, by

$$\dot{\Delta} = \dot{V}/(NA_b\ d)$$

which, when combined with (17) and (18) and the definition of the area fraction ω results in the following expression for the dilatation rate

$$\dot{\Delta} = \omega\dot{e} \tag{19}$$

Utilizing (14) the dilatation rate can be written as

$$\dot{\Delta} = [1 - \exp(-\bar{\lambda}e)]\dot{e}$$

which can be integrated directly to get the dilatation in terms of the strain

$$\Delta(e) = e + (1/\bar{\lambda})[\exp(-\bar{\lambda}e) - 1] \tag{20}$$

This equation indicates that, for small strains, the dilatation is essentially a term of second order in strain, i.e.,

$$\lim \Delta(e)/e \to 0,\ e \to 0$$

4 Tertiary Creep and Creep Fracture

The basic equations developed in the previous sections for uniaxial creep are presented in the following:

$$\dot{e} = D\sigma^n \exp[\beta(\sigma)e] \tag{15}$$

$$\Delta = e + (n/\beta)[\exp(-\beta e/n) - 1] \tag{20}$$

where we have introduced the function $\beta(\sigma)$ defined by

$$\beta(\sigma) = n\bar{\lambda}(\sigma) \geq 0 \tag{21}$$

For the constant stress tensile test the creep strain follows directly by simply integrating (15) to get

$$e(t) = ln[1 - D\beta(\sigma)\sigma^n t]^{-1/\beta} \tag{22}$$

which, for vanishing β (zero nucleation rate) reduces to the power law solution for steady creep

$$e(t) = D\sigma^n t$$

An expression for the critical time to fracture can be obtained by assuming that fracture occurs when all the grain boundaries become cavitated ($\omega \to 1$) which, by (14) is equivalent to requiring the strain to become infinite, i.e.,

$$\lim e(t) \to \infty,\ t \to [D\beta(\sigma)\sigma^n]^{-1}$$

This is a reasonable assumption since the final fracture process involves the formation and propagation of cracks together with plastic deformation occurring too rapidly to significantly affect fracture times. Equation (22) can be written in the simpler form

$$e(t) = ln[1 - t/t_F]^{-1/\beta} \tag{23}$$

where

$$t_F = [D\beta(\sigma)\sigma^n]^{-1}$$

The dilatation follows directly by employing equation (23) together with (20). The result is

$$\Delta(t) = ln(1 - t/t_F)^{-1/\beta} + (n/\beta)[(1 - t/t_F)^{1/n} - 1] \tag{24}$$

The form of equation (23) suggests a simple procedure for obtaining an expression for β from experimental data. First, the constants D,n are obtained from the initial linear portion of the creep curve by calculating the steady state slopes at two different stress levels [6]. By assuming the function β in the form of a polynomial in the stress and noting approximate

Downloaded 02 May 2010 to 171.66.16.54. Redistribution subject to ASME license or copyright; see http://www.asme.org/terms/Terms_Use.cfm

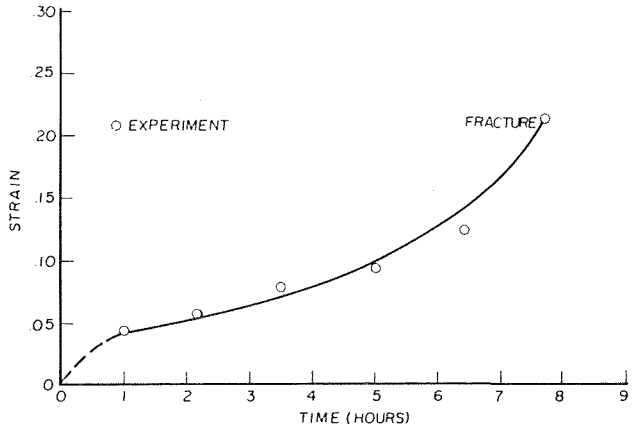

Fig. 4 Constant stress (5 ksi) creep test (copper) at 500°C

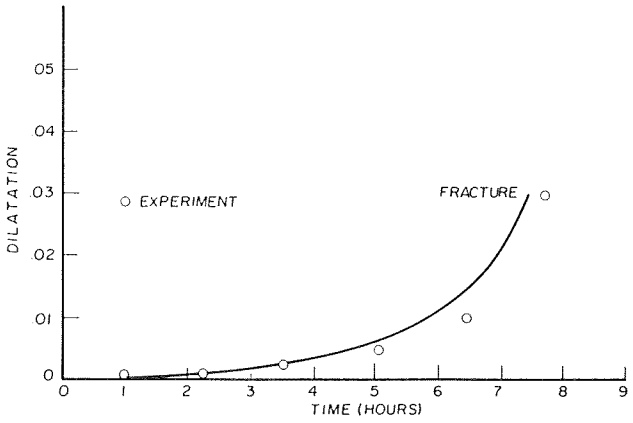

Fig. 5 Constant stress (5 ksi) creep test (copper) at 500°C

values of t_F from experimental data at different stress levels the coefficients of β can be determined. The more data points, i.e., stress levels and times to fracture obtained, the more accurate β will be. This simple procedure makes the need for the metallurgical parameters unnecessary since the dependence of the nucleation rate (λ) on the stress is unknown and would have to be determined from experiment anyway.

The behavior of the model just described was examined for the creep deformation of copper at constant stress. The experimental data of Boettner and Robertson [14], who determined strain and density changes with time for polycrystalline copper bars, was utilized and their results as well as the predictions of the model are shown in Fig. 4 and Fig. 5. Adjustment was made for elastic and transient creep. Agreement between the model and experiment is reasonable although the dilatation might be overestimated by the model. A possible reason for this could be that in the derivation of the dilatation rate equation it was assumed that cavities nucleate and instantaneously have the volume of the existing cavities and that the volume of cavities on the boundary grows with rate proportional to the axial strain rate, i.e., the cavity nucleates and instantaneously becomes constrained. In reality a cavity nucleates and only after a finite time will it become constrained with volume equal to that of the other cavities. This point, as well as the fact that the cavity density-strain relationship is not exactly linear (there is actually a slightly decreasing slope) could account for the discrepancy between the dilatation observed in the experiment and that predicted by the model.

5 A Multiaxial Form of the Creep Damage Equations

The equations developed in the preceding sections are valid for the uniaxial tension test. It is advantageous to have a multiaxial form of the equations available for situations involving more general types of applied loads. Such an equation can be developed by considering the dashpot elements of Section 2 to be continuum elements [1]. Following a procedure analogous to that given in the uniaxial formulation we have the strain rate in the uncavitated elements, in the direction of the maximum principal stress (assumed for the time being to be σ_1), given by

$$\dot{e}_1 = B J_2'^{(n-1)/2} \tau_1$$

where J_2' is the second invariant of the stress deviator tensor τ_{ij} and whose form in principal axes coordinates is simply

$$J_2' = (1/6)[(\sigma_1 - \sigma_2)^2 + (\sigma_2 - \sigma_3)^2 + (\sigma_3 - \sigma_1)^2]$$

σ_1, σ_2, σ_3 being the principal stresses. Also, τ_1 is the first component of the deviatoric stress referred to principal axes ($\tau_1 = (2/3)\sigma_1 - (1/3)(\sigma_2 + \sigma_3)$) while B is constant. This is none other then the multiaxial generalization of the power law for steady creep. The strain rate in the cavitated elements is given by

$${}^c\dot{e}_1 = B^c J_2'^{(n-1)/2}\, {}^c\tau_1 + f^c \sigma_1$$

where, as before, the last term represents the contribution to the strain rate from cavitation while the letter c indicates quantities acting in the cavitated elements. The constraint condition is simply that

$$\dot{e}_1 = {}^c\dot{e}_1$$

and since

$$f^c \sigma_1 >> B^c J_2'^{(n-1)/2}\, {}^c\tau_1$$

by equilibrium of forces we have a condition on the stresses identical with that given by (6). Hence the strain rate in the direction of the maximum principal stress is given by

$$\dot{e}_1 = B \bar{J}_2'^{(n-1)/2} \bar{\tau}_1 \tag{25a}$$

where

$$\bar{J}_2' = (1/6)\{[\sigma_1/(1-\omega) - \sigma_2]^2 + (\sigma_2 - \sigma_3)^2 + [\sigma_3 - \sigma_1/(1-\omega)]^2\} \tag{26}$$

and

$$\bar{\tau}_1 = (2/3)[\sigma_1/(1-\omega)] - (1/3)[\sigma_2 + \sigma_3]$$

These quantities can be simplified by noting that $\bar{\tau}_1$ can be written as

$$\bar{\tau}_1 = \tau_1 + (2/3)[\omega/(1-\omega)]\sigma_1 \tag{27}$$

and $\bar{J}_2'$ can be written, with the aid of (26) as

$$\bar{J}_2' = J_2' + \sigma_1[\sigma_1 - J_1/3][\omega/(1-\omega)] + [\sigma_1{}^2/3][\omega/(1-\omega)]^2 \tag{28}$$

where J_1, the first invariant of the stress, is just

$$J_1 = \sigma_1 + \sigma_2 + \sigma_3$$

The other components of strain rate i.e., $\dot{e}_2$, $\dot{e}_3$, can be obtained by noting, as in the case of uniaxial tension, that these components are directly proportional to their respective deviator stress components τ_2, τ_3. That is, from (19) and (7)

$$\dot{e}_2 = -(1/2)D\sigma^n/(1-\omega)^{n-1} = B\bar{J}_2'^{(n-1)/2}\tau_2 \tag{25b}$$

where we have used the fact that for uniaxial tension,

$$\bar{J}_2' = (1/3)[\sigma_1/(1-\omega)]^2$$

and

$$B = D3^{(n+1)/2}/2$$

Similiary,

$$\dot{e}_3 = B\bar{J}_2{}'^{(n-1)/2}\tau_3 \tag{25c}$$

Equations (25*a–c*) are the components of the strain rate tensor

Downloaded 02 May 2010 to 171.66.16.54. Redistribution subject to ASME license or copyright; see http://www.asme.org/terms/Terms_Use.cfm

in principal axes coordinates where the maximum principal stress is σ_1. A general form of the equations valid for any orthogonal coordinate system, and for maximum principal stress along any one of the principal axes, can be obtained. Following Hutchinson [3] we introduce the tensor **m** whose components, in principal axes coordinates, are given by

$$m_{ij} = \delta_{iI}\delta_{jI} \quad \text{(no sum on } I\text{)}$$

where I is the direction of the maximum principal stress. Then the components of the strain rate assume the form

$$\dot{e}_{ij} = B\bar{J}_2'^{(n-1)/2}\{\tau_{ij} + (2/3)[\omega/(1-\omega)]\sigma_I m_{ij}\} \tag{29}$$

where $\bar{J}_2'$, now a function of the damage variable ω, is given by

$$\bar{J}_2' = J_2' + \sigma_I[\sigma_I - J_1/3][\omega/(1-\omega)] + [\sigma_I^2/3][\omega/(1-\omega)]^2 \tag{30}$$

The dilatation rate follows directly as

$$\dot{\Delta} = \dot{e}_{kk} = B\bar{J}_2'^{(n-1)/2}(2/3)[\omega/(1-\omega)]\sigma_I \tag{31}$$

Equation (29) is a generalization of the power law for steady creep which governs the time-dependent deformation of a creep-cavitating body.[2]

To complete our multiaxial constitutive description the equation governing the evolution of the area fraction (14) must be modified to account for more general types of loading. Dyson and McLean [15] have conducted tension and torsion experiments on the superalloy Nimonic 80a and have concluded that, for this material, the cavity density is proportional to the effective strain

$$(\bar{e} = \sqrt{2(e_{ij} - 1/3\Delta\delta_{ij})(e_{ij} - 1/3\Delta\delta_{ij})}$$

the proportionality factor being a function of stress variable $\sigma_I/\bar{\sigma}$ where $\bar{\sigma}$ is the effective stress ($\bar{\sigma} = \sqrt{3\bar{J}_2'}$). Unfortunately there does not as yet exist sufficient experimental data to draw any general conclusions as to the appropriateness of these variables for a wider range of materials.

6 Summary and Conclusions

In this paper a constitutive equation characterizing the creep-damaging behavior of polycrystalline metals at elevated temperatures has been presented. The formulation is based on the micromechanical mechanisms of cavity nucleation and diffusional cavity growth as embodied by Dyson's constrained cavity growth mechanism [7]. The model is capable of describing steady creep and tertiary creep arising from grain boundary cavitation. In addition, dilatation arising from the cavitation process is accounted for although it is shown to be small in comparison to the creep strain. The strain rate equation for uniaxial creep deformation which is obtained is similar to the power law for steady creep and in fact, reduces to this form when either cavitation is ignored or the strains are very small. In this formulation, a single empirical function of applied stress is introduced, which is essentially the nucleation rate and which must be determined from creep fracture data for a given material. Comparison between the behavior predicted by the model and experimental data on the elevated temperature creep of copper yields reasonable agreement. Finally, a multiaxial form of the basic model is presented which clearly shows the effect of the entire stress state on the creep strain and dilatation.

[2] Note that if two (largest) or three of the principal stresses are equal then the strain rate is obtained directly from (26), and (27) with enhancement for those maximum stresses. For hydrostatic stress the strain rate simply vanishes.

Acknowledgment

This study was supported by the National Science Foundation under contract MEA-8307133. The author gratefully acknowledges the helpful comments of Professor M.P. Bieniek and Profesor C. Libove.

References

1 Dyson, B. F., Verma, A. K., and Szkipiak, Z. C., "The Influence of Stress State on Creep Resistance: Experiments and Modelling," *Acta. Metall.*, Vol. 29, 1981, pp. 1573-1580.

2 Raj, R., "Correlations Between Cavitation, Creep and Dilation for Multiaxial Loading," *Acta. Metall.*, Vol. 31, 1983, pp. 29-36.

3 Hutchinson, J. W., "Crack Tip Behavior for Metals Undergoing Creep Controlled Grain Boundary Cavitation," *Proceedings of the 9th U.S. National Congress of Applied Mechanics*, 1982, pp. 119-120.

4 Needham, N. G., and Greenwood, G. W., "The Creep of Copper Under Superimposed Hydrostatic Pressure," *Metal Sci.*, Vol. 9, 1975, pp. 258-262.

5 Miller, A., "An Inelastic Constitutive Model for Monotonic, Cyclic and Creep Deformation," ASME *Journal of Engineering Materials and Technology*, Vol. 98, 1976, pp. 97-105.

6 Levy, A. J., "Tertiary Creep and Creep Fracture," Ph.D. Thesis, Columbia University, New York, 1982.

7 Dyson, B. F., "Constraints on Diffusional Cavity Growth Rates," *Metal Sci.*, Vol. 10, 1976, pp. 349-353.

8 Hull, D., and Rimmer, D. E., "The Growth of Grain-Boundary Voids Under Stress," *Phil. Mag.*, Vol. 4, 1959, pp. 673-687.

9 Chang, T. J., Kogawa, K. I., Rice, J. R., and Sills, "Non-Equilibrium Models for Diffusive Cavitation of Grain Interfaces," *Acta Metall.*, Vol. 27, 1979, pp. 265-284.

10 Needham, N. G., and Gladman, J., "Nucleation and Growth of Creep Cavities in Type 347 Steel," *Metal Sci.*, Vol. 14, 1980, pp. 64-72.

11 Dyson, B. F., "Continuous Cavity Nucleation and Creep Fracture," *Scripta Metall.*, Vol. 17, 1983, pp. 31-37.

12 Raj, R., "Nucleation of Cavities at Second Phase Particles in Grain Boundaries," *Acta., Metall.*, Vol. 26, 1978, pp. 995-1006.

13 Greenwood, G., Int. Congress on Metals, Cambridge, 1973. *Microstructure and the Design of Alloys*, Vol. 2, pp. 91-105.

14 Boettner, R. C., and Robertson, W. D., "A Study of the Growth of Voids in Copper during the Creep Process by Measurement of the Accompanying Change in Density," *AIME Trans.*, Vol. 221, 1961, pp. 613-622.

15 Dyson, B. F., and McLean, D., "Creep of Nimonic 80A in Torsion and Tension," *Metal Sci.*, Vol. 1, 1977, pp. 37-45.

Downloaded 02 May 2010 to 171.66.16.54. Redistribution subject to ASME license or copyright; see http://www.asme.org/terms/Terms_Use.cfm

Nonproportional Loading Steps in Multiaxial Creep of 2618 Aluminum

J. L. Ding
Assistant Professor,
Department of Mechanical Engineering,
Washington State University,
Pullman, Wash. 99164
Mem. ASME

W. N. Findley
Professor of Engineering,
Brown University,
Providence, R.I. 02912
Life Fellow ASME

Experimental data on the creep behavior of 2618-T61 aluminum alloy under nonproportional loadings are presented. Among the important findings are the anisotropy induced by creep strain, synergistic effects during creep recovery, and strongly nonlinear material behavior at high stress levels. Data were compared with two theoretical models, a viscous-viscoelastic (VV) model and a viscoplastic (VP) model. In the VV model the time-dependent strain was decomposed into recoverable (viscoelastic) and nonrecoverable components. The VP model differs from the VV model in that all the time-dependent strain is assumed nonrecoverable. In each model, three viscoplastic flow rules based on different hardening natures, namely, isotropic strain hardening, kinematic hardening, and independent strain hardening were derived to describe the time-dependent nonrecoverable strain component, and compared with experiments. The viscoelastic component in the VV model was represented by the third-order multiple integral representation combined with the modified superposition principle. Predictions for all theories used material constants obtained from creep and recovery data only. Possible causes for the discrepancies between theories and experimental data were discussed. Further experimental and theoretical work necessary for the study of the time-dependent material behavior at high temperature were also suggested.

Introduction

Past experimental work in creep under multiaxial stresses were reviewed in [1].

The study of the time-dependent behavior of the current material started with a series of short term (2h per loading period) creep and stress relaxation tests under variable multiaxial stress states. A viscous-viscoelastic model (*VV* model) was developed to simulate the experimental observations [2–5].

The stress-strain-time relations under constant stress states were further refined in [6] through a set of 48 h creep and creep recovery data including aging and compression tests. Based on this relation, constitutive equations for variable stress states were developed, and evaluated through a set of experimental observations on the creep behavior under multistep proportional loadings [7].

In the present work, the creep behavior under multistep nonproportional loadings were studied. The capabilities of the constitutive relations developed in [7] for predicting the responses under these complex stress histories were evaluated.

Contributed by the Applied Mechanics Division and presented at the 1985 Joint ASME/ASCE Applied Mechanics, Fluids Engineering, and Bioengineering Conference, Albuquerque, N. Mex., June 24–26, 1985 of THE AMERICAN SOCIETY OF MECHANICAL ENGINEERS.

Discussion on this paper should be addressed to the Editorial Department, ASME, United Engineering Center, 345 East 47th Street, New York, N.Y. 10017, and will be accepted until two months after final publication of the paper itself in the JOURNAL OF APPLIED MECHANICS. Manuscript received by ASME Applied Mechanics Division, November, 1983; final revision, October, 1984. Paper No. 85-APM-32.

Material, Specimen, Apparatus, and Procedures

The material employed was aluminum alloy 2618-T61 from the same batch as that reported in [6, 7]. A more complete description of material and specimen were given in [2, 6]. The combined tension and torsion machine used for these experiments was described in [8]. The temperature control system and the data acquisition procedures were described in [2, 8]. All the tests were performed at a test temperature of 200°C. Except for the aging tests, the specimen was soaked at the test temperature for approximately 18 h prior to testing.

Experimental Results

Six experiments are reported whose loading programs and resulting total strain versus time are shown in Figs. 1-6. Letters *CA*, *CT* preceding the test number represent the axial strain data and the shear strain data, respectively, for that specified test. The first two periods of all these tests were reported in [6] for determining the stress-strain-time relation under constant stress states. Figures 2 and 6 (tests 35 and 43) are aging tests in which the specimen was soaked at the test temperature prior to testing for 312 and 114 h, respectively. Aging was found to be negligible within 312 h as described in [6].

The Effect of Previous Creep Strain on Subsequent Creep Under a Different Stress State. A typical example of the effect of prior shear creep strain on subsequent tensile creep is shown in Fig. 5(*b*). It was found that prior shear strain had the effect of increasing the subsequent tensile creep rate as shown by comparison of the axial creep curve in period 3 of Fig. 5(*b*) with that in period 1 of Fig. 4(*b*) and that in period 3 of Fig. 3(*b*), both of which are also inserted in Fig. 5(*b*). These

Copyright © 1985 by ASME
Downloaded 02 May 2010 to 171.66.16.54. Redistribution subject to ASME license or copyright; see http://www.asme.org/terms/Terms_Use.cfm

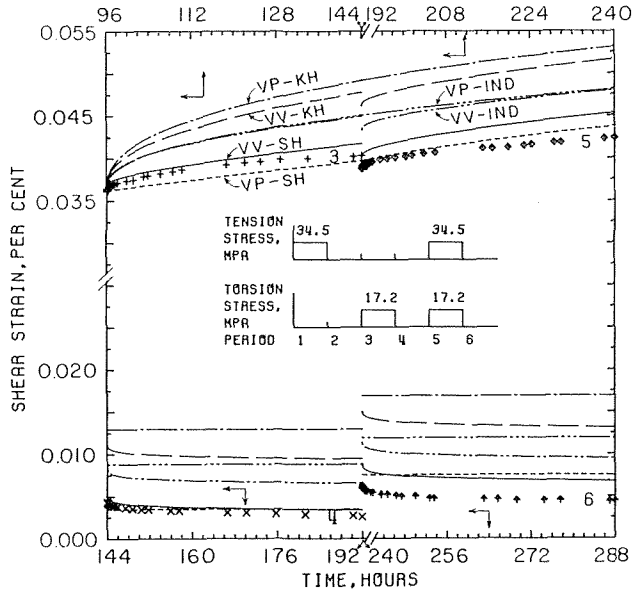

Fig. 1(*a*) Test CT33 (shear strain part of test 33). Period durations are 48 h. Experimental data are compared with several theoretical curves. The two orthogonal arrows adjacent to a group of curves point toward the two scales to be used with that period.

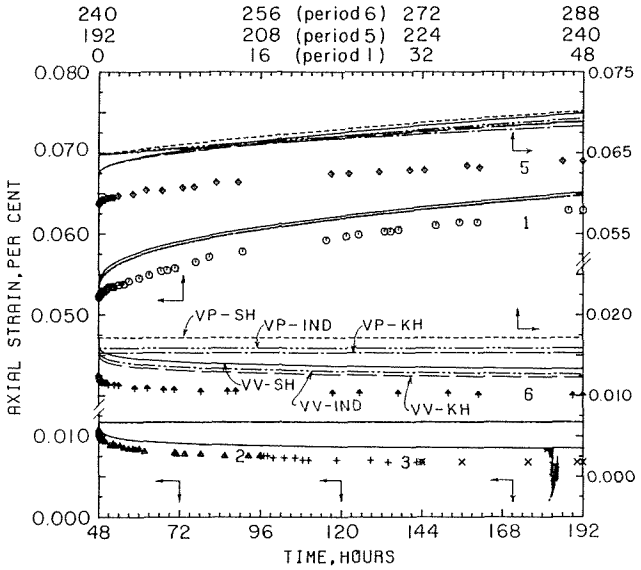

Fig. 1(*b*) Test CA33 (axial strain part of test 33)

Fig. 1

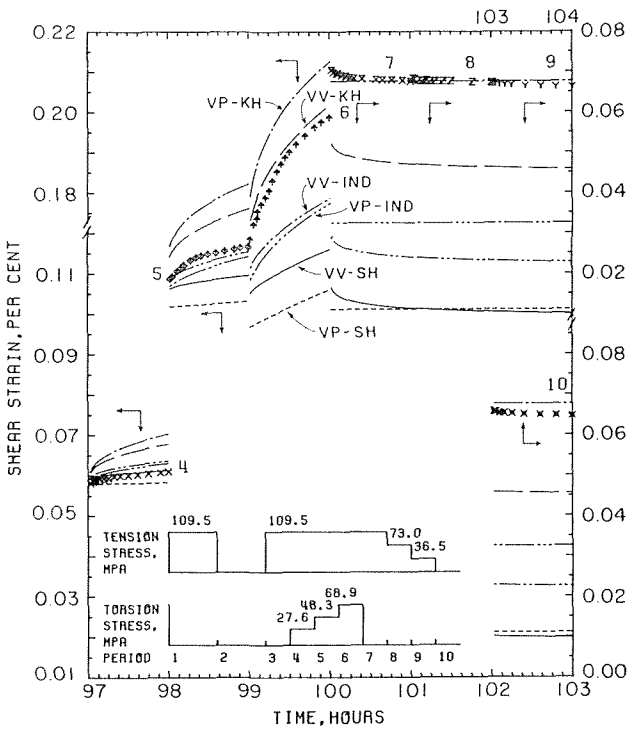

Fig. 2(*a*) Test CT35 (shear strain part of test 35). Durations are 48 h for periods 1 and 2, 1 h otherwise. Aged 312 h at 200°C

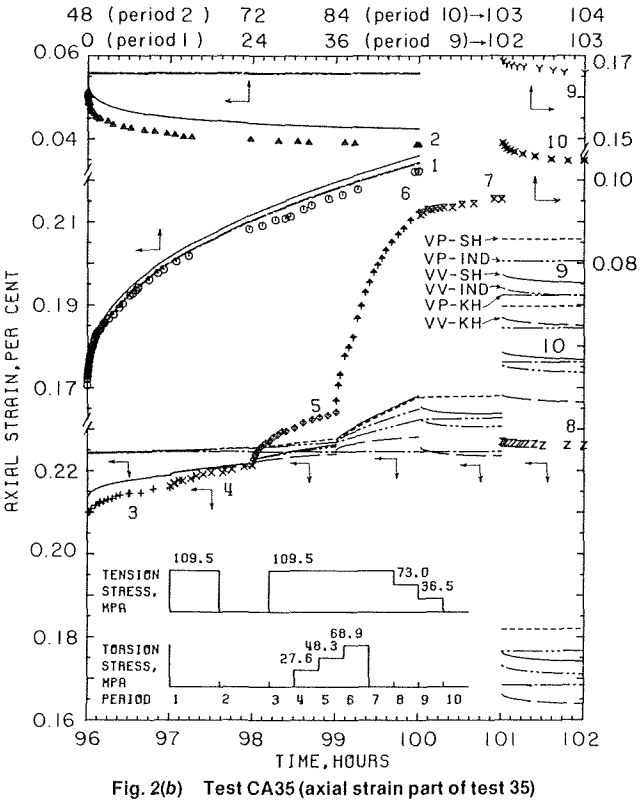

Fig. 2(*b*) Test CA35 (axial strain part of test 35)

Fig. 2

data were all obtained from pure tensile creep at the same stress level (137.2 MPa), but preceded by a pure shear creep step at different stress levels, i.e., 0.0, 79.2, and 101.4 MPa for Fig. 4(*b*) period 1, Fig. 3(*b*) period 3, and Fig. 5(*b*) period 3, respectively. As also implied by these data, the prestrain effect increased with the amount of previous creep strain (or stress level).

Similar observations were found on the effect of prior tension creep strain on the subsequent shear creep rate as shown in Fig. 4(*a*). The accumulated shear creep strain in period 3, which was preceded by a pure tension creep period, was larger than that in period 1 of Fig. 3(*a*), also shown in Fig. 4(*a*), which was obtained from a virgin specimen under the same shear stress. The same observation was found in Fig. 6(*a*) by comparing the shear creep curve in period 3 with that in period 1 of test 42, Fig. 5(*a*), which is also inserted in Fig. 6(*a*).

Other observations on prior creep strain effects are shown in Fig. 4(*b*). The fact that the tensile creep rate in period 5 was larger than that obtained from a virgin specimen (denoted by "A32, Fig. 6, [7], Period 1") seemed to imply that the strain-hardening effect induced by tensile creep at 137.2 MPa was overridden by the interruption of shear creep (period 3). Also,

Downloaded 02 May 2010 to 171.66.16.54. Redistribution subject to ASME license or copyright; see http://www.asme.org/terms/Terms_Use.cfm

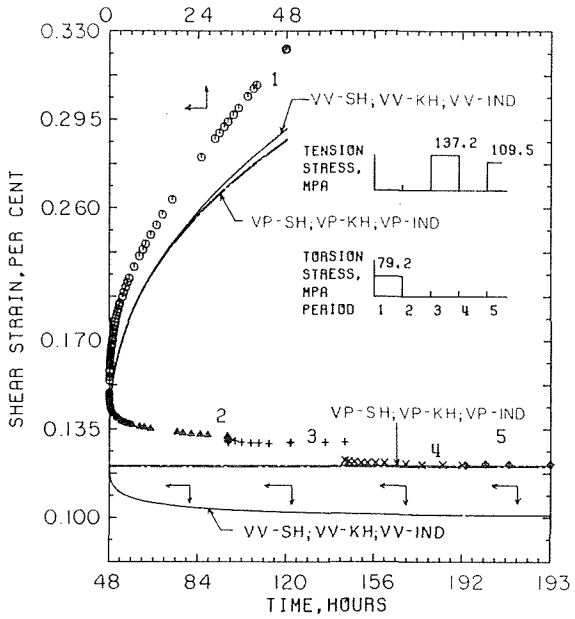

Fig. 3(*a*) Test CT38 (shear strain part of test 38). Durations are 48 h for periods 1-4, 1 h for period 5.

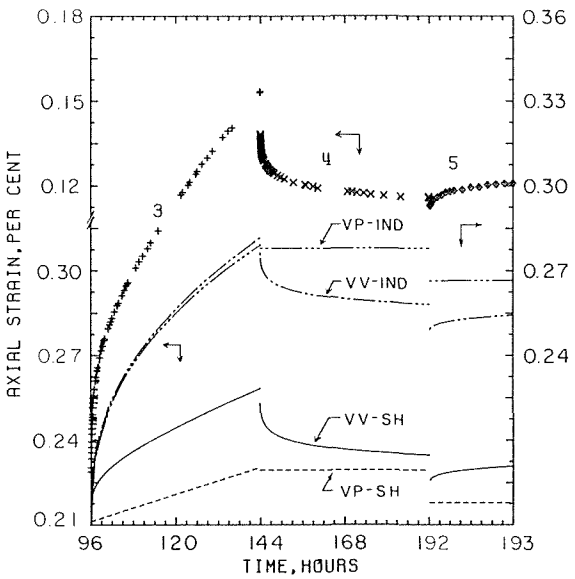

Fig. 3(*b*) Test CA38 (axial strain part of test 38). *VV·KH* and *VP·KH* are not shown because they are far out of scale.

Fig. 3

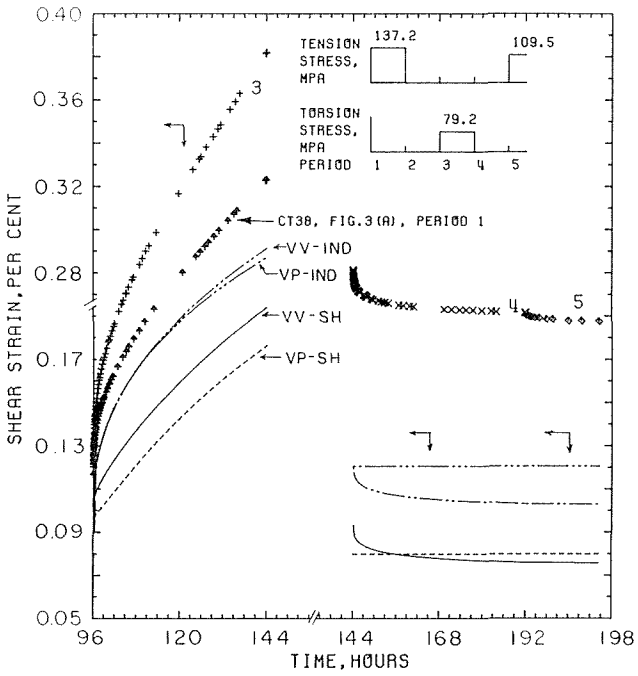

Fig. 4(*a*) Test CT39 (shear strain part of test 39). Durations are 48 h for periods 1-4, 5.15 h for period 5. CT38, Fig. 3(*a*), Period 1 uses the same origin and scale as period 3. *VV·KH* and *VP·KH* are not shown because they are far out of scale.

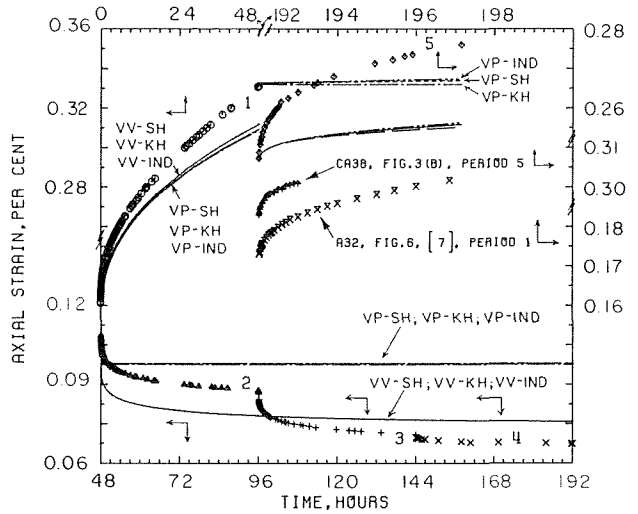

Fig. 4(*b*) Test CA39 (axial strain part of test 39)

Fig. 4

from the observation that the creep curve denoted by "CA38, Fig. 3(*b*), Period 5" was nearly parallel to that of "A32, Fig. 6 [7], Period 1", suggests that the strain-hardening effect induced by the tension creep in period 3 of test 38 might balance out the prior effect of torsion induced in period 1. Furthermore, the stress history dependence can also be seen in Fig. 4(*b*) by examining the tensile creep curves for CA39 in Period 5 and "CA38, Fig. 3(*b*), period 5" also shown in Fig. 4(*b*). Both were preceded by two other stresses: tension and then torsion for CA39 and torsion then tension for CA38, with the same stress levels in both.

Synergistic Effects on Creep Recovery. A transient increase of the axial creep recovery rate was found on the addition of shear stress during axial creep recovery, as shown in period 3 of Fig. 4(*b*) and period 3 of Fig. 6(*b*). The same is true for shear creep recovery during addition of tension as shown in period 3 of Fig. 5(*a*) and period 5 of Fig. 4(*a*). In period 3 of Fig. 3(*a*), this phenomenon seemed less significant. As would be expected, these effects diminished at low stress levels as shown in period 3 of Fig. 1(*b*).

Strongly Nonlinear Material Behavior at High Stress Levels. Due to the synergistic effects discussed in [6], adding a stress component in steps while the other stress components were kept constant, induced an increase of the creep rate associated with the constant stress components as shown in periods 4–7 of Fig. 2(*b*), periods 6–9 of Figs. 5(*a*) and 5(*b*), and periods 6–8 of Figs. 6(*a*) and 6(*b*). This synergistic effect became extremely significant when the effective stress exceeded 137.2 MPa (refer to Fig. 1 of [6]) as shown in period 6 of test 35, Figs. 2(*a*) and (*b*) and period 8 of test 43, Figs. 6(*a*) and (*b*). In period 9 of test 42, Fig. 5, the combined stress was so large that a jump in the strain reading was found at the end

Downloaded 02 May 2010 to 171.66.16.54. Redistribution subject to ASME license or copyright; see http://www.asme.org/terms/Terms_Use.cfm

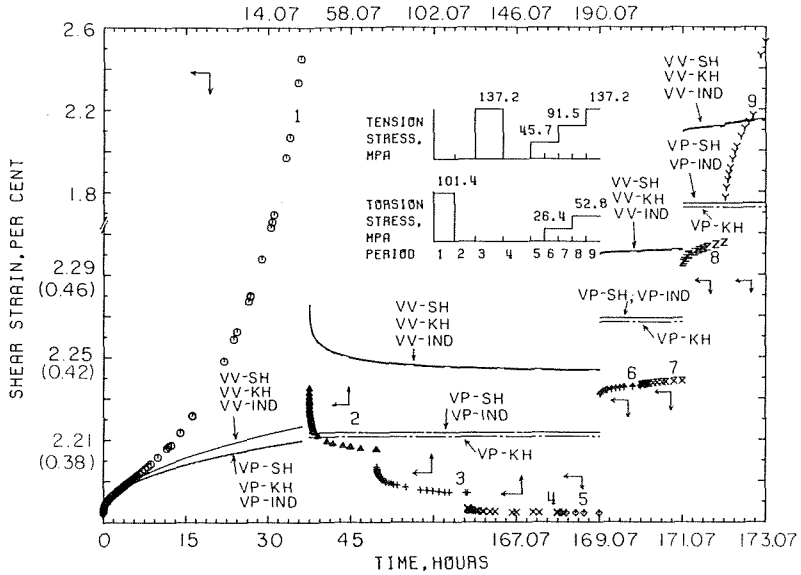

Fig. 5(*a*) Test CT42 (shear strain part of test 42). Durations are 36.07 h for period 1, 36 h for period 2, 48 h for periods 3 and 4, 1 h for periods 5-9. Experimental data and theory curves for periods 2-9 use different origins because of their large deviations. Ordinate numbers in parenthesis refer to theory curves.

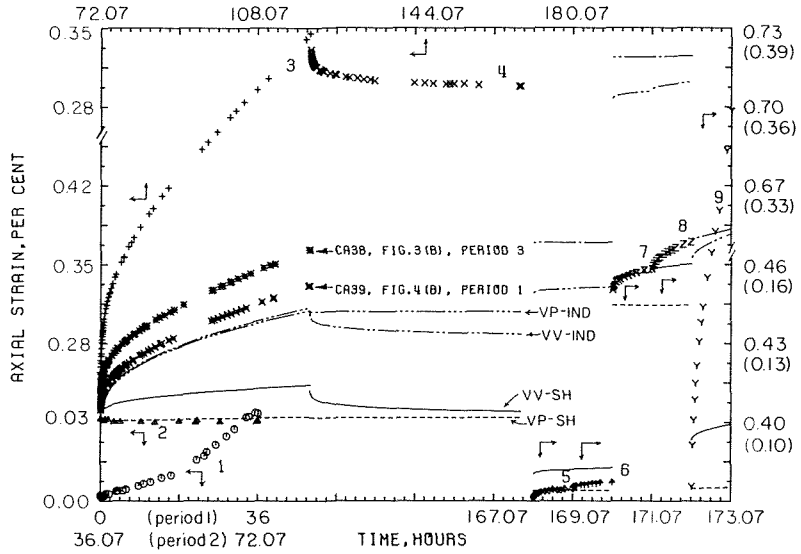

Fig. 5(*b*) Test CA42 (axial strain part of test 42). CA39, Fig. 4(*b*), Period 1 and CA38, Fig. 3(*b*), period 3 use the same origin and scale as period 3. Experimental data and theory curves for periods 5-9 are relative to different origins becuase of their large deviations. *VV-KH* and *VP-KH* are not shown because they are far out of scale. Ordinate numbers in parenthesis refer to theory curves.

Fig. 5

of that period which might be due to development of internal cracks in the material. This strong nonlinearity should be expected in view of the stress dependence of the viscous component shown in Fig. 10 of [6].

Tension Strain Accompanied by Torsion Creep. As mentioned in [6], some time-dependent tension strain was detected during creep in pure torsion in period 1, Fig. 5(*b*). This could possibly be due to the geometrical change caused by the large shear deformation. Since this was the only test showing a tensile strain during torsion creep and existed only during the tertiary stage, this factor was not considered in the analysis of the current work. In response to a reviewer's question: there is no detectable cross talk in tension-torsion strain measurements with the system employed [8] at constant temperature; and the weight of the lower grip was supported so that there was no axial stress during pure torsion.

Discussion. The anisotropic nature induced by creep deformation as observed in the effect of prior creep strain on subsequent creep under another stress state could be due to the interaction between the residual stress field due to prior creep and the subsequent applied stress. The synergistic effects observed during creep recovery may be explained the same way, i.e., they are due to the interaction of residual stress and the new applied stress. When the residual stress is relaxed to some extent this synergistic effect diminishes. The onset of fracture mechanisms may explain the strongly

Downloaded 02 May 2010 to 171.66.16.54. Redistribution subject to ASME license or copyright; see http://www.asme.org/terms/Terms_Use.cfm

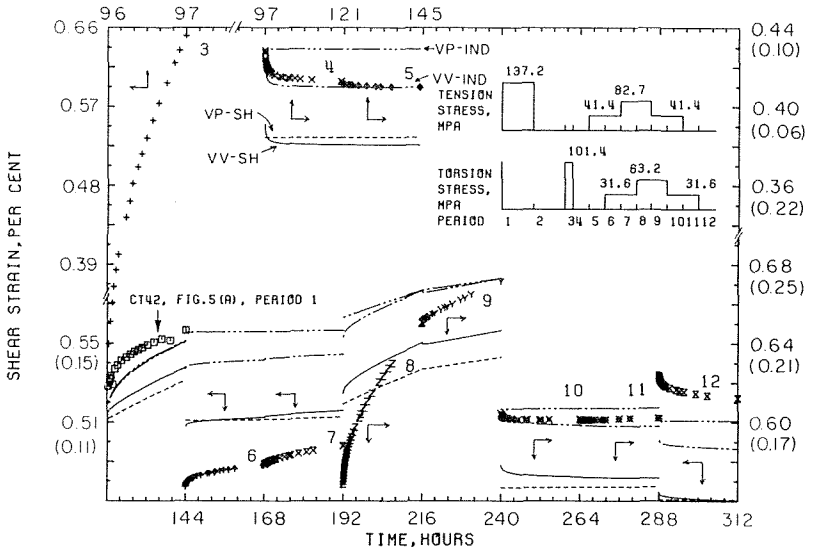

Fig. 6(*a*) Test CT43 (shear strain part of test 43). Durations are 48 h for periods 1 and 2, 1 h for period 3, 23 h for period 4, 24 h for periods 5-12. CT42, Fig. 5(*a*), periods 1 uses the same origin and scale as period 3. Experimental data and theory curves for periods 4-12 use different origins because of their large deviations. *VV-KH* and *VP-KH* are not shown because they are far out of scale. Ordinate numbers in parenthesis refer to theory curves. Aged 114 h at 200°C.

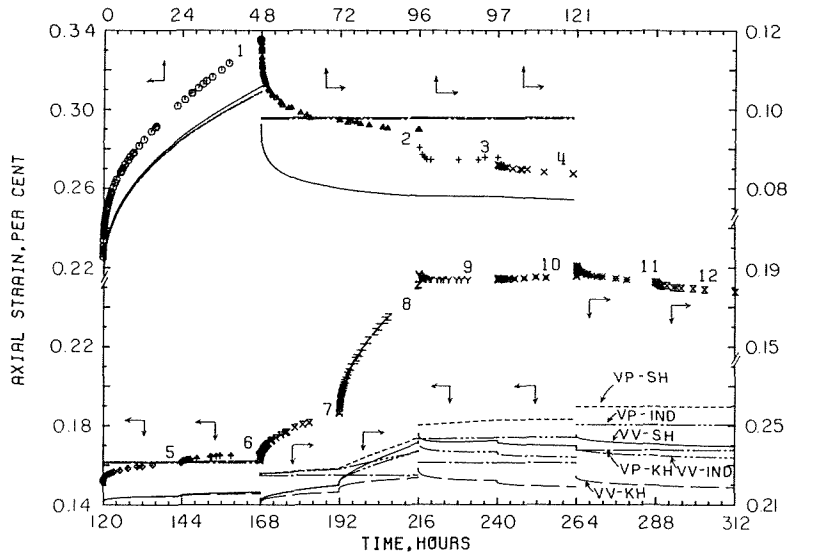

Fig. 6(*b*) Test CA43 (axial strain part of test 43)

Fig. 6

nonlinear behavior at high stress levels and part of the prior creep strain effect. Experiments on prior strain effects (as reviewed in [9], Chapter 12), usually subjected a specimen to cold-work before creep testing. In that case, it was found that prestraining was accompanied by a dramatic increase in the number of cavities developed during creep compared with nonprestrained material.

Constitutive Equations for Variable Stress States

In [7], two theoretical models, a viscous-viscoelastic (*VV*) model and a viscoplastic (*VP*) model, were developed to simulate the material behavior under multiaxial proportional loading steps. In the *VV* model, the total strain was decomposed into time-independent elastic ϵ^E, viscoelastic ϵ^{VE} (time-dependent recoverable) and viscous strain ϵ^V (time-dependent nonrecoverable). No time-independent plastic strain was found for this material in the stress range examined. The *VP* model differs from the *VV* model only in that all the time-dependent strain was assumed nonrecoverable. The constitutive relations for ϵ^{VE} and ϵ^V under variable stress states are as follows:

Viscoelastic Strain, ϵ_{ij}^{VE}. For a series of m steps in combined tension (σ) and torsion (τ) stress states, ϵ_{11}^{VE} was described as follows:

$$\epsilon_{11}^{VE} = F^{VE}(\sigma_1,\tau_1)[t^{n_1} - (t-t_1)^{n_1}] + \text{-----}$$
$$+ F^{VE}(\sigma_{m-1},\tau_{m-1})[(t-t_{m-2})^{n_1} - (t-t_{m-1})^{n_1}]$$
$$+ F^{VE}(\sigma_m,\tau_m)(t-t_{m-1})^{n_1},\ t_{m-1} < t, \qquad (1)$$

where $F^{VE}(\sigma,\tau) = F_1^+\sigma + F_3^+\sigma^3 + F_4^+\sigma\tau^2$ was the stress dependence of ϵ_{11}^{VE} under a constant stress state. Similarly, ϵ_{12}^{VE} was obtained by replacing $F^{VE}(\sigma,\tau)$ in equation (1) by $G^{VE}(\sigma,\tau) = G_1^+\tau + G_2^+\tau^3 + G_4^+\sigma^2\tau$; see [6,7].

Downloaded 02 May 2010 to 171.66.16.54. Redistribution subject to ASME license or copyright; see http://www.asme.org/terms/Terms_Use.cfm

Table 1 Back stress (α_{ij}, MPa) at the end of each period

Fig. no. (Test no.)	Period no.	*VV* Theory α_{11}	*VV* Theory α_{12}	*VP* Theory α_{11}	*VP* Theory α_{12}
1 (33)	1,2	22.957	0.000	22.971	0.000
	3,4	22.957	17.209	22.971	17.224
	5,6	22.966	17.219	22.976	17.229
2 (35)	1-2	72.846	0.000	72.915	0.000
	3	72.847	0.000	72.916	0.000
	4	72.966	26.674	72.969	27.038
	5	72.970	46.645	72.970	47.369
	6-10	72.970	64.697	72.970	66.700
3 (38)	1,2	0.000	78.912	0.000	79.103
	3-5	88.042	78.912	90.741	79.103
4 (39)	1,2	91.240	0.000	91.375	0.000
	3-5	91.240	76.966	91.375	78.680
5 (42)	1,2	0.000	99.641	0.000	100.855
	3,4	0.415	99.641	87.039	100.855
	5	2.302	99.641	87.039	100.855
	6	4.294	99.641	87.039	100.855
	7	4.600	99.641	87.039	100.855
	8	4.915	99.641	87.039	100.855
	9	4.929	99.641	87.155	100.855
6 (43)	1,2	91.240	0.000	91.375	0.000
	3-5	91.240	0.123	91.375	11.396
	6	91.240	31.239	91.375	31.449
	7	91.240	31.347	91.375	31.500
	8	91.240	62.008	91.375	62.801
	9-12	91.240	62.372	91.375	62.934

Note: $\alpha_{22} = \alpha_{33} = -(1/2)\alpha_{11}$ and $\alpha_{13} = \alpha_{31} = \alpha_{23} = \alpha_{32} = 0$.

Time-Dependent Nonrecoverable Strain, ϵ_{ij}^V. Two flow rules, isotropic strain hardening (*SH*) and kinematic hardening (*KH*), were developed for ϵ_{ij}^V under variable stress states in [7] as follows:

Isotropic Strain Hardening (SH):

$$\dot{\epsilon}_{ij}^V = \sigma_{ij}' n\, F(\tau_{\max})\{(\tfrac{1}{2}\gamma_{\max})/[\tau_{\max} F(\tau_{\max})]\}^{(n-1)/n}, \tag{2}$$

where the value of the constant n and the expression $F(\tau_{\max})$ were described in [7] and were different for *VV* and *VP* models.

Kinematic Hardening (KH).

$$\dot{\epsilon}_{ij}^V = C(\Sigma_{ij}/\|\Sigma_{ij}\|)\sinh(\|\Sigma_{ij}\|/K), \tag{3}$$

$$\dot{\alpha}_{ij} = -\frac{K(n-1)(b_1 n)^{1/(n-1)}\|\dot{\epsilon}_{ij}^V\|^{-1/(n-1)}}{(\|\dot{\epsilon}_{ij}^V\|^2 + C^2)^{1/2}}\dot{\epsilon}_{ij}^V, \tag{4}$$

where

$$\Sigma_{ij} = \sigma_{ij}' - \alpha_{ij}$$
$$b_1 = b_2 F(b_2)$$
$$b_2 = \|\alpha_{ij}\| + K\, ln\{(\|\dot{\epsilon}_{ij}^V\|/C) + [(\|\dot{\epsilon}_{ij}^V\|/C)^2 + 1]^{1/2}\},$$

where α_{ij} is the back stress, and C, n, and K are constants whose values are shown in [7] and depend on the model used, *VV* or *VP*. The function F and the constant n are the same as those used in (2). The intensity quantities $\|\Sigma_{ij}\|$, $\|\alpha_{ij}\|$, and $\|\dot{\epsilon}_{ij}^V\|$ are defined by maximum shear stress and maximum shear strain rate, respectively.

In the term, $(b_1 n)^{1/(n-1)}$, n is a positive number less than 1, thus it follows that a previous deformation history resulting in a nonzero value of $\|\alpha_{ij}\|$ has the effect of reducing the following work hardening rate $\dot{\alpha}_{ij}$ corresponding to the same strain rate. Furthermore, due to the strong nonlinearity of function F, b_1 increases very rapidly with increase of $\|\alpha_{ij}\|$. Neglecting metallurgical recovery effects, this evolution rule is similar to that used in [10] except for the stronger nonlinearity of the current equation. In [10], the evolution rule was in the form $\dot{\alpha}_{ij} = (c/\|\alpha_{ij}\|^{\beta})\dot{\epsilon}_{ij}^V$, where c, β are constants and the stress dependence of the flow rule is through a power law instead of the hyperbolic sine used here.

Since ϵ_{ij}^V is not recoverable, a constraint was imposed such that $\dot{\epsilon}_{ij}^V$ is zero whenever $\Sigma_{ij}\sigma_{ij}' \le 0$ (with no summation) see [7].

Independent Strain Hardening (*IND*). Since the stress-strain-time relation for ϵ_{ij}^V under constant stress states can be expressed as

$$\epsilon_{ij}^V = F(\tau_{\max})\sigma_{ij}' t^n, \tag{5}$$

differentiating both sides with respect to time yields the following expression:

$$\dot{\epsilon}_{ij}^V = n\, F(\tau_{\max})\sigma_{ij}' t^{n-1}. \tag{6}$$

In the derivation of an independent hardening flow rule, t was replaced by $\{|\epsilon_{ij}^V|/[F(\tau_{\max})|\sigma_{ij}'|]\}^{1/n}$ which was directly obtained from equation (5), where $|\epsilon_{ij}^V|$ and $|\sigma_{ij}'|$ are the absolute values of the specified strain and stress component. Substituting for t in (6) and simplifying, the independent strain hardening flow rule can be stated as follows:

$$\dot{\epsilon}_{ij}^V = sgn(\sigma_{ij}')n[F(\tau_{\max})|\sigma_{ij}'|]^{1/n}|\epsilon_{ij}^V|^{(n-1)/n}, \tag{7}$$

where the value of n and the expression for $F(\tau_{\max})$ are the same as used in equation (2) and different for *VV* and *VP* models. In constrast to the isotropic hardening flow rule [equation (2)], equation (7) is independent hardening in the sense that the strain path dependence of each specified strain-rate component $\dot{\epsilon}_{ij}^V$ was only through the corresponding strain component ϵ_{ij}^V instead of $\gamma_{\max}$ as used in equation (2).

Equation (7) can be integrated explicitly to get $|\epsilon_{ij}^V|$ as a functional of the stress histories as follows:

$$|\epsilon_{ij}^V| = \left\{\int_0^t [|\sigma_{ij}'(\xi)|F(\tau_{\max}(\xi))]^{1/n} d\xi\right\}^n. \tag{8}$$

Predictions By The Theories

In summary, there are two models: *VV* and *VP*. In each model three flow rules for the viscous component were compared, namely, isotropic strain hardening (*SH*), kinematic hardening (*KH*), and independent strain hardening

Downloaded 02 May 2010 to 171.66.16.54. Redistribution subject to ASME license or copyright; see http://www.asme.org/terms/Terms_Use.cfm

(*IND*). The modified superposition principle was used for representing the viscoelastic component under variable stress states. An IMSL subroutine DVERK based on the Runge-Kutta-Verner fifth and sixth-order method with automatic time step control was used for the numerical integration. Predictions of creep behavior were computed from the relations described in the foregoing using material constants determined from creep and recovery tests only under combinations of tension and torsion and reported in [6].

The results are shown in Figs. 1–6 in which *VV-SH* are represented by solid lines, *VP-SH* by dotted lines, *VV-KH* by dashed lines, *VP-KH* by dash-dot lines, *VV-IND* by double dots-dash lines, and *VP-IND* by triple dots-dash lines. The back stresses α_{ij} at the end of each period are given in Table 1. Experimental data for all periods are shown for comparison with theoretical curves. Most figures have several scales in order to have a scale suitable for each period presented. The two orthogonal arrows adjacent to a group of curves point toward the two scales to be used with that period.

Comparison of Theories With Experimental Data

Prestrain Effects. The differences between theories on predicting the effect of prior creep strain can be seen from the results in period 3 of Fig. 1(*a*). Since the tensile creep strain was assumed to have no effect on the shear creep from the *IND* approach, *VV-IND* and *VP-IND* predicted that the creep behavior in period 3 was exactly the same as that for a new material. Due to the hardening effect induced by the tensile creep strain in period 1, *VV-SH* and *VP-SH* predicted less creep strain than the *IND* approaches, while *VV-KH* and *VP-KH* predicted larger creep strain because a nonzero value of $\|\alpha_{ij}\|$ resulting from creep in period 1 reduced the subsequent work hardening rate as discussed earlier. In this test, *SH* was the best in representing the material behavior, which seemed to contradict the previous observation that prior creep strain had the effect of increasing the subsequent creep rate in a different direction. Stresses used for this test were at the lowest levels, mainly for checking the possible existence of a creep limit, which was not found. Since the scale in this figure was very small, this contradiction could be due to the deviations of the mathematical representation for the stress dependence of the ϵ^V component, see equation (5).

The differences between theories were larger for some tests at high stress levels, Figs. 3–6. Due to the term $(b_1 n)^{1/(n-1)}$ in equation (4) which increased very rapidly with increase of $\|\alpha_{ij}\|$ as mentioned earlier, the work hardening rate $\dot{\alpha}_{ij}$ for the subsequent creep period was limited. The predictions by the *VV-KH* and *VP-KH* were thus so very far out of scale that they are not shown in Figs. 3(*b*), 4(*a*), 5(*b*), and 6(*a*).

Synergistic Effects on Creep Recovery. The synergistic effects during creep recovery discussed earlier could not be described from the modified superposition principle. This can be easily seen from the expression for $F^{VE}(\sigma,\tau)$ in equation (1) by noting that shear stress has no effect on the value of F^{VE} when σ is zero. The same is true for G^{VE} on the effect of σ when τ is zero.

Another defect of the modified superposition principle can be seen in period 7 of Fig. 2(*b*) in which the *VV* model predicted creep recovery, which contradicted the experimental observation. The reason is that the modified superposition principle completely depends on how the current value of F^{VE} or G^{VE} is compared to the previous one. Removal of the shear stress results in a smaller value of F^{VE} due to the term $\sigma\tau^2$ and prediction of creep recovery from equation (1). The same phenomenon was found in period 9 of Fig. 6(*a*).

Strongly Nonlinear Material Behavior at High Stress Levels. A typical theoretical prediction is shown in Figs. 2(*a*) and (*b*). *VV-SH* and *VP-SH* underestimated both the axial strain and shear strain in periods 5 and 6. *IND* approaches predicted less axial strain but more shear strain than *SH* approaches in these periods. Reexamination of equation (2) and equation (7) showed that their differences depended on the relative role played by $|\epsilon_{ij}^V|$ in equation (7) versus $1/2\ \gamma_{\max}$ in equation (2) and $|\sigma'_{ij}|$ in equation (7) versus $\tau_{\max}$ inside the bracket of equation (2), and were strongly history-dependent. For example, in periods 4–6 of Fig. 2(*b*), $\tau_{\max}$ used in *SH* increased in steps with the addition of shear stress in contrast to the constant value of $|\sigma'_{11}|$ used in *IND* throughout these periods. Therefore, *SH* predicted higher axial creep strain than *IND*. In period 3 of Fig. 4(*a*) all the stress terms are equal in equation (2) and (7). However, due to the term $1/2\ \gamma_{\max}$, which is nonzero at the beginning of this period, *SH* predicted less shear creep strain than *IND* in which $|\epsilon_{12}^V|$ is zero at the beginning.

The *KH* approach for this case was even less satisfactory. As shown in Fig. 2(*b*) *VP-KH* was almost a horizontal line from period 3 to 7. This was due to the fact that α_{11} was almost equal to σ'_{11} at the end of period 1. The axial creep rates for the following periods were thus nearly zero irrespective of the addition of shear stress because Σ_{11} was nearly zero. The validity of the *KH* approach was thus seriously limited even though it seemed to give a better representation of the shear creep strain in this case. Similar results were found in Figs. 5 and 6.

Discussion

From the preceding comparisons, all theories suffered from some limitations on predicting the material behavior under nonproportional loadings. Implied by the observations on the prior creep strain effects, the constitutive equation based on the isotropic hardening nature seemed not suitable for the current material. However, *IND* approaches did not give an overwhelming improvement over the *SH* approaches either.

As shown from the tests reported here, several critical problems also existed in the current *KH* flow rule which was based on a state variable approach. In fact, prediction of the time-dependent material behavior under nonproportional loadings could be a critical challenge for most of the constitutive equations based on the same approaches in which usually a tensorial state variable (back stress) was associated with the kinematic hardening nature and a scalar state variable with the isotropic hardening nature, see [10–14]. In the proportional loadings, the differences between various theoretical approaches are really not significant, as shown in [7].

One subject that needs further experimental investigation is the verification of the assumption that $\dot{\epsilon}_{ij}^V$ is parallel to $\Sigma_{ij} = \sigma'_{ij} - \alpha_{ij}$ as used in state variable approaches.

Further theoretical considerations are also necessary on properly specifying and controlling the evolutions of the state variables for a particular material even though considerable progress on the general state variable theory has been achieved [14]. The overestimation of the prior creep strain effects and the discrepancies found in periods 3–7 of Fig. 2(*b*) could be related to these problems.

More consideration should also be given to the constraints imposed on the constitutive equations to deal with the case when σ'_{ij} is smaller than α_{ij}, such as that $\dot{\epsilon}_{ij}^V = 0$ whenever $\Sigma_{ij}\sigma'_{ij} \le 0$ (with no summation) used in the current *KH* flow rule. Most of the state variable theories did not take this into specific consideration, except for Robinson's work [10]. The difference between this constraint and that used in [10] is that the summation convention is applied to the condition of $\Sigma_{ij}\sigma'_{ij} \le 0$ in [10], i.e., $\dot{\epsilon}_{ij}^V$ is zero whenever $\Sigma_{ij}\sigma'_{ij} \le 0$. This dissimilarity can be seen by using period 3 of Fig. 3 as an example. In period 3, Σ_{12} is negative, Σ_{11} is positive and $\Sigma_{ij}\sigma'_{ij}$ is also positive. According to the constitutive equation in [10],

Downloaded 02 May 2010 to 171.66.16.54. Redistribution subject to ASME license or copyright; see http://www.asme.org/terms/Terms_Use.cfm

ϵ_{12}^{V} is negative in period 3, i.e., negative shear creep, which is not consistent with the experimental observation. However, by the constraint proposed in the current work, in period 3, ϵ_{12}^{V} is zero since $\Sigma_{12}\sigma_{12}'$ is zero and ϵ_{11}^{V} can undergo further creep because $\Sigma_{11}\sigma_{11}'$ is positive.

An even more essential question may be the appropriateness of imposing a constraint in the constitutive equations even though it seemed necessary according to the definition that ϵ^{V} is not recoverable. As shown in [15-17] $\sigma_{ij}\dot{\epsilon}_{ij}^{p}<0$ (where $\dot{\epsilon}_{ij}^{p}$ is the plastic strain rate) is allowable from the thermodynamic point of view. A possible improvement is to unify ϵ^{VE} and ϵ^{V}, i.e., let creep recovery correspond to the case when σ_{ij}' is smaller than α_{ij}. Then further creep or creep recovery are completely determined by the relative magnitude of the applied stress σ_{ij}' and back stress α_{ij}. This approach may also improve the defects of the modified superposition principle of not describing the observed synergistic effect during creep recovery. That is, $\|\Sigma_{ij}\|$ which controls the creep recovery rate, can be increased by the addition of applied stress. However, since Σ_{ij} could not change sign under constant stress states, the unified approach may not be able to accurately simulate the material behavior under some step down loadings in which strain recovery is followed by further creep as reported in [7], i.e., the direction of strain rate switches from a negative to a positive direction.

Since all the tests reported here, except for Fig. 1, were performed at relatively high stress states, see Fig. 1 of [6], it is possible that the mechanisms, which were involved in the tertiary stage like period 1 of Fig. 5, may also have come into effect in these tests. This would increase the difficulties of theoretical simulation of material behavior. Experimental study in the microscopic scale is essential for a complete understanding of the time dependence of material behavior.

Conclusions

Experimental observations on the creep behavior of AL2618-T61 under nonproportional loadings were presented. Among the important findings are anisotropy induced by creep strain; synergistic effects on creep recovery; and strongly nonlinear material behavior at high stress levels.

Theories with different hardening natures, i.e., isotropic strain hardening, kinematic hardening, and independent strain hardening, were evaluated with reference to the experimental data. The *VV* model with strain-hardening nature (either *SH* or *IND*) generally gave better predictions than the other theories considered. However, all theories were found to suffer from some disadvantages. Strain hardening approaches generally underestimated the effects of prior creep strain, while the kinematic hardening approaches overestimated them; and neither of them could simulate the strongly nonlinear material behavior at high stress levels which might be due to time-dependent fracture mechanisms. No overwhelming advantages over the other were found between the isotropic strain hardening and the independent strain-hardening flow rules. The constitutive equation for the viscoelastic component in the *VV* model based on the modified superposition principle could not predict the synergistic effects on creep recovery. It also had limitations on predicting the behavior under side step-down loadings (i.e., when only one of two stress components decreased).

Further experimental work is needed for the improvement of the constitutive equations based on state variable approaches, such as a systematic study of the direction of the strain rate vector under nonproportional loadings, and the microscopic deformation mechanisms involved. More theoretical study is also necessary on properly specifying and controlling the evolution of the state variables characterizing the material structure.

Acknowledgment

This work was supported by the Army Research Office, Research Grant Number DAAG29-81-K-0138. The material was contributed by the Aluminum Company of America. The authors are grateful to R. M. Reed for assistance in experiments and Ms. C. Gavin for typing the manuscript.

References

1 Findley, W. N., Cho, U. W., and Ding, J. L., "Creep of Metals and Plastic Under Combined Stresses, A Review," ASME *Journal of Engineering Materials and Technology*, Vol. 101, 1979, pp. 365-368.

2 Findley, W. N., and Lai, J. S., "Creep and Recovery of 2618 Aluminm Alloy Under Combined Stress With a Representation by a Viscous-Viscoelastic Model," ASME JOURNAL OF APPLIED MECHANICS, Vol. 45, 1978, pp. 507-514.

3 Lai, J. S., and Findley, W. N., "Creep of 2618 Aluminum Under Step Stress Changes Predicted by a Viscous-Viscoelastic Model," ASME JOURNAL OF APPLIED MECHANICS, Vol. 47, 1980, pp. 21-26.

4 Findley, W. N., and Lai, J. S., "Creep of 2618 Aluminum Under Side Steps of Tension and Torsion and Stress Reversal Predicted by a Viscous-Viscoelastic Model, ASME JOURNAL OF APPLIED MECHANICS, Vol. 48, 1981, pp. 47-54.

5 Lai, J. S., and Findley, W. N., "Simultaneous Stress Relaxation in Tension and Creep in Torsion of 2618 Aluminum at Elevated Temperature," ASME JOURNAL OF APPLIED MECHANICS, Vol. 49, 1982, pp. 19-25.

6 Ding, J. L., and Findley, W. N., "48 Hour Multiaxial Creep and Creep Recovery of 2618 Aluminum Alloy at 200°C," ASME JOURNAL OF APPLIED MECHANICS, Vol. 51, 1984, pp. 125-132.

7 Ding, J. L., and Findley, W. N., "Multiaxial Creep of 2618 Aluminum Under Proportional Loading Steps," ASME JOURNAL OF APPLIED MECHANICS, Vol. 51, 1984, pp. 133-140.

8 Findley, W. N., and Gjelsvik, A., "A Biaxial Testing Machine for Plasticity, Creep or Relaxation Under Variable Principal Stress Ratios," *Proceedings, American Society for Testing and Materials*, Vol. 62, 1962, pp. 1103-1118.

9 Gittus, J. H., *Creep Viscoelasticity and Creep Fracture in Solids*," Wiley, New York, 1975.

10 Robinson, D. N., "A Unified Creep-Plasticity Model for Structural Metals at High Temperature," ORNL-TM-5969, Oak Ridge National Laboratory, Oct. 1978.

11 Miller, A. K., "An Inelastic Constitutive Model for Monotonic, Cyclic, and Creep Deformation: Part 1—Equations Development and Analytical Procedures and Part 2—Applications to Type 304 Stainless Steel," ASME *Journal of Engineering Material and Technology*, Vol. 98, 1976, pp. 97-113.

12 Kreig, R. D., Swearengen, J. C., and Rohde, R. W., "A Physically Based Internal Variable Model for Rate Dependent Plasticity," in *Inelastic Behavior of Pressure Vessel and Piping Components*, PVP-PB-028, ASME, 1978, p. 15.

13 Hart, E. W., "Constitutive Relations for the Nonelastic Deformation of Metals," ASME *Journal of Engineering Material and Technology*, Vol. 98, 1976, pp. 193-202.

14 Onat, E. T., "Representation of Inelastic Behavior," in *Creep and Fracture of Engineering Materials and Structures*, Wilshire, B., and Owen, D. R. J., Eds., Pineridge Press, Swansea, U. K., 1981.

15 Kestin, J., and Rice, J. R., "Paradoxes in the Application of Thermodynamics to Strained Solids," in *A Critical Review of Thermodynamics*, Stuart, E. B. et al., Ed., Mono Book Corporation, Baltimore, 1970.

16 Rice, J. R., "Inelastic Constitutive Relations for Solids: An Internal Variable Theory and Its Application to Metal Plasticity," *J. Mech. Phys. Solids*, Vol. 19, 1971, pp. 433-455.

17 Rice, J. R., "Continuum Mechanics and Thermodynamics of Plasticity in Relation to Microscale Deformation Mechanics," in *Constitutive Equations in Plasticity*, Argon Ed., MIT Press, 1975.

Downloaded 02 May 2010 to 171.66.16.54. Redistribution subject to ASME license or copyright; see http://www.asme.org/terms/Terms_Use.cfm

A Viscoplastic Theory With Anisotropic Hardening and Its Application to Pressure-Shear Plate Impact Experiments

A. Gilat
Department of Engineering Mechanics,
The Ohio State University,
Columbus, Ohio 43210
Assoc. Mem. ASME

An elastic/viscoplastic theory that includes anisotropic strain hardening is presented. The theory is a combination of the elastic/viscoplastic formulation of Perzyna [4] and the anisotropic hardening model for time-independent plasticity of Mroz [6]. The theory is used in the analysis of pressure-shear plate impact experiments on commercially pure alpha titanium. Good agreement between theory and experiment is observed.

Introduction

Various forms of constitutive theories for viscoplasticity have been proposed. For a review reference is made, for example, to [1-4]. A widely used formulation for a general state of stress has been introduced by Perzyna [4]. The formulation consists of an assumed function which determines the magnitude of an effective plastic strain rate and a flow potential which gives the direction of the plastic strain rate vector. The flow potential at a point in stress space is a surface obtained by isotropic expansion of the yield surface through the point. The plastic strain rate vector is in the direction of the normal to the flow potential at that point. Hardening of the material during plastic deformation can be introduced by changes in the shape, size, and location of the yield surface. Perzyna [4] has presented the theory for isotropic hardening in which plastic work was used as a measure of the hardening. A formulation for a general hardening law has been presented by Eisenberg and Yen [5].

An anisotropic hardening model for time-independent plastic deformation has been introduced by Mróz [6]. In this model, the stress space is divided into regions by hypersurfaces $f_0, f_1, \ldots f_n$ where f_0 is the yield surface and $f_1, \ldots f_n$ are boundaries of regions of constant work hardening moduli. During plastic deformation the surfaces are allowed to translate and expand. The plastic strain rate vector is in the direction of the normal to the yield surface and its magnitude depends on the value of the work-hardening modulus in the region at which the yield surface is located. The translation direction of the surfaces depends on their relative positions and is obtained from the condition that the stress point remains on the yield surface. The Mroz model has been successfully applied in analysis of experiments that involve quasistatic cyclic nonproportional loadings [7].

In the present paper, the hardening model of Mróz [6] is introduced into the elastic/viscoplastic formulation of Perzyna [4]. The hardening model is modified to adapt it for use in a time-dependent theory. The stress point in the viscoplastic model does not remain on the yield surface. Consequently, the magnitude of the translation of the yield surface can not be obtained, as in the time-independent model, from the location of the stress point. In the model proposed here, the translation depends on the value of the hardening modulus in the region at which the yield surface is located. This will affect the magnitude of the plastic strain rate vector directly since it depends on the overstress (the distance between the stress point and the yield surface). The resultant model is used in the analysis of pressure-shear plate impact experiments. Other anisotropic hardening models, e.g., [8-10], for time-independent plasticity with features similar to the model used here have been introduced. These models can probably also be combined with the Perzyna model.

The pressure-shear plate impact experiment has been introduced by Abou-Sayed, Clifton, and Hermann [11] and further developed by Kim and Clifton [12]. In this experiment two parallel plates of the same material are impacted with their impact faces inclined relative to the direction of approach. Plastic waves of combined pressure and shear are produced at the impact face and propagate through the plates. The waves are monitored by measuring the motion (in-plane and normal components at the same point) of the rear surface of the target plate. The wave profiles can be computed once a constitutive relation for the plastic deformation is assumed. The validity of this relation is determined by comparing the theoretical and experimental wave profiles. Since the pressure and shear waves propagate through the plate at different speeds, every section of the plate experiences a different

Contributed by the Applied Mechanics Division and presented at the 1985 Joint ASME/ASCE Applied Mechanics, Fluids Engineering, and Bioengineering Conference, Albuquerque, N. Mex., June 24-26, 1985 of THE AMERICAN SOCIETY OF MECHANICAL ENGINEERS.

Discussion on this paper should be addressed to the Editorial Department, ASME, United Engineering Center, 345 East 47th Street, New York, NY. 10017, and will be accepted until two months after final publication of the paper itself in the JOURNAL OF APPLIED MECHANICS. Manuscript received by ASME Applied Mechanics Division, May, 1984; final revision, November, 1984. Paper No. 85-APM-37.

Copyright © 1985 by ASME
Downloaded 02 May 2010 to 171.66.16.54. Redistribution subject to ASME license or copyright; see http://www.asme.org/terms/Terms_Use.cfm

nonproportional loading path. This aspect of the experiment provides an opportunity to examine the effect of the hardening law in the constitutive relation.

Theoretical analysis of pressure-shear waves in an aluminum plate has been presented by Abou-Sayed and Clifton [13]. This analysis makes use of Perzyna's elastic/viscoplastic model with isotropic strain hardening. Gilat and Clifton [14] have extended the solution to include kinematic strain hardening and have applied it also to alpha titanium. Comparison of computed wave profiles with experimental results on 6061-T6 aluminum and commercially pure alpha titanium have shown [14] that the hardening model has only a minor effect on the profiles of the aluminum since 6061-T6 aluminum exhibits only small strain hardening. For the titanium, the isotropic hardening model predicts a stiffer material response than observed while the kinematic strain hardening model predicts a softer material response than observed.

The combined Perzyna-Mróz model is used here in the analysis of the pressure-shear plate impact experiment on titanium conducted in [14]. Good agreement between theoretical predictions and experimental results is obtained. The main difference between the model used here and the kinematic strain hardening is that the yield surface translates more rapidly during changes in the direction of the stress path. Consequently, when a change in direction occurs in the loading path, the material will harden in the new direction and soften in the old direction at a greater rate than in the kinematic strain hardening model. The rate of hardening in the new direction decreases if the loading direction does not change further.

Theoretical Analysis

Details of the theoretical analysis of elastic/viscoplastic pressure shear waves in a plate are given in [13]. Here, only the parts needed for the introduction of the anisotropic hardening model are reviewed. The total strain rate is assumed to have elastic and viscoplastic components in the form[1]

$$\dot{\epsilon}_{ij} = \frac{1+\nu}{E}\dot{\sigma}_{ij} - \frac{\nu}{E}\dot{\sigma}_{kk}\delta_{ij} + \dot{\epsilon}_{ij}^{vp} \tag{1}$$

where ν, E, and δ_{ij} are Poisson's ratio, Young's modulus, and the Kronecker delta, respectively. From Perzyna [4], the viscoplastic term in equation (1) is taken in the form

$$\dot{\epsilon}_{ij}^{vp} = <\phi(\bar{\tau},\bar{\gamma}^p)>\frac{\partial f}{\partial \sigma_{ij}} \tag{2}$$

where ϕ is equivalent plastic shear strain rate given by $\phi = (2\dot{\epsilon}_{ij}^{vp}\dot{\epsilon}_{ij}^{vp})^{1/2}$, $\bar{\gamma}^p$ is equivalent plastic shear strain $\bar{\gamma}^p = \int_0^t \phi dt$, $\bar{\tau}$ is effective shear-stress and f is the plastic flow potential. The definitions of $\bar{\tau}$, f, and $<\phi(\bar{\tau},\bar{\gamma}^p)>$ will be given. Equation (1) combined with equations of motion and compatibility relations constitute a hyperbolic system of five semilinear first-order partial differential equations. This system can be rewritten as ordinary differential equations along characteristics and then solved numerically by a finite differences method.

From Mróz [6], hypersurfaces $f_0, f_1, \ldots f_n$ are defined in the deviatoric stress space by

$$f_k(S_{ij},\alpha_{ij}^k) = \left[\frac{1}{2}(S_{ij}-\alpha_{ij}^k)(S_{ij}-\alpha_{ij}^k)\right]^{1/2} = K_k \quad k=0,1,\ldots n \tag{3}$$

in which S_{ij} is the stress deviator, $S_{ij} = \sigma_{ij} - 1/3\ \sigma_{kk}\ \delta_{ij}$, K_k are constants and α_{ij}^k is the position of the center of the surface f_k

[1] A superposed dot indicates differentiation with respect to time.

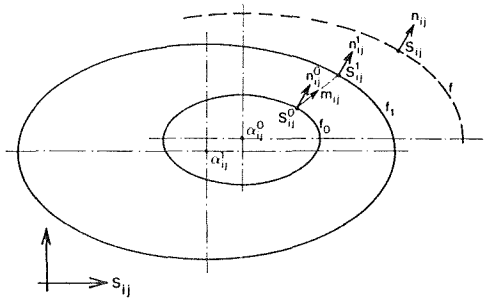

Fig. 1 Translation of surface f_0 inside surface f_1

(the values of K_k and the evolution equations for α_{ij}^k will be given). The flow potential f and the effective shear stress $\bar{\tau}$ are defined by

$$\bar{\tau} = f(S_{ij},\alpha_{ij}^0) = \left[\frac{1}{2}(S_{ij}-\alpha_{ij}^0)(S_{ij}-\alpha_{ij}^0)\right]^{1/2} \tag{4}$$

The function $<\phi(\bar{\tau},\bar{\gamma}^p)>$ in equation (2) is defined by

$$<\phi(\bar{\tau},\bar{\gamma}^p)> = \begin{cases} 0 & \text{for} \quad \bar{\tau} \le K_0 \\ \phi(\bar{\tau},\bar{\gamma}^p) & \text{for} \quad \bar{\tau} > K_0 \end{cases} \tag{5}$$

The plastic strain rate function ϕ, used also in [14], is taken from Hsu and Clifton [15]. The function is assumed to have a form suggested by concepts of dislocation dynamics

$$\phi(\bar{\tau},\bar{\gamma}^p) = bN\bar{v}(\bar{\tau},\bar{\gamma}^p) \tag{6}$$

where b is the Burgers vector and, for polycrystalline materials, N and $\bar{v}$ are defined as average values of dislocation density and dislocation velocity.

During plastic deformation the surfaces translate. The surfaces cannot intersect but consecutively contact and "push" each other. Thus, f_0 translates to touch f_1, next f_0 and f_1 translate together, while in contact, toward f_2 and so on.

Consider first the translation of f_0 inside f_1. A typical situation is shown in Fig. 1. The position of the centers of f_0 and f_1 is defined by α_{ij}^0 and α_{ij}^1. The applied stress is S_{ij}. The flow potential f is given by equation (4) and is the surface obtained by isotropic expansion of f_0 through S_{ij}. n_{ij} is the normal to the flow potential at S_{ij} and is given by

$$n_{ij} = \frac{\partial f}{\partial \sigma_{ij}} = \frac{\partial f}{\partial S_{ij}} = \frac{S_{ij}-\alpha_{ij}^0}{2\bar{\tau}} \tag{7}$$

S_{ij}^0 and S_{ij}^1 are points on the surfaces f_0 and f_1 at which the direction of the normals n_{ij}^0 and n_{ij}^1 to f_0 and f_1, respectively, are in the direction of n_{ij}. n_{ij}^0 and n_{ij}^1 are given by

$$n_{ij}^k = \left(\frac{\partial f_k}{\partial S_{ij}}\right)_{S_{ij}=S_{ij}^k} = \frac{S_{ij}^k - \alpha_{ij}^k}{2K_k} \quad k=0,1 \tag{8}$$

S_{ij}^0 and S_{ij}^1 are obtained from the condition that n_{ij}^0 and n_{ij}^1 are in the direction of n_{ij}

$$S_{ij}^k = \alpha_{ij}^k + \frac{K_k}{\bar{\tau}}(S_{ij}-\alpha_{ij}^0) \quad k=0,1 \tag{9}$$

The surface f_0 translates to contact the surface f_1 at a point at which the normals to both surfaces are in the direction of n_{ij}. To obtain such a translation, the instantaneous translation of f_0 is in the direction of the line connecting points S_{ij}^0 and S_{ij}^1 (the direction of m_{ij} in Fig. 1). Once f_0 contacts, f_1, f_1 will start to translate to contact f_2 at a point at which the normals to f_1 and f_2 are both in the direction of n_{ij} (shown in Fig. 2). During this translation, f_0 remains in contact with f_1, such that the normals to both surfaces at the contact point are

Downloaded 02 May 2010 to 171.66.16.54. Redistribution subject to ASME license or copyright; see http://www.asme.org/terms/Terms_Use.cfm

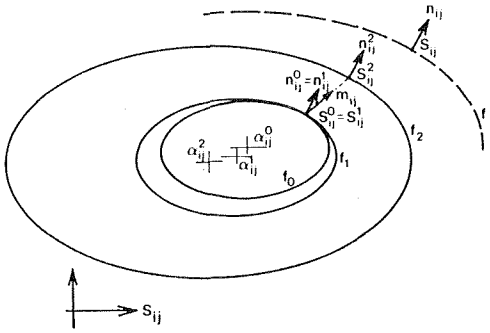

Fig. 2 Translation of surface f_1 inside surface f_2

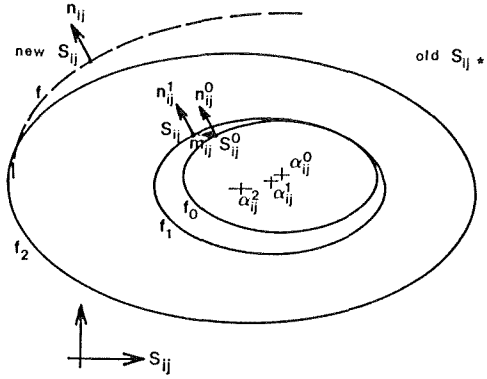

Fig. 3 Translation of surface f_0 inside surface f_1 following a change in loading direction

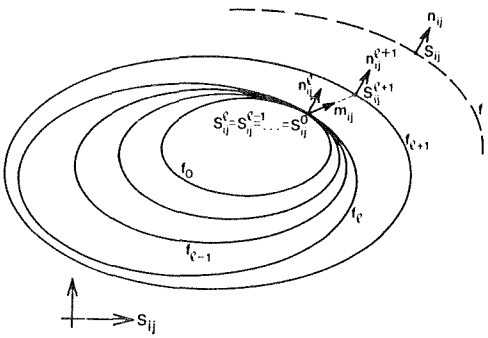

Fig. 4 Translation of surface f_l inside surface f_{l+1}

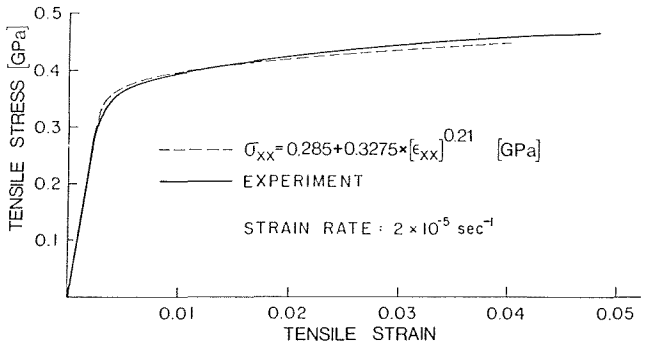

Fig. 5 Static uniaxial stress-strain curve for alpha titanium

in the direction of n_{ij}. If S_{ij} is changed during the translation of f_1 such that the direction of the normals to f_0 and f_1 at their contact point is not in the direction of n_{ij}, then f_1 stops translating and f_0 translates inside f_1 to make contact at a new point (shown in Fig. 3).

A general configuration is shown in Fig. 4. The surfaces f_0, f_1, . . . f_l are all in contact at one point $S_{ij}^0 = S_{ij}^1 = \ldots = S_{ij}^l$ such that the normals n_{ij}^0, n_{ij}^1, . . . ,n_{ij}^l are all in the same direction. Point S_{ij}^{l+1} is a point on f^{l+1} at which the normal n_{ij}^{l+1} to f_{l+1} is in the direction of n_{ij}. The normals n_{ij}^0, . . . , n_{ij}^{l+1} and the points S_{ij}^0, . . . ,S_{ij}^{l+1} are given by equations (8) and (9), respectively, with $k = 0, \ldots, l+1$. If in the next increment n_{ij} is in the direction of n_{ij}^l, then the surface f_l will translate to contact the surface f_{l+1} at a point at which the normals to f_l and f_{l+1} are in the direction of n_{ij}. To obtain such a translation, the instantaneous translation of f_l is in the direction of the line connecting points S_{ij}^l and S_{ij}^{l+1}.

$$\dot{\alpha}_{ij}^l = \dot{\mu}_l m_{ij} \tag{10}$$

where m_{ij} is a unit vector in the direction $s_{ij}^{l+1} - s_{ij}^l$ and $\dot{\mu}_l$ is given by

$$\dot{\mu}_l = \mu_l' \dot{\phi} \tag{11}$$

in which μ_l' is a constant. During the translation of f_l toward f_{l+1} the surfaces f_0, . . . f_{l-1} remain in contact with f_l at S_{ij}^l such that the normals to these surfaces at the point of contact are in the direction of n_{ij}. From this condition the centers of the surfaces f_0, . . . f_{l-1} are given by

$$\alpha_{ij}^k = S_{ij}^k - \frac{K_k}{K_l}(S_{ij}^l - \alpha_{ij}^l) \quad k = 0, \ldots, l-1 \tag{12a}$$

since $S_{ij}^k = S_{ij}^l$, α_{ij}^k can be written as

$$\alpha_{ij}^k = S_{ij}^l - \frac{K_k}{K_l}(S_{ij}^l - \alpha_{ij}^l) \quad k = 0, \ldots, l-1 \tag{12b}$$

If the next increment S_{ij} is changed such that n_{ij} is not in the direction of n_{ij}^0, . . . ,n_{ij}^l, then the surface f_l does not translate, but f_0 translates first inside f_1 and so on.

The constants μ_0', . . . ,μ_n' and K_0, . . . ,K_n are determined from a uniaxial static stress-strain curve. During quasi-static plastic deformation the stress state remains on the yield surface f_0. As f_0 translates and contacts the surfaces f_1, . . . f_l the stress state is the contact point. The non-zero components of the deviatoric stress tensor in a uniaxial tension test are $S_1 = 2\sigma_{xx}/3$ and $S_{22} = S_{33} = -\sigma_{xx}/3$. The normal n_{ij} is constant during this test and m_{ij} is a unit vector in the direction of n_{ij}. Using this information, equations (3) and (10), and for $\mu = \mu(\bar{\gamma}^p)$, the following expression is obtained for μ_l'.

$$\mu_l'(\bar{\gamma}^p) = \frac{\sqrt{2}}{3}\frac{d\sigma_{xx}}{d\epsilon_{xx}^p}\bigg|_{\epsilon_{xx}^p = \bar{\gamma}^p/\sqrt{3}} \tag{13}$$

Thus, μ_l' is related to the slope of the uniaxial stress-strain curve. The σ-ϵ curve is then approximated by n linear segments of constant plastic moduli E_0^p, . . . ,E_{n-1}^p. Every segment k is related to a region of constant strain hardening rate between two surfaces f_k and f_{k-1}. μ_k' in this region is given by

$$\mu_k' = \frac{\sqrt{2}}{3}E_k^p \tag{14}$$

The constants K are given by

$$K_k = \frac{1}{\sqrt{3}}(\sigma_{xx})_k \tag{15}$$

where $(\sigma_{xx})_k$ is the value of σ_{xx} in the beginning of the linear segment k.

Results

The anisotropic hardening model introduced in the preceding section was used in the analysis of pressure-shear impact experiments on commercially pure alpha titanium.

Downloaded 02 May 2010 to 171.66.16.54. Redistribution subject to ASME license or copyright; see http://www.asme.org/terms/Terms_Use.cfm

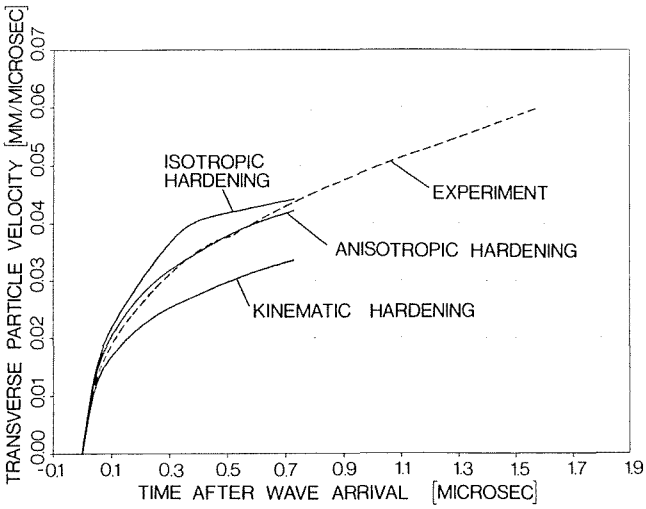

Fig. 6 Transverse velocity-time profiles at the rear surface of the specimen (shot #A-22). Titanium, impact velocity: 0.208 mm/μsec, angle: 26.6 deg., thickness 4.6 mm.

Results are shown here for shot #22 of reference [14]. In this shot the impact velocity is 0.208 mm/μsec, angle of inclination 26.6 deg, and specimen thickness 4.6 mm. The uniaxial static tension stress-strain curve of the material used, Fig. 5, was divided into nine linear sections. All the material constants are the same as in [14].

Transverse particle velocity-time profiles at the rear surface of the specimen are shown in Fig. 6. The figure shows the measured profile, the calculated profiles from isotropic and kinematic strain hardening models taken from [14], and the calculated profile from the anisotropic strain hardening model introduced here. The profile from the anisotropic hardening is between the profiles from kinematic and isotropic hardenings and is in good agreement with the measured profile.

The difference between the hardening models is demonstrated in Figs. 7 and 8 (the plots in Fig. 8 are taken from [16]). The figures show stress trajectories and trajectories of the center of the yield surfaces at a section of the plate located 1.84 mm from the impact face. For the coordinates chosen in these figures, the yield surface is a circle. The stress trajectory starts at point A when the elastic precursor of the compression normal wave arrives at that section. Initially, as the normal plastic wave arrives, $-(\sigma_{xx}-\sigma_{yy})/\sqrt{3}$ increases to reach a maximum at point B. Then, hydrostatic pressure builds up and the difference between σ_{xx} and σ_{yy} decreases. At point C the shear stress starts to increase due to the arrival of the shear wave, while the hydrostatic pressure continues to build up. At point D the normal wave that is reflected back fron the rear free surface arrives to the cross section as a tension wave. The jump from point D to point E corresponds to the arrival of the elastic precursor of the reflected wave. For each of the hardening models, the yield surfaces shown in the figures are the initial surface and the subsequent surface at the time when the reflected normal wave arrives (corresponds to point D on the stress trajectory). The location of the yield surfaces is shown by an asterisk. The flow potential at each point on the stress trajectory is the surface obtained by isotropic expansion of the curernt yield surface through the point. The plastic strain rate vector is in the direction of the normal to the flow potential at the point. The magnitude of the plastic strain rate is determined by the function ϕ in equation (2) which is a function of the overstress. The overstress, in the coordinates chosen in Figs. 7 and 8, is the distance between the stress point on the stress trajectory and the current yield surface.

The rate of translation and expansion in the kinematic and

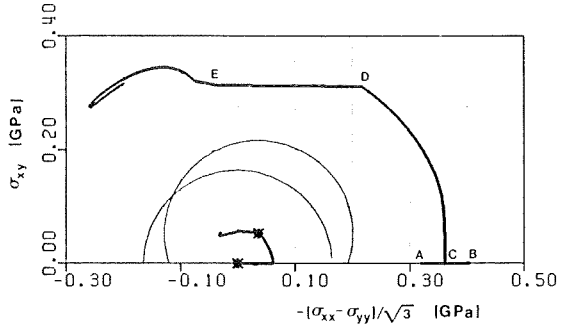

Fig. 7 Stress trajectory and translation of yield surface in the anisotropic hardening model

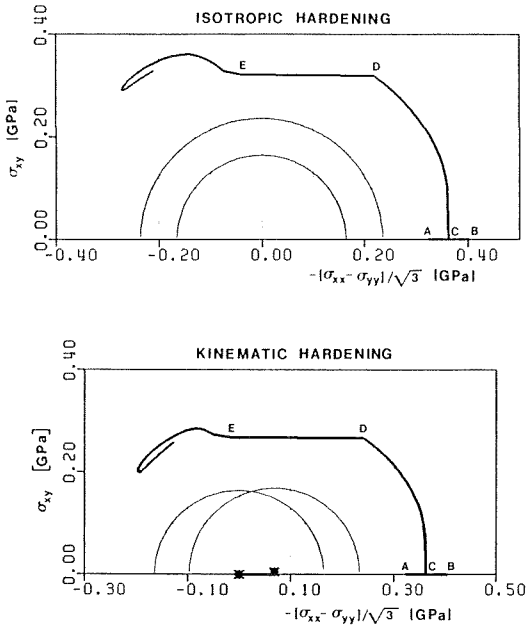

Fig. 8 Stress trajectories and changes in yield surface in the isotropic and kinematic hardening models

isotropic hardening models, respectively, was taken in [14] to be a function of the accumulated plastic strain which is related to the quasistatic stress strain curve. This curve, Fig. 5, shows a high rate of hardening for small strains and a decreasing rate of hardening as the strain increases. Consequently, the yield surface in the kinematic hardening translates considerably during the initial loading by the normal wave, but translates with a low rate later as the loading path changes when the shear wave arrives. Similarly, the rate of expansion of the yield surface in the isotropic hardening case is high initially and decreases as plastic strain accumulates.

The strain rates predicted by the three models are about the same during the initial proportional loading related to the compressive normal wave. During this loading the translation of the yield surface of the kinematic and anisotropic hardening models is about the same and the yield surface of the isotropic hardening expands by the same amount. The difference between the models appears when the loading direction changes. As shown in Fig. 8, the kinematic yield surface does not translate much to the new direction and the isotropic yield surface has already expanded in all directions. Consequently, following a change in the loading path, larger overstress values are observed for the kinematic hardening model. The higher overstress causes higher plastic strain rates, which leads to lower velocity time profiles. For the anisotropic hardening, Fig. 7 shows that the yield surface follows the stress trajectory. The calculated plastic strain rates

Downloaded 02 May 2010 to 171.66.16.54. Redistribution subject to ASME license or copyright; see http://www.asme.org/terms/Terms_Use.cfm

from the anisotropic hardening model are between the rates obtained by the isotropic and kinematic hardening models.

The normal particle velocity-time profile predicted by the anisotropic hardening model is almost identical to the profiles predicted by the isotropic and kinematic hardening models in [14], and thus, not shown here. This result indicates, as in [14], that the shear wave profiles in the pressure-shear plate impact experiment are sensitive to the plastic flow characteristics of the material and can be used as a sensitive indicator of the validity of proposed constitutive relations.

Concluding Remarks

Constitutive relations for rate-sensitive plastic deformation that include anisotropic hardening have been presented. These relations, which are a combination of Perzyna [4] formulation and Mróz [6] hardening model, can be applied to a general state of stress and loading history. Application of the constitutive relations in the analysis of results from pressure-shear plate impact experiment have shown that these relations model the material response adequately. The pressure-shear plate impact technique appears to be useful for studying constitutive relations for plasticity.

Acknowledgment

The author wishes to thank Professor R. J. Clifton of Brown University for helpful discussions and suggestions.

References

1 Cristescu, N., and Suliciu, I., *Viscoplasticity*, Martinus Nijhoff Publishers, 1982.

2 Clifton, R. J., "Plastic Waves: Theory and Experiment," *Mechanics Today*, Nemat-Nasser, S., ed., Pergamon Press, 1972, pp. 102-167.

3 Nicholas, T., in: *Impact Dynamics*, Zukas, J. A., Nicholas, T., Swift, H. F., Greszczuk, L. B. and Curran, D. R., eds. John Wiley & Sons, New York, 1982, Chapters 4 and 8.

4 Perzyna, P., "Fundamental Problems in Viscoplasticity," *Advances in Applied Mechanics*, Academic Press, New York, Vol. 9, 1966, pp. 243-377.

5 Eisenberg, M. A., and Yen, C. F., "A Theory of Multiaxial Anisotropic Viscoplasticity," ASME JOURNAL OF APPLIED MECHANICS, Vol. 48, 1981, pp. 276-284.

6 Mróz, Z., "On the Description of Anisotropic Workhardening," *J. Mech. Phys. Solids*, Vol. 15, 1967, pp. 163-175.

7 Lamba, H. S., and Sidebottom, O. M., "Cyclic Plasticity for Nonproportional Paths: Part 2—Comparison With Predictions of Three Incremental Plasticity Models," ASME *Journal of Engineering Materials and Technology*, Vol. 100, 1978, pp. 104-111.

8 Dafalias, Y. F., and Popov, E. P., "A Model of Nonlinearly Hardening Materials for Complex Loading," *Acta Mechanica*, Vol. 21, 1975, pp. 173-192.

9 Mróz Z., Shrivastava, H. P., and Dubey, R. N., "A Non-Linear Hardening Model and Its Application to Cyclic Loading," *Acta Mechanica*, Vol. 25, 1976, pp. 51-61.

10 Krieg, R. D., "A Practical Two Surface Plasticity Theory," ASME JOURNAL OF APPLIED MECHANICS, Vol. 42, 1975, pp. 641-646.

11 Abou-Sayed, A. S., Clifton, R. J., and Hermann, L., "The Oblique-Plate Impact Experiment," *Experimental Mechanics*, Vol. 16, 1976, pp. 127-133.

12 Kim, K. S., and Clifton, R. J., "Pressure-Shear Impact of 6061-T6 Aluminum," ASME JOURNAL OF APPLIED MECHANICS, Vol. 47, 1980, pp. 11-16.

13 Abou-Sayed, A. S., and Clifton, R. J., "Analysis of Combined Pressure-Shear Waves in an Elastic/Viscoplastic Material," ASME JOURNAL OF APPLIED MECHANICS, Vol. 44, 1977, pp. 79-84.

14 Gilat, A., and Clifton, R. J., "Pressure-Shear Waves in 6061-T6 Aluminum and Alpha Titanium," to be published in the *J. Mech. Phys. Solids*.

15 Hsu, J. C. C., and Clifton, R. J., "Plastic Waves in a Rate Sensitive Material Part I: Waves of Uniaxial Stress," *J. Mech. Phys. Solids*, Vol. 22, 1974, pp. 253-255.

16 Gilat, A., "An Experimental and Numerical Investigation of Pressure Shear Waves in 6061-T6 Aluminum and Alpha-Titanium," Ph.D. thesis, Brown University, Providence, R.I., 1982.

Downloaded 02 May 2010 to 171.66.16.54. Redistribution subject to ASME license or copyright; see http://www.asme.org/terms/Terms_Use.cfm

Optimal Cooling Paths for a Class of Thermorheologically Complex Viscoelastic Materials

B. D. Harper
Assistant Professor,
Department of Engineering Mechanics,
The Ohio State University,
Columbus, Ohio 43210-1181
Assoc. Mem. ASME

This paper concerns the optimal cooling of thin viscoelastic plates so as to minimize the residual thermal stresses upon completion of the cool-down process. The thermorheological behavior of the plate material is assumed complex in the sense that both horizontal and vertical shift factors are employed. The optimal path is shown to possess initial and final jump discontinuities and to depend on only one of the two components of the vertical shift factor. It is further demonstrated that significant reductions in the level of residual stress may be attained by following the optimal cooling path.

Introduction

An analytical method was recently developed to predict optimal temperature paths that minimize residual thermal stresses in thin plates of linear, thermorheologically simple, viscoelastic material [1,2]. This method has also been applied to cross-ply composite laminates and adhesive joints [3]. For a given, finite cooling time the optimal path was shown to contain jump discontinuities at the initial and final times.

This paper presents a scheme to predict optimal temperature paths for a class of thermorheologically complex materials. For the type of complex response considered here, all effects of temperature may be accounted for by vertical and horizontal shift factors (in contrast to simple response, which requires only a horizontal shift factor). In the present case, the optimal path is also found to possess initial and final jump discontinuities. In addition, it is shown that the optimal path depends on only one of the two components of the vertical shift factor. This fact is significant since transient temperature tests are required to uniquely separate the two components of the vertical shift [4–6], a procedure rarely employed in practice.

Analysis

Consider a linear viscoelastic material for which all effects of temperature may be correlated through a horizontal as well as a vertical shift factor. It has been noted previously [4,6] that a proper evaluation of transient temperature response requires the vertical shift to be represented as a product of two temperature-dependent functions. We consider, therefore, a thermoviscoelastic constitutive equation of the form

$$\sigma(t) = h_1(T(t)) \int_0^t E(\xi(t) - \xi(\tau)) \frac{d}{d\tau} [h_2(T(\tau))(\epsilon(\tau) - \alpha \Delta T(\tau))] d\tau \tag{1}$$

In (1) σ and ϵ denote stress and strain, respectively, $E(t)$ is the relaxation modulus, and $h(T) = h_1(T) h_2(T)$ is the vertical shift factor. Also, α is the linear coefficient of thermal expansion, T denotes temperature, ΔT the change in temperature from a reference value, while the reduced time ξ is defined by

$$\xi(u) = \int_0^u \frac{ds}{a(T(s))} \tag{2}$$

where $a(T)$ is the horizontal shift factor.

The significance of the horizontal and vertical shift factors can be demonstrated by plotting versus log t the relaxation modulus $E(t)$ obtained at an arbitrary reference temperature T_R and at an elevated temperature $T_e > T_r$. If (1) is valid, then the elevated temperature curve may be superimposed on the reference temperature curve by rigid horizontal and vertical shifts of magnitude log $a(T_e)$ and log $h(T_e)$, respectively. With this in mind, we see that the present constitutive model requires both horizontal and vertical shift factors to be positive-definite functions of temperature.

As in [1], consider a thin, isotropic viscoelastic plate that is fixed between rigid walls and is free of stress at some elevated temperature T_I. Subjecting this plate to a fluctuating ambient temperature $T(t)$ produces a spatially uniform stress $\sigma(t)$ given by

$$-\frac{1-\nu}{\alpha} \sigma(t) = h_1(T(t)) \int_0^t E(\xi(t) - \xi(\tau)) \frac{d\theta(T(\tau))}{d\tau} d\tau \tag{3}$$

provided heat conduction occurs rapidly compared with the time scale associated with viscoelastic relaxation processes.

In (3), ν is Poisson's ratio (assumed constant) and $\theta(T(t)) = h_2(T(t))(T(t) - T_I)$.

Contributed by the Applied Mechanics Division for publication in the JOURNAL OF APPLIED MECHANICS.

Discussion on this paper should be addressed to the Editorial Department, ASME, United Engineering Center, 345 East 47th Street, New York, N.Y. 10017, and will be accepted until two months after final publication of the paper itself in the JOURNAL OF APPLIED MECHANICS. Manuscript received by ASME Applied Mechanics Division, April, 1984; final revision, October, 1984.

Copyright © 1985 by ASME
Downloaded 02 May 2010 to 171.66.16.54. Redistribution subject to ASME license or copyright; see http://www.asme.org/terms/Terms_Use.cfm

Consider now the process of cooling the plate from the elevated temperature T_I to some final temperature T_F in a specified time interval t_f. Our objective is to determine an optimal temperature path $T(t)$ $0 \le t \le t_f$ which minimizes the stress $\sigma(t)$ following cool-down. This problem is directly related to that of determining optimal paths that minimize the residual stresses in an adhesive joint or a fiber-reinforced polymeric matrix composite [1–3] following cool-down from an elevated cure temperature (T_I) to some service temperature (T_F). In such cases, one is usually interested in minimizing the average residual stress experienced by a component during its service lifetime. In most practical situations, however, the service temperature history will not be known a priori. Consequently, optimal paths are sought that provide a minimal value for the stress experienced by a component immediately before it is put into service, i.e., at $t = t_f^+$.

As in [1] we assume that the optimal path possesses discontinuities at $t = 0$ and $t = t_f$, and is continuous over the open interval $(0,t_f)$. The necessity for making this assumption will be noted later. With these points in mind, equation (2) yields at time $t = t_f^+$.

$$-\frac{1-\nu}{\alpha}\sigma(t_f^+) = h_1(T_F)\int_{0^-}^{t_f^+} E(\xi(t_f)-\xi(\tau))\frac{d\theta(T(\tau))}{d\tau}d\tau \tag{4}$$

Note in (4) that the optimal path $T(t)$ does not depend on the component h_1 of the vertical shift factor since we wish to optimize the final value of σ and T_F is prescribed. In view of this, the problem reduces to one of finding an optimal path that minimizes the quantity $Q(t_f^+)$, where

$$Q(t_f^+) \equiv -\frac{1-\nu}{\alpha}\sigma(t_f^+)/h_1(T_F) = \int_{0^-}^{t_f^+} E(\xi(t_f) - \xi(\tau))\frac{d\theta(T(\tau))}{d\tau}d\tau \tag{5}$$

Integrating (5) by parts we obtain

$$Q(t_f^+) = E(0)\theta(T_F) + \int_0^{t_f} E'(\xi(t_f)-\xi(\tau))\frac{\theta(T(\tau))}{a(T(\tau))}d\tau \tag{6}$$

since $\theta(T_I) \equiv 0$. In equation (6) and the sequel, primes indicate derivatives with respect to the argument.

Letting $T(t)$ be the optimal path and designating $\tilde{T}(t) = T(t) + \epsilon\eta(t)$ as an adjacent path we write

$$\tilde{Q}(t_f^+) = E(0)\theta(T_F) + \int_0^{t_f} E'\left[\int_\tau^{t_f}\frac{ds}{a(T+\epsilon\eta)}\right]\frac{\theta(T(\tau)+\epsilon\eta(\tau))}{a(T(\tau)+\epsilon\eta(\tau))}d\tau \tag{7}$$

For any adjacent temperature path $\tilde{T}(t)$ we know

$$\frac{d}{d\epsilon}[\tilde{Q}(t_f^+)]_{\epsilon=0} = 0 = \int_0^{t_f}\left\{E''(t,t_f)\left[\int_t^{t_f} -\frac{a'(T(s))}{a^2(T(s))}\eta(s)ds\right]\frac{\theta(T(t))}{a(T(t))} + E'(t,t_f)\left[\frac{\theta'(T(t))a(T(t)) - a'(T(t))\theta(T(t))}{a^2(T(t))}\eta(t)\right]\right\}dt \tag{8}$$

where

$$E(t,t_f) = E\left[\int_t^{t_f}\frac{ds}{a(T(s))}\right] \tag{9}$$

Denoting

$$F(t) = \int_0^t E''(s,t_f)\frac{\theta(T(s))}{a(T(s))}ds \tag{10}$$

and integrating the first term in (8) by parts we obtain

$$\int_0^{t_f} F'(t)\left[\int_t^{t_f}\frac{a'(T(s))}{a^2(T(s))}\eta(s)ds\right]dt = F(t)\int_t^{t_f}\frac{a'(T(s))}{a^2(T(s))}\eta(s)ds\Big|_{t=0}^{t=t_f} + \int_0^{t_f} F(t)\frac{a'(T(t))}{a^2(T(t))}\eta(t)dt \tag{11}$$

The first term in (11) vanishes at both limits. Thus, equation (8) may be written

$$\int_0^{t_f}\left\{-\frac{a'(T(t))}{a^2(T(t))}\int_0^t E''(s,t_f)\frac{\theta(T(s))}{a(T(s))}ds + E'(t,t_f)\left[\frac{\theta'(T(t))a(T(t)) - a'(T(t))\theta(T(t))}{a^2(T(t))}\right]\right\}\eta(t)dt = 0 \tag{12}$$

Equation (12) will be zero for all η only if

$$E'(t,t_f)(\theta'(T(t))a(T(t)) - a'(T(t))\theta(T(t))) - a'(T(t))\int_0^t E''(p,t_f)\frac{\theta(T(p))}{a(T(p))}dp = 0 \tag{13}$$

Equation (13) represents Euler's equation for our problem and must be satisfied by the optimal path $T(t)$ for $0 < t < t_f$.

Since $\theta(T(t)) = h_2(T(t))(T(t) - T_I)$, equation (13) may also be written

$$E'(t,t_f)[a(T(t))\{h_2'(T(t))(T(t)-T_I) + h_2(T(t))\} - a'(T(t))h_2(T(t))(T(t)-T_I)] - a'(T(t))\int_0^t E''(p,t_f)\frac{h_2(T(p))(T(p)-T_I)}{a(T(p))}dp = 0 \tag{14}$$

Recalling that both $a(T)$ and $h_2(T)$ are positive-definite we note that if $T(0^+) \equiv T_0 = T_I$ (i.e., if no initial discontinuity exists) then equation (14) implies that $E'(0,t_f) = 0$, which is physically inadmissable, thus proving the existence of an initial discontinuity. Also, since (14) does not depend on the final temperature T_F, we would expect, in general, that $T(t_f^-) \equiv T_f \neq T_F$. The optimal temperature path will thus suffer an additional jump discontinuity at time $t = t_f$.

It is interesting to note that no optimal path can be found within the class of temperature paths considered here (i.e., those paths that are continuous over the open interval $0 < t < t_f$ with finite jump discontinuities at $t = 0$ and $t = t_f$) for the special case $h_2(T) \equiv a(T)$, since (14) would again yield $E'(0,t_f) = 0$ at $t = 0$. However, as discussed in the following section, available data preclude this possibility and it will not be considered here.

Setting $t = 0$ in (14) yields the magnitude of the initial discontinuity

$$T_0 - T_I = \frac{h_2(T_0)a(T_0)}{a'(T_0)h_2(T_0) - h_2'(T_0)a(T_0)} \tag{15}$$

An alternate form of Euler's equation may be obtained by differentiating (14) with respect to time. If the result of this differentiation is substituted back into (14), there results

$$\frac{dT}{dt} = -\frac{E''(t,t_f)}{E'(t,t_f)}\frac{a'(h_2'(T-T_I)+h_2}{a[a''(h_2'(T-T_I)+h_2) - a'(h_2''(T-T_I)+2h_2')]} \tag{16}$$

where $a = a(T(t))$ and $h_2 = h_2(T(t))$.

From thermodynamics we know $E''/E' < 0$ [7], while experience with polymeric resins indicates that $a > 0$, $a' < 0$, and $a'' > 0$ [8–10]. Certain assumptions regarding the temperature dependence of the function h_2 are required before any general observations about the nature of the optimal path may be inferred from (16). These assumptions are introduced in the following section.

Downloaded 02 May 2010 to 171.66.16.54. Redistribution subject to ASME license or copyright; see http://www.asme.org/terms/Terms_Use.cfm

Temperature Dependence of the Shift Factors

Available data [5,6,8,9] indicate that the horizontal shift factor $a(T)$ can be expressed

$$a(T) = \exp\left(-\gamma\left(\frac{T-T_R}{T_R}\right)\right) \tag{17}$$

where T_R is an arbitrarily chosen, but fixed reference temperature and γ is a positive constant.

It has been shown [4-6] that a unique decomposition of the vertical shift factor into its two components $h_1(T)$ and $h_2(T)$ requires transient temperature characterization tests. Unfortunately, data obtained from tests of this type are limited. Peretz and Weitsman [5] and Harper and Weitsman [6] used transient temperature tests to characterize the creep behavior of two resins according to

$$\epsilon_\sigma(t) = D_0 g_0(T)\sigma(t) + g_1(T)\int_0^t \Delta D(\xi(t) - \xi(\tau))\frac{d(g_2(T(\tau))\sigma(\tau))}{d\tau}\,d\tau \tag{18}$$

where $\epsilon_\sigma = \epsilon - \alpha\Delta T$. In (18), the reduced time ξ is given by (2), again with a horizontal shift factor $a(T)$. The vertical shift factor, however, is now given by $g(T) = g_1(T)g_2(T)$.

It is possible to relate the components of the vertical shift factor $h_1(T)$ and $h_2(T)$ in (1) to the components $g_1(T)$ and $g_2(T)$ in (18) as follows (see the Appendix)

$$h_1(T) = \frac{1}{g_2(T)}$$

$$h_2(T) = \frac{1}{g_1(T)} \tag{19}$$

In view of [5] we have

$$h_1(T) = \exp\left(-\psi\left(\frac{T-T_R}{T_R}\right)\right)$$

$$h_2(T) = \exp\left(\rho\left(\frac{T-T_R}{T_R}\right)\right) \tag{20}$$

where ψ and ρ are positive constants.

From (17) and (20) we observe that $a(T)$ is a monotonically decreasing function of temperature while $h_2(T)$ is a monotonically increasing function of temperature, thus excluding the possibility that $h_2(T) \equiv a(T)$. Recall from the preceding section that this is precisely the case for which (14) fails to yield an optimal path.

The Optimal Path for Power Law Response

Many polymeric materials exhibit power law response. For materials of this type the relaxation function may be expressed

$$E(t) = E_0 + E_1(t+t_0)^{-n} \tag{21}$$

where E_0, E_1, t_0, and n are constants.

It is common practice to characterize the thermoviscoelastic response of a material solely from isothermal experiments. If a material whose time-temperature behavior is described by (1) and (21) were characterized in this way, one would *incorrectly* find the material to be thermorheologically simple with an "apparent" horizontal shift factor [6]

$$b(T) = a(T)(h_1(T)h_2(T))^{1/n} \tag{22}$$

or, in view of (17) and (20)

$$b(T) = \exp\left(-\lambda\left(\frac{T-T_R}{T_R}\right)\right) \tag{23}$$

where

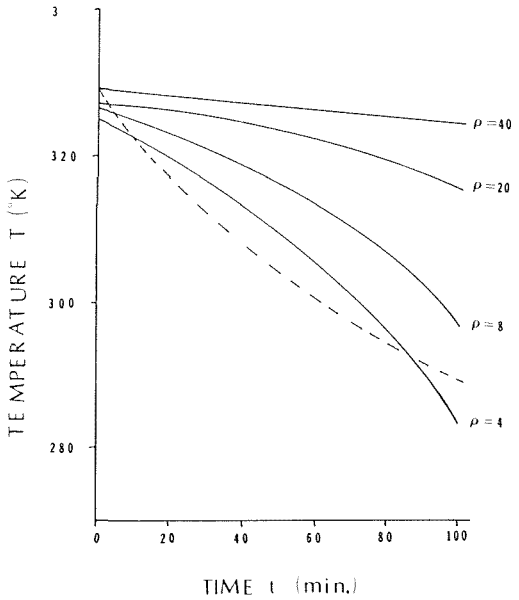

Fig. 1 Optimal temperature paths $T(t)$ for $\gamma = 40$ and $\rho = 4$, 8, 20, and 40 (solid lines) and for simple response with $\lambda = 70$ (dashed line)

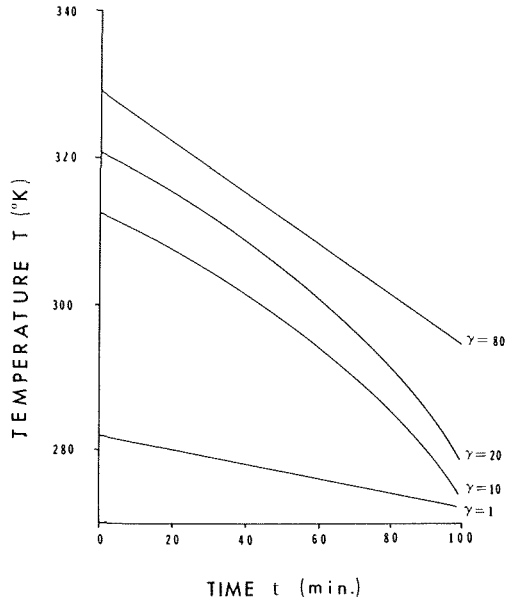

Fig. 2 Optimal temperature paths $T(t)$ for $\rho = 5$ and $\gamma = 1$, 10, 20, and 80

$$\lambda = \frac{\gamma n + \psi - \rho}{n} \tag{24}$$

If the material were, in reality, thermorheologically simple with horizontal shift factor $b(T)$, the optimal path would be given by [1]

$$T_0 - T_I = -T_R/\lambda$$

and

$$T = \frac{1}{C}\ln\left(\frac{L}{K+Ct}\right) \tag{25}$$

where $C = \lambda n/T_R(n+1)$. In (25), the values of L and K are found from the transcendental equation

$$L = \left[\frac{\lambda t_0 (K+Ct_f)^{1/n}e^{\lambda}}{T_R(n+1)}\right]^{n/n+1}$$

$$L = Ke^{CT_0} \tag{26}$$

The actual optimal path is, however, given by insertion of

Downloaded 02 May 2010 to 171.66.16.54. Redistribution subject to ASME license or copyright; see http://www.asme.org/terms/Terms_Use.cfm

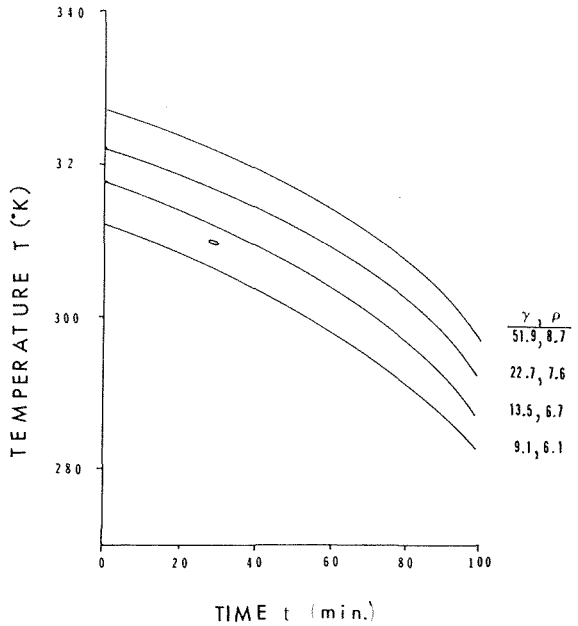

Fig. 3 Optimal paths $T(t)$ for various combination of γ and ρ selected so that $T_0 - T_s = 30°C$ in each case

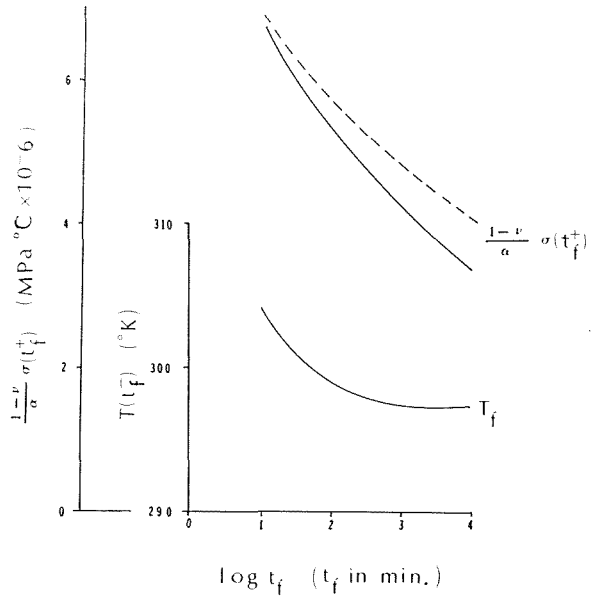

Fig. 4 The variation of $T(t_f^-) = T_f$ and the residual thermal stress $(1-\nu)/(\alpha)\,\sigma(t_f^+)$ with log t_f for $\gamma = 40$ and $\rho = 8.5$. The solid line corresponds to values of $(1-\nu)/(\alpha)\,\sigma(t_f^+)$ obtained by following the true optimal path, while the dashd line represents those values that result from following an optimal path for simple response with $\lambda = 70$.

(17), (20), and (21) into (15) and (16), which yields after several manipulations

$$T_0 - T_I = -\frac{T_R}{\gamma+\rho} \tag{27}$$

and

$$\frac{1}{T_R}\frac{dT}{dt} = -\left(\int_t^{t_f}\frac{ds}{a(T(s))} + t_0\right)^{-1}\frac{(n+1)}{a(T)(\gamma+\rho)}\frac{(T-T_s)}{(T-T_d)} \tag{28}$$

where

$$T_s = T_I - T_R/\rho$$

$$T_d = T_I - \frac{\gamma+2\rho}{\rho(\gamma+\rho)}T_R \tag{29}$$

Since γ and ρ are positive, equations (27) and (29) imply that $T_I > T_0 > T_s > T_d$. From (27) and (28) we see then that the optimal path drops suddenly from T_I to T_0 at $t=0$ and continues to decrease monotonically over $(0,t_f)$ reaching T_f at $t=t_f^-$. The optimal path then undergoes a second jump discontinuity at $t=t_f$ of magnitude $T_F - T_f$.

Computations

The solution for the optimal path $T(t)$ can be obtained from (28) by means of an iterative numerical scheme, as noted in reference [1].

In all computations we took $T_I = 333°K$, $T_F = 303°K$, $T_R = 303°K$, $\lambda = 70$, $n = 0.12$, $t_0 = 1$ min., $E_0 = 3000$MPa, and $E_1 = 30{,}000\text{MPa}\cdot\text{min}^n$.

Figure 1 exhibits optimal cooling paths $T(t)$ for $\gamma = 40$, $t_f = 100$ min., and $\rho = 4,8,20$, and 40. Since the optimal path is independent of ψ, a value of ψ (see equation (24)) may be chosen so that $\lambda = 70$ for all curves shown in Fig. 1. For comparison, the optimal path for a thermorheologically simple material with $\lambda = 70$ was calculated from (25) and (26), and is shown as a dashed line in Fig. 1. Note that this optimal path differs significantly in both a qualitative and quantitative sense from the optimal paths obtained from (28). These differences emphasize the need for considering transient temperature experiments when characterizing the thermoviscoelastic behavior of polymeric materials, since isothermal tests alone will not allow a unique determination of the horizontal and vertical shift factors [4-6].

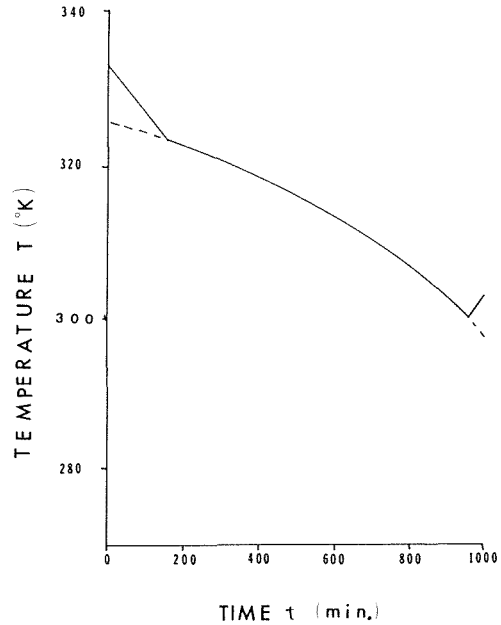

Fig. 5 "Modified" optimal path (solid curve) for $\gamma = 40$ and $\rho = 8.5$ with maximum heating and cooling rate of 0.05°C/min. The dashed curve represents the actual optimal cooling path for this case.

Figure 2 is similar to Fig. 1 except that ρ is held constant ($\rho = 5$) and optimal paths are calculated for $\gamma = 1$, 10, 20, and 80.

It turns out that the most significant parameter affecting the general shape of the optimal path is the temperature difference

$$T_0 - T_s = \frac{\gamma T_R}{\rho(\gamma+\rho)} \tag{30}$$

Figure 3 gives optimal paths for various values of γ and ρ, selected in such a way that $T_0 - T_s = 30°K$ in each case. Note that these curves are similar in shape, differing primarily in the value of T_0. Similar results are obtained for other values of $T_0 - T_s$.

Downloaded 02 May 2010 to 171.66.16.54. Redistribution subject to ASME license or copyright; see http://www.asme.org/terms/Terms_Use.cfm

The variation of the residual stress $(1-\nu)/(\alpha)\ \sigma(t_f^+)$ (equation (5)) with cooling time t_f is shown in Fig. 4 (solid line) for $\gamma = 40$ and $\rho = 8.5$. For comparison, $(1-\nu)/(\alpha)\ \sigma(t_f^+)$ was also calculated from (5) assuming that the optimal path is that for thermorheologically simple material (equation (25)) with $\lambda = 70$. This result is shown by the dashed line in Fig. 4. For $t_f = 10{,}000$ min., one achieves approximately a 20 percent reduction in the residual stress by following the true optimal path as opposed to the path calculated from (25).

Also shown in Fig. 4 are the variations of the terminal temperature $T(t_f^-) = T_f$ with cooling time t_f. Note that as t_f becomes large, T_f approaches a limiting value that happens to be the temperature T_s (equation (29)).

In practice, there will often be some restraint on the maximum cooling (heating) rate that may be attained, thus making it impossible to achieve the instantaneous temperature changes required to follow the optimal temperature path predicted by (15) and (16). If such is the case, one could consider a "modified" optimal path constructed so as to follow the true optimal path as closely as possible given the constraint upon cooling (heating) rate. Figure 5 displays such a "modified" optimal path for the case $\gamma = 40$ and $\rho = 8.5$ with maximum heating and cooling rate of 0.05°C/min. Following this "modified" optimal path results in a 1 percent increase in $\sigma(t_f^+)$ over that obtained by following the true optimal path. If the maximum heating and cooling rate could be increased from 0.05 to 5°C/min, the increase in $\sigma(t_f^+)$ would only be around 0.05 percent. Similar results were also found for other values of γ and ρ.

Conclusion

This paper presented a method for predicting optimal cooling paths that minimize residual thermal stresses in linear, thermorheologically complex, viscoelastic materials. These optimal paths were shown to possess both initial and final jump discontinuities, and to depend on only one of the two components of the vertical shift factor.

If the type of thermorheologically complex material considered in this study were characterized solely from isothermal experiments one would *incorrectly* conclude the material to be thermorheologically simple with an "apparent" horizontal shift factor that is a function of both the true horizontal and vertical shift factors. For this reason, optimal paths were also calculated for thermorheologically simple materials with appropriate "apparent" horizontal shift factors. It was shown that substantial reductions in residual stresses can be attained by following the true optimal path as opposed to the "optimal" path for simple response.

Finally, for those situations where the maximum heating and/or cooling rate is constrained, it was found that only slight (typically less than 1 percent) increases in residual stress result if one employs a "modified" optimal path that is constructed so as to reproduce the true optimal path as closely as possible without exceeding the maximum cooling (heating) rate allowed.

Acknowledgments

The author is grateful to Professor Y. Weitsman of Texas A&M University for several useful suggestions.

References

1 Weitsman, Y., "Optimal Cool-Down in Linear Viscoelasticity," ASME JOURNAL OF APPLIED MECHANICS, Vol. 47, No. 1, 1980, pp. 35-39.

2 Gurtin, M. E., and Murphy, L. F., "On Optimal Temperature Paths for Thermorheologically Simple Viscoelastic Materials," *Quart. App. Math.*, Vol. 38, No. 2, 1980, pp. 179-190.

3 Weitsman, Y., and Harper, B. D., "Optimal Cooling of Cross-Ply Composite Laminates and Adhesive Joints," ASME JOURNAL OF APPLIED MECHANICS, Vol. 49, 1982, pp. 735-739.

4 Weitsman, Y., "On the Thermoviscoelastic Characterization of Adhesives and Composites," in *Progress in Science and Engineering of Composites*, Hayashi, T., et al., eds., ICCM-IV, Tokyo, 1982, pp. 771-779.

5 Peretz, D., and Weitsman, Y., "The Non-Linear Thermoviscoelastic Characterization of FM-73 Adhesives," *Journal of Rheology*, Vol. 27, No. 2, 1983, pp. 97-114.

6 Harper, B. D., and Weitsman, Y., "A Characterization Method for a Class of Thermorheologically Complex Materials," to appear in the *Journal of Rheology*.

7 Schapery, R.A., "Viscoelastic Behavior and Analysis of Composite Materials," Vol. 2, *Mechanics of Composite Materials*, Sendeckj, G. P., ed., Academic Press, New York, 1974, pp. 86-165.

8 Beckwith, S. W., "Viscoelastic Characterization of a Nonlinear Glass/Epoxy Composite Including the Effect of Damage," Ph.D. dissertation, Texas A&M University, Dec. 1974.

9 Renton, W. J., and Ho, T., "The Effect of Environment on the Mechanical Behavior of AS/3501-6 Graphite Epoxy Material," final report, Vought Corp., Aug. 1978.

10 Ferry, J. D., *Viscoelastic Properties of Polymers*, Wiley, New York, 1961.

APPENDIX

The purpose of this Appendix is to justify the relations among the components of the vertical shift factor given in equations (19).

Consider a special case of equation (18) where $g_0 = g_1 g_2$ so that

$$\epsilon_o(t) = g_1(T)\int_0^t D(\xi(t)-\xi(\tau))\frac{d(g_2(T(\tau))\sigma(\tau))}{d\tau}\,d\tau \qquad (A1)$$

where $D(t) = D_0 + \Delta D(t)$ is the creep compliance.

Equation (A1) may also be expressed

$$\epsilon_o(\xi) = g_1(T(\xi))\int_0^\xi D(\xi-\xi')\frac{d(g_2(T(\xi'))\sigma(\xi'))}{d\xi'}\,d\xi' \qquad (A2)$$

where $\xi = \xi(t)$. Taking the Laplace transform of (A2) with respect to reduced time ξ yields

$$\{\epsilon_o/g_1\} = s\{D\}\{g_2\sigma\} \qquad (A3)$$

where s is the Laplace transform parameter and $\{F\}$ denotes the Laplace transform of F. Elementary considerations [7] give $s^2\{D\}\{E\} = 1$ where E is the relaxation modulus, so that (A3) becomes

$$\{g_2\sigma\} = s\{E\}\{\epsilon_o/g_1\} \qquad (A4)$$

which may be inverted to yield

$$\sigma(\xi) = \frac{1}{g_2}\int_0^\xi E(\xi-\xi')\frac{d}{d\xi'}\left[\frac{\epsilon_o}{g_1}\right]d\xi' \qquad (A5)$$

or, equivalently

$$\sigma(t) = \frac{1}{g_2(T)}\int_0^t E(\xi(t)-\xi(\tau))\frac{d}{d\tau}\left[\frac{\epsilon(\tau)-\alpha\Delta T(\tau)}{g_1(T(\tau))}\right]d\tau \qquad (A6)$$

Comparing (A6) with (1) we conclude

$$h_1(T) = \frac{1}{g_2(T)}$$

$$h_2(T) = \frac{1}{g_1(T)} \qquad (A7)$$

Downloaded 02 May 2010 to 171.66.16.54. Redistribution subject to ASME license or copyright; see http://www.asme.org/terms/Terms_Use.cfm

An Incremental Constitutive Relation of Unilateral Contact Friction for Large Deformation Analysis

J.-H. Cheng
Student Mem. ASME

N. Kikuchi
Mem. ASME

Department of Mechanical Engineering
and Applied Mechanics,
The University of Michigan,
Ann Arbor, Mich. 48109

An incremental constitutive relation of friction contact is presented for large deformation analysis. After a brief review of published explanations of friction, a model is constructed following the established concepts of plasticity theory. Extensive studies are laid on how the theory closely simulates the nature of friction and how the unknown parameters in the equation are to be determined from the existing experimental results. Possible extensions to allow considerations of temperature and nonlocal effects are discussed. Formulations of a quasistatic boundary value problem based on the updated Lagrangian approach are summarized. The elastoplastic material is assumed to behave according to the generalized Prandtl-Reuss constitutive equation. Finite element methods are employed to solve the problem. Two examples are selected to demonstrate the capability and adequacy of the proposed model.

1 Introduction

In this paper we present an incremental constitutive equation of unilateral friction contact conditions suitable for large deformation analysis. The theory is an extension and generalization of the works by Seguchi et al. [1], Fredriksson [2], and Michalowski and Mroz [3]. Applications of this mathematical model have been directed to the analysis of metal-forming processes involving large elastic-plastic deformations in the authors' recent work [4].

Recent advances in finite element methods have ushered a rapid increase of studies on friction contact problems. In a series of two papers, Chan and Tuba [5] poineered a possibility to solve friction contact problems using finite element methods. Since then many other alternatives have been proposed, e.g., Tsuta and Yamaji [6], Ohte [7], Schäfer [8], Francavilla and Zienkiewicz [9], Yamada et al. [10], Sachdeva and Ramakrishnan [11], Zied and Padovan [12], Mazurkiewicz and Ostachowicz [13], and Guerra and Browing [14] considered static contact conditions; Hughes et al. [15], Talaslidis and Panagiotopouls [16], and Osmont [17] studied dynamic/impact aspects. These models are, however, confined to linear-elastic problems only. Analyses of small deformation elastoplastic material response have also been carried out by Lee and Kobayashi [18], Hardy, Baronet, and Tordion [19], Dumas and Baronet [20], Lee, Masaki, and Kobayashi [21], and Kikuchi and Skalski [22] under the frictionless condition.

Currently one of the most dynamic research activities in the field of finite element methods is to attack nonlinear problems. Among many solution techniques, the incremental approach has been well established and widely used to formulate these problems. This trend has naturally come to bear on friction contact mechanics which are inherently nonlinear. In the course of its development, Seguchi et al. [1] introduced an incremental friction law based on the theory of plasticity. This idea is then taken by Fredriksson [2], and is extended to admit associated and nonassociated sliding rules by Michalowski and Mroz [3]. An interesting observation of these works is that the change of normal contact pressure is not taken into account in deriving an incremental constitutive relation for sliding friction, although it is an essential factor to be considered, especially in the analysis of metal-forming processes. Furthermore it is not clear how the "hardening" or "softening" parameter can be determined experimentally.

In this paper, we give an incremental friction law considering the influence of changing contact pressure and the objectivity requirement in a constitutive equation together with a method to determine the hardening or softening parameter from the experimental works by Courtney-Pratt and Eisner [23]. Possible extensions to include temperature and microstructural effects are discussed. A nonlocal form based on the work by Oden and Pires [24] is applied to resolve the latter effect. At the end, numerical examples are given to show some practical applications of the present theory.

Contributed by the Applied Mechanics Division and presented at the 1985 Joint ASME/ASCE Applied Mechanics, Fluids Engineering, and Bioengineering Conference, Albuquerque, N. Mex., June 24-26, 1985 of THE AMERICAN SOCIETY OF MECHANICAL ENGINEERS.

Discussion on this paper should be addressed to the Editorial Department, ASME, United Engineering Center, 345 East 47th Street, New York, N.Y. 10017, and will be accepted until two months after final publication of the paper itself in the JOURNAL OF APPLIED MECHANICS. Manuscript received by ASME Applied Mechanics Division, May, 1984; final revision, September, 1984. Paper No. 85-APM-24.

Copyright © 1985 by ASME
Downloaded 02 May 2010 to 171.66.16.54. Redistribution subject to ASME license or copyright; see http://www.asme.org/terms/Terms_Use.cfm

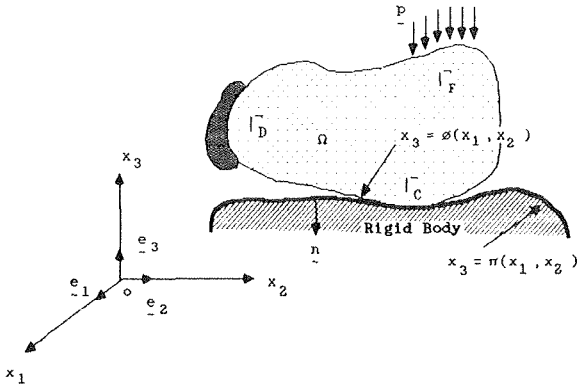

Fig. 1 A unilateral contact problem

2 Unilateral Contact in Normal Direction

Consider two bodies in contact. For simplicity, let us assume that one of them is rigid and is moving on the other deformable body whose surface can be described by a parametric equation

$$x_3 = \phi(x_1, x_2), \tag{1}$$

where a global Cartesian coordinate system x_1, x_2, x_3 with origin O and base vectors $\mathbf{e}_i$ (Fig. 1) is adopted to study contact conditions of two bodies. For some cases where a unique function description as (1) is not possible, local coordinate systems may then be introduced and the following discussions are still applicable provided that proper coordinate transformations are employed.

Denoting the possible contact region of deformable body by Γc, the nonpenetration restriction between the contact surfaces can be satisfied if the following inequality

$$\phi(x_1, x_2) + \Delta u_3 \leq \pi(x_1 + \Delta\hat{u}_1, x_2 + \Delta\hat{u}_2) + \Delta u^R{}_3, \tag{2}$$

holds for any displacement increment vector $\Delta\mathbf{u}(=\Delta u_i \mathbf{e}_i)$ evaluated at each point with the updated coordinate $\mathbf{x}(x_1, x_2, \phi(x_1, x_2))$ on the deformable surface Γc, where π is a parametric function to describe the rigid surface, $\Delta\hat{\mathbf{u}}(=\Delta\hat{u}_i \mathbf{e}_i)$ is the relative displacement increment vector between the deformable surface and the rigid surface moving at the prescribed increment $\Delta\mathbf{u}^R(=\Delta u^R i\mathbf{e}_i)$, i.e., $\Delta\hat{\mathbf{u}} = \Delta\mathbf{u} - \Delta\mathbf{u}^R$.

In an incremental approach, the equality in (2) can be used to determine an appropriate $\Delta\hat{\mathbf{u}}$ so as to just bring a (or some) material point(s) on the surface Γc to be in contact with the rigid surface. If the increment $\Delta\hat{\mathbf{u}}$ is small enough, (2) can be linearized as

$$n \cdot \Delta\mathbf{u} \leq n_3(\pi - \phi) + \mathbf{n} \cdot \Delta\mathbf{u}^R, \tag{3}$$

where $\mathbf{n}$ $(=n_i \mathbf{e}_i)$ is the unit vector "inward" normal to the rigid surface defined by

$$\mathbf{n} = \{ -\mathbf{e}_1(\partial\pi/\partial x_1) - \mathbf{e}_2(\partial\pi/\partial x_2) + \mathbf{e}_3 \} /$$

$$\sqrt{(\partial\pi/\partial x_1)^2 + (\partial\pi/\partial x_2)^2 + 1}. \tag{4}$$

The equality in (3) holds for any two in-contact points, since $\pi = \phi$ instantaneously, (3) becomes

$$\Delta u_n - \Delta g_n = 0 \qquad \text{on} \quad \Gamma^* c, \tag{5}$$

where Δu_n $(=\Delta\mathbf{u} \cdot \mathbf{n})$ is the increment of the normal displacement constrained by the given rigid surface motion Δg_n, a "*" on Γc is to indicate the in-contact portion of Γc.

To resolve this boundary constraint, we apply the exterior penalty method evolved from the early work of Courant, Friedrichs, and Lewy [25] and later elaborated by Zangwill [26]. The idea, as inspired by Courant [27], is to replace the rigid surface by a set of very stiff springs along the boundary. Mathematically, this can be expressed as

$$\Delta t_n = -k_n(\Delta u_n - \Delta g_n) \qquad \text{on} \quad \Gamma^* c, \tag{6}$$

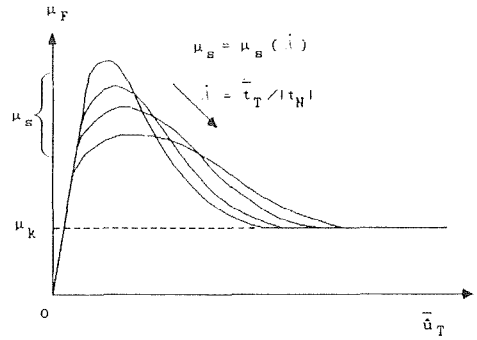

Fig. 2 A schematic diagram for the coefficient of friction as a function of sliding distance $\dot{\bar{u}}_T$ and tangential loading rate $\dot{\lambda}$

where Δt_n is the increment of normal contact pressure obtained by the penalization to the constraint (5), the penalty parameter k_n indicates the degree of approximation. The proofs of the existence of the solution to the penalized problem and its convergence to the original problem as $k_n \to \infty$ have been given by Kikuchi and Song [28]. Extensive studies on various unilateral contact problems can also be found in Kikuchi and Oden [29].

Equation (6) provides us a convenient way to change the first kind of boundary condition into the third kind of boundary condition, and to evaluate the increment of the contact pressure Δt_n as the solution Δu_n is obtained. The resultant contact pressure t_n is then updated by Δt_n accordingly. It is noted that the requirement for a point to remain on $\Gamma^*{}_c$ is that t_n has to be negative. Therefore, depending on the loading path, while at certain deformation stage the sign of Δt_n of an in-contact point becomes positive, which amounts to its tendency to leave the rigid surface, the point will stay in contact as long as t_n remains negative.

3 An Incremental Friction Law

Frictional effects play an important role in most of the practical applications. Although a tremendous amount of effort has been put into the investigation of this subject, a precise incremental friction law suitable for large deformation analysis with sufficient and appropriate experimental data is still lacking. In what follows, an attempt is made toward constructing an incremental friction law in analogy with the elastoplasticity theory, which is an extension of the works by Seguchi et al. [1], Fredriksson [2], and Michalowski and Mroz [3]. The discussion is, however, confined to static or quasistatic processes of which the response is assumed to be rate-independent.

According to the classical Amontons-Coulomb friction law, two material points on the contact surfaces stick together when the magnitude of the tangential traction vector is less than the product of friction coefficient and the absolute value of contact pressure. There is no relative motion between these two points, that is $\Delta u_{Ti} = \Delta g_{Ti}$, a similar constrained condition as (5), has to be imposed, where Δu_{Ti} is the tangential displacement increment of the deformable surface and Δg_{Ti} is the tangential component of the rigid surface motion. While we can use the same physical reasoning as in (6) to relate the increment of the tangential traction vector $\Delta\mathbf{t}_T$ to the increment of the relative tangential displacement vector $(\Delta\mathbf{u}_T - \Delta\mathbf{g}_T)$, the use of $\Delta\mathbf{t}_T$ is, however, limited to small deformation problems since $\Delta\mathbf{t}_T$ is not material frame indifferent, i.e., it is not objective to changes of the frame of reference. Nevertheless, by introducing a corotational traction increment $\mathbf{t}^\nabla(=t^\nabla i\mathbf{e}_i)$ similar to the definition of Zaremba-Jaumann as (see Malvern [30], pp. 380–403)

$$t^\nabla{}_i = \Delta t_i - \Omega_{ij} t_j, \tag{7}$$

we can write

Downloaded 02 May 2010 to 171.66.16.54. Redistribution subject to ASME license or copyright; see http://www.asme.org/terms/Terms_Use.cfm

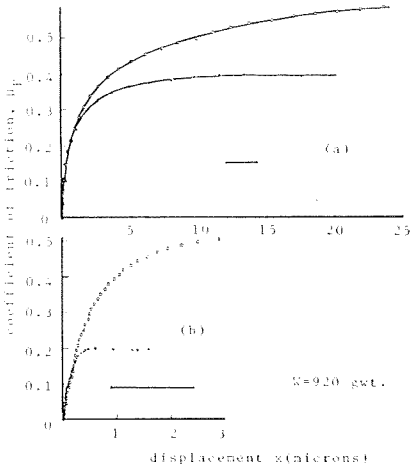

Fig. 3 The results of four sets of measurements of the coefficient of friction versus displacements before sliding. (*a*) Polished platinum; (*b*) steel. O, with clean surfaces; •, with surfaces flooded with a saturated solution of lauric acid in cetane, reproduced from Courtney-Pratt and Eisner [23].

$$t^{\nabla}{}_{Ti} = -k_T(\Delta u^e{}_{Ti} - \Delta g_{Ti}), \tag{8}$$

with (6) being modified into

$$t^{\nabla}{}_n = k_n(\Delta u_n - \Delta g_n) \tag{9}$$

where the components

$$t^{\nabla}{}_{Ti} = t^{\nabla}{}_i - t^{\nabla}{}_n n_i = \Delta t_{Ti} - \Omega_{kj} t_j(\delta_{ki} - n_k n_i), \tag{10}$$

and

$$t^{\nabla}{}_n = \mathbf{t}^{\nabla} \cdot \mathbf{n} = \Delta t_n - t_i \Omega_{ij} n_j, \tag{11}$$

are invariant with respect to rigid body rotations, $\mathbf{n}(=n_i\mathbf{e}_i)$ given in (4) is defined in the current state, $\Omega_{ij} = -\Omega_{ji} = (\Delta u_{j,i} - \Delta u_{i,j})/2$ is the "spin" tensor, the comma notation indicates the partial derivatives with respect to the coordinate $\mathbf{x}$ (Fig. 1), i.e., $\Delta u_{i,j} = \partial \Delta u_i / \partial x_j$, k_T is a penalty parameter representing a fictitious spring in the tangential direction so that as $k_T \to \infty$, the sticking condition $\Delta \mathbf{u}_T = \Delta \mathbf{g}_T$ is satisfied [28].

However, experimental evidence as described in the treatises of Bowden and Tabor [31], and Rabinowicz [32], has indicated that before sliding commences, a small amount of relative tangential displacement between two contact surfaces does exist due to the yielding of asperities, which are intrinsic to any unlubricated surface on a microscopic scale. A scrutiny of the studies by Courtney-Pratt and Eisner [23], Rabinowicz [33–34], Burwell and Rabinowicz [35], Johnson [36], Banerjee [37], Johannes, Green, and Brockley [38], and many others yields a fairly complete description of the friction coefficient μ_F (Fig. 2) as a function of the relative tangential displacement $\bar{u}_T$ $(=\sqrt{\hat{u}_{Ti}\hat{u}_{Ti}}$ and the rate of application of the tangential force $\dot{\lambda}$ $(=\dot{\bar{t}}_T/|t_n|)$, where $\dot{\bar{t}}_T)$ is the tangential loading rate. Similar relations have been discussed by Desai, Zaman, and Drumm [39] in a study of the behavior at junctions or interfaces between structural and geological materials and at joints in rock masses.

There are many concerns about describing the coefficient of friction in terms of a time parameter, such as Howe, Benton, and Puddington [40], Derjaguin, Push, and Tolstoi [41], Brockley and Davis [41], Kato and Matsubayashi [43], Kato, Sato, and Matsubayashi [44], and Richardson and Nolle [45]. However, in most of mechanics problems, when the displacement method is used, the governing equations are usually expressed in terms of the displacement or the velocity vector. It would then be a natural physical concept to state the friction law as in (8) and that discussions will be centered on achieving a general model that scrupulously simulates the response shown in Fig. 2.

Experiments often show that the initial effect of a normal force and an increasing tangential force is to increase the real contact area, which is made up of a large number of small regions of contact, or "junctions." At this stage, only relative microdisplacement in the junction occurs and there is no gross macroscopic sliding. With an increase in the magnitude of the microdisplacement, there is a corresponding increase in the coefficient of friction which reaches a maximum value μ_s at the onsetof the macroscopic sliding. It is well known that the friction force required to maintain sliding is usually less than the force required to initiate sliding. The kinetic friction coefficient (for surface in motion) generally has a positive slope at low sliding speeds (10^{-10}–10^{-4} cm/sec) and a negative slope at higher sliding speeds, which eventually becomes asymptotic to some constant value μ_k.

It is evident from these observations that, for a static or quasistatic process that is assumed to be independent of the loading rate, Fig. 2 can be regarded as a representation of the elastic-plastic behavior of interacting asperities (junctions) on contact surfaces. Thus, k_T of the surface property in (8) resembles the Young's modulus E of an elastic material and can be determined by $k_T = (d\mu_F/d\bar{u}_T)(W/A_c)$ from the experimental results. Two typical curves of μ_F for tests on polished platinum and steel are extracted from [23, Fig. 3, pp. 535] and are shown in Fig. 3, where $d\mu_F/d\bar{u}_T$ is the slope obtained from these curves in the "elastic" range, W is the applied normal load, and A_c is the true contact area under purely normal loading. It is for this reason that the superscript "e" is placed on the displacement increment $\Delta \mathbf{u}_T$ in (8) to indicate the elastic response of the asperity.

As in plasticity, the description of the response of an "elastic working-hardening" material can be completed by the following ingredients:

(*a*) A yield criterion, characterizing the initiation of the plastic flow.

(*b*) A flow rule, giving the relations between the plastic deformation increments, and the stress components.

(*c*) A hardening rule, representing the successive changes of yield loci with working hardening.

In this section, a model is presented as a continuation of (8) based on a Coulomb type of "slip" criterion [2] and an associated isotropic hardening rule. Another version adopting an associated kinematic hardening rule and thus taking the Bauschinger effect into account is given in the Appendix.

Consider a state of combined stresses produced by a normal loading and a tangential pull. Assume that there exists a Coulomb isotropic slip function

$$f(\mathbf{t}_T, \mu_F, t_n) = \bar{t}_T + \mu_F t_n, \tag{12}$$

where $\mathbf{t}_T$ and t_n are tangential and normal components of the traction vector defined by $\mathbf{t} = \mathbf{t}_T + t_n\mathbf{n}$, and $\bar{t}_T$, $(=\sqrt{t_{Ti}t_{Ti}})$ is the effective tangential traction. When the state of stress of a junction on $\Gamma^*{}_c$ is such that $f=0$, the junction is said to be yielded. And a plastic (sliding) displacement increment $\Delta u^P{}_{Ti}$ arises which is assumed to be a part of the following decomposition

$$\Delta u_{Ti} = \Delta u^e{}_{Ti} + \Delta u^P{}_{Ti}. \tag{13}$$

To describe the post-yield behavior, an associated flow rule

$$\Delta u^P{}_{Ti} = h(\partial f/\partial t_{Ti}) \tag{14}$$

is adopted, where h is a positive scalar function. If an isotropic hardening rule is chosen so that μ_F is a function of the component of the plastic displacement $u^P{}_{Ti}$, then since the necessary condition of subsequent loading from a plastic state to another plastic state is that

Downloaded 02 May 2010 to 171.66.16.54. Redistribution subject to ASME license or copyright; see http://www.asme.org/terms/Terms_Use.cfm

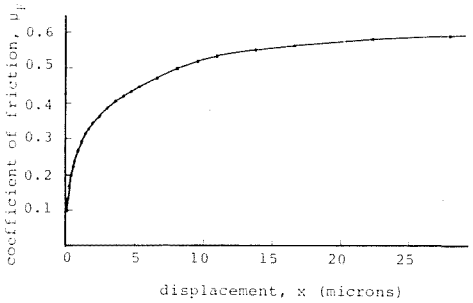

Fig. 4 The coefficient of friction versus the "irreversible" component of displacement, $\tilde{u}^p{}_T$, reproduced from Courtney-Pratt and Eisner [23]

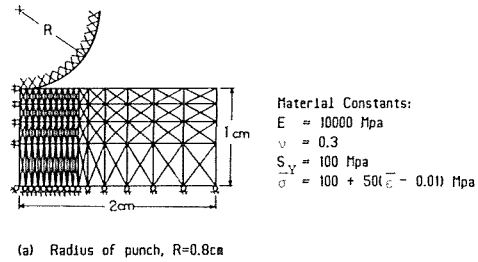

(a) Radius of punch, R=0.8cm

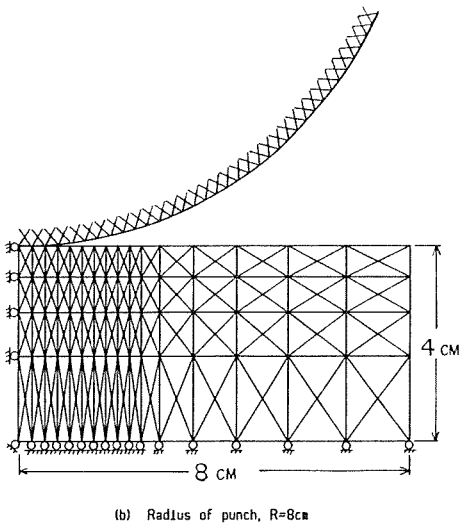

(b) Radius of punch, R=8cm

Fig. 5 Two initial configurations for a plane-strain indentation problem by a cylindrical rigid punch

$$f^{\nabla} = t^{\nabla}{}_{Ti}(\partial f/\partial t_{Ti}) + \Delta u^{p}{}_{Ti}(\partial f/\partial \mu_F)(\partial \mu_F/\partial u^{p}{}_{Ti})$$
$$t^{\nabla}{}_{n}(\partial f/\partial t_n) = 0, \tag{15}$$

h can be determined from (8) and (15) as

$$h = \frac{-k_T T_j(\Delta u_{Tj} - \Delta g_{Tj}) + \mu_F t^{\nabla}{}_n}{k_T + T_k t_n(\partial \mu_F/\partial u^{p}{}_{Tk})}, \tag{16}$$

where T_i is defined as $T_i = \partial f/\partial t_{Ti} = t_{Ti}/\tilde{t}_T$.

If an effective tangential plastic displacement $\tilde{u}^p{}_T$ is defined by

$$\tilde{u}^p{}_T = \sqrt{u^p{}_{Ti} u^p{}_{Ti}}, \tag{17}$$

then applying the chain rule

$$\partial \mu_F/\partial u^p{}_{Ti} = (\partial \mu_F/\partial \tilde{u}^p{}_T)(\partial \tilde{u}^p{}_T/\partial u^p{}_{Ti})$$
$$= (\partial \mu_F/\partial \tilde{u}^p{}_T)(u^p{}_{Ti}/\tilde{u}^p{}_T),$$

h becomes a well-defined quantity since the hardening or softening parameter $\partial \mu_F/\partial \tilde{u}^p{}_T$ can be obtained as the tangent of $\mu_F - \tilde{u}^p{}_T$ curve from an experiment. As an example, Fig. 4 shows a curve of $\mu_F - \tilde{u}^p{}_T$ for an experiment on polished platinum of very slow motions, which is reproduced from Courtney-Pratt and Eisner [23, p. 543].

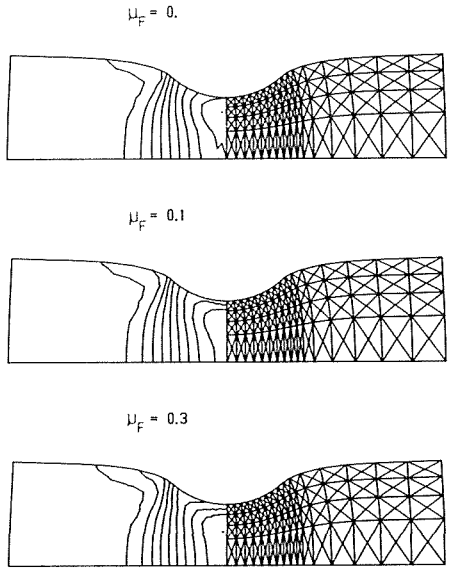

Fig. 6(a) Deformed meshes at 0.4 cm plane-strain indentation by a rigid punch (r = 0.8 cm) on an elastic slab with E = 10 GPa, ν = 0.3

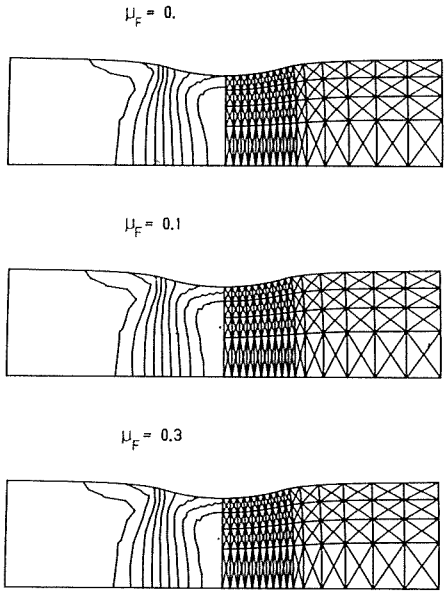

Fig. 6(b) Deformed meshes at 0.6 cm plane-strain indentation by a rigid punch (r = 8 cm) on an elastic slab with E = 10 GPa, ν = 0.3

Fig. 6

The conditions $f = 0$ and $f^{\nabla} = 0$ imply a path of successive plastic loading. However, if $f = 0$ and $f^{\nabla} < 0$ at time t, then we have $f < 0$ at the next instant of time and the junction is again deformed "elastically," that is, the junction reenters the sticking zone. This change is called unloading. And since $\Delta u^p{}_{Ti}$ must vanish during unloading, we have

$$f = 0 \quad \text{and} \quad T_i t^{\nabla}{}_{Ti} + \mu_F t^{\nabla}{}_n < 0$$
for unloading, otherwise
$$f = 0 \quad \text{and} \quad T_i t^{\nabla}{}_{Ti} + \mu_F t^{\nabla}{}_n \geq 0$$
for continued loading. (18)

Based on these loading criteria, an incremental constitutive relation for friction contact can be obtained by substituting (16) into (14) and applying (8) and (15), as

$$t^{\nabla}{}_{Ti} = -k_{ij}(\Delta u_{Tj} - \Delta g_{Tj}) - c T_i t^{\nabla}{}_n, \tag{19}$$

where

Downloaded 02 May 2010 to 171.66.16.54. Redistribution subject to ASME license or copyright; see http://www.asme.org/terms/Terms_Use.cfm

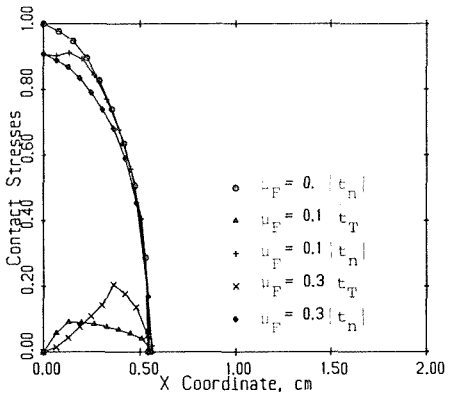

(a) R=0.8cm, Po=818Mpa

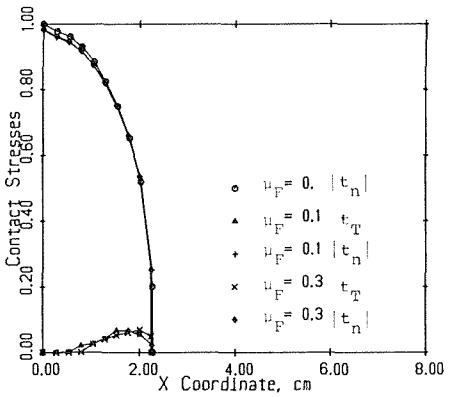

(b) R=8cm, Po=238Mpa

Fig. 7 Normalized contact stresses (by maximum contact pressure P_0) of a plane-strain indentation, evaluated at deformed meshes shown in Fig. 6, elasticity only

$$k_{ij} = k_T(\delta_{ij} - \alpha k_T T_i T_j / D_T), \tag{20}$$

$$c = \alpha k_T \mu_F / D_T, \tag{21}$$

$$D_T = k_T + T_k t_n (\partial \mu_F / \partial \tilde{u}^{\rho}{}_T)(u^{\rho}{}_{Tk} / \tilde{u}^{\rho}{}_T), \tag{22}$$

and

$$\alpha = \begin{cases} 0 & \text{for elastic loading or unloading,} \\ 1 & \text{for plastic loading.} \end{cases}$$

Remark 1 The preceding incremental friction law is derived for the isothermal case. Although much still remains unknown, the problem of temperature effect is getting more and more important in view of the high temperature levels and also severe temperature gradients encountered in present-day technology. A possible extension of this theory to include the thermal effect can be made by assuming that the coefficient of friction μ_F is a function of not only the relative tangential sliding displacement but also the temperature. Thus if we modify the Coulomb slip function (12) as

$$f(t_T, \mu_F(\tilde{u}^{\rho}{}_T, \theta), t_n) = \sqrt{t_{Ti} t_{Ti}} + \mu_F(\tilde{u}^{\rho}{}_T, \theta) t_n, \tag{23}$$

where θ is the temperature measured on the contact surfaces, then the constitutive relation (19) can be replaced by

$$t^{\nabla}{}_{Ti} = -k_{ij}(\Delta u_{Tj} - \Delta g_{Tj}) - c T_i t^{\nabla}{}_n - \beta T_i \Delta\theta, \tag{24}$$

where k_{ij} and c are the same as (20) and (21), respectively, and

$$\beta = t_n(\partial \mu_F / \delta\theta) / D_T \tag{25}$$

The temperature dependence appears as $\partial \mu_F / \partial \theta$ in (23) which is to be determined from experiments. Because of the practical difficulties involved in investigating this problem, it is not surprising that accurate information is lacking. More rigorous considerations and research efforts have to be directed to this subject.

Remark 2 For some problems, the contact region is relatively small, so that the height or the size of asperities does affect the surface properties. It is then necessary to introduce a nonlocal form as advocated by Oden and Pires [24]. The idea is to replace t_n in (22) by $t^*{}_n$ defined as

$$t^*{}_n(\mathbf{x}) = \int_{\Gamma^*{}_c} k(\mathbf{x};\mathbf{y}) t_n(\mathbf{y}) d\Gamma(\mathbf{y}), \tag{26}$$

where $k(\mathbf{x};\mathbf{y})$ is a kernal function with the property

$$\int_{\Gamma^*{}_c} \int_{\Gamma^*{}_c} k(\mathbf{x};\mathbf{y}) d\Gamma(\mathbf{y}) d\Gamma(\mathbf{x}) = 1,$$

and it becomes almost zero for $\mathbf{y}$ satisfying $|\mathbf{y} - \mathbf{x}| > \hat{a}$, $\hat{a}$ being a parameter representing the height and the size of asperities, i.e., the surface roughness. However, for many applications especially in the forming processes, the extent of contact is generally large enough and thus $t_n = t^*{}_n$ can be assumed without losing accuracy.

4 Finite Element Formulations (Updated Lagrangian Approach)

The application of finite element methods to large elastic-plastic deformation problems has been fruitful over the last two decades. Considerable amount of efforts have been given to solve nonlinear problems. A concise survey of the related literature was recently presented by Cheng and Kikuchi [4]. The updated Lagrangian approach originated by McMeeking and Rice [45] in 1975 has become the most used method in this area owing to its simplicity in the resulting incremental form and the advantage of using the updated finite element mesh as the reference configuration, a convenient state for describing the constitutive relations of history-dependent elastoplastic materials.

Based on the principle of virtual work [4] using the generalized Prandtl-Reuss stress-strain relations for finite deformations, the incremental equilibrium equation for a quasistatic problem can be written as

$$\int_{\Omega^t} \{ (D_{ijkl} - \delta_{jl}\sigma^t{}_{ik} - \delta_{il}\sigma^t{}_{jk}) \Delta u_{k,l} + \sigma^t{}_{jk} \Delta u_{i,k} \} \tilde{u}_{i,j} d\Omega^t + \int_{\Gamma^*{}_c} \{ k_n \Delta u_n \tilde{u}_n + k_{ij} \Delta u_{Tj} \tilde{u}_{Ti} - t^t{}_{Tj} (\Delta u_{j,i} - \Delta u_{j,t}) \tilde{u}_i / 2 \} d\Gamma^t = \int_{\Omega^t} \rho \Delta b_i \tilde{u}_i d\Omega^t + \int_{\Gamma^t{}_F} \Delta p_i \tilde{u}_i d\Gamma^t + \int_{\Gamma^*{}_c} \{ k_n \Delta g_n \tilde{u}_n + (k_{ji} \Delta g_{Tj} - c T_i \Delta t_n) \tilde{u}_i \} d\Gamma^t, \tag{27}$$

which has to be satisfied for an arbitrary virtual (variation of) displacement $\tilde{u}_i$ such that $\tilde{u}_i = 0$ on $\Gamma^t{}_D$ on which $\Delta\mathbf{u}$ ($= \Delta u_i \mathbf{e}_i$) is prescribed, where D_{ijkl} is the material constant tensor described by

$$D_{ijkl} = (E\nu/(1+\nu)(1-2\nu))\delta_{ij}\delta_{kl} + G(\delta_{ik}\delta_{jl} + \delta_{il}\delta_{jk}) - \alpha(3G)s_{ij}s_{kl}/(\bar{\sigma}^2(1 + H'/3G)), \tag{28}$$

in which E, G, ν are the Young's modulus, the shear modulus, and the Poisson's ratio, respectively, $\bar{\sigma} = \sqrt{3(s_{ij}s_{ij})/2}$ is the effective stress obtained from the deviatoric components $s_{ij} = \sigma_{ij} - \sigma_{kk}\delta_{ij}/3$ of the Cauchy stress tensor $\boldsymbol{\sigma}$ ($= \sigma_{ij}\mathbf{e}_i\mathbf{e}_j$), H' is the hardening parameter, α is determined through the Mises yield function

$$f(\sigma_{ij}, Y) = \sqrt{3(s_{ij}s_{ij})/2} - Y, \tag{29}$$

such that $\alpha = 0$ when $f < 0$ (elastic loading) or $f = 0$ but

Downloaded 02 May 2010 to 171.66.16.54. Redistribution subject to ASME license or copyright; see http://www.asme.org/terms/Terms_Use.cfm

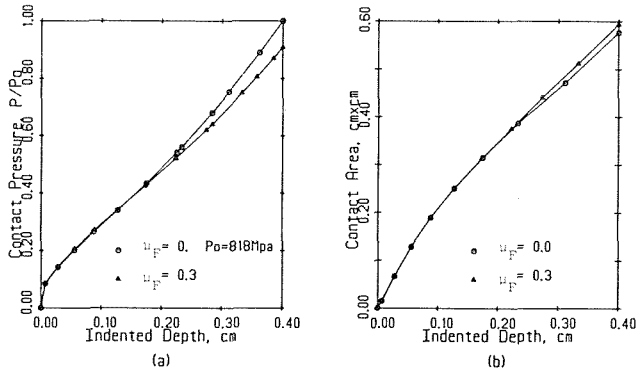

Fig. 8(*a*) Maximum contact pressure and (*b*) contact area versus depth of indentation for the case in Fig. 6(*a*)

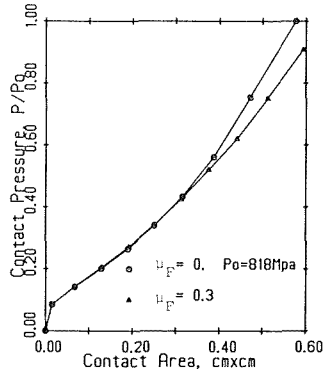

Fig. 9 Maximum pressure versus contact area

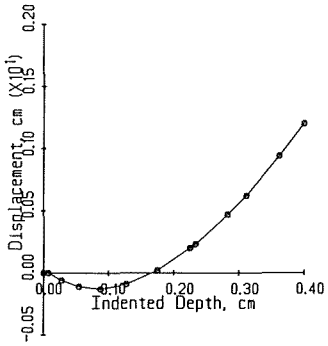

Fig. 10 Effective relative tangential displacement versus depth of indentation

$s_{ij}\Delta e_{ij} < 0$ (plastic unloading), otherwise $\alpha = 1$ if $f = 0$ and $s_{ij}\Delta e_{ij} \geq 0$ (plastic loading), $\Delta e_{ij} = (\Delta u_{i,j} + \Delta u_{j,i})/2$, the yield strength Y is a function of strain history, ρ is the mass density function, Δb_i are components of the body force vector, and Δp_i are components of the traction vector function prescribed on the surface Γ'_F whose unit normal vector is denoted by $\tilde{\mathbf{n}}$ $(= \tilde{n}_i \mathbf{e}_i)$. It is assumed that the whole boundary Γ' is made up of three portions Γ'_D, Γ'_F, Γ'_c which are mutually disjointed.

We obtain a suitable finite element formulation by discretizing the domain Ω' and the boundary Γ' into finite elements Ω'_e and Γ'_e. Within each element, interpolations are made to the variables $\Delta\mathbf{u}$, $\mathbf{u}$, $\Delta\mathbf{b}$, $\Delta\mathbf{p}$, $\Delta\mathbf{g}$, by properly chosen shape functions which lead to an algebraic matrix equation

$$[K]\{\Delta u\} = \{\Delta f\}, \tag{30}$$

where $[K]$ is a stiffness matrix depending on the deformation history, $\{\Delta f\}$ is a generalized load vector consisting of increments of body force and boundary conditions, and $\{\Delta\mathbf{u}\}$ is the unknown displacement increment to be solved. Detailed components in (30) are given in [4].

Since in the friction law the increment of tangential traction depends on the increment of contact pressure, which also must be determined, equation (30) is no longer linear unless Δt_n remains constant. However, in most cases, Δt_n is quite insensitive to change although a little difference does exist for each successive increment. Thus, the following subiteration scheme may be used to obtain fairly accurate solutions: At any incremental step, the equation is solved by using the values of Δt_n from the previous step and an iteration is made by keeping the computed Δt_n unchanged within this increment.

5 Numerical Examples

To demonstrate the capability and adequacy of the algorithms derived in this paper, two problems are solved using the computer code "EPAFRIC" (Elasto-Plastic Analysis of Friction Contact Problems) developed by the authors.

5.1 Plane-Strain Indentation Test. This example is the plane-strain indentation of a cylindrical rigid punch on a semi-infinite slab. To verify the accuracy of numerical solutions, the material is first assumed to be linearly elastic so that the nonlinearities are restricted to the surface of contact. The problem is described in Fig. 5 which shows two different initial configurations with finite element discretizations and material properties. Due to symmetry, half of the slab is analyzed. It is assumed that there is no hardening or softening effect for the sliding motion, i.e., $d\mu_F/d\bar{u}^P{}_T = 0$, or $\mu_F = \mu_s$ during the entire process. Figure 6 illustrates deformed meshes with contour lines of the equieffective stress $\bar{\sigma}$ at 0.4 cm and 0.6 cm depths of indentation, respectively. The extent of indentation is chosen to show the change of contact regions inspite of oversized elastic deformations imposed on the slab. Increments are determined by the code using either (2) so that at the end of each increment a nodal point on Γ_c just comes to contact with the rigid punch, or the Coulomb slip criterion (9), unless the value exceeds 0.05 cm, a given reference displacement increment.

The computed contact stresses are depicted in Fig. 7 for different coefficients of friction. It is seen that the contact pressure distributions for the smooth punch indentation ($\mu_F = 0$) are in excellent agreement with the classical Hertz's solution. The results of tangential tractions indicate that as the coefficients of static friction μ_s changes from 0.3 to 0.1, the span of sliding zone increases with a reduced peak value at the interface of sticking and sliding zones. Similar results have been obtained by Kikuchi [47] who solved the same problem using an iterative method. The smaller peak pressures with higher μ_s's are owing to the difference of the contact area. To see this, let us concentrate on the case of Fig. 5(*a*). The historical developments of the maximum contact pressure and contact area for $\mu_F = 0$ and $\mu_s = 0.3$ are shown in Fig. 8. Close investigations show that the contact area for $\mu_s = 0.3$ is smaller (thus with higher contact pressure) than that for $\mu_F = 0$ at the early stage of indentation, but the situation becomes reverse later on (Fig. 9). To demonstrate this change of contact area, Fig. 10 depicts the effective relative tangential displacement $\bar{u}_T$ of the point next to the axis as a function of indentation depth. The sign of $\bar{u}_T$ is included to indicate the direction of motion of the material point: the negative sign stands for a motion toward the center with respect to the rigid punch. When the contact points move out, the contact area increases. However, the relatively larger sliding motion for frictionless indentation allows only nine points (instead of 10 points for $\mu_s = 0.3$) in contact with the punch, thus results in a slightly smaller contact zone.

It should be mentioned that for some cases (e.g., $\mu_s = 0.1$), $\bar{t}_T > \mu_s |t_n|$ at the first incremental step after a point just

Downloaded 02 May 2010 to 171.66.16.54. Redistribution subject to ASME license or copyright; see http://www.asme.org/terms/Terms_Use.cfm

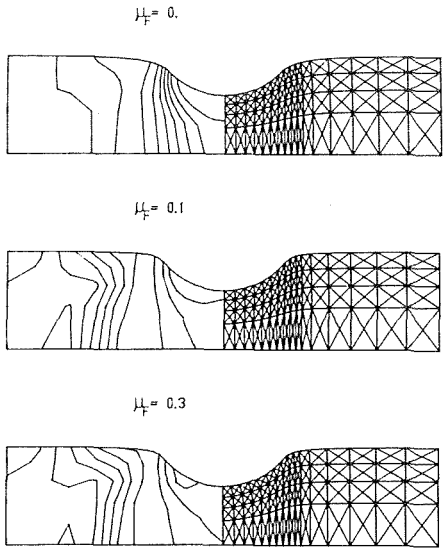

Fig. 11 Deformed meshes at 0.4 cm plane-strain indentation by a rigid punch ($r = 0.8$ cm) on an elastoplastic slab with $E = 10$ GPa, $\nu = 0.3$, $S_Y = 100$ MPa, and $\bar{\sigma} = 100 + 50(\bar{\epsilon} - 0.01$ MPa)

contacts the punch, i.e., $\Delta \bar{t}_T > \mu_s |\Delta t_n|$ initially, we will term it as initial sliding. When this occurs, Δt_{Ti} is set to be equal to $\mu_s |t_n| T_i$, where T_i is obtained from the displacement increment as $\Delta u_{Ti}/\|\Delta \mathbf{u}_T\|$ and the matrix equation (30) is resolved again. Also since unloading is to be predicted for each increment using (18), it is found that sometimes these initial sliding and resticking processes are coupled together. Subiterations are then required to settle this situation.

Allowing plastic deformations, the same problem is solved for $\mu_F = 0$ and $\mu_s = 0.3$ with the material yield strength $S_Y = 10$ kN/cm^2, and the post-yield behavior described by $\bar{\sigma} = 10 + 5\bar{\epsilon}^P$ kN/cm^2. Figure 11 shows the final deformed meshes after 0.4 cm of indentation from the initial configuration in Fig. 5(*a*). Very different stress distributions are observed since nonlinear plastic strains are involved. In all computations, a reference increment is chosen to be 0.005 cm which may be altered by three criteria: the Mises yield condition (29), the kinematic contact condition (2), and the turning point of sticking-sliding (12). The resultant contact stresses are exhibited in Fig. 12 in which all the stress values are normalized by P_o ($= 1.764 S_Y$), an analytical value at the threshold of plasticity due to Hertz. With the same total number of contact points in this instance, the maximum contact pressure is higher (smaller contact area) when the frictional effect is included. It is seen that distribution of contact pressure is not as smooth as in the linear-elasticity case (Fig. 13). A possible explanation of this oscillatory result is because of the requirement of vanishing volumetric plastic strain-increment Δe^P_{ii} in the plasticity theory. The material becomes incompressible or nearly incompressible when plastic deformations prevail. This constraint does present a serious problem and is called the locking phenonemon in the finite element approximations. Extensive discussions on this difficulty and possible remedies can be found in [4] and Nagtegaal, Parks, and Rice [48]. This observation can again be confirmed when we solve the same problem with a high work-hardening material ($H' = 50$ kN/cm^2) which allows larger components of elastic strain increment in the plastic region. The results are depicted in Fig. 14 which shows a less fluctuating distribution of the contact stresses. A comparison of the maximum contact pressures versus the contact area for both elastic and plastic loading conditions is given in Fig. 15.

5.2 Sheet Metal Forming. To demonstrate a practical application of this friction law, we choose to solve a forming

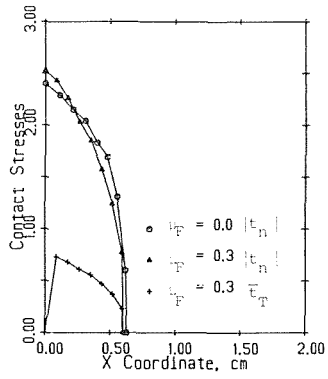

Fig. 12 Contact stresses (normalized by $P_0 = 17.6$ Mpa) of indentation tests on an elastoplastic slab

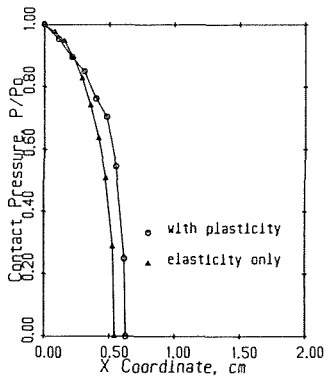

Fig. 13 Comparison of contact pressure for elastic and plastic indentation (frictionless)

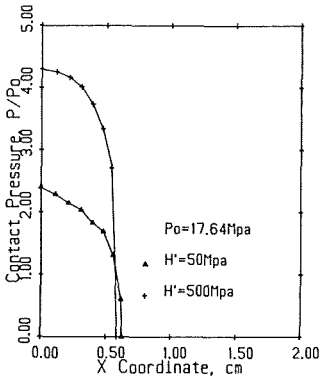

Fig. 14 Comparison of contact pressure for two plastic loading paths (frictionless indentation)

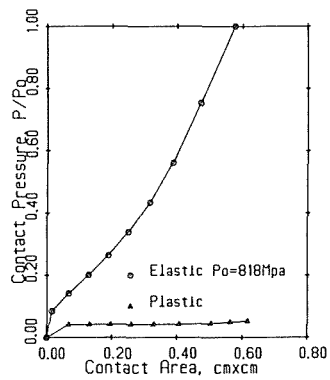

Fig. 15 Comparison of maximum contact pressure versus contact area for elastic and plastic plane-strain indentations

Downloaded 02 May 2010 to 171.66.16.54. Redistribution subject to ASME license or copyright; see http://www.asme.org/terms/Terms_Use.cfm

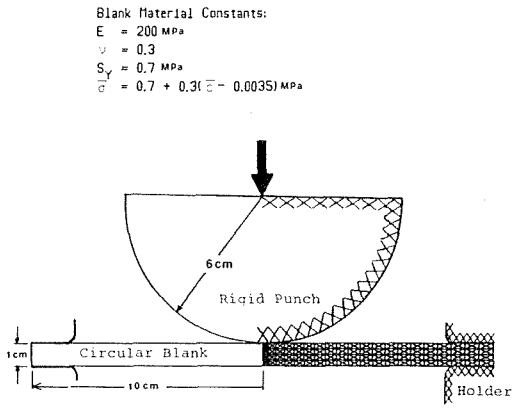

Fig. 16 The initial configuration for an axisymmetric sheet metal forming process with $\mu_F = 0.1$

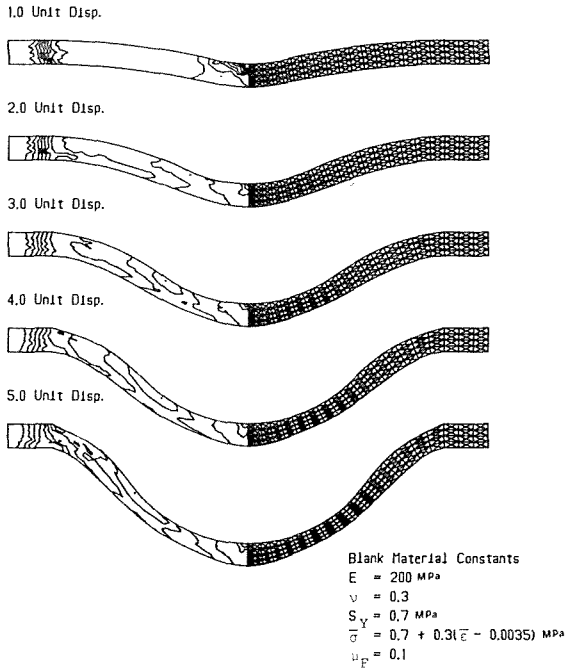

Fig. 17 Deformed meshes for a sheet metal forming process

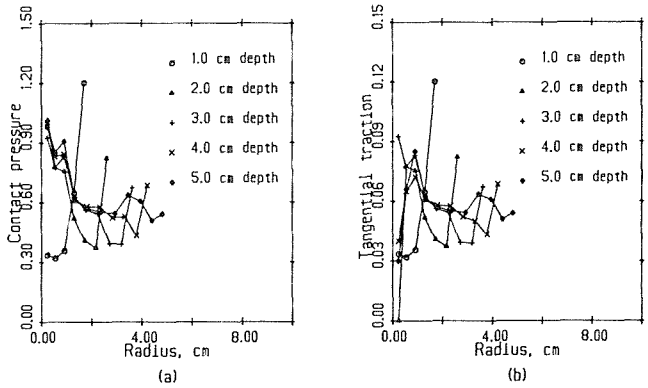

Fig. 18 (*a*) Contact pressures and (*b*) tangential tractions (normalized by $S_Y = 0.7$ MPa) for a sheet forming process at five deformed stages shown in Fig. 17, $\mu_F = 0.1$

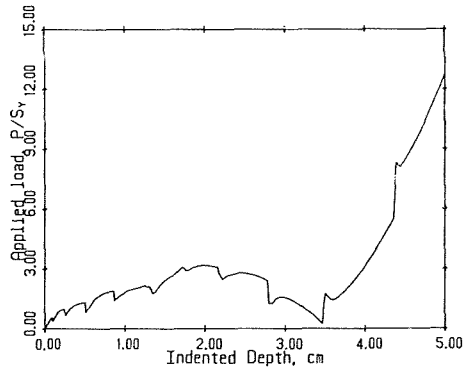

Fig. 19 Applied load (normalized by $S_Y = 0.7$ MPa) evaluated from the element stresses under the rigid punch during a sheet metal forming process, $\mu_F = 0.1$

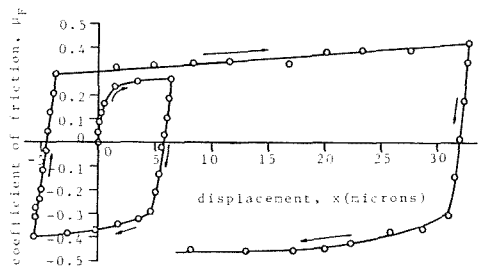

Fig. 20 The coefficient of friction versus displacement when the tangential force is oscillated with increasing amplitude. Polished platinum; normal load, $W = 920$ gwt., reproduced from Courtney-Pratt and Eisner [23].

process of thick sheet metal with the dimensions, material properties, and finite element discretization shown in Fig. 16. For simplicity, a circular blank with its flange fixed is studied. As the hemispherical punch moves downward, the blank is stretched and becomes thinner. Several stages of deformation patterns are presented in Fig. 17. The initial uniform thinning event ceases when plastic unloading occurs around the central portion at 0.1 cm of punch stroke. Because of this unloading process, only the annulus next to this unloading (elastic again) zone is undergoing plastic deformations at this early period of process, which leads to a localized neck known as the puckering phenomenon. The effect of the unloading process can be observed as a result of oscillatory contact stresses in Fig. 18 and a sudden drop of the applied load in Fig. 19, respectively. As the process goes on, a second neck is formed because of the fixed displacement boundary condition imposed around the edge of the blank (this portion remains elastic throughout). The ever-increasing applied load after 3.5 cm of punch stroke is again due to the locking phenomena described in the previous example. The elements become very stiff after nearly incompressible strain increments dominate the process.

6 Conclusion

The history-dependent frictional behavior of materials has been represented by an incremental constitutive relation among the increments of tangential traction vector, contact pressure, and relative tangential displacement. A generalization for large deformation analysis has been stressed. Attentions have been placed on the determination of parameters or surface properties from some existing experimental results and on the limitation and feasible applications of the current theory. To formulate the boundary value problem, the updated Lagrangian approach was adopted. Two problems have been solved to examine the quality of the solutions using finite element methods. The first example was a plane-strain indentation problem. The elastic frictionless solutions agreed well with Hertz's solutions. Discussions on the effect of friction forces and some difficulties arising from incompressible plastic deformations

Downloaded 02 May 2010 to 171.66.16.54. Redistribution subject to ASME license or copyright; see http://www.asme.org/terms/Terms_Use.cfm

have been discussed. Finally an example of stretch-forming of sheet metals was considered.

Acknowledgment

This research has been carried out under the sponsorship of the National Science Foundation, Grant MEA-8109221. This support is gratefully acknowledged.

References

1 Seguchi, Y., Shindo, A., Tomita, Y., and Sunohara, M., "Sliding Rule of Friction in Plastic Forming of Metal," *Computational Methods in Nonlinear Mechanics*, University of Texas at Austin, 1974, pp. 683-692.

2 Fredriksson, B., "Finite Element Solution of Surface Nonlinearities in Structural Mechanics With Special Emphasis to Contact and Fracture Mechanics Problems," *Comp. & Struct.*, Vol. 6, 1976, pp. 281-290.

3 Michalowski, R., and Mroz, Z., "Associated and Non-Associated Sliding Rules in Contact Friction Problems," *Arch. Mech.*, Vol. 30, 1978, pp. 259-276.

4 Cheng, J. H., and Kikuchi, N., "An Analysis of Metal Forming Processes Using Large Deformation Elastic-Plastic Formulations," to appear, 1983.

5 Chan, S. K., and Tuba, I. S., "A Finite Element Method for Contact Problem of Solid Bodies—Part I. Theory and Validation; Part II. Application to Turbine Blade Fastenings," *Int. J. Mech. Sci.*, Vol. 13, 1971, pp. 615-639.

6 Tsuta, T., and Yamaji, S., "Finite-Element Analysis of Contact Problem," *Theory and Practice in Finite-Element Structural Analysis*, Tokyo University Press, 1973, pp. 177-194.

7 Ohte, S., "Finite Element Analysis of Elastic Contact Problems," *Bull. JSME*, Vol. 16, 1973, pp. 797-804.

8 Schäfer, H., "A Contribution to the Solution of Contact Problems With the Aid of Bond Elements," *Comp. Meths. Appl. Mech. Eng.*, Vol. 6, 1975, pp. 335-354.

9 Francavilla, A., and Zienkiewicz, O. C., "A Note on Numerical Computation of Elastic Contact Problems," *Int. J. Num. Meth. Eng.*, Vol. 9, 1975, pp. 913-824.

10 Yamada, Y., Ezawa, Y., Nishiguchi, I., and Okabe, M., "Handy Incorporation of Bond and Singular Elements in Finite Element Solution Routine," *Trans. 5th Int. Conf. on SMIRT*, 1979.

11 Sachdeva, T. D., and Ramakrishnan, C. V., "A Finite Element Solution," *Int. J. Num. Meth. Eng.*, Vol. 17, 1981, pp. 1257-1271.

12 Zeid, I., and Padovan, J., "Finite Element Modeling of Rolling Contact," *Comp. & Struct.*, Vol. 14, 1981, pp. 163-170.

13 Mazurkiewicz, M., and Ostachowicz, W., "Theory of Finite Element Method for Elastic Contact Problems of Solid Bodies," *Comp. & Struct.*, Vol. 17, 1983, pp. 51-59.

14 Guerra, F. M., and Browning, R. V., "Comparison of Two Slideline Methods Using ADINA," *Comp. & Struct.*, Vol. 17, 1983, pp. 819-834.

15 Hughes, T. J. R., Taylor, R. L., Sackman, J. L., Curnier, A., and Kanoknukulchai, W., "A Finite Element Method for a Class of Contact-Impact Problems," *Comp. Meths. Appl. Mech. Eng.*, Vol. 34, 1982, pp. 847-859.

16 Talaslidis, D., and Panagiotopouls, P. D., "A Linear Finite Element Approach to the Solution of the Variational Inequalities Arising in Contact Problems of Structural Dynamics," *Int. J. Num. Meth. Eng.*, Vol. 18, 1982, pp. 1505-1520.

17 Osmont, D., "Computation of the Dynamic Response of Structures With Unilateral Constraints (Contact)—Comparison With Experimental Results," *Comp. Meths. Appl. Mech. Eng.*, Vol. 34, 1982, pp. 847-859.

18 Lee, C. H., and Kobayashi, S., "Elastoplastic Analysis of Plane-Strain and Axisymmetric Flat Punch Indentation by the Finite-Element Method," *Int. J. Mech. Sci.*, Vol. 12, 1970, pp. 348-370.

19 Hardy, C., Baronet, C. N., and Tordion, G. V., "The Elastoplastic Indentation of a Half-Space by a Rigid Sphere," *Int. J. Num. Meth. Eng.*, Vol. 3, 1971, pp. 451-462.

20 Dumas, G., and Baronet, C. N., "Elastoplastic Indentation of a Half-Space by an Infinitely Long Rigid Circular Cylinder," *Int. J. Mech. Sci.*, Vol. 13, 1971, pp. 519-530.

21 Lee, C. H., Masaki, S., and Kobayachi, S., "Analysis of Ball Indentation," *Int. J. Mech. Sci.*, Vol. 14, 1972, pp. 417-426.

22 Kikuchi, N., and Skalski, K., "An Elastoplastic Rigid Punch Problem Using Variational Inequalities," *Arch. Mech.*, Vol. 33, 1981, pp. 865-877.

23 Courtney-Pratt, J. S., and Eisner, E., "The Effect of a Tangential Force on the Contact Metallic Bodies," *Proc. Roy. Soc. A*, Vol. 238, 1957, pp. 529-550.

24 Oden, J. T., and Pires, E. B., "Nonlocal and Nonlinear Friction Laws and Variational Principles for Contact Problems in Elasticity," ASME JOURNAL OF APPLIED MECHANICS, Vol. 50, 1983, pp. 67-76.

25 Courant, R., Friedrichs, K., and Lewy, H., "On the Partial Difference Equations of Mathematical Physics," *IBM Journal*, Vol. 11, 1967, pp. 251-234.

26 Zangwill, W. I., "Nonlinear Programming Via Penalty Functions," *Management Science*, Vol. 13, 1967, pp. 344-358.

27 Courant, R., "Variational Methods for the Solutions of Problems of Equilibrium and Vibrations," *Bull. Amer. Math. Soc.*, Vol. 49, 1943, pp. 1-23.

28 Kikuchi, N., and Song, Y. J., "Penalty/Finite-Element Approximations of a Class of Unlilateral Problems in Linear Elasticity," *Q. Appl. Math.*, Vol. XXXIX, 1981, pp. 1-22.

29 Kikuchi, N., and Oden, J. T., *Contact Problems in Elasticity*, SIAM, Philadelphia, 1981.

30 Malvern, L. E., *Introduction to the Mechanics of a Continuous Medium*, Prentice-Hall, Englewood Cliffs, N.J., 1969.

31 Bowden, F. P., and Tabor, D., *The Friction and Lubrication of Solids*, Part II, Oxford at the Clarendon Press, London, 1964.

32 Rabinowicz, E., *Friction and Wear of Materials*, John Wiley & Sons, New York, 1965.

33 Rabinowicz, E., "The Nature of the Static and Kinetic Coefficients of Friction," *J. Appl. Phys.*, Vol. 22, 1951, pp. 1373-1379.

34 Rabinowicz, E., "The Intrinsic Variables Affecting the Stick-Slip Process," *Proc. Phys. Soc. London*, Vol. 71, 1958, pp. 668-675.

35 Burwell, J. T., and Rabinowicz, E., "The Nature of the Coefficient of Friction," *J. Appl. Phys.*, Vol. 24, 1953, pp. 136-139.

36 Johnson, K. L., "Surface Interaction Between Elastically Loaded Bodies Under Tangential Forces," *Proc. Roy. Soc. A.*, Vol. 230, 1955, pp. 531-548.

37 Banerjee, A. E., "Influence of Kinetic Friction on the Critical Velocity of Stick-Slip Motion," *Wear*, Vol. 12, 1968, pp. 107-116.

38 Johannes, M. A., Green, M. A., and Brockley, C. A., "The Role of the Rate of Application of the Tangential Force in Determining the Static Friction Coefficient," *Wear*, Vol. 24, 1973, pp. 381-385.

39 Desai, C. S., Zaman, M. M., and Drumm, E. C., "Cyclic Testing and Modelling of Interfaces," *Geotech. Eng. Div. ASCE*, to appear, 1984.

40 Howe, P. G., Benton, D. P., and Puddington, I. E., "London-Van der Wassls' Attractive Forces Between Glass Surfaces," *Canadian J. Chem.*, Vol. 33, 1955, pp. 1375-1383.

41 Derjaguin, B. V., Push, V. E., and Tolstoi, D. M., "A Theory of Stick-Slip Sliding of Solids," *Proc. Conf. Lub. Wear*, London, 1957, pp. 265-268.

42 Brockley, C. A., and Davis, H. R., "The Time-Dependence of Static Friction," *J. Lub. Tech.*, Vol. 90, 1968, pp. 35-41.

43 Kato, S., and Matsubayashi, T., "On the Dynamic Behavior of Machine Tool Slideway—1st Paper," *Bull. JSME*, Vol. 13, 1970, pp. 170-179.

44 Kato, S., Sato, N., and Matsubayashi, T., "Some Considerations on Characteristics of Static Friction of Machine Tool Slideway," ASME *Journal of Lubrication Technology*, Vol. 94, 1972, pp. 234-247.

45 Richardson, R. S. H., and Nolle, H., "Surface Friction under Time-Dependent Loads," *Wear*, Vol. 37, 1976, pp. 87-101.

46 McMeeking, R. M., and Rice, J. R., "Finite-Element Formulations for Problems of Large Elastic-Plastic Deformation," *Int. J. Solids Struct*, Vol. 11, 1975, pp. 601-616.

47 Kikuchi, N., "Penalty/Finite Element Approximations of a Class of Unilateral Contact Problems," *Penalty Methods in Finite Element Methods*, Reddy, J. N., ed., ASME, New York, 1982.

48 Nategaal, J. C., Parks, D. M., and Rice, J. R., "On Numerically Accurate Finite Element Solutions in the Fully Plastic Range," *Comp. Meths. Appl. Mech. Eng.*, Vol. 4, 1974, pp. 153-177.

49 Prager, W., "The Theory of Plasticity: A Survey of Recent Achievements," *Proc. Inst. Mech. Engs.*, Vol. 169, 1955, pp. 41-57.

50 Ziegler, H., "A Modification of Prager's Hardening Rule," *Q. Appl. Math.*, Vol. 17, 1959, pp. 55-65.

51 Hodge, P. G., Jr., "The Theory of Piecewise Linear Isotropic Plasticity," *IUTAM Colloquium on Deformation and Flow of Solids*, Madrid, Berlin, 1955, p. 147.

52 Tanaka, M., "Large Deflection Analysis of Elastic-Plastic Circular Plates with Combined Isotropic and Kinematic Hardening," *Ingenieur-Archiv*, Vol. 41, 1972, pp. 342-356.

53 Shiratori, E., Ikegami, K., and Yoshida, F., "Analysis of Stress-Strain Relations by Using an Anisotropic Hardening Plastic Potential," *J. Mech. Phys. Solids*, Vol. 27, 1979, pp. 213-229.

54 Hashiguchi, K., "Constitutive Equations of Elastoplastic Materials with Anisotropic Hardening and Elastic-Plastic Transition," ASME JOURNAL OF APPLIED MECHANICS, Vol. 48, 1981, pp. 297-301.

55 Tokuora, T., "Plastic Materials With Continuous Transition Between Loading and Unloading States," *Arch. Mech.*, Vol. 34, 1982, pp. 187-197.

APPENDIX

An Incremental Friction Law With Kinematic Hardening Rules

The isotropic hardening rule takes no account of the Bauschinger effect, which, however, seems to be an essential characteristic under the cyclic loadings. A typical experimental evidence shown in Fig. 20 is obtained from Courtney-Pratt and Eisner [23, Fig. 9, p. 544], on polished platinum when the tangential force is oscillated with increasing amplitude. Although currently in the plasticity theory, no single constitutive relation can perfectly describe this effect, there are, however, many proposed simple concepts such as Prager's kinematic hardening [49], Ziegler's modification [50], and Hodge's linear combination [51] of the isotropic hardening and the kinematic hardening, which have been widely applied to the plastic analysis of various struc-

Downloaded 02 May 2010 to 171.66.16.54. Redistribution subject to ASME license or copyright; see http://www.asme.org/terms/Terms_Use.cfm

tures. In this Appendix, we briefly present an alternative of (19) using Prager's kinematic hardening rule.

The kinematic hardening rule advanced by Prager assumes that the yield (sliding) surface does not change the shape but its center undergoes a translation represented by $\mathfrak{I}_{Ti}$ in a way that the successive loading surface may be expressed by

$$f(\mathbf{t}_T - \mathbf{J}_T, \mu_s, t_n) = \sqrt{(t_{T2} - \mathfrak{I}_{Ti})(t_{Ti} - \mathfrak{I}_{Ti})} + \mu_s t_n, \tag{31}$$

where μ_s is taken to be constant. If linear hardening is further assumed and the center moves in the direction of $\Delta \mathbf{u}^P{}_T$, we have

$$\mathfrak{I}^{\nabla}{}_{Ti} = -\eta \Delta u^{\rho}{}_{Ti}, \tag{32}$$

where η is a constant. Applying similar derivations in Section 3 yields

$$h = \frac{-k_T T_j (\Delta u_{Tj} - \Delta g_{Tj}) + \mu_s t^{\nabla} t_n}{k_T - \eta T_k (\partial f / \partial \mathfrak{I}_{Tk})} \tag{33}$$

and exactly the same form as (19) can be obtained except that c and D_T should be replaced by

$$c = \alpha k_T \mu_s / D_T, \tag{34}$$

$$D_T = k_T - \eta T_k (\partial f / \partial \mathfrak{I}_{Tk}). \tag{35}$$

It remains to determine η using experimental results. Consider a one-dimensional sliding test in the x-direction (so that only t_{Tx}, $\mathfrak{I}_{Tx}$ are nonzero) with a constant distribution of contact pressure t_n. Equation (31) imples that

$$t_{Tx} - \mathfrak{I}_{Tx} = \mu_s |t_n| = \text{constant}. \tag{36}$$

Thus,

$$\eta = -(\Delta \mathfrak{I}_{Tx} / \Delta u^{\rho}{}_{Tx}) = -(\Delta t_{Tx} / \Delta u^{\rho}{}_{Tx}), \tag{37}$$

and can be obtained from Fig. 4 as $(\partial \mu_F / \partial \tilde{u}^{\rho}{}_T)\ (W/A_c)$ accordingly.

Finally, if we introduce a proportional constant γ such that

$$t^{\nabla}{}_{Ti} = (1-\gamma)\mathfrak{I}^{\nabla}{}_{Ti} + \gamma t_n T_i (\partial \mu_F / \partial \tilde{u}^{\rho}{}_T) \Delta \tilde{u}^{\rho}{}_T, \tag{38}$$

then a more general constitutive relation of friction that contains the isotropic hardening and the kinematic hardening can be derived, as has been extensively studied on the plasticity theory by Hodge [51], Tanaka [52], Shiratori, Ikegami, and Yoshida [53], Hashiguchi [54], Tokuora [55], and so forth.

Downloaded 02 May 2010 to 171.66.16.54. Redistribution subject to ASME license or copyright; see http://www.asme.org/terms/Terms_Use.cfm

On the Uniqueness of Solution of the Initial Value Problem in Softening Materials

K. C. Valanis
College of Engineering,
University of Cincinnati,
Cincinnati, Ohio 45221
Mem. ASME

The initial value problem in finite "softening" material domains is discussed. An inequality that is true of all materials irrespective of their constitution is first established. It is then shown that the solution to this problem is unique when the attending constitutive equation satisfies another inequality, which is characteristic of material models that we call "positive." A number of constitutive equations that give rise to realistic softening behavior are shown to lead to a unique solution of the initial value problem.

Introduction

The paper, as the title indicates, deals with the questions of uniqueness of the solution of the initial value problem in softening materials in isothermal small strain fields. The constitutive modeling of such materials is a subject of great interest and its pursuit has led to many questions, some of which we address herewith. Specifically it has been recognized that elastic constitutive equations of softening materials are inappropriate, insofar as they lead to initial value problems that are not well posed. This has led to the larger question of which classes of constitutive equations are applicable to softening materials, yet lead to a unique solution of the initial value (wave propagation) problem.

In Section 1, softening is given a precise mathematical definition, and the difficulties associated with the elastic model are presented. In Section 2, the method of characteristics is used to demonstrate the ill posedness of the problem associated with this model. In Section 3 the question of uniqueness is examined, in its generality, and an inequality is established that *all* constitutive equations must satisfy. In Section 4 a general uniqueness criterion is established which when satisfied guarantees that the solution to the initial value problem will be unique, irrespective of the form of the constitutive equation.

In the subsequent sections, classical models are shown to satisfy this criterion and specifically in Section 5 a viscoelastic *softening* model is shown to have a unique solution. In Section 6 a degradation softening model which also has a unique solution is developed. In Section 7 a *broad class* of material models is introduced within the context of irreversible thermodynamics, which have softening capability, yet possess a unique solution to the initial value problem.

The conclusion is that softening models do not preclude the existence of a unique solution to the initial value problem, provided that they are properly formulated.

1 Definition of the Problem

Certain geomaterials when strained at a constant strain rate in a uniaxial stress field exhibit the phenomenon of "softening" [1]. This is characterized by a mechanical response whereby the stress rises monotonically with strain, reaches a maximum, and then decreases. In an alternative sense, as the strain increases, the tangent modulus decreases from an initial (positive) value, becoming zero (at the point of maximum stress) and finally negative.

More generally if $\epsilon(t)$ is a parametric representation of the strain path in strain space and $\sigma(t)$ the corresponding stress path in stress space, a material is said to be *softening* at a point on the strain path if, at this point,

$$\dot{\sigma}_{ij}\dot{\epsilon}_{i_j} < 0 \tag{1.1}$$

An elastic model with progressively fracturing elements in the presence of a strain fracture criterion can describe softening behavior quite well. See, for instance, Dougill [3]. When the axial strain is monotonically increasing, then the axial response can be represented by the relation

$$\sigma = E(\epsilon)\epsilon \tag{1.2}$$

where $E(\epsilon)$ is a monotonically decreasing function of ϵ, typically of the type

$$E(\epsilon) = E_0 e^{-k\epsilon} \tag{1.3}$$

More generally, and in the preceding context, if in the presence of monotonically increasing ϵ

$$\sigma = F(\epsilon) \tag{1.4}$$

then the material is said to soften if $F'(\epsilon)$ takes negative values in ϵ, $\epsilon_c < \epsilon < \infty$, where ϵ_c is the strain corresponding to the maximum stress σ_c. From a modeling point of view, the preceding approach is satisfactory, even though the strain rate

Contributed by the Applied Mechanics Division and presented at the 1985 Joint ASME/ASCE Applied Mechanics, Fluids Engineering, and Bioengineering Conference, Albuquerque, N. Mex., June 24-26, 1985 of THE AMERICAN SOCIETY OF MECHANICAL ENGINEERS.

Discussion on this paper should be addressed to the Editorial Department, ASME, United Engineering Center, and will be accepted until two months after final publication of the paper itself in the JOURNAL OF APPLIED MECHANICS. Manuscript received by ASME Applied Mechanics Division, April, 1984; final revision, September, 1984. Paper No. 85-APM-29.

Copyright © 1985 by ASME
Downloaded 02 May 2010 to 171.66.16.54. Redistribution subject to ASME license or copyright; see http://www.asme.org/terms/Terms_Use.cfm

dependence of materials that *do* soften has not been addressed in this treatment.

Difficulties arise when one attempts to solve the problem of wave propagation in such a material. Specifically the following situations arise.

(*i*) If an attempt is made to solve the problem by the method of characteristics one finds that in the domain where $F'(\epsilon) < 0$, the speed of propagation of the wave in question (stress, strain, or velocity) becomes imaginary and real characteristics of the solution cannot be found [4].

(*ii*) If the problem is solved numerically by a finite element technique then the solution depends on the size of the element to an *exacerbated* degree, but more importantly the solution does not appear to converge as the element size tends to zero [5].

(*iii*) The integral method (discussed in Section 3) which furnishes a proof of uniqueness when $F'(\epsilon) > 0$, fails when $F'(\epsilon) < 0$.

2 Method of Characteristics

Consider the initial value problem in one spatial dimension for the case of an elastic material, where

$$\sigma = f(\epsilon) \tag{2.1}$$

$$\frac{\partial \sigma}{\partial x} = \rho_0 \frac{\partial v}{\partial t} \tag{2.2}$$

in the usual notation. In view of equations (2.1) and (2.2)

$$f' \frac{\partial \epsilon}{\partial x} = \rho \frac{\partial v}{\partial t} \tag{2.3}$$

while the compatibility condition is

$$\frac{\partial \epsilon}{\partial t} = \frac{\partial v}{\partial x} \tag{2.4}$$

If we left $\mathbf{W}$ be the vector $\{\epsilon, v\}$ and x and t be denoted by x_1 and x_2, respectively, we then have the relations

$$f' \frac{\partial W_1}{\partial x_1} = \rho \frac{\partial W_2}{\partial x_2} \tag{2.5}$$

$$\frac{\partial W_1}{\partial x_2} = \frac{\partial W_2}{\partial x_1} \quad \text{or, curl } W = 0 \tag{2.6a,b}$$

The condition curl $\mathbf{W} = 0$, allows the potential representation

$$W_i = \phi_{,i} \tag{2.7}$$

in which case equation (2.5) becomes

$$f' \frac{\partial^2 \phi}{\partial x_1^2} = \rho \frac{\partial^2 \phi}{\partial x_2^2} \tag{2.8}$$

This last equation will be hyperbolic with real characteristics, if the characteristic equation

$$f' \left(\frac{\partial \xi}{\partial x_1} \right)^2 = \rho \left(\frac{\partial \xi}{\partial x_2} \right)^2 \tag{2.9}$$

where ξ is a characteristic curve, has real non-null solutions. This is possible if and only if $f' > 0$.

A softening *elastic* material such that $f' < 0$, does not have a hyperbolic wave equation and leads to physical results that are not physically acceptable. Thus a softening *elastic* model leads to wave problems that are not well posed.

3 The Question of Uniqueness of the Solution to Initial Value Problems

The Initial Value Problem. Let V and S be the volume and surface, respectively, of a three-dimensional continuum. Let $\sigma(\mathbf{x}, t)$, $\epsilon(\mathbf{x}, t)$, and $\mathbf{v}(\mathbf{x}, t)$ denote the stress field, strain field, and velocity field, respectively, in V. Furthermore, let $\sigma(\mathbf{x}, 0) = 0$, $\epsilon(\mathbf{x}, 0) = 0$, $\mathbf{v}(\mathbf{x}, 0) = 0$ in V. Also, let S_1 be the part of the surface over which the traction vector $\mathbf{T}(\mathbf{x}, t)$ is prescribed and S_2 the remaining part over which the velocity vector $\mathbf{v}(\mathbf{x}, t)$ is prescribed (so that $S_1 \cup S_2 = S$) in the time domain $0 < t < \infty$.

Limiting ourselves to isothermal small deformation we wish to examine conditions under which the solution $\sigma(\mathbf{x}, t)$, $\epsilon(\mathbf{x}, t)$, $\mathbf{v}(\mathbf{x}, t)$ in V is unique, for $0 < t < \infty$, when the following equations apply.

In V:

$$\sigma_{ij,j} = \rho \frac{\partial v_i}{\partial t} \tag{3.1}$$

$$\sigma_{ij} = F_{ij}[\epsilon_0^t(\tau)] \tag{3.2}$$

where equation (3.1) is Newton's Law of Motion and equation (3.2) is a statement to the fact that the present value of the stress tensor is related to the history of the strain tensor in the interval $0 \le \tau \le t$ by a functional relation. (The exact nature of this relation is at the moment left open.)

On S_1:

$$\sigma_{ij} n_j = T_i \tag{3.3}$$

We limit the discussion to solutions that are continuous and differentiable in V and in the time domain $0 < t < \infty$.

The Auxiliary Problem. Before we address the initial value problem, we pose the following related problem which we call the "auxiliary problem": If the solution is unique at time t under what conditions is it unique also at $t + \Delta t$ where Δt is a vanishingly small nonzero time interval? To answer this question we proceed as follows.

At $t + \Delta t$ let two different solutions exist, which we denote by $\sigma_2, \epsilon_2, \mathbf{v}_2$ and $\sigma_1, \epsilon_1, \mathbf{v}_1$, respectively. Since the solution fields are differentiable with respect to t and since they coincide at t, it follows that:

$$\Delta\sigma \overset{\text{def}}{=} \sigma_2 - \sigma_1 \simeq (\dot{\sigma}_2 - \dot{\sigma}_1)\Delta t \overset{\text{def}}{=} \Delta\dot{\sigma}\,\Delta t \tag{3.4a}$$

$$\Delta\epsilon \overset{\text{def}}{=} \epsilon_2 - \epsilon_1 \simeq (\dot{\epsilon}_2 - \dot{\epsilon}_1)\Delta t \overset{\text{def}}{=} \Delta\dot{\epsilon}\Delta t \tag{3.4b}$$

$$\Delta\mathbf{v} \overset{\text{def}}{=} \mathbf{v}_2 - \mathbf{v}_1 \simeq (\dot{\mathbf{v}}_2 - \dot{\mathbf{v}}_1)\Delta t \overset{\text{def}}{=} \Delta\dot{\mathbf{v}}\Delta t \tag{3.4c}$$

At this point let I denote the following integral

$$I = \int_V \Delta\sigma_{ij}\Delta\epsilon_{ij}\,dV = \Delta t^2 \int_V \Delta\dot{\sigma}_{ij}\Delta\dot{\epsilon}_{ij}\,dV \tag{3.5}$$

or

$$I = \Delta t \int_V \Delta\sigma_{ij}\Delta v_{i,j}\,dV \tag{3.6}$$

Upon application of the Gauss theorem to equation (3.6), one obtains equation (3.7).

$$I = \Delta t \int_S \Delta\sigma_{ij}\Delta v_i n_j\,dS - \Delta t \int_V \Delta\sigma_{ij,j}\Delta v_i\,dV \tag{3.7}$$

At this juncture we utilize equations (3.1) and (3.3) to obtain the following result:

$$I = \Delta t \int_S \Delta T_i \Delta v_i\,dS - \Delta t \int_V \rho\Delta\dot{v}_i\Delta v_i\,dV \tag{3.8}$$

In view of the boundary condition the first integral on the right-hand side of equation (3.8) vanishes and since $\Delta t \neq 0$, the following relation results:

$$\Delta t \int_V \Delta\dot{\sigma}_{ij}\Delta\dot{\epsilon}_{ij}\,dV + \frac{\partial}{\partial t}\int_V \frac{1}{2}\rho\Delta v_i\Delta v_i\,dV = 0 \tag{3.9}$$

This equation is pivotal in the proof of uniqueness of solution of the initial value problem in continuous media.

Downloaded 02 May 2010 to 171.66.16.54. Redistribution subject to ASME license or copyright; see http://www.asme.org/terms/Terms_Use.cfm

Before we proceed with the discussion of the conditions for uniqueness of the auxiliary solution we prove the following fundamental theorem.

Theorem. For all continuous media undergoing small, time-dependent isothermal deformation the following inequality always applies,

$$I \leq 0 \tag{3.10}$$

where the equality applies only in the specific case where the auxiliary solution to the initial value problem is unique, i.e., if in V, $\dot{\epsilon}_1 = \dot{\epsilon}_2$ and $\dot{v}_1 = \dot{v}_2$.

Proof. Let $I > 0$ and let K_Δ be defined by equation (3.11)

$$K_\Delta = \int_V \frac{1}{2} \rho \Delta v_i \Delta v_i \tag{3.11}$$

By definition K_Δ is always non-negative and zero only when the auxiliary solution is unique. Let there be (at least) two different solutions. Then it follows from equations (3.9) and (3.6) that if $I > 0$:

$$\frac{\partial K_\Delta}{\partial t} < 0 \tag{3.12}$$

However, since K_Δ is zero at t inequality (3.12) implies K_Δ will be *negative* in the interval Δt, contrary to equation (3.11). Hence, the integral I cannot be positive, which proves the theorem.

4 The Uniqueness of Solution of the Auxiliary Problem

Positive Material Models. We proceed to discuss a class of *positive* material models which are such that

$$\Delta \dot{\sigma}_{ij} \Delta \dot{\epsilon}_{ij} > 0 \; ; \; \|\Delta \dot{\sigma}\| > 0, \; \|\Delta \dot{\epsilon}\| > 0, \tag{4.1}$$

point-wise in V. Drucker [6] discussed the preceding inequality in the context of "stable materials," i.e., materials for which

$$\dot{\sigma}_{ij} \dot{\epsilon}_{ij} > 0 \tag{4.2}$$

In this discussion we avoid the word "material" by speaking instead of a "material model," i.e., the constitutive equation of a material. Also we avoid the word "stable" because as we will show, there are material models that violate inequality (4.2) but satisfy inequality (4.1) under proper conditions.

We will also show in the following that all positive material models impart a unique solution to the auxiliary problem.

Theorem. All positive material models impart a unique solution to the auxiliary initial value problem.

Proof. The proof is trivial. In view of inequality (4.1) and equation (3.5), I must be non-negative. However we have proved that I cannot be positive. Hence, it must be zero in which case $\Delta v_i = 0$ and the solution is unique.

Remark. Since nothing can be said about uniqueness if inequality (4.1) is violated we conclude that inequality (4.1) is in fact a *sufficient* condition for the uniqueness of the solution of the auxiliary problem.

Uniqueness of the Solution of the Initial Value Problem

Theorem. All positive material models impart a unique solution to the initial value problem.

Proof. To show that the actual solution to the initial value problem is unique, we appeal to the method of induction. If the solution is unique at $t = 0$ then it must be unique at Δt, $2\Delta t$, . . . and $t(=n\Delta t)$, i.e., in the entire interval $(0, t]$. However, the solution *is* unique at $t = 0$ in view of the prescribed initial conditions. Hence uniqueness follows.

5 Examples of Positive Models

All the following examples impart a unique solution to the wave propagation (initial value) problem.

***(i)* Linear-Elastic Model With Positive-Definite Stiffness Tensor.** This model has the well-known classical constitutive equation

$$\sigma = \underset{\sim}{C} \cdot \epsilon \tag{5.1}$$

Thus if $\|\Delta \dot{\sigma}\| > 0, \|\Delta \dot{\epsilon}\| > 0$, then

$$\Delta \dot{\sigma} \cdot \Delta \dot{\epsilon} = \Delta \dot{\epsilon} \cdot \underset{\sim}{C} \cdot \Delta \dot{\epsilon} > 0 \tag{5.2}$$

and the model is positive.

***(ii)* Linear-Viscoelastic Model With a Positive-Definite Initial Relaxation Tensor.** This model has again the well-known constitutive equation

$$\sigma(t) = \int_0^t \underset{\sim}{C}(t-\tau) \frac{\partial \epsilon}{\partial \tau}(\tau) d\tau \tag{5.3}$$

We impose the conditions

$$\dot{\epsilon} \cdot \underset{\sim}{C}(0) \cdot \dot{\epsilon} > 0, \|\dot{\epsilon}\| > 0 \tag{5.4}$$

and require that $\underset{\sim}{C}(t)$ is continuous and differentiable in $0 < t < \infty$, but nothing else is said about the behavior of $\underset{\sim}{C}(t)$.

It follows from equation (5.3) that

$$\dot{\sigma} = \underset{\sim}{C}(0)\dot{\epsilon} + \int_0^t \hat{\underset{\sim}{C}}(t-\tau) \cdot \dot{\epsilon}(\tau) d\tau \tag{5.5}$$

where

$$\hat{\underset{\sim}{C}}(t) = \frac{d\underset{\sim}{C}(t)}{dt} \tag{5.6}$$

Because of the continuity and differentiability properties of $\underset{\sim}{C}(t)$, it follows that the right-hand side of equation (5.5) does not depend on the current value of $d\epsilon/d\tau$, i.e., on $d\epsilon/d\tau|_{\tau=t}$. Thus $\Delta\dot{\sigma}$ and $\Delta\dot{\epsilon}$, in view of the notation of Section 3 (equations (3.4*a*) and (3.4*b*)) and equation (5.5), are related by the equation

$$\Delta \dot{\sigma} = \underset{\sim}{C}(0) \cdot \Delta \dot{\epsilon} \tag{5.7}$$

Hence,

$$\Delta \dot{\sigma} \cdot \Delta \dot{\epsilon} > 0 \tag{5.8}$$

in view of equation (5.4). The material model is therefore, positive.

Admissible Forms of $\underset{\sim}{C}(t)$. If the material is isotropic then $\underset{\sim}{C}(t)$ is given in terms of two relaxation functions $\lambda(t)$ and $\mu(t)$ as is well known. The inequality (5.4) then reduces to the form

$$\left(\lambda(0) + \frac{2\mu(0)}{3}\right) \epsilon_{kk} \epsilon_{ii} + 2\mu(0) e_{ik} e_{ik} > 0 \tag{5.9}$$

where $\mathbf{e}$ is the deviatoric part of ϵ. Evidently the required conditions are

$$\lambda(0) + 2\frac{\mu(0)}{3} > 0, \mu(0) > 0 \tag{5.10}$$

Otherwise any continuous differentiable form of $\lambda(t)$ and $\mu(t)$ is admissible (!), insofar as uniqueness of the solution of the initial value problem is concerned. Consider for instance the form shown in Fig. 1.

The shear stress response to a constant strain rate history is found upon use of equation (5.3), i.e.,

$$\tau = \dot{\gamma} \int_0^t \mu(\tau) d\tau \tag{5.11}$$

If specifically $\int_0^t \mu(\tau) d\tau > \int_t^\infty \mu(\tau) d\tau$ for some t then the shear stress response is given schematically in Fig. 2.

It is of importance to note that the material model exhibits "softening" in the conventionally defined sense, yet the

Downloaded 02 May 2010 to 171.66.16.54. Redistribution subject to ASME license or copyright; see http://www.asme.org/terms/Terms_Use.cfm

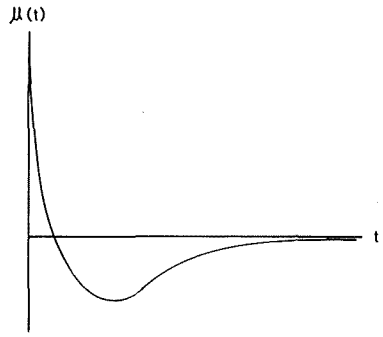

Fig. 1 An admissible form of μ

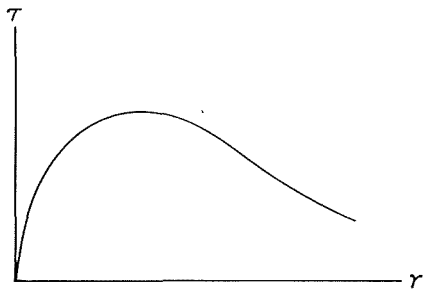

Fig. 2 The shear stress response of a softening material

model is positive and the associated wave propagation problem has a unique solution.

6 Degrading Materials

Softening. Concrete, rock, marble, and other geomaterials, when compressed uniaxially evince a response which consists of a rising stress-strain curve, characterized by a maximum stress beyond which the stress falls monotonically (asymptomically) to zero, thereby exhibiting a softening behavior.

The Degrading Elastic Solid. One popular model for this type of response is the degrading elastic solid described by the constitutive equation

$$\sigma = E_0 e^{-k\epsilon}\epsilon \tag{6.1}$$

or more generally

$$\sigma = F(\epsilon) \tag{6.2}$$

where $F'(\epsilon)$ - the derivative of F with respect to ϵ takes negative values in the range $\epsilon_c < \epsilon < \infty$, where ϵ_c is the strain corresponding to the maximum stress σ_c.

It follows from equation (6.2) that

$$(\dot{\sigma}_2 - \dot{\sigma}_1)(\dot{\epsilon}_2 - \dot{\epsilon}_1) = F'(\epsilon)(\dot{\epsilon}_2 - \dot{\epsilon}_1)^2 \tag{6.3}$$

In view of the character of $F'(\epsilon)$ (<0) in the range $\epsilon_c < \epsilon < \infty$, the right-hand side of equation (6.3) is negative-definite and uniqueness of the initial value problem cannot be proved.

An Appropriate Positive Degrading Model. It has been observed that degradation is associated with the creation of internal flaws such as voids, cracks, and a general disruption of the internal structure of a material. It is pertinent therefore to define an internal variable **q**, which could be a scalar, a vector, or a tensor of the second order, which is a measure of the density and directionality of such flaws in a material element.

Specifically in the uniaxial case one could define a linear degrading solid by the relation

$$\sigma = E(q)\epsilon \tag{6.4}$$

where, here, q is a scalar. We stipulate that $\dot{q}$ is non-negative and E is a positive monotonically decreasing function of q. The purpose here is to find a model that exhibits softening yet gives rise to a unique solution to the wave propagation problem. What is needed, basically, is an evolution equation for q, which ensures the non-negative character of the model.

A Simple Model. We first address a material that softens in axial compression. The tensile case follows similar lines. Let

$$\frac{dq}{dt} = k|\epsilon|^m \tag{6.5}$$

where m is a positive number. This is a simple model which stipulates that the rate of increase of the flaw density q is a power function of the absolute value of the current strain. It follows from equation (6.4) that

$$\dot{\sigma} = \dot{q}\left(\frac{dE}{dq}\right)\epsilon + E\dot{\epsilon} \tag{6.6}$$

It also follows from equations (6.5) and (6.6) that in the course of the axial test

$$\dot{\sigma} = \frac{dE}{dq}|\epsilon|^m\epsilon + E\dot{\epsilon} \tag{6.7}$$

Hence,

$$(\dot{\sigma}_2 - \dot{\sigma}_1)(\dot{\epsilon}_2 - \dot{\epsilon}_1) = E(q)(\dot{\epsilon}_2 - \dot{\epsilon}_1)^2 \tag{6.8}$$

In view of the fact that $E(q)$ is positive, the right-hand side of the equation (6.8) shows that the model is positive and that the solution to the wave propagation problem is unique.

Consider now the specific case where the axial test is performed at constant strain rate, i.e.,

$$\epsilon = \alpha t \tag{6.9}$$

and let $E(q)$ have the explicit functional form given by equation (6.10)

$$E(q) = E_0\exp(-\beta q^n) \tag{6.10}$$

Under these special circumstances equations (6.5) and (6.9) on one hand and (6.4) and (6.10) on the other give rise to the following relations

$$q = \frac{k}{\alpha}(\epsilon^{m+1})/(m+1) \tag{6.11}$$

$$\sigma = E_0\exp(-\beta q^n)\epsilon \tag{6.12}$$

where q was set to zero at $t = 0$. We introduce a simple change of variable by setting

$$Q = \beta q^n \tag{6.13}$$

whereupon equations (6.11) and (6.12) become

$$Q = Q_0\left(\frac{1}{\alpha}\right)^n \epsilon^p \tag{6.14}$$

$$\sigma = E_0\exp(-Q)\epsilon \tag{6.15}$$

where $Q_0 = \beta k^n$ and $p = n(m+1)$ (6.16)

This is a softening model, which however is positive and has a unique solution to the initial value problem.

To illustrate the behavior of the model a comparison is made with the experimental results of Dilger et al. [1] in Fig. 3 for the following values of the constants.

$Q_0 = 2.2 \times 10^3, E_0 = 5.2 \times 10^3$ ksi, $p = 1.26$ and $n = .024$

7 Uniqueness in an Internal Variable Context

We now consider the class of materials whose constitutive equations are derived by the internal variable theory of irreversible thermodynamics. In this case, there exists a free energy density ψ which is a function of the strain tensor ϵ and n internal variables $\mathbf{q}^{(n)}$ which could be tensors of any order. The pertinent constitutive equations are, then, the following

Downloaded 02 May 2010 to 171.66.16.54. Redistribution subject to ASME license or copyright; see http://www.asme.org/terms/Terms_Use.cfm

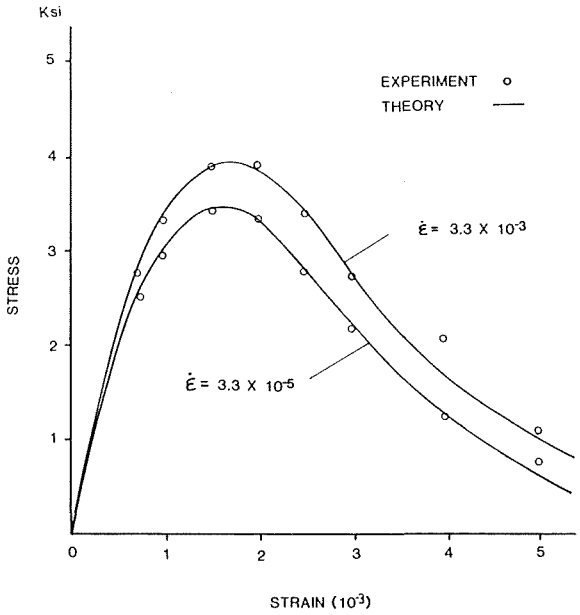

Fig. 3 Comparison of model prediction with experimental data

$$\sigma = \frac{\partial \psi}{\partial \epsilon} \tag{7.1}$$

$$\dot{\mathbf{q}}^{(r)} = \mathbf{f}^{(n)}(\epsilon, \mathbf{q}^{(r)}) \tag{7.2}$$

The functions $\mathbf{f}^{(n)}$ must satisfy the thermodynamic constraint of positive rate of irreversible entropy given in equation (7.3).

$$\dot{\psi}|_{\epsilon} = \frac{\partial \psi}{\partial \mathbf{q}}(r) \cdot \mathbf{f}^{(n)} < 0 \tag{7.3}$$

We wish to examine conditions that render the model positive. In view of equation (7.1) and (7.2)

$$\dot{\sigma}_{ij} = \frac{\partial^2 \psi}{\partial \epsilon_{ij} \partial \epsilon_{kl}} \dot{\epsilon}_{kl} + \frac{\partial^2 \psi}{\partial \epsilon_{ij} \partial q_{kl}(n)} f_{kl}^{(n)} \tag{7.4}$$

Thus, in direct notation,

$$\Delta \dot{\sigma} \cdot \Delta \dot{\epsilon} = \Delta \dot{\epsilon} \cdot \frac{\partial \psi}{\partial \epsilon^2} \cdot \Delta \dot{\epsilon} \tag{7.5}$$

since the second term on the right-hand side of equation (7.4) is a function of ϵ and $\mathbf{q}^{(n)}$.

As a consequence of the definition of positive materials (i.e., equation (4.1)) and Theorem II of Section 4, it follows that material models of this class, such that the fourth-order tensor $\partial^2 \psi / \partial \epsilon^2$ is positive-definite, possess a unique solution to the initial value problem. It is important to point out that this is true irrespective of the form of the functions $\mathbf{f}^{(n)}$ and ψ and irrespective of whether the thermodynamic inequality (7.3) is satisfied. Thus the constraint of positive rate of irreversible entropy is not relevant to the question of uniqueness of the initial value problem.

Uniqueness Condition. The uniqueness condition for the class of constitutive models where the constitutive response is determined by equations (7.1) and (7.2) is the following:

$$\xi \cdot \frac{\partial^2 \psi}{\partial \epsilon^2} \cdot \xi > 0 \tag{7.6}$$

for all ξ such that $\|\xi\| > 0$

The simple model in Section 6 is a case in point. In view of equation (6.4)

$$\psi = \frac{1}{2} E(q) \epsilon^2 \tag{7.7}$$

whereby

$$\sigma = \frac{\partial \psi}{\partial \epsilon} = E(q) \epsilon \tag{7.8}$$

as before, and in addition

$$\frac{\partial^2 \psi}{\partial \epsilon^2} = E(q) \tag{7.9}$$

Thus as pointed out, the model is positive if $E(q) > 0$. Since the rate equation for $\dot{q}$ is of the type given by equation (7.2) the initial value problem will have a unique solution.

However the entropy inequality inequality (7.3) requires that

$$\dot{E}(q) < 0 \tag{7.10}$$

or

$$\frac{dE}{dq} \dot{q} < 0, \dot{q} \neq 0 \tag{7.11}$$

If we demand that degradation is a nondecreasing function of time, i.e., that there can be no "healing" then $\dot{q}$ will always be non-negative in which case

$$\frac{dE}{dq} < 0 \tag{7.12}$$

As we showed in Section 6, inequality (7.12) leads to softening.

References

1 Dilger, W. H., Koch, R., and Kowalyczyk, R., "Ductility of Plain and Confined Concrete Under Different Strain Rates," The University of Calgary, Civil Engineering Report, 1982.

2 Hsu, T. T. C., et al., "Microcracking of Plain Concrete and the Shape of the Stress-Strain Curve," *J. Am. Concrete Inst.*, Vol. 60, 1963, p. 209.

3 Dougill, J. W., "On Stable Progressively Fracturing Solids," *ZAMP*, Vol. 27, 1976, p. 423.

4 Courant, R., and Hilbert, D., *Methods of Mathematical Physics, II*, Interscience, New York, 1962.

5 Pietruszczak St., and Mroz, Z., "Finite Element Analysis of Deformation Softening Materials," *Int. J. Num. Methods in Eng.*, Vol. 17, 1981, p. 327.

6 Drucker, D. C., "A Definition of a Stable Inelastic Material," ASME JOURNAL OF APPLIED MECHANICS, Vol. 26, 1959, p. 101.

Downloaded 02 May 2010 to 171.66.16.54. Redistribution subject to ASME license or copyright; see http://www.asme.org/terms/Terms_Use.cfm

The Uniaxial Unloading Behavior of Two Engineering Alloys at Room Temperature

E. Krempl
Fellow ASME

V. V. Kallianpur[1]

Department of Mechanical Engineering
Aeronautical Engineering and Mechanics,
Rensselaer Polytechnic Institute,
Troy, N.Y. 12180

A computer-controlled servohydraulic testing machine was used to study the unloading behavior from the fully plastic region of AISI Type 304 Stainless Steel and of the Ti-7Al-2Cb-1Ta Titanium alloy at room temperature. Load and displacement control were used and in some tests the magnitude of the loading rate was changed by two orders of magnitude at the point of unloading. Unloading behavior from the fully plastic region depends strongly on the control mode (the boundary condition) and is not linearly elastic, but curved. In displacement control, positive slopes larger than the elastic one are obtained leaving the unloading point. Small negative slopes and creeping out may be observed in load control. At some region below the maximum stress and above zero stress the unloading curve attains an elastic slope. At zero stress the slope is less than the elastic one. The observed behavior is influenced by the presence of significant rate dependence of the deformation behavior (viscosity effects).

Introduction

Results of experiments on specimens representing a uniaxial state of stress have frequently been used to model material behavior and to check constitutive equations for inelastic deformation of materials. Among the many properties of interest is the behavior during unloading when it occurs beyond the linear-elastic range.

Plasticity theory says that unloading behavior from the fully plastic region is linearly elastic and this assumption has been tacitly carried over to the modeling of the deformation behavior of metals in general. As a consequence it is widely accepted that metals show linear-elastic unloading behavior. A recent example is given in [1, 2] where the elastic unloading behavior after prior plastic deformation figures prominently in the evaluation of the capabilities of the endochronic theory.

The initial endochronic theory [3] did not exhibit an elastic slope during initial unloading. This fact was noticed [4, 5] and led to the introduction of a new endochronic time which results in elastic unloading [6]. Further elastic unloading is presumed in finite deformation theories of plasticity which use the multiplicative decomposition of the deformation gradient, see [7, 8].

These theoretical considerations do not address the question of real material behavior. Although early experiments show that unloading is not strictly linear-elastic [9], very little additional information on this subject has been published.[2]

Accordingly, this paper reports the results of experiments regarding the unloading behavior of two engineering alloys at room temperature.

Test Conditions and Test Material

All tests were run on specimens representing the uniaxial state of stress at room temperature on AISI Type 304 Stainless Steel and on the high-strength Ti-7Al-2Cb-1Ta Titanium alloy. Test methods, specimen size, and heat treatment of the materials are given in [10–12].

In the present tests the function generator used in [10–12] was replaced by an MTS 463 Data/Control Processor which employs a PDP 11/23 minicomputer and permits arbitrary loading rate changes initiated by a suitable program. All other conditions including the displacement measurement on the cylindrical section of the specimens (gage length) are identical to the ones used in [10–12].

The displacement measurement on the gage length, the use of a servocontrolled testing machine, and the slow motions used in the tests ensure that the measured responses represent real material behavior under load (stress) and displacement (strain) control with virtually no testing machine bias. Strain control simulates a very stiff conventional testing machine whereas stress control changes the characteristics to that of a

[1] Presently at General Electric Co., Schenectady, N.Y.

Contributed by the Applied Mechanics Division and presented at the 1985 Joint ASME/ASCE Applied Mechanics, Fluids Engineering, and Bioengineering Conference, Albuquerque, N. Mex., June 24–26, 1985 of THE AMERICAN SOCIETY OF MECHANICAL ENGINEERS.

Discussion on this paper should be addressed to the Editorial Department, ASME, United Engineering Center, 345 East 47th Street, New York, N.Y. 10017, and will be accepted until two months after final publication of the paper itself in the JOURNAL OF APPLIED MECHANICS. Manuscript received by ASME Applied Mechanics Division, June, 1984; final revision October, 1984. Paper No. 85-APM-31.

[2] The first appearance of a hysteresis loop during cycling with increasing amplitude in the "macroscopically elastic region" is of interest in determining "microyielding." These studies [22, 23] show deviation from linear elasticity in the elastic region of plasticity theory.

Copyright © 1985 by ASME
Downloaded 02 May 2010 to 171.66.16.54. Redistribution subject to ASME license or copyright; see http://www.asme.org/terms/Terms_Use.cfm

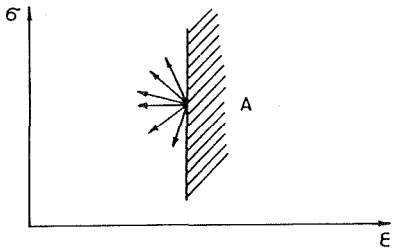

Fig. 1(*a*)

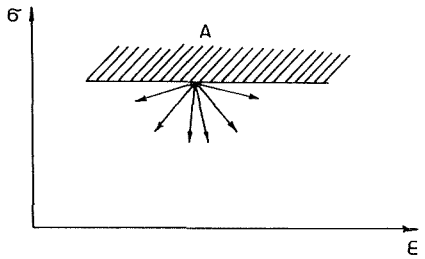

Fig. 1(*b*)

Fig. 1 Schematic showing the influence of control on the unloading behavior. Hatched half-planes going through the point of unloading, *A* are inaccessible. Figure 1(*a*) is for strain control and Fig. 1(*b*) for stress control.

soft machine. Indeed the servocontrolled system constitutes the best experimental method to realize slow homogeneous motions of defined time variation in solids. In the present paper only piecewise-linear command signals will be employed. The time rates of the input signals are therefore piecewise-constant.

Test Results

The Influence of Stress and Strain Control on the Unloading Behavior. The engineering stress (small strain) rate before and after reversal are designated by $\dot{\sigma}^-$ ($\dot{\epsilon}^-$) and $\dot{\sigma}^+$ ($\dot{\epsilon}^+$), respectively. The ratios

$$\delta = \dot{\epsilon}^+ / \dot{\epsilon}^- \tag{1}$$

and

$$\gamma = \dot{\sigma}^+ / \dot{\sigma}^- \tag{2}$$

can be imposed on the specimens by a suitable control program.[3] Reversal with constant loading-rate magnitude corresponds to $\delta = -1 (\gamma = -1)$. If the rate magnitude is increased at reversal $\delta < -1 (\gamma < -1)$ and if it is decreased, $-1 < \delta < 0 (-1 < \gamma < 0)$.

Behavior for $\delta = -1$ and $\gamma = -1$. Figure 1(*a*) shows the kinematically possible motions in the σ (engineering stress) versus ϵ (engineering strain) plane for strain control[4] for a reversal of the loading rate. Figure 1(*b*) is for reversal under stress control.

For strain control the half-plane to the right of the vertical line through the reversal point is inaccessible. For stress control the plane above the horizontal line through the reversal point cannot be reached.

Experiments using strain control exhibit a sharp corner at the unloading point with immediate positive slope larger than the modulus of elasticity E (see Figs. 6 and 7 in [10], Figs. 1, 15, and 16 in [11], and Figs. 2, 3, and 10 in [12]). For stress control and slow loading-rate magnitudes, a small negative slope is observed shortly after the point of reversal (see Figs. 1, 12, and 13 of [11] and Figs. 3 and 4 of [12]). For fast stress rates the portion of the curve exhibiting negative slope becomes very small, see Fig. 4 of [12]. As the stress decreases a positive slope is obtained and the unloading behavior in stress control is indistinguishable from that of strain control.

The slope at zero stress in each case is less than the elastic modulus and the unloading curve is not a straight line. However, a region exists below the stress at reversal and above zero where the unloading curve exhibits elastic slope (see Figs. 1 and 13 of [11] and Figs. 2 and 3 of [12]). The plastic power $\sigma(\dot{\epsilon} - \dot{\sigma}/E)$ can be negative during unloading as zero stress is approached.

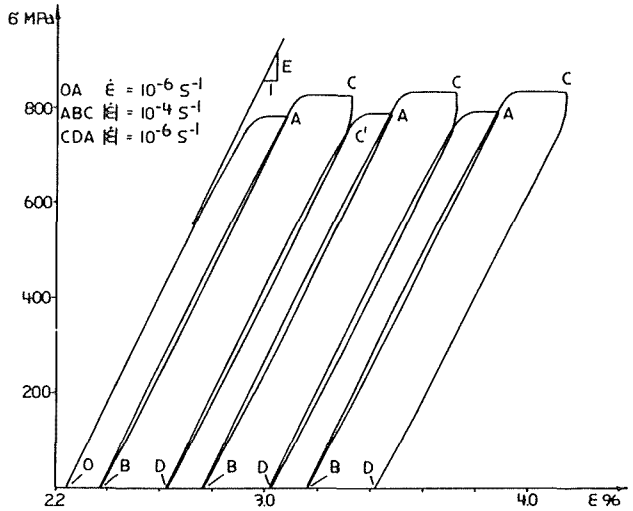

Fig. 2 Strain-controlled loading and unloading involving strain-rate changes of two orders of magnitude for the high-strength Ti-alloy

Behavior for $\delta << -1 (\gamma << -1)$ and $1/\delta << -1) (1/\gamma << -1)$. Experience has shown the rate effects are significant if the changes involve orders of magnitude [10, 12]. Therefore the experimental results shown in the following involve rate changes of at least two orders of magnitude.

The behavior of the Ti-alloy under strain control is shown in Fig. 2. At points A, $\delta = -10^2$ and at points C, $\delta = -10^{-2}$. Starting from A, the unloading slope is elastic and

[3]The ratios that can be realized are limited by the response characteristic of the testing system.

[4]Stress control implies traction boundary conditions whereas displacement boundary conditions are represented by strain control.

Nomenclature

σ = engineering stress
$\dot{\sigma}$ = engineering stress rate
$\dot{\sigma}^-$ = engineering stress rate before reversal
$\dot{\sigma}^+$ = engineering stress rate after reversal
ϵ = engineering strain
$\dot{\epsilon}$ = engineering strain rate
$\dot{\epsilon}^-$ = engineering strain rate before reversal
$\dot{\epsilon}^+$ = engineering strain rate after reversal

Downloaded 02 May 2010 to 171.66.16.54. Redistribution subject to ASME license or copyright; see http://www.asme.org/terms/Terms_Use.cfm

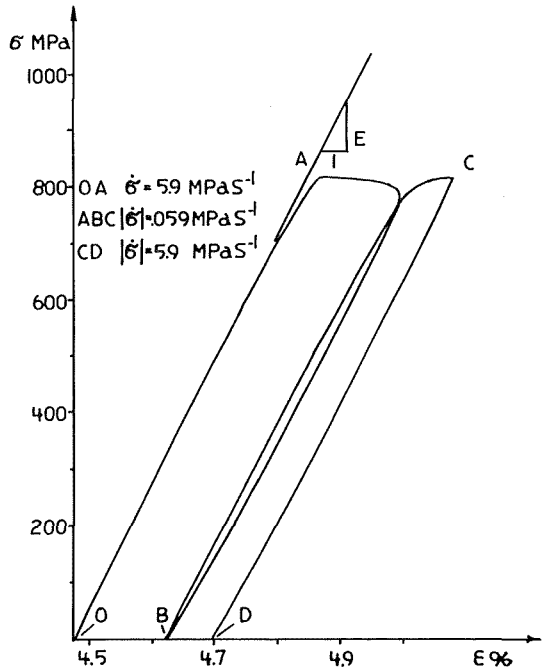

Fig. 3 Stress-controlled loading and unloading for the Ti-alloy involving stress-rate changes of two orders of magnitude. Prior tensile deformation.

reduces continuously as the stress decreases to zero. At C an almost vertical drop is seen. As the stress decreases, the slope gradually decreases. At an interval of stresses below C', the slope is equal to the elastic modulus and then, as in the case of "fast" unloading, reduces further. At zero stress the slope is less than the elastic modulus.

The behavior in stress control is shown in Fig. 3 and is completely different from that under strain control. At A, $\gamma = -10^{-2}$ and a small negative slope follows with considerable accumulation of strain. Gradually the slope increases and becomes positive and subsequently changes in the way that was observed for strain control. At C, $\gamma = -10^{2}$, the unloading slope is very close to E and continues to decrease.

The slope at zero stress as it is approached from above is always less than the slope leaving zero stess. This observation is true for all reloadings from zero stress and the corner at this point seems to be a characteristic of metal behavior that results in a small hysteresis loop for zero-to-tension loading.

The behavior of Type 304 Stainless Steel exhibits the same differences between stress and strain control. Details can be found in [13].

Repeated Loading and Unloading. In [2] repeated loading and unloading cycles were considered as part of a thermodynamic argument, see Fig. 3 of [2]. The results of the strain-controlled tests on the Ti-alloy shown in Fig. 4 depict the behavior of an engineering alloy under repeated loading and unloading cycles.

The origin of Fig. 4 was reached from the compression side and subsequent tensile loading exhibits an early departure from linearity due to the Bauschinger effect. Intermediate loading and unloading cycles were started at a maximum strain of 3.6 percent. After the cycles it was decided to move to the fully plastic range and the actual test consisting of 1620 cycles started at about 4.2 percent maximum strain. It is seen that the maximum stress of a cycle drops by about 90 MPa and that the loading-unloading behavior appears to be nearly a straight line. A detailed analysis, however, shows that the slopes upon approaching and departing from the minimum

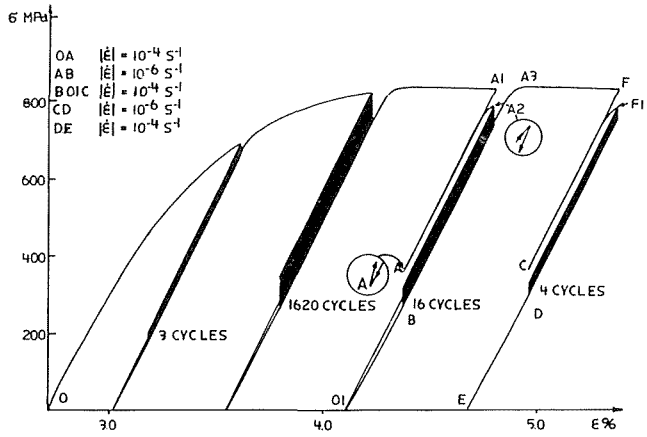

Fig. 4 Strain-controlled partial unloading cycles for a Ti-alloy specimen depicting stress drops that gradually subside

(maximum) strain are different; each time a corner is formed as shown in the inserts of Fig. 4.

At 4.8 percent, the same test is repeated with the exception that the strain rate is reduced by two orders of magnitude at point A. This reduction does not affect the stress-strain behavior at low stress levels but, when the maximum stress is approached, a significant decrease in slope is observed. On subsequent cycles the behavior is nearly a straight line. The 16 cycles at $|\dot{\epsilon}| = 10^{-6}$ s^{-1} correspond to the same test time ($\sim$ 36 hr) as the 1620 cycles at $|\dot{\epsilon}| = 10^{-4}$ s^{-1}. The stress drop[5] at 4.8 percent involving $|\dot{\epsilon}| = 10^{-6}$ s^{-1} is slightly greater than that associated with 10^{-4} s^{-1} at 4.22 percent. However, the maximum and minimum stresses at the last cycle are equal in both cases.

The experiment commencing at F (5.4 percent maximum strain) with subsequent reduction in strain rate for four cycles is added to show repeatability of the observations. The same set of experiments was conducted at compression with the same qualitative behavior.

It is clear from Fig. 4 that the gradual reduction in the maximum stress is controlled by the strain rate and, therefore, by viscous effects. The analysis of the rate dependence of the stress drop for various tests is shown in Fig. 5 where the stress drop is plotted on a linear scale versus the logarithm of test duration. It is seen that the results are separated according to the strain rates used. At test times in excess of 2×10^4 s, the tests with the slow strain rate show a greater stress drop than the ones with 10^{-4} s^{-1}.

No saturation of the stress drop is evident in Fig. 5 on the semilogarithmic plot. The straight lines indicate that stress drop per decade is constant but takes 10 times longer with the passage of each decade. Therefore stress drop slows down considerably. Assuming that the trend shown in Fig. 5 continues indefinitely and, considering that the total possible drop to zero stress is approximately 370 MPa at Points A and C in Fig. 4, it is easy to estimate that the time required for the total drop is approximately 3×10^6 (3×10^{13}) years at the strain rate of 10^{-6} s^{-1} (10^{-4} s^{-1}).

For a strain rate of 10^{-4} s^{-1}, the stress drops shown in Fig. 5 seem to be independent of strain range and of the sign of the stresses.

It is interesting to note that the many intermediate cycles do not appear to affect the subsequent behavior. By extrapolating, say from point $A1$ to $A3$, a continuous curve OF in Fig. 4 can be obtained which is very close to the uninterrupted stress-strain curve.

[5]The stress drop is defined as the difference between the maximum stress at which unloading commences initially and the maximum stress in subsequent cycles. See points $A1(F)$ and $A2(F1)$, respectively, in Fig. 4.

Downloaded 02 May 2010 to 171.66.16.54. Redistribution subject to ASME license or copyright; see http://www.asme.org/terms/Terms_Use.cfm

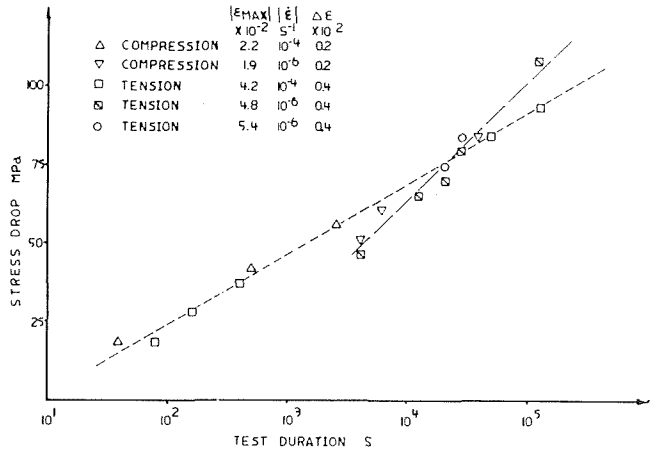

Fig. 5 Stress drops for the Ti-alloy at a given maximum strain versus time under cyclic load in tests such as the one shown in Fig 4. The stress drop is measured from the maximum stress (such as points *A*I or *F* in Fig. 4) and the test duration commences at these points.

The behavior of Type 304 Stainless Steel follows the same qualitative trends [13].

Discussion

Although the experiments have been conducted at specific strain values, the unloading and cyclic behaviors shown in Figs. 2-4 are not peculiar to these strain values. It is our experience that they are typical for tests conducted in tension or compression when plastic flow is well established. The unloading and cyclic behavior depicted is typical for these two materials for unloading from anywhere in the plastic range.

The results presented clearly show that the unloading behavior of Type 304 Stainless Steel and of the Ti-alloy does not correspond to the classical notions. Additional limited experiments on SAE 1020 Steel, on A533B Pressure Vessel Steel, and on commercially pure copper show qualitatively the same behavior as the two engineering alloys studied here. Purely elastic unloading is not observed with these metals.

The detailed behavior shortly after reversal is determined by the type of control and rate of unloading. Beyond this short region the behavior is not very sensitive to loading rate and type of control. As the stress decreases, the unloading curve assumes elastic slope at some positive stress. From this stress on, the slope decreases further and is less than the elastic one at zero stress.

When the unloading rate is reversed at any stress including zero stress, the slope leaving this stress is found to be greater than the slope approaching this stress; a corner is formed. This qualitative property is not dependent on the type of control and on the rate of loading, and is found in tension and compression.

The present results are qualitatively in agreement with early results [9] on a variety of other metals. (The influence of control on the behavior immediately after resersal was not studied in [9].) They do not corroborate the idealizations commonly used [1, 2, 7]. Rather, these tests suggest that rate dependence (or viscous behavior) is an important part of metal deformation and must be considered even at room temperature.

It is interesting to compare the results of the tests reported herein with the predictions of the "unified theories." In these theories the total strain rate $\dot{\epsilon}$ is the sum of the inelastic $\dot{\epsilon}_{in}$ and the elastic strain rate $\dot{\sigma}/E$ where E is the modulus of elasticity

$$\dot{\epsilon} = \dot{\sigma}/E + \dot{\epsilon}_{in}. \tag{3}$$

In these theories plasticity (time-independent) and creep are not separately recognized and it is postulated that all inelastic deformation is rate-dependent.

Table 1(*a*) Measured and predicted slopes immediately after a rate change for the Ti-alloy

Strain at Start of Test (%)	δ	γ	$d\sigma/d\epsilon^+/E$ Measured (approx.)	$d\sigma/d\epsilon^+/E$ Predicted
2.25	-10^{2}		1.03	1
2.25	-10^{-2}		45	100
4.50		-10^{-2}	-0.02^a	-0.03
4.50		-10^{2}	1.07	1.13
5.90		-10^{2}	1.17	1.06
5.90		-10^{2}	1.12	1.96
6.25		-10^{-2}	-0.03	-3×10^{-4}

$^a d\sigma/d\epsilon^- = 0.76E$

Table 1(*b*) Measured and predicted slopes after a rate change for type 304 stainless steel

Strain at Start of Test (%)	δ	γ	$d\sigma/d\epsilon^+/E$ Measured (approx.)	$d\sigma/d\epsilon^+/E$ Predicted
1.00	-10^{2}		1.2	1
1.00	-10^{-2}		47	100
0.65		-10^{2}	1.09	1
0.65		-10^{-2}	-0.01^a	0.008
10.00	-10^{2}		1.3	1
10.00	-10^{2}		1.2	1
10.00	-10^{-2}		30	100
10.00	-10^{-2}		30	100

$^a d\sigma/d\epsilon^- = 0.45E$

While the various theories differ in the dependence of the inelastic strain rate on other variables, they have one property in common; the inelastic strain rate does not depend on time derivatives for any quantity and is, therefore, continuous upon a discontinuous change in stress or strain rate.

By writing equation (3) immediately before and after a jump in stress or strain rate and by using (1) and (2) and the chain rule, the slopes immediately before ($d\sigma^-/d\epsilon$) and immediately after a jump ($d\sigma^+/d\epsilon$) can be calculated.

They are for strain control

$$\frac{d\sigma^+}{d\epsilon} = E\left[1 - \frac{1}{\delta}\left(1 - \frac{1}{E}\frac{d\sigma^-}{d\epsilon}\right)\right] \tag{4}$$

and for stress control

$$\frac{d\sigma^+}{d\epsilon} = E\left(1 - \frac{1}{\gamma}\left(1 - \frac{E}{d\sigma/d\epsilon^-}\right)\right)^{-1}. \tag{5}$$

The limits of the predictions of (4) and (5) for $(d\sigma^-)/(d\epsilon)E << 1$ are given in [14, 15] and numerical experiments in [14, 15] illustrate the unloading behavior which is very comparable to the behavior observed in Figs. 2 and 3.[6] In the present tests, rate changes involving two orders of magnitude are used and the results of the prediction and of the experiment are listed in Tables 1(*a*), and 1(*b*) for the Ti-alloy and the stainless steel, respectively. In the assessment of the experimental results it should be stressed that the theory requires that the slope be determined leaving the point of rate change. This is strictly not possible. The results reported are the best values obtainable with a straight edge and they are susceptible to considerable error, specifically for steep and shallow slopes. Nevertheless theory and experiment are in broad agreement regarding the influence of control and of rate increases (decreases). Where necessary, the influence of $d\sigma/d\epsilon^-$ has been considered in evaluating (5), e.g., point A in Fig. 3.

The predictions of equations (4) and (5) not only apply to the theories discussed in [14, 15] but also to those postulated

[6] Similar observations are made in [16].

Downloaded 02 May 2010 to 171.66.16.54. Redistribution subject to ASME license or copyright; see http://www.asme.org/terms/Terms_Use.cfm

in [17-19] and others that have the structure given in (3). The prediction of subsequent behavior may be quite different for various approaches.

The prediction for rate changes of a theory using

$$\dot{\epsilon} = \dot{\sigma}/E + \dot{\epsilon}_{in} + \dot{\epsilon}_{pl} \tag{6}$$

where $\dot{\epsilon}_{pl}$ is the rate-independent plastic strain [20] would be very different. This fact was pointed out in [21]. Indeed the behavior under jumps in loading rate of a real metal could be used to see whether its behavior can be modeled by either the "unified" theories (3) or by the ones represented by (6).

"Dissipation" in cyclic deformation is another point of discussion in [1] and [2]. Specifically, a strain cycle starting at ϵ_1 and returning to ϵ_1 with a reversal point at $\epsilon_2 < \epsilon_1$ is considered in [1, 2]. The work done in such a cycle is called dissipation and postulated to be non-negative in [1].

The experiments reported herein include such strain cycles. As an example we consider the cycle CDC' in Fig. 2. For this strain cycle, the net work

$$\int_C^{C'} \sigma d\epsilon > 0 \tag{7}$$

since the reloading curve is above the unloading curve (the strain at points C and C' is the same). This behavior is rather general and is due to the corners that are being formed at the reversal points, see Figs. 2-4. Even in the small strain cycles of Fig. 4, these corners are present as indicated by the inserts. Corners are also evident for all metals tested in [9] with the exception of an aluminum alloy, which showed almost linear behavior.

Owing to these properties, the net work in such a strain cycle is generally non-negative.

However, that need not always be the case as demonstrated by the strain cycles AlAA2 and FCF1 in Fig. 4. For these cycles, the net work is obviously negative. Similar observations were made in compression testing for the Ti-alloy and in tension for Type 304 Stainless Steel.

These examples show that for the *two engineering alloys tested* the *net work* in the strain cycle under consideration *can be negative or zero or positive*. Even when it is negative no instabilities were found.[7] Therefore the non-negative value of the net work (called dissipation in [1]) cannot be postulated as a general principle.

It might be argued that the negative net work for cycles A1AA2 and FCF1 in Fig. 4 is brought about by the reduction in rate at A, or C, and that such cycles are not possible in rate-independent materials where rate changes do not affect the deformation behavior.

Although this may be true, we are not in a position to make a statement about the actual behavior of rate-independent materials. The engineering alloys tested by us so far do not conform to the rate-independent idealization.

It appears to us that there is no basic reason why the net work in such a cycle cannot be negative. If this happens, the first law of thermodynamics requires only the internal energy (at point A2(F1) be less than at point A1(F).[8] We therefore agree with the opinion expressed in [2].

Given the ever-decreasing rate of stress drop shown in Fig. 5, we do not suppose that the drop continues until the minimum stress is zero. Rather, we think that the cycle will stabilize at some stress level somewhat below point B in Fig. 4.

[7]There is no significantly different behavior for the cycles with and cycles without strain-rate changes.

Acknowledgment

The support of the National Science Foundation is gratefully acknowledged. Mr H. Lu contributed to the analysis.

References

1 Rivlin, R. S., "Some Comments on the Endochronic Theory of Plasticity," *Int. J. Solids and Structures*, Vol. 17, 1981, pp. 231-248.

2 Valanis, K. C., "On the Substance of Rivlin's Remarks on the Endochronic Theory," *Int. J. Solids and Structures*, Vol. 17, 1981, pp. 249-265.

3 Valanis, K. C., "A Theory of Viscoplasticity Without a Yield Surface," Parts I and II, *Archives of Mechanics*, Vol. 23, 1971, pp. 517-551.

4 Walker, K. P., and Krempl, E., "An Implicit Functional Representation of Stress-Strain Behavior," *Mech. Res. Communications*, Vol. 4, 1978, pp. 185-190.

5 Valanis, K. C., and Read, H. E., "A Theory of Plasticity for Hysteretic Materials—I: Shear Response," *Computers and Structures*, Vol. 8, 1978, pp. 503-510.

6 Valanis, K. C., "Fundamental Consequences of a New Intrinsic Time Measure-Plasticity as a Limit of Endochronic Theory," *Archives of Mechanics*, Vol. 32, 1980, pp. 171-191.

7 Lee, E. H., "Elastic-Plastic Deformations at Finite Strains," ASME JOURNAL OF APPLIED MECHANICS, Vol. 36, 1969, pp. 1-6.

8 Nemat-Nasser, S., "On Finite Deformations in Elastoplasticity," *Int. J. Solids and Structure*, Vol. 18, 1982, pp. 857-872.

9 Dalby, W. E., "Researches on the Elastic Properties and the Plastic Extension of Metals," *Phil. Trans. Roy. Soc. London*, Vol. 221, 1921, pp. 117-138.

10 Krempl, E., "An Experimental Study of Room-Temperature Rate Sensitivity, Creep and Relaxation on Type 304 Stainless Steel," *J. Mech. Phys. Solids*, Vol. 27, 1979, pp. 363-375.

11 Kujawski, D., Kallianpur, V., and Krempl, E., "An Experimental Study of Uniaxial Creep, Cyclic Creep and Relaxation of AISI Type 304 Stainless Steel at Room Temperature," *J. Mech. Phys. Solids*, Vol. 28, 1980, pp. 129-148.

12 Kujawski, D., and Krempl, E., "The Rate(Time)-Dependent Behavior of Ti-7Al-2Cb-1Ta Titanium Alloy at Room Temperature Under Quasi-Static Monotonic and Cyclic Loading," ASME JOURNAL OF APPLIED MECHANICS, Vol. 48, 1981, pp. 55-63.

13 Kallianpur, V. V., Ph.D. thesis, Rensselaer Polytechnic Institute, Troy, N.Y., May 1983.

14 Cernocky, E. P., "Comparison of the Unloading and Reversed Loading Behavior of Three Viscoplastic Constitutive Thoeries," *Int. J. Non-Linear Mechanics*, Vol. 17, 1982, pp. 255-266.

15 Cernocky, E. P., "An Examination of Four Viscoplastic Constitutive Theories in Uniaxial Monotonic Loading," *Int. J. Solids and Structures*, Vol. 18, 1982, pp. 989-1005.

16 Patel, N. R., and Bieniek, M. P., "An Analysis of Viscoplastic Behavior of Metals," *Materials Science and Engineering*, Vol. 40, 1979, pp. 123-134.

17 Hart, E. W., "Constitutive Relations for the Nonelastic Deformation of Metals," *ASME Journal of Engineering Materials and Technology*, Vol. 98, 1976, pp. 193-201.

18 Miller, A. K., "An Inelastic Constitutive Model for Monotonic, Cyclic and Creep Deformation, Parts I and II," *ASME Journal of Engineering Materials and Technology*, Vol. 98, 1976, pp. 97-113.

19 Rohde, R. W., Swearengen, J. C., "Deformation Modeling Applied to Stress Relaxation of Four Solder Alloys," *ASME Journal of Engineering Materials and Technolgy*, Vol. 102, 1980, pp. 207-214.

20 Cristescu, N., and Suliciu, I., *Viscoplasticity*, Martinus Nijhoff, 1982, especially p. 39 ff.

21 Krempl, Discussion of "Time-independent and Time-dependent Deformation of Metals," by T. H. Alden in ASTM STP 765, American Society for Testing and Materials, 1982, pp. 48-49.

22 Brown, N., and Ekvall, R. A., "Temperature Dependence of the Yield Points in Iron," *Acta Met.*, Vol. 10, 1962, pp. 1101-1107.

23 Hecker, S. S., in: *Consitutive Equations in Viscoplasticity: Computational and Engineering Aspects*, ASME New York, 1976, pp. 1-33.

[8]Adiabatic conditions and no external heat supply are assumed.

Downloaded 02 May 2010 to 171.66.16.54. Redistribution subject to ASME license or copyright; see http://www.asme.org/terms/Terms_Use.cfm

Acoustoelastic Response of a Polycrystalline Aggregate With Orthotropic Texture

G. C. Johnson

Department of Mechanical Engineering,
University of California,
Berkeley, Calif. 94720
Assoc. Mem. ASME

Estimates of the effective second-order and third-order elastic constants of a polycrystalline aggregate exhibiting texture are presented for the case of orthotropic sample symmetry and cubic crystalline symmetry. The nature of the texture is brought into the analysis through the crystallites' orientation distribution function which is written in a series of generalized spherical harmonics. The effective response is evaluated using a Voigt-type procedure in which the crystal stiffnesses are averaged over the orientation distribution function. In evaluating the results, it is found that only seven terms in the expansion for the orientation distribution function are required for the exact representation of the effective properties.

Introduction

In the development of acoustoelasticity as a tool for the nondestructive evaluation of stress, it has become increasingly apparent that the characterization of the structural materials being examined as isotropic is overly simplistic. Most of these materials are actually polycrystalline aggregates whose forming (rolling, drawing, forging, etc.) leaves the grains in certain preferred orientations and hence causes the aggregate response to be anisotropic. The purpose of this paper is to provide a method for the estimation of the effective elastic and acoustoelastic constants for such textured materials based on the knowledge of the elastic constants of the constituent crystals and the orientation distribution of the grains within the aggregate.

Acoustoelasticity is a technique that has been examined as a possible method for evaluating active and residual stresses within a structural component. It is based on the observation that the speeds at which waves propagate through a body depend on the state of stress or deformation to which that body is subjected. To model the observed response, the theory associated with acoustoelasticity is based on an assumption that the strain energy (from which the constitutive relation between stress and strain is obtained) is a cubic function of the strain. As a result, the material response is characterized by the coefficients of the quadratic and cubic terms in the strain energy, called the second-order elastic constants (SOEC) and third-order elastic constants (TOEC), respectively. The acoustoelastic response is obtained by considering the motion of the infinitesimal wave superposed on a state of finite homogeneous deformation of the material. The usual result of this type of evaluation is a set of equations for the velocities of plane waves as functions of the strain, with the coefficients in the equations being particular combinations of the SOEC and TOEC.

To be able to estimate the acoustoelastic response of a material, then, its elastic constants must be known. For an isotropic material there are two independent SOEC and three independent TOEC, while for a plate with rolling texture there are nine SOEC and 20 TOEC which must be evaluated. The work presented in this paper gives a method for estimating these 29 elastic constants from the nine elastic constants of the cubic crystals which make up the aggregate. The technique employed to obtain the estimates is a simple Voigt-type procedure in which the second and third-order stiffness tensors are averaged over the orientation distribution function for the crystallites. The results for the SOEC are equivalent to previous estimates of such quantities by Bunge [1], Morris [2], and Sayers [3]. The results for the TOEC contain as a special case the work by Johnson [4, 5] who gives estimates for an aggregate that exhibits transverse isotropy.

The term "effective properties" is used to describe the physical properties of a homogeneous medium that exhibits orthotropic symmetry and that in some sense approximates the macroscopic response of the actual inhomogeneous polycrystalline aggregate. All effective property estimates given in the paper are based on the Voigt assumption that the strain in the actual material is the same as in the effective medium, which because of its homogeneity can support a uniform strain field. Another technique, called Reuss-type averaging, makes the similarly extreme assumption that the stress in the aggregate is the same as the stress in the effective medium. In actuality, the strain and stress vary from point to point because of the inhomogeneous nature of the material (differing orientations of the grains). For the SOEC, a

Contributed by the Applied Mechanics Division and presented at the 1985 Joint ASME/ASCE Applied Mechanics, Fluids Engineering, and Bioengineering Conference, Albuquerque, N. Mex., June 24-26, 1985 of THE AMERICAN SOCIETY OF MECHANICAL ENGINEERS.

Discussion on this paper should be addressed to the Editorial Department, ASME, United Engineering Center, 345 East 47th Street, New York, N.Y. 10017, and will be accepted until two months after final publication of the paper itself in the JOURNAL OF APPLIED MECHANICS. Manuscript received by ASME Applied Mechanics Division, March, 1984; final revision, October, 1984. Paper No. 85-APM-23.

Copyright © 1985 by ASME
Downloaded 02 May 2010 to 171.66.16.54. Redistribution subject to ASME license or copyright; see http://www.asme.org/terms/Terms_Use.cfm

substantial body of work exists giving methods for improving on the estimates obtained by the Voigt and Reuss procedures (see Christensen [6] and Hashin [7] for surveys of this work). To date, however, no techniques other than those based on the Voigt or Reuss assumptions have been used to obtain estimates of the TOEC of an aggregate.

The Textured Aggregate

In describing the character of the polycrystalline aggregate, we adopt the methods and terminology of the field of quantitative texture analysis [8–12]. We consider a sample made up of a large number of crystallites whose orientations are not necessarily random. To describe the nonrandom nature of the grains, a distribution function w is introduced, which gives the probability that any particular crystallite will be oriented in a given way. The assumption is made that a single such orientation distribution function (ODF) is appropriate for all of the grains. That is, the material is taken to be statistically homogeneous.

In this work, the ODF w is taken to be known or at least obtainable in some manner. The details of how w can be obtained from a crystallographic examination of the aggregate will not be considered here, but may be found in a number of references (for example [8–12]). By way of background, though, the nature of the texture of an aggregate may be found in a series of x-ray diffraction measurements displayed as pole figures. A pole figure gives, on a spherical projection, the variation of pole density with pole orientation, relative to a set of aggregate axes, for a selected crystal plane (the pole being the normal to that plane). Intensities are plotted as multiples of the intensity expected from a specimen in which the grains are randomly oriented. These contour plots (the pole figures) are descriptive representations of the texture, and are the quantities that are examined to obtain the ODF. Roe [8] and Bunge [9] gave independent, but equivalent methods for "inverting the pole figures" to obtain the ODF based on an expansion of w in a series of generalized spherical harmonics. The present work makes use of this representation for w, with the notation chosen to be consistent with that of Roe [8, 10]. This facilitates the comparison of the results of this work by Morris [2] and Sayers [3]. As noted, however, the methods of Roe [8] and Bunge [9] are equivalent, and the notation can be put in the alternate form by use of the comparison given in Section 4.10 of reference [11].

To discuss the orientation of a crystallite, let us introduce a set of sample-fixed axes with coordinates X_i, and for a typical grain, a set of crystal-fixed axes with coordinates $X^*{}_i$. The orientation of this grain relative to the sample is then given by the transformation relating X_i to $X^*{}_i$, which is

$$X^*{}_i = t_{ij} X_j. \tag{1}$$

The proper orthogonal transformation tensor t_{ij} can be expressed in terms of Euler angles θ, ψ, and ϕ as

$$t_{ij} = \begin{bmatrix} \cos\phi & \sin\phi & 0 \\ -\sin\phi & \cos\phi & 0 \\ 0 & 0 & 1 \end{bmatrix} \begin{bmatrix} \cos\theta & 0 & -\sin\theta \\ 0 & 1 & 0 \\ \sin\theta & 0 & \cos\theta \end{bmatrix} \begin{bmatrix} \cos\psi & \sin\psi & 0 \\ -\sin\psi & \cos\psi & 0 \\ 0 & 0 & 1 \end{bmatrix}. \tag{2}$$

Given that the specification of the three Euler angles is sufficient to describe the orientation of a grain, we take the ODF to be a function of θ, ψ, and ϕ (or equivalently of ξ, ψ, and ϕ where $\xi = \cos\theta$). Further, since w is a probability distribution function, it is subject to the condition that its integral over all possible orientations is unity. That is,

$$\int_0^{2\pi} \int_0^{2\pi} \int_{-1}^{1} w(\xi,\psi,\phi)\, d\xi\, d\psi\, d\phi = 1. \tag{3}$$

To streamline the notation somewhat, we borrow from Bunge [11] and let the scalar g represent the orientation $\{\xi, \psi, \phi\}$. Then equation (3) can be rewritten

$$\int w(g)\, dg = 1. \tag{4}$$

The expansion of w in a series of generalized spherical harmonics takes the form [8]

$$w(g) = \sum_{l=0}^{\infty} \sum_{m=-l}^{l} \sum_{n=-l}^{l} W_{lmn} Z_{lmn}(\xi) e^{-im\psi} e^{-in\phi} \tag{5}$$

where the $Z_{lmn}(\xi)$ are the Jacobi polynomials (or augmented Jacobi polynomials [13]). These functions form an orthonormal basis with respect to the first index on the interval -1 to 1 so that

$$\int_{-1}^{1} Z_{kmn}(\xi) Z_{lmn}(\xi)\, d\xi = \delta_{kl}. \tag{6}$$

The number of coefficients, W_{lmn}, which must be evaluated for a particular aggregate depends on the symmetries exhibited by the crystals as well as the statistical symmetries of the sample. In this work, we restrict our attention to samples with orthotropic symmetry (rolling texture) made up of crystals of the cubic classes with the highest symmetry ($m3m$, 432, and $\bar{4}3m$). Such crystals have three independent SOEC and six independent TOEC, while as discussed earlier, the sample requires nine SOEC and 20 TOEC for its complete characterization. We take the sample axes X_i to be chosen as the axes defining the three mutually perpendicular symmetry planes of the orthotropic body. For a rolled plate these would be the rolling, normal, and transverse directions. Similarly, the crystal axes $X^*{}_i$ are given by the [100], [010], and [001] crystallographic directions.

Given the large class of materials for which such aggregate and crystal symmetries are appropriate, a number of investigations into the characterization of such materials have been conducted [8, 10, 13]. Among the results of these investigations are restrictions on the coefficients W_{lmn} and relations between various Jacobi polynomials $Z_{lmn}(\xi)$. We summarize here those characteristics pertinent to the present analysis. For the coefficients W_{lmn}:

(*a*) The W_{lmn}'s are all real so that equation (5) may be written [3, 13]

$$w(g) = \sum_{l=0}^{\infty} \sum_{m=-l}^{l} \sum_{n=-l}^{l} W_{lmn} Z_{lmn}(\xi) \cos(m\psi + n\phi). \tag{7}$$

(*b*) W_{lmn} is zero unless l and m are even and $n = 4k$, $k = 0, \pm 1, \pm 2, \ldots$.

(*c*) The coefficients are such that

$$W_{lmn} = W_{l\bar{m}n} = W_{lm\bar{n}} = W_{l\bar{m}\bar{n}} \tag{8}$$

where $\bar{m}$ represents $-m$.

(*d*) The remaining coefficients are not all independent. Specifically, Roe [10] has shown that for this case

$$\begin{aligned} W_{000} &= \sqrt{2}/8\pi^2, \quad W_{2m0} = 0 \\ W_{4m4} &= 5 W_{4m0}/\sqrt{70} = \sqrt{70} W_{4m0}/14 \\ W_{6m4} &= -\sqrt{14} W_{6m0}/2. \end{aligned} \tag{9}$$

For the Jacobi polynomials $Z_{lmn}(\xi)$:

(*a*) For m and n even [8, 13]

$$Z_{lmn} = Z_{l\bar{m}n} = Z_{lm\bar{n}} = Z_{l\bar{m}\bar{n}}$$

and

$$Z_{l\bar{m}n}(\xi) = Z_{lm\bar{n}}(\xi) = Z_{lmn}(-\xi). \tag{10}$$

(*b*) The Jacobi polynomials can be expressed as functions of the angle θ in the form

$$Z_{lmn}(\theta) = \frac{\sqrt{D_{lmn}}}{2^k l_{mn}} \sum_{s=0}^{l} E_{lmns} \cos(s\theta) \tag{11}$$

Downloaded 02 May 2010 to 171.66.16.54. Redistribution subject to ASME license or copyright; see http://www.asme.org/terms/Terms_Use.cfm

where the coefficients D_{lmn}, k_{lmn}, and E_{lmns} have been tabulated by Morris and Heckler [13] for l from 0 to 16.

Evaluation of Effective Elastic Constants

In estimating the effective elastic constants of the aggregate, we employ a simple Voigt-type procedure in which the stiffness tensors are averaged. To do this, we first consider the strain energy density in a typical grain as a function of the strain referred to that grain's crystal-fixed axes. The assumption is then made that the strain in the aggregate relative to the sample axes is independent of position. This allows us to write the crystallite's strain energy density as a function of the aggregate strain. Finally, the strain energy density of the aggregate is taken to be the average of the crystallite strain energy densities, weighted by the ODF w.

Let E_{ij} and E^*_{ij} be the Lagrangian strain tensors referred to the sample axes X_i and the crystal axes X^*_i, respectively. From equation (1) it follows that

$$E^*_{ij} = t_{ik} t_{jl} E_{kl}. \tag{12}$$

If we make the Voigt assumption that E_{kl} is independent of position and known, then the strain E^*_{ij} in a particular grain is determined solely by the orientation of that grain.

Within a grain, the strain energy density Φ^* is taken to be

$$\rho_0 \Phi^* = \frac{1}{2} C^*_{ijkl} E^*_{ij} E^*_{kl} + \frac{1}{6} C^*_{ijklmn} E^*_{ij} E^*_{kl} E^*_{mn} \tag{13}$$

where ρ_0 is the mass density of the undeformed crystal, and the second and third-order stiffness tensors C^*_{ijkl} and C^*_{ijklmn} are consistent with Brugger's convention [14] in that

$$C^*_{ijkl} = \frac{\partial^2 (\rho_0 \Phi^*)}{\partial E^*_{ij} \partial E^*_{kl}}, \quad C^*_{ijklmn} = \frac{\partial^3 (\rho_0 \Phi^*)}{\partial E^*_{ij} \partial E^*_{kl} \partial E^*_{mn}}. \tag{14}$$

Given equation (12), the expression for Φ^* can be expressed in terms of E_{ij} as

$$\rho_0 \Phi^* = \frac{1}{2} \bar{C}_{ijkl} E_{ij} E_{kl} + \frac{1}{6} \bar{C}_{ijklmn} E_{ij} E_{kl} E_{mn} \tag{15}$$

where

$$\begin{aligned} \bar{C}_{ijkl} &= t_{pi} t_{qj} t_{rk} t_{sl} C^*_{pqrs}, \\ \bar{C}_{ijklmn} &= t_{pi} t_{qj} t_{rk} t_{sl} t_{um} t_{vn} C^*_{pqrsuv}. \end{aligned} \tag{16}$$

The strain energy density of the aggregate is defined as the average of Φ^* weighted by w,

$$\rho_0 \Phi = \rho_0 \int \Phi^*(g)\, w(g)\, dg. \tag{17}$$

In terms of effective stiffnesses, the aggregate strain energy density is written

$$\rho_0 \Phi = \frac{1}{2} C_{ijkl} E_{ij} E_{kl} + \frac{1}{6} C_{ijklmn} E_{ij} E_{kl} E_{mn} \tag{18}$$

where

$$\begin{aligned} C_{ijkl} &= \int \bar{C}_{ijkl}(g)\, w(g)\, dg, \\ C_{ijklmn} &= \int \bar{C}_{ijklmn}(g)\, w(g)\, dg. \end{aligned} \tag{19}$$

Following the earlier work on transversely isotropic aggregates [4, 5], the strain energy for the crystal is written in the form given by Smith and Rivlin [15],

$$\begin{aligned} \rho_0 \Phi^* = {} & \beta_1^* I_1^2 + \beta_2^* I_2 + \beta_3^* J_2 + \gamma_1^* I_1^3 + \gamma_2^* I_1 I_2 \\ & + \gamma_3^* I_3 + \gamma_4^* I_1 J_2 + \gamma_5^* J_3 + \gamma_6^* K_3 \end{aligned} \tag{20}$$

where the β^*'s and γ^*'s are the independent SOEC and TOEC, respectively, the I's are the principal invariants of the strain tensor,

$$I_1 = E^*_{kk}, \; I_2 = \frac{1}{2} (E^*_{ij} E^*_{ij} - E^*_{kk} E^*_{ll}), \; I_3 = \det E^*_{ij}, \tag{21}$$

while the remaining terms are invariant under the symmetry transformations of the cubic crystal and are given as

$$\begin{aligned} J_2 &= E_{11}^* E_{22}^* + E_{22}^* E_{33}^* + E_{33}^* E_{11}^*, \\ J_3 &= E_{11}^* E_{22}^* E_{33}^*, \; K_3 = E_{12}^* E_{23}^* E_{31}^*. \end{aligned} \tag{22}$$

We note that if the crystal is isotropic with respect to its SOEC, then $\beta_3^* = 0$ and if it is isotropic with respect to its TOEC then $\gamma_4^* = \gamma_5^* = \gamma_6^* = 0$. The extent to which these four constants differ from zero is a measure of the degree of anisotropy of the crystal.

The coefficients of the stiffness tensors for the crystal may be written in terms of this set of elastic constants as

$$C^*_{1111} = 2\beta^*_1, \; C^*_{1212} = \beta^*_2/2, \; C^*_{1122} = 2\beta^*_1 - \beta^*_2 + \beta^*_3 \tag{23}$$

and

$$\begin{aligned} & C^*_{111111} = 6\gamma^*_1, \; C^*_{111212} = \gamma^*_2/2, \; C^*_{111122} = 6\gamma^*_1 - 2\gamma^*_2 + 2\gamma^*_4, \\ & C^*_{112323} = (\gamma^*_2 - \gamma^*_3)/2, \; C^*_{122331} = \gamma^*_3/4 + \gamma^*_6/8 \\ & C^*_{112233} = 6\gamma^*_1 - 3\gamma^*_2 + \gamma^*_3 + 3\gamma^*_4 + \gamma^*_5. \end{aligned} \tag{24}$$

The representation given in equation (20) for Φ^* in terms of E^*_{ij} may be rewritten using equations (15) and (16) to express Φ^* in terms of E_{ij} as

$$\begin{aligned} \rho_0 \Phi^* = {} & \beta_1^* I_1^2 + \beta_2^* I_2 + \beta_3^* T_{ijkl} E_{ij} E_{kl} \\ & + \gamma_1^* I_1^3 + \gamma_2^* I_1 I_2 + \gamma_3^* I_3 + [\gamma_4^* T_{ijkl} \delta_{mn} \\ & + \gamma_5^* t_{1i} t_{1j} t_{2k} t_{2l} t_{3m} t_{3n} \\ & + \gamma_6^* t_{1i} t_{2j} t_{2k} t_{3l} t_{3m} t_{1n}] E_{ij} E_{kl} E_{mn} \end{aligned} \tag{25}$$

where

$$T_{ijkl} = t_{1i} t_{1j} t_{2k} t_{2l} + t_{2i} t_{2j} t_{3k} t_{3l} + t_{3i} t_{3j} t_{1k} t_{1l} \tag{26}$$

and I_1, I_2, and I_3 being invariants have the same form as in equation (21) with E^*_{ij} replaced by E_{ij}.

The calculation of the effective elastic stiffnesses, equation (19), then requires the evaluation of integrals of the type

$$K_{ijkl} = \int T_{ijkl}(g)\, w(g)\, dg \tag{27}$$

and

$$K_{ijklmn} = \int t_{1i} t_{1j} t_{2k} t_{2l} t_{3m} t_{3n} w(g)\, dg \tag{28}$$

for the appropriate values of the indices. Note that while the stiffness tensors exhibit the usual symmetries, for example $C_{ijkl} = C_{ijlk} = C_{jikl} = C_{klij}$, the integrals K_{ijkl} and K_{ijklmn} do not exhibit the same symmetries. To obtain the stiffnesses given by equation (19), the integrals, equations (27) and (28), are combined with the appropriate elastic constants in the manner given by equation (25). For example,

$$\begin{aligned} C_{1122} &= 2\beta_1^* - \beta_2^* + \beta_3^* (K_{1122} + K_{2211}) \\ C_{111122} &= 6\gamma_1^* - 2\gamma_2^* + 2\gamma_4^* (K_{1111} + K_{1122} + K_{2211}) \\ &\quad + 2\gamma_5^* (K_{111122} + K_{112211} + K_{221111}) \\ &\quad + 2\gamma_6^* (K_{111212} + K_{121112} + K_{121211}) \end{aligned} \tag{29}$$

In computing these integrals, $w(g)$ in the form of equation (7) was used with the Jacobi polynomials expanded as in equation (11). The actual evaluation of the integrals was carried out with the help of the symbolic manipulation program called MACSYMA [16]. MACSYMA (we used the VAXIMA version set up to run on the VAX-11/780) is a powerful program that can perform a wide variety of algebraic and analytic tasks while keeping the results in symbolic (i.e., not strictly numerical) form. This has allowed our results to be exact within the framework of the problem being solved.

Recall that the representation for $w(g)$ in equation (7) is an infinite series over the three indices of the Jacobi polynomial. The number of terms required for the exact representation of K_{ijkl} and K_{ijklmn}, however, is finite. This is because the elements of the integrands of equations (27) and (28) are simple combinations of sines and cosines of the three Euler angles. The orthogonality of the series for w then results in the series for K_{ijkl} and K_{ijklmn} terminating after a relatively few

Downloaded 02 May 2010 to 171.66.16.54. Redistribution subject to ASME license or copyright; see http://www.asme.org/terms/Terms_Use.cfm

Table 1 Coefficients of A_p in C_{ijkl}

$ijkl$	$a_0^{(1)}$	$a_1^{(1)}$	$a_2^{(1)}$	$a_3^{(1)}$
1111	2	−3	1	−1
1122	−1	−1	0	1
1133	−1	4	−1	0
2222	2	−3	−1	−1
2233	−1	4	1	0
3333	2	−8	0	0
2323	−1	4	1	0
3131	−1	4	−1	0
1212	−1	−1	0	1

Table 2 Coefficients of A_p in C_{ijklmn}

$ijklmn$	$a_0^{(2)}$	$a_1^{(2)}$	$a_2^{(2)}$	$a_3^{(2)}$
111111	6	−9	3	−3
111122	0	−5	1	1
111133	0	5	−1	−1
222211	0	−5	−1	1
222222	6	−9	−3	−3
222233	0	5	1	−1
333311	0	0	−1	0
333322	0	0	1	0
333333	6	−24	0	0
112233	−3	7	0	1
112323	−1	4	1	0
113131	−1	4	−1	0
111212	−1	−1	0	1
222323	−1	4	1	0
223131	−1	4	−1	0
221212	−1	−1	0	1
332323	−1	4	1	0
333131	−1	4	−1	0
331212	−1	−1	0	1
233112	0	0	0	0

terms. For the case of K_{ijkl}, the quantity being integrated, T_{ijkl}, contains terms that are at most fourth order in the trigonometric functions and hence the resulting expressions (K_{ijkl}) contain coefficients W_{pqr} only for which p is less than or equal to 4. Further, because of the restrictions imposed by symmetry, equations (8) and (9), the only coefficients that contribute to K_{ijkl} are W_{400}, W_{420}, and W_{440}. For K_{ijklmn}, the maximum power of the trigonometric functions is six. The result is that in addition to the three coefficients for which $p = 4$, there are four more, W_{600}, W_{620}, W_{640}, and W_{660} that contribute. These seven terms of the expansion of $w(g)$ then provide all of the information needed to obtain a complete representation for the effective stiffnesses, C_{ijkl} and C_{ijklmn}.

In presenting the results, the effective elastic constants are written in terms of the elastic constants of the cubic crystal as

$$C_{ijkl} = C^*_{ijkl} + \beta^*_3 \sum_{p=0}^{3} a_p^{(1)} A_p \tag{30}$$

and

$$C_{ijklmn} = C^*_{ijklmn} + \gamma^*_4 \sum_{p=0}^{3} a_p^{(2)} A_p + \gamma^*_5 \sum_{p=0}^{7} b_p B_p + \gamma^*_6 \sum_{p=0}^{7} c_p C_p \tag{31}$$

where

$$A_0 = \frac{1}{5}, A_1 = \frac{4\sqrt{2}}{35}\pi^2 W_{400}, A_2 = \frac{16\sqrt{5}}{35}\pi^2 W_{420} \tag{32}$$

$$A_3 = \frac{8\sqrt{35}}{35}\pi^2 W_{440};$$

$$B_0 = \frac{1}{35}, B_1 = \frac{4\sqrt{2}}{385}\pi^2 W_{400}, B_2 = \frac{16\sqrt{5}}{77}\pi^2 W_{420},$$

Table 3 Coefficients of B_p in C_{ijklmn}

$ijklmn$	b_0	b_1	b_2	b_3	b_4	b_5	b_6	b_7
111111	2	−9	3	−3	−5	15	−3	1
111122	6	−37	9	1	−1	1	1	−1
111133	6	13	−1	−9	6	−16	2	0
222211	6	−37	−9	1	−1	−1	1	1
222222	2	−9	−3	−3	−5	−15	−3	−1
222233	6	13	1	−9	6	16	2	0
333311	6	−32	−10	0	−8	16	0	0
333322	6	−32	10	0	−8	−16	0	0
333333	2	−24	0	0	16	0	0	0
112233	−19	63	0	9	2	0	−2	0
112323	−5	30	11	−2	2	0	−2	0
113131	−1	2	−1	2	6	−16	2	0
111212	−1	7	−2	1	−1	1	1	−1
222323	−1	2	1	2	6	16	2	0
223131	−5	30	−11	−2	2	0	−2	0
221212	−1	7	2	1	−1	−1	1	1
332323	−1	12	−1	0	−8	−16	0	0
333131	−1	12	1	0	−8	16	0	0
331212	−5	−25	0	9	2	0	−2	0
233112	2	−14	0	−2	2	0	−2	0

Table 4 Coefficients of C_p in C_{ijklmn}

$ijklmn$	c_0	c_1	c_2	c_3	c_4	c_5	c_6	c_7
111111	16	−18	12	−12	−5	15	−3	1
111122	−8	14	−8	4	−1	1	1	−1
111133	−8	4	−4	8	6	−16	2	0
222211	−8	14	8	4	−1	−1	1	1
222222	16	−18	−12	−12	−5	−15	−3	−1
222233	−8	4	4	8	6	16	2	0
333311	−8	24	4	0	−8	16	0	0
333322	−8	24	−4	0	−8	−16	0	0
333333	16	−48	0	0	16	0	0	0
112233	16	−28	0	−8	2	0	−2	0
112323	−12	−11	−11	3	2	0	−2	0
113131	6	9	−4	−3	6	−16	2	0
111212	6	−8	3	4	−1	1	1	−1
222323	6	9	4	−3	6	16	2	0
223131	−12	−11	11	3	2	0	−2	0
221212	6	−8	−3	4	−1	−1	1	1
332323	6	2	7	0	−8	−16	0	0
333131	6	2	−7	0	−8	16	0	0
331212	−12	16	0	−8	2	0	−2	0
233112	−26	10	0	3	2	0	−2	0

$$B_3 = \frac{8\sqrt{35}}{385}\pi^2 W_{440}, B_4 = \frac{8\sqrt{26}}{1001}\pi^2 W_{600}, \tag{33}$$

$$B_5 = \frac{8\sqrt{2730}}{15015}\pi^2 W_{620}, B_6 = \frac{16\sqrt{91}}{1001}\pi^2 W_{640},$$

$$B_7 = \frac{8\sqrt{6006}}{1001}\pi^2 W_{660};$$

and

$$C_0 = B_0/8, C_1 = B_1/2, C_2 = B_2/4, C_3 = B_3/4$$
$$C_4 = B_4, C_5 = B_5, C_6 = B_6, C_7 = B_7. \tag{34}$$

The coefficients $a_p^{(1)}$, $a_p^{(2)}$, b_p, and c_p are listed in Tables 1-4, respectively.

The results for the second-order stiffnesses are not new, but rather reproduce the expressions given by Morris [2] and Sayers [3] for this same problem. The results for the third-order stiffnesses, however, give for the first time a method for estimating the TOEC and hence the effective acoustoelastic response of an aggregate with a realistic texture. The idealized texture of transverse isotropy treated earlier [4, 5] is obtained by letting W_{400} and W_{600} be the only nonzero terms in the expansion for the ODF. In this special case, the results here agree with those of the previous work [4, 5].

Conclusions

A method for estimating the effective SOEC and TOEC of

Downloaded 02 May 2010 to 171.66.16.54. Redistribution subject to ASME license or copyright; see http://www.asme.org/terms/Terms_Use.cfm

a polycrystalline aggregate exhibiting rolling texture has been presented. Based on a Voigt-type averaging procedure, which takes the strain to be homogeneous throughout the aggregate, the results give the 29 independent effective constants of the aggregate in terms of the nine independent constants of the crystal and a total of seven coefficients representing the texture. Within the framework of the problem being solved, the results presented are exact.

The assumption made in the Voigt-type averaging is rather severe. An analogous procedure of the Reuss-type may be used by assuming that the stress is homogeneous throughout the aggregate – a similarly severe assumption. Thus while the method presented here offers a degree of simplicity which makes the exercise tractable, the results obtained may or may not be quantitatively accurate estimates of the actual aggregate response. The extent to which they are quantitatively accurate probably depends on the degree of isotropy found in the SOEC of the crystallites.

The next step in the development of this technique is obvious – a real material must be examined both crystallographically to generate the ODF and acoustoelastically to generate the actual SOEC and TOEC of the aggregate. The elastic constants estimated by this technique will then be compared with those obtained experimentally.

Acknowledgment

This work was supported by the National Science Foundation under Grant No. MEA-8116376.

References

1 Bunge, H.-J., "Uber die elastischen Konstanten kubischer Materialien mit beliebiger Textur," *Krist. Tech.*, Vol. 3, 1968, pp. 431–438.

2 Morris, P. R., "Averaging Fourth-Rank Tensors With Weight Functions," *J. Appl. Phys.*, Vol. 40, 1969, pp. 447–448.

3 Sayers, C. M., "Ultrasonic Velocities in Anisotropic Polycrystalline Aggregates," *J. Phys. D*, Vol. 15, 1982, pp. 2157–2167.

4 Johnson, G. C., "Acoustoelastic Response of Polycrystalline Aggregates Exhibiting Transverse Isotropy," *J. Nondestructive Eval.*, Vol. 3, 1982, pp. 1–8.

5 Johnson, G. C., "The Effect of Texture on Acoustoelasticity," *Review of Progress in Quantitative Nondestructive Evaluation*, Vol. 2*B*, Thompson, D. O., and Chimenti, D. E., eds., Plenum Press, 1983, pp. 1295–1308.

6 Christensen, R. M., *Mechanics of Composite Materials*, Wiley-Interscience, New York, 1979.

7 Hashin, Z., "Analysis of Composite Materials—A Survey," ASME JOURNAL OF APPLIED MECHANICS, Vol. 50, 1983, pp. 481–505.

8 Roe, R.-J., "Description of Crystallite Orientation in Polycrystalline Materials. III, General Pole Figure Inversion," *J. Appl. Phys.*, Vol. 36, 1965, pp. 2024–2031.

9 Bunge, H.-J., "Zur Darstellung allgemeiner Texturen," *Z. Metallkunde*, Vol. 56, 1965, pp. 872–874.

10 Roe, R.-J., "Inversion of Pole Figures for Materials Having Cubic Crystal Symmetry," *J. Appl. Phys.*, Vol. 37, 1966, pp. 2069–2072.

11 Bunge, H.-J., *Texture Analysis in Materials Science*, Butterworths, London, 1982.

12 Bunge, H.-J., and Esling, C., eds., *Quantitative Texture Analysis*, Deutsche Gesellschaft für Metallkunde, 1982.

13 Morris, P. R., and Heckler, A. J., "Crystallite Orientation Analysis for Rolled Cubic Materials," *Adv. X-Ray Anal.*, Vol. 11, 1968, pp. 454–472.

14 Brugger, K., "Thermodynamic Definition of Higher Order Elastic Coefficients," *Phys. Rev.*, Vol. 133, 1964, pp. *A*1611–*A*1612.

15 Smith, G. F., and Rivlin, R. S., "The Strain-Energy Function for Anisotropic Elastic Materials," *Trans. Am. Math. Soc.*, Vol. 88, 1958, pp. 175–193.

16 The Mathlab Group, *MACSYMA Reference Manual*, Version Ten, Laboratory for Computer Science, MIT, 1983.

Downloaded 02 May 2010 to 171.66.16.54. Redistribution subject to ASME license or copyright; see http://www.asme.org/terms/Terms_Use.cfm

Scattering of a Rayleigh Wave by an Elastic Quarter Space

A. K. Gautesen
Ames Laboratory[1] and
Department of Mathematics,
Iowa State University,
Ames, Iowa 50011

We study the two-dimensional, steady-state problem of the scattering of waves in a homogeneous, isotropic, linear-elastic quarter space. We derive decoupled equations for the Fourier transforms of the normal and tangential displacements on the free surfaces. For incidence of a Rayleigh surface wave, we plot the amplitudes and phases of the surface waves reflected and transmitted by the corner. These curves were obtained numerically.

1 Introduction

We consider the two-dimensional problem of steady-state wave propagation in a homogeneous, isotropic, linear-elastic quarter space, where we impose traction-free boundary conditions on the free surfaces. In a review on the corresponding problem for a wedge, Knopoff [1] discusses the difficulties associated with this problem and attempts by other authors to deal with them. In the usual manner, we obtain an integral representation for the displacements, with the unknowns being the normal and tangential displacements on the free surfaces. We separate this problem into two independent problems in which the displacements are symmetric and antisymmetric with respect to the plane that makes a 45 deg angle with each of the free surfaces. Then the normal displacements as well as the tangential displacements on the free surfaces are equal for the symmetric problem and have opposite signs for the antisymmetric problem. By application of the boundary conditions, we obtain for each problem a coupled pair of integral equations for the normal and tangential displacements on the free surfaces.

We were able to decouple the Fourier transforms of these equations to achieve a separate integral equation for the transform of the normal displacement and a separate equation for the transform of the tangential displacement. These equations were still too complicated to be amenable to an analytic solution. Thus, we solved them numerically. For the incident wave, we chose a Rayleigh surface wave of unit amplitude propagating on one of the free surfaces toward the corner. We chose a set of complex-valued approximating functions and determined the values of the corresponding unknown constants by a least squares fit. From the equations for the normal displacements we computed the amplitude and phase of the Rayleigh surface wave reflected by the corner, as well as the surface wave transmitted by the corner, for Poisson's ratio running from 0.025 to 0.475 at intervals of 0.025. As a check on the accuracy of this computation we computed independently, by the same technique, these same quantities from the equations for the tangential displacements. The agreement between the values obtained for the amplitudes and phases of the reflection and transmission coefficients by the two independent computations is good enough to strongly suggest that our results are correct. We also give a table which compares the values of these coefficients obtained by other authors [2–9] (either experimentally or numerically) with our results.

In the next section we formulate the problem and derive the decoupled equations. In Section 3, we analyze the equations for incidence of a Rayleigh surface wave. In the last section, we discuss our numerical results.

2 Formulation and Derivation

We consider two-dimensional, steady-state wave propagation in a homogeneous, isotropic, elastic quarter space which occupies the first quadrant of the Cartesian plane (see Fig. 1). We will denote this region by I, the boundary of this region by B, and the remaining region in the Cartesian plane by E. Motion is generated by incident waves $\mathbf{u}^{in}$ from line-loads located in region I. These waves satisfy the differential equation

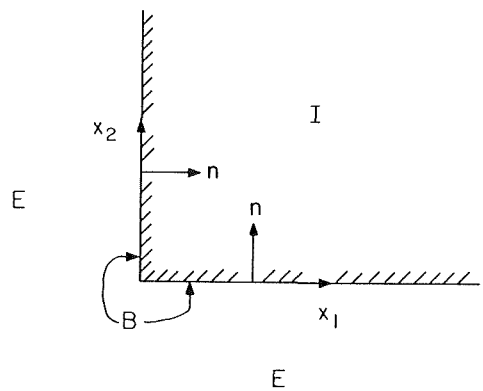

Fig. 1 Geometry and coordinate system

[1]Operated for the U.S. Department of Energy by Iowa State University under contract #W-7405-eng-82.

Contributed by the Applied Mechanics Division and presented at the 1985 Joint ASME/ASCE Applied Mechanics, Fluids Engineering, and Bioengineering Conference, Albuquerque, N. Mex., June 24-26, 1985 of THE AMERICAN SOCIETY OF MECHANICAL ENGINEERS.

Discussion on this paper should be addressed to the Editorial Department, ASME, United Engineering Center, 345 East 47th Street, New York, N.Y. 10017, and will be accepted until two months after final publication of the paper itself in the JOURNAL OF APPLIED MECHANICS. Manuscript received by ASME Applied Mechanics Division, September, 1984. Paper No. 85-APM-30.

Copyright © 1985 by ASME
Downloaded 02 May 2010 to 171.66.16.54. Redistribution subject to ASME license or copyright; see http://www.asme.org/terms/Terms_Use.cfm

$$(Lu^{in})_i = 0, \quad \mathbf{x}\epsilon E \tag{2.1}$$

where

$$(Lu)_i = \tau_{ij,j} + \rho\omega^2 u_i \tag{2.2}$$

$$\tau_{ij} = \lambda u_{k,k}\delta_{ij} + \mu(u_{i,j} + u_{j,i}) \tag{2.3}$$

ρ is the density of the elastic solid, ω is circular frequency of the incident wave, λ and μ are the Lame constants, and δ_{ij} is the Kronecker delta. Here, we have used the convention that a repeated roman subscript implies summation from 1 to 2 and the shorthand notation:

$$u_{i,j} = \partial u_i / \partial x_j \tag{2.4}$$

In the sequel, we find it convenient to divide the incident field $\mathbf{u}^{in}$ into two fields $\mathbf{u}^{inl}$, $l = 1,2$ which are symmetric ($l = 2$) and antisymmetric ($l = 1$) with respect to the line $x_1 = x_2$ in the Cartesian plane, Thus,

$$u_i^{inl}(x_1,x_2) = \frac{1}{2}\begin{cases} u_i^{in}(x_1,x_2) - u_{3-i}^{in}(x_2,x_1), & l=1 \\ u_i^{in}(x_1,x_2) + u_{3-i}^{in}(x_2,x_1), & l=2 \end{cases} \tag{2.5}$$

where $\mathbf{u}^{in}$ is recovered from $\mathbf{u}^{inl}$ by

$$u_i^{in} = \sum_{l=1}^{2} u_i^{inl} \tag{2.6}$$

Note that $\mathbf{u}^{inl}$ also satisfies (2.1) and has the property that

$$u_i^{inl}(x_1,x_2) = (-1)^l u_{3-i}^{inl}(x_2,x_1) \tag{2.7}$$

The total and scattered fields corresponding to $\mathbf{u}^{inl}$ also have the property defined by (2.7). Hereafter, we drop the superscript l for simplicity of notation. We emphasize that the equations derived in the following must be solved for both $l = 1$ and $l = 2$ and the corresponding results added as in (2.6).

The total field $\mathbf{u}$ is related to the scattered field $\mathbf{u}^{sc}$ by

$$\mathbf{u} = \mathbf{u}^{sc} + \mathbf{u}^{in}, \quad \mathbf{x}\epsilon I \tag{2.8}$$

The scattered field satisfies the differential equations

$$(Lu^{sc})_i = 0, \quad \mathbf{x}\epsilon I \tag{2.9}$$

and the boundary conditions

$$\tau_{ij}^{sc} n_j = -\tau_{ij}^{in} n_j, \quad \mathbf{x}\epsilon B \tag{2.10}$$

where $\mathbf{n}$ is the unit interior normal to I as shown in Fig. 1.

We will now obtain an expression for the total field in terms of displacements on the free surfaces B. For any pair $(\mathbf{u}^{\alpha}, \mathbf{u}^{\beta})$ we have the identity

$$u_i^{\alpha}(Lu^{\beta})_i - u_i^{\beta}(Lu^{\alpha})_i = [u_i^{\alpha}\tau_{ij}^{\beta} - u_i^{\beta}\tau_{ij}^{\alpha}]_{,j} \tag{2.11}$$

The free space Green's displacement tensor $u_{i;k}^{G}(\mathbf{x}-\mathbf{y})$ satisfies

$$(Lu_{i;k}^{G})_i = -\delta_{ik}\delta(\mathbf{x}-\mathbf{y}) \tag{2.12}$$

where $\delta(\mathbf{x})$ is the Dirac delta function. In (2.11), we choose $u_i^{\alpha} = u_{i;k}^{G}$ and $u_i^{\beta} = u_i^{sc}$, then integrate over the region I, employ the divergence theorem, and substitute from (2.12) and (2.9). The result is

$$u_k^{sc}(\mathbf{y})H(I) = \int_B \{u_i^{sc}(\mathbf{x})\tau_{ij;k}^{G}(\mathbf{x}-\mathbf{y}) - \tau_{ij}^{sc}(\mathbf{x})u_{i;k}^{G}(\mathbf{x}-\mathbf{y})\}n_j(\mathbf{x})ds_x \tag{2.13}$$

where s_x denotes arc length along the boundary B, $\mathbf{x}$ denotes a point on B, and

$$H(I) = \begin{cases} 1, & \mathbf{y}\epsilon I \\ 0, & \mathbf{y}\epsilon E \end{cases} \tag{2.14}$$

We remark that (2.13) is valid for both $\mathbf{y}\epsilon I$ and $\mathbf{y}\epsilon E$, and that the integral about infinity vanishes since $\mathbf{u}^{sc}$ is outgoing for $\mathbf{x}$ in I. In (2.12), we now substitute $u_i^{\alpha} = u_{i;k}^{G}$ and $u_i^{\beta} = u_i^{in}$, integrate over the region E exterior to the quarterspace, and substitute from (2.12) and (2.1) to achieve the result:

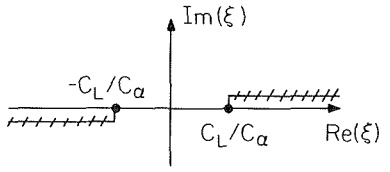

Fig. 2 Branches of γ^{α}

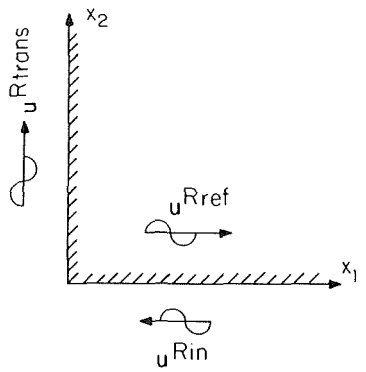

Fig. 3 Incident, reflected, and transmitted surface waves

$$u_k^{in}(\mathbf{y})H(E) = -\int_B \{u_i^{in}(\mathbf{x})\tau_{ij;k}^{G}(\mathbf{x}-\mathbf{y}) - \tau_{ij}^{in}(\mathbf{x})u_{i;k}^{G}(\mathbf{x}-\mathbf{y})\}n_j(\mathbf{x})ds_x \tag{2.15}$$

Subtracting (2.15) from (2.13) and substituting from (2.8) and (2.10) yields

$$u_k(\mathbf{x})H(I) = u_k^{in}(\mathbf{x}) - \int_B \tau_{ij;k}^{G}(\mathbf{x}-\mathbf{y})n_j(\mathbf{y})u_i(\mathbf{y})ds_y \tag{2.16}$$

where the roles of $\mathbf{x}$ and $\mathbf{y}$ have been interchanged and the identity

$$\tau_{ij;k}^{G}(-\mathbf{x}) = -\tau_{ij;k}^{G}(\mathbf{x}) \tag{2.17}$$

has been used. Also, $\tau_{ij;k}^{G}$ is defined in the Appendix by (A.1).

The importance of (2.16) is that it is valid for all $\mathbf{x}$, not just for $\mathbf{x}\epsilon I$. We let x_2 approach zero from the lower half-plane (i.e., from within the region E) and drop the subscript 1 on x_1 to achieve

$$u_k^{in}(x,0) = \int_0^{\infty} \{\tau_{i2;k}^{G}(x-s,0^-)v_i(s) + (-1)^l \tau_{ii;k}^{G}(x,-s)v_{3-i}(s)\}ds, \quad -\infty < x < \infty \tag{2.18}$$

where we have written out the integral over each of the free surfaces, defined

$$v_i(s) = u_i(s,0^+) \tag{2.19}$$

and used the symmetry relation:

$$u_i(0^+,s) = (-1)^l v_{3-i}(s) \tag{2.20}$$

We remark that if we had let x_2 approach zero from the upper half-plane, we would also have obtained (2.18).

The important property of (2.18) is that this equation is valid on the entire real line and not just on the semi-infinite interval $0 < x < \infty$. We introduce the Fourier transform and its inverse defined by

$$\bar{v}(\xi) = k_L \int_{-\infty}^{\infty} \exp[ik_L \xi x]v(x)dx \tag{2.21}$$

$$v(x) = \frac{1}{2\pi}\int_{-\infty}^{\infty} \exp[-ik_L \xi x]\bar{v}(\xi)d\xi \tag{2.22}$$

where

$$c_L^2 = (\lambda + 2\mu)/\rho, c_T^2 = \mu/\rho \tag{2.23}$$

$$k_{\alpha} = \omega/c_{\alpha}, \quad \alpha = L,T \tag{2.24}$$

Downloaded 02 May 2010 to 171.66.16.54. Redistribution subject to ASME license or copyright; see http://www.asme.org/terms/Terms_Use.cfm

The Fourier transform of (2.18) is

$$2\kappa^2\bar{u}_1^{in}(\xi,0)=\kappa^2\bar{v}_1(\xi)+\xi[a(\xi)-2\gamma^L\gamma^T]\bar{v}_2(\xi)/\gamma^L$$
$$+(-1)^l\{a(\xi)\bar{v}_1(\gamma^T)+2\xi^2\bar{v}_1(\gamma^L)+2\xi\gamma^T\bar{v}_2(\gamma^T)$$
$$+\xi a(\gamma^L)\bar{v}_2(\gamma^L)/\gamma^L\} \tag{2.25}$$

$$2\kappa^2\bar{u}_2^{in}(\xi,0)=-\xi[a(\xi)-2\gamma^L\gamma^T]\bar{v}_1(\xi)/\gamma^T$$
$$+\kappa^2\bar{v}_2(\xi)+(-1)^l\{-\xi a(\xi)\bar{v}_1(\gamma^T)/\gamma^T+2\xi\gamma^L\bar{v}_1(\gamma^L)$$
$$-2\xi^2\bar{v}_2(\gamma^T)+a(\gamma^L)\bar{v}_2(\gamma^L)\} \tag{2.26}$$

where (A-6)-(A.12) have been used and

$$a(\xi)=\kappa^2-2\xi^2 \tag{2.27}$$
$$\kappa=c_L/c_T \tag{2.28}$$
$$\gamma^\alpha=(c_L^2/c_\alpha^2-\xi^2)^{1/2},\quad \alpha=L,T \tag{2.29}$$

The branches of γ^α are shown in Fig. 2. Eliminating $\bar{v}_1(\xi)$ and $\bar{v}_2(\xi)$ from (2.25) and (2.26) yields the pair of equations

$$\bar{w}_1(\xi)=R(\xi)\bar{v}_1(\xi)+(-1)^l\{a^2(\xi)\bar{v}_1(\gamma^T)$$
$$+4\xi^2\gamma^L\gamma^T\bar{v}_1(\gamma^L)+2\xi\gamma^T[a(\xi)\bar{v}_2(\gamma^T)$$
$$+a(\gamma^L)\bar{v}_2(\gamma^L)]\} \tag{2.30}$$

$$\bar{w}_2(\xi)=R(\xi)\bar{v}_2(\xi)+(-1)^l\{2\xi\gamma^L a(\xi)[-\bar{v}_1(\gamma^T)$$
$$+\bar{v}_1(\gamma^L)]-4\xi^2\gamma^L\gamma^T\bar{v}_2(\gamma^T)+a(\xi)a(\gamma^L)\bar{v}_2(\gamma^L)\} \tag{2.31}$$

where

$$\bar{w}_1(\xi)=2\kappa^2\gamma^T[\kappa^2\gamma^L\bar{u}_1^{in}(\xi,0)-\xi(a(\xi)$$
$$-2\gamma^L\gamma^T)\bar{u}_2^{in}(\xi,0)]/(\xi^2+\gamma^L\gamma^T) \tag{2.32}$$

$$\bar{w}_2(\xi)=2\kappa^2\gamma^L[\xi(a(\xi)-2\gamma^L\gamma^T)\bar{u}_1^{in}(\xi,0)$$
$$+\kappa^2\gamma^T\bar{u}_2^{in}(\xi,0)]/(\xi^2+\gamma^L\gamma^T) \tag{2.33}$$

and R is the Rayleigh function defined by

$$R(\xi)=a^2(\xi)+4\xi^2\gamma^L\gamma^T \tag{2.34}$$

At this point, we interject some remarks. A standard method of analyzing this problem is to compute the tractions on the free surfaces and then apply the boundary conditions (2.10). This leads to a pair of integral equations that are valid on the semi-infinite interval $0<x<\infty$. We found a complicated sequence of linear transformations that transformed these integral equations into (2.18). This tedious calculation is omitted. For incidence of a plane wave corresponding to transverse motions at the specific angle of 45 deg, this antisymmetric problem can be solved in closed form by the method of images. We found that this solution satisfied (2.18). The author is unaware of any other incident wave for which the problem has an exact solution. Recalling that

$$\bar{v}_i(\xi)=k_L\int_0^\infty \exp[ik_L\xi x]u_i(x,0^+)dx \tag{2.35}$$

we note that $\bar{v}_i(\xi)$ is an analytic function of ξ in the upper half of the complex ξ-plane.

The coupling of $\bar{v}_1$ and $\bar{v}_2$ in equations (2.30) and (2.31) is via the terms in square brackets. These terms are an odd function of ξ for real ξ. Taking the even part of (2.30) and (2.31), we obtain for ξ real

$$\bar{w}_1(\xi)+\bar{w}_1(-\xi)=R(\xi)[\bar{v}_1(\xi)+\bar{v}_1(-\xi)]$$
$$+2(-1)^l\{a^2(\xi)\bar{v}_1(\gamma^T)+4\xi^2\gamma^L\gamma^T\bar{v}_1(\gamma^L)\},$$
$$-\infty<\xi<\infty \tag{2.36}$$

$$\bar{w}_2(\xi)+\bar{w}_2(-\xi)=R(\xi)[\bar{v}_2(\xi)+\bar{v}_2(-\xi)]$$
$$+2(-1)^l\{-4\xi^2\gamma^L\gamma^T\bar{v}_2(\gamma^T)+a(\xi)a(\gamma^L)\bar{v}_2(\gamma^L)\},$$
$$-\infty<\xi<\infty \tag{2.37}$$

These decoupled equations will be analyzed in the next section for incidence of a Rayleigh surface wave.

3 Analysis for Surface Wave Incidence

We consider a Rayleigh surface wave incident on the lower free surface (see Fig. 3) with displacements defined by

$$\mathbf{u}^{Rin}(x_1,0)$$
$$=(-\sin\theta_R,\cos\theta_R)\exp[-ik_Rx_1]/\cos^{1/2}(2\theta_R) \tag{3.1}$$

where

$$\theta_R=2i\cosh^{-1}(c_T/c_R) \tag{3.2}$$
$$k_R=\omega/c_R \tag{3.3}$$

and c_R is the speed of Rayleigh waves determined from

$$R(c_L/c_R)=0 \tag{3.4}$$

This wave gives rise to a reflected surface wave on the same free surface defined by

$$\mathbf{u}^{Rre}(x_1,0)$$
$$=R^c(\sin\theta_R,\cos\theta_R)\exp[ik_Rx_1]/\cos^{1/2}(2\theta_R) \tag{3.5}$$

and to a transmitted surface wave defined by

$$\mathbf{u}^{Rtr}(0,x_2)$$
$$=T^c(\cos\theta_R,\sin\theta_R)\exp[ik_Rx_2]/\cos^{1/2}(2\theta_R) \tag{3.6}$$

where R^c and T^c are the reflection and transmission coefficients, respectively. When we separate this problem into an antisymmetric ($l=1$) and symmetric problem ($l=2$), we find that the displacement of the surface waves $\mathbf{u}^R$ on the lower free surface is

$$2\mathbf{u}^R(x_1,0)=\mathbf{u}^{Rin}(x_1,0)+A_l\mathbf{u}^{Rre}(x_1,0) \tag{3.7}$$

where

$$A_l=R^c+(-1)^lT^c \tag{3.8}$$

The Fourier transform of (3.7) is

$$2\bar{\mathbf{u}}^R(\xi,0)=i\{(-\sin\theta_R,\cos\theta_R)/(\xi-\kappa_R)$$
$$+A_l(\sin\theta_R,\cos\theta_R)/(\xi+\kappa_R)\}/\cos^{1/2}(2\theta_R) \tag{3.9}$$

where

$$\kappa_R=c_L/c_R \tag{3.10}$$

For this problem, $\mathbf{u}^{in}=\mathbf{0}$, and hence $\bar{\mathbf{w}}(\xi)=\mathbf{0}$ in (2.36) and (2.37). Motions are generated by the incoming Rayleigh surface wave. We therefore write

$$\bar{v}_1(\xi)=\bar{u}_1{}^R(\xi,0)+\sin\theta_R\bar{v}_1{}^P(\xi)/[2\cos^{1/2}(2\theta_R)] \tag{3.11}$$

$$\bar{v}_2(\xi)=\bar{u}_2{}^R(\xi,0)+\cos\theta_R\bar{v}_2{}^P(\xi)/[2\cos^{1/2}(2\theta_R)] \tag{3.12}$$

where $\bar{v}_i^P(\xi)$ is analytic in the upper half of the complex ξ-plane as well as in a neighborhood of $\xi=\pm\kappa_R$. The poles at $\xi=\pm\kappa_R$ in $\bar{v}_i(\xi)$, which yield the Rayleigh surface waves, are contained in $\bar{u}_i^R(\xi,0)$. Upon substitution of (3.11) and (3.12) into (2.36) and (2.37), we obtain the result

$$R(\xi)[\bar{v}_1^P(\xi)+\bar{v}_1^P(-\xi)]/2+(-1)^l\{a^2(\xi)\bar{v}_1{}^P(\gamma^T)$$
$$+4\xi^2\gamma^L\gamma^T\bar{v}_1^P(\gamma^L)\}=-i[Q_1^-(\xi)+A_lQ_1^+(\xi)],$$
$$-\xi<\infty<\xi \tag{3.13}$$

$$R(\xi)[\bar{v}_2^P(\xi)+\bar{v}_2^P(-\xi)]/2+(-1)^l\{-4\xi^2\gamma^L\gamma^T\bar{v}_2^P(\gamma^T)$$
$$+a(\xi)a(\gamma^L)\bar{v}_2^P(\gamma)^L\}=i[Q_2^-(\xi)-A_lQ_2^+(\xi)],$$
$$-\xi<\infty<\xi \tag{3.14}$$

where

$$Q_1^\pm(\xi)=(-1)^l\{a^2(\xi)/(\kappa_R\pm\gamma^T)+4\xi^2\gamma^L\gamma^T/(\kappa_R$$
$$\pm\gamma^L)\}+\kappa_RR(\xi)/(\kappa_R^2-\xi^2) \tag{3.15}$$

$$Q_2^\pm(\xi)=(-1)^l\{-4\xi^2\gamma^L\gamma^T/(\kappa_R\pm\gamma^T)+a(\xi)a(\gamma^L)/$$
$$(\kappa_R\pm\gamma^L)\}+\kappa_RR(\xi)/(\kappa_R^2-\xi^2) \tag{3.16}$$

To determine A_l from either (3.13) or (3.14), we evaluate these equations at $\xi=\kappa_R$. Note that by (3.4) $R(\kappa_R)$ vanishes and that $\bar{v}_i^P(\pm\kappa_R)$ is bounded. The results are

Downloaded 02 May 2010 to 171.66.16.54. Redistribution subject to ASME license or copyright; see http://www.asme.org/terms/Terms_Use.cfm

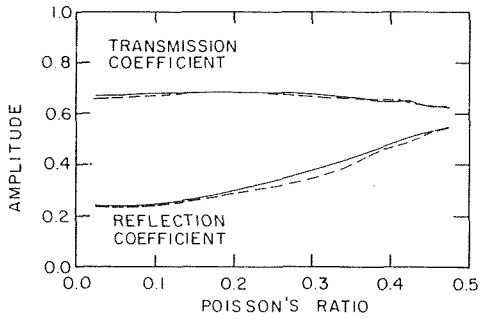

Fig. 4 Amplitudes of the reflection and transmission coefficients versus Poisson's ratio; – – – from (3.14) and --- from (3.13)

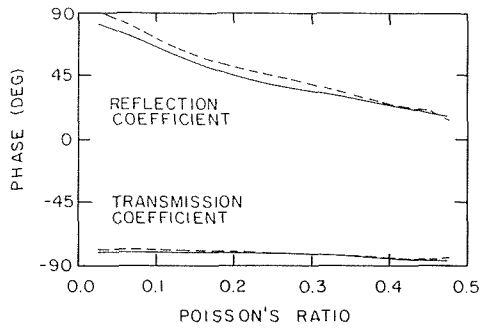

Fig. 5 Phases in degrees of the reflection and transmission coefficients versus Poisson's ratio; – – – from (3.14) and --- from (3.13)

$$Q_1^+(\kappa_R)A_l = -Q_1^-(\kappa_R) + i(-1)^l\{a^2(\kappa_R)\tilde{v}_1^P(\gamma_R^T) + 4\kappa_R^2\gamma_R^L\gamma_R^T\tilde{v}_1^P(\gamma_R^L)\} \tag{3.17}$$

$$Q_2^+(\kappa_R)A_l = Q_2^-(\kappa_R) + i(-1)^l\{-4\kappa_R^2\gamma_R^L\gamma_R^T\tilde{v}_2^P(\gamma_R^T) + a(\kappa_R)a(\gamma_R^L)\tilde{v}_2^P(\gamma_R^L)\} \tag{3.18}$$

where

$$\gamma_R^\alpha = i[(c_L/c_R)^2 - (c_L/c_\alpha)^2]^{1/2}, \quad \alpha = L,T \tag{3.19}$$

After substitution for A_l in (3.13) from (3.17) and for A_l in (3.14) from (3.18), we obtain two linear, uncoupled equations for $\tilde{v}_1^P$ and $\tilde{v}_2^P$.

To solve the resulting equations numerically, we used a set of approximating functions $\{F_n(\xi)\}$ which are related to $\tilde{v}_j^P(\xi)$ by

$$\tilde{v}_j^e(\xi) \equiv \frac{1}{2}\{\tilde{v}_j^P(\xi) + \tilde{v}_j^P(-\xi)\} = \sum_{n=0}^{N} a_{nj}F_n(\xi), \quad -\infty < \xi < \infty \tag{3.20}$$

Since $\tilde{v}_j^P(\xi)$ is analytic in the upper half of the complex ξ-plane, we determine $\tilde{v}_j^P(\xi)$ from

$$\tilde{v}_j^P(\xi) = \frac{i}{\pi}\sum_{n=0}^{N} a_{nj}I_n(\xi) \tag{3.21}$$

where

$$I_n(\xi) = \int_{-\infty}^{\infty} \frac{F_n(s)}{\xi - s}\,ds \tag{3.22}$$

We first tried $F_n(\xi) = [G_n(\xi) + G_n(-\xi)]/2$, where

$$G_n(\xi) = [(i-\xi)/(i+\xi)]^n \tag{3.23}$$

which gave $I_n(\xi) = -i\pi G_n(\xi)$ and

$$\tilde{v}_j^e(\xi) = \sum_{n=0}^{N} a_{nj}\cos(n\theta), \quad -\pi < \theta < \pi \tag{3.24}$$

where $\xi = \tan(\theta/2)$. This led to poor results – perhaps, because of slow convergence near the branch points ($\xi = -1, -\kappa$) of $\tilde{v}_j^P(\xi)$. Instead, we used

$$F_n = H(\xi)[G_n(\bar{\kappa}+\xi) + G_n(\bar{\kappa}-\xi)] \tag{3.25}$$

where

$$\bar{\kappa} = (1+\kappa)/2 \tag{3.26}$$

$$H(\xi) = \gamma^L - \gamma^T \tag{3.27}$$

This choice meant that $I_n(\xi)$ had to be computed numerically. We wrote

$$I_n(\xi) = \int_{-\infty}^{\infty}\left\{\frac{G_n(s+\bar{\kappa}) - G_n(\xi+\bar{\kappa})}{\xi - s}\right\}H(s)\,ds + \int_{-\infty}^{\infty}\frac{G_n(\bar{\kappa}-s)}{\xi-s}H(s)\,ds + G_n(\xi+\bar{\kappa})\int_{-\infty}^{\infty}\frac{H(s)}{\xi-s}\,ds \tag{3.28}$$

The last integral in (3.28) is known in closed form. In the first integral we closed the contour in the upper half of the complex s-plane, and in the second integral we closed the contour in the lower half of this plane. The only contributions to these integrals are from the branches. After transforming (e.g. $s = t/\kappa$) the branch line integrals to the interval [0,1], we evaluated the resulting integrals by a 16-point Gaussian quadrature formula which accounted for the square-root behavior of the integrand near the end point. We remark that if n is too large, the numerical quadrature breaks down due to the oscillations in G_n.

Table 1 Amplitudes of the reflection and transmission coefficients

Source	Poisson's ratio	Reflection coefficient	Transmission coefficient
De Bremaecker [2] (Experimental, 1958)	0.17	0.38	0.63
This study	0.17	0.27	0.68
Pilant et al. [3] (Experimental, 1964)	0.25	0.252	0.670
Munasinghe [4] (Numerical, 1973)	0.245	0.36	0.64
Bond [5] (Numerical, 1979)	0.24	0.43	0.57
This study	0.25	0.32	0.68
Viktorov [6] (Experimental, 1962)	0.34	0.60	0.70
Cuozzo et al. [7] (Analytical, 1977)	0.33	0.38	0.75
Bond [5] (Experimental, 1979)	0.34	0.37	0.60
Bond [5] (Numerical, 1979)	0.34	0.47	0.59
Achenbach et al. [8] (Analytical, 1980)	0.33	0.40	0.60
Kinra and Vu [9] (Tone-burst, 1983)	0.34	0.43	0.61
Kinra and Vu [9] (Spectroscopy, 1983)	0.34	0.43	0.59
This study	0.33	0.39	0.67

4 Discussion of Results

With F_n defined by (3.25) and $N = 15$ in (3.20), we determined the constants a_{nj} for a given Poisson's ratio by a least square fit to (3.13) and (3.14) at 76 values of ξ on the interval $(0,\infty)$. We then chose 19 values of Poisson's ratio at intervals of 0.025 and beginning at $\nu = 0.025$. Next we computed the reflection and transmission coefficients, which follow from (3.8) as

$$R^c = (A_1 + A_2)/2 \tag{4.1}$$

$$T^c = (A_2 - A_1)/2 \tag{4.2}$$

where A_l, $l = 1,2$, is given by (3.17) when (3.13) is solved or by (3.18) when (3.14) is solved. Writing these coefficients as

Downloaded 02 May 2010 to 171.66.16.54. Redistribution subject to ASME license or copyright; see http://www.asme.org/terms/Terms_Use.cfm

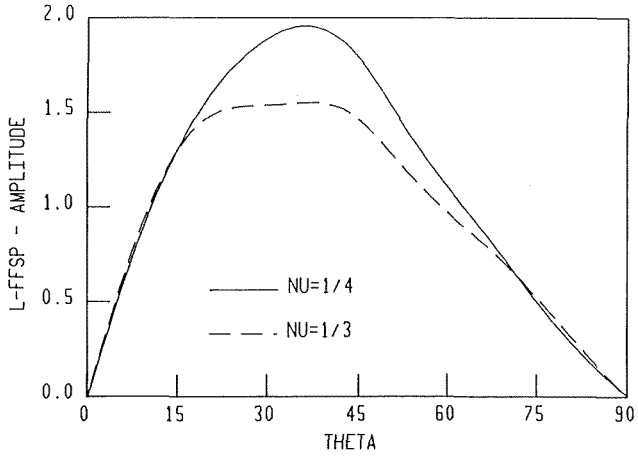

Fig. 6 Amplitude of $D^L(\theta)$ versus θ for $\nu = 1/4$ and 1/3

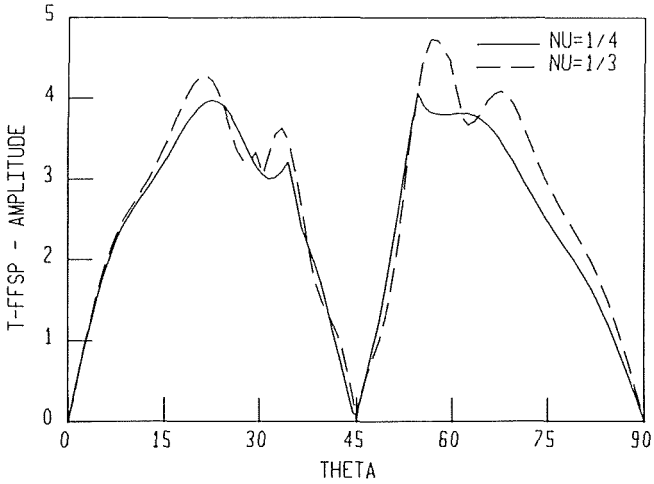

Fig. 7 Amplitude of $D^T(\theta)$ versus θ for $\nu = 1/4$ and 1/3

$$\text{Amp. exp}[i\ \text{Phase}] \tag{4.3}$$

we plotted, as a solid line, the amplitudes of these coefficients in Fig. 4 and the corresponding phases (in degrees) in Fig. 5 when A_l, $l=1,2$, is determined from the solution to (3.14). In these figures we also plotted, as a dashed line, the same curves when A_l, $l=1,2$, is determined from the solution to (3.13). The solid and dashed curves should, of course, coincide. However, they are sufficiently close so that we can assume that our results are reasonably accurate.

We note that the amplitude of the transmission coefficient is fairly constant—varying between 0.63 and 0.68. Its phase is also fairly constant—varying between -78 and -87 deg. As Poisson's ratio increases from 0.025 to 0.475, the amplitude of the reflection coefficient increases from 0.24 to 0.55, while its phase decreases from about 86 to 15 deg.

In Table 1, we compare the values of the reflection and transmission coefficients obtained in this work with those obtained either experimentally or numerically by other authors.

To obtain expressions for the farfield scattering patterns (FFSPs) $D^L(\theta)$ and $D^T(\theta)$, we let $r\to\infty$ in (2.16) to achieve

$$u_k^{sc} \sim q_k D^L(\theta) G^L(r) + (-1)^k q_{3-k} D^T(\theta) G^T(r) \quad \text{(no sum)} \tag{4.4}$$

where

$$(q_1, q_2) = (\cos\theta,\ \sin\theta) = \mathbf{x}/r \tag{4.5}$$

$$G^\alpha(r) = \exp[i(k_\alpha r + \pi/4)]/(8\pi k_\alpha r)^{1/2}, \quad \alpha = L, T \tag{4.6}$$

Gautesen [10] has shown that for this problem,

$$i\kappa^2 D^L(\theta) = 4q_1 q_2\{\bar v_1(q_1) + \bar v_1(-q_1) + (-1)^l[\bar v_1(q_2) + \bar v_1(-q_2)]\} \tag{4.7}$$

$$iD^T(\theta) = 4\kappa q_1 q_2\{\bar v_2(\kappa q_1) + \bar v_2(-\kappa q_1) - (-1)^l[\bar v_2(\kappa q_2) + \bar v_2(-\kappa q_2)]\} \tag{4.8}$$

In Figs. 6 and 7 we have plotted the amplitudes of $D^L(\theta)$ and $D^T(\theta)$, respectively, versus θ for $\nu = 1/4$, 1/3. Gautesen [10] has shown analytically that $D^T(45\ \text{deg}) = 0$. We see in Fig. 7 that this fact is confirmed by our numerical results.

References

1 Knopoff, L., "Elastic Wave Propagation in a Wedge," in: *Wave Propagation in Solids*, Miklowtz, J., ed., ASME, New York, 1969, pp. 3-42.

2 De Bremaecker, J. C., "Transmission and Reflection of Rayleigh Waves at Corners," *Geophysics*, Vol. 23, 1958, pp. 253-256.

3 Pilant, W. L., Knopoff, L., and Schwab, F., "Transmission and Reflection of Surface Waves at a Corner," *J. Geophys. Res.*, Vol. 69, 1964, pp. 291-297.

4 Munasinghe, M., and Farnell, G. W., "Transmission and Reflection of Acoustic Surface Waves at Corners," *Ultrason. Int.*, 1973, pp. 250-255.

5 Bond, L. J., "A Computer Model of the Interaction of Acoustic Surface Waves With Discontinuities," *Ultrasonics*, Vol. 17, 1979, pp. 71-77.

6 Viktorov, I. A., "Rayleigh Waves in the Ultrasonic Range," *Soviet Phys. Acoustics*, Vol. 8, 1962, pp. 119-129.

7 Cuozzo, F. C., Cambiaggio, E. L., Damiano, J. P., and River, E., "Influence of Elastic Properties on Rayleigh Wave Scattering by Normal Discontinuities," *IEEE Trans. Sonics and Ultrason.*, Vol. SU-24, 1977, pp. 280-289.

8 Achenbach, J. D., Gautesen, A. K., and Mendelsohn, D. A., "Ray Analysis of Surface-Wave Interaction With an Edge Crack," *IEEE Trans. Sonics and Ultrason.*, Vol. SU-27, 1980, pp. 124-129.

9 Kinra, V. K., and Vu, B. Q., "Diffraction of Rayleigh Waves in a Quarter Space," *Mech. Res. Com.*, Vol. 10, 1983, pp. 193-198.

10 Gautesan, A. K., "Scattering of a Plane Longitudinal Wave by an Elastic Quarter Space," submitted.

APPENDIX

In this Appendix, we give the fundamental stress tensor and its Fourier transform. This tensor is defined by

$$-4i\ \tau_{ij;k}^G(x,y) = (1-2\kappa^{-2})[H_0^{(1)}(k_L r)]_{,k}\delta_{\theta\pi} - 2k_T^{-2}[H_0^{(1)}(k_L r) - H_0^{(1)}(k_T r)]_{,ijk} + [H_0^{(1)}(k_T r)]_{,j}\delta_{ik} + [H_0^{(1)}(k_T r)]_{,i}\delta_{jk} \tag{A.1}$$

where k_α and κ are given by (2.24) and (2.28), $H_0^{(1)}$ is the outgoing, zeroth-order Hankel function, and

$$r = (x^2 + y^2)^{1/2} \tag{A.2}$$

The Fourier transform of (A.1) is

$$-(2/k_L)\bar\tau_{ij;k}^G(\xi,y) = (P_k^L/\gamma^L)[\delta_{ij} + 2\kappa^{-2}(P_i^L P_j^L - \delta_{ij})]E^L + (\gamma^T)^{-1}[\delta_{ik}P_j^T + \delta_{jk}P_i^T - 2\kappa^{-2}P_i^T P_j^T P_k^T]E^T \tag{A.3}$$

where γ^α is defined by (2.29)

$$(P_1^\alpha, P_2^\alpha) = (-\xi, \gamma^\alpha \operatorname{sgn}(y)), \quad \alpha = L, T \tag{A.4}$$

$$E^\alpha = \exp[ik_L\ \gamma^\alpha\ |y|], \quad \alpha = L, T \tag{A.5}$$

With $a(\xi)$ defined by (2.27), the explicit expressions for the transforms used in this work are

$$-(2/k_L)\bar\tau_{12;1}^G(\xi,0^\pm) = -(2/k_L)\bar\tau_{22;2}^G(\xi,0^\pm) = \pm 1 \tag{A.6}$$

$$-(2\kappa^2/k_L)\bar\tau_{22;1}^G(\xi,0^\pm) = \xi[2\gamma^L\gamma^T - a(\xi)]/\gamma^L \tag{A.7}$$

$$-(2\kappa^2/k_L)\bar\tau_{12;2}^G(\xi,0^\pm) = \xi[a(\xi) - 2\gamma^L\gamma^T]/\gamma^T \tag{A.8}$$

$$-(2\kappa^2/k_L)\bar\tau_{11;1}^G(\xi,y) = -\xi[2\gamma^T E^T + a(\gamma^L)E^L/\gamma^L] \tag{A.9}$$

$$-(2\kappa^2/k_L)\bar\tau_{21;1}^G(\xi,y) = \operatorname{sgn}(y)[a(\xi)E^T + 2\xi^2 E^L] \tag{A.10}$$

$$-(2\kappa^2/k_L)\bar\tau_{11;2}^G(\xi,y) = \operatorname{sgn}(y)[-2\xi^2 E^T + a(\gamma^L)E^L] \tag{A.11}$$

$$-(2\kappa^2/k_L)\bar\tau_{21;2}^G(\xi,y) = \xi[a(\xi)E^T/\gamma^T - 2\gamma^L E^L] \tag{A.12}$$

Downloaded 02 May 2010 to 171.66.16.54. Redistribution subject to ASME license or copyright; see http://www.asme.org/terms/Terms_Use.cfm

An Experimental Study of the Reflection and Transmission of Flexural Waves at Discontinuities

J. F. Doyle
Associate Professor.

S. Kamle
Former Graduate Student.

School of Aeronautics and Astronautics,
Purdue University,
West Lafayette, Ind. 47907

The research reported is the study of the transmission and reflection characteristics of flexural waves at structural discontinuities. A Fast Fourier Transform (FFT) computer algorithm is used to characterize the dispersive flexural waves. The incident wave is propagated through two types of discontinuities namely, a stepped beam and the free end of a beam. At each stage, comparison with experimental results are made.

Introduction

It has long been understood that the likelihood of failure of an impacted body is not just a matter of the total momentum or energy transferred. A very important factor is the time period over which the energy is transferred. That is, the rate at which the structure can absorb or disperse the energy plays a vital role; if the energy cannot spread into the body fast enough then other mechanisms such as plasticity or fracture are needed to absorb the energy. One area where these considerations are of importance is in the design of large flexible space structures. These are large lightweight framed structures whose structural performance (e.g., alignment of solar disks) must not be impaired. Another area is that of the large framed structures used in offshore oil drilling. These are susceptible to impact from icebergs and boats.

The ability of framed structures to withstand an impact depends not only on its ability to withstand it right at the site of impact, but also on its ability to propagate the energy throughout the whole structure. Much research has been done considering, on the one hand, the local behavior near the impact site, and on the other, the global vibrational aspects. It seems, however, to fully understand the dynamic response of framed structures that it is necessary to be able to track the energy propagation through the structure. Specifically it is necessary to see how the waves, having emanated from the impact site, behave at joints, to know what portion of the energy is transmitted, and what portion is reflected.

The presence of joints can affect the dynamic response in a variety of ways. For example, the reflected portion may add to the input energy at the impact site and thus increase the likelihood of local failure. Or, the joint can cause a change in the types of waves reflected and transmitted: a flexural wave on reaching a joint generates not only flexural waves, but also longitudinal and torsional waves. These new types of loading can cause structural failures not anticipated by the designer. A more subtle effect occurs when the wave is unable to disperse quickly enough past the joint, thus causing a "trapping" of the wave. While this may not cause structural failure it could adversely affect the performance of the structure.

The literature on the reflection and transmission of flexural waves at discontinuities is not very large. Reference [1] considered waves incident at either a fixed or free end of a beam. Reference [2] considered waves incident on an L joint while reference [3] considered both L and T joints. Reference [4] investigated two rods at arbitrary angles while reference [5] considered a Y junction. These last four references studied incident longitudinal waves but not incident flexural waves. They also report on the use of a rigid intersection element. Reference [6] considered sinusoidal waves in nonhomogeneous beams and compared both the Euler-Bernoulli and Timoshenko beam theories.

The present paper attempts to develop an experimental methodology for analyzing the effect of structural joints on wave propagation. Particular attention is paid to flexural waves because they are dispersive. The results are divided into two main categories; characterizing the incident wave, which will be done using a frequency analysis, and investigating the effect of the joint on the wave. For the present, however, only discontinuities of material and cross-section in collinear bars will be reported on, but the methodology used is applicable to any discontinuity.

Characterization of the Incident Wave

When a beam is impacted, the resulting flexural wave is comprised of many frequency components as shown in Fig. 1. Each component will travel at a different speed according to its dispersion relation also shown in Fig. 1. Consequently, the strain response detected at two different locations will appear quite different as shown in Fig. 2. That they are different is because of the so-called dispersive nature of flexural waves, and this makes characterizing the waves in the time domain difficult. The characterization must be done in the frequency domain and use is made of a Fast Fourier Transform (FFT) numerical algorithm to accomplish this.

Contributed by the Applied Mechanics Division for publication in the JOURNAL OF APPLIED MECHANICS.

Discussion on this paper should be addressed to the Editorial Department, ASME, United Engineering Center, 345 East 47th Street, New York, N.Y. 10017, and will be accepted until two months after final publication of the paper itself in the JOURNAL OF APPLIED MECHANICS. Manuscript received by ASME Applied Mechanics Division, September, 1983; final revision, October, 1984.

Copyright © 1985 by ASME
Downloaded 02 May 2010 to 171.66.16.54. Redistribution subject to ASME license or copyright; see http://www.asme.org/terms/Terms_Use.cfm

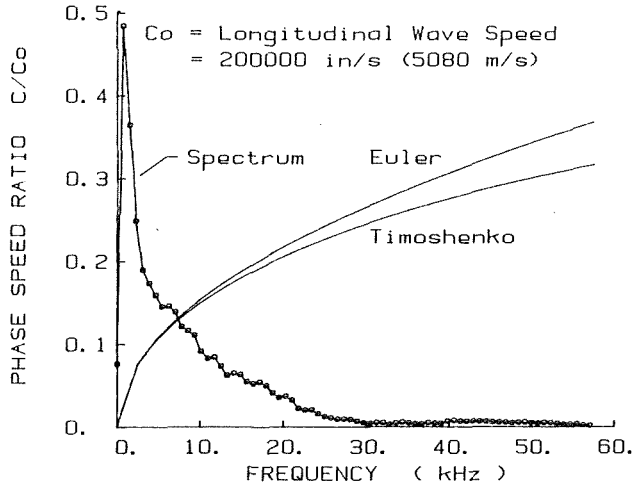

Fig. 1 Amplitude spectrum for a typical strain history and the dispersion relations for two beam models

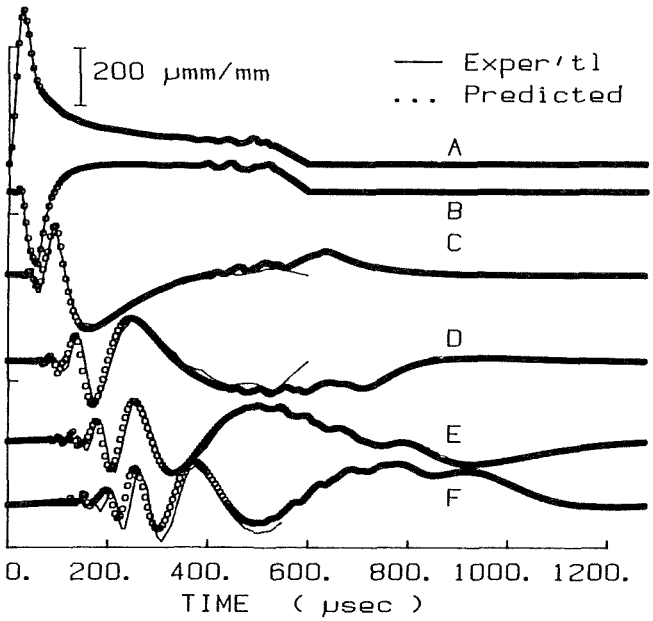

Fig. 2 Predictions of strain at *C*, *D*, *E*, *F* based on sampling at *A* and *B*

The FFT is actually a quick way of obtaining the Discrete Fourier Transform of a signal and is defined as:

$$A_r = \sum_{K=0}^{N} x_K e^{\frac{-2\pi i r K}{N}} \qquad r,K = 0,1,2,\ldots N-1$$

$$i = \sqrt{-1}$$

where x_K is the sample value of the signal at time $(K-1)\Delta t$ and A_r is its FFT at the frequency $r/N\Delta t$. Unlike the Fourier Transform the FFT samples on a finite window $N\Delta t$ and has a finite frequency range $1/\Delta t$. Consequently, the sampled signal is actually considered to be periodic with the period $N\Delta t$ as shown in Fig. 4. This will be significant when the wave is propagating.

In all the results to follow, a strain gage signal of about 600 μs is padded with zeroes to give a total signal length (or window) of 1280 μs. The sampling is done every 5 μs so that a total of 256 points are used with a Nyquist frequency of 100 kHz.

It is seen from Fig. 1 that most of the significant amplitudes occur in the frequency range where there is little difference between the Timoshenko and Bernoulli-Euler beam models.

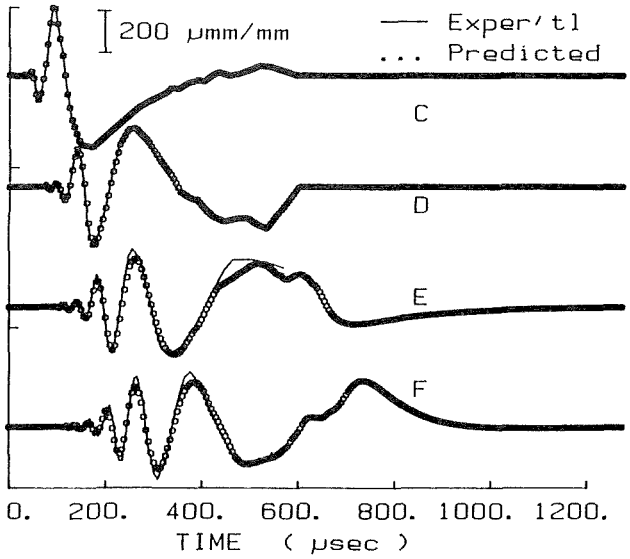

Fig. 3 Predictions of strain at *E* and *F* based on sampling at *C* and *D*

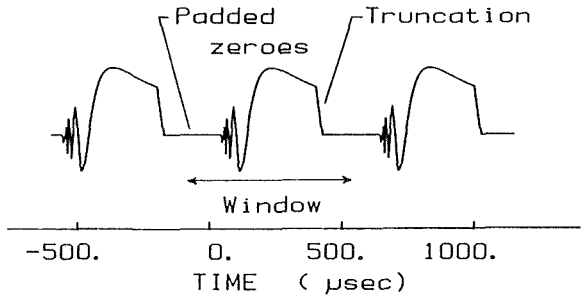

Fig. 4 The FFT represents the signal as periodic with a period the window size

Consequently, the simpler Bernoulli-Euler beam model will be used in the analysis to follow.

The differential equation of flexural motion in a beam is given by

$$EI\frac{\partial^4 v}{\partial x^4} + \rho\, A\frac{\partial^2 v}{\partial t^2} = 0$$

where $v(x,t)$ is the vertical deflection, EI is the stiffness, and ρA is the mass per unit length. This admits harmonic solutions of the form

$$v(x,t) = Ae^{i(kx+\omega t)} \qquad k = \pm\left[\omega^2\frac{\rho A}{EI}\right]^{1/4}, \quad \pm i\left[\omega^2\frac{\rho A}{EI}\right]^{1/4}$$

which corresponds to two wave motions and two spatially damped vibrations. Obviously, the complete spectrum of frequency components can propagate in the beam. Considering only a forward moving wave then for a general disturbance, the displacements and strains can be written as

$$v(x,t) = \Sigma[Ae^{-ikx} + Be^{kx}]e^{i\omega t}$$

$$e(x,t) = -\frac{h}{2}\frac{\partial^2 v}{\partial x^2} = \frac{h}{2}\Sigma\, k^2[Ae^{-ikx} - Be^{kx}]e^{i\omega t}$$

where the summation is with respect to all frequency components and A, B, and k are understood to be frequency dependent. To characterize the wave, it is necessary to know the spectra $A(\omega)$, $B(\omega)$. If a Fast Fourier Transform (FFT) is taken of the strain history, then it can be approximated with a finite set of frequency components, that is

$$e(x,t) = \sum_{n=0}^{N} \hat{e}(x,\omega_n)e^{i\omega_n t}$$

Downloaded 02 May 2010 to 171.66.16.54. Redistribution subject to ASME license or copyright; see http://www.asme.org/terms/Terms_Use.cfm

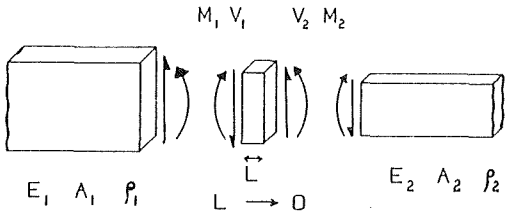

Fig. 5 A model for the joint of a stepped beam

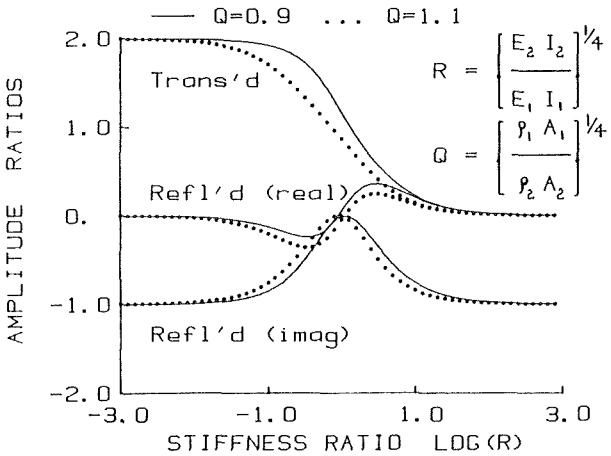

Fig. 6 Behavior of the transmitted and reflected waves as a function of stiffness and density

where $\hat{e}(x,\omega_n)$ is the FFT component at frequency ω_n of the strain history at x. If the strain is sampled at two locations then A and B at discrete frequencies can be solved for as

$$A_n = A_n(\omega_n) = [\hat{e}(x_1,\omega_n)e^{-k_n x_2} - \hat{e}(x_2,\omega_n)e^{-k_n x_1}]/Q_n$$

$$B_n = B_n(\omega_n) = [\hat{e}(x_1,\omega_n)e^{-ik_n x_2} - \hat{e}(x_2,\omega_n)e^{-ik_n x_1}]/Q_n$$

$$Q_n = e^{-ik_n x_1 - k_n x_2} - e^{-ik_n x_2 - k_n x_1}$$

Note that in general A_n and B_n are complex.

In summary, to characterize the disturbance in a beam it is necessary to sample this disturbance at two locations, obtain the FFT components and then solve for A_n and B_n simultaneously. This is different than what was reported by Yew et al. in reference [7]. They assumed essentially that the e^{-kx} terms are negligible and consequently did sampling at only one location. This is generally true when the measurements are taken a distance away from the origin of the waves (i.e., when x is large). However, if the signal originates from an impact and the signal is sampled near the impact site then both A and B are necessary to characterize the wave.

Propagating the Wave

Once the wave has been characterized in the form

$$v(x,t) = \Sigma[A_n e^{-ik_n x} + B_n e^{-k_n x}]e^{i\omega t}$$

then it is propagated simply by changing x. However it must be realized that the term inside the square bracket is the FFT of the signal within the time window of the sample. Consequently, the window must be chosen so as to allow the wave to propagate without moving out of the window (or the wave from the neighboring period moving into the window). This was handled by padding the sampled signal with zeros so as to almost double the time period (as shown in Fig. 4).

Figure 2 shows a comparison of the experimental strains at A, B, C, D, E, and F with those predicted based on sampling at A and B. Obviously agreement is exact at the first two locations. For larger x, the wave has moved and the padded zeros are disturbed. It is noted that these disturbances which arise at large time are due entirely to the numerical representation of the wave and not due to any wave phenomena.

Figure 3 is similar to Fig. 2 except that the sampling was done at C and D. There is less spurious disturbances at large time and the predicted and measured strains show improved agreement. In the later work to be reported on, it is this set of sampling positions that will be used to characterize the incident wave. It is noted in passing, however, that it is possible to sample at more than two positions and get an average.

Improvement can be achieved by choosing a larger sampling window. In the present case a strain signal of about 600 μsec was used because reflections are beginning to enter the picture. Schemes of extending the sample in the presence of reflections are being investigated.

Analysis of Discontinuity

The analysis will be restricted to bars that have discontinuity in stiffness and density, but remains collinear. Such a bar is shown in Fig. 5 along with a model of the joint. The joint is assumed to be rigid but of very small mass. Let the displacements for bars 1 and 2 be

$$v_1(x,t) = \Sigma[A_n e^{-ik_{1n}x} + C_n e^{ik_{1n}x} + D_n e^{k_{1n}x}]e^{i\omega_n t}$$

$$v_2(x,t) = \Sigma[\bar{A}_n e^{-ik_{2n}x} + \bar{B}_n e^{-k_{2n}x}]e^{i\omega_n t}$$

where it is assumed that only a propagating wave is incident on the joint and is represented by the A_n term. Note that bar 1 also contains a reflected wave (C_n) and a ringing term (D_n). For convenience, the joint is located at $x = 0$.

Continuity conditions at the joint gives (with $L = 0$)

Displacement: $v_1 = v_2$

Slope: $$\frac{\partial v_1}{\partial x} = \frac{\partial v_2}{\partial x}$$

Moment: $$E_1 I_1 \frac{\partial^2 v_1}{\partial x^2} = E_2 I_2 \frac{\partial^2 v_2}{\partial x^2}$$

Shear: $$E_1 I_1 \frac{\partial^3 v_1}{\partial x^3} = E_2 I_2 \frac{\partial^3 v_2}{\partial x^3}$$

In terms of the coefficients these become with $x = 0$

$$[C_n + D_n] - [\bar{A}_n + \bar{B}_n] = -A_n$$

$$R[iC_n + D_n] + Q[i\bar{A}_n + \bar{B}_n] = iRA_n$$

$$[-C_n + D_n] + R^2Q^2[\bar{A}_n - \bar{B}_n] = A_n$$

$$[-iC_n + D_n] - RQ^3[i\bar{A}_n - \bar{B}_n] = -iA_n$$

where $R = [E_2 I_2 / E_1 I_1]^{1/4}$ and $Q = [\rho_2 A_2 / \rho_1 A_1]^{1/4}$. Solving in terms of A_n gives

$$C_n = A_n[2RQ(R^2 - Q^2) - i(1 - R^2Q^2)^2]/D$$

$$D_n = A_n(1 - R^4Q^4)[1 - i]/D$$

$$\bar{A}_n = A_n 2(1 + R^2Q^2)(R + Q)/(DQ)$$

$$\bar{B}_n = -A_n 2(1 - R^2Q^2)(R + iQ)/(DQ)$$

$$D = 2RQ(R^2 + Q^2) + (1 + R^2Q^2)$$

The strains in bars 1 and 2 are obtained simply by differentiating the displacements.

The behavior of the coefficients of the propagating components is shown in Fig. 6 for various values of stiffness and density. Note that while the reflected wave may have a phase change, the transmitted wave is always in phase with the incident wave (since $\bar{A}_n$ is always real).

From this analysis it can be concluded that depending on

Downloaded 02 May 2010 to 171.66.16.54. Redistribution subject to ASME license or copyright; see http://www.asme.org/terms/Terms_Use.cfm

the discontinuity, amplitude, phase as well as wave number changes can occur.

Two discontinuities were tested here. In the first case, a stepped beam was used with area ratio 2:1 but no thickness change. The results for the transmitted wave at 25 mm from the discontinuity are shown in Fig. 7 along with the predicted results as if no discontinuity were present. There is an amplification in magnitude but very little phase change. The agreement with experiment is very close.

Figure 8 shows the results for the wave reflected from a free end and measured 75 mm from this end. There is very little amplitude change between the incident and reflected waves, but their superposition causes a significant change in the observed strain history. It is remarkable that this predicted behavior follows quite closely that observed experimentally.

Conclusion

A methodology for analyzing structural joints due to incident flexural waves has been developed. The results show that it is possible to track the wave as it passes through the joint thus allowing evaluation of the adequacy of the models used to describe the joint. This will be especially beneficial when complicated multimember joints are analyzed.

There are, however, a few further developments that need to be considered. First, while the majority of frequency components were in the range described adequately by the Bernoulli-Euler beam theory, some high frequency components showed the need for a Timoshenko beam description. This could be included and even in an approximate way would probably be sufficient. Secondly, ways of obtaining larger samples artificially so as to better characterize the incident wave should be investigated. For example, the experimental signal (before reflections become significant), could be augmented with the long-time exact solution for an infinite beam. This primarily will have a beneficial effect on the low-frequency components.

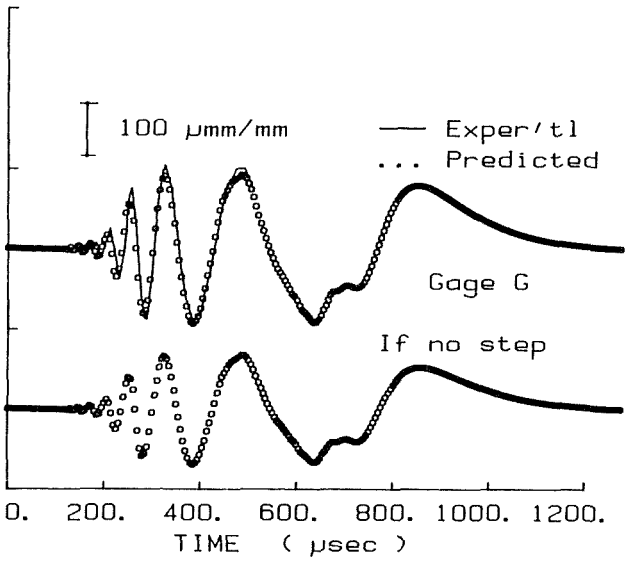

Fig. 7 Prediction of strain 25.4 mm after step

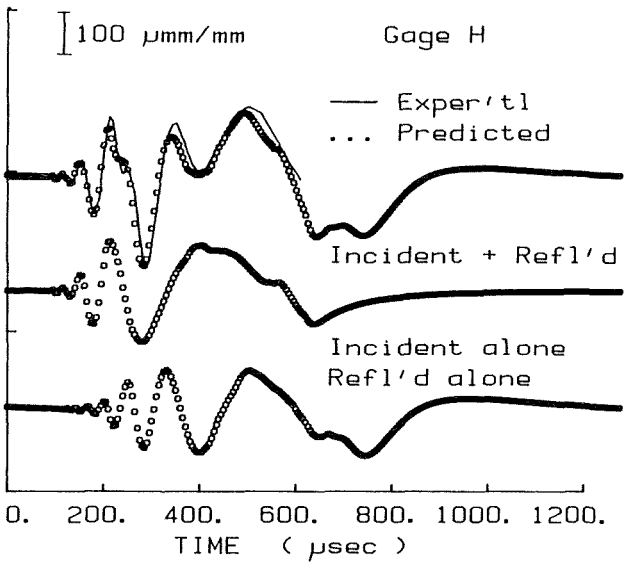

Fig. 8 Prediction of strain 76 mm from a free end

References

1 Ripperger, E. Q., and Abramson, H. N., "Reflection and Transmission of Elastic Pulses in a Bar at a Discontinuity in Cross Section," *Third Midwestern Conf. on Solid Mechs.*, 1957, pp. 135-138.

2 Mandel, J. A., Mathur, R. K., and Chang, Y. C., "Stress Waves at Rigid Right Angle Joint," *J. Eng. Mechs. Div., ASCE*, Vol. 97, Aug. 1971, pp. 1173-1185.

3 Atkins, K. J., and Hunter, S. C., "The Propagation of Longitudinal Elastic Waves Around Right-Angled Corners in Rods of Square Cross Section," *Q. J. Mechs. and Applied Math.*, Vol. 28, May 1975, pp. 245-260.

4 Lee, J. P., and Kolsky, H., "The Generation of Stress Pulses at the Junction of Two Noncollinear Rods," ASME JOURNAL OF APPLIED MECHANICS, Vol. 39, 1972, pp. 809-813.

5 Desmond, T. P., "Theoretical and Experimental Investigation of Stress Waves at a Junction of Three Bars," ASME JOURNAL OF APPLIED MECHANICS, Vol. 48, 1981, pp. 148-154.

6 Reismann, H., and Yamaguchi, T., "Wave Motion in Non-Homogeneous Beams and Plates—A Comparison of Two Theories," *SM Archives*, Vol. 6, No. 2, 1981, pp. 213-277.

7 Yew, E. H., and Chen, C. S., "Experimental Study of Dispersive Waves in Beam and Rod Using FFT," ASME JOURNAL OF APPLIED MECHANICS, Vol. 45, 1978, pp. 940-942.

APPENDIX

Experimental Set-Up

The schematic of the experimental setup is shown in Fig. *A*1. The hard-copy plots of the data are digitized for data analysis in the computer. Triggering was achieved by connecting a 22.5V battery to both the beam and the ball. Contact between the two closed the circuit and sent the trigger voltage to the Biomation. There were not enough preamps to record all the gages simultaneously, but by using the contact trigger and dropping the ball from the same height, then as nearly as

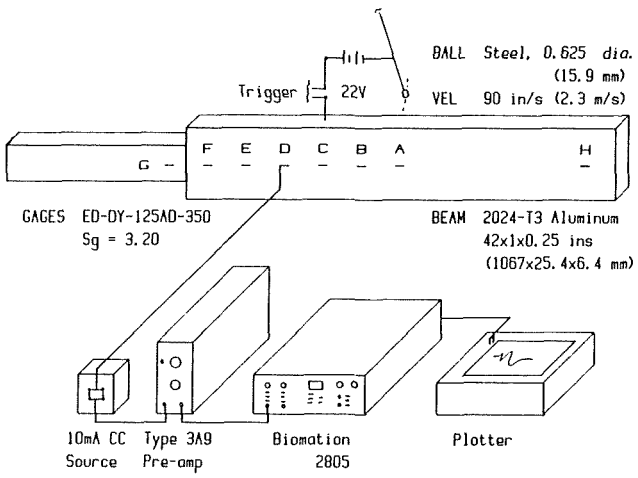

Fig. A1 Schematic of experimental setup

Downloaded 02 May 2010 to 171.66.16.54. Redistribution subject to ASME license or copyright; see http://www.asme.org/terms/Terms_Use.cfm

possible, the exact impact was reproduced and groups of gages (three) could be recorded sequentially. It may be pointed out that the grouping was random so that there would not be a trend in any errors.

The beam was stepped on one end with the second bar being half the area and about 250 mm long. The gages were located as indicated in Table $A1$.

All of the equipment had the necessary frequency response to capture the strain signals i.e., up to about 50 kH_z. An area of concern however is the length of the gage (3 mm (0.125 in.)). For the Bernoulli-Euler beam the relation between frequency and wavelength is

$$f = \frac{EI}{\rho A}\frac{2}{\lambda^2} = \frac{0.091}{\lambda} MH_z$$

where λ is the wavelength in inches. Certainly wavelengths on the order of the gagelength and less could not be picked up, i.e., frequencies of about 5.8 MH_z. Wavelengths corresponding to a frequency of 50 kH_z are on the order of 10 times the gage size. This is acceptable.

Table $A1$ Gage locations

Gage	Distance from impact site	
	mm	in.
A	0	0
B	45	1.75
C	114	4.5
D	216	8.5
E	318	12.5
F	394	15.5
Step	419	16.5
G	445	17.5
H	283	11.125
free end	356	14.0

Downloaded 02 May 2010 to 171.66.16.54. Redistribution subject to ASME license or copyright; see http://www.asme.org/terms/Terms_Use.cfm

Prediction of Impact Force and Duration Due to Low-Velocity Impact on Circular Composite Laminates

K. N. Shivakumar
Research Associate Professor,
Old Dominion University.

W. Elber
Head,
Fatigue and Fracture Branch.

W. Illg
Senior Scientist,
Fatigue and Fracture Branch.

NASA Langley Research Center,
Hampton, Va. 23665

Two simple and improved models – energy-balance and spring-mass – were developed to calculate impact force and duration during low-velocity impact of circular composite plates. Both models include the contact deformation of the plate and the impactor as well as bending, transverse shear, and membrane deformations of the plate. The plate was a transversely isotropic graphite/epoxy composite laminate and the impactor was a steel sphere. In the energy-balance model, a balance equation was derived by equating the kinetic energy of the impactor to the sum of the strain energies due to contact, bending, transverse shear, and membrane deformations at maximum deflection. The resulting equation was solved using the Newton-Raphson numerical technique. The energy-balance model yields only the maximum force; hence a less simple spring-mass model is presented to calculate the force history. In the spring-mass model, the impactor and the plate were represented by two rigid masses and their deformations were represented by springs. Springs define the elastic contact and plate deformation characteristics. Equations of equilibrium of the resulting two degree-of-freedom system, subjected to an initial velocity, were obtained from Newton's second law of motion. The two coupled nonlinear differential equations were solved using Adam's numerical integration technique. Calculated impact forces from the two analyses agreed with each other. The analyses were verified by comparing the results with reported test data.

Introduction

Low-velocity impact of composite laminates has been a subject of importance since the last decade. The invisible damage caused by mild impacts was found to decrease residual strengths. Many researchers have studied this problem in different ways. Yet the problem still poses many challenges. Methods reported [1–8] to date to predict the impact force, including the effect of contact deformation, can be classified into two categories: (1) the Hertz method and (2) the modified Hertz method. The Hertz method, which includes only the contact deformation for plates supported at the outer boundary, overestimates impact force by several orders of magnitude [3]. The modified Hertz method includes the plate flexural deflection in addition to contact deformation. Impact of rectangular [5–7], circular [4], and cantilever [3] plates was studied based on small deflection thin plate theory. Recent studies [8, 9], however, have shown that the laminates (plates) undergo large deflection and transverse shear deformation when the impact occurs at low velocity. The modified Hertz method [3–7], which neglects these two effects, underestimates the impact force for thin plates and overestimates the force for thick plates. Hence, it is necessary to develop a more general analysis that includes both large deflection and transverse shear effects, so that a wider range of plate thickness and impact velocities could be analyzed accurately. An exact solution for the low-velocity impact on composite laminates involves a three-dimensional nonlinear dynamic analysis of a laminate attached to a central mass through a Hertzian spring. Such an analysis is mathematically highly complex and numerically intractable even with modern computers. The objective of this paper is, therefore, to develop improved, yet simple, analyses to calculate the impact force and duration for a low-velocity impact on circular laminates.

The particular problem considered in this study was a circular laminated plate impacted at its center by a stiff sphere. The plate was assumed to be made up of a quasi-isotropic laminate having transversely isotropic material properties. The plate boundary was either clamped or simply supported. During impact, the plate and the impactor undergo contact deformation and the plate further undergoes bending, transverse shear, and membrane deformations.

Contributed by the Applied Mechanics Division for publication in the JOURNAL OF APPLIED MECHANICS.

Discussion on this paper should be addressed to the Editorial Department, ASME, United Engineering Center, 345 East 47th Street, New York, N.Y. 10017, and will be accepted until two months after final publication of the paper itself in the JOURNAL OF APPLIED MECHANICS. Manuscript received by ASME Applied Mechanics Division, October, 1983; final revision, July, 1984.

Copyright © 1985 by ASME
Downloaded 02 May 2010 to 171.66.16.54. Redistribution subject to ASME license or copyright; see http://www.asme.org/terms/Terms_Use.cfm

Table 1 Bending and membrane stiffness parameters of centrally loaded plates

Boundary conditions	Edge conditions	Bending stiffness, K_b	Membrane stiffness parameters, K_m
Clamped[a]	Immovable	$\frac{4\pi E_r h^3}{3(1-\nu_r^2)a^2}$	$\frac{(353-191\nu_r)\pi E_r h}{648(1-\nu_r)a^2}$
	Moveable	$\frac{4\pi E_r h^3}{3(1-\nu_r^2)a^2}$	$\frac{191\pi E_r h}{648a^2}$
Simply supported[b]	Immovable	$\frac{4\pi E_r h^3}{3(3+\nu_r)(1-\nu_r)a^2}$	$\frac{\pi E_r h}{(3+\nu_r)^4 a^2}\left\{\frac{191}{648}(1+\nu_r)^4+\frac{41}{27}(1+\nu_r)^3+\frac{32}{9}(1+\nu_r)^2+\frac{40}{9}(1+\nu_r)+\frac{8}{3}+\frac{1}{(1-\nu_r)}\left[\frac{(1+\nu_r)^4}{4}+2(1+\nu_r)^3+8(1+\nu_r)^2+16(1+\nu_r)+16\right]\right\}$
	Movable	$\frac{4\pi E_r h^3}{3(3+\nu_r)(1-\nu_r)a^2}$	$\frac{\pi E_r h}{a^2(3+\nu_r)^4}\left[\frac{191}{648}(1+\nu_r)^4+\frac{41}{27}(1+\nu_r)^3+\frac{32}{9}(1+\nu_r)^2+\frac{40}{9}(1+\nu_r)+\frac{8}{3}\right]$

[a] From reference [13].
[b] Derived using Babuno-Galerkin variational method, as reported in reference [13].

Early studies [1, 8, 10] have shown that the impact duration is many times longer than the time for generated stress waves to travel to the outer boundary of the plate and to return. Furthermore, the effects of higher modes, especially when the plate undergoes large deflection, are small and can be neglected. Therefore, assuming the first mode vibration of the plate, two simple models were proposed: (1) an energy-balance model and (2) a spring-mass model. The energy-balance model is a first-mode approximation of the spring-mass model to calculate the magnitude of impact force. The energy-balance model (equating the kinetic energy of the impactor before the impact to the deformation energies of the plate-impactor system) yielded an energy equation which could be solved for maximum force using a desk top calculator. However, to calculate the complete force history during impact, the spring-mass model was developed. In the spring-mass model, the impactor and the plate were represented by two rigid masses and the associated deformation characteristics were represented by springs. Equations of motion of the two masses were obtained using Newton's second law of motion. The resulting coupled nonlinear differential equations then were solved using Adam's numerical integration technique. The two analyses were compared with each other and with reported data [4, 9].

Description of the Problem

Figure 1 (top) shows a spherical impactor of radius R_I, mass M_I, and velocity V_0 striking the center of a circular plate of radius a and thickness h. The plate is assumed to be made up of a quasi-isotropic laminate having transversely isotropic material properties. A cylindrical coordinate system with the origin at the center of the plate is assumed. A representative θ = constant section of the plate is shown in the figure. During impact ($t > 0$), the impact force induces two types of deformations [4]: (1) contact deformation α in the impactor and the plate (See Fig. 1), and (2) transverse deflection w of the plate, which is measured from its midsurface (see Fig. 1). The deformation α is the measure of how much the centers of the plate and the impactor approach each other. The impact force P and the contact deformation are related by the well-known Hertz law [2, 11]. The transverse deflection w is the sum of bending w_b and transverse shear w_s deformations of the plate. (From hee on "transverse shear" is referred to as shear.) Furthermore, the membrane deformation is caused by the stretching associated with the deflection w of the plate. If w is small compared to plate thickness ($w/h \leq 0.2$), the membrane effect could be neglected [12].

After the plate-impactor contact, the impact force P (see Fig. 1) acts over an area of contact between the impactor and the plate. The area of contact depends on the force and moduli of the impactor and plate. The plate load and deflection are related by the stiffness associated with bending, shear and membrane deformations. Because the area of contact is small, it was assumed that the impact force was centrally concentrated. The expressions for bending stiffness K_b and membrane stiffness K_m parameters were derived using the Babunov-Galerkin variational method [13]. These stiffness expressions for K_b and K_m are given in Table 1 for the four plate boundaries, namely, clamped (edge moveable or immoveable) and simple supported (edge moveable or immoveable). The transverse shear stiffness K_s expression was derived assuming the impact force to be distributed over the region of contact [14]. This K_s expression was verified by comparing the calculated shear deformation with Woinowsky-Krieger's [12] results for isotropic plates. The formulation and results of the proposed two models, energy-balance model and spring-mass model, are presented in the following sections.

Energy-Balance Model

Analysis. The energy-balance (*E-B*) model was based on the principle of conservation of total energy of the plate-impactor system. In this analysis, the kinetic energy of the impacting mass was equated to the sum of the energies due to contact, bending, shear, and membrane deformations. The energy losses from material damping, surface friction, and higher mode vibrations [10] were neglected. The resulting equation was solved for the impact force using the standard Newton-Raphson numerical technique.

The maximum kinetic energy of the impactor before impact, at $t = 0$, is $1/2\, M_I V_0^2$. After $t = 0$, the plate-impactor system undergoes contact, bending-shear, and membrane

Downloaded 02 May 2010 to 171.66.16.54. Redistribution subject to ASME license or copyright; see http://www.asme.org/terms/Terms_Use.cfm

deformations. The corresponding stored deformation energies are E_c, E_{bs}, and E_m, respectively. Then, from the principle of conservation of total energy, the energy-balance equation of the plate-impactor system is

$$\frac{1}{2} M_I V_0^2 = E_c + E_{bs} + E_m \tag{1}$$

The energies E_c, E_{bs}, and E_m were calculated using the corresponding force-deformation relations as follows.

The impact force P and contact deformation α relation for impact of two bodies of revolution is given by the Hertz law [2],

$$P = n\alpha^{3/2} \tag{2}$$

where n is the contact stiffness parameter, which depends on material and geometrical properties of the plate and the impactor. The expression for n, for a spherical isotropic impactor and transversely isotropic composite plate, is given by [11]

$$n = \frac{4\sqrt{R_I}}{3\pi(K_1 + K_2)} \tag{3}$$

where

$$K_1 = \left(\frac{1 - \nu_I^2}{\pi E_I}\right)$$

and

$$K_2 = \frac{\sqrt{A_{22}}[(\sqrt{A_{11}A_{22}} + G_{zr})^2 - (A_{12} + G_{zr})^2]^{1/2}}{2\pi\sqrt{G_{zr}}(A_{11}A_{22} - A_{12}^2)}$$

$$A_{11} = E_z(1 - \nu_r)\beta$$

$$A_{22} = \frac{E_r\beta(1 - \nu_{zr}^2\delta)}{(1 + \nu_r)}$$

$$A_{12} = E_r\nu_{zr}\beta$$

$$\beta = \frac{1}{1 - \nu_r - 2\nu_{zr}^2\delta}$$

$$\delta = E_r/E_z$$

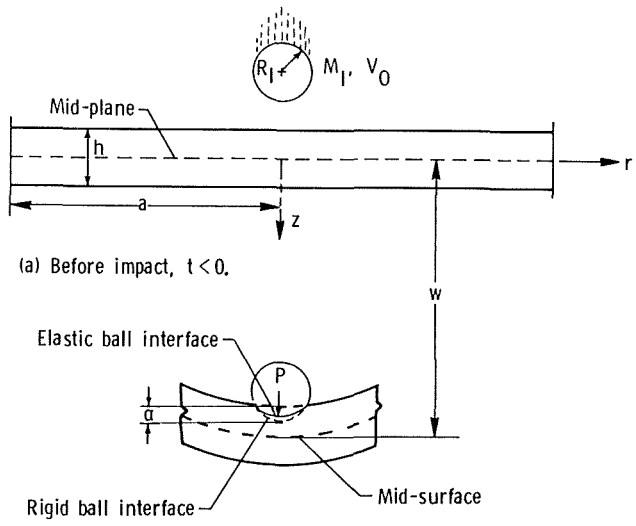

Fig. 1 Central transverse impact on a circular plate

The constants E_I and ν_I are, respectively, Young's modulus and Poisson's ratio of the impactor. The constants E, G, and ν are, respectively, Young's modulus, shear modulus, and Poisson's ratio of the plate, while the subscripts r and z refer to radial and thickness directions, respectively.

The contact energy E_c is then the integral of the product of the impact force and contact deformation:

$$E_c = \int_0^\alpha P\, d\alpha$$

The impact force P is replaced by the function α from equation (2), then after integration and simplification E_c becomes

$$E_c = \frac{2}{5}\frac{P^{5/3}}{n^{2/3}} \tag{4}$$

The reactive force P from the plate can be resolved into two components

$$P = P_{bs} + P_m \tag{5}$$

where P_{bs} is the force associated with bending and shear deformations and the P_m is the force associated with mem-

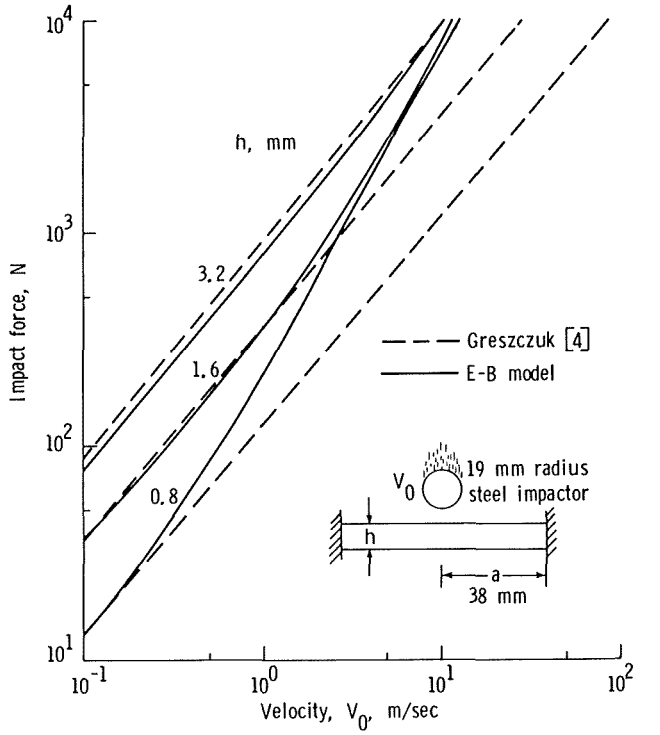

Fig. 2 Predicted impact force for clamped (immovable support) composite plates (graphite/epoxy quasi-isotropic laminate)

Table 2 Material properties

Properties	Steel	Aluminum	Graphite/Epoxy (T300/5208)
E_r, GPa	199.95	68.95	50.81
E_z, GPa	199.95	68.95	11.78
G_r, GPa	75.17	25.92	19.38
G_{zr}, GPa	75.17	25.92	4.11
ν_r	0.33	0.33	0.31
ν_{zr}	0.33	0.33	0.06
ρ, density, kg/m^3	7971.8	2768.0	1611

[a] Quasi-isotropic laminate

Downloaded 02 May 2010 to 171.66.16.54. Redistribution subject to ASME license or copyright; see http://www.asme.org/terms/Terms_Use.cfm

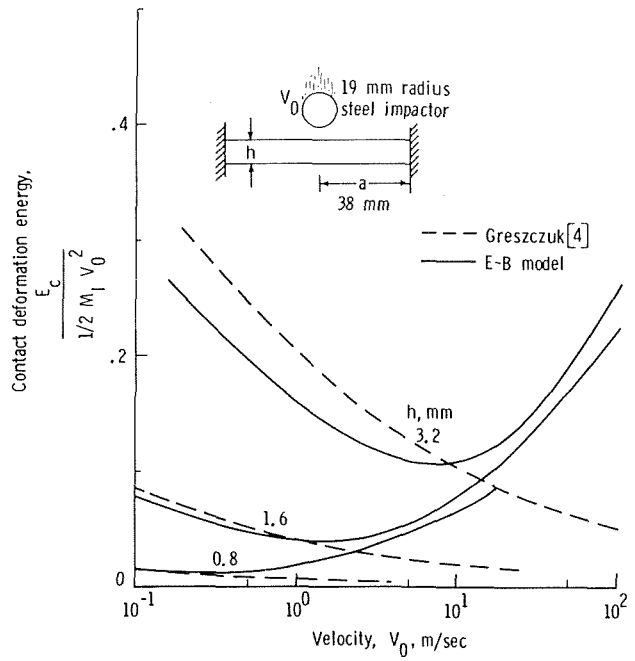

Fig. 3 Predicted contact energy ratio for clamped composite plate (graphite/epoxy quasi-isotropic laminate)

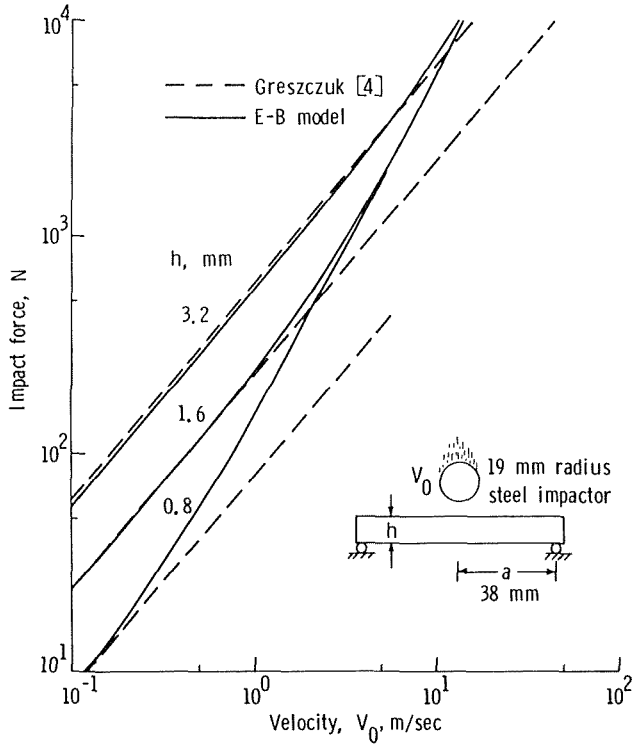

Fig. 4 Predicted impact force for simply-supported plate (graphite/epoxy quasi-isotropic laminate)

brane deformation. Using the force-deflection relation reported in reference [13], the force P is written as

$$P = K_{bs} w + K_m w^3 \tag{6}$$

where $K_{bs} = (K_b K_s)/(K_b + K_s)$ is the effective stiffness due to bending and shear. The constants K_b, K_s, and K_m are bending, shear, and membrane stiffnesses, respectively, of the laminate. Expressions for K_b and K_m for the four plate boundary conditions are given in Table 1. The shear stiffness K_s was derived starting from the shear stress-strain relation for transverse loading of a circular laminate [14]. It is given by

$$K_s = \frac{4\pi G_{zr} h}{3} \left(\frac{E_r}{E_r - 4\nu_{rz} G_{zr}} \right) \left(\frac{1}{4/3 + \log a/a_c} \right) \tag{7}$$

The contact radius a_c is the radius of contact between the impactor and the laminate, which depends on the force P, and which is expressed as [4]

$$a_c = \left[\frac{3\pi}{4} P(K_1 + K_2) R_I \right]^{1/3} \tag{8}$$

The impact force P is initially unknown, hence an initial value of $a_c = h/2$ was used in equation (7) for the estimation of P. The bending-shear energy E_{bs}, and membrane energy E_m of the laminate, were obtained by integrating the forces P_{bs} and P_m (from equations (5) and (6)) with respect to w. Therefore,

$$E_{bs} = \frac{1}{2} K_{bs} w^2 \tag{9}$$

and

$$E_m = \frac{1}{4} K_m w^4 \tag{10}$$

Substituting equations (4), (9), and (10) in equation (1), and then simplifying using equation (6), the energy-balance equation becomes

$$M_I V_0^2 = K_{bs} w^2 + \frac{K_m w^4}{2} + \frac{4}{5} \left[\frac{(K_{bs} w + K_m w^3)^5}{n^2} \right]^{1/3} \tag{11}$$

The deflection w is calculated solving equation (11), using the Newton-Raphson numerical technique. The inverse procedure of calculating the impact velocity for a chosen value of w can also be followed. The impact force P is then calculated by substituting the value of w into equation (6). The analysis was repeated for different plate configurations and impact velocities. Typical results for the *E-B* model are presented in the next section.

Results. The impactor was a steel sphere of radius 19 mm, and the plate was a quasi-isotropic graphite/epoxy laminate of radius 38 mm. Material properties of the impactor and the laminate used in the analysis are given in Table 2. Clamped and simply-supported plate boundaries were examined.

Figure 2 shows impact force versus impact velocity for three different plate thicknesses: 3.2, 1.6, and 0.8 mm for a plate radius of 38 mm. The plate boundary was clamped and edge immoveable. The case of $h = 3.2$ mm ($a/h = 12$) was a moderately thick plate, wherein the transverse shear deformation is significant, and $h = 0.8$ mm was a thin plate wherein the membrane stretching is large. The solid lines represent the *E-B* model results and the broken lines represent Greszczuk's [4] results, in which both large deflection and shear deformation effects were neglected. The two analyses agree over only limited velocity ranges, depending on the plate thickness. Greszczuk's analysis predicts higher impact force for thick plates ($h = 3.2$ mm) than the *E-B* model for not including the transverse shear flexibility (plate deflections were in the small deflection range). At higher velocities, the plate deflection becomes larger and the associated membrane stiffening counteracts shear flexibility; hence, the two results approach each other before crossing at $V_0 = 8.5$ m/sec. For thin plates, the two analyses agree only at very low velocities (less than 1 m/sec, which is not of practical interest); at higher velocities Greszczuk's analysis yields lower impact force than the *E-B* model for not including the membrane stiffening.

Figure 3 shows the variation of contact deformation energy with impact velocity for the same plates. The contact energy is normalized with respect to the kinetic energy of the impactor, i.e., $E_c/(1/2\ M_I V_0^2)$. As before, solid lines represent the *E-B* model results and broken lines represent the Greszczuk analysis. The *E-B* model results show that the contact

Downloaded 02 May 2010 to 171.66.16.54. Redistribution subject to ASME license or copyright; see http://www.asme.org/terms/Terms_Use.cfm

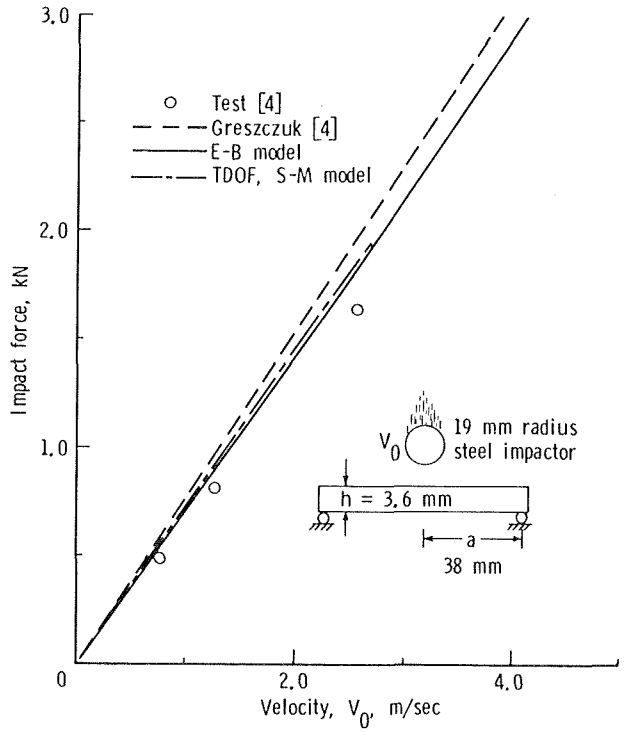

Fig. 5 Test-analysis of impact force versus impact velocity for a simply-supported plate (graphite/epoxy quasi-isotropic laminates)

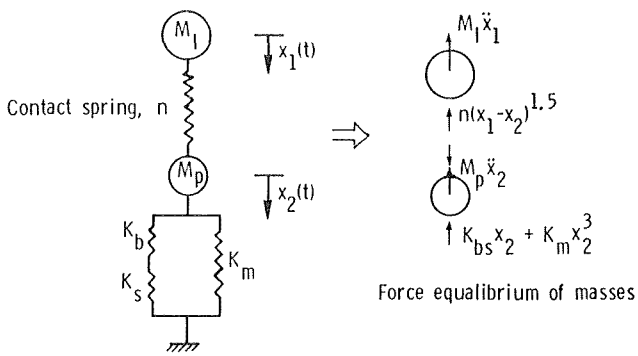

(a) Two degree-of-freedom spring-mass model.

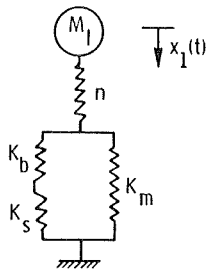

(b) Single degree-of-freedom spring-mass model.

Fig. 6 Spring-mass models for low-velocity impact of a circular plate

deformation energy initially decreases with increase in impact velocity, and finally increases at higher velocities, whereas Greszczuk's analysis shows a monotonic decrease in contact energy. This difference is due to neglecting the effect of large deflection (membrane stiffening) in the Greszczuk's analysis. But the two results agree very well for thin laminates at very low impact velocities (a region of academic interest). Examining the contact energy for thin plates in Fig. 3, one can conclude that contact effects may be neglected for very thin plates.

Figure 4 shows maximum impact force versus velocity for the same plates but with simply supported edges (roller supports). The *E-B* model and the Greszczuk analysis agree well for $h = 3.2$ mm, due to the counteracting effect of membrane stiffening and the transverse shear flexibility in the plate. Furthermore, the two analyses agree for thin plates at very low velocities. But at higher velocities, the *E-B* model predicts higher impact force than the Greszczuk analysis. Comparison of results from Figs. 2 and 4 show that for a given impact velocity, the clamped plate (due to higher bending and membrane stiffness) experiences higher impact force than the simply-supported plate.

Figure 5 compares the predicted and measured [4] impact forces for a simply-supported plate of radius 38 mm and thickness of 3.6 mm. Notice that the ordinate scale in Fig. 5 is linear, whereas in Fig. 4 it was log-log. Calculated impact forces are represented by curves, and the test results [4] by symbols. The broken line (---) is from the spring-mass model, which will be explained in the next section. Results from the *E-B* model agree well with test data at low velocities, and reasonably well at higher velocities. The discrepancy may be due to plate damage during the impact ($P = 1.6$ KN, $V_0 = 2.54$ m/sec). However, predictions from the present *E-B* model are closer to test data than are Greszczuk's predictions.

Spring-Mass Model

Analysis. The energy-balance model presented in the preceding section estimates the impact force fairly accurately. But it does not predict the history of force, velocity or displacement throughout the impact. So an alternate model, namely a "spring-mass" model (*S-M* model), is presented here. The *S-M* model is an extension of Lee's spring-mass model for impact of beams [1]. In the present *S-M* model (Fig. 6), the impactor and the plate were represented by two rigid masses M_I and M_P, respectively. The early studies [15] on free vibrations of plates with an attached central concentrated mass have indicated that the effective mass of the plate contributing to inertial effects is one-fourth of its total mass. Hence, in the present analysis also, the effective plate mass M_p was taken as one-fourth of the total mass of the plate. The two masses were connected through a Hertzian spring that represented the contact load-deformation characteristics [11]. The transverse load-deformation behavior of the plate was represented by a combination of bending, shear, and membrane springs (see Fig. 6(*a*)). The spring combination below the plate mass satisfy the following conditions: impact force is shared by bending, shear and membrane deformations of the plate; for thin plates the spring combination reduces to the thin plate theory due to relatively low bending stiffness ($K_{bs} = 1/(1/K_b + 1/K_s) \approx K_b$); for small plate deflections ($w < 0.2\,h$), the spring combination reduces to the small deflection theory due to relatively small force carried by membrane stretching ($P = K_m w^3$). Bending and membrane stiffness expressions for four types of plate boundaries are given in Table 1; the shear stiffness expression is given by equation (7). Again, material damping, plate damage, and surface friction where neglected.

Let $x_1(t)$ and $x_2(t)$ (see Fig. 6(*a*)) represent the displacement responses of the two masses at any time t after impact. The corresponding velocities were represented by $\dot{x}_1(t)$ and $\dot{x}_2(t)$. The dot indicates the differentiation with respect to time t. The transverse deflection of the plate is given by $w = x_2(t)$ and the contact deformation is given by $\alpha = x_1(t) - x_2(t)$. Throughout the analysis the impactor mass M_I was assumed to be in contact with the plate. Applying Newton's second law of motion, equations of equilibrium of the two degree-of-

Downloaded 02 May 2010 to 171.66.16.54. Redistribution subject to ASME license or copyright; see http://www.asme.org/terms/Terms_Use.cfm

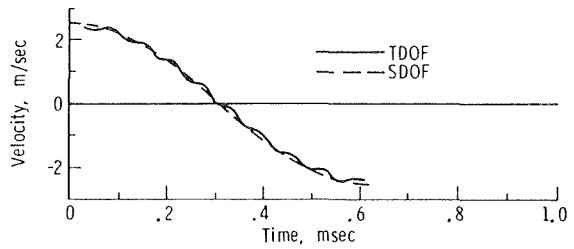

(a) Velocity response of the impactor.

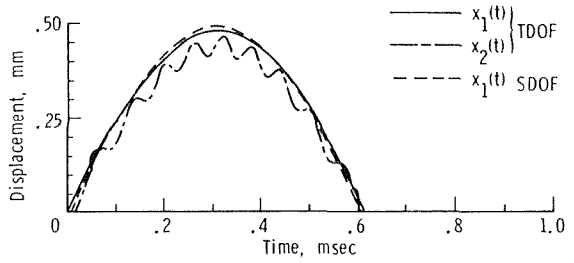

(b) Displacement response of the impactor and the plate.

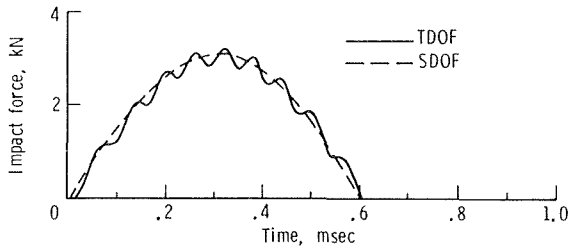

(c) Impact force response.

Fig. 7 Impact response of an aluminum plate using spring-mass models (a = 38mm, h = 3.2mm, steel impactor, R_I = 19mm)

freedom (TDOF) spring-mass systems are written as (see Fig. 6(a))

$$M_I\ddot{x}_1 + \lambda n\,|(x_1 - x_2)|^{1.5} = 0 \tag{12}$$

$$M_P\ddot{x}_2 + K_{bs}x_2 + K_m x_2^3 - \lambda n\,|(x_1 - x_2)|^{1.5} = 0 \tag{13}$$

and

$$\lambda = 1 \quad \text{for} \quad x_1 > x_2$$

$$\lambda = -1 \quad \text{for} \quad x_1 < x_2$$

Initial conditions of the two masses are: $x_1(0) = 0$ and $\dot{x}_1(0) = V_0$ for the mass M_I; and $x_2(0) = \dot{x}_2(0) = 0$ for the plate mass M_P. The coupled nonlinear differential equations were solved using Adam's numerical integration technique. Calculations were stopped when the plate displacement $x_2(t)$ became zero or negative. The impact force experienced by the plate was calculated by substituting $x_2(t)$ in place of w in equation (6).

If the effective plate mass M_P is less than 0.071 times the impactor mass (or impactor mass M_I is greater than 3.5 times the total plate mass), reference 15 suggested that the plate mass could be neglected. The two degree-of-freedom system then reduces to a single degree-of-freedom (SDOF) system as shown in Fig. 6(b). Then the equation of equilibrium of M_I is written as

$$M_I\ddot{x}_1 + K_{bs}w + K_m w^3 + n\alpha^{1.5} = 0 \tag{14}$$

and

$$x_1 = w + \alpha \tag{15}$$

Initial conditions are $t = 0$, $x_1(0) = 0$, and $\dot{x}_1(0) = V_0$.

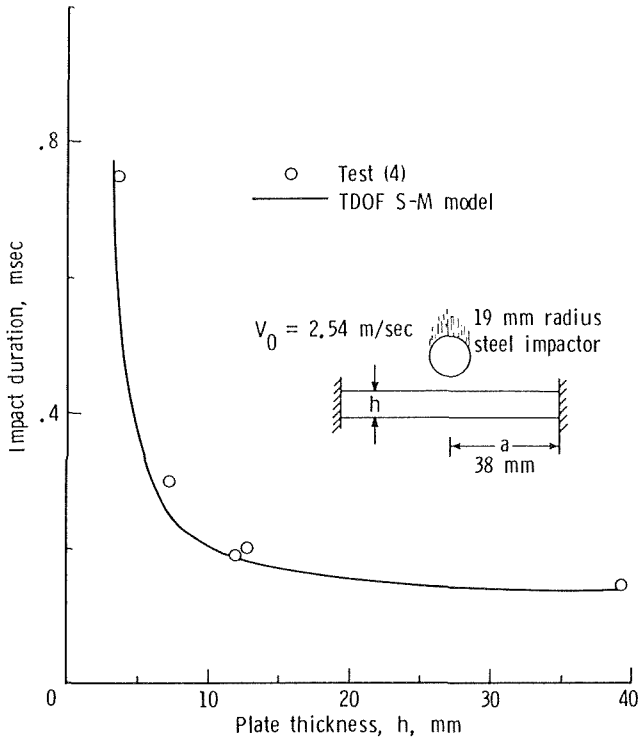

Fig. 8 Influence of plate thickness on impact duration for an aluminum plate

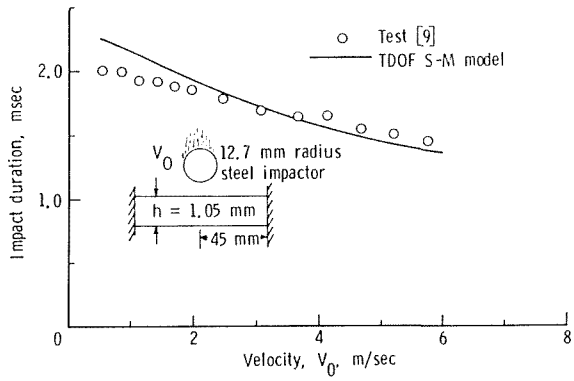

(a) Predicted and measured impact duration.

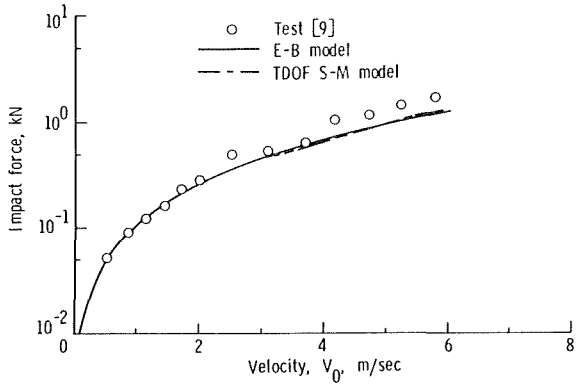

(b) Predicted and measured impact force.

Fig. 9 Impact on a clamped graphite/epoxy quasi-isotropic laminate

Equations (14) and (15) were solved numerically for $x_1(t)$ and P as before. It may be noted here that the energy-balance equation (11) is the time integral of the equation (14).

Downloaded 02 May 2010 to 171.66.16.54. Redistribution subject to ASME license or copyright; see http://www.asme.org/terms/Terms_Use.cfm

Results. Impact force and the duration due to an impact of a steel ball on a circular plate were calculated using the *S-M* model. Two impactor sizes 19 mm and 12.8 mm, and two types of plate materials, aluminum and graphite/epoxy, were used in the analysis. The analysis was first verified by comparing the calculated impact durations with reported test results [4] for aluminum plates. Then, impact force and the duration were calculated for graphite/epoxy laminates, and compared with reported results.

Figure 7 shows velocity, displacement, and force responses of impactor and plate when a steel ball of radius 19 mm impacted on an aluminum plate (a = 38 mm) at a velocity of 2.54 m/sec. Solid lines represent the two degree-of-freedom (TDOF) spring-mass results and broken lines represent the single degree-of-freedom (SDOF) spring-mass results. In Fig. 7(a), the velocity of the impactor decreases from an initial velocity of 2.54 m/sec to zero and then to −2.54 m/sec. The incident and the rebound velocities were equal because energy losses in the system were neglected. The time elapsed during the impactor velocity excursion from +2.54 m/sec to −2.54 m/sec is defined as the impact duration. The duration was 0.607 m/sec from both TDOF and SDOF analyses. The perturbations in the TDOF results are due to interacting inertial forces of the two masses.

Figure 7(b) shows the displacement response of the impactor (x_1) and the plate (x_2) masses calculated from the two spring-mass models. The impactor and target displacements were zero initially and then attained maximum when the impactor velocity reached zero, before becoming zero again. In the case of the TDOF analysis, the plate displacement x_2 was higher than the impactor x_1 for a few microseconds in the early part and later part of the impact event. The separation of masses was not allowed, since the impactor was assumed in contact with the plate throughout the analysis. These small disturbances were due to inertial effects of the plate; inclusion of material damping would have reduced these disturbances.

Figure 7(c) shows variation of plate reaction with time. The absolute maximum reaction experienced by the plate during the impact event is defined as the impact force. The SDOF curve passes through the mean of the TDOF results. In Fig. 7(a)-(c) (M_I/M_P = 23), the TDOF and SDOF agree very well; hence, for large ratio of impactor mass to plate mass, the inertial effects of the plate may be neglected.

Figure 8 compares predicted and measured [4] impact durations on aluminum plates of various thicknesses. The solid line represents the TDOF *S-M* model results and symbols are from test data [4]. The analysis agrees reasonably well with test results. The discrepancy may be due to two main assumptions in the analysis: the plate is perfectly elastic, whereas in the tests local plastic deformation is possible; and the boundary is perfectly clamped, whereas, actually, rubber grip pads were used in the test [4]. Furthermore, impact duration is seen to decrease with plate thickness.

Returning to Fig. 5, it shows the comparison of impact force calculated from spring-mass model, energy-balance model, and Greszczuk's analysis and test data [4] for simply-supported composite plates. Calculated forces from the spring-mass model and energy-balance model agree very well, and both agree with test data, except at the higher impact velocity.

Figure 9(a) shows the comparison of predicted and measured [9] impact duration for a clamped composite plate at various velocities. The plate was an eight-ply graphite/epoxy composite with quasi-isotropic laminate and 45 mm radius. The TDOF spring-mass model results agree with test data [9], except at low velocities. Calculated impact forces (Fig. 9(b)) for the same configurations agree reasonably well with test data [9]. Results from the energy-balance model are also shown and are very close to the TDOF spring-mass model results.

Conclusions

Two simple and improved models, an energy-balance model and a spring-mass model, were developed to calculate impact force and duration associated with low-velocity impact on circular composite plates. Both models include the contact deformation of the plate and the impactor as well as the bending, shear, and membrane deformations of the plate. The plate materials were transversely isotropic graphite/epoxy laminate or aluminum and the impactor was a steel sphere.

The energy-balance model was based on the principle of conservation of total energy. This analysis yielded a simple energy-balance equation, which was used to calculate maximum impact force. The spring-mass model was based on the response analysis of the plate and the impactor assuming them as a combination of rigid masses and springs. The resulting equations were solved to calculate the impact force history. The analysis led to the following conclusions:

1. The energy-balance model is simple, and accurately predicts the maximum impact force; the spring-mass model, which is less simple, predicts the complete force history.

2. Impact forces calculated from the two models agreed with each other and with reported data. Also, impact durations from the spring-mass model agreed with reported test data.

3. Thin plates undergo membrane stretching and the calculated impact forces are greater than those based on small deflection theory.

4. Thick plates undergo significant transverse shear deformation that must be accounted to predict the impact force accurately.

5. When the impactor mass is large compared to the plate mass, the inertial effects of the plate are negligible. Hence, the plate-impactor system could be represented by a single degree-of-freedom system.

References

1 Lee, E. H., "Impact of a Mass Striking a Beam," ASME JOURNAL OF APPLIED MECHANICS, Dec. 1940, pp. A-129–A-138.

2 Goldsmith, W., *Impact*, Edward Arnold Ltd., London, 1960.

3 Preston, J. L., Jr., and Cook, T. S., "Impact Response of Graphite/Epoxy Flat Laminates Using Projectiles That Simulate Aircraft Engine Encounters," ASTM STP568, American Society for Testing Materials, 1975, pp. 49–71.

4 Greszczuk, L. B., "Damage in Composite Materials Due to Low Velocity Impact," in Zukas, J. A., et al. eds., *Impact Dynamics*, John Wiley & Sons, New York, 1982.

5 Sun, C. T., and Chattopadhyay, S., "Dynamic Response of Anisotropic Plates Under Initial Stress Due to Impact of a Mass," ASME JOURNAL OF APPLIED MECHANICS, Vol. 42, 1975, pp. 693–698.

6 Dobyns, A. L., and Porter, T. R., "A Study of the Structural Integrity of Graphite/Epoxy Composite Structure Subjected to Low Velocity Impact," *Polymer Engineering and Science*, Vol. 21, June 1981, pp. 493–498.

7 Dobyns, A. L., "Analysis of Simply-Supported Orthotropic Plates Subjected to Static and Dynamic Loads," AIAA paper No. 80-0680, 1980.

8 Elber, W., "Failure Mechanics in Low-Velocity Impacts on Thin Composite Plates," NASA TP 2152, May 1983.

9 Lal, K. M., "Prediction of Residual Tensile Strength of Transversely Impacted Composite Laminates," Housner, J. M., and Noor, A. K., eds., *Research in Structural and Solid Mechanics*, NASA CP 2245, 1982, pp. 97–112.

10 Lord Rayleigh, "On the Prediction of Vibrations by Forces of Relatively Long Duration, With Application to the Theory of Collisions," *Philosophical Magazine*, Series 6, Vol. 11, 1906, pp. 283–292.

11 Conway, H. D., and Angew, Z., "The Pressure Distribution Between Two Elastic Bodies in Contact," *Journal of Mathematics and Physics*, Vol. 7, 1956, pp. 460–465.

12 Timoshenko, S. P., and Woinowsky, S., *Theory of Plates and Shells*, McGraw-Hill, New York, 1959.

13 Volmir, A. S., "A Translation of Flexible Plates and Shells," AFFDL-TR-66-216, Apr. 1967.

14 Lukasiewiez, S. A., "Introduction of Concentrated Loads in Plates and Shells," *Progress in Aerospace Science*, Vol. 17, 1976, pp. 109–146.

15 Leissa, A. W., "Vibrations of Plates," NASA SP-160, 1969.

Downloaded 02 May 2010 to 171.66.16.54. Redistribution subject to ASME license or copyright; see http://www.asme.org/terms/Terms_Use.cfm

V. I. Fabrikant
Department of Mechanical Engineering,
Concordia University,
Montreal, Quebec, Canada H3G 1M8

A. P. S. Selvadurai
Department of Civil Engineering,
Carleton University,
Ottawa, Ontario, Canada K1S 5B6

G. D. Xistris
Department of Mechanical Engineering,
Concordia University,
Montreal, Quebec, Canada, H3G 1M8
Mem. ASME

Asymmetric Problem of Loading Under a Smooth Punch

This paper examines the three-dimensional elastostatic problem related to the interaction between a smoothly indenting rigid circular punch on a transversely isotropic elastic half-space and an internal concentrated force. The localized force acts at an arbitrary point within the half-space region. The analysis of the problem focuses on the evaluation of the resultant displacement and rotation experienced by the rigid punch.

Introduction

Classical elastostatic contact problems are primarily concerned with the indentation of an elastic body, such as a half-space region, by a directly loaded rigid punch with an arbitrary planform. Extensive accounts of this class of contact problems dealing with the rigid indentors possessing either smooth, adhesive, or frictional interfaces are given by Galin [1], Lur'e [2], De Pater and Kalker [3], and Gladwell [4]. In a different category of elastostatic problems, the contact between the rigid indentor and the elastic half-space region is perturbed by forces that are applied at the interior of the half-space region. This class of problems is of particular interest to geomechanical applications wherein the internal forces can be visualized as forces transmitted by anchoring regions located in the vicinity of structural foundations [5]. Also in the particular case when the internal force migrates to the traction-free surface of the half-space the resulting problem models the interaction between existing structural foundation and a surcharge load applied in its vicinity [6].

This paper examines the three-dimensional elastostatic contact problem of a rigid circular punch resting in a smooth contact with the surface of a transversely isotropic elastic medium. The punch is subjected to external loads which act directly on the punch and internal forces which act at the interior of the transversely isotropic elastic half-space region. The external loads correspond to central force N and a moment M which acts about the y-axis. The internal loading corresponds to a concentrated force P which acts at the location (r,θ,h) and along the positive z-direction. It is assumed that throughout the application of the loads N, M, and P complete contact is maintained at the smooth interface. The analysis of the three-dimensional contact problem yields results for the rigid displacement and rotation experienced by the punch due to the application of the combined loading system. Specific results are developed for the situations where locally distributed external surface loads are applied at the half-space region exterior to the indenting rigid circular punch.

Contributed by the Applied Mechanics Division for publication in the JOURNAL OF APPLIED MECHANICS.

Discussion on this paper should be addressed to the Editorial Department, ASME, United Engineering Center, 345 East 47th Street, New York, N.Y. 10017, and will be accepted until two months after final publication of the paper itself in the JOURNAL OF APPLIED MECHANICS. Manuscript received by ASME Applied Mechanics Division, December, 1983; final revision, September, 1984.

Formulation of the Problem and Solution

Consider a transversely isotropic half-space $z \geq 0$ with the planes of elastic symmetry parallel to the boundary. A smooth circular flat-ended punch of radius a is pressed against the half-space by an axial force N and is acted upon by a moment M about the y-axis. An additional force P is applied in the positive z-direction at an arbitrary point (r,θ,h) inside the half-space region. The analysis concentrates on the assessment of stresses developed at the punch elastic half-space interface and the determination of relationships between the forces applied and the corresponding generalized displacements of the punch.

Let δ denote the normal displacement of the punch. Introduce the complex angular displacement.

$$\gamma_c = \gamma_x + i\gamma_y = \gamma e^{i\psi} \tag{1}$$

Considering the linear-elastostatic boundary-value problem, it can be shown that the governing integral equation is

$$H\int_0^a \int_0^{2\pi} \frac{\sigma(\rho_0,\phi_0)\rho_0 d\rho_0 d\phi_0}{\sqrt{\rho^2+\rho_0^2-2\rho\rho_0\cos(\phi-\phi_0)}} = w(\rho,\phi) \tag{2}$$

Here σ denotes the normal stresses at the contact region, and w is the normal displacement. Since the indenting punch is rigid, its displacements due to the simultaneous action of N, P and M can be written in the form

$$w(\rho,\phi) = \delta + \gamma\ \rho\ \sin(\phi-\psi) - \frac{PH}{\nu_1^2-\nu_2^2}\left[\frac{D_1}{R_1} - \frac{D_2}{R_2}\right] \tag{3}$$

where

$$H = \frac{(\nu_1+\nu_2)C_{11}}{2\pi(C_{11}C_{33}-C_{13}^2)}, \quad \nu_{1,2}{}^2 = Q \pm \sqrt{Q^2 - C_{33}/C_{11}} \tag{4}$$

Copyright © 1985 by ASME
Downloaded 02 May 2010 to 171.66.16.54. Redistribution subject to ASME license or copyright; see http://www.asme.org/terms/Terms_Use.cfm

$$Q=(C_{11}C_{33}-C_{13}^2-2C_{13}C_{44})/2C_{11}C_{44},$$

$$D_j=\nu_j^2+C_{13}/C_{11};\ j=1,2$$

$$R_j^2=\rho^2+r^2-2\rho r\cos(\phi-\theta)+h_j^2,\ h_j=h/\nu_j$$

and C_{ij} are the elastic constant of the half-space. The last term in (3) is essentially the surface displacement, derived for the Mindlin's problem in [7].

The exact closed-form solution of (2) is given in [8] as

$$\sigma(y,\phi)=-\frac{1}{\pi^2 Hy}L(y)\frac{d}{dy}\int_y^a\frac{tdt}{\sqrt{t^2-y^2}}$$

$$L\left(\frac{1}{t^2}\right)\frac{d}{dt}\int_0^t\frac{\rho d\rho}{\sqrt{t^2-\rho^2}}L(\rho)w(\rho,\phi) \tag{5}$$

Here the operator L is understood as

$$L(k)f(\rho,\phi)=\sum_{n=-\infty}^{\infty}k^{|n|}f_n(\rho)e^{in\phi}, \tag{6}$$

and $f_n(\rho)$ are the Fourier coefficients of $f(\rho,\phi)$

$$f_n(\rho)=\frac{1}{2\pi}\int_0^{2\pi}f_n(\rho,\phi)e^{-in\phi}d\phi \tag{7}$$

The following integral representation of L is valid for $|k|<1$

$$L(k)f(\rho,\phi)=\frac{1}{2\pi}\int_0^{2\pi}\lambda(k,\phi-\phi_0)f(\rho,\phi_0)d\phi_0 \tag{8}$$

where

$$\lambda(k,\psi)=\frac{1}{1-ke^{i\psi}}+\frac{1}{1-ke^{-i\psi}}-1=\frac{1-k^2}{1+k^2-2k\cos\psi} \tag{9}$$

Notice the properties of the L-operators [8]

$$L(k)L(k_1)=L(kk_1),\ L(1)f=f \tag{10}$$

Formal substitution of (3) into (5) gives the solution to the problem. Evaluation of all the integrals is elementary, except for the integral involving R_j. Some preliminary considerations are necessary. The following integral representation was established in [8]

$$\frac{1}{R}=\frac{1}{\sqrt{\rho^2+\rho^2-2\rho\rho_0\cos(\phi-\phi_0)}}=\frac{2}{\pi}$$

$$\int_0^{\min(\rho,\rho_0)}\frac{\lambda\left(\frac{x^2}{\rho\rho_0},\phi-\phi_0\right)dx}{\sqrt{\rho^2-x^2}\sqrt{\rho_0^2-x^2}} \tag{11}$$

Strictly speaking, R_j is different from R but some algebraic transformations can make them similar, so that the representation (11) can be applied, namely

$$\frac{1}{R_j}=\frac{1}{\sqrt{l_{1j}^2+l_{2j}^2-2l_{1j}l_{2j}\cos(\phi-\theta)}} \tag{12}$$

Here

$$l_{kj}=\frac{1}{2}\left(\sqrt{(\rho+r)^2+h_j^2}+(-1)^k\sqrt{(\rho-r)^2+h_j^2}\right) \tag{13}$$

Notice also that

$$l_{1j}l_{2j}=\rho r,\quad l_{1j}^2+l_{2j}^2=\rho^2+r^2+h_j^2 \tag{14}$$

Now the following integral representation of R_j^{-1} is valid

$$\frac{1}{R_j}=\frac{2}{\pi}\int_0^{l_{1j}}\frac{\lambda\left(\frac{x^2}{\rho r},\phi-\theta\right)dx}{\sqrt{l_{1j}^2-x^2}\sqrt{l_{2j}^2-x^2}} \tag{15}$$

Using properties of the L-operators, one finds

$$L(\rho)\frac{1}{R_j}=\frac{2}{\pi}\int_0^{l_{1j}}\frac{\lambda\left(\frac{x^2}{r},\phi-\theta\right)dx}{\sqrt{l_{1j}^2-x^2}\sqrt{l_{2j}^2-x^2}} \tag{16}$$

Now it is necessary to evaluate the integral in (5)

$$\int_0^t\frac{\rho d\rho}{\sqrt{t^2-\rho^2}}L(\rho)\frac{1}{R_j} \tag{17}$$

Substituting (16) into (17) and changing the order of integration yields

$$\frac{2}{\pi}\int_0^t\frac{\rho d\rho}{\sqrt{t^2-\rho^2}}\int_0^{l_{ij}}\frac{\lambda\left(\frac{x^2}{r},\phi-\theta\right)dx}{\sqrt{l_{1j}^2-x^2}\sqrt{l_{2j}^2-x^2}}$$

$$=\frac{2}{\pi}\int_0^{l_{ij}(t)}\frac{\lambda\left(\frac{x^2}{r},\phi-\theta\right)dx}{\sqrt{r^2-x^2}}$$

$$\int_{g_j(x)}^t\frac{\rho d\rho}{\sqrt{t^2-\rho^2}\sqrt{\rho^2-g_j^2(x)}}=\int_0^{l_{ij}(t)}\frac{\lambda(x^2/r,\phi-\theta)}{\sqrt{r^2-x^2}} \tag{18}$$

Here the properties (14) were used, and the integral

$$\int_a^b\frac{\rho d\rho}{\sqrt{b^2-\rho^2}\sqrt{\rho^2-a^2}}=\frac{\pi}{2}$$

The notations introduced in (18) are

$$l_{kj}(t)=\frac{1}{2}\left[\sqrt{(r+t)^2+h_j^2}+(-1)^k\sqrt{(r-t)^2+h_j^2}\right]$$

$$g_j(x)=x\sqrt{1+\frac{h_j^2}{r^2-x^2}} \tag{19}$$

Substitution of (18) in (5) allows the evaluation of the contact stresses in the following form

$$\sigma(\rho,\phi)=\frac{\delta+2\gamma\rho\sin(\phi-\theta)}{\pi^2 H\sqrt{a^2-\rho^2}}-\frac{P}{{\nu_1}^2-{\nu_2}^2}$$

$$[D_1\sigma_1(\rho,\phi)-D_2\sigma_2(\rho,\phi)] \tag{20}$$

where

$$\sigma_j(\rho,\phi)=-\frac{1}{\pi^2\rho}L(\rho)\frac{d}{d\rho}\int_\rho^a\lambda\left(\frac{l_{ij}^2(t)}{rt^2},\phi-\theta\right)$$

$$\frac{t\,dl_{1j}(t)}{\sqrt{t^2-\rho^2}\sqrt{r^2-l_{1j}^2(t)}} \tag{21}$$

Integration and differentiation in (21) can be performed, and the result can be expressed in elementary functions:

$$\sigma_j(\rho,\phi)=\frac{1}{\pi^2}\frac{h_j}{R_j^3}\left[\frac{R_j}{\xi_j}+\tan^{-1}\frac{\xi_j}{R_j}\right],$$

where

$$\xi_j=\frac{h_j\sqrt{a^2-\rho^2}}{\sqrt{l_{2j}^2(a)-a^2}}$$

and l_{2j} is defined by (19). In the particular case of $h=0$, $l_{2j}(a)=r$, and the following simplification takes place:

$$\sigma_j(\rho,\phi)=\frac{1}{\pi^2}\frac{\sqrt{r^2-a^2}}{\sqrt{a^2-\rho^2}(r^2+\rho^2-2r\rho\cos(\phi-\theta))}, \tag{22}$$

which is in correspondence with the result reported in [8].

The integral of stresses should give the axial force N

$$N=\int_0^a\int_0^{2\pi}\sigma(\rho,\phi)\rho d\rho d\phi \tag{23}$$

Integration of (21) can be performed as follows

$$\int_0^a\int_0^{2\pi}\sigma_j(\rho,\phi)\rho d\rho d\phi$$

$$=\frac{2}{\pi}\int_0^a\frac{d\,l_{1j}(t)}{\sqrt{r^2-l_{1j}^2(t)}}=\frac{2}{\pi}\sin^{-1}\left(\frac{l_{1j}(a)}{r}\right) \tag{24}$$

Downloaded 02 May 2010 to 171.66.16.54. Redistribution subject to ASME license or copyright; see http://www.asme.org/terms/Terms_Use.cfm

The remaining integrals are elementary, and the final result for N takes the form:

$$N=\frac{2}{\pi}\left[\frac{a\delta}{H}-\frac{P}{\nu_1{}^2-\nu_2{}^2}\left(D_1\sin^{-1}\frac{l_{11}(a)}{r}-D_2\sin^{-1}\left(\frac{l_{12}(a)}{r}\right)\right)\right] \tag{25}$$

Introduce the complex moment

$$M=M_x+iM_y \tag{26}$$

From the equilibrium considerations

$$M=-i\int_0^a\int_0^{2\pi}\sigma(\rho,\phi)\rho^2e^{i\phi}d\rho d\phi \tag{27}$$

Again the integration of (21) can be performed in the following manner:

$$-i\int_0^a\int_0^{2\pi}\sigma_j(\rho,\phi)\rho^2e^{i\phi}d\rho d\phi=\frac{2i}{\pi}$$

$$\int_0^a\rho^2d\rho\frac{d}{d\rho}\int_\rho^a e^{i\theta}\frac{l_{1j}^2(t)dl_{1j}(t)}{rt\sqrt{t^2-\rho^2}\sqrt{r^2-l_{1j}^2(t)}}$$

$$=-\frac{4i}{\pi}\int_0^a\rho d\rho\int_\rho^a\frac{e^{i\theta}l_{1j}^2(t)dl_{1t}(t)}{rt\sqrt{t^2-\rho^2}\sqrt{r^2-l_{1j}^2(t)}}$$

$$=-\frac{4i}{\pi}\frac{e^{i\theta}}{r}\int_0^a\frac{l_{1j}^2(t)dl_{1j}(t)}{t\sqrt{r^2-l_{1j}^2(t)}}\int_0^t\frac{\rho d\rho}{\sqrt{t^2-\rho^2}}$$

$$=-\frac{4i}{\pi}\frac{e^{i\theta}}{r}\int_0^a\frac{l_{1j}^2(t)dl_{1j}(t)}{\sqrt{r^2-l_{1j}^2(t)}}$$

$$=-\frac{2i}{\pi}e^{i\theta}\left[r\sin^{-1}\left(\frac{l_{1j}(a)}{r}\right)-l_{1j}(a)\sqrt{1-\frac{l_{1j}^2(a)}{r^2}}\right] \tag{28}$$

The expression for the moment can be written as

$$M=\frac{2}{\pi}\left[\frac{2}{3}a^3\gamma e^{i\psi}+\frac{P\,i\,e^{i\theta}}{\nu_1{}^2-\nu_2{}^2}(D_1f_1(r)-D_2f_2(r))\right] \tag{29}$$

where the notations

$$f_j(r)=r\sin\frac{l_j(r)}{r}-l_j(r)\sqrt{1-\frac{l_j{}^2(r)}{r^2}} \tag{30}$$

$$l_j(r)=\frac{1}{2}\left[\sqrt{(r+a)^2+h_j^2}-\sqrt{(r-a)^2+h_j^2}\right]\quad\text{for}\quad j=1,2 \tag{31}$$

were introduced for convenience.

When M and P are prescribed, the angle of inclination of the punch γ and its direction ψ can be defined from (29) by separation of the real and imaginary parts. For the case $M=0$, $\psi=\theta-\pi/2$, and the modulus of the angle of inclination is defined by

$$\gamma=\frac{3P}{2a^3(\nu_1^2-\nu_2^2)}[D_1f_1(r)-D_2f_2(r)] \tag{32}$$

The value of the moment, which equilibrates the action of the force P, can be obtained, from (29), as

$$M_e=\frac{2}{\pi}\frac{P\,i\,e^{i\theta}}{\nu_1{}^2-\nu_2{}^2}[D_1f_1(r)-D_2f_2(r)] \tag{33}$$

Examples

Consider the case of a uniformly distributed loading of stress intensity p, acting over the segment $\theta_1\le\theta\le\theta_2$, $r_1\le r\le r_2$. The relationship between the normal displacement and the applied forces can be obtained from (25). The result is

$$N=\frac{2}{\pi}\left[\frac{a\delta}{H}+\frac{p(\theta_2-\theta_1)}{\nu_1{}^2-\nu_2{}^2}\sum_{j=1}^{2}(-1)^jD_j(\chi_j(r_2)-\chi_j(r_1))\right] \tag{34}$$

where

$$\chi_j(r)=\int r\sin^{-1}\frac{l_j(r)}{r}dr=\frac{r^2}{2}\sin^{-1}\frac{l_j(r)}{r}+\frac{h_j[2a^2-l_j^2(r)]}{2\sqrt{a^2-l_j^2(r)}} \tag{35}$$

Integration by parts was used to obtain (35) with subsequent change of variable.

$$r=y\sqrt{1+\frac{h_j^2}{a^2-y^2}},\quad l_j(r)=y \tag{36}$$

The relationship between the angular displacement and the moment takes the form

$$M=\frac{2}{\pi}\left[\frac{2}{3}a^3\gamma e^{i\psi}-\frac{p(e^{i\theta_2}-e^{i\theta_1})}{\nu_1{}^2-\nu_2{}^2}\sum_{j=1}^{2}(-1)^jD_j(F_j(r_2)-F_j(r_1))\right] \tag{37}$$

Here

$$F_j(r)=\int f_j(r)rdr=\frac{r^3}{3}\sin^{-1}\left(\frac{l_j(r)}{r}\right)+\frac{r(a^2-2l_j^2(r))}{3l_j(r)}\sqrt{r^2-l_j^2(r)}+\frac{2a^3}{3}\tanh^{-1}\left[\frac{l_j(r)}{a}\sqrt{1-\frac{l_j^2(r)}{r^2}}\right]-\frac{h_j(3a^2+h_j^2)}{3}\sin^{-1}\left(\frac{l_j(r)}{\sqrt{a^2+h_j^2}}\right) \tag{38}$$

The integration (38) was performed by parts and using the substitution (36). It is evident from (37) that for the case of complete annulus $\theta_1=0$, $\theta_2=2\pi$, and the last term in (37) becomes equal to zero, simplifying (37) as

$$M=\frac{4a^3}{3\pi}\gamma e^{i\psi} \tag{39}$$

Other cases of loading can also be considered. The integration becomes more complicated. For example, for the case of loading $p=k\rho$, formula (34) takes the form

$$N=\frac{2}{\pi}\left[\frac{a\delta}{H}+\frac{k(\theta_2-\theta_1)}{\nu_1{}^2-\nu_2{}^2}\sum_{j=1}^{2}(-1)^jD_j(\xi_j(r_2)-\xi_j(r_1))\right] \tag{40}$$

Here

$$\xi_j(r)=\int r^2\sin^{-1}\frac{l_j(r)}{r}dr=\frac{r^3}{3}\sin^{-1}\frac{l_j(r)}{r}+\frac{h_jr(2a^2-l_j^2(r))}{6\sqrt{a^2-l_j^2(r)}}+\frac{a(a^2-3h_j^2)}{6}\tanh^{-1}\left[\frac{l_j(r)}{a}\sqrt{1-\frac{l_j^2(r)}{r^2}}\right]-\frac{h_j(3a^2-h_j^2)}{6}\sin^{-1}\frac{l_j(r)}{\sqrt{a^2+h_j^2}} \tag{41}$$

Discussion

Some particular cases are of interest. Consider the geometric interpretation of $l_j(r)$; as one can see, the maximum value of l_j is a, therefore certain simplification can be obtained in (29) for $a/r<<1$, namely

$$M=\frac{4}{3\pi}\left[a^3\gamma_c-\frac{M_p}{\nu_1{}^2-\nu_2{}^2}\left(D_1\frac{l_1^3(r)}{r^3}-D_2\frac{l_2^3(r)}{r^3}\right)\right] \tag{42}$$

Downloaded 02 May 2010 to 171.66.16.54. Redistribution subject to ASME license or copyright; see http://www.asme.org/terms/Terms_Use.cfm

where

$$M_p = -i\,r\,P\,e^{i\theta} \tag{43}$$

is the complex moment of the force P about the origin. Formula (42) shows that the influence of the force P on the angular displacement of the punch is reduced approximately proportionally to the order of the cube of the ratio $l_j(r)/r$.

Significant simplifications occur with $h \to 0$ formulas (20), (25), and (29) take the form

$$\sigma(\rho,\phi) = \frac{\delta + 2\gamma\rho\sin(\phi-\psi)}{\pi^2 H\sqrt{a^2-\rho^2}} - \frac{P}{\pi^2}\,\frac{\sqrt{r^2-a^2}}{\sqrt{a^2-\rho^2}(\rho^2+r^2-2\rho r\cos(\phi-\theta))} \tag{44}$$

$$N = \frac{2}{\pi}\left[\frac{a\delta}{H} - P\sin^{-1}\frac{a}{r}\right] \tag{45}$$

$$M = \frac{2}{\pi}\left[\frac{2}{3}a^3\,\gamma\,e^{i\psi} + P\,i\,e^{i\theta}\left(r\sin^{-1}\frac{a}{r} - a\sqrt{1-\frac{a^2}{r^2}}\right)\right] \tag{46}$$

Formulas (44), (45), and (46) are in agreement with the results reported in [9]. Formulas (34), (37), and (40) change with $h \to 0$ as follows

$$N = \frac{2}{\pi}\left\{\frac{a\delta}{H} - p(\theta_2-\theta_1)[\chi(r_2)-\chi(r_1)]\right\} \tag{47}$$

where

$$\chi(r) = \frac{r^2}{2}\sin^{-1}\frac{a}{r} + \frac{a\sqrt{r^2-a^2}}{2}$$

$$M = \frac{2}{\pi}\left\{\frac{2}{3}a^3\gamma e^{i\psi} + p(e^{i\theta_2} - e^{i\theta_1})[F(r_2)-F(r_1)]\right\} \tag{48}$$

where

$$F(r) = \frac{r^3}{3}\sin^{-1}\frac{a}{r} - \frac{ar}{3}\sqrt{r^2-a^2} + \frac{2}{3}\tanh^{-1}\sqrt{1-\frac{a^2}{r^2}} \tag{49}$$

$$N = \frac{2}{\pi}\left\{\frac{a\delta}{H} - k(\theta_2-\theta_1)[\xi(r_2)-\xi(r_1)]\right\} \tag{50}$$

where

$$\xi(r) = \frac{r^3}{3}\sin^{-1}\frac{a}{r} - \frac{ra}{6}\sqrt{r^2-a^2} + \frac{a^3}{6}\tanh^{-1}\sqrt{1-\frac{a^2}{r^2}} \tag{51}$$

Notice that

$$\lim_{h\to 0}\frac{h_j}{\sqrt{a^2-l_j^2(r)}} = \frac{\sqrt{r^2-a^2}}{a} \tag{52}$$

All the results presented are valid for the case of an isotropic body provided that

$$H = (1-\nu^2)/\pi E,\quad D_1 = D_2 = (1-\nu)^{-1},\quad \nu_1 = \nu_2 = 1 \tag{53}$$

where ν is the Poisson ratio and E is the modulus of elasticity. Formulas (25) and (29) will change for the case of isotropy as follows

$$N = \frac{2}{\pi}\left\{\frac{\pi E}{1-\nu^2}a\delta - P\left[\sin^{-1}\left(\frac{l_{10}}{r}\right) + \frac{h^2 l_{10}}{2(1-\nu)\sqrt{r^2-l_{10}^2}(l_{20}^2-l_{10}^2)}\right]\right\} \tag{54}$$

$$M = \frac{2}{\pi}\left\{\frac{2}{3}a^3\,\gamma\,e^{i\psi} + P\,i\,e^{i\theta}\left[f(r) + \frac{1}{1-\nu}f'(r)\right]\right\}, \tag{55}$$

where

$$l_{10} = \frac{1}{2}\left[\sqrt{(r+a)^2+h^2} - \sqrt{(r-a)^2+h^2}\right],$$

$$l_{20} = \frac{1}{2}\left[\sqrt{(r+a)^2+h^2} + \sqrt{(r-a)^2+h^2}\right],$$

$$f(r) = r\sin^{-1}\frac{l_{10}}{r} - l_{10}\sqrt{1-\frac{l_{10}^2}{r^2}}$$

$$f'(r) = \frac{h^2 l_{10}^3}{r\sqrt{r^2-l_{10}^2}(l_{20}^2-l_{10}^2)}$$

Notice that for $h \to 0$ formulas (54) and (55) correspond to (45) and (46). It is of interest to compare the results of an action of a concentrated force P with those of a uniform pressure

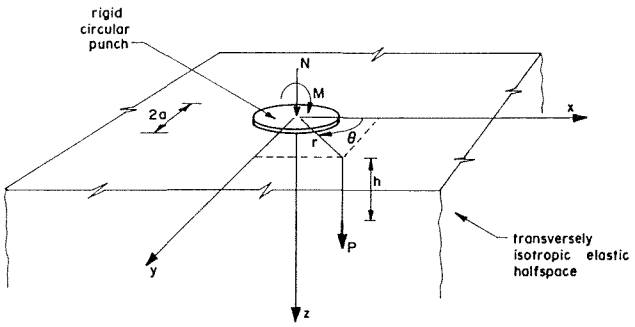

Fig. 1 Scheme of loading

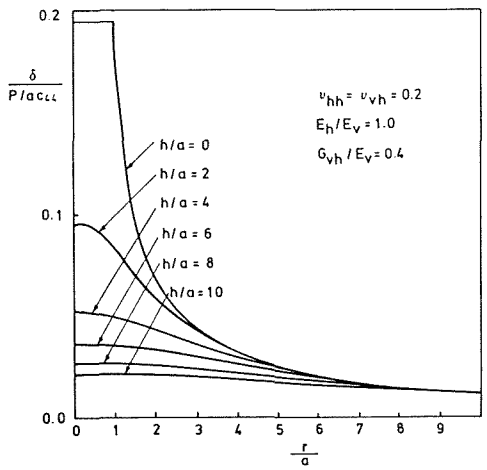

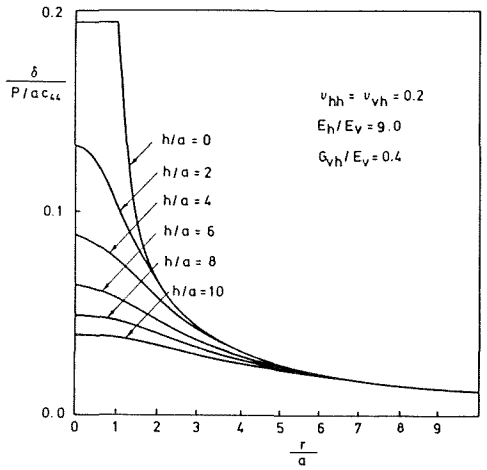

Fig. 2 Axial displacement of the rigid punch due to action of internal force

Downloaded 02 May 2010 to 171.66.16.54. Redistribution subject to ASME license or copyright; see http://www.asme.org/terms/Terms_Use.cfm

distributed over circle $\rho \le r_2$, such that $P = \pi r_2^2 p$. Formula (25) for this case gives

$$N = \frac{2}{\pi}\left\{\frac{a\delta}{H} - \frac{P}{\nu_1^2 - \nu_2^2}\left[D_1 \tan^{-1}\frac{a}{h_1} - D_2 \tan^{-1}\frac{a}{h_2}\right]\right\} \tag{56}$$

In the case of a uniform pressure, from (34) one deduces

$$N = \frac{2}{\pi}\left\{\frac{a\delta}{H} + \frac{P}{\nu_1^2 - \nu_2^2}\sum_{j=1}^{2}(-1)^j D_j\left[\sin^{-1}\frac{l_j(r_2)}{r_2} + \frac{h_j}{r_2^2}\left(\frac{2a^2 - l_j^2(r_2)}{\sqrt{a^2 - l_j^2(r_2)}} - 2a\right)\right]\right\} \tag{57}$$

when $r_2 \to 0$ formula (57) transforms into (56). Numerical calculations show that the term in square brackets in (57) decreases with increase in r_2. This implies that the normal displacement due to a concentrated force is greater than that produced by a distributed load with an equal total force.

Numerical Results

For the purposes of illustrating the influences of anisotropy and the location of the internal force on the displacement of the rigid punch numerical results were evaluated for the central displacement of the punch δ defined by equation (25). In the absence of the external force N we have

$$\frac{\delta}{P/aC_{44}} = F\left(\frac{C_{ij}}{C_{44}}, \frac{r}{a}, \frac{h}{a}\right)$$

The elastic constants of the transversely isotropic material (C_{ij}) can be assigned by examining typical values of the elastic constants used in engineering practice (i.e., E_h, E_v, ν_{hh}, ν_{vh}, and G_{vh}; where the suffixes v and h refer to the vertical (z) and horizontal (r) principal directions). Following Selvadurai [10] we get $\nu_{hh} = \nu_{vh} = 0.2$; $G_{vh}/E_v = 0.4$, and $E_h/E_v = 1$ or 9. In terms of the tensorial quantities these two groups of elastic constant yield $C_{11}/C_{44} = 2.7777$; $C_{13}/C_{44} = 0.6944$; $C_{33}/C_{44} = 2.7777$ (which corresponds to $E_h/E_v = 1$) and $C_{11}/C_{44} = 150$; $C_{13}/C_{44} = 56.25$; $C_{33}/C_{44} = 25$ (which corresponds to $E_h/E_v = 9$).

Figure 2 illustrates the manner in which the central rigid displacement of the punch is influenced by the location of the internal force. These results indicate trends that are consistent with Saint Venant-type phenomena. The influence of material anisotropy becomes dominant only in certain situations where the internal force migrates to the proximity of the rigid punch.

Conclusions

The present paper gives the complete solution to the problem of interaction between a smoothly indenting punch and a half-space and an internally placed concentrated force. The methodology outlined here enables the evaluation of both the displacements of the rigid punch and the stresses and displacements within the half-space region. It may be observed that certain results of a global nature (such as the displacements and rotations of the punch) can be obtained, in principle, by the application of Betti's reciprocal theorem. As has been observed by Shield [11], Shield and Anderson [12], and Selvadurai [13], in connection with punch and inclusion problems, the auxiliary solution required for the application of the reciprocal theorem pertains to the classical solution of the directly loaded punch or inclusion. While the procedure may be straightforward in principle, the resulting analysis may require the evaluation of complicated infinite integrals. Furthermore the applications of reciprocity principles lend themselves to the evaluation of results of a global nature and results such as contact stresses and the state of stress and strain within the elastic half-space can only be obtained by a complete analysis of the mixed boundary value problems.

References

1 Galin, L. A., "Contact Problems in the Theory of Elasticity," Tech. Rep. G16447, North Carolina State College, 1961.

2 Uflyand, Ya. S., "Survey of Articles on the Application of Integral Transforms in the Theory of Elasticity, Tech. Rep. AFOSR-65-1556, North Carolina State University, 1965.

3 dePater, A. D., and Kalker, J. J., eds., "The Mechanics of Contact Between Deformable Bodies," *Proc. I.U.T.A.M. Symp.*, Enschede, Delft University Press, 1975.

4 Gladwell, G. M. L., *Contact Problems in the Classical Theory of Elasticity*, Sijthoff and Noordhoff, Amsterdam, 1980.

5 Selvadurai, A. P. S., "A Theoretical Estimate of the Tilt of a Surface Foundation Due to an Inclined Anchor Load Applied at the Interior of the Soil Medium," *International Journal for Numerical and Analytical Methods in Geomechanics*, Vol. 5, 1981, pp. 369-378.

6 Selvadurai, A. P. S., "Fundamental Results Concerning the Settlement of a Rigid Foundation on an Elastic Medium Due to an Adjacent Surface Load, *International Journal for Numerical and Analytical Methods in Geomechanics*, Vol. 7, 1983, pp. 209-223.

7 Shield, R. T., "Notes on Problems in Hexagonal Aeolotropic Materials, *Proc. Cambr. Phil. Soc.*, Vol. 47, 1951, pp. 401-409.

8 Fabrikant, V. I., and Sankar, T. S., "On Contact Problems in an Inhomogeneous Half-Space," *International Journal of Solids and Structures*, Vol. 20, 1984, pp. 159-166.

9 Gladwell, G. M. L., and Fabrikant, V. I., "The Interaction Between a System of Circular Punches on an Elastic Half-Space," ASME JOURNAL OF APPLIED MECHANICS, Vol. 49, 1982, pp. 341-344.

10 Selvadurai, A. P. S., "The Elastic Settlement of a Rigid Circular Foundation Anchored to a Transversely Isotropic Elastic Rock Mass," *Proc. Int. Conf. on Structural Foundations on Rock*, Sydney, Pells, P. J. N., ed., A. A. Balkema, 1980, pp. 23-28.

11 Shield, R. T., "Load-Displacement Relations for Elastic Bodies," *J. Appl. Math. Phys. (ZAMP)*, Vol. 18, 1967, pp. 682-693.

12 Shield, R. T., and Anderson, C. A., "Some Least Work Principles for Elastic Bodies," *J. Appl. Math. Phys. (ZAMP)*, Vol. 17, 1966, pp. 663-676.

13 Selvadurai, A. P. S., "Betti's Reciprocal Relationships for the Displacements of an Elastic Infinite Space Bounded Internally by a Rigid Inclusion," *J. Struct. Mech.*, Vol. 9, 1981, pp. 199-210.

Downloaded 02 May 2010 to 171.66.16.54. Redistribution subject to ASME license or copyright; see http://www.asme.org/terms/Terms_Use.cfm

Stability of a Rigid Body With an Oscillating Particle: An Application of MACSYMA

L. A. Month
Department of Mechanical Engineering,
University of California at Berkeley,
Berkeley, Calif. 94720

R. H. Rand
Department of Theoretical
and Applied Mechanics,
Cornell University,
Ithaca, N.Y. 14853
Mem. ASME

This problem is a generalization of the classical problem of the stability of a spinning rigid body. We obtain the stability chart by using: (i) the computer algebra system MACSYMA in conjunction with a perturbation method, and (ii) numerical integration based on Floquet theory. We show that the form of the stability chart is different for each of the three cases in which the spin axis is the minimum, maximum, or middle principal moment of inertia axis. In particular, a rotation with arbitrarily small angular velocity about the maximum moment of inertia axis can be made unstable by appropriately choosing the model parameters. In contrast, a rotation about the minimum moment of inertia axis is always stable for a sufficiently small angular velocity. The MACSYMA program, which we used to obtain the transition curves, is included in the Appendix.

Introduction

This paper concerns the stability of the steady rotation of a rigid body containing a particle that oscillates sinusoidally along a principal axis. In the limiting case where the particle has zero mass, the solution to this problem reduces to the classical result that rotations about the axes of largest and smallest moment of inertia are stable, while a rotation about the middle moment of inertia axis is unstable [3]. The presence of the oscillating particle makes the stability criterion much more complicated.

Mathematically, this problem involves the stability of an equilibrium position in a nonlinear dynamical system that is parametrically driven by a periodic forcing function. Such stability problems may be efficiently investigated by using Floquet theory [9], which yields information about the asymptotic behavior of the system based on the system's performance over one period of the forcing function. Moreover, Floquet theory may be used in the context of perturbation methods to obtain stability criterion in the form of power series expansions in some small parameter.

While such analytical computations are straightforward [9], the grueling algebra involved has limited their use in the past. With the recent advent of computer algebra, however, new possibilities arise. Computer algebra systems such as MACSYMA [8] permit the exact handling of algebraic expressions involving unevaluated variables (represented, as usual, by letters). Differentiation and integration are supported, and, in general, any routine computations that a person can do by hand can now be done with greater speed and accuracy by computer. Moreover, MACSYMA uses exact (rational) arithmetic, so that the roundoff error usually associated with computer solutions is absent.

In this paper we show how such computations can be applied to the problem at hand. We include the listing of a MACSYMA program which computes stability transition curves in the form of power series expansions out to arbitrary order (limited only by the memory size of the computer).

The problem of a rigid body carrying an oscillating particle has been previously investigated by Kane [5]. He derived the governing equations and presented a preliminary stability analysis, obtaining the lowest order approximation for the stability transition curves. He concluded that rotations about the middle moment of inertia axis could be made stable, and that rotations about the largest and smallest moment of inertia axes could be made unstable, by choosing the parameters appropriately.

In this paper we will extend Kane's analysis in two ways. Firstly, we will use computer algebra to develop stability criterion in the form of power series expansions in a small parameter. Secondly, we will use numerical integration in the setting of Floquet theory to obtain results valid over a wider range of parameter values. This work will reveal an entirely unexpected family of regions of stability and instability in the parameter plane. In addition we will show that rotations about the minimum moment of inertia axis have different stability properties than rotations about the maximum moment of inertia axis.

Theory

In this section we set up the problem and derive certain properties of the stability transition curves. We begin by stating the governing equations of motion (from [5]):

Contributed by the Applied Mechanics Division and presented at the 1985 Joint ASME/ASCE Applied Mechanics, Fluids Engineering, and Bioengineering Conference, Albuquerque, N. Mex., June 24-26, 1985 of THE AMERICAN SOCIETY OF MECHANICAL ENGINEERS.

Discussion on this paper should be addressed to the Editorial Department, ASME, United Engineering Center, 345 East 47th Street, New York, N.Y., 10017, and will be accepted until two months after final publication of the paper itself in the JOURNAL OF APPLIED MECHANICS. Manuscript received by ASME Applied Mechanics Division, August, 1984; final revision October, 1984. Paper No. 85-APM-28.

Copyright © 1985 by ASME
Downloaded 02 May 2010 to 171.66.16.54. Redistribution subject to ASME license or copyright; see http://www.asme.org/terms/Terms_Use.cfm

$$(I_2 - I_3)\omega_2\omega_3 - I_1\dot{\omega}_1 = 0$$
$$(I_3 - I_1)\omega_3\omega_1 - I_2\dot{\omega}_2 - s\mu(s(\dot{\omega}_2 - \omega_1\omega_3) + 2\dot{s}\omega_2) = 0$$
$$(I_1 - I_2)\omega_1\omega_2 - I_3\dot{\omega}_3 - s\mu(s(\dot{\omega}_3 + \omega_1\omega_2) + 2\dot{s}\omega_3) = 0 \quad (1)$$

where dots represent differentiation with respect to time t, and where I_i and ω_i are the principal moments of inertia and the corresponding angular velocities, respectively. The particle is assumed to move along the I_1 axis, with $s = s(t)$ as its distance from the center of mass of the rigid body. The parameter $\mu = mM/(m+M)$, where m and M are the masses of the particle and rigid body, respectively.

Throughout this paper we will be interested in the stability of a steady rotation about the axis on which the particle is constrained to move:

$$\omega_1 = \omega = \text{constant}, \quad \omega_2 = 0, \quad \omega_3 = 0. \quad (2)$$

To investigate the stability of this solution, we define the following small deviations from steady state:

$$x_1 = \omega_1 - \omega, \quad x_2 = \omega_2, \quad x_3 = \omega_3. \quad (3)$$

We substitute (3) into (1) and linearize in the x_i to obtain these linear variational equations:

$$d/dt\ x_1 = 0$$
$$d/dt\,((I_2 + \mu s^2)\,x_2) + (I_1 - I_3 - \mu s^2)\ \omega x_3 = 0$$
$$d/dt\,((I_2 + \mu s^2)\,x_2) + (I_1 - I_3 - \mu s^2)\ \omega x_3 = 0. \quad (4)$$

The solution (2) is said to be stable if all solutions to (4) are bounded, and unstable if an unbounded solution to (4) exists. We may thus ignore the first equation of (4) which cannot produce instability.

We prescribe the motion $s(t)$ of the particle to be sinusoidal,

$$s = s(t) = A\cos\Omega\ t. \quad (5)$$

To nondimensionalize (4), we set

$$J_2 = I_2/I_1, \quad J_3 = I_3/I_1 \quad (6)$$

and define $\tau = \Omega t$, giving

$$(f_2\ x_2)' + g_3 x_3 = 0, \quad (f_3\ x_3)' - g_2\ x_2 = 0 \quad (7)$$

where primes represent differentiation with respect to τ and where, for $i = 2,3$,

$$f_i = J_i + \epsilon\cos^2\tau$$

$$g_i = \sqrt{\frac{K\ J_2\ J_3}{(1-J_2)(1-J_3)}}\,(1 - f_i) \quad (8)$$

in which ϵ and K are dimensionless parameters:

$$\epsilon = \mu\ A^2/I_1 = (m\ M/(m+M))\ A^2/I_1 \quad (9)$$

$$K = \frac{(1-J_2)(1-J_3)}{J_2 J_3}\,(\omega/\Omega)^2. \quad (10)$$

In the case that $\epsilon = 0$, equations (7) may be written in the form:

$$x_i'' + K\ x_i = 0, \quad i = 2,3. \quad (11)$$

This limit corresponds to the classical problem in which the particle has no mass or does not move. Equation (11) will have no unbounded solutions only if $K > 0$, i.e., if $(1-J_2)$ $(1-J_3) > 0$, i.e., if the rotation axis has the largest or smallest principal moment of inertia.

Equations (7) thus depend on four dimensionless parameters: ϵ, K, J_2, and J_3. For a particular rigid body, J_2 and J_3 are fixed, while ϵ and K, respectively, reflect the forcing amplitude and the ratio of spin frequency ω to forcing frequency Ω. To reduce the size of the parameter space from 4 to 2, we view J_2 and J_3 as fixed, and are interested in which points in the K-ϵ plane correspond to stable, and which to unstable motions (2). Since $\epsilon > 0$ from (9), we are interested only in the upper half of the K-ϵ plane. Moreover, we note that three distinct cases occur: If $(1-J_2)$ $(1-J_3) > 0$ then $K > 0$ and we are interested only in the first quadrant of the K-ϵ plane. We have two cases $J_2 < 1$, $J_3 < 1$ or $J_2 > 1$, $J_3 > 1$. These cases correspond to a rotation about the maximum or minimum moment of inertia axis, respectively. The third case, in which the rotation is about the middle moment of inertia axis, involves $K < 0$ and restricts our attention to the second quadrant of the K-ϵ plane.

In particular we are interested in the transition curves that separate regions of stability from regions of instability in the appropriate quadrant of the K-ϵ plane. On such a curve, it is well known from Floquet theory that there must exist periodic solutions having the period of the forcing function ($= \pi$ from equation (8)), or twice that period. This result follows from the Hamiltonian nature of the problem ([1], p. 203; [9], p. 197): equations (7) may be written in Hamiltonian form,

$$q' = \partial H/\partial p, \quad p' = -\partial H/\partial q \quad (12)$$

where $q = f_3\,x_3$, $p = f_2\,x_2$, and

$$H = \left(\frac{g_3}{f_3}\,q^2/2 + \frac{g_2}{f_2}\,p^2/2\right).$$

Thus, to find transition curves in the K-ϵ plane, it is sufficient to look for periodic solutions of period π or 2π. We begin by finding those points on the positive K axis from which regions of instability originate. When $\epsilon = 0$, equation (11) shows that equations (7) have period $2\pi/\sqrt{K}$. Hence for a transition point on the positive K axis we require (11) to exhibit solutions with period $2\pi/N$, $N = 0, 1, 2, \ldots$ since all such solutions will have period 2π; (e.g., a solution of period π may also be considered to have period 2π, but not vice versa). $N = 0$ corresponds to a constant solution (which occurs in equations (7) for $K = \epsilon = 0$), which may also be thought of as a periodic function of period 2π. This gives

$$2\pi\sqrt{K} = 2\pi/N \quad \text{or} \quad K = N^2, \quad N = 0,1,2, \ldots. \quad (13)$$

For $\epsilon = 0$ and $K < 0$, equation (11) has unbounded solutions, and therefore the entire negative K axis is unstable.

At each of the points $K = N^2$, $\epsilon = 0$, we expect two transition curves to intersect the K axis, the solution on one behaving like $\sin N\tau$, and on the other like $\cos N\tau$ for $\epsilon = 0$. An exception is the $N = 0$ case, where we expect a single transition curve with solution behaving like a constant for $\epsilon = 0$. This situation is so far reminiscent of Mathieu's equation ([2], p. 65),

$$x'' + (\delta + \epsilon\ \cos\ 2t)\ x = 0 \quad (14)$$

which is the paradigm for problems in Floquet theory.

We now note a surprising difference between the behavior of equations (7) and the Mathieu equation (14). The $N = 0$ transition curve (which intesects the origin $K = \epsilon = 0$) is the straight line $K = 0$ for equations (7), whereas it is a curved line having a complicated power series expansion in ϵ for Mathieu's equation (see [8]). This may be proved as follows: When $K = 0$, $g_2 = g_3 = 0$ in equation (8), and equations (7) become

$$(f_2\ x_2)' = 0 \quad \text{and} \quad (f_3\ x_3)' = 0. \quad (15)$$

These equations have the general solution

$$x_2 = c_1/f_2 \quad \text{and} \quad x_3 = c_2/f_3 \quad (16)$$

where c_1 and c_2 are arbitrary constants. From equations (8), f_2 and f_3 are periodic with period π, and hence, from Floquet theory, all points on the ϵ axis are transition points.

Note that this implies that for equations (7), stability is not possible for negative K near the origin. This is in contrast to the behavior of Mathieu's equation, in which the transition

Downloaded 02 May 2010 to 171.66.16.54. Redistribution subject to ASME license or copyright; see http://www.asme.org/terms/Terms_Use.cfm

curve through $\delta=\epsilon=0$ bends to the left and thus carries a region of stability into the negative K half-plane.

We are interested in using computer algebra to obtain approximate expressions for each of the two transition curves that go through the points $K=N^2$, $\epsilon=0$. Before proceeding with this computation, however, we note a remarkable symmetry property that these transition curves possess.

Theorem: Let

$$K=F(\epsilon;J_2,J_3) \quad \text{and} \quad K=G(\epsilon;J_2,J_3) \tag{17}$$

represent the two transition curves emanating from a single transition point on the K axis. Then the functions F and G interchange when J_2 and J_3 are interchanged:

$$F(\epsilon;J_3,J_2)=G(\epsilon;J_2,J_3) \tag{18}$$

Before proving this theorem, we note that it implies that when $J_2=J_3$, each pair of transition curves emanating from the same point on the K axis coalesce. This means that in the case of a dynamically symmetric rigid body, all the associated regions of instability disappear.

Proof: We begin by writing equations (7) in the form of a single second-order equation. We solve the first of equations (7) for x_3 and substitute into the second, giving:

$$(f_3(f_2\ x_2)'/g_3)'+g_2x_2=0. \tag{19}$$

Alternately, we could have eliminated x_2 giving:

$$(f_2(f_3x_3)'/g_2)'+g_3x_3=0. \tag{20}$$

On a transition curve there exists a solution to equation (19) of period 2π which may be expanded in a Fourier series:

$$x_2(\tau)=\sum_{n=0}^{\infty} a_n\ \cos\ n\tau+b_n\ \sin\ n\tau. \tag{21}$$

We substitute (21) into (19), collect terms, and equate coefficients of cos $n\tau$ and sin $n\tau$ to zero. As in the case of Mathieu's equation (see [9], p. 204), this results in two *uncoupled* sets of homogeneous linear algebraic equations, respectively on the a_n and b_n coefficients. Thus we may obtain an even periodic solution (if all the b_n equal zero) or an odd periodic solution (if all the a_n equal zero), each case giving rise to separate transition curves. If we suppose that on the transition curve $K=F$ in (17), x_2 is an even periodic function, then on $K=G$, x_2 will be odd.

Next we show that whenever $x_2(\tau)$ is even, $x_3(\tau)$ must be odd. We replace τ by $-\tau$ in equation (7) and use $x_2(-\tau)=x_2(\tau)$, giving

$$-(f_2(\tau)\ x_2(\tau))'+g_3(\tau)\ x_3(-\tau)=0,$$
$$-(f_3(\tau)\ x_3(-\tau))'-g_2(\tau)\ x_2(\tau)=0$$

from which it follows that $x_3(-\tau)=-x_3(\tau)$ by comparison with (7).

Finally, we note that when J_2 and J_3 are interchanged, the linear differential operators defined by equations (19) and (20) interchange. Thus

$$x_2(\tau;J_2,J_3)=x_3(\tau;J_3,J_2).$$

This means that the transition curve on which x_2 was even and x_3 was odd interchanges with the one on which x_2 was odd and x_3 was even, i.e., equation (18) holds.

Computer Algebra

We use a well-known perturbation method [9] to obtain approximate expressions for the transition curves that intersect the K axis at $K=N^2$. Our setup and computer algebra implementation will closely follow the treatment of Mathieu's equation ([8], pp. 87–94).

The procedure will be to expand x_2 and K in equation (19) in power series in ϵ. When $\epsilon=0$, equation (19) reduces to equation (11), and has two linearly independent periodic solutions, one even and one odd: cos $N\tau$ and sin $N\tau$, where $N=1,2,3,\ldots$ tags the particular transition curves we are approximating. To treat each value of N as similarly as possible, we begin by defining a new independent variable z:

$$z=N\tau. \tag{22}$$

Then when $\epsilon=0$, equation (19) exhibits the solutions cos z and sin z, independent of N.

Then we expand:

$$K=N^2(1+K_1\ \epsilon+K_2\ \epsilon^2+\ \ldots) \tag{23}$$

$$x_2(z)=x_{20}(z)+x_{21}(z)\ \epsilon+x_{22}(z)\ \epsilon^2+\ \ldots \tag{24}$$

where $x_{20}(z)$ is taken either as cos z or sin z, each choice giving a distinct transition curve.

The method entails substituting (22)–(24) into (8) and (19), collecting terms, and equating coefficients of powers of ϵ to zero. This yields a sequence of differential equations on the $x_{2i}(z)$. The constants K_i are obtained by requiring the resulting solutions to be bounded (periodic) functions of z. It is sufficient to choose the constants of integration in these equations to be zero, since for a transition curve we are interested in any periodic solution of period π or 2π.

This method involves a great deal of algebra. Even explicitly computing equation (19), which contains 28 terms, would be difficult to do correctly by hand. The substitution of equations (23) and (24), and collection of terms would have been virtually impossible without computer algebra.

The MACSYMA program which we used, and an explanation of how it works, is presented in the Appendix. In the following we present a sample of the program's output, namely an expression for the $N=1$ transition curve corresponding to the choice $x_{20}(z)=\sin z$ expanded out to 0(3). The quantities J_{12} and J_{13} are respectively defined as $1-J_2$ and $1-J_3$:

$$\begin{aligned}
K=1+\ & \frac{(((J_{13}+3J_{12})J_2+J_{12}J_{13})J_3+3J_{12}J_{13}J_2)\epsilon}{4J_{12}J_{13}J_2J_3} \\
&+(((7J_{13}^2+18J_{12}J_{13}+71J_{12}^2)J_2^2 \\
&+(-2J_{12}J_{13}^2+18J_{12}^2J_{13})J_2-9J_{12}^2J_{13}^2)J_3^2 \\
&+((18J_{12}J_{13}^2+62J_{12}^2J_{13})J_2^2+18J_{12}^2J_{13}^2J_2)J_3 \\
&-9J_{12}^2J_{13}^2J_2^2)\epsilon^2/(128J_{12}^2J_{13}^2J_2^2J_3^2) \\
&+(((41J_{13}^3+69J_{12}J_{13}^2+283J_{12}^2J_{13}+1655J_{12}^3)J_2^3 \\
&+(-85J_{12}J_{13}^3-102J_{12}^2J_{13}^2+283J_{12}^3J_{13})J_2^2 \\
&+(27J_{12}^2J_{13}^2-171J_{12}^3J_{13}^2)J_2+153J_{12}^3J_{13}^3)J_3^3 \\
&+((69J_{12}J_{13}^3+166J_{12}^2J_{13}^2+1205J_{12}^3J_{13})J_2^3 \\
&+(-102J_{12}^2J_{13}^3+166J_{12}^3J_{13}^2)J_2^2 \\
&-171J_{12}^3J_{13}^3J_2)J_3^2+((-117J_{12}^2J_{13}^3 \\
&-315J_{12}^3J_{13}^2)J_2^3-117J_{12}^3J_{13}^3J_2^2)J_3 \\
&+135J_{12}^3J_{13}^3J_2^3)\epsilon^3/(4096J_{12}^3J_{13}^3J_2^3J_3^3)+\ \ldots .
\end{aligned} \tag{25}$$

As noted previously in property (18), the $N=1$ transition curve corresponding to the choice $x_{20}(z)=\cos z$ is identical to equation (25) with J_2 and J_{12}, respectively, interchanged with J_3 and J_{13}.

Note that in equation (25), J_2 and J_3 are left as algebraic parameters. Inspection of equation (25) and the corresponding expression for the other $N=1$ transition curve suggested property (18) to us, which we were then able to substantiate theoretically.

As another example of the utility of having algebraic expressions like equation (25), we obtained an expression for the width of the region of instability associated with equation (25), and tried to find a condition on J_2 and J_3 (in addition to

Downloaded 02 May 2010 to 171.66.16.54. Redistribution subject to ASME license or copyright; see http://www.asme.org/terms/Terms_Use.cfm

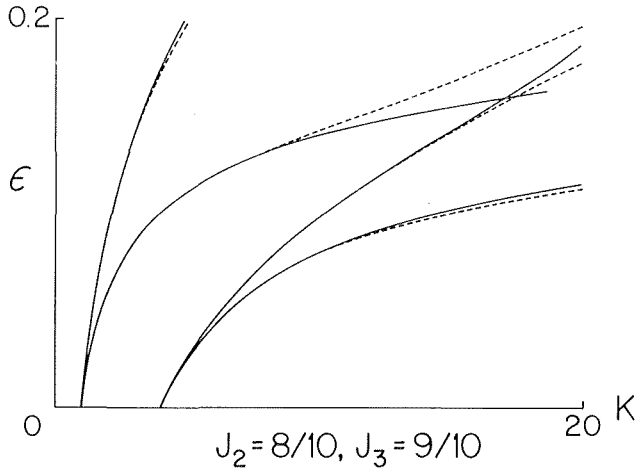

Fig. 1(*a*) $J_2 = 8/10$ and $J_3 = 9/10$. Rotations about maximum axis. The solid lines are analytical expressions for the transition curves. They include terms of 0(8) for $N = 1$ and 0(7) for $N = 2$. The dashed lines represent transition curves calculated numerically.

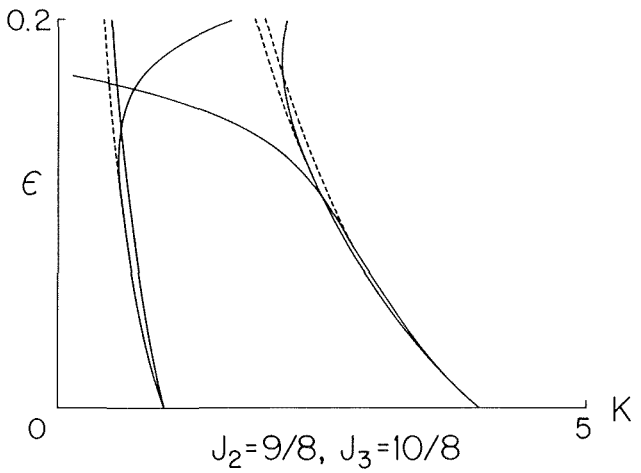

Fig. 1(*b*) $J_2 = 9/8$ and $J_3 = 10/8$. Rotation about minimum axis. The solid lines are analytical expressions for the transition curves. They include terms of 0(8) for $N = 1$ and 0(7) for $N = 2$. The dashed lines represent transition curves calculated numerically.

Fig. 1

the already discussed condition $J_2 = J_3$) which would make this region as small as possible. In the notation of equation (17), we computed $F(\epsilon;J_2,J_3) - G(\epsilon;J_2,J_3)$. We found that while the resulting expression generally had a term or order ϵ, we could eliminate this lowest order term by choosing $J_2 + J_3 = 1$. While this condition does not eliminate the $N = 1$ region entirely (as the $J_2 = J_3$ condition does), it also does not require the body to be dynamically symmetric. In fact, since in physical variables this becomes $I_2 + I_3 = I_1$ (see equation (6)), it can only be applied to situations in which the spin axis is the axis of largest moment of inertia. Incidentally, we note that this condition, $J_2 + J_3 = 1$, does not play any such instability-minimizing role with regard to the $N = 2$ transition region (which generally has a width of order ϵ^2).

This ability of computer algebra programs to leave parameters unevaluated offers a characteristic advantage over traditional computer calculations. However, it takes up a lot of memory. We carried out all these computations on Cornell's DEC 2060 mainframe computer. We found that we could obtain expressions in the form of equation (25) valid to 0(4) before limitations in the computer's memory size stopped us from going further. However, if we assigned J_2 and J_3 numerical values before running the computation, we found we could get results valid to 0(8).

To check our computer algebra computations and to investigate the dynamics of this problem when ϵ is not necessarily small, we used numerical integration.

Numerical Integration

The procedure for using Floquet theory and numerical integration to determine the stability of a first-order system of differential equations (such as equations (7)) is well known [9] and may be outlined as follows:

1. Numerically integrate from 0 to π (= the period of the forcing function) for two sets of initial conditions:
   (*i*) $x_2(0) = 1$, $x_3(0) = 0$, and
   (*ii*) $x_2(0) = 0$, $x_3(0) = 1$.

2. Find the eigenvalues of the resulting fundamental solution matrix M (evaluated at time π). If both eigenvalues have absolute values less than unity, then the motion is stable, and so on.

3. In the case of a Hamiltonian system (cf. equation (12)), the eigencomputation is simplified since the associated matrix M has determinant unity. In this case it is sufficient that the absolute value of the trace of the matrix M be less than 2.

We used a fourth-order Runge-Kutta scheme to implement the preceding algorithm. By choosing various parameter values (we fixed J_2 and J_3, and varied K and ϵ), we were able to approximate the location of transition curves (on which the trace of the matrix M is ± 2).

In what follows, we present some numerical results for a rigid body with principal moments of inertia in the ratio 8:9:10. In the case in which the spin axis is the axis of the largest moment of inertia, this gives $J_2 = 8/10$ and $J_3 = 9/10$. When the spin axis corresponds to the middle moment of inertia, we have $J_2 = 10/9$ and $J_3 = 8/9$. If the spin axis is the axis of the smallest moment of inertia, then $J_2 = 9/8$ and $J_3 = 10/8$.

To begin with, we set $J_2 = 8/10$ and $J_3 = 9/10$ in our MACSYMA program and obtained computer algebra expressions for the first four transition curves ($N = 1$ and 2). As an example, we present the transition curve corresponding to equation (25), but carried out to 0(8):

$$K = 1 + \frac{475\,\epsilon}{48} + \frac{1321375\,\epsilon^2}{18432} + \frac{3429696875\,\epsilon^3}{7077888} + \frac{25933872809375\,\epsilon^4}{8153726976} + \frac{573740794468203125\,\epsilon^5}{28179280429056} + \frac{27429354565142230468 75\,\epsilon^6}{21641687369515008} + \frac{12676914311735148281640625\,\epsilon^7}{16620815899787526144} + \frac{11832356872679546545169921875\,\epsilon^8}{2692572175765579235328} + \ldots . \tag{26}$$

In addition we obtained analogous expressions for the case $J_2 = 9/8$ and $J_3 = 10/8$. In Figs. 1(*a*) and 1(*b*), we present a plot of the first four computer algebra generated curves (one of which is equation (26)), and we compare them to points obtained by the previously described numerical integration scheme. The agreement is excellent for values of ϵ less than about 0.1.

In Figs. 2–4, we present the results of numerical integration for the cases ($J_2 = 8/10$, $J_3 = 9/10$), ($J_2 = 10/9$, $J_3 = 8/9$), and ($J_2 = 9/8$, $J_3 = 10/8$), respectively. Note the presence of an entire family of transition curves in Fig. 2 that do not intersect the K axis. These curves are not displayed in Fig. 1(*a*) and

Downloaded 02 May 2010 to 171.66.16.54. Redistribution subject to ASME license or copyright; see http://www.asme.org/terms/Terms_Use.cfm

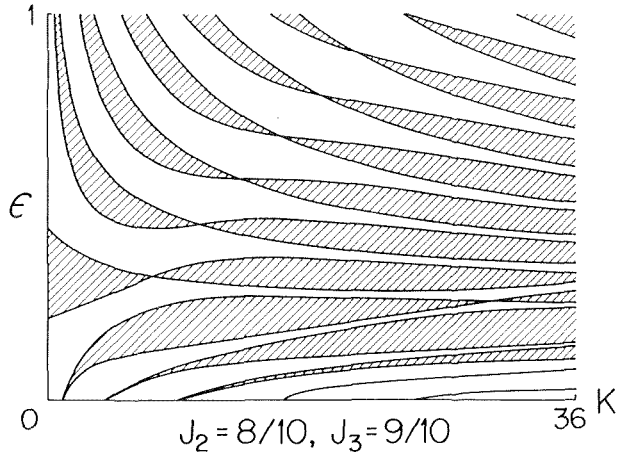

Fig. 2 $J_2 = 8/10$ and $J_3 = 9/10$ stability chart for rotation about maximum principal axis. Here shaded regions are unstable and unshaded regions are stable.

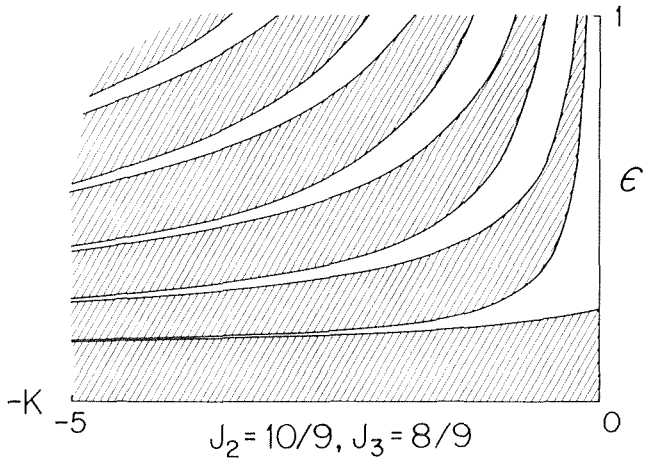

Fig. 3 $J_2 = 10/9$ and $J_3 = 8/9$ stability chart for rotation about middle principal axis. Here shaded regions are unstable and unshaded regions are stable.

cannot be found by a perturbation method, which is based on a small ϵ analysis. Similarly in Fig. 3, there is a family of transition curves, none of which intersect the K axis. (Note that for this case the small ϵ perturbation theory predicts instability for all $K<0$.) In Fig. 4 all the transition curves intersect the K axis.

Note that Fig. 2 predicts that even when the angular velocity ω of the rigid body about its axis of rotation is small (in which case K will be small from equation (10)), instability is possible if the amplitude of the motion of the oscillating particle is appropriately chosen. Similarly in the case of Fig. 3 note that when K is nearly zero the motion can be made stable by choosing the forcing amplitude sufficiently large. In the case of Fig. 4, when K is very small the motion is always stable.

These last considerations are based on the existence of transition curves which intersect the ϵ axis. With the numerical results of Figs. 2–4 as motivation, we look for the points of intersection of these transition curves with the ϵ axis by using a perturbation method.

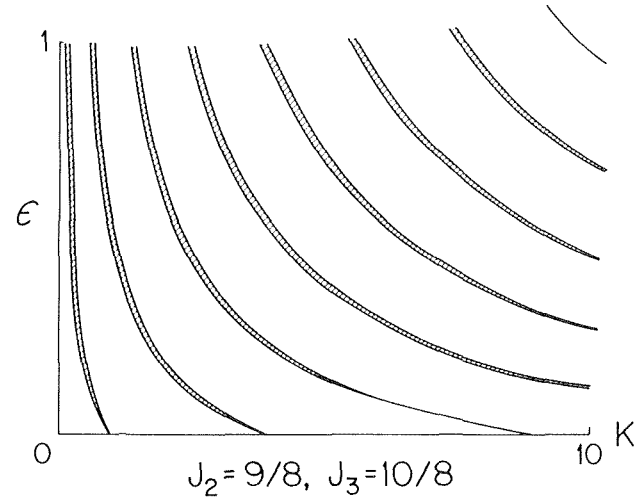

Fig. 4 $J_2 = 9/8$ and $J_3 = 10/8$ stability chart for rotation about minimum principal axis. Here shaded regions are unstable and unshaded regions are stable.

More Perturbations

When K is small, equations (7) simplify because the functions g_i in (8) also become small. For convenience we set, for $i = 2, 3$,

$$g_i = \sqrt{K}\ G_i \tag{27}$$

where $G_i = J^*(1 - f_i)$,

$$J^* = \sqrt{\frac{J_2 J_3}{(1-J_2)(1-J_3)}}.$$

We look for a solution to equations (7) that is valid when K is small by using the two variable expansion method [6]. We replace τ as independent variable by two new variables, ξ and η:

$$\xi = \tau, \quad \eta = \sqrt{K}\,\tau. \tag{28}$$

Then

$$\frac{d}{d\tau} = \frac{\partial}{\partial \xi} + \sqrt{K}\ \frac{\partial}{\partial \eta}. \tag{29}$$

We expand $x_2(\xi, \eta)$ and $x_3(\xi, \eta)$ in power series in $\sqrt{K}$:

$$x_i = x_{i0} + \sqrt{K}\, x_{i1} + \ \ldots \ \text{i} = 2,3. \tag{30}$$

Substituting (29) and (30) into (7) and collecting terms gives:

$$(f_2\ x_{20})_\xi = 0, \quad (f_3\ x_{30})_\xi = 0 \tag{31}$$

$$(f_2\ x_{21})_\xi = -(f_2\ x_{20})_\eta - G_3\ x_{30} \tag{32}$$

$$(f_3\ x_{31})_\xi = -(f_3\ x_{30})_\eta + G_2\ x_{20}. \tag{33}$$

The zeroth-order equations (31) are easily solved:

$$x_{20} = A(\eta)/f_2, \ x_{30} = B(\eta)/f_3. \tag{34}$$

Note that the "constants" of integration (A and B) in equations (34) are functions of the slow time variable η.

Substituting (34) into the first-order equation (32) gives:

$$(f_2\ x_{21})_\xi = -A' - J^*\ B\frac{1-f_3}{f_3} \tag{35}$$

where primes represent differentiation with respect to η.

For equation (35) to have bounded solutions, we require that the right-hand side of (35) have average value zero over one forcing period:

$$-A' - J^*B\left(\frac{1}{\sqrt{(J_3)(J_3+\epsilon)}} - 1\right) = 0 \tag{36}$$

where we have used the fact that

$$\int_0^\pi \frac{1}{f_3}\,d\xi = \int_0^\pi \frac{d\xi}{J_3 + \epsilon\cos^2\xi} = \frac{\pi}{\sqrt{(J_3)(J_3+\epsilon)}}. \tag{37}$$

A similar treatment of equation (33) gives the condition:

$$-B' + J^*A\left(\frac{1}{\sqrt{(J_2)(J_2+\epsilon)}} - 1\right) = 0. \tag{38}$$

Equations (36) and (38) can be written in the form:

Downloaded 02 May 2010 to 171.66.16.54. Redistribution subject to ASME license or copyright; see http://www.asme.org/terms/Terms_Use.cfm

$$A'' + J^{*2}\left(\frac{1}{\sqrt{(J_2)(J_2+\epsilon)}} - 1\right)\left(\frac{1}{\sqrt{(J_3)(J_3+\epsilon)}} - 1\right)A = 0 \quad (39)$$

which will have bounded solutions as long as ϵ does not lie between the critical values:

$$\epsilon = \frac{1-J_2^2}{J_2} \quad \text{and} \quad \epsilon = \frac{1-J_3^2}{J_3}. \quad (40)$$

The preceding analysis was for the case in which J^* was positive, i.e., for rotations about the largest or smallest principal axis. The same analysis can be applied to rotations about the middle principal axis by expanding in a power series in $\sqrt{-K}$, and so on. This results in precisely the same expressions for the critical values (40).

Since ϵ is defined to be positive, the critical values occur only when $1-J_2^2$ or $1-J_3^2 > 0$. Thus we have three cases. If $J_2 < 1$ and $J_3 < 1$ (a rotation about the maximum moment of inertia axis) there are two ϵ intercepts. In fact for $J_2 = 8/10$, $J_3 = 9/10$, equation (40) gives the critical values:

$$\epsilon = 9/20,\ 19/90 \quad (41)$$

in agreement with the numerical results. If $J_2 > 1$ and $J_3 < 1$ (a rotation about the middle moment of inertia axis) there is one transition curve bifurcating from the positive ϵ axis. For $J_2 = 10/9$ and $J_3 = 8/9$, equation (40) gives the values:

$$\epsilon = 17/72,\ -19/90. \quad (42)$$

The positive value is in agreement with the numerical results presented in Fig. 3. If $J_2 > 1$ and $J_3 > 1$ (a rotation about the minimum moment of inertia axis) then there are no ϵ intercepts. The numerical results in Fig. 4 illustrate this case when $J_2 = 9/8$ and $J_3 = 10/8$.

Conclusions

In this investigation of the effects of an oscillating particle on the steady rotation of a rigid body, we have used computer algebra to obtain closed-form analytical approximations for transition curves. These expressions permitted us to draw certain conclusions that would have been hard to ascertain by traditional numerical approaches. For example, we showed that if a dynamically asymmetric rigid body rotates about, and carries an oscillating particle on, its largest principal axis, then the $N=1$ instability region can be made small by choosing the sum of the two smaller principal moments of inertia equal to largest principal moment of inertia, $I_2 + I_3 = I_1$.

Similarly, we used expressions generated by computer algebra to motivate us to show: (*i*) that the symmetric rigid body (for which $I_2 = I_3$) has no regions of instability emanating from points on the K axis, and (*ii*) that the ϵ axis ($K=0$) is an exact transition curve.

We supplemented our computer algebra-perturbation method approach with numerical integration based on Floquet theory. This permitted us to find the structure of the stability chart far from the K axis. Figures 2 and 3 exhibit families of transition curves that are disconnected from those curves that emanate from the K axis. This situation is quite unlike that occurring in Mathieu's equation. Figure 4 does not have transition curves disconnected from the K axis.

In particular we were able to conclude that a rigid body which is slowly rotating about its axis of largest moment of inertia (i.e., one for which K is small), can be made unstable by oscillating a particle along this axis with the appropriate amplitude. Similarly, we found that the normally unstable motion of a rigid body slowly rotating about its axis of middle moment of inertia could be made stable by oscillating a particle along this axis with an amplitude that depended on the system parameters. In contrast the normally stable motion of a rigid body slowly rotating about its axis of minimum moment of inertia remains stable even when a particle oscillating along this axis is added. If K is not small all cases exhibit regions of stability and instability. We also note the surprising result that the presence of the oscillating particle causes the stability properties of a rotation about the minimum moment of inertia axis to be different from that about the maximum moment of inertia axis; cf. Figs. 2 and 4.

Because of the linear nature of the stability analysis, we are not able to predict what the motion will be like once it becomes unstable. Although such questions are certainly of interest in this application, they are not the subject of this paper. These considerations fall under the category of nonlinear parametric excitation, a subject that has just begun to be investigated in much simpler systems [4, 7].

References

1 Arnold, V. I., *Ordinary Differential Equations*, MIT Press, Cambridge, Mass., 1973.

2 Cesari, L., *Asymptotic Behavior and Stability Problems in Ordinary Differential Equations*, 3rd Ed., Springer Verlag, New York, 1971.

3 Goldstein, H., *Classical Mechanics*, Addison Wesley, Reading, Mass., 1980.

4 Holmes, C. A., and Rand, R. H., "Coupled Oscillators as a Model for Nonlinear Parametric Excitation," *Mechanics Research Comm.*, Vol. 8, No. 5, 1981, pp. 263-268.

5 Kane, T. R., "Stability of Steady Rotations of a Rigid Body Carrying an Oscillating Particle," *Proceedings of the 4th U.S. National Congress of Applied Mechanics*, Berkeley, Calif., 1962, pp. 235-238.

6 Kervorkian, J., and Cole, J. D., *Perturbation Methods in Applied Mathematics*, Springer Verlag, New York, 1981.

7 Month, L. A., and Rand, R. H., "Bifurcation of 4:1 Subharmonics in the Nonlinear Mathieu Equation," *Mechanics Research Comm.*, Vol. 9, No. 4, 1982, pp. 233-240.

8 Rand, R. H., *Computer Algebra in Applied Mathematics: An Introduction to MACSYMA*, Pitman, 1984.

9 Stoker, J. J., *Nonlinear Vibrations*, Wiley-Interscience, New York, 1950.

APPENDIX

MACSYMA is a *functional* language, i.e., programs are written in the form of user-defined functions. For an introduction to programming in MACSYMA, see [8]. The program presented in the following consists of a main function, called TC (for Transition Curve) and of eight other functions that are called by TC.

We offer a brief summary of how each of these functions works. TC begins by "killing" Y_0, i.e., by expunging any value that the function $Y_0(z)$ may have had from a previous run. Then some "pattern matching" functions are called to prepare for their use later in the program to solve the perturbation differential equations. Here two rules named C and S are defined, which will provide a particular solution to the nonhomogeneous equation $y'' + y = f(z)$ when $f(z)$ is a sine or cosine. (Although MACSYMA has a differential equation solver called ODE2 as one of its standard functions, it is relatively inefficient time-wise, compared to pattern matching. The authors thank Professor Jim Geer of SUNY Binghamton for suggesting this use of pattern matching.)

Next TC calls INPUT which queues the user to enter the transition curve number and the degree of truncation from the keyboard. The function SETUP1 then performs the expansions (23) and (24) (with a slight change of notation).

TC then calls SETUP2 which contains the expanded differential equation (19). Here MACSYMA was used to derive the listed equation, and then the MACSYMA editor was used to build the rest of the function SETUP2 around the derived equation. This function does the job of substituting the expansions into the differential equation and collecting terms. The perturbation equations are stored in an array called EQ.

Next $Y_0(z)$ is defined as SIN(Z) and a function named FINDTC is called. The latter performs a FOR-DO loop in which the functions STEP1, STEP2, and STEP3 are called. At the Ith stage of the process, STEP1 plugs all the previously

Downloaded 02 May 2010 to 171.66.16.54. Redistribution subject to ASME license or copyright; see http://www.asme.org/terms/Terms_Use.cfm

found perturbation results into the Ith perturbation differential equation. The function OUTOFPOIS is used to convert trig expressions like $\cos^2 z$ to the form $(1+\cos 2z)/2$. (We note that OUTOFPOIS, which is part of the MACSYMA Poisson series package, works more efficiently than the function TRIGREDUCE used in [8].)

STEP2 eliminates secular terms and obtains a value for the Ith coefficient in the expansion (23) for K.

STEP3 uses the previously defined pattern matching rules to solve the Ith differential equation.

Finally OUTPUT displays the resulting expression for the transition curve on the video screen.

When the function FINDTC is finished, control is returned to TC, which now defines $Y_0(z)$ to be COS(Z), and FINDTC is once again called.

Here is the program listing (the E-labels that precede the function definitions may be ignored):

```
(E4) TC( ):=(KILL (Y0), MATCHDECLARE (NN, TRUE),
DEFRULE (C, COS (NN Z), COS(NN Z)/(1-NN NN)),
DEFRULE (S, SIN (NN Z), SIN(NN Z)/(1-NN NN)), INPUT( ), SETUP1( ),
SETUP2( ), Y0(Z):=SIN(Z), FINDTC( ),
Y0(Z):=COS(Z), FINDTC( ),
(E5) INPUT( ):=(N:
READ ("ENTER TRANSITION CURVE NUMBER N"),
M: READ ("ENTER DEGREE OF TRUNCATION"))
(E6) FINDTC( ):=(FOR I THRU M
DO BLOCK (STEP1( ), STEP2( ), PRINT(F_I),
IF I=M THEN GO(END), STEP(3), PRINT(E_I), END),
OUTPUT( ))
(E7) SETUP1(1):=(W:1, FOR I THRU M DO W: W+K_I E^I,
                 X:Y0(Z), FOR I THRU M DO X: X+Y_I(Z) E^I)
```

$$(E8)\ \text{SETUP2( )}:=(\text{TEMP1: EV}\Big(-\frac{2E^3X\cos^4\left(\frac{Z}{N}\right)\sin^2\left(\frac{Z}{N}\right)}{J_{13}J_2J_3N^2}$$

$$+\frac{6E^2X\cos^2\left(\frac{Z}{N}\right)\sin^2\left(\frac{Z}{N}\right)}{J_2J_3N^2}+\frac{2E^2X\cos^2\left(\frac{Z}{N}\right)\sin^2\left(\frac{Z}{N}\right)}{J_{13}J_2N^2}$$

$$+\frac{2EX\sin^2\left(\frac{Z}{N}\right)}{J_2N^2}+\frac{4E^3X_Z\cos^5\left(\frac{Z}{N}\right)\sin\left(\frac{Z}{N}\right)}{J_{13}J_2N}$$

$$-\frac{6E^2X_Z\cos^3\left(\frac{Z}{N}\right)\sin\left(\frac{Z}{N}\right)}{J_2J_3N}+\frac{2E^2X_Z\cos^3\left(\frac{Z}{N}\right)\sin\left(\frac{Z}{N}\right)}{J_{13}J_2N}$$

$$-\frac{2EX_Z\cos\left(\frac{Z}{N}\right)\sin\left(\frac{Z}{N}\right)}{J_3N}-\frac{4EX_Z\cos\left(\frac{Z}{N}\right)\sin\left(\frac{Z}{N}\right)}{J_2N}$$

$$-\frac{2EX_Z\cos\left(\frac{Z}{N}\right)\sin\left(\frac{Z}{N}\right)}{J_{13}N}-\frac{E^3X_{ZZ}\cos^6\left(\frac{Z}{N}\right)}{J_{13}J_2J_3}$$

$$+\frac{2E^3X\cos^6\left(\frac{Z}{N}\right)}{J_{13}J_2J_3N^2}-\frac{E^3WX\cos^6\left(\frac{Z}{N}\right)}{J_{12}J_{13}^2}+\frac{E^2X_{ZZ}\cos^4\left(\frac{Z}{N}\right)}{J_2J_3}$$

$$-\frac{E^2X_{ZZ}\cos^4\left(\frac{Z}{N}\right)}{J_{13}J_3}-\frac{E^2X_{ZZ}\cos^4\left(\frac{Z}{N}\right)}{J_{13}J_2}$$

$$-\frac{2E^2X\cos^4\left(\frac{Z}{N}\right)}{J_2J_3N^2}+\frac{2E^2X\cos^4\left(\frac{Z}{N}\right)}{J_{13}J_2N^2}+\frac{2E^2WX\cos^4\left(\frac{Z}{N}\right)}{J_{12}J_{13}}$$

$$+\frac{E^2WX\cos^4\left(\frac{Z}{N}\right)}{J_{13}^2}+\frac{EX_{ZZ}\cos^2\left(\frac{Z}{N}\right)}{J_3}+\frac{EX_{ZZ}\cos^2\left(\frac{Z}{N}\right)}{J_2}$$

$$-\frac{EX_{ZZ}\cos^2\left(\frac{Z}{N}\right)}{J_{13}}-\frac{2EX\cos^2\left(\frac{Z}{N}\right)}{J_2N^2}$$

$$-\frac{2EWX\cos^2\left(\frac{Z}{N}\right)}{J_{13}}-\frac{EWX\cos^2\left(\frac{Z}{N}\right)}{J_{12}}$$

$$+X_{ZZ}+WX,\ \text{DIFF}\Big),$$

```
TEMP1 : TAYLOR (TEMP1, E, 0, M),
FOR I THRU M DO EQ_I : COEFF (TEMP1, E, I))
(E9) STEP1(): = (TEMP1 : EV(EQ_I,
MAKELIST ([E_J, F_J], J, 1, I-1), DIFF),
TEMP1 : EV(TEMP1, Z=NU), TEMP1 : OUTOFPOIS (TEMP1),
TEMP1 : EV(TEMP1, U=Z/N))
(E10) STEP2( ) : = (F_I : SOLVE (COEFF(TEMP1, Y_0(Z)), K_I),
                    TEMP1 : EXPAND (EV(TEMP1, F_I)))
(E11) STEP3( ) : = (TEMP1 : -EV(TEMP1, Y_1(Z)=0),
TEMP1 : APPLYB1 (TEMP1, S), E_I : Y_I(Z) = APPLYB1 (TEMP1, C))
(E12) OUTPUT( ) : = (TEMP1 : N^2
EV(W, MAKELIST ([F_J], J, 1, M)),
TEMP1 : TAYLOR (TEMP1, E, 0, M), PRINT ("K=", TEMP1))
```


Downloaded 02 May 2010 to 171.66.16.54. Redistribution subject to ASME license or copyright; see http://www.asme.org/terms/Terms_Use.cfm

A Study of Dynamic Instability of Plates by an Extended Incremental Harmonic Balance Method

C. Pierre[1]
Graduate Research Assistant.

E. H. Dowell
Dean of Engineering,
Mem. ASME

School of Engineering,
Duke University,
Durham, N.C. 27706

The dynamic instability of plates is investigated with geometric nonlinearities being included in the model, which allows one to determine the amplitude of the parametric vibrations. A modal analysis allowing one spatial mode is performed on the nonlinear equations of motion and the resulting nonlinear Mathieu equation is solved by the incremental harmonic balance method, which takes several temporal harmonics into account. When viscous damping is included, a new algorithm is proposed to solve the equation system obtained by the incremental method. For this purpose, a new characterization of the parametric vibration by its total amplitude—or Euclidian norm—is introduced. This algorithm is particularly simple and convenient for computer implementation. The instability regions are obtained with a high degree of accuracy.

1 Introduction

When a flat plate is subjected to a periodic, in-plane load of the form $P_0 + P_t \cos \theta t$, it may either remain straight or exhibit lateral deflections. The latter phenomenon is referred to as parametric instability, because it occurs over continuous zones of the (P_0, P_t, θ) parameter space. At the principal parametric resonance, the exciting frequency θ lies near twice the natural frequency of the system, and the frequency of the parametric vibration is half the pulsating load frequency θ. The linear theory can only predict the frequencies at which lateral vibration would occur, and determining the amplitude of the vibration requires a nonlinear formulation.

Parametric instability has been studied by a variety of authors. In the well-known text by Bolotin, *The Dynamic Stability of Elastic Systems* [1], a detailed linear theory of the phenomenon is proposed. Moreover, Bolotin obtained an expression for the amplitude of the parametric vibration of plates as a function of the load frequency and the load amplitude, by allowing one spatial mode for the deflection of the plate, and by using a first harmonic approximation for the temporal part in the nonlinear calculation. Nayfeh and Mook [2] also proposed an extensive study of parametric instability.

Using a computer analysis approach, Lau et al. [3] proposed an incremental method to obtain the parametric instability boundary of columns. The method easily treats strong geometrical nonlinearities and provides highly accurate results. Nevertheless, although Lau was able to solve for a damped system in the linear case, the characterization he adopted for the ampltitude of the vibration did not allow him to treat a geometrically nonlinear system with linear viscous damping.

In the present paper the dynamic instability of plates is considered, and the boundary regions of instability are determined for a single spatial mode model, nonlinear system, by applying and extending the incremental harmonic balance method. In particular, the solution procedure proposed generalizes the incremental method when linear viscous damping is included in the nonlinear model.

2 Equation of Dynamic Instability of Plates

Consider a rectangular plate subjected to a uniformly distributed, compressive, periodic in-plane load per unit length $P(t) = P_0 + P_t \cos \theta t$. The plate is shown in Fig. 1. The nonlinear equations for large deflections are the well-known Von-Karman equations [4], which are solved through a modal analysis by expanding the lateral deflection w:

$$w(x,y,t)/h = \sum_k f_k(t)\,\psi_k(x,y) \tag{1}$$

where the ψ_k's are the spatial modes of free transverse vibration, which depend on the boundary conditions, and where the f_k's are the associated dimensionless generalized coordinates. For instance, if the plate is simply supported on all edges, $\psi(x,y) = \sin(m\pi x/a) \cdot \sin(n\pi y/b)$; if the plate is pinned at its leading and trailing ends with free side edges, $\psi(x) = \sin(m\pi x/a)$. For the sake of simplicity, a single-term model expansion is considered. After some tedious calculation, the modal analysis leads to the same nonlinear differential equation with variable coefficients—the Mathieu equation—for the two boundary configurations mentioned in the foregoing [1, 5]:

[1]Formerly, Graduate Research Assistant, Princeton University.

Contributed by the Applied Mechanics Division, and presented at the 1985 Joint ASME/ASCE Applied Mechanics, Fluids Engineering, and Bioengineering Conference, Albuquerque, N. Mex., June 24-26, 1985 of THE AMERICAN SOCIETY OF MECHANICAL ENGINEERS.

Discussion on this paper should be addressed to the Editorial Department, ASME, United Engineering Center, 345 East 47th Street, New York, N.Y. 10017, and will be accepted until two months after final publication of the paper itself in the JOURNAL OF APPLIED MECHANICS. Manuscript received by ASME Applied Mechanics Division, March, 1984; final revision, October, 1984. Paper No. 85-APM-33.

Copyright © 1985 by ASME
Downloaded 02 May 2010 to 171.66.16.54. Redistribution subject to ASME license or copyright; see http://www.asme.org/terms/Terms_Use.cfm

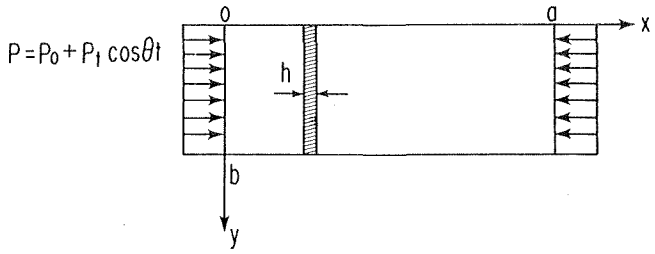

Fig. 1 Geometry of plate under uniform compressive load

$$\frac{d^2f}{dt^2} + \omega_L{}^2 f(1 - 2\lambda \cos\theta t) + \gamma f^3 = 0 \tag{2}$$

where $\omega_L = \omega_0(1 - P_0/P^*)^{1/2}$ is the transverse vibration natural frequency of a plate loaded by the constant axial force P_0, $\lambda = P_t/[2(P^* - P_0)]$ is the coefficient of excitation, ω_0 is the free transverse vibration natural frequency, P^* is the static buckling critical load, and γ is the nonlinear coefficient, the expressions of these parameters depending on the boundary configuration [5].

Since the plate is most likely to vibrate at the frequency $\theta/2$—the first region of instability, the following set of variables is used [3]: the parametric vibration natural frequency $\omega = \theta/2$, the reduced vibration natural frequency $\Omega = \omega/\omega_L$, a new time scale $\tau = \omega t$, and the reduced nonlinear coefficient $K = \gamma/\omega_L{}^2$. The latter variables are employed in equation (2), and for a single spatial mode model, the boundaries of dynamic instability are determined by:

$$\Omega^2 \frac{d^2f}{d\tau^2} + 2\zeta\Omega \frac{df}{d\tau} + (1 - 2\lambda \cos 2\tau)f + Kf^3 = 0 \tag{3}$$

when linear viscous damping is introduced into the model.

3 Determination of the Boundaries of Parametric Instability for a Nonlinear System With Viscous Damping

3.1 A Brief Review of the Incremental Harmonic Balance Method. The method used to solve equation (3) is basically an incremental harmonic balance method discussed by Lau in [3]. As pointed out by Lau, the method is convenient for computer implementation, is not limited by weak nonlinearities or small exciting parameters, and provides very accurate results. The first step of the incremental harmonic balance method is a Newton-Raphson procedure: the current state of vibration corresponding to a point (Ω_0, λ_0) on the instability boundary is denoted by $f_0(\tau)$. A neighboring state is reached through a parameter incrementation:

$$\begin{aligned} \lambda &= \lambda_0 + \Delta\lambda \\ \Omega &= \Omega_0 + \Delta\Omega \\ f &= f_0 + \Delta f \end{aligned} \tag{4}$$

Substituting the expansions (4) into equation (3) and neglecting the nonlinear terms of $\Delta\lambda$, $\Delta\Omega$, Δf, a linearized incremental equation is obtained:

$$\Omega_0^2 \Delta\ddot{f} + 2\zeta\Omega_0 \Delta\dot{f} + (1 - 2\lambda_0 \cos 2\tau)\Delta f + 3Kf_0^2 \Delta f = R - 2\zeta\Delta\Omega\dot{f}_0 + 2\Delta\lambda f_0 \cos 2\tau - 2\Delta\Omega\Omega_0\ddot{f}_0 \tag{5a}$$

$$R = -[\Omega_0^2\ddot{f}_0 + 2\zeta\Omega_0\dot{f}_0 + (1 - 2\lambda_0 \cos 2\tau)f_0 + Kf_0^3] \tag{5b}$$

where $\cdot = d/d\tau$. R is the corrective term that goes to zero when the solution is reached.

Although equation (5*a*) is linear, it has variable coefficients, and thus is difficult to solve. Hence, an approximate solution will be obtained by assuming a periodic solution and using Galerkin's method, which is the second step of the method. The functions f_0 and Δf can be written as

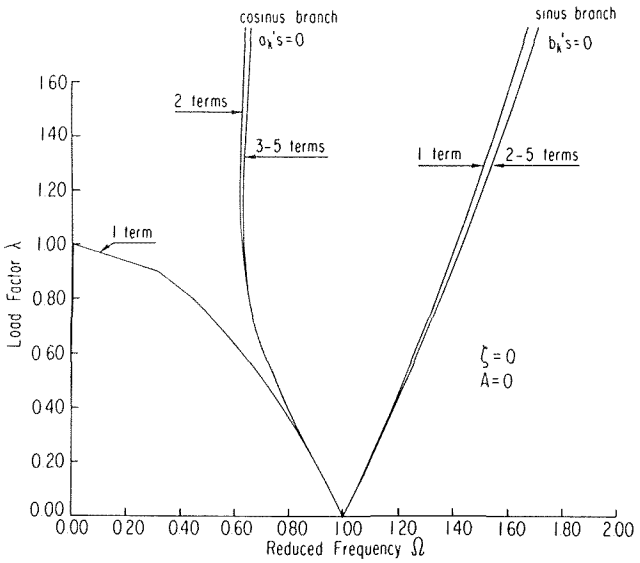

Fig. 2 Influence of the number of temporal harmonics terms on the principal region of instability for a zero damping coefficient

$$f_0(\tau) = \sum_{k=1,3,\ldots}^{2N-1} (a_k \sin k\tau + b_k \cos k\tau) \tag{6}$$

$$\Delta f(\tau) = \sum_{k=1,3,\ldots}^{2N-1} (\Delta a_k \sin k\tau + \Delta b_k \cos k\tau) \tag{7}$$

for the first region of instability, corresponding to a solution of period 2π. The summation is on $k = 2, 4, \ldots, 2N$ for the second region of instability, corresponding to a solution of period π. N is the number of temporal terms taken into account.

Let us define the amplitude vector by $\mathbf{a} = (a_1, a_3, \ldots, a_{2N-1}, b_1, b_3, \ldots, b_{2N-1})^T$ and its corresponding increment accordingly, where a bold face letter denotes a vector. Galerkin's method is used with Δa_k's and Δb_k's as generalized coordinates leading to an incremental system of $2N$ linear equations in the terms of the Δa_k's and Δb_k's:

$$[C]\Delta\mathbf{a} = \mathbf{R} + \Delta\lambda\,\mathbf{P} + \Delta\Omega\,\mathbf{Q} \tag{8}$$

See [3, 5] for the detailed expressions of $[C]$, $\mathbf{P}$, $\mathbf{Q}$, and $\mathbf{R}$.

3.2 The Algorithms Associated With the Incremental Method. On a boundary of parametric instability, a current state of vibration of the system is defined by a triplet (f, Ω, λ) solution of equation (3). By considering equation (6), one may note that the vibration is represented in an equivalent manner by f or by the converged amplitude vector $\mathbf{a}$, hence, the vibration may be characterized by the norm of the amplitude vector $\mathbf{a}$, that is $\|\mathbf{a}\|$. The choice of norm will be discussed later in this paragraph. Then, in the $(\|\mathbf{a}\|, \Omega, \lambda)$ space, the boundaries of dynamic instability are surfaces, whose projections in the two-dimensional (Ω, λ), respectively, $(\Omega, \|\mathbf{a}\|)$ space are boundary curves of instability with $\|\mathbf{a}\|$, respectively, λ as a parameter. In the following paragraphs, special attention will be focused on the algorithms that allow us to obtain a solution $(\|\mathbf{a}\|, \Omega, \lambda)$, hence (f, Ω, λ) on a boundary of parametric instability, and moreover, to follow this solution along the curves defined in the foregoing.

Returning to equation (8), the problem is to solve, at each incremental step, a linear system of $2N$ equations with $2N+2$ unknows $\Delta\mathbf{a}$, $\Delta\Omega$, $\Delta\lambda$. Hence, one needs to add two constraints being relations between $\Delta\mathbf{a}$, $\Delta\Omega$, and $\Delta\lambda$, which are determined as follows. Consider, for example, the boundary curves in the (Ω,λ) plane, with $\|\mathbf{a}\|$ as a parameter, that is, the

Downloaded 02 May 2010 to 171.66.16.54. Redistribution subject to ASME license or copyright; see http://www.asme.org/terms/Terms_Use.cfm

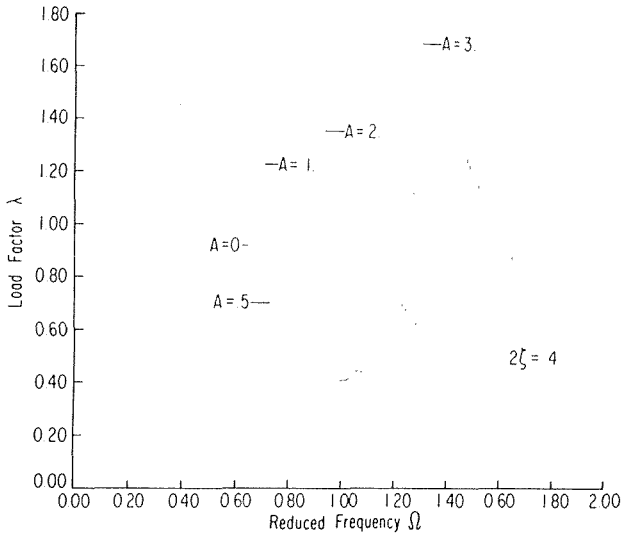

Fig. 3 Nonlinear effects of amplitude on the principal instability region for a damping coefficient $2\zeta = 0.4$ and for $A = 0, 0.5, 1.0, 2.0, 3.0$

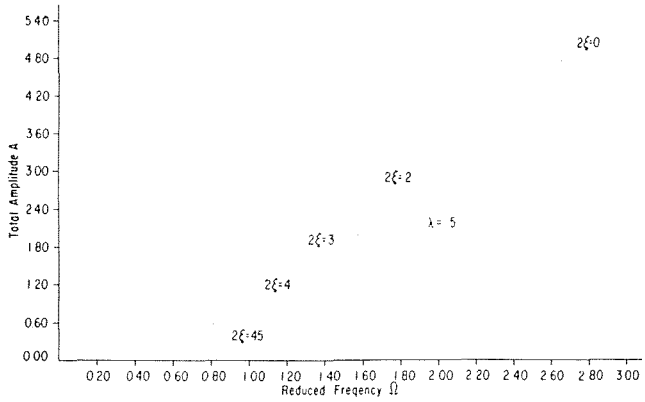

Fig. 4 Nonlinear influence of the amplitude on the reduced frequency for a coefficient of excitation $\lambda = 0.5$, and for various damping coefficient $2\zeta = 0.0, 0.2, 0.3, 0.4, 0.45$

value of $\|\mathbf{a}\|$ is fixed for each curve. To obtain a point on such a curve, the quantity $\|\mathbf{a}\|$ has to be constant through the incremental steps, determining the first constraint to be:

$$\overline{\|\mathbf{a}\| = \|\mathbf{a} + \Delta\mathbf{a}\|} \tag{9}$$

The second constraint is either $\Delta\lambda = 0$ or $\Delta\Omega = 0$. If $\Delta\lambda = 0$, λ is said to be an active increment [3], i.e., the boundary curve is obtained by incrementing λ from point to point. This is the so-called λ-incrementation [3]. Similarly, if $\Delta\Omega = 0$, Ω is the active increment (Ω-incrementation). The second constraint $\Delta\lambda = 0$ or $\Delta\Omega = 0$ is determined by the local shape of the curve: In practice, the active increment is chosen as the one that varies faster. As can be seen in Fig. 3, the slope of the curve λ versus Ω determines λ as the active increment, except for the possible U-turn portion of the curve, where an Ω-incrementation is necessary locally.

Similarly, for a point located on a curve of the (Ω, $\|\mathbf{a}\|$) - plane, with λ as a parameter, the first constraint is λ = constant, i.e., $\Delta\lambda = 0$. And considering the high value of the slope, near the Ω-axis of the curve $\|\mathbf{a}\|$ versus Ω shown in Fig. 4, the active increment has to be $\|\mathbf{a}\|$, implying relation (9) except for the possible U-turn portion of the curve, which requires an Ω-incrementation. Note that the existence of U-turn portions of the curves requires that the computer program has the capability of automatically changing the incrementation parameter. The preceeding development gives rise to the following possibilities:

(*a*) U-turn of the curves $\|\mathbf{a}\|$ versus Ω.

Then $\Delta\Omega = \Delta\lambda = 0$, and equation (8) becomes:

$$[C]\Delta\mathbf{a} = \mathbf{R} \tag{10}$$

which can be solved directly for $\Delta\mathbf{a}$.

(*b*) All other sections of the boundary curves.

Then constraints are $\|\mathbf{a}\| = \|\mathbf{a} + \Delta\mathbf{a}\|$ and $\Delta\Omega = 0$ or $\Delta\lambda = 0$. Because of their similarity, only the first of these two cases is chosen. Hence, at each step, one has to solve:

$$\begin{cases} [C]\Delta\mathbf{a} = \mathbf{R} + \Delta\lambda\,\mathbf{P} \\ \|\mathbf{a}\| = \|\mathbf{a} + \Delta a\| \end{cases} \tag{11}$$

The methods for solving system (11) now depend on the choice of the norm for the amplitude vector. Among several possibilities, the two following norms have been studied:

the so-called infinite norm:

$$\|\mathbf{a}\|_\infty = \max_{i=1,3\,..\,2N-1} \{|a_i|, |b_i|\} \tag{12}$$

the Euclidian norm

$$\|\mathbf{a}\|_2 = \left(\sum_{i=1,3}^{2N-1} (a_i^2 + b_i^2) \right)^{1/2} \tag{13}$$

These choices and the corresponding methods used to solve system (11) are discussed in the two following sections.

3.3 System Without Viscous Damping ($\zeta = 0$). Here the boundary curves consist of two different branches corresponding to decoupled "sinus" and "cosinus" vibrations; see Fig. 2. For example, let us consider the case of a "sinus" response, i.e., all the Δb_k's are very small or equal to zero. The most natural way to characterize the vibration is certainly to consider the amplitude a_1 of the first temporal harmonic, which is predominant. This is equivalent to choosing the infinite norm defined by (12); $\|\mathbf{a}\|_\infty = |a|_1$. This approach is adopted by Lau in [3]. Then the constant-norm condition becomes $\Delta a_1 = 0$ and the system (11) may be partitioned as follows [6]:

$$\begin{cases} \mathbf{C}_{12}^T \Delta\mathbf{a}' = R_1 + \Delta\lambda P_1 \\ [\mathbf{C}_3]\Delta\mathbf{a}' = \mathbf{R}' + \Delta\lambda\mathbf{P}' \end{cases} \tag{14}$$

where:

$$[C] = \left[\begin{array}{c|c} \mathbf{C}_1 & \mathbf{C}_{12}^T \\ \hline \mathbf{C}_{21} & [C_3] \end{array}\right] \quad \Delta\mathbf{a} = \begin{bmatrix} 0 \\ \Delta\mathbf{a}' \end{bmatrix} \quad \mathbf{R} = \begin{bmatrix} R_1 \\ \mathbf{R}' \end{bmatrix} \quad \mathbf{P} = \begin{bmatrix} P_1 \\ \mathbf{P}' \end{bmatrix}$$

T denotes a transpose. Solving these equations for $\Delta\lambda$, one obtains:

$$\Delta\lambda = \frac{\mathbf{C}_{12}^T [C_3]^{-1}\mathbf{R}' - R_1}{P_1 - \mathbf{C}_{12}^T [C_3]^{-1}\mathbf{P}'} \tag{15}$$

Then, knowing $\Delta\lambda$, $\Delta\mathbf{a}'$ is deduced:

$$\Delta\mathbf{a}' = [C_3]^{-1}\{\mathbf{R}' + \Delta\lambda\mathbf{P}'\} \tag{16}$$

3.4 An Original Method for a Nonlinear System Including Viscous Damping. When viscous damping is included, the boundary curves no longer consist of two different branches, but of one single branch with a U-turn portion; see Fig. 3. The "sinus" and "cosinus" vibrations are no longer decoupled. If the system is linear, i.e., $K = 0$, it is still possible to characterize the vibration by a_1 or b_1, since then only the relative values of the components of $\mathbf{a}$ are required. This is the way Lau handled viscous damping in the linear system.

Downloaded 02 May 2010 to 171.66.16.54. Redistribution subject to ASME license or copyright; see http://www.asme.org/terms/Terms_Use.cfm

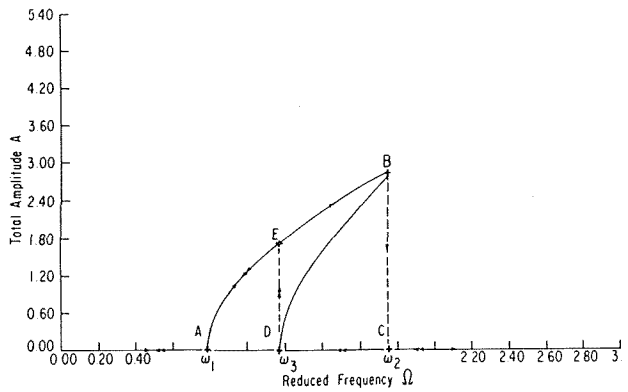

Fig. 5 Physical interpretation of the curves *A* versus Ω, with λ as a parameter

Nonetheless, for a nonlinear system, the knowledge of the relative values of the components of **a** is not sufficient, and one would need to represent the vibration by $(a_1^2 + b_1^2)^{1/2}$, amplitude of the first harmonic. However, such a representation of the vibration complicates the solution of system (11). It appears that a better characterization of the vibration is obtained by considering its so-called "total" amplitude, the Euclidian norm of the amplitude vector, given by equation (13). Let us denote $\|\mathbf{a}\|_2$ by A. A^2 is proportional to the energy of the vibration, which is the sum of each harmonic energy. System (11) becomes:

$$\begin{cases} [C]\Delta\mathbf{a} = \mathbf{R} + \Delta\lambda\mathbf{P} \\ (a_1 + \Delta a_1)^2 + \cdots + (a_{2N-1} + \Delta a_{2N-1})^2 + (b_1 + \Delta b_1)^2 \\ \qquad + \cdots (b_{2N-1} + \Delta b_{2N-1})^2 = {A_0}^2 \end{cases} \tag{17}$$

where A_0 is the value assigned to the constant amplitude. System (17) cannot be solved directly because of the nonlinear constraint. However, it is possible to use an approach provided by an analysis of the path deflection versus load in a nonlinear buckling problem [7], the latter giving rise to the same type of nonlinear constraint. The method is as follows: System (17) may be rewritten as:

$$\Delta\mathbf{a} = [C]^{-1}\{\mathbf{R} + \Delta\lambda\mathbf{P}\} \tag{18a}$$

$$(\mathbf{a} + \Delta\mathbf{a})^T(\mathbf{a} + \Delta\mathbf{a}) = {A_0}^2 \tag{18b}$$

Substituting the expression (18*a*) of $\Delta\mathbf{a}$ into equation (18*b*) and expanding the resulting relation leads to a quadratic expression in $\Delta\lambda$:

$$a_1\Delta\lambda^2 + a_2\Delta\lambda + a_3 = 0 \tag{19a}$$

where:

$$\begin{aligned} a_1 &= ([C]^{-1}\mathbf{P})^T([C]^{-1}\mathbf{P}) \\ a_2 &= ([C]^{-1}\mathbf{P})^T\mathbf{a} + \mathbf{a}^T([C]^{-1}\mathbf{P}) + ([C]^{-1}\mathbf{P})^T[C]^{-1}\mathbf{R} \\ &\quad + ([C]^{-1}\mathbf{R})^T[C]^{-1}\mathbf{P} \\ a_3 &= \mathbf{a}^T\mathbf{a} + \mathbf{a}^T[C]^{-1}\mathbf{R} + ([C]^{-1}\mathbf{R})^T\mathbf{a} \\ &\quad + ([C]^{-1}\mathbf{R})^T([C]^{-1}\mathbf{R}) - {A_0}^2. \end{aligned} \tag{19b}$$

The coefficients a_1, a_2, a_3 are easily obtained by a computer calculation. The nonlinear system (17) has been reduced to a quadratic equation in $\Delta\lambda$, whose roots are designated by $\Delta\lambda_1$ and $\Delta\lambda_2$. Using these values, the two corresponding amplitude vectors are obtained:

$$\Delta\mathbf{a}_i = [C]^{-1}\{\mathbf{R} + \Delta\lambda_i\mathbf{P}\} \quad i = 1,2 \tag{20}$$

Of course, only one of the roots $\Delta\lambda_1$ and $\Delta\lambda_2$ is a relevant solution. To determine it, the following criterion is used:

$$\mathbf{a}^T(\mathbf{a} + \Delta\mathbf{a}) > 0 \tag{21}$$

This means that the direction of the amplitude vector remains the same after incrementation. Hence, between $(\Delta\mathbf{a}_1, \Delta\lambda_1)$ and $(\Delta\mathbf{a}_2, \Delta\lambda_2)$, criterion (21) determines the solution $(\Delta\mathbf{a}, \Delta\lambda)$ of system (17). This latter method, which allows the presence of viscous damping in the system, has been chosen to solve the system obtained by the incremental harmonic balance method at each step; thus the relevant characterization of the vibration by its total amplitude has been considered. The method is particularly convenient for computer implementation. Of course, the method is also valid when there is no viscous damping.

3.5 Results and Discussion. Figure 2 shows the principal instability region for a zero amplitude i.e., for a linear calculation, with different numbers of harmonic terms in the temporal expansion, for $\zeta = 0$. It can be seen that a three-term expansion gives highly accurate results. It is also worth mentioning the importance of the third harmonic: a first harmonic approximation is sufficient only for small values of the coefficient of excitation. The following results are obtained by considering a three-term expansion. The reduced nonlinear coefficient has been taken equal to 0.341.

Figure 3 represents the nonlinear effect of amplitude on the principal instability region for $2\zeta = 0.4$ in the (Ω, λ)-plane. One may note that, when viscous damping is taken into account, a minimum coefficient of excitation is necessary to make parametric vibration occur. It can be seen from Fig. 3 that the value $\lambda_{\min} = 2\zeta$ predicted by Bolotin [1] is a good approximation for the linear case.

Figure 4 shows the dependence of the critical reduced frequency on the "total" amplitude for various damping coefficients and for $\lambda = 0.5$. When the damping coefficient is different from zero, the curves no longer consist of two distinct branches, but of one closed path. Since λ has to be greater than $\lambda_{\min} \simeq 2\zeta$, there are no curves A versus Ω, corresponding to values of 2ζ greater than 0.5. It can be seen that the greater ζ is, the smaller the amplitude of the vibration for given λ is. At the limit $2\zeta \simeq 0.5$, there is only a zero amplitude vibration near $\Omega = 1$: the curve is restricted to a point on the axis $A = 0$.

The boundary curves in the (Ω, A)-plane have an important physical meaning. Let us imagine that, for given ζ and constant λ, the excitation frequency is increased, starting from zero. Considering the instability region in the (Ω, A)-plane represented on Fig. 5, the response of the system can be analyzed as follows: for Ω smaller than ω_1, there are only in-plane vibrations. At $\Omega = \omega_1$, parametric resonance occurs, the amplitude of the steady vibrations increasing with Ω. When Ω reaches the maximum value of ω_2, a jump phenomenon occurs and the parametric vibrations stop abruptly. Finally, for Ω greater than ω_2, the plate vibrates in its own plane. On the other hand, when Ω decreases from a large value, there are only in-plane vibrations, until Ω reaches ω_3 at which there is a jump phenomenon and resonance appears. Then, the amplitude of the vibrations decreases with Ω and goes to zero as Ω goes to ω_1. Hence, it turns out that steady vibrations only occur on the part AB of the curve, which is the stable side of the boundary. The branch BD, which does not represent an actual response, is the unstable side. Moreover, by considering the instability region in the (Ω, λ)-plane for the given amplitude A, only the points located on the left part, such that Ω has the smallest value for given λ, correspond to actual steady vibrations.

As a conclusion, for a nonlinear system, only vibrations with steady-state amplitudes exist in the instability regions. This result has been confirmed experimentally [1], since no vibrations with amplitudes increasing unboundedly with time have ever been observed. Also see the work of Somerset and Evan-Iwanowski [8-10].

3.6 Validity of the Method. The results provided by the

Downloaded 02 May 2010 to 171.66.16.54. Redistribution subject to ASME license or copyright; see http://www.asme.org/terms/Terms_Use.cfm

incremental method have been checked by a direct time-integration of the motion performed on the Mathieu equation (3). The method used is a classical fourth-order Runge-Kutta integration. For example, in Fig. 3, consider a point on the boundary curve $A = 1$. To obtain a vibration amplitude equal to 1, the point must be chosen on the left part of the curve. A point belonging to the right part of the curve would also represent a steady vibration, but with an amplitude that characterizes another curve whose left part intersects the initial curve at this point. A periodic motion of period 2π is reached after a transient phase. The amplitudes of the harmonics are obtained by performing a Fourier transform on the numerical values obtained by the time integration, and then by comparing them with the amplitudes obtained by the incremental method. Due to lack of space, detailed results cannot be presented in this paper. However, the agreement between the two methods was found to be excellent.

4 Concluding Remarks

The incremental harmonic balance method presented by Lau in [3] has been successfully applied to the investigation of dynamic instability of plates. The characterization of the parametric vibration by its total amplitude, which is by itself a very relevant choice, has allowed one to treat easily the case when viscous damping is included in the nonlinear model. For that purpose, an original and efficient algorithm has been developed, which easily handles the nonlinear constraint introduced in the incremental system of equations by the consideration of the total amplitude. The boundaries of the first region of instability have been obtained by considering several temporal harmonics and with an excellent accuracy in the (Ω, λ) and (Ω, A)-planes. The results have been checked by a direct time integration. The consideration of the boundary curves in the (Ω, A)-plane when viscous damping is included has led to a physical interpretation of the response of the system and, moreover, to the determination of the stable and unstable parts of the boundary curves.

The authors have studied in some detail the effect of multiple spatial modes and the determination of the most critical mode through direct numerical integration [5]. However, lack of space precludes the authors from presenting results in the present paper. Furthermore, it is believed that the incremental method could be generalized to deal with several spatial modes. This is left for a future study.

Acknowledgment

This work was supported by National Science Foundation Grant No. MEA-8315193, Division of Mechanical Engineering and Applied Mechanics. Dr. Elbert Marsh is the grant monitor.

References

1 Bolotin, V. V., *The Dynamic Stability of Elastic Systems*, Holden-Day, San Francisco, 1964.

2 Nayfeh, A. H., and Mook, D. T., *Nonlinear Oscillations*, John Wiley & Sons, New York, 1979.

3 Lau, S. L., Cheung, Y. K., and Wu, S. Y., "A Variable Parameter Incrementation Method for Dynamic Instability of Linear and Nonlinear Elastic Systems," ASME JOURNAL OF APPLIED MECHANICS, Vol. 49, 1982, pp. 849-853.

4 Timoshenko, S. P., and Gere, J. M., *Theory of Elastic Stability*, McGraw-Hill, New York, 1961.

5 Pierre, C., "An Incremental Approach to the Theory of Dynamic Instability of Plates," Master's Thesis, Princeton University, Oct. 1983.

6 Haisler, W. E., Stricklin, J. A., and Key, J. E., "Displacement Incrementation in Nonlinear Structural Analysis by the Self-Correcting Method," *International Journal for Numerical Methods in Engineering*, Vol. 11, 1977, pp. 3-10.

7 Crisfield, M. A., "A Fast Incremental/Iterative Solution Procedure that Handles "Snap-Through," *Computers and Structures*, Vol. 13, 1981, pp. 55-62.

8 Somerset, J. H., "Large Amplitude Stabilization of Parametrically Excited Plate Vibrations," PhD Thesis, Syracuse University, June 1965.

9 Somerset, J. H., and Evan-Iwanowski, R. M., "Experiments on Large Amplitude Parametric Vibration of Rectangular Plates," *Developments in Theoretical and Applied Mechanics*, Vol. 3, Proc. 3rd Southeastern Conf. on Theoretical and Applied Mechanics, Columbia, S.C., Apr., 1966, Pergamon Press.

10 Somerset, J. H., and Evan-Iwanowski, R. M., "Influence of Nonlinear Inertia on the Parametric Response of Rectangular Plates," *Int. J. Nonlinear Mechanics*, Vol. 2, 1967, pp. 217-232.

Downloaded 02 May 2010 to 171.66.16.54. Redistribution subject to ASME license or copyright; see http://www.asme.org/terms/Terms_Use.cfm

On the Recursive Determination of Body Frames for Multibody Dynamic Simulation

R. E. Roberson
Department of Applied Mechanics and Engineering Science, University of California San Diego, La Jolla, Calif. 92037

In multibody dynamic simulation it often is convenient to choose new body axes such that all body frames are parallel to the attitude reference frame when the system of bodies is in a prescribed configuration consistent with the interbody constraints. Computational details are given of how this may be done efficiently using a recursive method.

1 Introduction

Each body of a multibody system has its own local vector triad used as a body frame for the resolution of the vectors and dyadics associated with that body. These often can be regarded as "plan axes" because they usually are established by the construction drawings of the physical bodies. Plans offer natural origins for the frames as well as natural orientations for their base vectors. (Without loss in generality it is assumed that the latter are orthonormal and dextral.) It cannot be taken for granted that the origin lies at the center of mass of the body or that the base vectors are aligned with principal axes of inertia. When implementing a digital dynamic simulation it is easy enough to shift the origins to the centers of mass of the respective bodies but, as is well known, there is little point to rotating axes to coincide with principal axes unless the multibody system is of very specialized type.

When a set of bodies is combined to form a single multibody system, the plan axes may be in any helter-skelter arrangement, with no systematic relationship among them. Yet a certain order is desirable in practice, as detailed later, so there may be a persuasive reason to choose a new set of body axes in many or all bodies. This paper gives a criterion for the choice of body axes and shows how to construct the new axes by a computationally efficient procedure.

2 Background on System Structure

It is assumed that the interconnection of the multibody system is characterized by a graph, as described in [1] and the literature cited there. The graph consists of n_V+1 vertices enumerated $0,1,\ldots,n_V$ and n_B branches (directed edges) enumerated $1,2,\ldots,n_B$, with $n_B \geq n_V$. (If $n_B = n_V$ the graph is a tree.) In that formalism the 0-vertex represents a known reference frame with respect to which the motion of the system is described, while the remaining vertices represent physical bodies. Each branch represents the totality of interactions existing between the two vertices it connects. The branch directions can be assigned arbitrarily: they merely establish positive senses for interaction forces and torques, translation vectors, and orientations. For simulation purposes, the only graphs considered are connected graphs in which no vertex lies at both ends of the same branch and no pair of vertices is connected by more than one branch.

In symbolic terms, if a branch number is b, the vertex from which the branch originates is denoted $(b+)$ and the vertex on which the branch terminates is denoted $(b-)$. Numerically, the relation between branch and vertex numbers is established by two arrays of length n_B containing the same information as would be found in the incidence matrix of the graph. These arrays, together with values of n_V and n_B, are the global quantities used to describe the structure of the multibody system.

A first preparatory step for simulation is the selection of a spanning tree, a process that can be done algorithmically by any of various standard methods. This matter need not be discussed here; the interested reader is referred to [2, 3]. Suffice it to say that the root of the spanning tree is the 0-vertex and that any two vertices v_i, v_j may be ordered by a weak ordering relationship "$\leq$," defined such that $v_i = v_j$ if the two vertices are identical, while $v_i < v_j$ if the simple chain (in the spanning tree) from v_j to the 0-vertex passes through v_i.

Let identifiers *nv*, *nb* stand for n_V and n_B. The number of arcs of the graph (branches of the spanning tree) equals n_V, while $n_B - n_V$ is the number of chords (branches of the original graph not in the spanning tree). Three integer arrays are filled in the process of generating a spanning tree. The first, *astack* [1:*nv*], contains the arc numbers in the order of their discovery when the search for the tree is started at the 0-vertex. For present purposes an important property of this array is that the branch listed at each index value is not closer to the 0-vertex than any other branch having a smaller index value in the array. That is, as one encounters successive branch numbers in *astack*, they correspond to branches "further out" in the tree relative to the root. Another point is that a branch number is entered into this array with positive algebraic sign when that branch is directed toward the 0-vertex, and with negative sign if it is directed oppositely.

Contributed by the Applied Mechanics Divison for publication in the JOURNAL OF APPLIED MECHANICS.

Discussion on this paper should be addressed to the Editorial Department, ASME, United Engineering Center, 345 East 47th Street, New York, N.Y. 10017, and will be accepted until two months after final publication of the paper itself in the JOURNAL OF APPLIED MECHANICS. Manuscript received by ASME Applied Mechanics Division, March, 1984; Final revision, January, 1985.

Copyright © 1985 by ASME
Downloaded 02 May 2010 to 171.66.16.54. Redistribution subject to ASME license or copyright; see http://www.asme.org/terms/Terms_Use.cfm

The contents of a specific element of a second array *vin* [1:*nv*] is the number of the vertex at the "inboard" end of the arc having the same index value in *astack* (i.e., closer to the 0-vertex). A third array, *vout* [1:*nv*], contains at that index value the number of the "outboard" vertex attached to the same arc. Thus if arc number b is positive, *vin* contains $(b-)$ while *vout* contains $(b+)$. If arc number b is negative, *vin* contains $(b+)$ while *vout* contains $(b-)$[1].

3 Nature of the Problem

The reason for choosing new body frames now can be described using graph terminology. Denote by $\mathbf{e}^i$ the vector array of base vectors $[\mathbf{e}_1{}^i\ \mathbf{e}_2{}^i\ \mathbf{e}_3{}^i]^T$ in body i. The two bodies connected by branch b have body frames $\mathbf{e}^{(b+)}$ and $\mathbf{e}^{(b-)}$. The relationship between these frames is important, arising time and time again in the calculations involved in multibody simulation. It can be represented generically as

$$\mathbf{e}^{(b-)} = B^b \mathbf{e}^{(b+)} \tag{1}$$

The question is how the direction cosine matrix B^b should be formed.

Suppose that a physical connection exists between the two bodies, coupling them such that their relative rotation is constrained to occur about a single unit axis $\mathbf{u}$. Typical situations are line hinges and shafts rotating in bearings. More complicated relative rotations change the description in detail, but not the conclusions. If there is no kinematical connection at all between the two bodies there is no problem, but this is rarer in multibody modeling situations.

Vector $\mathbf{u}$ is not an eigenvector of B^b unless it happens to have the same components in both body frames. Thus one must assume in general that B^b does not have a simple representation in terms of the components of $\mathbf{u}$ and the angle of rotation θ about $\mathbf{u}$. The best one can do is to write

$$B^b = C_o{}^u C(\theta) \tag{2}$$

where ${}^uC(\theta)$ is a canonical rotation matrix whose eigenvector is $\mathbf{u}$ and whose rotation angle is θ, and C_0 is a constant matrix[2]. (Alternatively, the two matrices on the right could have been written in the opposite order.) Although it is not too difficult to construct C_0, every time one needs to resolve vectors from one frame into the other frame—and this happens often—an extra matrix multiplication by C_0 is required. The computational burden would be far less if the relationship between the contiguous frames could be described by a single canonical rotation matrix.

Our goal, then, is to define new body frames $\boldsymbol{\epsilon}^i$ in terms of $\mathbf{e}^i$ for all bodies such that the relationship between the new frames takes the simple form

$$\boldsymbol{\epsilon}^{(b-)} = {}^uC(\theta)\,\boldsymbol{\epsilon}^{(b+)} \tag{3}$$

One is immediately confronted by a problem. Several branches may be incident on a single vertex i. If $\boldsymbol{\epsilon}^i$ is chosen so that equation (3) is satisfied for one of these branches, can we be assured that the same choice causes that equation to hold for all the incident branches? The answer, of course, is that we cannot.

A way out of the difficulty is as follows. Imagine the multibody system to be in an arbitrary but physically realizable configuration, one consistent with all the constraints acting between pairs of bodies and between bodies and the outside environment. This will be called a "feasible configuration." While the system is held fixed in this configuration we can imagine embedding $\boldsymbol{\epsilon}^i$-frames in all bodies such that they are all congruent in direction. For definiteness, suppose that they all coincide (except for origin location) with the reference frame $\mathbf{e}^o$. For every branch, then, $\boldsymbol{\epsilon}^{(b-)} = \boldsymbol{\epsilon}^{(b+)}$ for the feasible configuration. Any physical hinge axis has the same vector components in both frames, so it is an eigenvector of the direction cosine matrix relating these two frames in *every* feasible configuration. The relationship between contiguous frames is that given by equation (3), the simple form we seek.

The parallelism of the ϵ-frames provides a criterion for body frame choice. It remains to generate these new frames efficiently from our knowledge of a feasible configuration.

4 Recursive Generation of Body Frames

It is assumed that a feasible configuration is available in the form of direction cosine matrices $B_0{}^b$ satisfying equation (1). These matrices are gotten directly or in some indirect form from the system plans. Suppose that within body i the plan axes $\mathbf{e}^i$ and the new axes $\boldsymbol{\epsilon}^i$ henceforth called the "simulation body axes," are related according to

$$\boldsymbol{\epsilon}^i = \boldsymbol{\Gamma}^i \mathbf{e}^i \tag{4}$$

For a certain index value, let a be the contents of *astack*, i be the contents of *vin*, j be the contents of *vout*. As stated previously, if $a>0$, $i=(b-)$ and $j=(b+)$ whereas if $a<0$ the inerpretations of i and j are reversed. put $b=|a|$ and $\delta = \text{sgn}\,(a)$. From equation (1)

$$\mathbf{e}^i = B_o{}^b \mathbf{e}^j \quad (\delta>0) \tag{5a}$$

$$\mathbf{e}^j = B_o{}^b \mathbf{e}^i \quad (\delta<0) \tag{5b}$$

But equation (5*b*) gives

$$\mathbf{e}^i = (B_o{}^b)^T \mathbf{e}^j = (B_o{}^b)^{-1} \mathbf{e}^j$$

so in all cases one gets

$$\mathbf{e}^i = (B_o{}^b)^\delta \mathbf{e}^j \tag{6}$$

Using equation (4) written for i and j on the two sides of equation (6), one is led to

$$\boldsymbol{\epsilon}^i = \boldsymbol{\Gamma}^i (B_o{}^b)^\delta (\boldsymbol{\Gamma}^j)^T \boldsymbol{\epsilon}^j \tag{7}$$

Requiring that $\boldsymbol{\epsilon}^i = \boldsymbol{\epsilon}^j$ in this specific feasible configuration implies the unique choice

$$\boldsymbol{\Gamma}^j = \boldsymbol{\Gamma}^i (B_o{}^b)^\delta \tag{8}$$

Equation (8) is a recursive relationship. When $i=0$ one can define $\boldsymbol{\epsilon}^0$ as precisely $\mathbf{e}^o$, so $\boldsymbol{\Gamma}^o$ is the identity matrix. As one increases the index in arrays *astack*, *vin*, *vout* the Γ-matrix for the outboard vertex is gotten from the known B_o-matrix and the Γ-matrix for the inboard vertex. But the latter already has been calculated because that vertex was previously encountered as the outboard vertex of another arc.

The complete set of simulation body frames is generated by one 3×3 matrix multiplication for each system arc, reduced by the number of arcs incident on the reference vertex, for which there are implied multiplications by the identity matrix. Embedding simulation body frames in the several bodies can be done as an off-line preliminary operation, although their subsequent motions with respect to each other is gotten as a part of the dynamic simulation itself. Also, all body-related vectors and the inertia matrices can be converted off-line to components in the ϵ-frames. The kinematics of the actual simulation need concern only equations having the form of equation (3) saving a great deal of computational labor over kinematics based on equation (1).

It may be felt that it is a nuisance to be confronted by B_o-matrices in equation (8) which are sometimes transposed, sometimes not. This is no real problem. In most practical

[1] To the reader unfamiliar with the details of the formalism this may seem to be a strange and unnecessarily complicated way of arranging matters. Be assured that any a priori choice of branch directions which improves matters in this regard also imposes some restriction on generality. An a posteriori reversal of certain directions after the spanning tree has been generated is easy in practice and usually acceptable. One can construct specific examples, though, for which it is undesirable. The route followed here is completely general.

[2] An implied superscript b on both matrices on the right side of equation (2) is suppressed for typographical convenience.

Downloaded 02 May 2010 to 171.66.16.54. Redistribution subject to ASME license or copyright; see http://www.asme.org/terms/Terms_Use.cfm

situations the signs of all the elements of *astack* can be made the same by reversing certain arcs after the spanning tree is chosen. (This may be inconvenient only in exceptional problems of combined rotation and translation between bodies.) If all signs are made the same, one may wish that the all be negative (outward pointing arcs). If so, it is more convenient to define body frames by the transposed matrices

$$\Delta^i = (\mathbf{\Gamma}^i)^T \tag{9}$$

and to rewrite equation (8) as

$$\Delta^j = B_o{}^b \Delta^i \tag{10}$$

5 Consistency in Systems With Circuits

A potentially troublesome numerical problem remains. All attention so far has been focused on the arcs of the graph, yet the $B_0{}^b$ also are defined for the chords in the feasible configuration. Indeed, one must treat all branches the same before a spanning tree is generated, for one may not know in advance which will become arcs and which chords. If c denotes a chord, the condition

$$\mathbf{e}^{(c-)} = B_o{}^c \mathbf{e}^{(c+)} \tag{11}$$

leads to

$$\boldsymbol{\epsilon}^{(c-)} = \Gamma^{(c-)} B_o{}^c (\Gamma^{(c+)})^T \boldsymbol{\epsilon}^{(c+)} \tag{12}$$

Because all the ϵ-frames already have been made parallel, equation (12) implies that

$$\Gamma^{(c+)} = \Gamma^{(c-)} B_o{}^c \tag{13}$$

must be satisfied, in which all matrices already are known or calculated. It is too much to expect that these equations will be satisfied to full numerical precision even for one chord, much less for all.

The pragmatic solution is to assume that the $B_o{}^c$ gotten from the plan are just approximations and that the "true" $B_o{}^c$ in the feasible configuration are just those that satisfy equation (13). There is some danger to this, in that it could contribute to the mathematical "locking" of a subsystem that is always a potential source of trouble in mechanical systems with circuits—one for which no completely satisfactory solution yet seems to exist.

An interesting question is the degree to which a similar recursive calculation can be incorporated into other multibody formalisms. This is a larger topic than can be done justice here, but a work in preparation [4] will address this question among others.

References

1 Schwertassek, R., and Roberson, R. E., "A State-Space Dynamical Representation for Multibody Mechanical Systems. Part 1: Systems With Tree Configurations; Part 2: Systems With Closed Loops," *Acta Mechanica*, Vol. 50, 1984, pp. 141-161 and Vol. 51, 1984, pp. 15-29.

2 Roberson, R. E., "The Path Matrix of a Graph, Its Construction and Its Use in Evaluating Certain Products," *Computer Meth. Appl. Mech. Eng.*, Vol. 42, 1984, pp. 47-56.

3 Roberson, R. E., *Lectures on the Dynamics of Multibody Systems*, Nanjing, 1984 (Chinese).

4 Schwertassek, R., and Roberson, R. E., "A Perspective on Computer-Oriented Dynamical Formalisms and Their Implementations," Symposium on the Dynamics of Multibody System, Udine, Italy, Sept. 1985.

Downloaded 02 May 2010 to 171.66.16.54. Redistribution subject to ASME license or copyright; see http://www.asme.org/terms/Terms_Use.cfm

R. Cohen

I. Porat

Faculty of Mechanical Engineering,
Technion-Israel Institute
of Technology,
Haifa, Israel

Coupled Torsional and Transverse Vibration of Unbalanced Rotor[1]

A model of an unbalanced rotor, driven by a torsion-flexible shaft through a constant velocity joint, is used to investigate the combination-resonance effect in coupled torsional-transverse vibration. Analysis of the nonlinear equations of motion by an asymptotic method yields the instability zones of the system. Results are in very good agreement with those obtained by direct numerical solution of the equations of motion.

1 Introduction

Two types of coupling between the equations of torsion and those of transverse motion of a rotor are known, one (widely treated, especially in the context of rotor stability in helicopters) associated with asymmetry of the elastic coefficients of the shaft and bearings, and the other (the subject of this paper) associated with the imbalance effect.

The latter type involves three main aspects:

(*a*) Variation of the gyroscopic moment, as a result of speed fluctuations due to torsion.

(*b*) The axial torque produced by misalignment of the mass and rotational centers of the rotor.

(*c*) Transverse components due to the axial torque.

An early work in this context is due to Tondl [1], who studied a turbogenerator model consisting of a pair of unbalanced rotors connected by a massless flexible shaft. Using a modification of the Floquet theory, he found that instability zones can be expected when the rotational velocity is equivalent to the sum or difference of one of the torsional and one of the bending resonance frequencies. One of his conclusions is that the combined effect of the flexural and torsional stiffnesses manifests itself not so much in actual instability – which is an exception – but in reduction of the effective positive damping in sensitive regions. Loewy [2] also dealt with the problem of coupled vibration, but arbitrary omission of nonlinear terms in deriving the equations of motion, and errors introduced in their solution, resulted in incorrect conclusions. Rabkin [3] studied a multirotor system with flexible shafts under a pulsating torque; his treatment and conclusions are much like those of Tondl. Broniarek [4, 5], in his study of a continuous flexible rotor on short bearings, also took the gyroscopic effects into account and found the conditions for synchronous and asynchronous instability. Wachel's work [6] described field measurements of the coupled vibration on a large industrial compressor train, the conclusion being that the main source of vibration is the gearbox, especially if failure of a gear tooth causes excitation corresponding to the torsional natural frequency.

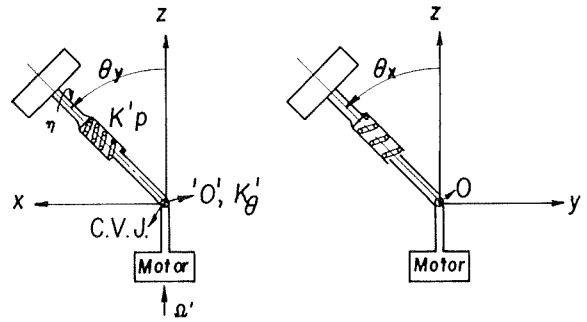

Fig. 1 Rotor driven by constant velocity joint and shaft rigid to bending and flexible to torsion

The present paper deals with a model of an unbalanced rotor, driven by a shaft rigid to bending and flexible to torsion, the rotational velocity and the lateral angular displacements being introduced by means of a constant-velocity joint. In this model the rotor has only two transverse degrees of freedom (angular displacements) as against four (linear *and* angular displacements) in the general case of a rotor on a flexible shaft. The advantage is that in spite of its relative simplicity, the model incorporates all the aforementioned coupling effects while avoiding the complexity of the general case. The nonlinear equations of motion are investigated by an asymptotic approach which is a modification of the Mitropolski method [7] (also known as the KBM method [8], after the Soviet team Krylov, Bogoliubov, and Mitropolski). This approach does not yield a closed solution, but permits determination of the stability conditions at the combination resonance (C.R.) and provides an insight into the special phenomenon noted by Valeev [9], namely that in certain cases, superimposed damping causes for considerable enlargement of the instability zones.

2 Equations of Motion (Fig. 1)

The equations of motion can be written out in a fixed coordinate system, with third-order terms omitted, as follows:

[1]The results presented in this paper form part of a Thesis submitted by the first author in partial fulfillment of requirements for the D.Sc. degree at the Faculty of Mechanical Engineering, Technion-Israel Institute of Technology, Haifa, Israel.

Contributed by the Applied Mechanics Division for publication in the JOURNAL OF APPLIED MECHANICS.

Discussion on this paper should be addressed to the Editorial Department, ASME, United Engineering Center, 345 East 47th Street, New York, N.Y. 10017, and will be accepted until two months after final publication of the paper itself in the JOURNAL OF APPLIED MECHANICS. Manuscript received by ASME Applied Mechanics Division, January, 1984; final revision, December, 1984.

Copyright © 1985 by ASME
Downloaded 02 May 2010 to 171.66.16.54. Redistribution subject to ASME license or copyright; see http://www.asme.org/terms/Terms_Use.cfm

$$I'\frac{d^2\theta_x}{dt^2}+I'_p\frac{d\phi'}{dt}\frac{d\theta_y}{dt}+K'_\theta\theta_x=K'_p\eta\theta_y/2-D'_\theta\frac{d\theta_x}{dt}+meL\left[\frac{d^2\phi'}{dt^2}\cos\phi'-\left(\frac{d\phi'}{dt}\right)^2\sin\phi'\right]$$

$$I'\frac{d^2\theta_y}{dt^2}-I'_p\frac{d\phi'}{dt}\frac{d\theta_x}{dt}+K'_\theta\theta_y=-K'_p\eta\frac{\theta_x}{2}-D'_\theta\frac{d\theta_y}{dt}+meL\left[\frac{d^2\phi'}{dt^2}\sin\phi'+\left(\frac{d\phi'}{dt}\right)^2\cos\phi'\right] \quad (1)$$

$$I'_p\frac{d^2\phi'}{dt^2}+K'_p\eta=-D'_p\frac{d\eta}{dt}+meL\left[\frac{d^2\theta_x}{dt^2}\cos\phi'+\frac{d^2\theta_y}{dt^2}\sin\phi'\right]+\frac{I'_p}{2}\left[\frac{d^2\theta_y}{dt^2}\theta_x-\frac{d^2\theta_x}{dt^2}\theta y\right]$$

where θ_x and θ_y are the inclination angles and ϕ' the rotation angle of the rotor, m its mass, e the imbalance, I' and I'_p the transverse and polar moments of inertia, D'_θ and D'_p damping coefficients proportional to the inclination and torsion angle rates, respectively, K'_p and K'_θ – the torsional stiffness of the shaft and the angular (inclinational) stiffness of the joint. In (1), $d\phi'/dt = \Omega' + \dot{\eta}$, where Ω' is the rotational velocity of the motor and η the torsion angle of the shaft. θ_x, θ_y, e, D'_θ, D'_p, and η are assumed to be small parameters.

The left-hand side of the two first equations represents the common linearity of a symmetric rotor with angular transverse degree of freedom only, and that of the third equation – the uncoupled torsional behavior of such a rotor. The terms containing I'_p $(d\phi'/dt)$ in the first two equations represent the gyroscopic moment exerted on the rotor as a result of the motor velocity Ω' and the torsion rate $\dot{\eta}$ of the shaft; those containing the imbalance – the moments due to misalignment of the rotor mass center and the axis of rotation; nonlinear terms containing $K'_p\ \eta$ – the influence of the axial torque on the transverse moments which appear while the rotor is inclined [10]. Finally, the last term on the right-hand side of the third equation represents (in this case of small inclination angles) the influence of the precession rate of the rotor on the axial torque.

Equations (1) in normalized form read:

$$\begin{aligned}
I\ddot{\theta}_x+I_p\dot{\phi}'\dot{\theta}_y+\theta_x&=K_p\eta\theta_y/2-D_\theta\dot{\theta}_x+E[\ddot{\phi}'\cos\phi'-\dot{\phi}'^2\sin\phi']\\
I\ddot{\theta}_y-I_p\dot{\phi}'\dot{\theta}_x+\theta_y&=-K_p\eta\theta_x/2-D_\theta\dot{\theta}_y+E(\ddot{\phi}'\sin\phi'+\dot{\phi}'^2\cos\phi') \quad (2)\\
I_p\ddot{\phi}'+K_p\eta&=-D_p\dot{\eta}+E(\ddot{\theta}_x\cos\phi'+\ddot{\theta}_y\sin\phi')+\frac{I_p}{2}(\ddot{\theta}_y\theta_x-\ddot{\theta}_x\theta_y)
\end{aligned}$$

where

$$\begin{aligned}
&I=I'/mL^2;\quad I_p=I'_p/mL^2;\quad K_p=K'_p/K'_\theta;\quad E=e/L\\
&D_p=D'_p/\sqrt{mK'_\theta L^2};\quad D_\theta=D'_\theta/\sqrt{mK'_\theta L^2}; \quad (3)\\
&\Omega=\Omega'\sqrt{mL^2/K'_\theta}\quad \tau=t\sqrt{K'_\theta/mL^2},\\
&\text{and from now on } \frac{d}{d\tau}=(\ )^\bullet
\end{aligned}$$

3 The Combination Resonance (C.R.)

One means of determining the stability of the system consists in transforming equations (2) to a rotational coordinate system, thus omitting their periodic coefficients, and to perform afterward a linearization of the equations through a perturbation applied to their quasistationary solution (defined as the one for which the derivatives of θ_x, θ_y, and η vanish). This procedure – not followed up here – shows that instability (within the bounds of our approximations) through the coupling effect in question may occur only around a C.R. velocity, for which

$$\Omega=\omega_1+\omega_2$$

ω_1 and ω_2 being one of the transverse and torsional natural frequencies, respectively.

Resorting to the complex value

$$\theta=\theta_x+i\theta_y \quad (4)$$

equation (2) becomes

$$I\ddot{\theta}-iI_p\Omega\dot{\theta}+\theta=(iE\Omega^2e^{i\phi})+\epsilon\left\{E(\dddot{\eta}+2i\Omega\ddot{\eta}-\Omega^2\dot{\eta})e^{i\phi}+iI_p\ddot{\eta}\dot{\theta}-\frac{iK_p}{2}\theta\eta-D_\theta\dot{\theta}\right\}+\epsilon^2\ \ldots \quad (5a)$$

$$\ddot{\eta}+\omega_2^2\eta=\epsilon\left[\frac{E}{I_p}(\ddot{\theta}_x\cos\phi+\ddot{\theta}_y\sin\phi)-\frac{D_p}{I_p}\dot{\eta}+\tfrac{1}{2}(\ddot{\theta}_y\theta_x-\ddot{\theta}_x\theta_y)\right]+\epsilon^2\ \ldots\ . \quad (5b)$$

where ϵ designates terms of the second order [i.e., smaller by one order than the left-hand side terms of (5)] and,

$$\phi'=\phi+\eta \quad (6)$$

where ϕ is the rotation angle imparted by the motor. For the three natural frequencies we have, respectively,

$$\omega_{1,3}=(I_p\Omega/2I)\pm[(I_p\Omega/2I)^2+1/I]^{1/2},\quad (\omega_3<0) \quad (7)$$

and

$$\omega_2=(K_p/I_p)^{1/2} \quad (8)$$

Substituting (7) and (8) in (3), the C.R. velocity becomes

$$\Omega=\left[(2I-I_p)\sqrt{\frac{K_p}{I_p}}\pm\sqrt{I_pK_p+4(I-I_p)}\right]/2(I-I_p) \quad (9)$$

For a given system, at most two rotational velocities are possible (when $I_p/I<K_p$, only one) for which C.R. instability may occur.

As a modification of Mitropol'ski's method [7], it is assumed that in the C.R. regions the exciting rotational velocity Ω can be partitioned between the two degrees of freedom, namely

$$\Omega=\Omega_1+\Omega_2;\quad \Omega_1\simeq\omega_1;\quad \Omega_2\simeq\omega_2 \quad (10)$$

so that each degree of freedom is excited near its natural frequency. The solution of (5) is correspondingly assumed in the form

$$\begin{aligned}
\theta&=u_{10}+a_1e^{i(\phi_1+\psi_1)}+\epsilon u_{11}+\epsilon^2\ \ldots\ .\\
\eta&=a_2\cos(\phi_2+\psi_2)+\epsilon u_{21}+\epsilon^2\ \ldots\ .
\end{aligned} \quad (11)$$

where

$$\phi=\phi_1+\phi_2;\quad \dot{\phi}_1=\Omega_1(\simeq\omega_1);\quad \dot{\phi}_2=\Omega_2(\simeq\omega_2) \quad (12)$$

u_{10} is added here for the first-order excitation terms of the θ degree of freedom which differ in frequency from the natural one (since by assumption the rotational velocity differs from the critical one). For the amplitudes a_1 and a_2, and for the phase angles ψ_1 and ψ_2 in (14), the following derivatives are assumed:

$$\begin{aligned}
\dot{a}_1&=\epsilon A_{11}+\epsilon^2A_{12}+\ \ldots\ .;\qquad \dot{a}_2=\epsilon A_{21}+\epsilon^2A_{22}+\ \ldots\ .\\
\dot{\psi}_1&=(\omega_1-\Omega_1)+\epsilon B_{11}+\epsilon^2B_{12}+\ \ldots\ .;\\
\dot{\psi}_2&=(\omega_2-\Omega_2)+\epsilon B_{21}+\epsilon^2B_{22}+\ \ldots
\end{aligned} \quad (13)$$

where A_{ij} and B_{ij} are functions of a_1, a_2, ψ_1 and ψ_2. It can be readily shown that the last two variables may be unified into a common phase angle:

Downloaded 02 May 2010 to 171.66.16.54. Redistribution subject to ASME license or copyright; see http://www.asme.org/terms/Terms_Use.cfm

$$\beta = \psi_1 + \psi_2 \tag{14}$$

so that $A_{ij} = A_{ij}(a_1, a_2, \beta)$ and $B_{ij} = B_{ij}(a_1, a_2, \beta)$.

For A_{ij} and B_{ij} to be uniquely defined, we impose the requirement that the periodic functions u_{1j} and u_{2j} do not contain the first harmonics of θ and η, $(\phi_1 + \psi_1)$ and $(\phi_2 + \psi_2)$, respectively, which is equivalent to

$$\begin{aligned}
&\int_0^{2\pi} u_{1j}[a_1, a_2, \phi, (\phi_1 + \psi_1), \\
&\qquad (\phi_2 + \psi_2)] e^{i(\phi_1 + \psi_1)} d(\phi_1 + \psi_1) = 0 \\
&\int_0^{2\pi} u_{2j}[a_1, a_2, \phi, (\phi_1 + \psi_1), \\
&\qquad (\phi_2 + \psi_2)] \sin(\phi_2 + \psi_2) d(\phi_2 + \psi_2) = 0 \\
&\int_0^{2\pi} u_{2j}[a_1, a_2, \phi, (\phi_1 + \psi_1), \\
&\qquad (\phi_2 + \psi_2)] \cos(\phi_2 + \psi_2) d(\phi_2 + \psi_2) = 0
\end{aligned} \tag{15}$$

Physically, equation (15) is equivalent to choosing a_1 and a_2 as the full amplitudes of the first principal vibration harmonics (or to u_{ij} containing no secular terms). Substituting (10) and (12) in (13), we have ($i = 1, 2$)

$$\begin{aligned}
\ddot{a}_i = {} & \frac{\partial A_{i1}}{\partial \beta}(\omega_0 - \Omega) + \epsilon^2 \left[\frac{\partial A_{i1}}{\partial a_1} A_{11} + \frac{\partial A_{i1}}{\partial a_2} A_{21} \right. \\
& \left. + \frac{\partial A_{i1}}{\partial \beta}(B_{11} + B_{21}) + \frac{\partial A_{i2}}{\partial \beta}(\omega_0 - \Omega) \right] + \epsilon^3 \ldots
\end{aligned} \tag{16}$$

$$\begin{aligned}
\ddot{\psi}_i = {} & \epsilon \frac{\partial B_{i1}}{\partial \beta}(\omega_0 - \Omega) + \epsilon^2 \left[\frac{\partial B_{i1}}{\partial a_1} A_{11} + \frac{\partial B_{i1}}{\partial a_2} A_{21} \right. \\
& \left. + \frac{\partial B_{i2}}{\partial \beta}(\omega_0 - \Omega) + \frac{\partial B_{i1}}{\partial \beta}(B_{11} + B_{21}) \right] + \epsilon^3 \ldots
\end{aligned}$$

where $\omega_0 = \omega_1 + \omega_2$. Expanding the right-hand side of (15) in Taylor series, near the solution (11), one gets for the first-harmonics terms of the transverse motion:

$$\begin{aligned}
& \left[I(\omega_0 - \Omega) \frac{\partial A_{11}}{\partial \beta} - a_1 B_{11}(2I\omega_1 - I_p \Omega) \right] \\
& \quad + i \left[a_1 I(\omega_0 - \Omega) \frac{\partial B_{11}}{\partial \beta} + A_{11}(2I\omega_1 - I_p \Omega) \right] = \\
& = -\frac{E a_2}{2} \left[(\omega_2 - \Omega)^2 + c\left(I_p \omega_2 \Omega - \frac{K_p}{2} \right) \right] [\cos\beta - i \sin\beta] \\
& \quad - i a_1 D_\theta \omega_1
\end{aligned} \tag{17}$$

while for the remaining terms

$$\begin{aligned}
[I\ddot{u}_{11} - i I_p \Omega \dot{u}_{11} + u_{11}] = {} & -\frac{E a_2}{2} [(\omega_2 + \Omega)^2 \\
& - c(1_p \Omega \omega_2 + K_p/2)] e^{i(\phi + \phi_2 + \psi_2)} + Ec\, D_\theta \Omega e^{i\phi} + \\
& + \frac{i a_1 a_2}{2} [(I_p \omega_1 \omega_2 - K_p/2) e^{i(\phi_1 - \phi_2 + \psi_1 - \psi_2)} \\
& - (I_p \omega_1 \omega_2 + K_p/2) e^{i(\phi_1 + \phi_2 + \psi_1 + \psi_2)}].
\end{aligned} \tag{18}$$

The particular solution to (17) becomes, after resolution into its real and imaginary parts:

$$\begin{aligned}
A_{11} &= G_1 a_2 \sin\beta - a_1 d_\theta \\
B_{11} &= \frac{G_1 a_2}{a_1} \cos\beta
\end{aligned} \tag{19}$$

where

$$\begin{aligned}
G_1 &= \frac{E}{2} [(\omega_2 - \Omega)^2 + c(I_p \Omega \omega_2 - K_p/2)] / [I(\omega_1 - \omega_2 + \Omega) - I_p \Omega] \\
d_\theta &= D_\theta \omega_1 / (2I\omega_1 - I_p \Omega) \\
c &= \Omega^2 / [(I_p - I)\Omega^2 + 1]
\end{aligned} \tag{20}$$

Similar treatment for the torsional degree of freedom yields:

$$\begin{aligned}
A_{21} &= G_2 a_1 \sin\beta - a_2 d_p \\
B_{21} &= \frac{G_2}{a_2} a_1 \cos\beta
\end{aligned} \tag{21}$$

where

$$\begin{aligned}
G_2 &= E\left[\frac{\omega_1^2}{I_p} - \frac{c}{2}(\omega_1^2 - \Omega^2) \right] / (\Omega - \omega_1 + \omega_2); \\
d_p &= D_p / 2I_p
\end{aligned} \tag{22}$$

and all terms are a function of the first harmonics $(\phi_2 + \psi_2)$, thus $u_{21} = 0$.

Summing the first approximation, we obtain the following set of three first-order differential equations to be solved numerically:

$$\begin{aligned}
\theta &= a_1 e^{i(\phi_1 + \psi_1)} + iEc\, e^{i\phi} + \epsilon u_{11} + \epsilon^2 \ldots \\
\eta &= a_2 \cos(\phi_2 + \psi_2) + \epsilon^2 \ldots
\end{aligned}$$

where

$$\begin{aligned}
\dot{a}_1 &= A_{11} = -d_\theta a_1 + G_1 a_2 \sin\beta \\
\dot{a}_2 &= A_{21} = -d_p a_2 + G_2 a_1 \sin\beta \\
\dot{\beta} &= (\omega_0 - \Omega) + \left[G_1 \frac{a_2}{a_1} + G_2 \frac{a_1}{a_2} \right] \cos\beta
\end{aligned} \tag{23}$$

4 Stability of the System

In (23) d_θ and d_p are positive, and it can be shown that for positive ω_1 and ω_2, G_1 and G_2 are of the same sign. For convenience, we resort to the amplitude ratio

$$a' = a_2 / a_1 \tag{24}$$

which, substituted with its derivatives in (23), yields a set in only two variables:

$$\begin{aligned}
\dot{a}' &= -(d_p - d_\theta) a' + (G_2 - G_1 a'^2) \sin\beta \\
\dot{\beta} &= (\omega_0 - \Omega) + \left(G_1 a' + \frac{G_2}{a'} \right) \cos\beta
\end{aligned} \tag{25}$$

To determine the stability, a perturbation is applied to the quasistationary solution:

$$-(d_p - d_\theta) a'_0 + (G_2 - G_1 a_0'^2) \sin\beta_0 = 0 \tag{26a}$$

$$(\omega_0 - \Omega) + \left(G_1 a_0' + \frac{G_2}{a_0'} \right) \cos\beta_0 = 0 \tag{26b}$$

namely, denoting the variations of the quasistationary variables by $\Delta a'$ and $\Delta\beta$, we have the set

$$\begin{aligned}
\Delta\dot{a}' &= -[(d_p - d_\theta) + 2G_1 a_0' \sin\beta_0] \Delta a' + \Delta\beta (G_2 - G_1 a_0'^2) \cos\beta_0 \\
\Delta\dot{\beta} &= \Delta a' \left(G_1 - \frac{G_2}{a_0'^2} \right) \cos\beta_0 - \Delta\beta \left(G_1 a_0' + \frac{G_2}{a_0'} \right) \sin\beta_0
\end{aligned} \tag{27}$$

for which the stability requirement is readily obtainable as

$$(G_2 / a_0' + G_1 a_0') \sin\beta_0 > 0 \tag{28}$$

Since a_1 and a_2 are taken positive, so is a_0'. Thus, stability of (27) is conditional on sin β_0 – subject to (28) – being of the same sign as G_1 and G_2. In other words, if (26) has a quasistationary solution satisfying (28), then (25) is stable around this solution.

It should be emphasized that this does not necessarily imply stability of the amplitudes a_1 and a_2 themselves, which is obtainable by substituting sin β_0 in the first two equations of (23):

$$\begin{aligned}
\dot{a}_1 &= -d_\theta a_1 + G_1 a_2 \sin\beta_0 \\
\dot{a}_2 &= -d_p a_2 + G_2 a_1 \sin\beta_0
\end{aligned} \tag{29}$$

Unlike (25), the preceding set is linear, since β_0 is taken constant.

Stability of (29) thus requires

Downloaded 02 May 2010 to 171.66.16.54. Redistribution subject to ASME license or copyright; see http://www.asme.org/terms/Terms_Use.cfm

Table 1

Fig.	Rotational velocity	System parameters	Damping	$a_0' = \frac{a_1}{a_2}$	β_0
		$\omega_1 = 1.29$	$D_\theta = D_p = 0$	2.27	1.36
2	3.25	$\omega_2 = 1.96$	$D_\theta = 0.01$	2.76	1.37
		$\Omega - \omega_0 \simeq 6.10^{-3}$	$D_p 0.01$	1.08	1.41
		$\omega_1 = 1.31$	$D_\theta = D_p = 0$		
3	3.40	$\omega_2 = 1.96$	$D_\theta = 0.07$	14.3	0.30
		$\Omega - \omega_0 \simeq 0.126$	$D_p 0.03$	0.163	0.74

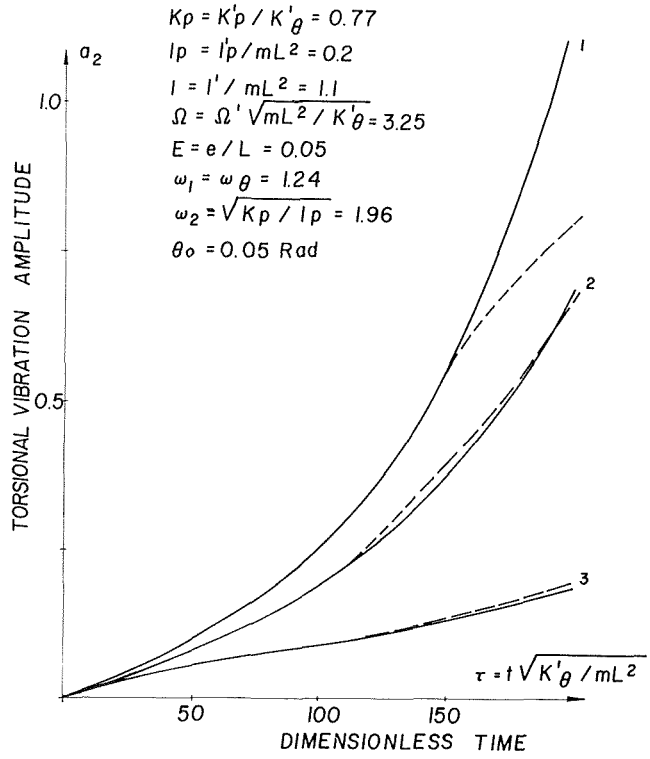

Fig. 2 Torsional vibration amplitude at combination resonance frequency. — Approximate method (23); and ····· Exact method. (1) No damping, $D_\theta = D_p = 0$. (2) Purely angular damping, $D_\theta = D_\theta' I \sqrt{mK_\theta' L^2} = 0.01$. (3) Purely torsional damping, $D_p = D_p' I \sqrt{mL^2 K_\theta'} = 0.01$.

$$d_\theta d_p > G_1 G_2 \sin\beta_0 \tag{30}$$

The amplitudes, and thus the system itself, are stable, provided G_1 and G_2 are of the same sign as $\sin\beta_0$, only if *both* types of damping are present.

In an *undamped* system (or in the particular case $d_\theta = d_p$), there are two conditions for (26) being satisfied:

$$\sin\beta_0 = 0, \tag{31a}$$

or

$$G_2 - G_1 a_0'^2 = 0 \tag{31b}$$

The first condition implies a periodic behavior according to (28), and the second – stability of a' and β according to (28), and deviation of a_1 and a_2 according to (30). But substitution of (31*b*) in (26*b*) shows that this is possible in an undamped system only provided

$$|(\omega_1 + \omega_2 - \Omega)| < 2(G_1 G_2)^{1/2} \tag{32}$$

As the rotational speed deviates from the focal point of the C.R., at which the left-hand side of (32) vanishes, the latter usually increases more steeply than its right-hand counterpart. The velocity for which (32) is no longer satisfied delimits the instability zone for an undamped system. A system with only *one* kind of damping, d_θ or d_p, is unstable in the velocity ranges outside (32) with G_1 and G_2 still of the same sign, since it admits a quasistationary solution as per (26) and (28), even though (32) is not satisfied.

5 Results and Conclusions

In Fig. 2, the numerical results for the approximated set (23) (the amplitudes and phase angle, obtained directly) are compared with the numerical results of the exact equations, which represent the complete motion of the rotor. The compared results were duly obtained under identical perturbation with the appropriate initial conditions. This comparison is carried out for the C.R. frequency ($\Omega = 3.25$) in the three basic variants – *no damping*, *purely torsional* damping, and *purely angular* damping. It is seen that agreement is excellent (deviation of only a few percent) at amplitudes less than 0.5 rad, but above 0.6 rad (12 times the initial perturbation) the approximated set for the no damping variant yields a much steeper plot. This could be expected, as for amplitudes close to unity, θ and η cannot be treated as "small" parameters anymore.

Figure 3, which compares the three variants for an off-C.R. situation ($\Omega = 3.4$), confirms the analytical conclusions from equations (32) and (30) for no-damping and single-damping variants, respectively: in the former case the amplitudes vary periodically throughout,[2] while in the latter periodicity prevails only until the amplitude ratio stabilizes, and the subsequent pattern is monotonic.

The difference between the C.R. and off-C.R. situations in terms of β and a' is shown in Table 1. In the first situation, there is no significant difference between the three variants: β is close to $\pi/2$ [as per equation (26*b*)] and a' is of the same order of magnitude. In the second, β_0 tends to zero; as expected, for the purely torsional variant, a_0 is much larger, and for the purely angular variant, much smaller than their C.R. counterpart.[3]

The considerable broadening of the instability zone due to superimposition of angular damping d_θ on a previously undamped system is illustrated in Fig. 4.

The interpretation is as follows: according to (11), θ and η are close to their natural frequencies

$$[\theta \cong a_1 e^{i(\phi_1 + \psi_1)} \text{ and } \eta \cong a_2 \cos(\phi_2 + \psi_2)]$$

while according to (12) and (13),

$$\dot\phi_1 + \dot\psi_1 = \omega_1 + \epsilon B_{11}; \quad \dot\phi_2 + \dot\psi_2 = \omega_2 + \epsilon B_{21}$$

Thus, the deviation from the natural frequencies depends on

[2] The periodic beats shown in Fig. 3 (undamped case) have a frequency of 0.13, namely the difference of the rotational velocity (3.4) and the C.R. frequency ($\omega_1 + \omega_2 = 1.31 + 1.96 = 3.27$); they overlie the vibrations of the two degrees of freedom θ and η, which are not shown.

[3] It should be noted that in principle, combination resonance is possible also when ω_1 (or ω_3) is negative (differential harmonic oscillation), in which case G_1 and G_2 differ in sign. These regions, however, can be shown to be stable and are irrelevant to our analysis. In other words, within the framework of our basic assumptions (unbalanced symmetric rotor and symmetric stiffness of the joint), instability occurs only under summed combination harmonic oscillation.

Downloaded 02 May 2010 to 171.66.16.54. Redistribution subject to ASME license or copyright; see http://www.asme.org/terms/Terms_Use.cfm

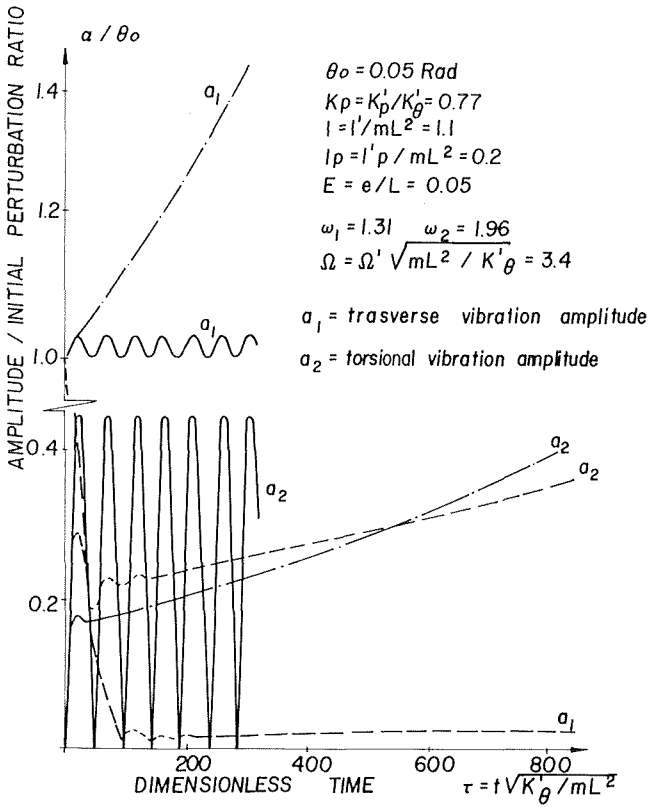

Fig. 3 Amplitude variation at rotational velocity deviating from combination resonance frequency. (1) — No damping, $D_\theta = D_p = 0$. (2) — • — • — Purely torsional damping, $D_p = D'_p/\sqrt{mK_\theta L^2} = 0.05$. (3) --- Purely angular damping, $D_\theta = D'_\theta/\sqrt{mK_\theta L^2} = 0.07$.

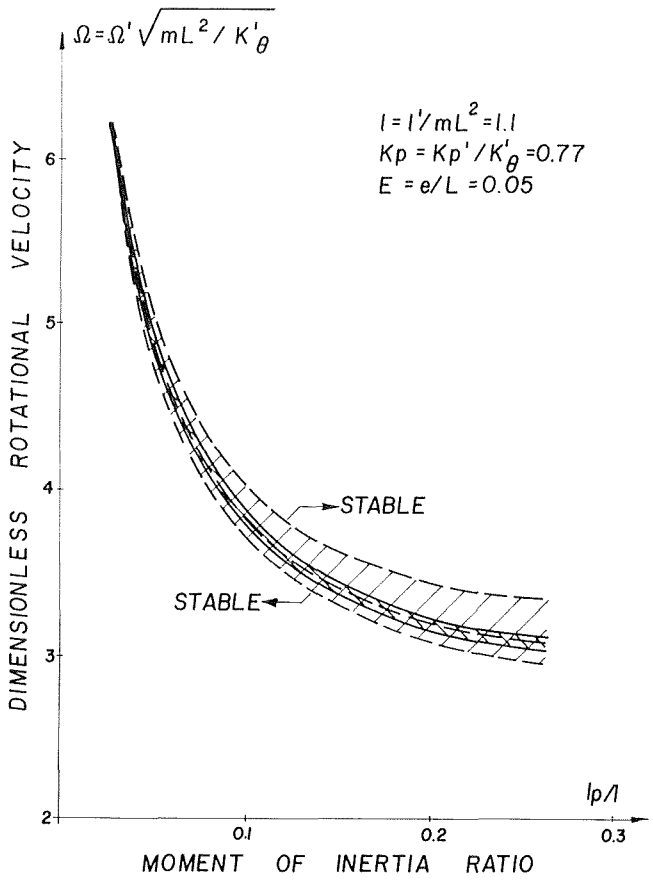

Fig. 4 Instability zones of rotor. — • — • — Combination resonance focal point. — Instability limit for $D_\theta = D_p = 0$. --- Instability limit for $D_\theta = 0.05$ and $D_p = 0$.

the absolute values of B_{11} and B_{21}. According to (19), (21), and (31*b*), for an undamped system

$$a'_0 = (G_2/G_1)^{1/2} \quad \text{and} \quad B_{11} = B_{21} = (G_1 G_2)^{1/2} \cos\beta_0.$$

Accordingly, so long as (32) is satisfied, the frequencies of the two degrees of freedom deviate equally from their natural counterparts ω_1 and ω_2. On further deviation from the C.R. focal point, a' and β are no longer constant and B_{11} and B_{21} become periodic. As a result, the excitation frequencies are no longer fixed and the system ceases to be unstable.

When *angular* damping d_θ is superimposed, equation (31) becomes irrelevant. So long as the rotational velocity remains close to the focal point of the C.R., there is no meaningful change in a'_0 and β_0. Subsequently, a'_0 becomes larger and β_0 smaller so that B_{11} increases and B_{21} decreases, tending to zero. Thus, while the damped angular frequency deviates considerably from ω_1, its undamped torsional counterpart remains close to ω_2, which causes instability. This process continues until at some distance from the focal point G_1 or G_2 changes sign and the system restabilizes.

When *torsional* damping is superimposed, the picture is reversed, and as Ω deviates from the focal point, a'_0 becomes smaller – B_{21} increasing and B_{11} decreasing – the undamped angular degree of freedom continues to be excited at its natural frequency ω_1 and the damped torsional degree of freedom deviates more and more from its natural frequency, while the system remains unstable.

The advantages of the approximate asymptotic method used in this work over the exact one can be summed up as follows:

It involves first-order rather than second-order equations.

The amplitude envelope and phase angles result directly, so that larger integration and output steps may be adopted; the behavior of the system is easily observable even if the instability is small.

Stabilization of the amplitude ratio and common phase angle, when the system itself is unstable, is readily understood by this method.

The method can readily be extended to the general case of four transverse degrees of freedom; this entails instability zones not necessarily associated with the combination resonance zones.

References

1 Tondl, E., *Some Problems of Rotor Dynamics*, Publishing House of the Czechoslovak Academy of Science, Prague, 1965, pp. 242-260.

2 Loewy, R. G., and Piarulli, V. J., *Dynamics of Rotating Shafts*, The Shock and Vibration Information Center, U.S. Department of Defense, 1969, pp. 53-61.

3 Rabkin, M. A., "Combined Flexural-Torsional Vibrations of Multidisk Rotors," *Soviet Applied Mechanics*, Vol. 9, No. 3, 1973, pp. 310-315.

4 Broniarek, C., "On Problems of Nonlinear Flexural-Torsional Vibration of Rotating Shaft with Distributed Parameters," *Bulletin de 'Academie Polonaise des Sciences*, Vol. XIV, No. 10, 1966, pp. 595(979)-604(988).

5 Broniarek, C., "The Problem of Dynamic Instability of Nonlinear Coupled Torsional-Flexural Vibrations of a Shaft Rotating With Unbalanced Mass which is Continuously Distributed Along the Shaft Axis," *Archives de Mecanique Appliquee* (Poland), Vol. 3, No. 19, 1967, pp. 445-469.

6 Wachel, J. C., and Szenasi, F. R., "Field Verification of Lateral-Torsional Coupling Effects on Rotor Instabilities in Centrifugal Compressors," NASA Conference Publication 2133 (AD A 088-701), May 1980, pp. 15-34.

7 Mitrolpol'ski, Yu. A., *Problems of the Asymptotic Theory of Nonstationary Vibrations*, Israel Program for Scientific Translations, Jerusalem, 1965.

8 Meirovitch, L., *Methods of Analytical Dynamics*, McGraw-Hill, New York, 1970, pp. 302-309.

9 Valeev, K. G., "On the Danger of Combination Resonances," *Journal of (Soviet) Applied Mathematics and Mechanics*, Vol. 27, No. 6, 1963, pp. 1745-1759.

10 Porat, I., "Moments Transmission by a Universal Joint," *Mechanism and Machine Theory*, Vol. 15, No. 4, 1980, pp. 245-254.

Downloaded 02 May 2010 to 171.66.16.54. Redistribution subject to ASME license or copyright; see http://www.asme.org/terms/Terms_Use.cfm

D. R. Otis
University of Petroleum & Minerals,
Dhahran, Saudi Arabia,
and Department of
Mechanical Engineering,
University of Wisconsin,
Madison-Wis. 53706

Laminar Start-Up Flow in a Pipe

A numerical solution is presented for the laminar start-up flow in a circular pipe. It is an extension of the Szymanski solution to include a parameter accounting for the head that must be devoted to the acceleration of the flow. Velocity profiles, wall shear stress, mean velocity history, and start-up time constants are given as a function of the new parameter.

Introduction

The Szymanski solution for laminar start-up flow was first reported in 1932 [1] and is referenced in advance fluid mechanics textbooks [2]. It concerns the flow of an incompressible fluid initially at rest in a long circular pipe, and where a constant pressure gradient ($-G$) is suddenly imposed. The differential equations and boundary conditions are

$$\frac{\partial u}{\partial t} = \frac{G}{\rho} + \nu\left(\frac{\partial^2 u}{\partial r^2} + \frac{1}{r}\frac{\partial u}{\partial r}\right) \tag{1}$$

$$u = 0 \quad \text{at} \quad r = R \quad \text{for all} \quad t$$

$$u = 0 \quad \text{at} \quad t = 0 \quad \text{for all} \quad r \tag{2}$$

The equation is linear, and by separation of variables Szymanski obtained the following solution:

$$u(r,t) = \frac{G}{4\mu}(a^2 - r^2) - \frac{2Ga^2}{\mu}\sum_{n=1}^{\infty}\frac{J_0\left(\lambda_n \frac{r}{a}\right)}{\lambda_n^3 J_1(\lambda_n)} \exp\left(-\lambda_n^2 \frac{\nu t}{a^2}\right) \tag{3}$$

with λ_n the positive roots of

$$J_0(\lambda_n) = 0 \tag{4}$$

His results for the velocity distribution are reproduced in Table 1.

Szymanski took the pressure gradient as constant. But in actual fact, it is usually not the pressure gradient that remains constant, but rather it is the total head, H_0 (see Fig. 1). As the flow accelerates, a portion of this head must be utilized to establish the kinetic head of the flow. This is illustrated in Fig. 1 where the energy grade lines are drawn to illustrate (*a*) just after valve opening, (*b*) at a later time, and (*c*) after steady state is established. Initially the total head is available to establish the pipe pressure gradient required to overcome the frictional head loss, i.e.,

$$G = G_0 \equiv \gamma H_0 / L \tag{5}$$

As the flow develops, the pressure gradient along the pipe is diminished because of the velocity head development as the flow accelerates in the reservoir. Along a streamline from the reservoir free surface to the pipe entrance, the fluid on average has acquired the velocity head $\overline{u^2}/2g$ with

$$\overline{u^2} \equiv \frac{\int u^3 r dr}{\int u r dr} \tag{6}$$

and the head that remains to drive the pipe flow is (see Fig. 1)

$$H_L = H_0 - \frac{\overline{u^2}}{2g}$$

and the corresponding pressure gradient is

$$G \equiv \frac{\gamma H_L}{L} - \frac{\gamma}{L}\frac{\overline{u^2}}{2g}$$

or

$$G = G_0 - \overline{\rho u^2}/2L \tag{7}$$

As a result, equation (1) becomes nonlinear with G depending on an integral of the velocity cubed, and a numerical solution is required. It is surprising that this effect has been overlooked in most treatments of the laminar start-up problem. In contrast, it is usually always recognized and properly included in the simpler one-dimensional turbulent start-up analyses where constant friction factor is assumed (see for example Streeter and others [3]). Even the recent and excellent paper by Letelier and Leutheusser [4] does not seem to discuss this effect though it falls within their classification scheme (their Case 4) and would probably be amenable to solution by the approximate method they have developed.

One may ask whether the kinetic head could be of any practical importance in a realistic laminar flow situation. In fact, the motivation for this work came from an unnamed researcher whose experimental results differed from the

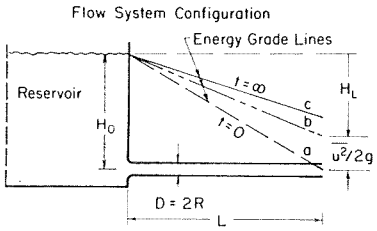

Fig. 1 The flow system configuration defining certain variables and indicating the time variation of the energy grade line after sudden valve opening

Contributed by the Applied Mechanics Division for publication in the JOURNAL OF APPLIED MECHANICS.

Discussion on this paper should be addressed to the Editorial Department, ASME, United Engineering Center, 345 East 47th Street, New York, N.Y. 10017, and will be accepted until two months after final publication of the paper itself in the JOURNAL OF APPLIED MECHANICS. Manuscript reviewed by ASME Applied Mechanics Division, January, 1984; final revision, September, 1984.

Copyright © 1985 by ASME
Downloaded 02 May 2010 to 171.66.16.54. Redistribution subject to ASME license or copyright; see http://www.asme.org/terms/Terms_Use.cfm

Table 1 Velocity distribution ($V(,X,T)$; $M=0$) V = -velocity; X = radial position, T = time, all dimensionless

X \ T	0.05	0.10	0.20	0.60	0.30	0.40	0.50	0.80	1.00	∞
0	0.200	0.385	0.651	0.965	0.804	0.890	0.938	0.989	0.997	
	(.200)[a]	(.385)	(.652)	-	(.805)	(.890)	(.939)	-	(.997)	(1.000)
0.1	0.199	0.383	0.646	0.956	0.797	0.882	0.929	0.979	0.987	-
	(.200)	(.384)	(.647)	-	(.797)	(.882)	(.929)	-	(.987)	(.990)
0.2	0.199	0.378	0.631	0.927	0.775	0.856	0.902	0.950	0.957	-
	(.199)	(.379)	(.631)	-	(.776)	(.857)	(.902)	-	(.957)	(.960)
0.3	0.198	0.369	0.605	0.880	0.739	0.814	0.856	0.900	0.907)	-
	(.198)	(.370)	(.606)	-	(.739)	(.814)	(.856)	-	(.907)	(.910)
0.4	0.195	0.355	0.567	0.813	0.687	0.754	0.792	0.831	0.837	-
	(.194)	(.355)	(.568)	-	(.687)	(.754)	(.792)	-	(.837)	(.840)
0.5	0.189	0.332	0.516	0.727	0.619	0.676	0.709	0.743	0.748	-
	(.189)	(.333)	(.517)	-	(.619)	(.677)	(.709)	-	(.748)	(.750)
0.6	0.178	0.300	0.450	0.621	0.534	0.580	0.606	0.634	0.638	-
	(.178)	(.300)	(.451)	-	(.536)	(.580)	(.607)	-	(.638)	(.640)
0.7	0.159	0.254	0.368	0.490	0.430	0.465	0.485	0.506	0.509	-
	(.160)	(.254)	(.368)	-	(.430)	(.465)	(.485)	-	(.509)	(.510)
0.8	0.127	0.191	0.266	0.351	0.307	0.331	0.343	0.357	0.359	
	(.127)	(.191)	(.267)	-	(.308)	(.331)	(.344)	-	(.359)	(.360)
0.9	0.076	0.108	0.144	0.185	0.164	0.176	0.182	0.189	0.190	
	(.076)	(.108)	(.145)	-	(.165)	(.176)	(.182)	-	(.190)	(.190)
$-(\partial V/\partial X)^{b}_{X=1}$	0.891	1.204	1.560	1.956	1.753	1.862	1.922	1.986	1.996	2.000
$V/V(\infty)$[c]	0.275	0.461	0.699	0.970	0.831	0.905	0.947	0.991	0.997	1.000

Notes: [a] Szymanski's values shown in parenthesis for comparison.
[b] Wall shear stress.
[c] Average velocity normalized to unity for $T\rightarrow\infty$.

Szymanski solution because of the very effect here described. A realistic example is developed later (in the Discussion of Results Section) and the results are as follows: for SAE 10W-30 oil driven by a head of 1.053 m, the start-up process in a 10-cm diameter pipe with a length of 6.25 m will occur in less than half the time predicted by Szymanski, and the steady-state average velocity attained will be one-half the Szymanski value. This is hardly a small effect!

Definition of the Start-Up Parameter

In this section the start-up parameter, M, will be defined. With the flow velocity denoted by $u(r,t)$, the average velocity is defined by

$$\overline{u(t)} \equiv (2/R^2)\int_0^R u(r,t)rdr \tag{8}$$

The steady-state velocity distribution is denoted by $u(r,\infty)$ and the steady-state average velocity is defined by

$$\overline{u(\infty)} \equiv (2/R^2)\int_0^R u(r,\infty)rdr \tag{9}$$

A bar denotes an average across the flow cross section, and a subscript 0 corresponds to $M=0$ (the Szymansky problem).

In equation (7) $\overline{u^2}$ is unknown and must be computed at each step of the numerical solution. But one can obtain the *steady-state* average velocity from equation (7) by simple algebra. The steady-state solution is the parabolic velocity distribution of Poiseuille for which

$$G = 32\mu\ \overline{u(\infty)}/D^2 \tag{10}$$

and

$$\overline{u(\infty)^2} = 2\ \overline{u(\infty)}^2 \tag{11}$$

Substituting into equation (7), then

$$(32\mu\ \overline{u(\infty)}/D^2) = G_0 - \rho\ \overline{u(\infty)}^2 \tag{12}$$

and this quadratic in $\overline{u(\infty)}$ can be solved to yield

$$\overline{u(\infty)} = (G_0D^2/32\mu)\left[\frac{\sqrt{1+8M}-1}{4M}\right] \tag{13}$$

where the start-up flow parameter is defined by

$$M \equiv (G_0D^4/8\nu^2\rho L) \tag{14}$$

Note that the quantity in brackets in equation (13) tends to unity in the limit as $M\rightarrow 0$, so that the coefficient, $G_0D^2/32\mu$ can be identified as the steady-state average velocity for the Szymanski problem.

The limit $M\rightarrow 0$, can be identified with a long pipe (i.e., $L\rightarrow\infty$). A greater physical insight can be gained by relating M to the following two velocities: the first is the flow velocity attained with no friction, namely

$$(2gH_0)^{1/2}$$

and the second is the average velocity attainable in Poiseuille flow if all the head is available to overcome the viscous losses, namely

$$G_0D^2/32\mu$$

The parameter M is the square of their ratio.

Equation Formulation and Normalization

The partial differential equation, equation (1), will be made

Downloaded 02 May 2010 to 171.66.16.54. Redistribution subject to ASME license or copyright; see http://www.asme.org/terms/Terms_Use.cfm

dimensionless by introducing the following normalized variables for velocity, radius and time:

$$V \equiv u/2\overline{u(\infty)}$$
$$X \equiv r/R$$
$$T \equiv \nu t/R^2 \quad (15)$$

These are the same as Szymanski's variables except that $\overline{u(\infty)}$ depends on the parameter M as given by equation (13). Substitute into equation (1), use equation (7), and normalize the average kinetic energy as follows:

$$\overline{V^2} \equiv \overline{u^2}/2\overline{u(\infty)}^2 \quad (16)$$

With these substitutions the differential equation for $V(X,T)$ becomes

$$\frac{\partial V}{\partial T} = \frac{\partial^2 V}{\partial X^2} + \frac{1}{X}\frac{\partial V}{\partial X} + \frac{16\,M}{\sqrt{1+8M}-1}[1-M\overline{V^2}] \quad (17)$$

The steady-state solution is

$$V(X,\infty) = 1 - X^2 \quad (18)$$

as can easily be verified by direct substitution using equation (13). Equation (18) is simply the parabolic velocity distribution of Poiseuille flow. The complete solution to equation (17) can then be expressed as

$$V(X,t) = 1 - X^2 + W(X,T) \quad (19)$$

where $W(X,T)$ must satisfy

$$\frac{\partial W}{\partial T} = \frac{\partial^2 W}{\partial X^2} + \frac{1}{X}\frac{\partial W}{\partial X} + G_w \quad (20)$$

where

$$G_w \equiv \frac{16\,M}{\sqrt{1+8M}-1}[1-M\overline{V^2}] - 4$$

with boundary conditions

$$W(X,0) = X^2 - 1; \quad W(1,T) = 0 \quad (21)$$

The problem is now one of solving equations (20) and (21) for W. (Note: One could just as easily perform the numerical solution on equation (17) for $V(X,T)$. But this last transformation forces the numerical solution for W and V to be exactly correct at $T=0$ and at $T=\infty$ and thereby minimizes the error that can be introduced by the numerical procedure.)

The Finite Difference Equations

The finite difference equations are taken from Albasiny [5] as summarized by Smith [6] and can be written:

For $i=0$

$$\frac{W_0' - W_0}{\Delta T} = \frac{2}{(\Delta X)^2}(W_1' - W_0' + W_1 - W_0) + G_w \quad (22)$$

For $i=1,2,\ldots,N-1$

$$\frac{W_i' - W_i}{\Delta T} = \frac{1}{2(\Delta X)^2}[(1+1/2i)W_{i+1}' - 2W_i' + (1-1/2i)W_{i-1}'] + \frac{1}{2(\Delta X)^2}[(1+1/2i)W_{i+1} - 2W_i + (1-1/2i)W_{i-1}] + G_w \quad (23)$$

For $i=N$

$$W_N' = 0 \quad (24)$$

where the cylinder dimensionless radius, X, has been divided into N equal increments, $\Delta X = 1/N$, with $i=0$ on the axis and $i=N$ at the wall. The primes denote the new values computed for the next time step from the old values (unprimed). This Crank-Nicolson method [6] is implicit in that the value for the W_i' depends not only on the old values W_{i-1}, W_i, and W_{i+1}, but also on the adjacent new values W_{i-1}' and W_{i+1}'. The calculation procedure involves recursive relations that are excellently explained and demonstrated by Smith [6], and which for the present problem become:

$$W_N' = 0 \quad (25)$$

$$W_{N-1}' = S_{N-1}/\alpha_{N-1} \quad (26)$$

$$W_i' = 1/\alpha_i[S_i + C_i W_{i+1}'] \quad i = N-2, N-3, \ldots, 0 \quad (27)$$

where

$$A_i = (1 - 1/2i)\epsilon \quad (28)$$
$$B_i = 1 + 2\epsilon \quad (29)$$
$$C_i = (1 + 1/2i)\epsilon \quad (30)$$
$$D_i = A_i W_{i-1} + (1-2\epsilon)W_i + C_i W_{i+1} + G_w \Delta T \quad (31)$$
$$\alpha_i = B_i - A_i C_{i-1}/\alpha_{i-1} \quad (32)$$
$$S_i = D_i + A_i S_{i-1}/\alpha_{i-1} \quad (33)$$
$$\epsilon = \Delta T/2\Delta X^2 = N^2 \Delta T/2 \quad (34)$$
$$G_w = \frac{16\,M}{\sqrt{1+8M}-1}[1-M\overline{V^2}) - 4 \quad (35)$$

and with the following special values for $i=0$:

$$\alpha_0 = B_0 = 1 + 4\epsilon \quad (36)$$
$$S_0 = D_0 = (1-4\epsilon)W_0 + 4\epsilon W_1 + G_w \Delta T \quad (37)$$

The A_i, B_i, and C_i can be computed once for all times, but the D_i, α_i, and S_i change with each time step. The time step is determined by the value selected for ϵ. Values of $\epsilon = 0.4$ and $N=20$ were used in most of the calculations except for small times and near the wall where $N=80$ was required to obtain the wall shear stress with sufficient accuracy (see discussion of results section).

Three additional relations are required for $\bar{V}$, $\overline{V^2}$, and for the wall shear stress. Using the normalized variables, equations (8) and (6) become

$$\bar{V} = 4\int_0^1 VX\,dX \quad (38)$$

$$\overline{V^2} = (4/\bar{V})\int V^3 X\,dX \quad (39)$$

and these two integrals are evaluated at each time step by applying Simpson's Rule [7] over the $N+1$ nodes.

The shear stress is computed at each time step by using a four point parabolic least squares fit following Scheid [7] as follows:

$$\left.\frac{dV}{dX}\right|_{X=0} = (N/20)[9V_{N-3} - 17V_{N-2} - 13V_{N-1}] \quad (40)$$

Equations (22) to (40) form the complete set from which all numerical results were obtained.

Computer Calculations

The equations were programmed in Applesoft BASIC (noncompiled) for the Apple 2 Plus microcomputer. Calculations were made for $M=0$, 0.1, 0.2, 0.5, 1.0, and 2.0. The computed velocity distribution for $M=0$ can be compared to the Szymanski solution in Table 1. They are almost identical. The agreement is taken as evidence that the numerical procedure presented here is sufficiently accurate. Trying various time and spacial increments has resulted in the choice of $N=20$ as more than adequate, and with $\epsilon=0.4$ this results in a computation time of about 30 min. per run. About 10 hr of computing time produced the results given in this paper.

Discussion of Results

The results are contained in Tables 1–4 and Figs. 3–7. The

Downloaded 02 May 2010 to 171.66.16.54. Redistribution subject to ASME license or copyright; see http://www.asme.org/terms/Terms_Use.cfm

Table 2 Velocity distribution ($V(X,T)$; $M=0.5$)

X \ T	0.04	0.08	0.12	0.16	0.20	0.24	0.28	0.32	0.36
0	0.256	0.487	0.667	0.793	0.875	0.926	0.957	0.975	0.986
0.1	0.256	0.485	0.664	0.787	0.868	0.918	0.948	0.966	0.976
0.2	0.255	0.481	0.652	0.770	0.846	0.893	0.921	0.937	0.947
0.3	0.254	0.472	0.632	0.740	0.808	0.850	0.875	0.890	0.899
0.4	0.252	0.457	0.601	0.696	0.755	0.790	0.811	0.823	0.831
0.5	0.247	0.433	0.557	0.635	0.683	0.711	0.728	0.737	0.743
0.6	0.236	0.395	0.495	0.555	0.591	0.612	0.624	0.631	0.635
0.7	0.215	0.339	0.412	0.455	0.479	0.493	0.500	0.505	0.507
0.8	0.175	0.258	0.304	0.330	0.344	0.351	0.355	0.357	0.358
0.9	0.107	0.147	0.168	0.179	0.184	0.187	0.188	0.189	0.190
$-(\partial V/\partial X)_{x=1}$	1.270	1.658	1.841	1.928	1.968	1.985	1.993	1.997	1.998
$V/V(\infty)$	0.367	0.607	0.762	0.860	0.918	0.953	0.973	0.985	0.991

Table 3 Velocity distribution ($V(X,T)$; $M=1.0$)

X \ T	0.004	0.01	0.02	0.04	0.08	0.12	0.16	0.20	0.30
0	0.032	0.080	0.159	0.312	0.578	0.764	0.877	0.939	0.991
0.1	0.032	0.080	0.159	0.312	0.576	0.760	0.871	0.931	0.981
0.2	0.032	0.080	0.159	0.312	0.570	0.747	0.851	0.907	0.952
0.3	0.032	0.080	0.159	0.317	0.560	0.723	0.816	0.865	0.904
0.4	0.032	0.080	0.159	0.308	0.542	0.686	0.765	0.805	0.835
0.5	0.032	0.080	0.158	0.302	0.512	0.633	0.696	0.726	0.747
0.6	0.032	0.080	0.156	0.288	0.466	0.560	0.606	0.626	0.639
0.7	0.032	0.079	0.150	0.262	0.399	0.464	0.493	0.504	0.510
0.8	0.032	0.074	0.132	0.213	0.302	0.341	0.355	0.360	0.360
0.9	0.028	0.056	0.088	0.130	0.171	0.187	0.191	0.192	0.190
$-(\partial V/\partial X)_{x=1}$	0.451	0.789	1.136	1.548	1.924	2.034	2.047	2.034	2.007
$V/V(\infty)$	0.058	0.136	0.253	0.448	0.715	0.863	0.938	0.973	0.997

Table 4 Velocity distribution ($V(X,T)$; $M=2.0$)

X \ T	0.004	0.01	0.02	0.04	0.08	0.12	0.16	0.20	0.30
0	0.041	0.102	0.202	0.390	0.686	0.861	0.945	0.981	0.999
0.1	0.041	0.102	0.202	0.390	0.684	0.855	0.938	0.972	0.989
0.2	0.041	0.102	0.202	0.390	0.678	0.839	0.914	0.945	0.960
0.3	0.041	0.102	0.202	0.389	0.664	0.811	0.875	0.899	0.910
0.4	0.041	0.102	0.202	0.385	0.641	0.767	0.817	0.834	0.840
0.5	0.041	0.102	0.202	0.377	0.605	0.704	0.739	0.749	0.750
0.6	0.041	0.102	0.199	0.360	0.549	0.620	0.640	0.643	0.641
0.7	0.041	0.101	0.191	0.326	0.467	0.510	0.517	0.515	0.511
0.8	0.040	0.095	0.167	0.265	0.352	0.371	0.369	0.365	0.360
0.9	0.036	0.072	0.112	0.161	0.198	0.201	0.197	0.193	0.190
$-(\partial V/\partial X)_{x=1}$	0.577	1.009	1.441	1.912	2.196	2.165	2.089	2.039	2.003
$V/V(\infty)$	0.074	0.174	0.322	0.559	0.841	0.955	0.991	1.000	1.001

normalized velocity distribution is plotted (Fig. 3) at several times and for $M=0$ and 1.0. For $M=0$, the profile develops and approaches the steady-state parabolic distribution at $T\approx 1.0$. For $M=1.0$, the approach to steady state is more rapid ($T\approx 0.34$), and the profiles during corresponding times of their development tend to be "flatter." Note that the velocity distribution is normalized to make $V(0,\infty)=1.0$, but the actual velocities attained depend strongly on M as given by equation (13).

The velocity distribution for $M=0$ is compared in Table 1 with the Szymanski solution (Szymanski's values are shown in parenthesis), and the agreement is excellent. The region that places the greatest demand on the numerical procedure is at the wall for small times, a region of nonuniform convergence as discussed by Szymanski. The wall shear stress is plotted in Fig. 4, and it can be observed that the stress rises rapidly, much faster than does the average flow velocity (which is plotted in Fig. 6). This is because the effects of viscosity are at first felt only in a thin layer near the wall, a boundary layer, and the shear stress rises rapidly in this region. With the passage of time, the boundary layer grows to fill the pipe.

The wall shear stress history is plotted for small values of T

Downloaded 02 May 2010 to 171.66.16.54. Redistribution subject to ASME license or copyright; see http://www.asme.org/terms/Terms_Use.cfm

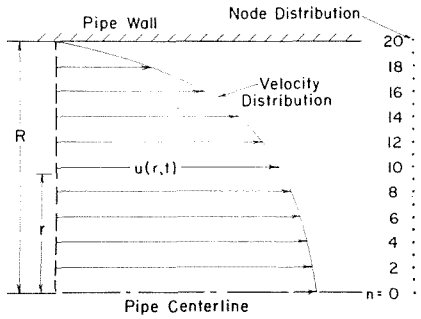

Fig. 2 Definition of circular pipe flow coordinate system and radial position of nodes used in the numerical calculations

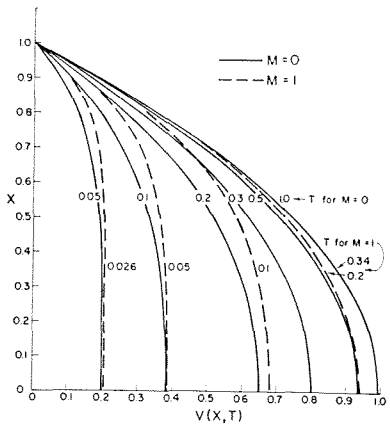

Fig. 3 Dimensionless velocity distribution for $M = 0$ and 1, with values for time chosen in each case to correspond roughly to similar stages in the development of the profile

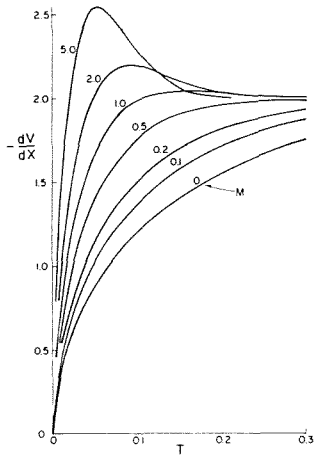

Fig. 4 Dimensionless wall shear stress versus time for various M values. All curves approach 2.0 as $T \to \infty$.

in Fig. 5 where computations for $N = 20$, 40, and 80 are compared. The larger number of spatial nodes results in improved accuracy, but for $T > 0.02$, 20 nodes appear to be adequate. The wall shear stress at $T = 0$ is zero, as can be determined by differentiating the Szymanski solution (equation (3)) and evaluating the velocity gradient there as follows:

$$\left.\frac{\partial V}{\partial X}\right|_{\substack{X=1 \\ T=0}} = -2 - 8\sum_{n=1}^{\infty} 1/\lambda_n^2 \tag{41}$$

where $J_0(\lambda_n) = 0$. The first 20 roots are given by Abramowitz [8], and using McMahon's expansion for the next 80 roots one obtains

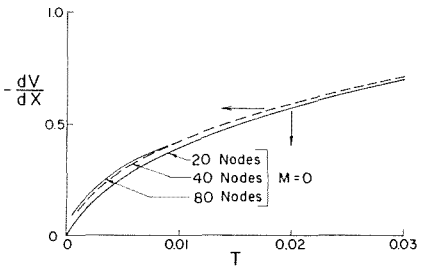

Fig. 5 Dimensionless wall shear stress for small values of T comparing the numerical results for $n = 20$, 40, and 80 nodes

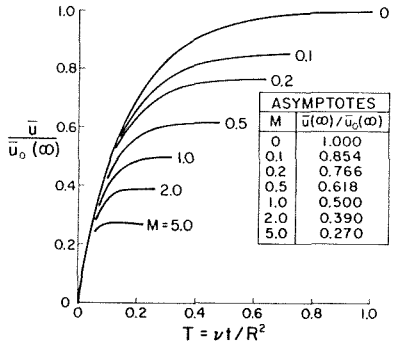

Fig. 6 Average velocity versus time normalized to the steady-state average velocity for $M = 0$. This normalization differs from that of Fig. 3 and Tables 1-4.

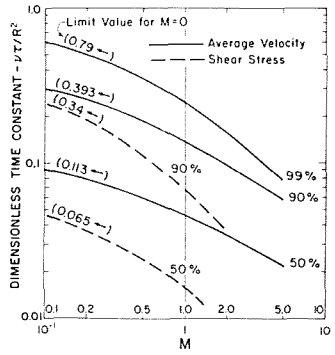

Fig. 7 Start-up time constants required to attain 50, 90, and 99 percent of steady-state average velocity (_____) and 50 and 90 percent of the steady-state wall shear stress (------)

$$\sum_{n=1}^{100} 1/\lambda_n^2 = 0.24899 \approx 0.250 \tag{42}$$

which by direct substitution yields zero for the velocity gradient. The rate of change of shear stress with time can be shown to become infinite, and there lies the difficulty in maintaining accuracy at this point. But it has little effect on the calculation for $T > 0.02$ (see Fig. 5). For $M < 1$, the wall shear stress rises monotonically with time. But for $M > 1$, the shear stress overshoots the steady-state value, such behavior resulting from the fact that the time constant for flow start-up decreases with M, whereas the time constant for boundary layer growth is independent of M. It would appear from Fig. 4 that the shear stress increases much more rapidly with time as M increases. In fact, this is only due to the way in which the variables have been normalized. The use of $\bar{u}(\infty)$ to normalize velocity is useful in making the steady-state centerline velocity equal to unity for all M, but the actual value of $\bar{u}(\infty)$ decreases with M as shown by equation (13).

The normalized average velocity defined in equation (38) is plotted in Fig. 6 versus time for several values of M. Note the slight overshoot for $M > 1$ which is much less pronounced

Downloaded 02 May 2010 to 171.66.16.54. Redistribution subject to ASME license or copyright; see http://www.asme.org/terms/Terms_Use.cfm

than for the shear stress (Fig. 4). The most striking feature of the velocity plots is the rapid decrease in start-up time constant with increasing M.

The start-up velocity time constants are plotted in Fig. 7 for attainment of 50, 90, and 99 percent of the steady-state average velocity. Time constants for the establishment of the shear stress based on Fig. 4 are also shown.

The following example will illustrate situations that would show a substantial departure from the classical solution for $M=0$. Equation (13) can be rearranged in the form

$$\frac{L}{D} = \frac{Re_\infty}{16}\left[1/((1+8M)^{1/2}-1)\right]$$

where $Re_\infty \equiv \overline{u(\infty)}D/\nu$. Consider flows for which $M=1.0$ and $Re_\infty = 2000$ (the upper limit for laminar flow). Then

$$\frac{L}{D} = 62.5$$

Select SAE 10W-30 at 25°C (spatial gravity = 0.88, $\nu = 1.14 \times 10^{-4}$ m^2/s) and a 10-cm diameter pipe. The pipe length would be $L = 6.25$ m and the corresponding head would be (from equation (14))

$$H_0 = \frac{2048\nu^2\rho}{\gamma D^2}\left(\frac{L}{D}\right)^2 M = 1.053 \text{ m}.$$

And one can see from Figs. 3, 4, 6, and 7 that the results would differ substantially from the Szymanski solution. Equation (13) shows that the final average velocity would be just one-half of the value for $M=0$.

It seems strange that such a large effect has not been reported. Leteliar and Leutheusser [9] report data showing agreement with the Szymanski result, but their experiments were for very low values of M (my calculations show their M values were less than 0.01). I can only conclude that researchers measuring values differing from the classical solution have been timid in contesting what has been a textbook standard, and so they have not recognized the importance of the start-up parameter, M.

Acknowledgment

I appreciate the environment at UPM-Dhahran which allowed time for this work, and helpful discussions with colleagues, especially H. Badr on numerical methods. John Olsen prepared the figures and Mary Stampfli was the technical typist, both from U.W.-Madison. Thanks to two reviewers for constructive comments and corrections.

References

1 Szymanski, P., "Quelques Solutions Exactes des Équations de l' Hydrodynamique du Fluide Visquex Dans le Case d'un Tube Cylindrique," *J. de Math. Pures et Appliquees*, Series 9, 11, 67, 1932.

2 Batchelor, G. K., *An Introduction to Fluid Mechanics*, Cambridge U. Press 1970; Schlichting, H., *Boundary Layer Theory*, 7th ed., McGraw Hill, p. 92; White, F. M., *Viscous Fluid Flow*, McGraw-Hill, 1974, p. 142; Telionis, D. P., *Unsteady Viscous Flows*, Springer-Verlag, New York, 1981, p. 91.

3 Streeter, V. L., and Wylie, E. B., *Fluid Mechanics*, 7th ed., McGraw-Hill, 1979, p. 491; Daugherty, R. L., and Franzini, J. B., *Fluids Mechanics*, McGraw-Hill, 1977, p. 423; Rouse, H., *Elementary Mechanics of Fluid*, Wiley, 1946, p. 125.

4 Letelier S., M. F., and Leutheusser, H. J., "Unified Approach to the Solution of Problems of Unsteady Laminar Flow in Long Pipes," ASME JOURNAL OF APPLIED MECHANICS, Vol. 50, Mar. 1983, pp. 9-12.

5 Albasimy, E. L., "On the Numerical Solution of a Cylindrical Heat-Conduction Problem," *Quart. J. Mech. and App. Math.*, Vol. 13, Part 3, 1960, pp. 374-384.

6 Smith, G. D., *Numerical Solution of Partial Differential Equations*, Oxford University Press 1974, pp. 17-23, 44, 45, 52-54.

7 Scheid, Francis, *Theory and Problems of Numerical Analysis*, Schaum's Outline Series, McGraw-Hill, 1968.

8 Abramowitz, M., and Stegun, A., ed., *Handback of Mathematical Functions With Formulas, Graphs, and Mathematical Tables*, U.S. Dept. of Commerce, N.B.S. Appl. Math. Series 55.

9 Letelier S., M. F., and Leutheusser, H. J., "Skin Friction in Unsteady Laminar Pipe Flow," *J. of the Hydraulics Div.*, Jan. 1976, pp. 41-56.

Downloaded 02 May 2010 to 171.66.16.54. Redistribution subject to ASME license or copyright; see http://www.asme.org/terms/Terms_Use.cfm

Effect of Hinge Gap on Aerodynamics of Thin Airfoils Having an Oscillating Flap

S. Ando
Professor,
Department of
Aeronautical Engineering,
Nagoya University,
Nagoya, Japan

D.-H. Lee
Assistant Professor,
Doctor of Engineering,
Department of Mechanical
Engineering,
Ulsan Institute of Technology,
Ulsan, Korea

Nonsteady load distributions on a thin airfoil in inviscid incompressible flow having an oscillating flap with a narrow hinge gap are investigated. The angle of attack is assumed to be zero in front of the hinge gap. The problem is first attacked numerically through Poisson's integral equation to compare it with analytical methods derived later. The logarithmic singularity in the kernal function is treated with special care. Secondly the method of matched asympototic expansions is used to analyze the problem. It brings forth simple closed-form expressions. Comparisons of results of the two methods show excellent agreement with each other, when gap width-to-chord ratio is less than 0.1. In the Appendix, a simplified method is presented where no inner solution needs to be considered. It is useful for the gap/chord ratio less than 0.01.

1 Introduction

There are many published works on steady aerodynamics of airfoils having gaps, but rather few on the unsteady case. Of special interest for steady case among many approaches is one presented by White and Landah [1], since it shows useful physical meanings in closed, explicit forms. They used the method of matched asymptotic expansions (MAE) (cf. Van Dyke [2],) with a small parameter, gap width/airfoil-chord-length ratio. We extended the idea of White and Landahl to the unsteady case for arbitrary but smooth upwash mode (Ando & Lee [3]). A pressure matching was used there rather than the streamwise velocity matching of White and Landahl [1]. A difficulty that stems from a nonlinearity in the inner solution was easily resolved for thin airfoils.

In this paper we expand this idea to oscillating flap cases when a narrow hinge gap exists. This is not so straightforward, because there is a singularity of pressure at the hinge even without a hinge gap. Many fundamental results are similar to those for smooth upwash [3], but most of them were not pointed out by White and Landahl [1]. Volume flow rate through the gap is almost proportional to the "pressure loading" at the hinge when there is no gap. Many results agree quite satisfactorily with those of Vortex Lattice Method (VLM). The composite solution of the pressure loading shows no significant differences from the outer solution with the desired accuracy of the approximation for the generalized forces. This fact simplifies later applications considerably. Modification of lift and pitching moment due to the hinge gap are expressed by closed explicit formulas.

Contributed by the Applied Mechanics Division for publication in the JOURNAL OF APPLIED MECHANICS.
Discussion on this paper should be addressed to the Editorial Department, ASME, United Engineering Center, 345 East 47th Street, New York, N.Y. 10017, and will be accepted until two months after final publication of the paper itself in the JOURNAL OF APPLIED MECHANICS. Manuscript received by ASME Applied Mechanics Division, May, 1982; final revision, April, 1983.

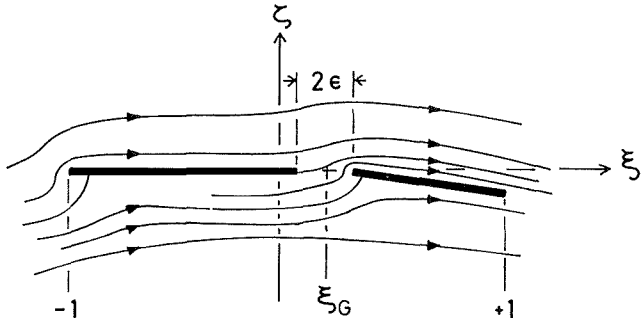

Fig. 1 Analytical model of flapped airfoil, and some notations

Three solution methods are considered as in the case of smooth upwash [3]. One is designated as the "analytical solution," based on the method of MAE. The second is the "numerical solution," based on VLM. It is used as a reference solution against which the others are compared. The third is the "simplified analytical solution," which exhibits worse accuracies, but requires no inner solution. Both analytical solutions are useful for not so large values of (reduced frequency) × (gap/chord ratio). Throughout this paper, the fluid is assumed to be incompressible and inviscid.

2 Numerical Solution

For a thin airfoil executing a simple harmonic motion in time in incompressible inviscid flow of stream velocity U, the following well-known Poisson's integral equation is useful (cf. Bisplinghoff et al. [4])

$$\frac{w(x)}{U} = \frac{k}{2\pi}\int_{-1}^{1} P(\xi)\left(\frac{1}{s} - ie^{-is}\left\{\gamma + ln|s| + C_i(|s|)\right.\right.$$

Copyright © 1985 by ASME
Downloaded 02 May 2010 to 171.66.16.54. Redistribution subject to ASME license or copyright; see http://www.asme.org/terms/Terms_Use.cfm

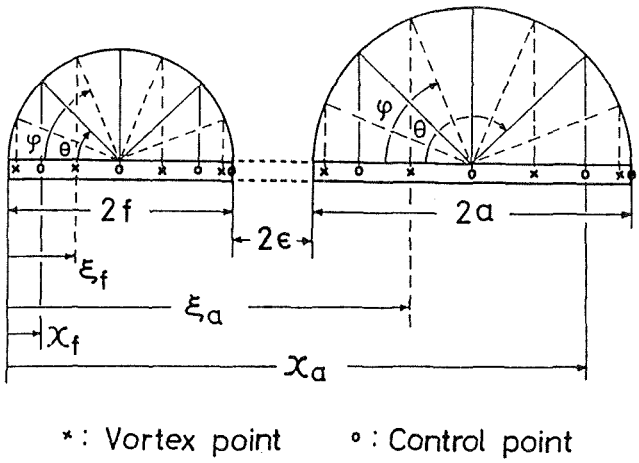

Fig. 2 Numerical model of flapped airfoil, and 2-SCM (semi-circle division)

$$+i\left[Si(s)+\frac{\pi}{2}\right]\Big\}\Big)d\xi$$

$$Ci^*(|s|)=\int_0^{|s|} t^{-1}(\cos t-1)dt, \quad s=k(x-\xi) \tag{1}$$

where γ = Euler's constant. Note that w, P, and later some additional quantities denote complex amplitudes. The semichord length is assumed to be unity. The reduced frequency k is defined as angular frequency divided by U. P denotes $(P_l-P_u)/\rho U^2$, upward lift distribution divided by (air mass density) $\times U^2$. The parameter w denotes the velocity component in the ζ direction. See Fig. 1.

When the well-known VLM is adopted, (1) must be discretized to give a system of algebraic linear equation; see Fig. 2. Then the unknowns $P(\xi_i)$, $i=1,2,\ldots$ are determined for given values $w(x_j)$, $j=1,2,\ldots$. To obtain satisfactory convergence characteristics, a logarithmic singularity in the kernal should be treated carefully (Ando and Ichikawa [5]). This method appears quite good for an arbitrary ratio of gap width-to-chord length, and may be said to be "almost exact."

3 Analytical Method

As is well known, Schwarz gave an inversion formula of (1) [4].

$$P(\xi)=\frac{2}{\pi}[1-C(k)]\sqrt{\frac{1-\xi}{1+\xi}}\int_{-1}^{1}\sqrt{\frac{1+\xi_1}{1-\xi_1}}w(\xi_1)d\xi_1$$

$$+\frac{2}{\pi}\int_{-1}^{1}\left[\sqrt{\frac{1-\xi}{1+\xi}}\sqrt{\frac{1+\xi_1}{1-\xi_1}}\frac{1}{\xi-\xi_1}-ik\,\Lambda(\xi,\xi_1)\right]w(\xi_1)d\xi_1 \tag{2}$$

where

$$\Lambda(\xi,\xi_1)=ln\left|\frac{1-\xi\xi_1+\sqrt{1-\xi_1^2}\sqrt{1-\xi^2}}{\xi-\xi_1}\right|$$

and $C(k)$ denotes the well-known Theodorsen's circulation function; see Bisplinghoff, et al. [4] p. 271. Let us consider the following normal displacement of a thin airfoil

$$\zeta=-(\xi-\xi_G)H(\xi-\xi_G)e^{i\omega t} \tag{3}$$

where ω and t denote angular frequency and time variable, respectively. H denotes the unit step function. Then we have the corresponding complex amplitude of the normal velocity

$$w=-[1+ik(\xi-\xi_G)]H(\xi-\xi_G) \tag{4}$$

Equation (4) refers to an airfoil without a hinge gap, and so we rewrite this w as w_R hereafter. If (4) is substituted into (2), we obtain

$$P_R=\frac{2}{\pi}\sqrt{\frac{1-\xi}{1+\xi}}\Big\{R_0+ik\Big(R_1(1+\xi)+(\pi-\varphi_G)(\xi-\xi_G)$$

$$\left[1+\frac{ik}{2}(1+\xi)\right]\Big)\Big\}+\frac{2}{\pi}\Lambda(\xi,\xi_G)\Big[1+2ik(\xi-\xi_G)$$

$$-\frac{k^2}{2}(\xi-\xi_G)^2\Big] \tag{5}$$

where

$$\varphi_G=\arccos(-\xi_G)$$

$$R_0(\xi_G,k)=(\pi-\varphi_G)\Big\{C(k)+ik\Big[1+[C(k)$$

$$-1]\left(\frac{1}{2}-\xi_G\right)\Big]\Big\}+\sqrt{1-\xi_G^2}\Big\{C(K)-1+ik\Big[1+[C(k)$$

$$-1]\left(1-\frac{1}{2}\xi_G\right)\Big]\Big\} \tag{6}$$

$$R_1(\xi_G,k)=\pi-\varphi_G+\frac{ik}{2}[\sqrt{1-\xi^2}-\xi_G(\pi-\varphi_G)] \tag{7}$$

In what follows we consider the case when there is a narrow hinge gap. The method of matched asymptotic expansion (MAE) will be used with a small parameter ϵ, ratio of gap width-to-chord length. However a p-matching will be adopted in our method rather than the u-matching of White and Landahl [1]. The reason stems from the difference between steady and nonsteady cases [3].

(A) **Outer Solution.** For the outer solution, a narrow hinge gap may be assumed to present a point source-like effect. Hence we assume

$$w=w_R+Q\,\epsilon\,\delta(\xi-\xi_G) \tag{8}$$

and substitute it into (2). Then the two-terms outer solution of P is obtained

$$P^\circ=P_R+\frac{2}{\pi}Q\,\epsilon\Big\{\sqrt{\frac{1-\xi}{1+\xi}}\sqrt{\frac{1+\xi_G}{1-\xi_G}}\Big[1-C(k)$$

$$+\frac{1}{\xi-\xi_G}\Big]-ik\,\Lambda\,(\xi,\xi_G)\Big\} \tag{9}$$

where Q is an unknown, and δ denotes Dirac's delta function.

(b) **Inner Solution.** Let us introduce the following inner variables

$$\bar{\xi}=(\xi-\xi_G)/\epsilon, \quad \bar{\zeta}=\zeta/\epsilon \tag{10}$$

The inner solution P^i should be a nonlinear form according to Bernoulli's equation, since all disturbances are not always small in the inner region. But fortunately the "linearized form" of P becomes acceptable provided that the wing thickness is zero and only the region $|\bar{\xi}|\geqq 1$ is concerned [3]. Hence

$$P^i=2\left[ik\phi^i+\frac{1}{\epsilon}\frac{\partial\phi^i}{\partial\bar{\xi}}\right] \tag{11}$$

where ϕ^i denotes the inner solution of the perturbation velocity potential:

$$\phi^i=\phi_0^i+\epsilon\phi_1^i+\epsilon^2\phi_2^i \tag{12}$$

Here

$$\phi_0^i=A \tag{13}$$

$$\phi_1^i=(B+C\bar{\xi})ln\,|\bar{\xi}+\sqrt{\bar{\xi}^2-1}|+(B-C)\sqrt{\bar{\xi}^2-1}+D \tag{14}$$

$$\phi_2^i=\bar{\xi}^2(E+F\,ln\,\bar{\xi}) \tag{15}$$

where A, B, C, D, E, and F are unknown constants, which

Downloaded 02 May 2010 to 171.66.16.54. Redistribution subject to ASME license or copyright; see http://www.asme.org/terms/Terms_Use.cfm

may depend on k. While they may be independent of $\bar{\xi}$ as well as ϵ, except for the quite weak form $ln\ \epsilon$. ϕ_1^i was introduced by inspecting equation (60) of White and Landahl [1]. Non-steadiness would bring no significant changes in flow properties in the inner region: the time variable t may participate as merely a parameter. ϕ_2^i of (15) was determined by considering the inner limit of the outer solution. See Appendix A. It is necessary for the final expression of P^i to be valid up to $0(\epsilon)$. Introduction of (12)–(15) into (11) yields

$$P^i = 2\{B\sqrt{(\bar{\xi}+1)/(\bar{\xi}-1)} + C\ ln\ |\bar{\xi}+\sqrt{\bar{\xi}^2-1}\,| + ikA\}$$
$$+ 2\epsilon\{\bar{\xi}(E+F\ \ln\ \bar{\xi}) + ik[(B+C\bar{\xi})ln\,|\bar{\xi}+\sqrt{\bar{\xi}^2-1}\,|$$
$$+ (B-C)\sqrt{\bar{\xi}^2-1} + D]\} \tag{16}$$

It should be noted that (16) is valid only for $|\bar{\xi}| \geqq 1$. Moreover, the factor $\text{sgn}(\bar{\xi})$ resulting from the root symbol, a double-valued function, was omitted for simplicity. Equation (16) represents a two-terms inner solution. Note that E and F, resulting from $0(\epsilon^2)$-term, ϕ_2^i, remain as $0(\epsilon)$-terms in P^i. P^i should satisfy the Kutta condition at the front end of the gap, $\bar{\xi} = -1$. Thus we have

$$ikA - \epsilon E - ik\epsilon D = 0. \tag{17}$$

(C) Matching. First we must obtain P^{oi}, the inner limit of the outer solution, by substituting $\xi = \xi_G + \epsilon\bar{\xi}$ into (9) and then expanding in a power series in ϵ

$$P^{oi} = F_0 - \frac{2}{\pi}\ ln\bar{\xi} + \frac{2}{\pi}\frac{Q}{\bar{\xi}} + \epsilon\left\{\bar{\xi}\left[F_1 - \frac{4}{\pi}ikln\ \bar{\xi}\right]\right.$$
$$\left. + \left[1 - C(k) - \frac{1}{1-\xi_G^2} + ik\ ln\left|\frac{2(1-\xi_G^2)}{\epsilon\bar{\xi}}\right|\right]\right\} + HOT \tag{18}$$

where

$$F_0 = \frac{2}{\pi}\left[R_0\sqrt{\frac{1-\xi_G}{1+\xi_G}} + ln\left|\frac{2(1-\xi_G^2)}{\epsilon}\right| + ik\ R_1\sqrt{1-\xi_G^2}\right] \tag{19}$$

$$F_1 = \frac{2}{\pi}\left\{\left[ik(\pi-\varphi_G) - \frac{R_0}{1-\xi_G^2}\right]\sqrt{(1-\xi_G)/(1+\xi_G)}\right.$$
$$+ ik[ik(\pi-\varphi_G)/2 - R_1\xi_G/(1-\xi_G^2)]\sqrt{1-\xi_G^2}$$
$$\left. - \xi_G/(1-\xi_G^2) + 2ik\ ln\,|2(1-\xi_G^2)/\epsilon|\right\} \tag{20}$$

$$HOT = 0[\epsilon^2 \times (k, kln\epsilon, k^2 ln\epsilon)] \tag{21}$$

Note that $P_R(\xi_G + \epsilon\bar{\xi})$ cannot be written down in the usual series,

$$\lim_{\epsilon\to 0} P_R(\xi_G + \epsilon\bar{\xi})$$
$$= P_R(\xi_G) + \epsilon\bar{\xi}P_{R,\xi}(\xi_G) + \ldots\ldots\ldots\ldots \tag{22}$$

like in the smooth upwash case (Ando and Lee [3]). The reason is that $P_R(\xi_G)$, $P_{R,\xi}(\xi_G)$, $\ldots\ldots\ldots$ do not exist here. It is noteworthy that an interesting simple relation exists between F_0 and $P_R(\epsilon\to\xi_G)$;

$$F_0 - \frac{2}{\pi}ln\bar{\xi} = \lim_{\epsilon\to 0} P_R(\xi_G + \epsilon\bar{\xi}). \tag{23}$$

or

$$F_0 + \frac{2}{\pi}ln\epsilon = \text{finite} = P_R(\xi) + \frac{2}{\pi}ln\,|\xi - \xi_G| \tag{24}$$
$$\text{for}\quad \epsilon\to 0,\ \xi\to\xi_G$$

Second let us obtain P^{io}, the outer limit of the inner solution, by introducing $\bar{\xi} = (\xi - \xi_G)/\epsilon$ in (16) and then making $\epsilon\to 0$

$$P^{io} = 2\{ikA + B + C\ ln\,|2(\xi-\xi_G)/\epsilon|$$
$$+ (\xi-\xi_G)[E + F\ ln\,|(\xi-\xi_G)/\epsilon|] + ik(B - C$$
$$+ C\ ln\,|2(\xi-\xi_G)/\epsilon|)] + \epsilon[B/(\xi-\xi_G) + ik(D$$
$$+ B\ ln\,|2(\xi-\xi_G)/\epsilon|)]\} + HOT \tag{25}$$

where HOT is given again by (21). Now apply the limit matching principle (cf. Van Dyke [2]), $P^{oi} = P^{io}$. Then we have

$$2(ikA + B + C\ ln\ 2) = F_0 \tag{26}$$
$$C = -1/\pi \tag{27}$$
$$2[E + ik(B - C + C\ ln\ 2)] = F_1 \tag{28}$$
$$F + ikC = -2ik/\pi \tag{29}$$
$$B = Q/\pi \tag{30}$$
$$ik(B\ ln\ 2 + D) = \frac{Q}{\pi}\left[1 - C(k) - \frac{1}{1-\xi_G^2}\right.$$
$$\left. - ik\ ln\left|\frac{2(1-\xi_G^2)}{\epsilon}\right|\right] \tag{31}$$

Equations (17) and (26)–(31) determine all the unknown constants. Let Q thus obtained by Q_1, i.e.,

$$Q_1 = \frac{2}{\pi}\ \frac{F_0 + (2/\pi)\ ln\ 2 - \epsilon[F_1 + 2ik(\ ln\ 2 - 1)/\pi]}{1 - \epsilon\left\{1 - C(k) - 1/(1-\xi_G^2) - ik\left[\ ln\left|\frac{4(1-\xi_G^2)}{\epsilon}\right| - 1\right]\right\}} \tag{32}$$

Note the following instructive qualitative properties of (32):

(*a*) $Q_1 \simeq 0(ln\ \epsilon)$ as $\epsilon\to 0$. Then (8) shows the gap flow rate to be $0(\epsilon\ ln\ \epsilon)$. This agrees with the steady case, studied by White and Landahl [1].

(*b*) Q_1 is influenced dominantly by F_0, which in turn is connected closely with $P_R(\epsilon\to\epsilon_G)$ as shown by (24). This is similar to one obtained for the smooth upwash case by Ando and Lee [3]. But the situation is more complicated because of the logarithmic singularity in P_R at the flap hinge.

(D) Composite Solution. The composite solution P^c is defined by

$$P^c = P^o + P^i - P^{io} \tag{33}$$

which is constructed by using equations (9), (16), and (18) or (25). But this expression is lengthy, and so we omit it here.

(E) Lift and Pitching Moment. A satisfactory expression of the lift should be obtained by the following way

$$L^c = \left[\int_{-1}^{\xi_G-\epsilon} + \int_{\xi_G+\epsilon}^{1}\right]P^c(\xi)d\xi \tag{34}$$

On the other hand, a simpler solution obtained from the outer solution is

$$L^0 = \int_{-1}^{1} P^0(\xi)d\xi \tag{35}$$

After somewhat lengthy elementary calculations, we find

$$L^0 - L^c = HOT \tag{36}$$

Thus within the desired accuracy, L^0 gives a satisfactory value which will hereafter be written simply as L

$$L = L_R + \Delta L\ \epsilon + HOT \tag{37}$$

where

$$L_R = 2(R_0 + \sqrt{1-\xi_G^2}) + ik[R_1 - (\pi-\varphi_G)(1+2\xi_G)$$
$$- 2\xi_G\sqrt{1-\xi_G^2}] + k^2[\xi_G(\pi-\varphi_G) - (1$$
$$+ 2\xi_G^2)\sqrt{1-\xi_G^2}/3]/2 \tag{38}$$
$$\Delta L = -2Q_1[C(k)\sqrt{(1+\xi_G)/(1-\xi_G)} + ik\sqrt{1-\xi_G^2}] \tag{39}$$

Downloaded 02 May 2010 to 171.66.16.54. Redistribution subject to ASME license or copyright; see http://www.asme.org/terms/Terms_Use.cfm

In the same way, one obtains for the nose-down pitching moment about the midchord point

$$M = M_R + \Delta M\,\epsilon + \text{HOT} \tag{40}$$

where

$$M_R = -R_0 + \xi_G\sqrt{1-\xi_G^2} + ik(\pi - \varphi_G)(1+\xi_G - ik/8) + ik\sqrt{1-\xi_G^2}[2(1-\xi_G^2) + ik\xi_G(2\xi_G^2 - 5)/8]/3 \tag{41}$$

$$\Delta M = -Q_1\{[2\xi_G - 1 - C(k)]\sqrt{(1+\xi_G)/(1-\xi_G)} + ik\xi_G\sqrt{1-\xi_G^2}\} \tag{42}$$

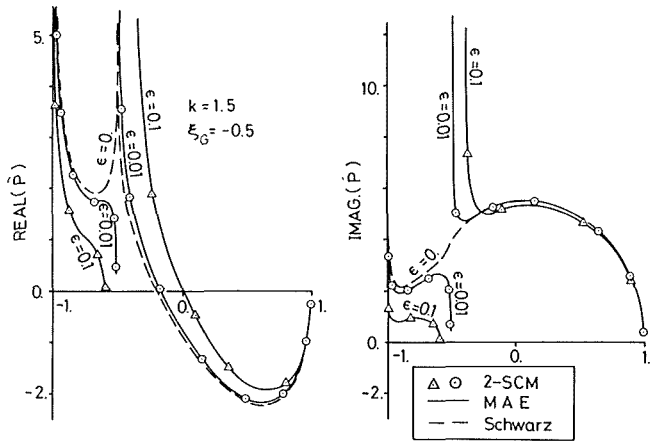

Fig. 3(*a*) Real and imaginary parts of P versus ξ; comparison between analytical and numerical methods for $\xi_G = -0.5$, $k = 1.5$, and $\epsilon = 0.1$ and 0.01

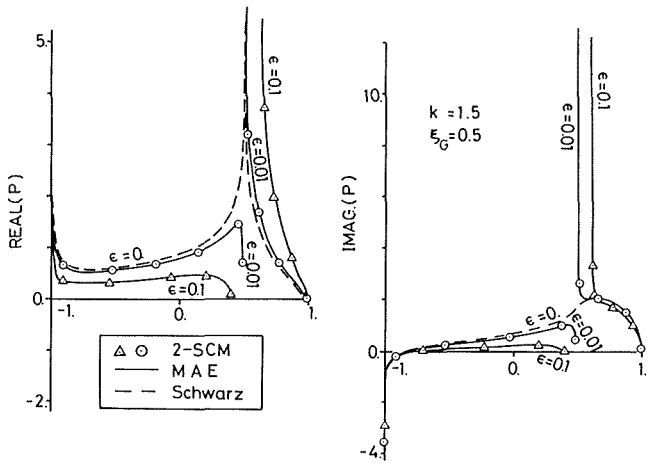

3(*b*); Continued for $\xi_G = +0.5$, $k = 1.5$, and $\epsilon = 0.1$ and 0.01

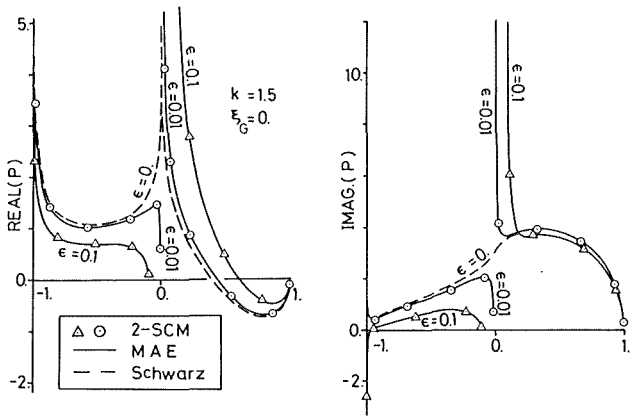

3(*c*); Continued for $\xi_G = 0$, $k = 1.5$, and $\epsilon = 0.1$ and 0.01

It is noteworthy that both ΔL and ΔM are apparently the same as the continuous upwash case [3]. All differences between the continuous and discontinuous cases lie only in the contents of Q_1.

3 Results of Calculations

Calculations are made mainly for pressure loadings. Analytical results are compared with numerical ones obtained using total number of divisions $M = 60$; see Fig. 3. The numerical results may be almost exact. The changes in the loading P due to the hinge gap are similar to those of the continuous upwash case [3]. Accuracy of the analytical results are seen more quantitatively in Fig. 4, where the "error-index" E^T is used. See Appendix C for the definition of E^T; this gives a measure of the relative error between the analytical and the numerical methods. The analytical method is satisfactory for $\epsilon < 0.1$, if an error less than 5 percent is required. This figure also shows accuracy of the simplified analytical solutions (see Appendix B) which become useful for $\epsilon < 0.01$.

Figure 5 shows the polar diagram of Q_1/π for $\xi_G = 0$ and $\epsilon = 0.01$ and 0.001, using k as a parameter. Comparison is seen against the continuous upwash case [3]. Note that the phase of Q_1 is late as compared with the flap angle except for the very small range of k near unity, for every case. Figure 6 shows the polar diagram of $L/2\pi$ for $\epsilon = 0$, 0.01 and $\xi_G = 0$, ± 0.5. The phase change is similar to that of Q_1, qualitatively. But the tendency, that the absolute value of lift for $\epsilon = 0.01$ is larger than for $\epsilon = 0$ as k increases, for the discontinuous case is weaker than for the continuous case.

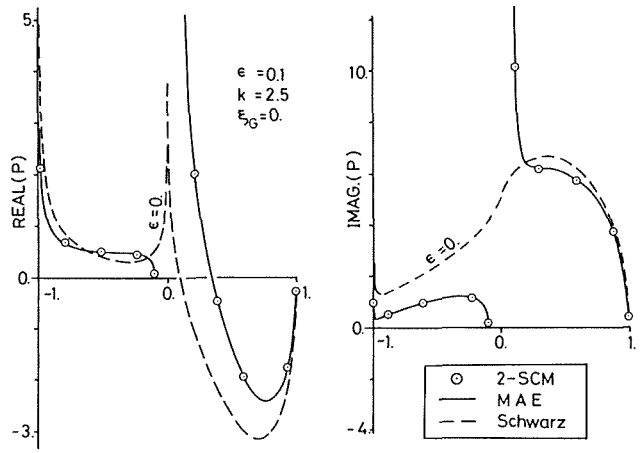

3(*d*); Continued for $\xi_G = 0$, $k = 0.5$, and $\epsilon = 0.1$

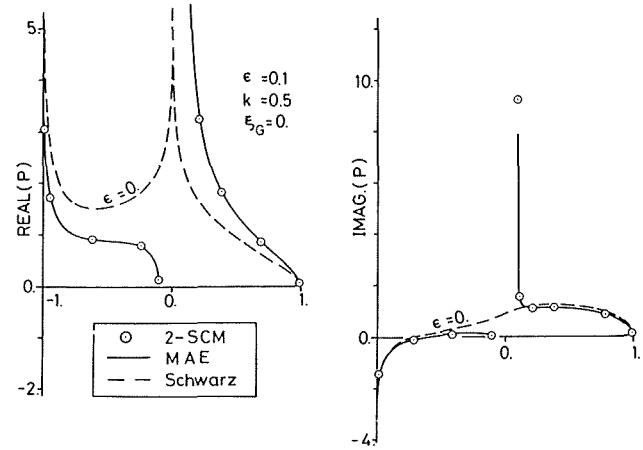

3(*e*) Continued for $\xi_G = 0$, $k = 2.5$, and $\epsilon = 0.1$

Fig. 3

Downloaded 02 May 2010 to 171.66.16.54. Redistribution subject to ASME license or copyright; see http://www.asme.org/terms/Terms_Use.cfm

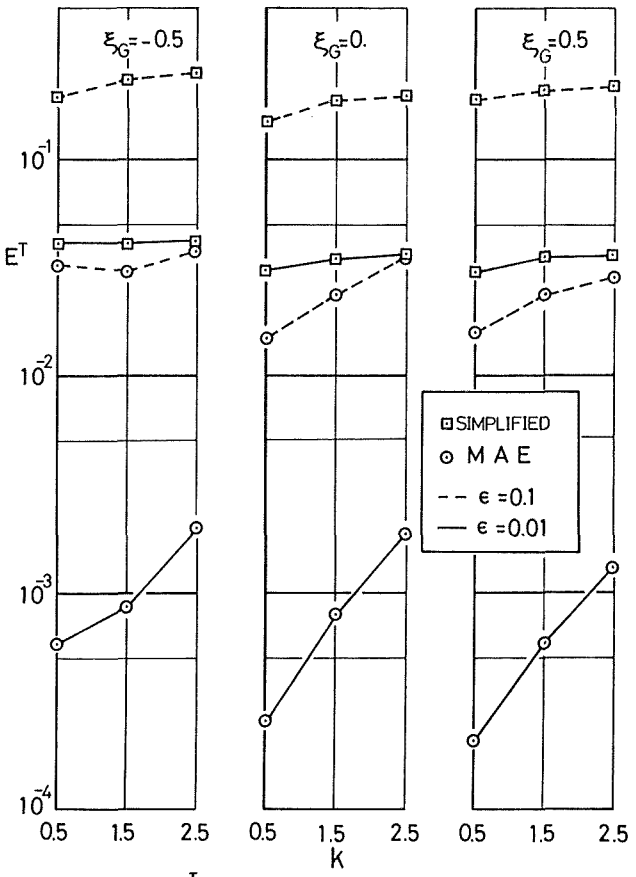

Fig. 4 Error-index E^T versus k for both analytical methods; $\xi_G = 0$, and ± 0.5

5 Conclusions

The effect of a narrow hinge gap on aerodynamics of a thin airfoil having an oscillating trailing edge flap is investigated for incompressible and inviscid flow.

(*a*) Numerical calculations on the basis of Vortex Lattice Method are carried out, as accurate reference results.

(*b*) Analytical method. This is derived using the method of matched asymptotic expansions. A pressure-matching scheme is adopted. A logarithmic singularity of loading at the hinge (which exists even for no gap) requires some new special consideration. Volume flow rate through the hinge gap is roughly proportional to $\epsilon/n\ \epsilon$, for $\epsilon \to 0$, and is governed dominantly by the loading at the hinge station for the case of no gap. Omitted terms in this solution are $0(\epsilon^2, k\epsilon^2, k\epsilon^2 ln\ \epsilon, k^2\epsilon^2 ln\ \epsilon)$. Sample numerical calculations show that the analytical method is satisfactory when $\epsilon < 0.1$ for $k < 2.5$. The effect of hinge gap on lift and pitching moment is expressed by closed formulas.

(*c*) Simplified analytical method. Derivation of this requires no inner solution. It is useful when $\epsilon < 0.01$ for $k < 2.5$.

References

1 White, R. B., and Landahl, M. T., "Effect of Gaps on the Loading Distribution of Planar Lifting Surfaces," *AIAA J.*, Vol. 6, No. 4, 1968, pp. 626-631.

2 Van Dyke, M., *Perturbation Methods in Fluid Mechanics*, Parabolic Press, Stanford, Calif., 1975.

3 Ando, S., and Lee, D. H., "Unsteady Incompressible Inviscid Aerodynamics of Thin Airfoil With Narrow Gaps," *AIAA J.*, Vol. 20, No. 1, 1982, pp. 4-8.

4 Bisplinghoff, R. L., Ashley, H., and Halfman, R. L.; *Aeroelasticity*, Addison-Wesley, Reading, Mass., 1955, p. 325.

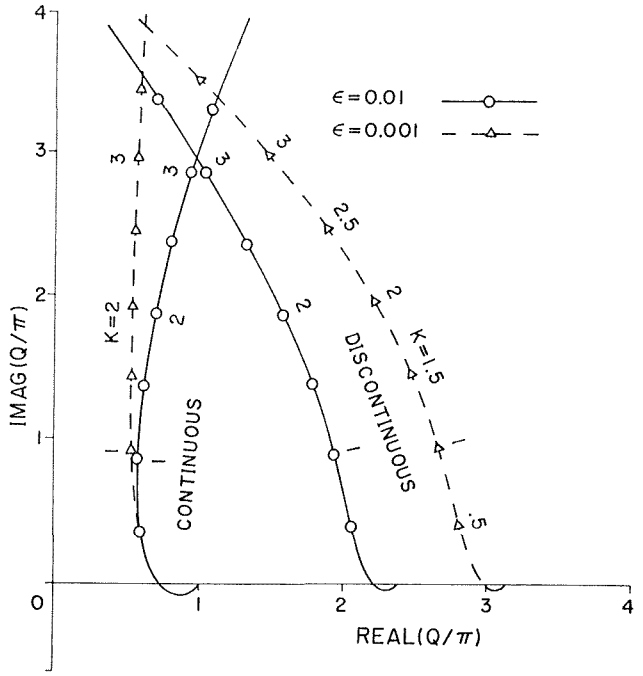

Fig. 5 Polar diagram of Q_1/π for both continuous and discontinuous upwash: $\epsilon = 0, 0.01$ and $\xi_G = 0$.

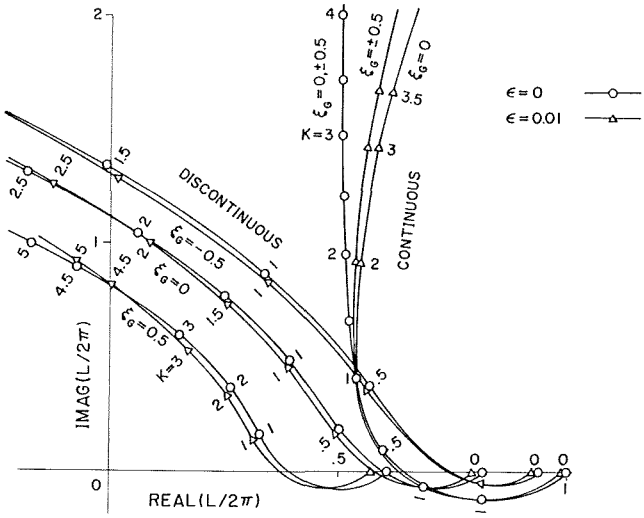

Fig. 6 Polar diagram of $L/2\pi$ for both continuous and discontinuous upwash: $\epsilon = 0, 0.01$ and $\xi_G = 0, \pm 0.5$

5 Ando, S., and Ischikawa, A., "The Use of an Error Index to Improve Numerical Solutions for Unsteady Lifting Airfoils," *AIAA J.*, Vol. 21, No. 1, 1983, pp. 47-54.

APPENDIX *A*

Derivation of ϕ_2^i

This is obtained by using the relation

$$\phi_R^{oi} = \phi^{io}(Q=0) \tag{A1}$$

The perturbation velocity potential ϕ_R^o without hinge gap is obtained through Schwarz' theory (cf. Bisplinghoff et al. [4]

$$\phi_R^o(\xi) = -\frac{2}{\pi}\int_{-1}^{1} \Lambda(\xi,\xi_1) w(\xi_1) d\xi_1 - \frac{\Omega}{\pi}\int_1^{\infty} \frac{\partial \Lambda_2}{\partial \lambda} e^{-ik\lambda} d\lambda \tag{A2}$$

where

$$\Omega = \frac{4}{\pi i k}\int_{-1}^{1} \sqrt{\frac{1+\xi_1}{1-\xi_1}}\, w(\xi_1) d\xi_1 / [H_1^{(2)}(k) + iH_0^{(2)}(k)] \tag{A3}$$

Downloaded 02 May 2010 to 171.66.16.54. Redistribution subject to ASME license or copyright; see http://www.asme.org/terms/Terms_Use.cfm

$$\frac{\partial \Lambda_2}{\partial \lambda} = \sqrt{\frac{1-\xi}{1+\xi}}\left[\frac{1}{\sqrt{\lambda^2-1}} + \sqrt{\frac{\lambda+1}{\lambda-1}}\frac{1}{\xi-\lambda}\right] \tag{A4}$$

Substitute (4) into (A2) and (A3) and then carry out integrations if possible. Put $\xi = \xi_G + \epsilon\bar{\xi}$ and obtain an asymptotic forms for small ϵ. The λ-integral in (A2) may be expanded in a regular $(\epsilon\bar{\xi})$-power series formally, paying no attention that the coefficients are not expressed explicitly. Thus we may write ϕ_R^{oi} in the following way

$$\phi_R^{oi} \equiv \lim_{\epsilon\to 0} \phi_R^o(\xi_G + \epsilon\bar{\xi}) = A_1 + \epsilon\bar{\xi}(A_2 + A_3 ln\ \bar{\xi}) + (\epsilon\bar{\xi})^2(A_4 + A_5 ln\bar{\xi}) + 0(\epsilon^3) \tag{A5}$$

where A_1 ----- A_5 are not obtained explicitly.

Next $\phi^{io}(Q=0)$ must be written down. Leaving ϕ_2^i only, we have from (12)–(15),

$$\phi^{io}(Q=0) = \lim_{\bar{\xi}\to\infty} \phi^i(Q=0) = A_0 + \epsilon\bar{\xi}[(B_o - C_o + C_0\ ln\ 2) + C_0\ ln\ \bar{\xi}] + \epsilon^2\phi_2^{io}(Q=0) \tag{A6}$$

where suffix o refers values for $Q=0$.

Comparison of (A5) with (A6), term-by-term for the same ϵ-power, leads us to $A_1 \mapsto A_0$, $A_2 \mapsto B_0 - C_0 + C_0\ ln2$, $A_3 \mapsto C_0$, and

$$\phi_2^{io}(Q=0) \mapsto \bar{\xi}^2(A_4 + A_5 ln\bar{\xi}) \tag{A7}$$

the last of which is nothing but the form of (15) in the text. It is clear that an alternative expression

$$\phi_2^i = (\bar{\xi}^2 - 1)\{E' + F' ln[\bar{\xi} + \sqrt{\bar{\xi}^2 - 1}]\} \tag{A8}$$

will still be useful. However the simpler form was selected in the text.

APPENDIX B

Simplified Analytical Method

Now let us construct a method through which the unknown parameter Q in the outer solution will be determined without using the inner solution. For this purpose we adopt the condition used for smooth upwash case by Ando and Lee [3]

$$P^0(\xi_G - \epsilon) = 0 \tag{B1}$$

which means the "Kutta condition" at the front end of the gap. There is no logical basis of this assumption, since the outer solution can give no details at or near the gap. Denoting Q obtained through (B1) as Q_2, we have

$$Q_2 = \frac{2}{\pi}\frac{F_0 - \epsilon F_1}{1 - \epsilon[1 - C(k) - 1/(1-\xi_G^2) - ik\ ln\,|2(1-\xi_G^2)/\epsilon|]} \tag{B2}$$

Then P^0 with Q_2 in place of Q is used as P, in this method.

APPENDIX C

Definition of the Error-Index E^T

We define the error-index E^T as follows.

$$E^T = \frac{\sum_{i=1}^{M}\{|Re(P_{Ai} - P_{Ni})| + |Im(P_{Ai} - P_{Ni})|\}h_i}{\sum_{i=1}^{M}\{|Re\ P_{Ni}| + |Im\ P_{Ni}|\}h_i} \tag{C1}$$

$( )_A$ = analytical or simplified analytical solutions,
$( )_i$ = value at the ith error evaluation station
$( )_N$ = numerical solution
h_i = length of the ith segment
Re, Im = real and imaginary parts
M = total number of the error-evaluation stations

Error evaluation points selected here are the loading points for VLM; hence $M = 60$.

Downloaded 02 May 2010 to 171.66.16.54. Redistribution subject to ASME license or copyright; see http://www.asme.org/terms/Terms_Use.cfm

Time-Dependent Stokes Flow Induced by Instantaneous Sources

O. O. Ajayi
Senior Lecturer.

A. Falade
Senior Lecturer.

Faculty of Engineering,
University of Lagos,
Lagos, Nigeria

Analytical solutions are provided for Stokes flow fields induced by an instantaneous thermal source located (i) in an infinite fluid and (ii) at the center of a solid spherical surface. In both cases it is assumed that the flow is driven by a body force that arises from buoyancy effects in the fluid due to the gradient of the source's temperature field. In accordance with Stokes approximation, convective acceleration terms are left out of the momentum equations but the local acceleration term is retained. The retention of the local acceleration term is crucial if all the salient features of the flow, especially in its early stages, are to be included in the solution for low Prandtl number. The evolution of the flow field in each of the two cases is demonstrated by plotting streamline patterns at various times. The influence of Prandtl number on flow field development is also discussed. Problem (i) is the fundamental one for this class of problems. From its solution, solutions to problems where the heat-generating rate is a general but known function of position and time to bounded and unbounded domains may be synthesised using well-known techniques. These results may be fruitfully applied to such practical problems as the motion of vessels in which nuclear wastes are stored, the fluid dynamics of weak point explosions, and the cooling of electrical and electronic equipments.

1 Introduction

Determination of the flow field induced by a heat-generating body inside the fluid surrounding the body is essential to the solution of many engineering problems. Some examples of such problems are (1) motion of vessels used for storage of nuclear wastes, (2) cooling of components of electrical equipments and, (3) the fluid dynamics of weak explosions. Providing the heat-generating rate is not excessive, the flow may be modeled as a Stokes flow field which is driven by the body force due to buoyancy effect of the temperature gradient created in the fluid by the heat-generating body. In other words, one may neglect the convective acceleration terms in the Navier-Stokes equation and adopt Boussinesq approximation to express the buoyancy force field in terms of the temperature field.

Recently, Krenk [1] investigated the development with time of the fluid motion induced when a heat-generating sphere is buried in a fluid of infinite extent. The approach adopted by Krenk is that of first determining the steady flow field outside a sphere due to a step-function spatial temperature variation and then integrating this field to obtain the field due to any spatial temperature variation. A more fundamental approach is to determine the time-dependent flow field generated by an instantaneous source of heat located at the center of the solid sphere. The flow field for other spherically symmetric heat source distributions where the rate of heat generation depends on time and spatial coordinates in a known manner can be determined by using well-known superposition techniques. For this reason we provide the analytical solution to the source-in-sphere problem. Following this approach, one needs to prescribe only the nature of the heat source and *not* the temperature field due to the source in order to calculate the resulting flow field.

In Krenk's treatment [1], the local acceleration term was left out of the momentum equations, even though the solution derived from these equations was later used to determine the flow field due to a time-dependent temperature field. As will be evident later, this quasisteady treatment involves, albeit tacitly, the assumption that the Prandtl number is high. This may be established by the following heuristic argument. It is implied in the quasistatic solution of Krenk that the velocity distribution corresponding to the spatial temperature distribution at a particular instant is set up simultaneously as the temperature distribution (which is the driving force of the flow field). This requires that the rate of momentum transfer, especially in the region close to the source where temperature varies rapidly, be much larger than the rate of heat transfer and hence that $\mathrm{Pr} \gg 1$.

In the recent past many investigations have been conducted into many other problems of buoyancy driven flows. Among these, we find the studies of (*i*) the steady two-dimensioal natural convection flow due to a horizontal line source (Zeldovich [2], Yih [3], Serruk [4], Crane [5], Spalding and Cruddace [6], Brodowicz and Kierkus [7], Forstrom and Sparrow [8], etc.); (*ii*) the three-dimensional temperature field above a concentrated heat source on a vertical adiabatic surface (Carey and Mollendorf [9]); (*iii*) the natural convection flows at small Grashoff number from cylinders and

Contributed by the Applied Mechanics Division for publication in the JOURNAL OF APPLIED MECHANICS.

Discussion on this paper should be addressed to the Editorial Department, ASME, United Engineering Center, 345 East 47th Street, New York, N.Y. 10017, and will be accepted until two months after final publication of the paper itself in the JOURNAL OF APPLIED MECHANICS. Manuscript received by ASME Applied Mechanics Division, January, 1984; final revision, August, 1984.

Copyright © 1985 by ASME
Downloaded 02 May 2010 to 171.66.16.54. Redistribution subject to ASME license or copyright; see http://www.asme.org/terms/Terms_Use.cfm

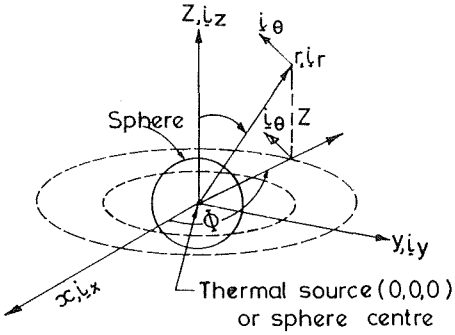

Fig. 1 Cartesian coordinates (x, y, z) and spherical polar coordinates (r, θ, ϕ) having a common origin at the location of the thermal source (or center fo the sphere in Case (*ii*)). The two system are related by the transformations $Z = r\cos$, $y = r\sin\theta\sin\phi$, $x = r\sin\theta\cos\theta$.

spheres (Mahoney [10]); and (*iv*) the convective flow within closed spheres and cyilnders (Kee et al. [11]lk) worthy of note, in the context of this paper.

Another result which is useful in its own right but which to our knowledge has not been given elsewhere is that of the time-dependent Stokes flow field due to an instantaneous thermal point source in an infinite fluid. The utility of this result, which indeed is the Green's function for this class of problems, derives from the fact that flow fields due to sources in the presence of solid boundaries can be synthesised from this result, using the method of images or some other well-known reflection techniques. For this reason, we consider it worthwhile to provide the solution to this problem.

In our analysis of the source-in-sphere problem, we assume that the sphere is neutrally buoyant in the fluid. Following Krenk, it is also assumed that the temperature field is not influenced by the flow field. It can be shown by a dimensional analysis that for the free convection problems under consideration here, this assumption would not lead to significant error if $\mathrm{Pr} \ll 1$. It can thus be seen that this assumption is not consistent with a quasistatic treatment of the flow field.

In Section 2, the two problems are formulated. Analytical solutions to these problems are provided in Section 3. In Section 4 streamline patterns of the flow fields at various times are presented. The influence of Prandtl number on the rate of flow development is also discussed in that section.

2 Formulation

(*A*) Source in an Unbounded Fluid. We consider an unbounded incompressible viscous fluid of density ρ and kinematic viscosity ν. In our solution method, we find it convenient to work in spherical polar coordinates (r, θ, ϕ) in which $\theta = 0$ and $\phi = 0$ are coincident with the z and x- axes, respectively, of the three-dimensional rectangular coordinates system (x, y,z) (see Fig. 1). At the origin O of the coordinate system, a certain quantity of heat is instantaneously released (through an explosion for instance) at time $t = 0$. Let the quantity of heat be ρcQ where c is the specific heat of fluid. We are interested in determining the temperature distribution within the fluid as well as the development of the induced fluid motion. The heat flow equation is

$$\frac{\partial T}{\partial t} = -\nabla.(T\mathbf{V}) + k\nabla^2 T + Q\delta(t)\delta(r). \tag{1}$$

Here T, $\mathbf{V}$, and k are the fluid temperature, velocity vector, and thermal diffusivity, respectively, t is time and r is the radius vector measured from the origin O, ∇ and ∇^2 are the gradient and Laplacian operators, respectively, $\delta(\mathbf{r})\delta(t)$ is the dimensional Dirac's delta function defined by $\int_0\int_v \delta(\mathbf{r})\delta(t)dVdt = 1$ where the volume v includes the source. Using continuity equation

$$\nabla.\mathbf{V} = 0, \tag{2}$$

equation (1) may be rewritten as

$$\frac{\partial T}{\partial t} = -\mathbf{V}.\nabla T + k\nabla^2 T + Q\delta(t)\delta(\mathbf{r}). \tag{3}$$

Equation (3) may be made dimensionless by defining dimensionless radius vector ($\tilde{\mathbf{R}}$), dimensionless time ($\tilde{t}$), temperature ($\tilde{T}$), and velocity vector ($\tilde{\mathbf{V}}$) as follows:

$$\begin{aligned} \mathbf{r} &= a_0\tilde{\mathbf{R}}, \\ t &= a_0^2\tilde{t}/k, \\ T &= \nu^2\tilde{T}/ca_0^3, \\ \mathbf{V} &= \nu\tilde{\mathbf{V}}/a_0, \end{aligned} \tag{4}$$

where a_0 is a characteristic length, which when no natural dimension of length exists may be chosen as $(\nu^2/g)^{1/3}$ or $(\beta Q)^{1/3}$. On substituting (4) into (1), we have

$$\frac{1}{\mathrm{Pr}}\frac{\partial\tilde{T}}{\partial\tilde{t}} = -\tilde{\mathbf{V}}.\tilde{\nabla}\tilde{T} + \frac{1}{\mathrm{Pr}}\tilde{\nabla}^2\tilde{T} + \delta(\tilde{\mathbf{R}})\delta(\tilde{t}), \tag{5}$$

where $\tilde{\nabla}$ is the dimensionless gradient operator and $\mathrm{Pr} = \nu/k$ = Prandtl number of fluid. If Pr is small, the convection term on the right-hand side of (5) may be neglected in favor of diffusion and heat source terms. It is assumed here that this is indeed the case. This assumption implies that the velocity field has no effect on the temperature field so that the dimensional heat flow equation now reduces to

$$\frac{\partial T}{\partial t} = k\nabla^2 T + Q\delta(\mathbf{r})\delta(t). \tag{6}$$

On account of the symmetry of the temperature problem, the temperature distribution is independent of θ and ϕ. Consequently the form of (6) which is most convenient to work with in the calculation of the temperature field is

$$\frac{\partial T}{\partial t} = \frac{k}{r^2}\frac{\partial}{\partial r}\left(r\frac{\partial T}{\partial r}\right) + Q\delta(t)\delta(\mathbf{r}). \tag{7}$$

Equation (7) is to be solved subject to the initial condition

$$T = 0 \quad \text{when} \quad t = 0. \tag{8}$$

For situations when T is not initially zero, (7) and (8) may still be used provided T is now interpreted as the temperature change in the fluid due to the instantaneous release of heat. The solution to (7) and (8) is well known, (see reference [12] for an equivalent solution). It is

$$T(r,t) = \frac{Q}{8(\pi kt)^{3/2}}e^{-r^2/4kt} \tag{9}$$

(*B*) The Flow Field. We adopt Boussinesq approximation and hold that the density of the fluid at temperature T is

$$\rho = \rho_0(1 - \beta T) \tag{10}$$

where ρ_0 is the density at $T = 0$ and β is the coefficient of volumetric thermal expansion. In other respects the fluid is considered incompressible so that the applicable form of the continuity equation is (2).

Neglecting convective acceleration terms (Stokes approximation) but retaining the buoyancy body force term we have as the momentum equation

$$\frac{\partial V}{\partial t} + \frac{1}{\rho}\nabla\tilde{p} = \nu\nabla^2\mathbf{V} + \beta gT\tilde{z}. \tag{11}$$

In (11) $\tilde{p}$ is pressure, g is the acceleration due to gravity, and $\tilde{z}$ is the unit vector in the positive z-direction. To eliminate $\tilde{p}$, we take the curl of (11) to obtain

$$\frac{\partial}{\partial t}\mathrm{Curl}\ \mathbf{V} = \beta g\nabla T\tilde{z} + \nu\nabla^2(\mathrm{Curl}\ \mathbf{V}). \tag{12}$$

Downloaded 02 May 2010 to 171.66.16.54. Redistribution subject to ASME license or copyright; see http://www.asme.org/terms/Terms_Use.cfm

Taking advantage of the axial symmetry of the velocity field, we may immediately satisfy (2) by defining a stream function ψ such that

$$\mathbf{V}=\left(\frac{1}{r^2}\frac{\partial\psi}{\partial\mu},\frac{1}{r\sin\theta}\frac{\partial\psi}{\partial r},0\right). \tag{13}$$

Here $\mu = \cos\theta$. Substituting (13) into (12) we obtain the scalar equation

$$\left\{E^2-\frac{1}{Pr}\frac{\partial}{\partial\tau}\right\}E^2\psi=\frac{\beta g}{\nu}r\frac{\partial T}{\partial r}\sin^2\theta \tag{14}$$

as the equation satisfied by ψ. In (14) $\tau = \nu\tau$ and E is the differential operator defined by

$$E^2=\frac{\partial^2}{\partial r^2}+\frac{1-\mu^2}{r^2}\frac{\partial^2}{\partial\mu^2}.$$

If T is replaced by the expression given in (9), we now have

$$D^2\left\{D^2-\frac{1}{\mathrm{Pr}}\frac{\partial}{\partial\tau}\right\}\psi=-\frac{\beta gQR^2e^{-R^2/4\tau}}{16\nu p\pi^{3/2}\tau^{5/2}}\sin\theta \tag{15}$$

where $R = r.p$, $p = (\mathrm{Pr})^{1/2}$ and the operator

$$D^2=\frac{\partial^2}{\partial R^2}+\frac{1-\mu^2\partial^2}{R^2\partial\mu^2}. \tag{16a}$$

Nondimensionalising (15) in terms of the dimensionless variables defined in (4) we have

$$\left(\tilde{E}^2-\frac{1}{\mathrm{Pr}}\frac{\partial}{\partial\tilde{t}}\right)\tilde{E}^2\tilde{\psi}=\frac{-\beta gQ\,\tilde{R}^2e^{-R^2/4\tilde{t}}}{16\nu^2\pi^{3/2}t^{5/2}}, \tag{16b}$$

where $\tilde{\psi}=\psi/\nu a_0$ and

$$E^2\equiv\frac{\partial^2}{\partial\tilde{R}^2}+\frac{(1-\mu^2)}{\tilde{R}^2}\frac{\partial^2}{\partial\mu^2}.$$

The quasistatic solution of Krenk corresponds to the case where $\mathrm{Pr}\gg 1$ so that the second term on the left-hand side of (16*b*) is negligible. Thus to apply this solution to the temperature field (9), which as we have shown, is only accurate for $\mathrm{Pr}\ll 1$ is inconsistent.

The boundary conditions to be satisfied by ψ are

(*i*) $\psi=0$ at $R=0$,
(*ii*) **V** remains finite as $R\to\infty$,
(*iii*) The order of singularity in ψ at the origin is minimum. (17)

(*C*) Point Source in Solid Sphere. In this case we suppose that the point source is enveloped by a solid sphere of radius a_0 whose center is coincident with the point source. For the sake of simplicity we assume that the thermal diffusivity of the sphere and that of the fluid are the same. In principle it is possible to solve (14) for a temperature distribution corresponding to the case of different thermal diffusivities. We however leave this case out of this paper partly because of the complexity of the analysis and partly because all the essential features of the flow would be revealed by the simpler solution in which equal values of diffusivity are assumed. Thus the temperature distribution is still given by (9). The equation of motion is still (15) but the boundary conditions (17) are now replaced by

(1) **V** = 0 on $r=a_0$,
(2) **V** is finite as $|r|\to\infty$. (18)

3 Solution

(*A*) Source in Infinite Fluid. To solve (15) first set

$$\left(D^2-\frac{1}{\mathrm{Pr}}\frac{\partial}{\partial\tau}\right)\psi(R,\mu,\tau)=\phi(R,\tau)(1-\mu^2). \tag{19}$$

Then substitute (19) in (15) and take the Laplace transform to get

$$\frac{d^2}{dR^2}\bar{\phi}(R,s)-\frac{2\bar{\phi}(R,s)}{R^2}=\lambda(i\alpha)^{3/2}R^{1/2}G_{3/2}(i\alpha R) \tag{20}$$

Here $\lambda=-\dfrac{\beta gQ}{8\nu p\pi^{3/2}}$,

$$\bar{\phi}=\int_0^\infty\phi(R,\tau)e^{-s\tau}d\tau,$$

$$\alpha=\sqrt{s},$$

$$G_m(x)=\frac{\pi}{2\sin}^{mx}\{J_{-m}(x)-(\cos m\pi-i\sin m\pi)J_m(x)\},$$

and $J_m(x)$ is the Bessel function of the first kind of order m. The complete solution of (20) is

$$\bar{\phi}(R,s)=\lambda\left\{(C(s)R^2+\frac{E(s)}{R}+\frac{R^{1/2}G_{3/2}(i\alpha R)}{(i\alpha)^{1/2}}\right\}$$

where $C(s)$ and $E(s)$ are functions of integration that depend only on s. If we write

$$\int_0^\infty\psi(R,\mu,\tau)e^{-s\tau}d\tau=(1-\mu^2)\bar{\chi}(R,s),$$

and set $\bar{\psi}(R,s)=R^{1/2}\bar{\chi}(R,s)$ we deduce from (19) that the equation satisfied by $\bar{\chi}$ is

$$\frac{d^2\bar{\chi}}{dR^2}+\frac{1}{R}\frac{d\bar{\chi}}{dR}+\left\{\frac{\alpha^2}{\mathrm{Pr}}-\frac{(3/2)^2}{R^2}\right\}\bar{\chi}=\frac{\bar{\phi}(R,s)}{R^{1/2}} \tag{21}$$

It is elementary to show that the complete solution of (21) is

$$\bar{\chi}(R,s)=J_{3/2}\left(\frac{\xi}{p}\right)\int_{a_1}^R x^{1/2}G_{3/2}\left(\frac{\eta}{p}\right)\bar{\phi}(x,s)\,dx$$

$$-G_{3/2}\left(\frac{\xi}{p}\right)\int_{a_2}^R x^{1/2}J_{3/2}\left(\frac{\eta}{p}\right)\bar{\phi}(x,s)\,dx \tag{22}$$

where a_1 and a_2 are constants of integration,

$$\xi=i\alpha R,\ \text{and}\ \eta=i\alpha x.$$

It can be readily verified that conditions (17) are satisfied if

$$C(s)=E(s)=a_1=0\quad\text{and}\quad a_2=\infty.$$

Whence

$$\bar{\chi}(R,s)=\frac{\lambda}{(i\alpha)^{1/2}}\left[G_{3/2}\left(\frac{\xi}{p}\right)\int_0^R x\,J_{3/2}\left(\frac{\eta}{p}\right)G_{3/2}(\eta)\,dx\right.$$

$$\left.-J_{3/2}\left(\frac{\xi}{p}\right)\int_\infty^R x\,G_{3/2}\left(\frac{\eta}{p}\right)G_{3/2}(\eta)\,dx\right]. \tag{23}$$

It is to be noted that while the velocity field derived from (23) dies out at infinity, it behaves like $1/R$ at the origin. On evaluating the integrals in (23), we have

$$\bar{\chi}(R,s)=\left(\frac{\pi}{2}\right)^{1/2}\frac{\lambda\mathrm{Pr}}{\mathrm{Pr}-1}\left[\frac{1}{s\sqrt{s}}\left\{e^{-R\sqrt{s}}-\frac{e^{-r\sqrt{s}/p}}{p}\right\}\right.$$

$$\left.+\frac{1}{Rs^2}\left\{e^{-r\sqrt{s}}-e^{-R\sqrt{s}/p}\right\}\right]. \tag{24}$$

After inverting (24) we obtain

$$\psi(R,\mu,\tau)=\left(\frac{\pi}{2}\right)^{1/2}\frac{\lambda p}{\mathrm{Pr}-1}\left[\left(\frac{\tau}{p}\right)^{1/2}\{p\,e^{-r^2\mathrm{Pr}/4\tau}-e^{-r^2/4\tau}\}\right.$$

$$+\frac{r}{2}\left\{erfc\left(\frac{r}{2\tau^{1/2}}\right)-\mathrm{Pr}\;erfc\left(\frac{rp}{2\tau^{1/2}}\right)\right\}$$

$$\left.+\frac{\tau}{r}\left\{erfc\left(\frac{rp}{2\tau^{1/2}}\right)-erfc\left(\frac{r}{2\tau^{1/2}}\right)\right\}\right]\sin^2\theta. \tag{25}$$

Downloaded 02 May 2010 to 171.66.16.54. Redistribution subject to ASME license or copyright; see http://www.asme.org/terms/Terms_Use.cfm

(B) Source at the Center of a Sphere. For this case, the solution of (21) which satisfies (18) is

$$\bar{\chi}(R,s) = J_{3/2}\left(\frac{\xi}{p}\right)\int_{\infty}^{R} x^{1/2} G_{3/2}\left(\frac{\eta}{p}\right)\tilde{\phi}(x,s)\,dx$$

$$- G_{3/2}\left(\frac{\xi}{p}\right)\int_{a_0}^{R} x^{1/2} J_{3/2}\left(\frac{\eta}{p}\right)\tilde{\phi}(x,s)\,dx, \tag{26}$$

where

$$\tilde{\phi}(x,s) = \lambda\left\{\frac{E(s)}{x} - x^{1/2}\frac{G_{3/2}(\eta)}{(i\alpha)^{1/2}}\right\}$$

and

$$\int_{a_0}^{\infty} x^{1/2} G_{3/2}\left(\frac{\eta}{p}\right)\tilde{\phi}(x,s)\,dx = 0. \tag{27}$$

From (27) it is determined that

$$E(s) = -\frac{(i\alpha a_0)^{1/2}}{s} p\left[\frac{i\alpha a_0}{p} G_{3/2}(i\alpha a_0) + \frac{i\pi \mathrm{pr}\, e^{-\alpha a_0}\dfrac{(p-1)}{p}}{2(p+1)G_{1/2}(i\alpha a_0/p)}\right].$$

This leads to

$$\bar{\psi}(R,s) = \bar{\psi}_{ps}(R,s) + \left(\frac{\pi}{2}\right)^{1/2}\lambda \mathrm{Pr}\left[\frac{e^{-a_0 s^{1/2}}}{Rs^2} - \frac{\mathrm{Pr}\, e^{-(a_0 - a_0/p + R/p)\sqrt{s}}}{R(\mathrm{Pr}-1)s^2} + \frac{e^{-R\sqrt{s}/p}}{R(\mathrm{Pr}-1)s^2} + \frac{a_0}{R(\mathrm{Pr}-1)}\frac{e^{-a_0 s^{1/2}}}{s\sqrt{s}} - \frac{p e^{-(a_0 - a_0/p + R/p)\sqrt{s}}}{(p^2-1)s\sqrt{s}} + \frac{e^{-R\sqrt{s}/p}}{p(\mathrm{Pr}-1)s\sqrt{s}}\right], \tag{28}$$

where $\bar{\psi}_{ps}(R, s)$ is the expression on the right-hand side of (24). The inversion of (28) is straight forward. It is

$$\psi(R,\tau) = \psi_{ps}(R,\tau) + \left(\frac{\pi}{2}\right)^{1/2}\lambda \mathrm{Pr}\left[\frac{1}{R}\left\{\left(\tau + \frac{a_0^2}{2}\right)erfc\left(\frac{a_0}{2\tau^{1/2}}\right) - a_0\left(\frac{\tau}{\pi}\right)^{1/2} e^{-a_0^2/4\tau}\right\} - \frac{\mathrm{Pr}}{R(\mathrm{Pr}-1)}\left\{\left(\tau + 1/2(a_0 - a_0/p + R/p)^2 erfc\left(\frac{a_0 - a_0/p + R/p}{2\tau^{1/2}}\right) - (a_0 - a_0/p + R/P)\left(\frac{\tau}{\pi}\right)^{1/2} e^{-(a_0 - a_0/p + R/p)^2/4\tau}\right\} + \frac{1}{R(\mathrm{Pr}-1)}\left\{\left(\tau + \frac{R^2}{2\mathrm{Pr}}\right)erfc\left(\frac{R}{2p\tau^{1/2}}\right) - \frac{R}{p}\left(\frac{\tau}{\pi}\right)^{1/2}\cdot \cdot e^{-r^2/(4\mathrm{Pr}\tau)}\right\} + \frac{a_0}{(p+1)}\left\{2\left(\frac{\tau}{\pi}\right)^{1/2} e^{-a_0^2/4\tau} - a_0 erfc\left(\frac{a_0}{2\tau^{1/2}}\right)\right\} - \frac{p}{(\mathrm{Pr}-1)}\left\{2\left(\frac{\tau}{\pi}\right)^{1/2} e - (a_0 - a_0/p + R/p)^2 4\tau - (a_0 - a_0/p + R/p)\, x\, erfc\left(\frac{a_0 - a_0/p + R/p}{2\tau^{1/2}}\right)\right\} + \frac{1}{p(\mathrm{Pr}-1)}\left\{2\left(\frac{\tau}{\pi}\right)^{1/2} e^{-R^2/4\tau\mathrm{Pr}} - \frac{R}{p} erfc\left(\frac{R}{2p\tau^{1/2}}\right)\right\}\right]. \tag{29}$$

In (29) $\psi_{ps}(R, \tau)$ is $\psi(R, \mu, \tau)$ of (25) divided by $\sin^2\theta$.

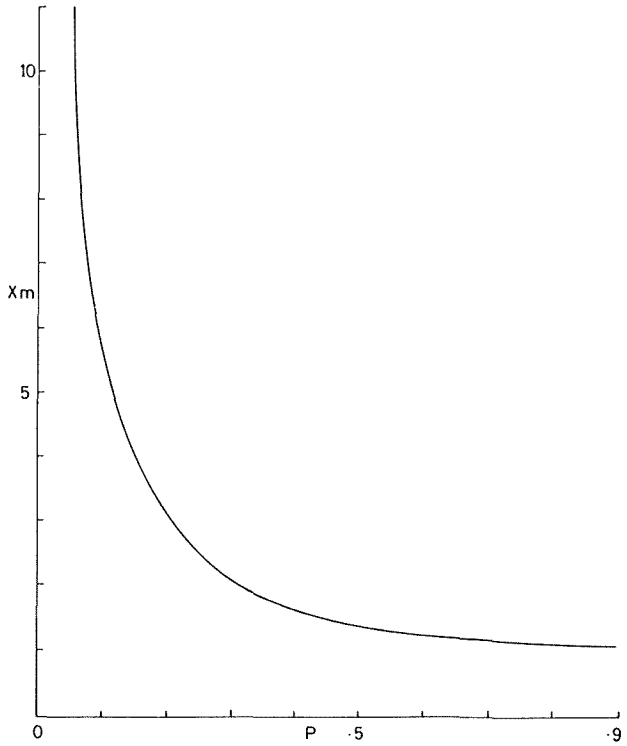

Fig. 2 Values of spatial positions x_m, of the stagnation points for various values of $p = (\mathrm{Pr})^{1/2}$ where Pr is the Prandtl number and x_m is a dimensionless quantity

4 Discussion

(A) Point Source in an Infinite Fluid. It is evident from (25) that the stream function ψ does not depend on r and t individually but through the single dimensionless variable

$$x = (\nu t)^{1/2}/R = \frac{(kt)^{1/2}}{r}$$

In terms of this similarity variable the alternative representation for this stream function is

$$\psi = \frac{\left(\frac{\pi}{2}\right)^{1/2}\lambda p^2 R}{P^2 - 1}\left[(x^2 - 1/2)erfc\left(\frac{1}{2x}\right) - \left(x^2 - \frac{1}{2p^2}\right)erfc\left(\frac{1}{2px}\right) + \frac{x}{\pi^{1/2}} e^{-1/(4x^2)} - \frac{x}{p\pi^{1/2}} - e^{-1/(4p^2x^2)}\right](1-\mu^2). \tag{30}$$

Our computations reveal that ψ attains its maximum value at some point (x_m, μ_m). It is clear from equation (30) that $\mu_m = 0$ and that $x_m d$ depends on the Prandtl number (p^2). The

Downloaded 02 May 2010 to 171.66.16.54. Redistribution subject to ASME license or copyright; see http://www.asme.org/terms/Terms_Use.cfm

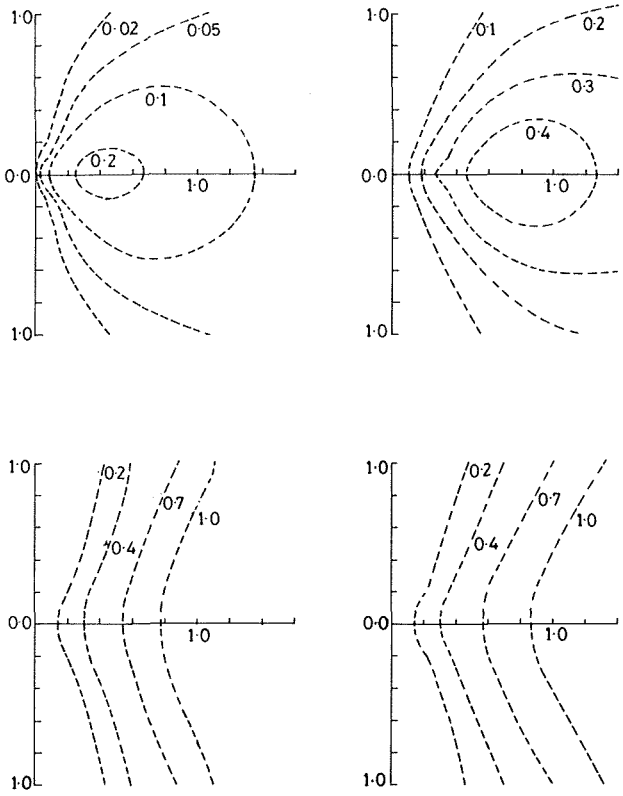

Fig. 3(*a*) (*i*) $\tau = 0.049$, (*ii*) $\tau = 0.196$, (*iii*) $\tau = 3.92$, and (*iv*) $\tau = 19.6$

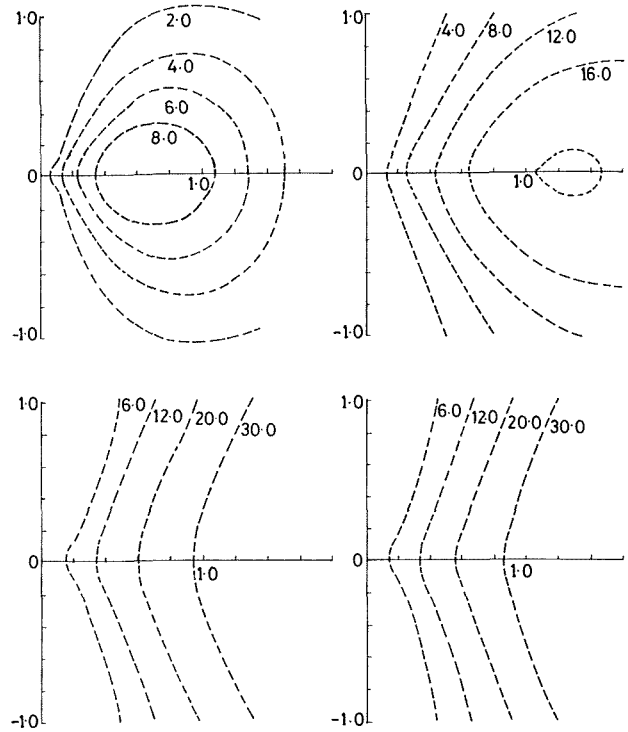

Fig. 3(*b*) (*i*) $\tau = 0.259$ and (*ii*) $\tau = 103.68$ 1.870 (*iii*) $\tau = 20.74$ (*iv*) $\tau = 103.7$

Fig. 3 Streamline patterns of the flow field induced by a point source in a fluid of infinite extent for various values of $\tau = \nu t$. The numbers on the curves are the values of $10^4 \psi$.

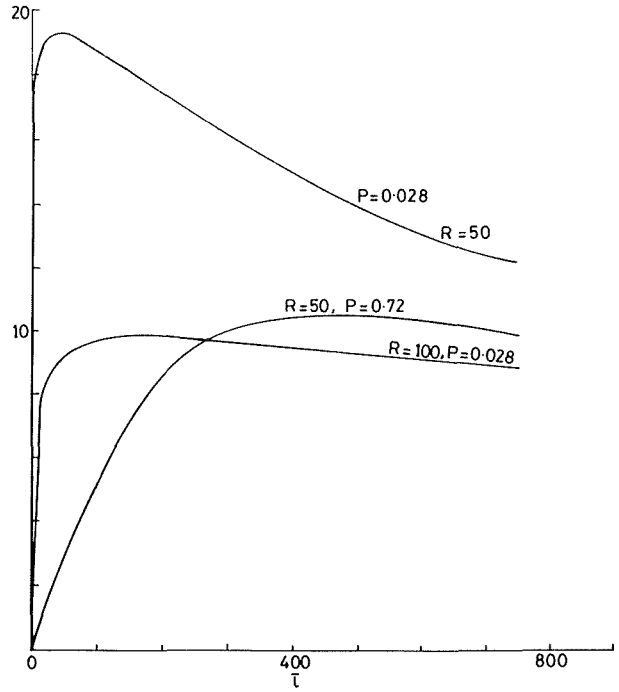

Fig. 4 The magnitude of the fluid velocity at some selected points plotted against variable $\tau = \nu t$

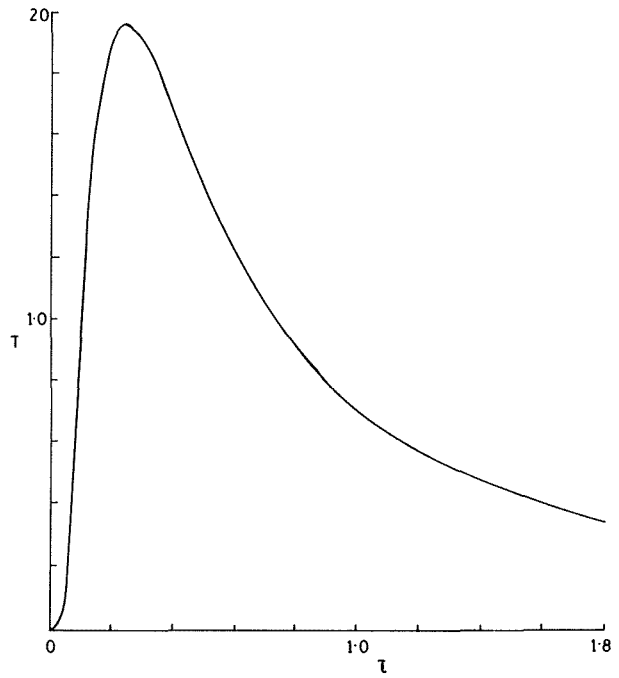

Fig. 5 The variation of temperature *T* with variable τ, where $\tau = \nu t$, for the case Pr = 0.028 and at the point whose distance, R, from the origin is 50 units

variation of x_m with p is shown in Fig. 2 from which it is deducible that, at any given time, the position of the stagnation points ($x = x_m$, $\mu = 0$) moves farther away from the source as p increases. As shown in Figs. 3(*a*) and (*b*), the stagnation points recede to infinity as τ increases for any given value of p. The speed of recession of the stagnation points is $\nu 1/2/(2x_m t^{1/2})$ along the $\mu = 0$ axis. From this and from Fig. 2 it can be deduced that the larger the value of p, the faster the stagnation point recedes to infinity. Taking the speed of stagnation point as an index of the rate of evolution of the flow field in response to the changes in the temperature field, we are led by this result to the conclusion that the flow field

Downloaded 02 May 2010 to 171.66.16.54. Redistribution subject to ASME license or copyright; see http://www.asme.org/terms/Terms_Use.cfm

could only be set up instantaneously if the Prandtl number is infinite. Whence the quasisteady treatment of Krenk [1] is once again shown to be valid only for $\Pr \gg 1$.

The flow patterns for $\Pr = 0.028$ and $\Pr = 0.72$ are each plotted for four different values of τ in Figs. 3(*a*) and (*b*), respectively. In the initial stages of flow development the flow pattern is in the form of closed loops. Indeed this closed loop structure may be derived from (30). It may be shown that for values of τ and R satisfying the conditions $R \gg \tau$, (30) has the asymptotic form

$$\psi = \frac{A \sin^2 \theta}{R}$$

where A is a constant. In other words the flow pattern has a dipole structure in the neighborhood of $R = 0$ during the period immediately following the release of the source's energy. It is readily observable from Figs. 3(*a*) and (*b*) that for larger values of τ the geometry of the closed loops are considerably different from those corresponding to smaller times, although the asymmetry of the streamlines about $\mu = 0$ line is preserved at all times.

(*B*) Point Source-In-Sphere Problem. The variation of velocity with time for three combinations of R and Pr namely ($R = 50$, $\Pr = 0.720$); ($R = 50$, $\Pr = 0.028$); and ($R = 100$, $\Pr = 0.028$) have been calculated from equation (29). The results are plotted in Fig. 4. The velocities at these large distances from the sphere are of significance in that they approximate the velocities with which the heat-generating sphere would move in a quiescent fluid medium if the sphere were unconstrained. Figure 4 reveals that, for the three combinations of R and Pr plotted, the velocity increases very rapidly from zero at $\tau = 0$ to a maximum value of V_m at $\tau = \tau_0$. Thereafter the velocities decrease at an ever decreasing rate to zero (at $\tau = \infty$). The values V_m and τ_0 increases with both R and Pr. It is also to be noted that (29) can be rearranged in such a form as to explicitly show the exclusive dependence of the flow field on two similarity variables, $R/(2p\tau^{1/2})$ and $a_0/(2p\tau)^{1/2}$ as well as on the parameter p (or Pr). The second similarity variable is a consequence of the introduction of the sphere radius into the problem as a natural dimension of length.

In Fig. 5 is plotted the variation of temperature T at $R = 50$ with time parameter τ for $\Pr = 0.028$. This curve is of the same general shape as the curves in Fig. 4. However, as expected, the attainment of maximum temperature is achieved much more rapidly than that of velocity at the same location.

The patterns of the flow generated by the point source at the center of a sphere submerged in a fluid of same thermal properties are plotted in Figs. 6(*a-c*). These figures correspond to $\tau = 0.00098$, 0.00392, and 0.392, respectively. For larger times ($\tau = 0.00392$, $\tau = 0.392$) there is qualitative agreement between our results and those of Krenk [1]. However Fig. 6(*a*) reveals that at the very early stages of the

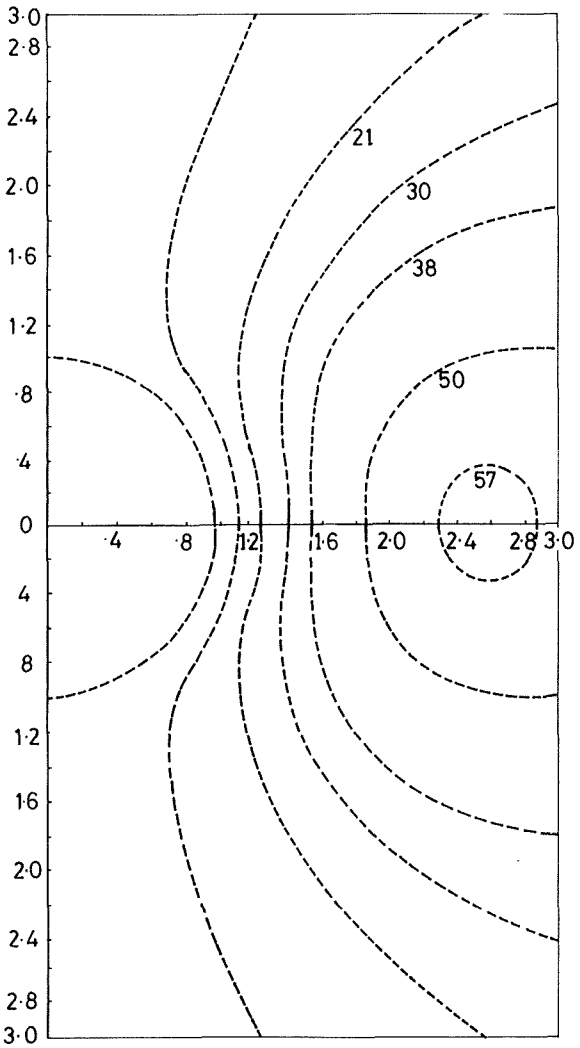

Fig. 6(*a*) $\tau = 0.00098$

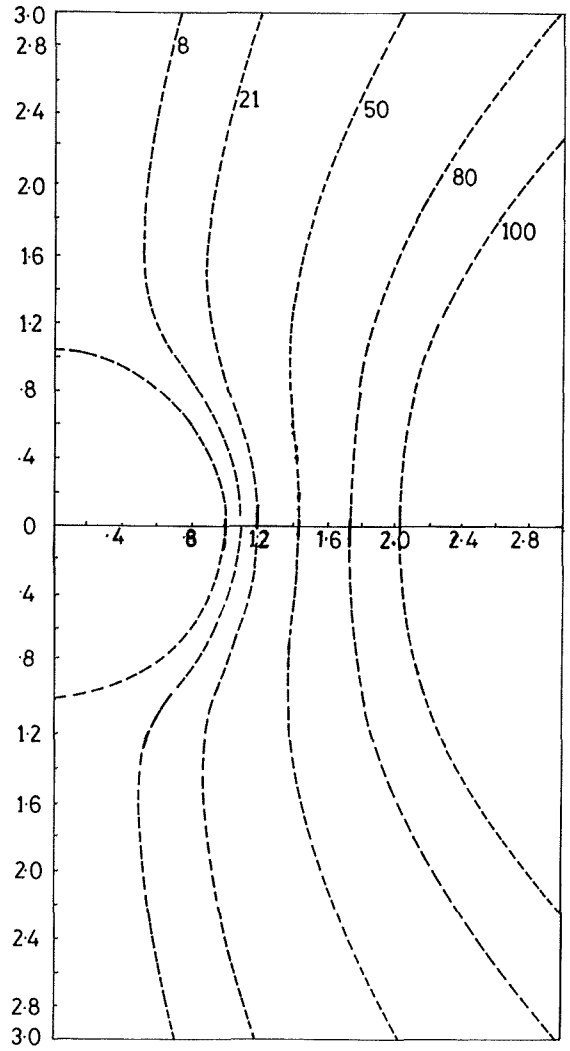

Fig. 6(*b*) $\tau = 0.00398$

Downloaded 02 May 2010 to 171.66.16.54. Redistribution subject to ASME license or copyright; see http://www.asme.org/terms/Terms_Use.cfm

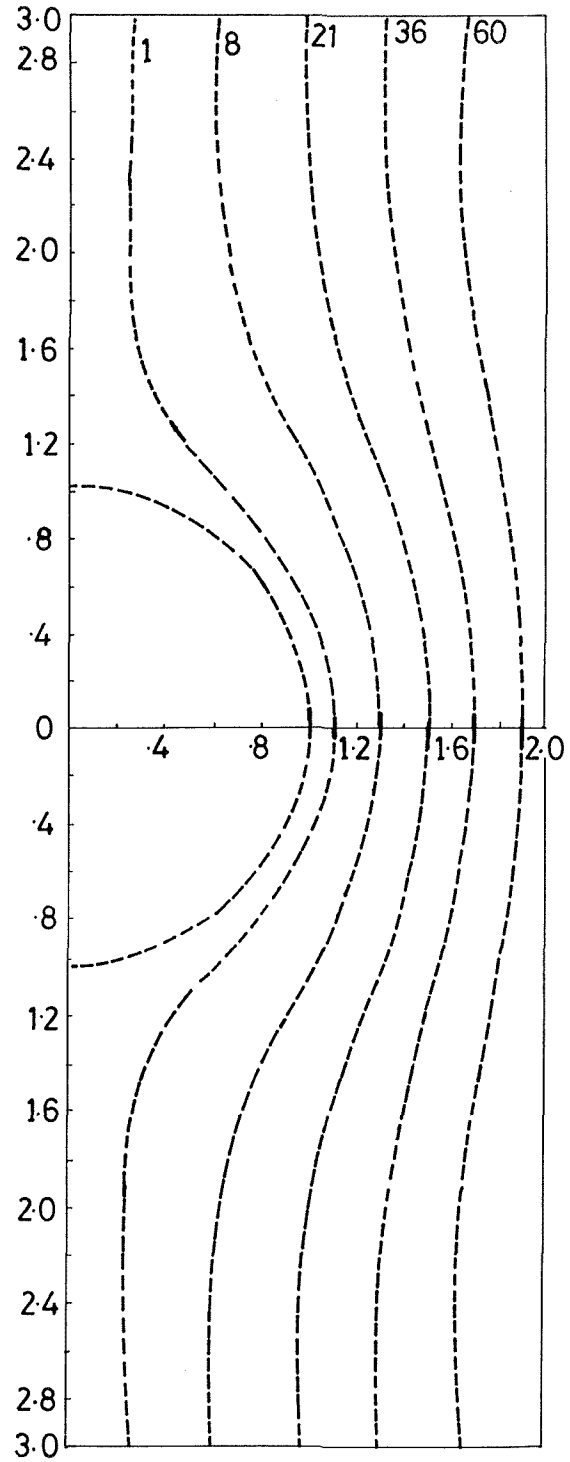

Fig. 6(c) $\tau = 0.392$

Fig. 6 Streamline patterns of the flow field set up for the point source-in-sphere problem for various values of $\tau = \nu t$. The numbers on the curve are values of $10^4 \psi$

flow closed streamlines appear in the flow. As in the point source-in-infinite-fluid case, these closed streamlines are symmetrical about the $\theta = \pm \pi/2$ axis and enclose the stagnation points (points of maximum ψ). It can be readily shown from (29) that the distance of the stagnation point from the sphere center increases as τ increases.

5 Conclusions

The solutions presented in the preceding sections are valid for small values of the Prandtl number. For moderate and large values of Pr, it would no longer be justifiable to neglect the influence of the velocity field on the temperature field. In that situation, the energy and momentum equations ((3) and (11)) are coupled and the temperature field is no longer spherically symmetric. For the case $\mathrm{Pr} \gg 1.0$ some simplification in the analysis may be achieved by treating the velocity field as a quasistatic Stokes flow in the manner of Krenk [1]. It would however not be justifiable under this circumstance to ignore interaction between velocity and temperature fields.

The results of our calculations confirm the expectation that the rate of development of the flow generated by an instantaneous point source of heat in an incompressible viscous fluid of infinite extent would increase as the Prandtl number increases. In the early stages of the flow, the streamlines are in the form of closed loops. These closed loop structures would not be present if the local acceleration term is ignored (i.e. if $\mathrm{Pr} \gg 1$) as revealed by Krenk's result.

References

1 Krenk, S., "Creeping Viscous Flow Around A Heat-Generating Solid Sphere," ASME JOURNAL OF APPLIED MECHANICS, Vol. 48, No. 2, 1981, pp. 239-242.

2 Zeldovich, Y. B., "Limiting Laws of Rising Convection Currents," *Zh. Eksp Teor. Fiz.*, Vol. 7, No. 12, 1937, pp. 1463-1465.

3 Yih, C. S., "Convection Due to a Point Source of Heat," *Proc. First U.S. Nat. Congress on Appl. Mech.*, 1952, pp. 941-947.

4 Serruk, L. G., "Laminar Convection Over a Heated Wire," *J. Appl. Math. Mech.*, Vol. 22, 1958, pp. 807-812.

5 Crane, L. J., "Thermal Convection From a Horizontal Wire," *Z. Angew Math. Phys.*, Vol. 10, 1959, pp. 453-460.

6 Spalding, D. B., and Cruddace, R. G., "Theory of Steady Laminar Flow Above a Line Heat Source in a Fluid of Large Pr and Temperature-Dependent Viscosity," *Int. J. Heat Mass Transfer*, Vol. 3, 1961, pp. 55-59.

7 Brodowicz, K., and Kierkus, W. T., "Experimental Investigation of Laminar Free Convection Flow in Air Above a Horizontal Wire with Constant Heat Flux," *Int. J. Heat Mass Transfer*, Vol. 9, 1966, pp. 81-94.

8 Forstrom, R. J., and Sparrow, E. M., "Experiments on the Bouyant Plume Above a Heated Horizontal Wire," *Int. J. Heat Mass Transfer*, Vol. 10, 1967, pp. 321-331.

9 Carey, V. P., and Mollendorf, J. C., "The Temperature Field Above a Concentrated Heat Source on a Vertical Adiabatic Surface," *Int. J. Heat Mass Transfer*, Vol. 20, 1977, pp. 1059-1067.

10 Mahoney, J. J., "Heat Transfer at Small Grashoff Number," *Proc. Roy. Soc. Lond.*, Series *A*, Vol. 238, 1956, pp. 412-423.

11 Kee, R. J., Landram, C. S., and Miles, J. C., "Steady Flow Field Due to Constant Internally Distributed Steady Heat Sources," ASME *Journal of Heat Transfer*, Vol. 98, 1976, pp. 55-61.

12 Carslaw, H. S., and Haeger, J. C., *Conduction of Heat in Solids*, Clarendon Press, Oxford, 1959.

Downloaded 02 May 2010 to 171.66.16.54. Redistribution subject to ASME license or copyright; see http://www.asme.org/terms/Terms_Use.cfm

Journal of Applied Mechanics

Design Data and Methods

Axisymmetric Postbuckling of Orthotropic Tapered Thick Annular Plates

P. C. Dumir[1]

The postbuckling parameters of clamped and simply supported tapered thick annular plates with free hole are presented for several values of annular ratio, thickness-to-radius ratio, orthotropic parameter, and taper ratio.

Some investigators have dealt with the axisymmetric postbuckling of orthotropic thin annular plates [1-5] and isotropic thick circular plates [6] of uniform thickness. Here the geometrically nonlinear postbuckling parameters are presented for polar orthotropic thick annular plates with free hole and linear variation of thickness, subjected to inplane radial load at the outer edge.

Assuming shear deformations in the sense of Mindlin's theory and including geometric nonlinearity in the sense of Von Karman, the compatibility and equilibrium equations can be expressed in the following dimensionless form:

$$(\rho+\xi)^2\psi'' + (\rho+\xi)\psi' - \beta\psi - (\rho+\xi)\frac{h'}{h}$$

$$[(\rho+\xi)\psi' - \nu_\theta\psi] + 6(\beta-\nu_\theta^2)(\rho+\xi)\frac{h}{h_0}w'^2 = 0 \quad (1)$$

$$(\rho+\xi)^2\phi'' + (\rho+\xi)[1+3(\rho+\xi)\frac{h'}{h}]\phi'$$

$$-\left[\beta - 3\nu_\theta(\rho+\xi)\frac{h'}{h} + \frac{12(\beta-\nu_\theta^2)}{\beta\eta^2}k^2\Gamma(\rho+\xi)^2\right]\phi$$

$$-\frac{12(\beta-\nu_\theta^2)}{\beta\eta^2}k^2\Gamma(\rho+\xi)^2w' = 0 \quad (2)$$

$$\frac{12(\beta-\nu_\theta^2)}{\beta\eta^2}k^2\Gamma(\rho+\xi)[\phi+(1+\xi)w'] + \psi w' = 0 \quad (3)$$

where

$$(\,)' = \frac{\partial(\,)}{\partial\rho}, \quad \rho = \frac{r-b}{a-b}, \quad \xi = \frac{b}{(a-b)}, \quad \eta = \frac{h_0}{a}$$

$$\beta = \frac{E_\theta}{E_r} = \frac{\nu_\theta}{\nu_r}, \quad \Gamma = \frac{G_{rz}}{E_r}, \quad D_0 = \frac{E_\theta h_0^3}{12(\beta-\nu_\theta^2)}, \quad k^2 = \frac{5}{6}$$

$$w = \frac{w^*}{h_0}, \quad \phi = \frac{a}{h_0}\phi^*, \quad \psi = \frac{(a-b)}{D_0}\psi^*, \quad (4)$$

$$\frac{h}{h_0} = 1+\alpha\rho \ (\alpha\geq 0); \quad \frac{h}{h_0} = \frac{(1+\alpha\rho)}{(1+\alpha)} \ (\alpha<0) \quad (5)$$

The inner and outer radii of the annulus are b and a, and h_0 is the minimum thickness. The transverse displacement, shear rotation, and stress function are w^*, ϕ^* and ψ^*, respectively. The boundary conditions are:

$$\rho=0: \quad \phi' + \nu_\theta\phi/\xi = 0, \quad \psi = 0$$

$$\rho=1: \quad w=0, \quad \psi = \frac{12(\beta-\nu_\theta^2)}{(1+\xi)}\frac{E_r}{E_\theta}\bar{N} \quad (6)$$

$\phi=0$ (clamped) or $\phi' + \nu_\theta\phi/(1+\xi) = 0$ (simply supported)

where

$$\bar{N} = \frac{a^2}{h_0^3}\cdot\frac{N_r(1)}{E_r} \quad (7)$$

is the dimensionless edge load.

The equations are discretized by using an orthogonal point collocation method with the N collocation points located at the zeros of Nth degree Legendre polynomials. Since there are $3N$ collocation equations and five boundary conditions, the variables ψ, w, and ϕ are approximated as:

$$\psi = \sum_{m=1}^{N+2}\rho^{m-1}a_m, \quad w = \sum_{m=1}^{N+1}\rho^{m-1}b_m, \quad \phi = \sum_{m=1}^{N+2}\rho^{m-1}c_m \quad (8)$$

The buckling load is obtained by solving the linear eigenvalue problem associated with (1)-(3) with $w' \equiv 0$ in (1). The method of solution for the postbuckling response is similar to the one employed by Dumir et al. [7]. The central deflection is incremented in steps of $\Delta w(0) = 0.1$ and the equations (1)-(3) and (6) are solved iteratively for $\bar{N}$. The nonlinear terms are linearized at step J as

$$(w'\psi)_J = w'_{J_p}\psi_J, \quad (w')^2_J = w'_{J_p}w'_J \quad (9)$$

[1]Assistant Professor, Department of Applied Mechanics, Indian Institute of Technology, Delhi, India 110016.

Manuscript received by ASME Applied Mechanics Division, August, 1984; final revision, January, 1985.

Copyright © 1985 by ASME

Downloaded 02 May 2010 to 171.66.16.54. Redistribution subject to ASME license or copyright; see http://www.asme.org/terms/Terms_Use.cfm

Table 1 Comparison of postbuckling results for orthotropic uniform thin annulus with free hole ($b/a = 0.4$, $\beta = 5$, $\nu_\theta = 1/3$, $\Gamma = 0.375$)

$w(0)$	$-\bar{N}$			
	Simply Supported		Clamped	
	Huang [4] (thin plate)	Present ($\eta = 0.002$)	Huang [4] (thin plate)	Present ($\eta = 0.002$)
0.0	1.2550	1.2549	4.0824	4.0822
0.6	1.3970	1.3972	4.4487	4.4491
1.2	1.8118	1.8119	5.4879	5.4881
1.8	2.4814	2.4815	7.0870	7.0885
2.4	3.4020	3.4024	9.1739	9.1765

Table 2 Comparison of postbuckling parameters for isotropic thick plate of uniform thickness [$\beta = 1$, $\nu_\theta = 0.3$, $\Gamma = 0.5/(1+\nu_\theta)$]

	η	$-\bar{N}_0$		$10C_1$		-10^3C_2	
		Present	Raju and Rao [6]	Present	Raju and Rao [6]	Present	Raju and Rao [6]
Clamped	0.001	1.34449	1.34455	2.0277	2.028	5.795	5.836
	0.200	1.15131	1.15133	2.3635	2.364	11.508	11.529
Simply	0.001	0.38441	0.38441	2.7015	2.702	4.656	4.647
Supported	0.200	0.36682	0.36681	2.8298	2.830	7.183	7.205

Table 3 Buckling and postbuckling parameters for clamped plates

		$b/a = 0.3$				$b/a = 0.4$			$b/a = 0.5$		
β	α	η	$-\bar{N}_0$	$10C_1$	-10^3C_2	$-\bar{N}_0$	$10C_1$	-10^3C_2	$-\bar{N}_0$	$10C_1$	10^3C_2
1	−0.2	0.001	1.7324	1.556	3.084	2.0652	1.240	1.510	2.7603	0.870	0.574
		0.10	1.6688	1.595	3.715	1.9825	1.272	1.993	2.6249	0.896	0.862
		0.15	1.5951	1.645	4.695	1.8874	1.311	2.655	2.4715	0.927	1.270
	0.0	0.001	1.3644	1.998	4.830	1.6904	1.507	2.236	2.3383	1.012	0.821
		0.10	1.3222	2.044	5.786	1.6316	1.543	2.825	2.2356	1.040	1.151
		0.15	1.2728	2.102	7.042	1.5631	1.588	3.617	2.1180	1.076	1.615
	0.2	0.001	1.9879	1.665	3.476	2.5373	1.203	1.449	3.5977	0.782	0.493
		0.10	1.9104	1.715	4.226	2.4235	1.242	1.945	3.3906	0.813	0.759
		0.15	1.8213	1.779	5.372	2.2939	1.291	2.620	3.1602	0.851	1.141
3	−0.2	0.001	3.4932	1.812	5.218	3.6086	1.851	4.983	4.0724	1.651	3.061
		0.10	3.2640	1.890	6.866	3.3770	1.920	6.747	3.7943	1.712	4.564
		0.15	3.0140	1.986	9.147	3.1227	2.002	9.155	3.4906	1.785	6.688
	0.0	0.001	2.7035	2.459	9.794	2.8236	2.432	8.370	3.2815	2.059	4.698
		0.10	2.5605	2.544	12.101	2.6753	2.509	10.700	3.0921	2.128	6.545
		0.15	2.4003	2.649	15.200	2.5087	2.602	13.821	2.8812	2.211	9.107
	0.2	0.001	3.8636	2.154	8.134	4.0897	2.061	6.171	4.8735	1.672	3.130
		0.10	3.6177	2.246	10.470	3.8273	2.144	8.332	4.5215	1.746	4.726
		0.15	3.3487	2.358	13.631	3.5395	2.244	11.320	4.1408	1.836	7.009
10	−0.2	0.001	8.9585	1.776	2.450	9.1098	1.785	3.455	9.2727	1.912	5.539
		0.10	7.7287	1.953	5.971	7.8572	1.944	6.711	8.0124	2.043	9.278
		0.15	6.5600	2.154	12.201	6.6638	2.131	12.814	6.8016	2.194	15.543
	0.0	0.001	7.3926	2.188	3.900	7.3232	2.307	6.656	7.3225	2.533	10.101
		0.10	6.5405	2.359	7.824	6.4978	2.456	10.560	6.5159	2.662	15.004
		0.15	5.6936	2.558	14.722	5.6710	2.632	17.090	5.7008	2.810	22.360
	0.2	0.001	11.0660	1.787	3.275	10.7432	1.962	6.050	10.6370	2.176	8.277
		0.10	9.5242	1.947	6.628	9.3405	2.100	9.726	9.2483	2.302	13.080
		0.15	8.0625	2.132	12.990	7.9215	2.260	15.972	7.9000	2.445	20.462

where the predicted term w'_{j_p} is taken as the mean of its value at the two preceding iterations. For the first iteration, w'_{j_p} is extrapolated quadratically from its value at three preceding steps.

The postbuckling response so obtained to $w(0) = 1$ is approximated by a least squares fit with the expression:

$$\frac{\bar{N}}{\bar{N}_0} = 1 + C_1[w(0)]^2 + C_2[w(0)]^4 \tag{10}$$

where $\bar{N}$ is the edge load for $w(0)$ and $\bar{N}_0$ is the buckling load. As a check on the accuracy of the method, the results for an orthotropic thick annulus with $\eta = 0.002$ are compared with the thin-plate results of Huang [4] in Table 1. The postbuckling parameters for an isotropic uniform thick plate are compared with the finite element results of Raju and Rao [6] in Table 2. A close agreement among the results can be noted. Seven collocation points have yielded accurate results.

Postbuckling parameters $\bar{N}_0$, C_1, C_2 are presented in Tables 3 and 4 for clamped and simply supported plates. The larger Poisson's ratio and G_{rz}/E_{min} have been taken as 0.25 and 0.4, respectively. It is observed that the buckling load increases with the degree of orthotropicity and decreases with the thickness-to-radius ratio. The effect of η is more pronounced for the orthotropic plates due to the smaller value of transverse shear modulus compared to the inplane Young's moduli. The effect of η is much smaller for the simply supported plates as compared to the clamped ones.

References

1 Uthgenant, E. B., and Brand, R. S., "Buckling of Orthotropic Annular Plates," *AIAA Journal*, Vol. 8, No. 11, 1970, pp. 2102-2104.

2 Uthgenant, E. B., and Brand, R. S., "Postbuckling of Orthotropic Annular Plates," ASME JOURNAL OF APPLIED MECHANICS, Vol. 40, 1973, pp. 559-564.

3 Huang, C. L., "Postbuckling of an Annulus," *AIAA Journal*, Vol. 11, No. 12, 1973, pp. 1608-1612.

4 Huang, C. L., "On Postbuckling of Orthotropic Annular Plates," *International Journal of Nonlinear Mechanics*, Vol. 10, 1975, pp. 63-74.

5 Reddy, B. S., and Alwar, R. S., "Postbuckling Analysis of Orthotropic Annular Plates," *Acta Mechanica*, Vol. 39, 1981, pp. 289-296.

Downloaded 02 May 2010 to 171.66.16.54. Redistribution subject to ASME license or copyright; see http://www.asme.org/terms/Terms_Use.cfm

Table 4 Buckling and postbuckling parameters for simply supported plates

		$b/a = 0.3$				$b/a = 0.4$			$b/a = 0.5$		
β	α	η	$-\bar{N}_0$	$10C_1$	-10^3C_2	$-\bar{N}_0$	$10C_1$	-10^3C_2	$-\bar{N}_0$	$10C_1$	-10^3C_2
1	−0.2	0.001	0.4057	2.746	5.689	0.3635	3.093	4.771	0.3287	3.357	3.283
		0.10	0.4016	2.768	6.392	0.3603	3.111	5.496	0.3263	3.372	3.989
		0.15	0.3965	2.794	7.283	0.3564	3.134	6.414	0.3232	3.391	4.881
	0.0	0.001	0.2758	3.913	9.452	0.2475	4.314	7.505	0.2254	4.591	4.987
		0.10	0.2738	3.937	10.393	0.2460	4.334	8.446	0.2242	4.608	5.882
		0.15	0.2713	3.967	11.590	0.2441	4.359	9.632	0.2227	4.629	7.009
	0.2	0.001	0.3607	3.491	6.713	0.3256	3.774	4.986	0.2990	3.945	3.141
		0.10	0.3577	3.516	7.563	0.3233	3.796	5.798	0.2971	3.968	3.886
		0.15	0.3540	3.548	8.641	0.3204	3.823	6.824	0.2949	3.991	4.829
3	−0.2	0.001	1.0795	2.346	3.870	1.0352	2.619	5.791	0.9700	2.973	6.195
		0.10	1.0515	2.395	4.970	1.0103	2.662	7.126	0.9490	3.012	7.782
		0.15	1.0184	2.455	6.422	0.9807	2.716	8.857	0.9238	3.060	9.821
	0.0	0.001	0.7915	3.190	6.624	0.7407	3.614	9.562	0.6845	4.075	9.624
		0.10	0.7760	3.241	8.084	0.7275	3.661	11.330	0.6736	4.118	11.670
		0.15	0.7574	3.303	9.974	0.7116	3.718	13.600	0.6604	4.170	14.281
	0.2	0.001	1.0916	2.763	5.151	1.0065	3.148	6.958	0.9243	3.515	6.480
		0.10	1.0667	2.816	6.485	0.9858	3.197	8.563	0.9073	3.561	8.263
		0.15	1.0370	2.881	8.239	0.9611	3.258	10.641	0.8870	3.617	10.551
10	−0.2	0.001	2.9092	2.385	0.924	2.9713	2.337	1.345	2.9925	2.425	3.303
		0.10	2.7247	2.509	3.539	2.7803	2.457	3.908	2.8019	2.535	6.072
		0.15	2.5231	2.661	7.420	2.5717	2.605	7.691	2.5934	2.670	10.060
	0.0	0.001	2.3728	2.857	0.621	2.3491	2.807	1.691	2.2811	3.161	5.383
		0.10	2.2481	2.980	3.568	2.2274	3.026	4.694	2.1678	3.171	8.822
		0.15	2.1085	3.130	7.804	2.0910	3.171	8.964	2.0401	3.406	13.581
	0.2	0.001	3.5448	2.249	0.221	3.4284	2.358	1.261	3.2445	2.650	4.185
		0.10	3.3149	2.370	2.586	3.2139	2.474	3.754	3.0540	2.760	7.201
		0.15	3.0644	2.517	6.104	2.9790	2.617	7.392	2.8494	2.894	11.440

6 Raju, K. K., and Rao, G. V., "Postbuckling Analysis of Moderately Thick Elastic Circular Plates," ASME JOURNAL OF APPLIED MECHANICS, Vol. 50, 1983, pp. 468-70.

7 Dumir, P. C., Nath, Y., and Gandhi, M. L., "Nonlinear Axisymmetric Static Analysis of Orthotropic Thin Annular Plates," *International Journal of Nonlinear Mechanics*, Vol. 19, No. 3, 1984, pp. 255-72.

Downloaded 02 May 2010 to 171.66.16.54. Redistribution subject to ASME license or copyright; see http://www.asme.org/terms/Terms_Use.cfm

Journal of Applied Mechanics

Brief Notes

A Brief Note is a short paper that presents a specific solution of technical interest in mechanics but which does not necessarily contain new general methods or results. A Brief Note should not exceed 1500 words *or equivalent* (a typical one-column figure or table is equivalent to 250 words; a one line equation to 30 words). Brief Notes will be subject to the usual review procedures prior to publication. After approval such Notes will be published as soon as possible. The Notes should be submitted to the Technical Editor of the JOURNAL OF APPLIED MECHANICS. Discussions on the Brief Notes should be addressed to the Editorial Department, ASME, United Engineering Center, 345 East 47th Street, New York, N. Y. 10017, or to the Technical Editor of the JOURNAL OF APPLIED MECHANICS. Discussions on Brief Notes appearing in this issue will be accepted until two months after publication. Readers who need more time to prepare a Discussion should request an extension of the deadline from the Editorial Department.

Theoretical and Experimental Analysis of Flexural Vibration of the Viscoelastic Timoshenko Beam

T. Nakao[1], T. Okano[1], and I. Asano[1]

Introduction

The first and best-known theory of flexural vibration of beams, including the effect of shear deflection and rotary inertia, is that of Timoshenko [1]. A few papers describing vibrations of the viscoelastic Timoshenko beams have been published [2, 3]. It is assumed in these studies that the damping factor associated with the dynamic Young's modulus is identical to that associated with the shear modulus. This assumption is well justified in the case of isotropic materials and it reduces the complexity of the resulting equation. However, in the analysis of anisotropic materials that have generally much higher shear deflections in comparison with isotropic materials, the damping factors must be introduced separately in the equation.

In this paper, the forced vibration of an anisotropic, viscoelastic Timoshenko beam with free ends is discussed both theoretically and experimentally. Experiments were made on free-free wooden beams. Wood is particularly interesting as an experimental material because it is both anisotropic and viscoelastic.

Theoretical Analysis

When damping is taken into consideration, the differential equations for rotational and translational motion of an element can be obtained as follows:

$$E_b I\frac{\partial^2\psi}{\partial x^2}+\eta_b I\frac{\partial^3\psi}{\partial x^2\partial t}+\frac{AG}{\kappa}\left(\frac{\partial y}{\partial x}-\psi\right)+\frac{A\eta_s}{\kappa}\frac{\partial\left(\frac{\partial x}{\partial x}-\psi\right)}{\partial t}-\rho I\frac{\partial\psi^2}{\partial t^2}=0, \tag{1}$$

$$\rho A\frac{\partial^2 y}{\partial t^2}+\frac{AG}{\kappa}\left(\frac{\partial^2 y}{\partial x^2}-\frac{\partial\psi}{\partial x}\right)+\frac{A\eta_s}{\kappa}\frac{\partial\left(\frac{\partial^2 y}{\partial x^2}-\frac{\partial\psi}{\partial x}\right)}{\partial t}=w(x,t), \tag{2}$$

where y = lateral deflection, ψ = slope of lateral bending deflection, x = index of position along the beam axis, E_b = dynamic Young's modulus of the Timoshenko theory, G = shear modulus, I = moment of inertia of a cross section around the principal axis normal to the plane of motion, κ = numerical factor depending on the shape of the cross section, ρ = density, A = cross-sectional area, η_b = coefficient of viscosity for normal stress in bending, and η_s = coefficient of viscosity for shear stress in bending.

Eliminating ψ from these two equations and considering that any mode of vibrations is produced by a shearing force $w(x,t) = F P(x) \sin\omega t$, the following equation can be obtained:

$$\frac{G}{\kappa}E_b I\frac{\partial^4 y}{\partial x^4}+\frac{\rho A}{\kappa}\left(G\frac{\partial^2 y}{\partial t^2}+\eta_s\frac{\partial^3 y}{\partial t^3}\right)-\rho I\left(E_b+\frac{G}{\kappa}\right)\frac{\partial^4 y}{\partial x^2\partial t^2}$$
$$-\rho I\left(\eta_b+\frac{\eta_s}{\kappa}\right)\frac{\partial y^5}{\partial x^2\partial t^3}+\frac{I}{\kappa}(E_b\eta_s+G\eta_b)\frac{\partial^5 y}{\partial x^4\partial t}$$
$$+\rho^2 I\frac{\partial^4 y}{\partial t^4}+\frac{I\eta_b\eta_s}{\kappa}\frac{\partial^6 y}{\partial x^4\partial t^2}$$
$$=\left(\frac{G}{\kappa}P(x)-\frac{E_b I}{A}P''(x)-\frac{\rho\omega^2 I}{A}P(x)\right)F\sin\omega t, \tag{3}$$

where F is the amplitude of vibrating force, $P(x)$ is a normal function, and is the circular frequency. The deflection at any location can be represented by

$$y=P(x)\,Y(t), \tag{4}$$

Substituting equation (4) in equation (3), we obtain:

[1]Graduate Student, Associate Professor, and Professor, respectively, Department of Forest Products, Faculty of Agriculture, The University of Tokyo, Tokyo 113, Japan.

Contributed by the Applied Mechanics Division for publication in the JOURNAL OF APPLIED MECHANICS. Manuscript received by ASME Applied Mechanics Division, June, 1984; final revision, January, 1985.

Copyright © 1985 by ASME
Downloaded 02 May 2010 to 171.66.16.54. Redistribution subject to ASME license or copyright; see http://www.asme.org/terms/Terms_Use.cfm

Table 1 Dimensions and resonance frequencies of different specimens

(*a*) Sitka spruce (*Picea sitchensis* Carr.)					
length (cm) (*L*)	thickness (cm) (*T*)	breadth (cm) (*R*)	*h*/*l*	density (g/cm^3)	frequency (Hz)
33.0	6.00	2.00	0.18	0.42	2226
31.0	5.00	1.90	0.16	0.42	2221
28.0	3.90	1.70	0.14	0.42	2236
25.5	3.10	1.55	0.12	0.42	2224
18.0	1.45	1.10	0.08	0.42	2177
(*b*) Rosewood (*Dalbergia* sp.)					
length (cm) (*L*)	thickness (cm) (*T*)	breadth (cm) (*R*)		density (g/cm^3)	
25.0–40.0	2.5	0.7		1.04	

Notes: *L*: Longitudinal direction; *T*: tangential direction; *R*: radial direction.
h/*l*: Thickness/length.

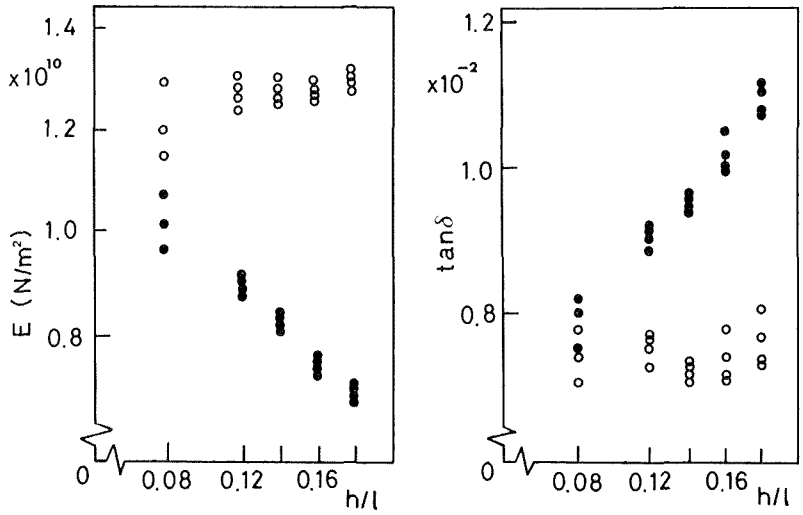

Fig. 1 Effect of the ratio of the thickness to the length on the dynamic Young's modulus and loss tangent in a constant resonance frequency. Note: •: according to the Bernoulli-Euler theory, and ○: according to the viscoelastic Timoshenko theory.

$$a\frac{d^4Y}{dt^4}+b\frac{d^3Y}{dt^3}+c\frac{d^2Y}{dt^2}+d\frac{dY}{dt}+e\,Y=f\sin\omega t \tag{5}$$

and the amplitude of the steady state solution can be expressed as follows:

$$A_m=f[(a\omega^4-c\omega^2+e)^2+(b\omega^3-d\omega)^2]^{-1/2}. \tag{6}$$

By using the following relations [4, 5]:

$$\tan\delta_b=\omega_r\eta_b/E_b,\ \tan\delta_s=\omega_r\eta_s/G, \tag{7}$$

where ω_r is resonance frequency for vibration of viscoelastic body, $\tan\delta_b$ is loss tangent for normal stress in the Timoshenko theory, and $\tan\delta_s$ is loss tangent for shear stress, and

$$\frac{P''''(x)}{P(x)}\bigg|_{x=\frac{l}{2}}=\left\{1+\left(\frac{h^2}{12}\left(\frac{k}{l}\right)^2\frac{\kappa E_b}{G}\right)^2\right\}\left(\frac{k}{l}\right)^4=S\left(\frac{k}{l}\right)^4, \tag{8}$$

$$\frac{P''(x)}{P(x)}\bigg|_{x=\frac{l}{2}}=-\frac{h^2}{12}\left(\frac{k}{l}\right)^2\frac{\kappa E_b}{G}\left(\frac{k}{l}\right)^2=T\left(\frac{k}{l}\right)^2, \tag{9}$$

coefficients in equations (5) and (6) can be written at the end of a free-free beam with a rectangular cross section, as follows:

$$a=\frac{\kappa\rho h^2}{12G},$$

$$b=\frac{l}{\omega_r}\left(\tan\delta_s-\frac{h^2}{12}\left(\frac{k}{l}\right)^2\left(\frac{\kappa E_b}{G}\tan\delta_b+\tan\delta_s\right)T\right),$$

$$c=1-\frac{h^2}{12}\left(\frac{k}{l}\right)^2\left(\frac{\kappa E_b}{G}+1\right)T+\tan\delta_b\tan\delta_s S\left(\frac{\omega_n}{\omega_r}\right)^2,$$

$$d=(\tan\delta_b+\tan\delta_s)S\omega_n{}^2/\omega_r{}^2,\quad e=\omega_n{}^2S,$$

$$f=\frac{F}{\rho A}\left(1-\frac{\kappa E_b}{G}\frac{h^2}{12}\left(\frac{k}{l}\right)^2T-\frac{\kappa\rho}{G}\frac{h^2}{12}\omega^2\right), \tag{10}$$

where h and l are the thickness and length of the beam, respectively, ω_n is the resonant circular frequency for vibration of the elastic beam, and the nondimensional frequency k is represented as follows:

$$k=l(\omega_n{}^2\rho A/E_bI)^{1/4}.$$

Now equation (6) can be written as:

$$A_m=f\,[S^2(\omega_n{}^2-\omega^2)^2+(d-b\omega^2)^2\omega^2]^{-1/2}. \tag{11}$$

Analogous to the elementary theory, actual damping factor $\tan\delta_a$ is obtained as follows:

$$\tan\delta_a=(d-b\omega^2)/(S\omega_n). \tag{12}$$

By the relations, $\omega\approx\omega_n\approx\omega_r$, we obtain the following approximate equation:

$$\tan\delta_a=\left[\Lambda\left(1-\frac{G}{\kappa E_b}\right)\tan\delta_s+\tan\delta_b\right]\Big/(\Lambda+1), \tag{13}$$

Downloaded 02 May 2010 to 171.66.16.54. Redistribution subject to ASME license or copyright; see http://www.asme.org/terms/Terms_Use.cfm

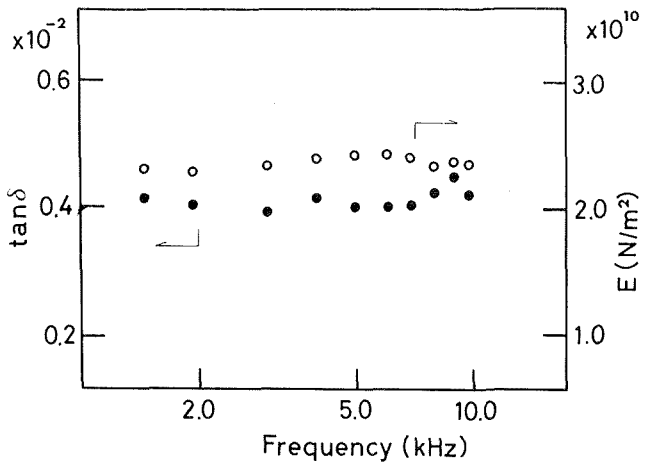

Fig. 2 Frequency dependence of the dynamic Young's modulus and loss tangent by the longitudinal vibration method

when we set $(1-G/(\kappa E_b)) = 1$, we obtain the following simple expression:

$$\tan\delta_a = (\Lambda\tan\delta_s + \tan\delta_b)/(\Lambda+1), \tag{14}$$

where

$$\Lambda = \left\{\frac{1}{12}\left(\frac{h}{l}\right)^2 \frac{\kappa E_b}{G}\right\}^2 k^4,$$

and k^4 can be approximately calculated as follows [2]:

$$k^4 = m^4/T_g,$$

where

$$T_g = 1 + \frac{1}{6}\left(\frac{h}{l}\right)^2 mf(m)\left(3 - \frac{\kappa E_b}{G}\right) + \frac{1}{12}\left(\frac{h}{l}\right)^2 m^2 f^2(m)\left(1 + \frac{\kappa E_b}{G}\right) - \frac{\kappa\rho h^2}{12G}\omega_r^2, \tag{15}$$

$m = 4.730$ and $f(m) = 0.9825$ for mode of vibration, p, $= 1$, $m = 7.853$ and $f(m) = 1.008$ for $p = 2$, and subsequently $m = (2p+1)\pi/2$ and $f(m) = 1$ for all values of p. Comparing the values of $\tan\delta_a$ calculated from equations (13) and (14) with the accurate value from equation (8), equation (14), which has more simple form than equation (13), gives the more exact values of $\tan\delta_a$ than equation (13).

Experimental Result and Discussion

The experiments reported in the following were carried out on wooden beams with a rectangular cross section. For wide beams the theory of plates (for example, Mindlin theory [6]) must be used in the analysis of the experiments. Species, dimensions, and density are shown in Table 1. All measurements were carried out at 20°C and 65 percent R.H. The viscoelastic moduli were measured by flexural [7, 8], longitudinal [9], and torsional [10] forced-vibration methods of free-free beams. The resonance frequency curves were recorded with an FFT analyzer. The elastic moduli were calculated only from the resonant frequencies and E_b according to the Timoshenko theory and G/κ were evaluated by applying Hearmon's procedure [7]. The loss tangent $\tan\delta_a$ according to the elementary Berunoulli-Euler theory was calculated by the band-width method [4]. The loss tangent $\tan\delta_b$ according to the present theory was calculated from the equation (14), in which the provisional value of $\tan\delta_s$ by the torsional vibration method is given in advance.

The complex Young's moduli were obtained for beams for Sitka spruce. Table 1 shows that the ratios of the thickness to the length are 0.08–0.18 and from the experiment, the resonant frequencies are almost the same. In this case, the frequnency dispersion of viscoelastic moduli is negligible and the constant values of the moduli are expected to be obtained. E_a and $\tan\delta_a$ according to the elementary Bernoulli-Euler theory and E_b and $\tan\delta_b$ according to the viscoelastic Timoshenko theory were calculated and plotted in Fig. 1 as functions of the ratio of the thickness to the length. E_b was experimentally obtained by measuring the resonance frequencies of the first, second, and third modes for each specimen. The other viscoelastic moduli were obtained from the first mode. The provisional value of $\tan\delta_s$ in equation (14) was 0.0145. Figure 1 shows that E_a decreases and $\tan\delta_a$ increases with increasing ratio of the thickness to the length. On the other hand, E_b and $\tan\delta_b$ remain almost constant. In addition, the provisional value for $\tan\delta_s = 0.0145$ is in a good agreement with the result obtained by the torsional vibration method.

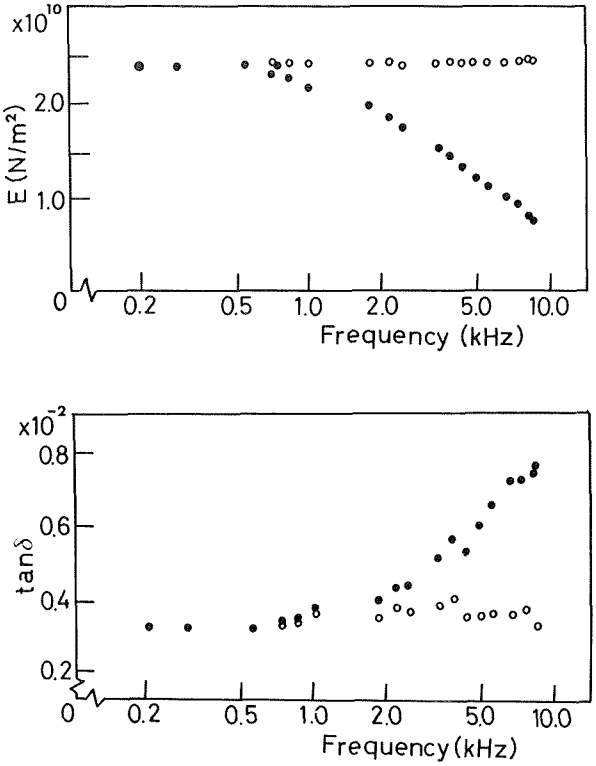

Fig. 3 Frequency dependence of the dynamic Young's modulus and loss tangent. Note: •: according to the Bernoulii-Euler theory, and ○: according to the viscoelastic Timoshenko theory.

The dynamic Young's modulus E_l and the loss tangent $\tan\delta_l$ for Rosewood were measured by the longitudinal vibration method and plotted in Fig. 2 as a function of frequency. Figure 2 shows that there is no definite trend in the effect of frequency on both E_l and $\tan\delta_l$.

E_a and $\tan\delta_a$ according to the elementary theory and E_b and $\tan\delta_b$ according to the viscoelastic Timoshenko theory were measured for Rosewood and are plotted in Fig. 3. The resonant curve was obtained for the first–sixth mode. The provisional value of $\tan\delta_s$ was 0.011–0.012. Figure 3 shows that E_b and $\tan\delta_b$ are both independent of frequency up to 10kHz. These results are in an agreement with those shown in Fig. 2. The provisional value of $\tan\delta_s = 0.011$–0.012 was somewhat larger than the value of $\tan\delta_s = 0.009$ by the torsional vibration method. This difference is probably due to the uncertainty in measuring $\tan\delta$ at higher modes, and is tolerable.

Acknowledgment

The assistance of Professor Anatole Sarko, State University

Downloaded 02 May 2010 to 171.66.16.54. Redistribution subject to ASME license or copyright; see http://www.asme.org/terms/Terms_Use.cfm

of New York, who refined the manuscript, is acknowledged with gratitude.

References

1 Timoshenko, S. P., "On the Correction for Shear of the Differential Equation for Transverse Vibration of Prismatic Bars," *Philosophical Magazine*, Vol. 41, 1921, pp. 744-746.

2 Snowdon, J. C., "Transverse Vibration of Beams With Internal Damping, Rotary Inertia, and Shear," *The Journal of the Acoustic Society of America*, Vol. 35, 1963, pp. 1997-2006.

3 Huang, T. C., and Huang, C. C., "Free Vibration of Viscoelastic Timoshenko Beams," ASME JOURNAL OF APPLIED MECHANICS, Vol. 38, June 1971, pp. 515-521.

4 Horio, M., and Onogi, S., "Forced Vibration of Reed as a Method of Determining Viscoelasticity," *Journal of Applied Physics*, Vol. 22, 1951, pp. 977-981.

5 Goens, E., "Über die Bestimmung des Elastizitätsmoduls von Stäben mit Hilfe von Biegungsschwingungen," *Annalen der Physik*, Vol. 11, 1931, pp. 649-676.

6 Mindlin, R. D., "Influence of Rotatory Inertia and Shear on Flexural Motions of Isotropic, Elastic Plates," ASME JOURNAL OF APPLIED MECHANICS, Vol. 18, 1951, pp. 31-38.

7 Hearmon, R. F. S., "The Influence of Shear and Rotatory Inertia on the Free Flexural Vibration of Wooden Beams," *British Journal of Applied Physics*, Vol. 9, 1958, pp. 381-388.

8 Kollmann, F., Krech, H., "Dynamische Messung der Elastischen Holzeigenschaften und der Dämpfung," *Holz als Roh- und Werkstoff*, Vol. 18, 1960, pp. 41-54.

9 Krüger, F., and Rohloff, E., "Uber die inner Reibung von Holz," *Zeitschrift fur Physik*, Vol. 110, 1938, pp. 58-69.

10 Becker, H. F., "Messung der Schubmoduln von Vollholz mit Akustischen Torsionsschwingungen," *Holz als Roh- und Werkstoff*, Vol. 31, 1973, pp. 207-210.

An Action-Based Method for the Kinetic Stability of Potential But Nonconservative Systems

J. G. Papastavridis[1]

1 Introduction

In a previous paper [1] the author has examined anew an old stability/instability-of-motion-theorem of Kelvin and Tait. This theorem is based on the extremal properties of the system's Lagrangean Action A_L (= time-integral of twice the system's kinetic energy), along a fundamental trajectory I. As opposed to the customary *fixed* endpoints treatments, that are based on Jacobi's geodesic form of A_L, the new treatment in [1] employs the general *variable time-endpoints* formulation: by examining the sign of A_L's second such variation, it leads to the concept of the Lagrangean (or Maupertuisian or isoenergetic/nontautochronous) Kinetic Foci (LKF). These foci, in general different from the more familiar Hamiltonian (or tautochronous) Kinetic Foci (HKF), (see e.g., [2], [3, Ch. 29, Sect. 345]), are related to the *orbital* stability/instability of I against isoenergetic disturbances: their complete absence signifies instability, whereas their presence indicates stability (for some time, at least); see e.g., [1], [2], [4, Ch. 12, Sections 13/15, 17].

The theory developed in [1] applies to holonomic, scleronomic, and *conservative* systems. For such systems, the Lagrangean L is (explicitly) independent of time t, i.e., $\partial \mathrm{L}/\partial t = 0$, and therefore an energy integral exists (Jacobi's theorem); this energy constancy along I is crucial to the LKF determination.

This investigation pushes these stability/instability – kinetic foci ideas a bit further to the case where L *may contain the time explicitly*, i.e., $\partial \mathrm{L}/\partial t \neq 0$, and consequently Jacobi's integral does not exist; the system although potential (or "gradient") is nevertheless nonconservative! As a rule this situation appears when: (i) the chosen set of generalized coordinates $q(t)$ describe the system's motion relative to a *noninertial* frame and/or (ii) when a, usually external time (only) – dependent force $Q(t)$ is acting on it (i.e., when the system is not "closed").

Here the starting point is not A_L, but a nonconservative generalization of it proposed a long time ago by Whittaker [5, Section 100, example 1] in the following *Example/Theorem*: "Skew that the principle of Least Action can be extended to systems for which the integral of energy does not exist, in the following form. Let the expression $(\partial \mathrm{L}/\partial \dot{q}_k)\dot{q}_k - \mathrm{L}$ be denoted by h; then the integral

$$\int \left(\frac{\partial \mathrm{L}}{\partial \dot{q}_k} \dot{q}_k + t \frac{dh}{dt} \right) dt, \tag{0}$$

has a stationary value for any part of an actual trajectory as compared with other paths between the same terminal points for which h has the same terminal values"; in the definition of h, in (0), and throughout the rest of this paper the customary summation convention is employed; here $k = 1, 2, \ldots, N =$ # d.o.f. This "new" nonconservative action-like functional in (0), to be denoted by A_w, is introduced in Section 2, and its *first noncontemporaneous* variation around I, $\Delta(I)$, is studied; the stationarity requirement $\Delta A_w = 0$ then leads to the correct boundary conditions for the coordinate and "energy" variations, thus proving Whittaker's theorem. Section 3 examines next A_w's *second* Δ-variation and its sign changes, in particular, the conditions that turn it (positive) semi-definite, i.e., $\Delta^2 A_w = 0$; the satisfaction of the secondary (or accessory) boundary conditions leads to a new determinantal equation, the roots of which yield all the *nontautochronous* AND *nonisoenergetic* (or perhaps "quasi-isoenergetic") kinetic foci on I. The paper ends with a discussion of the significance of A_w and its foci to the stability/instability of trajectories.

2 The First Variation

The mechanical system under consideration is discrete and holonomic, with generalized coordinates $q = \{q_k(t)\}$, kinetic energy $T = T(q,\dot{q},t)$ (where $\dot{q} = \{\dot{q}_k(t)\}$ = generalized velocities, and $(\cdots)\cdot \equiv d(\cdots)/dt$, t = time), potential energy $V = V(q,\dot{q},t)$, and additional nonconservative generalized forces $Q_k = Q_k(t)$. The Lagrangean is then

$$\mathrm{L} = \mathrm{L}(q,\dot{q},t) = T - V + Q_k q_k. \tag{1}$$

From the well-known theorem (see e.g., [4, Chapter 7, Section 2]),

$$\frac{d}{dt}\left(\frac{\partial \mathrm{L}}{\partial \dot{q}_k} \dot{q}_k - \mathrm{L} \right) = -\frac{\partial \mathrm{L}}{\partial t}, \tag{2}$$

it is clear that for the foregoing system the quantity $h(I,t) \equiv h \equiv (\partial \mathrm{L}/\partial \dot{q}_k)\dot{q}_k - \mathrm{L}$ is not constant along I anymore; in fact

$$\dot{h} = -\frac{\partial \mathrm{L}}{\partial t} = -\frac{\partial (T-V)}{\partial t} - \dot{Q}_k q_k \neq 0; \tag{3}$$

in *conservative* systems h is the familiar *Jacobi's integral*.

Along the fundamental actual path L of the system, and between two arbitrary instants t_1 and t_2 $(>t_1)$, following Whittaker, the action-like functional

$$A_w(I;t_1,t_2) \equiv A_w = \int_{t_1}^{t_2} \left(\frac{\partial \mathrm{L}}{\partial \dot{q}_k} \dot{q}_k + t \frac{dh}{dt} \right) dt, \tag{4}$$

is defined; A_w is actually the general form of Hamilton's *Characteristic Function* (frequently denoted by A or V; see e.g., [4, Chapter 12, Section 16]). If the system is *scleronomic* then $\partial T/\partial t = 0$, and A_w reduces to

[1]School of Engineering Science and Mechanics, Georgia Institute of Technology, Atlanta, Ga. 30332. Manuscript received by ASME Applied Mechanics Division, July, 1984; final revision, January, 1985.

Downloaded 02 May 2010 to 171.66.16.54. Redistribution subject to ASME license or copyright; see http://www.asme.org/terms/Terms_Use.cfm

of New York, who refined the manuscript, is acknowledged with gratitude.

References

1 Timoshenko, S. P., "On the Correction for Shear of the Differential Equation for Transverse Vibration of Prismatic Bars," *Philosophical Magazine*, Vol. 41, 1921, pp. 744-746.

2 Snowdon, J. C., "Transverse Vibration of Beams With Internal Damping, Rotary Inertia, and Shear," *The Journal of the Acoustic Society of America*, Vol. 35, 1963, pp. 1997-2006.

3 Huang, T. C., and Huang, C. C., "Free Vibration of Viscoelastic Timoshenko Beams," ASME JOURNAL OF APPLIED MECHANICS, Vol. 38, June 1971, pp. 515-521.

4 Horio, M., and Onogi, S., "Forced Vibration of Reed as a Method of Determining Viscoelasticity," *Journal of Applied Physics*, Vol. 22, 1951, pp. 977-981.

5 Goens, E., "Über die Bestimmung des Elastizitätsmoduls von Stäben mit Hilfe von Biegungsschwingungen," *Annalen der Physik*, Vol. 11, 1931, pp. 649-676.

6 Mindlin, R. D., "Influence of Rotatory Inertia and Shear on Flexural Motions of Isotropic, Elastic Plates," ASME JOURNAL OF APPLIED MECHANICS, Vol. 18, 1951, pp. 31-38.

7 Hearmon, R. F. S., "The Influence of Shear and Rotatory Inertia on the Free Flexural Vibration of Wooden Beams," *British Journal of Applied Physics*, Vol. 9, 1958, pp. 381-388.

8 Kollmann, F., Krech, H., "Dynamische Messung der Elastischen Holzeigenschaften und der Dämpfung," *Holz als Roh- und Werkstoff*, Vol. 18, 1960, pp. 41-54.

9 Krüger, F., and Rohloff, E., "Uber die inner Reibung von Holz," *Zeitschrift fur Physik*, Vol. 110, 1938, pp. 58-69.

10 Becker, H. F., "Messung der Schubmoduln von Vollholz mit Akustischen Torsionsschwingungen," *Holz als Roh- und Werkstoff*, Vol. 31, 1973, pp. 207-210.

An Action-Based Method for the Kinetic Stability of Potential But Nonconservative Systems

J. G. Papastavridis[1]

1 Introduction

In a previous paper [1] the author has examined anew an old stability/instability-of-motion-theorem of Kelvin and Tait. This theorem is based on the extremal properties of the system's Lagrangean Action A_L (= time-integral of twice the system's kinetic energy), along a fundamental trajectory I. As opposed to the customary *fixed* endpoints treatments, that are based on Jacobi's geodesic form of A_L, the new treatment in [1] employs the general *variable time-endpoints* formulation: by examining the sign of A_L's second such variation, it leads to the concept of the Lagrangean (or Maupertuisian or isoenergetic/nontautochronous) Kinetic Foci (LKF). These foci, in general different from the more familiar Hamiltonian (or tautochronous) Kinetic Foci (HKF), (see e.g., [2], [3, Ch. 29, Sect. 345]), are related to the *orbital* stability/instability of I against isoenergetic disturbances: their complete absence signifies instability, whereas their presence indicates stability (for some time, at least); see e.g., [1], [2], [4, Ch. 12, Sections 13/15, 17].

The theory developed in [1] applies to holonomic, scleronomic, and *conservative* systems. For such systems, the Lagrangean L is (explicitly) independent of time t, i.e., $\partial \mathrm{L}/\partial t = 0$, and therefore an energy integral exists (Jacobi's theorem); this energy constancy along I is crucial to the LKF determination.

This investigation pushes these stability/instability – kinetic foci ideas a bit further to the case where L *may contain the time explicitly*, i.e., $\partial \mathrm{L}/\partial t \neq 0$, and consequently Jacobi's integral does not exist; the system although potential (or "gradient") is nevertheless nonconservative! As a rule this situation appears when: (i) the chosen set of generalized coordinates $q(t)$ describe the system's motion relative to a *noninertial* frame and/or (ii) when a, usually external time (only) – dependent force $Q(t)$ is acting on it (i.e., when the system is not "closed").

Here the starting point is not A_L, but a nonconservative generalization of it proposed a long time ago by Whittaker [5, Section 100, example 1] in the following *Example/Theorem*: "Skew that the principle of Least Action can be extended to systems for which the integral of energy does not exist, in the following form. Let the expression $(\partial \mathrm{L}/\partial \dot{q}_k)\dot{q}_k - \mathrm{L}$ be denoted by h; then the integral

$$\int \left(\frac{\partial \mathrm{L}}{\partial \dot{q}_k} \dot{q}_k + t \frac{dh}{dt} \right) dt, \tag{0}$$

has a stationary value for any part of an actual trajectory as compared with other paths between the same terminal points for which h has the same terminal values"; in the definition of h, in (0), and throughout the rest of this paper the customary summation convention is employed; here $k = 1, 2, \ldots, N =$ # d.o.f. This "new" nonconservative action-like functional in (0), to be denoted by A_w, is introduced in Section 2, and its *first noncontemporaneous* variation around I, $\Delta(I)$, is studied; the stationarity requirement $\Delta A_w = 0$ then leads to the correct boundary conditions for the coordinate and "energy" variations, thus proving Whittaker's theorem. Section 3 examines next A_w's *second* Δ-variation and its sign changes, in particular, the conditions that turn it (positive) semi-definite, i.e., $\Delta^2 A_w = 0$; the satisfaction of the secondary (or accessory) boundary conditions leads to a new determinantal equation, the roots of which yield all the *nontautochronous* AND *nonisoenergetic* (or perhaps "quasi-isoenergetic") kinetic foci on I. The paper ends with a discussion of the significance of A_w and its foci to the stability/instability of trajectories.

2 The First Variation

The mechanical system under consideration is discrete and holonomic, with generalized coordinates $q = \{q_k(t)\}$, kinetic energy $T = T(q,\dot{q},t)$ (where $\dot{q} = \{\dot{q}_k(t)\}$ = generalized velocities, and $(\cdots)\cdot \equiv d(\cdots)/dt$, t = time), potential energy $V = V(q,\dot{q},t)$, and additional nonconservative generalized forces $Q_k = Q_k(t)$. The Lagrangean is then

$$\mathrm{L} = \mathrm{L}(q,\dot{q},t) = T - V + Q_k q_k. \tag{1}$$

From the well-known theorem (see e.g., [4, Chapter 7, Section 2]),

$$\frac{d}{dt}\left(\frac{\partial \mathrm{L}}{\partial \dot{q}_k} \dot{q}_k - \mathrm{L} \right) = -\frac{\partial \mathrm{L}}{\partial t}, \tag{2}$$

it is clear that for the foregoing system the quantity $h(I,t) \equiv h \equiv (\partial \mathrm{L}/\partial \dot{q}_k)\dot{q}_k - \mathrm{L}$ is not constant along I anymore; in fact

$$\dot{h} = -\frac{\partial \mathrm{L}}{\partial t} = -\frac{\partial (T-V)}{\partial t} - \dot{Q}_k q_k \neq 0; \tag{3}$$

in *conservative* systems h is the familiar *Jacobi's integral*.

Along the fundamental actual path L of the system, and between two arbitrary instants t_1 and t_2 $(>t_1)$, following Whittaker, the action-like functional

$$A_w(I;t_1,t_2) \equiv A_w = \int_{t_1}^{t_2} \left(\frac{\partial \mathrm{L}}{\partial \dot{q}_k} \dot{q}_k + t \frac{dh}{dt} \right) dt, \tag{4}$$

is defined; A_w is actually the general form of Hamilton's *Characteristic Function* (frequently denoted by A or V; see e.g., [4, Chapter 12, Section 16]). If the system is *scleronomic* then $\partial T/\partial t = 0$, and A_w reduces to

[1]School of Engineering Science and Mechanics, Georgia Institute of Technology, Atlanta, Ga. 30332. Manuscript received by ASME Applied Mechanics Division, July, 1984; final revision, January, 1985.

Copyright © 1985 by ASME
Downloaded 02 May 2010 to 171.66.16.54. Redistribution subject to ASME license or copyright; see http://www.asme.org/terms/Terms_Use.cfm

$$\int_{t_1}^{t_2}\left[2T+t\left(\frac{\partial V}{\partial t}-\dot{Q}_k q_k\right)\right]dt$$

thus generalizing the Lagrangean Action A_L to the nonconservative case. *Whittaker's theorem* now reads as follows: if

$$\Delta q_k(t_1)=0,\quad \Delta q_k(t_2)=0,$$

and (5)

$$\Delta h(t_1)=0,\quad \Delta h(t_2)=0,$$

then

$$\Delta A_w=0, \tag{6}$$

for variations around an *actual I*.

Here $\Delta(\cdots)$ is the well-known *noncontemporaneous* path variation operator,[1] and is related to the familiar contemporaneous (virtual) operator $\delta(\cdots)$ by

$$\Delta(\cdots)=\delta(\cdots)+\frac{d(\cdots)}{dt}\Delta t, \tag{7}$$

$$\delta t=0.$$

Proof:

First, invoking (2), one readily transforms (4) to the customary characteristic function form

$$A_w=\int_1^2\left(\mathrm{L}+h+t\frac{dh}{dt}\right)dt=\int_1^2 \mathrm{L}dt+\{ht\}_1^2,\left(\int_1^2\equiv\int_{t_1}^{t_2}\right). \tag{8}$$

Operating now with $\Delta(\cdots)$ on (8) one successively finds

$$\Delta A_w=\Delta\int_1^2 \mathrm{L}dt+\Delta\{ht\}_1^2$$

$$=\int_1^2\delta\mathrm{L}dt+\{\mathrm{L}\Delta t\}_1^2+\{\Delta ht+h\Delta t\}_1^2$$

$$=-\int_1^2\mathcal{E}_k\cdot\delta q_k dt+\left\{\frac{\partial \mathrm{L}}{\partial\dot{q}_k}(\Delta q_k-\dot{q}_k\Delta t)+(\mathrm{L}+h)\Delta t+\Delta ht\right\}_1^2$$

$$=-\int_1^2\mathcal{E}_k\cdot\delta q_k dt+\left\{\frac{\partial \mathrm{L}}{\partial\dot{q}_k}\Delta q_k+t\Delta h\right\}_1^2, \tag{9}$$

where

$$\mathcal{E}_k=\mathcal{E}_k(\mathrm{L})\equiv\left(\frac{\partial \mathrm{L}}{\partial\dot{q}_k}\right)^{\cdot}-\left(\frac{\partial \mathrm{L}}{\partial q_k}\right)$$

$$=\left[\left(\frac{\partial T}{\partial\dot{q}_k}\right)^{\cdot}-\left(\frac{\partial T}{\partial q_k}\right)\right]-\left[\left(\frac{\partial V}{\partial\dot{q}_k}\right)^{\cdot}-\frac{\partial V}{\partial q_k}+Q_k\right], \tag{9a}$$

and $\Delta^T h\equiv h[I+\Delta(I),t+\Delta t]-h[I,t]=\Delta h+\tfrac{1}{2}\Delta^2 h+\ldots$. Invoking now (5), and since along I $\mathcal{E}_k(\mathrm{L})=0$, the theorem (6) follows; instead of the first of (5) one could achieve stationarity by using the *periodic* conditions

$$\Delta q_k(t_1)=\Delta q_k(t_2)\neq 0, \tag{10}$$

provided that similar conditions hold for the generalized momenta $p_k=\partial L/\partial\dot{q}_k$ at t_1, t_2.

3 The Second Variation

Equation (6) denotes the *stationarity* of A_w under the variations (5). The *extremality* question now requires study of the sign of A_w's *second* Δ-variation $\Delta^2 A_w$. Applying $\Delta(\cdots)$ once more on ΔA_w, in the convenient ("Jacobi's") form (9), readily yields

$$\Delta^2 A_w=\Delta(\Delta A_w)$$

$$=-\int_1^2(\delta\mathcal{E}_k\cdot\delta q_k+\underline{\mathcal{E}_k\cdot\delta^2 q_k})\,dt$$

$$+\{\underline{-\mathcal{E}_k\cdot\delta q_k\Delta t}\}_1^2$$

$$+\left\{\Delta\left(\frac{\partial \mathrm{L}}{\partial\dot{q}_k}\right)\Delta q_k+\left(\frac{\partial \mathrm{L}}{\partial\dot{q}_k}\right)\Delta^2 q_k+\Delta t\Delta h+t\Delta^2 h\right\}_1^2$$

(as (9*a*) shows, the underlined terms cancel)

$$=-\int_1^2 J_k\cdot\delta q_k dt+\{\Delta p_k\Delta q_k+p_k\Delta^2 q_k\}_1^2+\{\Delta t\Delta h+t\Delta^2 h\}_1^2, \tag{11}$$

where

$$\delta\mathcal{E}_k(\mathrm{L})\equiv\delta\mathcal{E}_k\equiv J_k(\delta q)\equiv J_k; \tag{12}$$

the equations

$$J_k=0, \tag{13}$$

(plus appropriate *initial* conditions at t_1) are the well-known Jacobi-Poincare "equations aux variations."

As equation (11) shows, if $I+\Delta(I)$ is an *adjacent motion*, i.e., if between t_1 and t_2 the variations satisfy (13), then

$$\Delta^2 A_w=\{\Delta p_k\Delta q_k+p_k\Delta^2 q_k\}_1^2+\{\Delta t\Delta h+t\Delta^2 h\}_1^2. \tag{14}$$

If further, the variations are *cotermini*, i.e., if $\Delta^T q\equiv$ total Δ-variation of $q_k=\Delta q_k+\tfrac{1}{2}\Delta^2 q_k+\cdots=0$ at t_1 and t_2, or if they are *periodic* as in (10), then the first group of boundary terms in (14) cancels. If finally the variations are also *isoenergetic at the endpoints*, i.e., if $\Delta^T h=0$, at t_1 and t_2, then

$$\Delta^2 A_w=0. \tag{15}$$

Denote now by $\{t_1'\}$ the set of all roots of equation (15) to the *right* of t_1; they determine the configurations $\{q_k(t_1')\}\equiv\{q_{k1}'\}$ on I. These configurations shall be termed the *Nonconservative and Nontautochronous Kinetic Foci* (NNKF) with respect to $q_k(t_1)\equiv q_{k1}$. Since the number of the roots $\{t_1'\}$ can be zero, finite, or countably infinite (and is completely unrelated to the system's number of degrees of freedom), so can be the number of the NNKF. The *first* such root $t_{1,1}'$ and corresponding focus $q_{k1,1}'$, however, are important for $\Delta^2 A_w$'s *sign*, and consequently for A_w's *extremality*: by *Legendre*'s test (see e.g., [4, Chapter 12, Section 3]), for very *short* time intervals t_2-t_1, and for *scleronomic* systems at least,[2] $\Delta^2 A_w$ = positive-definite (i.e., A_w = minimum). Therefore for $t_2=t_{1,1}'$, $\Delta^2 A_w$ = positive-*semi*-definite; for $t_2>t_{1,1}'$, $\Delta^2 A_w$ = sign-indefinite (i.e., A_w = min/max).

Just like the *conservative but nontautochronous* foci of the *Lagrangean* Action, and the *nonconservative but tautochronous* foci of the *Hamiltonian* Action, the NNKF presence on I (or not) signifies the *orbital* stability (or instability) of I against the nonconservative *and* nontautochronous class of disturbances; for the former two, see e.g., [1], [2], and [4, Chapter 12, Sections 13/15, 17], and references therein. The analytical determination of the $\{t_1'\}$s proceeds as follows:

(i) First, one finds the general solutions of I, i.e., of the second-order system (9*a*) = 0:

$$q_k=q_k(t;c_1,c_2,\cdots,c_{2N}).$$

[1] Denoted in [1] by $\hat{\delta}(\ldots)$.

[2] For such systems, A_w's integrand equals $2T+t(\partial V/\partial t)-\dot{Q}_k q_k\equiv a_w$, and therefore $[\partial^2 a_w/\partial\dot{q}_k\partial\dot{q}_m]=\{\partial^2(2T)/\partial\dot{q}_k\partial\dot{q}_m\}$ → positive definite matrix$(k,m=1,2,\ldots N)$; recall that V can depend on $\dot{q}$ *linearly* at most! (see e.g., [6, pp. 66-68]).

Downloaded 02 May 2010 to 171.66.16.54. Redistribution subject to ASME license or copyright; see http://www.asme.org/terms/Terms_Use.cfm

In the variational formulation, t_1, $q_{k1} = q_k(t_1)$, and $q_{k2} = q_k(t_2)$ are given, but t_2 *is not*. t_2 can be found only if one specifies the value of h there, i.e., $h[q(t_2,c), \dot{q}(t_2,c), t_2] = h_2$, equivalent to a *transversality* condition. In short: the system

$$\left.\begin{aligned} q_k(t_1;c) &= q_{k1} : \text{given} \\ q_k(t_2;c) &= q_{k2} : \text{given} \\ h(c;t_2) &= h_2 : \text{given} \end{aligned}\right\} (2N+1) \text{ equations}, \tag{16}$$

yields the following (unique or not) solutions:

$$\begin{aligned} &c_l = c_l(q_{k1}, q_{k2}, h_2) \\ &(l = 1,2, \ldots, 2N), \\ &t_2 = t_2(q_{k1}, q_{k2}, h_2). \end{aligned} \tag{17}$$

(ii) Consider now a fixed set of values of the $\{c_l\}s$, as given by (17): They specify a definite dynamical trajectory. It is well-known that the family of dynamical trajectories adjacent to I corresponds to the values $\{c_l + \delta c_l\}$, where δc = small variations around c, and has *general* solutions $\{q_k(t;c) + \delta q_k(t;c,\delta c\}$, where

$$\delta q_k(t) = \frac{\partial q_k}{\partial c_l}\delta c_l$$

$$(k = 1,2, \ldots, N; \quad l = 1,2, \ldots, 2N), \tag{18}$$

i.e., a linear superposition of the system of $2N$ independent particular solutions $\{\partial q_k/\partial c_l\}$ evaluated for this fixed set of $\{c_l\}s$. Now, the boundary conditions of the so-called "accessory" problem that produces (15) (with $t_2 \to t_1'$) are:

$$\left.\begin{aligned} \Delta q_k(t_1) &= \delta q_k(t_1) + \dot{q}_k(t_1)\Delta t_1 = 0, \\ \Delta q_k(t_1') &= \delta q_k(t_1') + \dot{q}_k(t_1')\Delta t_1' = 0, \\ \Delta h(t_1) &= \delta h(t_1) + \dot{h}(t_1)\Delta t_1 = 0, \\ \Delta h(t_1') &= \delta h(t_1') + \dot{h}(t_1')\Delta t_1' = 0 \end{aligned}\right\} (2N+2) \text{ equations} \tag{19}$$

Introduction of (18) into (19), and since $h = h(c,t)$, yields

$$\begin{aligned} &\left(\frac{\partial q_k}{\partial c_l}\right)_1 \delta c_l + \left(\frac{\partial q_k}{\partial t}\right)_1 \Delta t_1 + (0)\Delta t_1' = 0, \\ &\left(\frac{\partial q_k}{\partial c_l}\right)_1' \delta c_l + (0)\Delta t_1 + \left(\frac{\partial q_k}{\partial t}\right)_1' \Delta t_1' = 0, \\ &\left(\frac{\partial h}{\partial c_l}\right)_1 \delta c_l + \left(\frac{\partial h}{\partial t}\right)_1 \Delta t_1 + (0)\Delta t_1' = 0, \\ &\left(\frac{\partial h}{\partial c_l}\right)_1' \delta c_l + (0)\Delta t_1 + \left(\frac{\partial h}{\partial t}\right)_1' \Delta t_1' = 0. \end{aligned} \tag{20}$$

This is a homogeneous $(2N+2) \times (2N+2)$ system for the $\{\delta c_l\}$s, *and* Δt_1 and $\Delta t_1'$. The vanishing of its coefficient determinant (for nontrivial solutions) i.e.,

$$\Delta_w(t_1,t_1') = \begin{vmatrix} (\partial q_k/\partial c_l)_1 & (\partial q_k/\partial t)_1 & 0 \\ (\partial q_k/\partial c_l)_1' & 0 & (\partial q_k/\partial t)_1' \\ (\partial h/\partial c_l)_1 & (\partial h/\partial t)_1 & 0 \\ (\partial h/\partial c_l)_1' & 0 & (\partial h/\partial t)_1' \end{vmatrix} = 0, \quad (k = 1,2, \ldots N;\ l = 1,2, \ldots, 2N) \tag{21}$$

yields the locations of the NNKF; the subdeterminant inside Δ_w indicated by solid lines is the *Mayer's* determinant whose zeros yield the HKF[3].

The stability/instability criterion can now be formulated as follows: starting from an initial configuration $C_1(t_1)$ on I, one first solves the determinantal equation (21) and finds all its (real) roots to the right of t_1. These roots $\{t_1'\}$ yield all the common points or NNKF $\{q_k(t_1'): C_1'\}$ of I with $I + \Delta(I)$, after C_1. Now, the more (less) such roots I has, and the more (less) densely these roots are distributed on it, the more (less) orbitally stable I will be; when the number of $\{t_1'\}$ is finite, the largest of them indicates the maximum duration of stability of I, starting from C_1.

The next step should be to generalize these ideas to the case of non-Lagrangean possessing systems, i.e., when $Q_k = Q_k(q, \dot{q}, t)$.

The author would like to thank the unknown reviewer for his helpful criticism and suggestions.

Acknowledgment

The support of the U.S. National Science Foundation (Grant MEA-8303663) is gratefully acknowledged.

References

1 Papastavridis, J. G., "On a Lagrangean Action-based Kinetic Instability Theorem of Kelvin and Tait," to appear in *Int. J. Engr. Sc.* during second half of 1985.

2 Papastavridis, J. G., "Toward an Extremum Characterization of Kinetic Stability," *Journal of Sound and Vibration*, Vol. 87, 1983, pp. 573-587.

3 Poincaré, H., *Les methodes nouvelles de la mecanique celeste*, Vol. 3, Dover, N.Y. (originally appeared in 1899).

4 Lur'é, *Mecanique Analytique*, Vol. 2, Librairie Universitaire, Louvain, Belgium, 1968 (original in Russian, 1961).

5 Whittaker, E. T., *A Treatise on the Analytical Dynamics of Particles and Rigid Bodies*, Cambridge U.P., Cambridge, 4th edition, 1937; Dover, N.Y., 1944.

6 Gantmacher, F., *Lectures in Analytical Mechanics*, Mir Publishers, Moscow, 1970.

7 Bliss, G. A., "The Problem of Bolza in the Calculus of Variations," *Annals of Mathematics*, Vol. 33, 1932, pp. 261-273.

Steady-State Response of an Internally Damped Cylindrical Shell Translationally or Rotationally Driven at an Edge

T. Irie[4] and Y. Kobayashi[4]

Introduction

This Brief Note presents an analysis of the steady-state response of internally damped circular cylindrical shells translationally or rotationally driven at an edge. The vibration theory has great importance in many engineering applications such as in the design of tanks, casings, etc. Although a number of papers are available on the free vibration of circular cylindrical shells, the forced response of the shells has been presented in only a few papers cited in a recent one by Irie et al. (1984). There have been also many papers available on the earthquake response of deformable liquid storage tanks (cylindrical shells), including the recent studies of Haroun and Housner (1981) and Haroun (1983). However, no papers have been presented for the dynamic response of the shells reported here.

For this purpose, the equations of vibration of an internally

[3]The above procedure, i.e., equations (19) - (21), is clearly *necessary* for equation (15) to hold; for its *sufficiency* see e.g. [7].

[4]Department of Mechanical Engineering, Faculty of Engineering, Hokkaido University, Sapporo, 060 Japan.

Manuscript received by ASME Applied Mechanics Division, October, 1984; final revision, February, 1985.

Downloaded 02 May 2010 to 171.66.16.54. Redistribution subject to ASME license or copyright; see http://www.asme.org/terms/Terms_Use.cfm

In the variational formulation, t_1, $q_{k1} = q_k(t_1)$, and $q_{k2} = q_k(t_2)$ are given, but t_2 *is not*. t_2 can be found only if one specifies the value of h there, i.e., $h[q(t_2,c), \dot{q}(t_2,c), t_2] = h_2$, equivalent to a *transversality* condition. In short: the system

$$\left.\begin{aligned} q_k(t_1;c) &= q_{k1} : \text{given} \\ q_k(t_2;c) &= q_{k2} : \text{given} \\ h(c;t_2) &= h_2 : \text{given} \end{aligned}\right\} (2N+1) \text{ equations}, \tag{16}$$

yields the following (unique or not) solutions:

$$\begin{aligned} &c_l = c_l(q_{k1}, q_{k2}, h_2) \\ &(l = 1,2, \ldots, 2N), \\ &t_2 = t_2(q_{k1}, q_{k2}, h_2). \end{aligned} \tag{17}$$

(ii) Consider now a fixed set of values of the $\{c_l\}s$, as given by (17): They specify a definite dynamical trajectory. It is well-known that the family of dynamical trajectories adjacent to I corresponds to the values $\{c_l + \delta c_l\}$, where δc = small variations around c, and has *general* solutions $\{q_k(t;c) + \delta q_k(t;c,\delta c\}$, where

$$\delta q_k(t) = \frac{\partial q_k}{\partial c_l}\,\delta c_l$$

$$(k = 1,2, \ldots, N; \quad l = 1,2, \ldots, 2N), \tag{18}$$

i.e., a linear superposition of the system of $2N$ independent particular solutions $\{\partial q_k/\partial c_l\}$ evaluated for this fixed set of $\{c_l\}s$. Now, the boundary conditions of the so-called "accessory" problem that produces (15) (with $t_2 \to t_1'$) are:

$$\left.\begin{aligned} \Delta q_k(t_1) &= \delta q_k(t_1) + \dot{q}_k(t_1)\Delta t_1 = 0, \\ \Delta q_k(t_1') &= \delta q_k(t_1') + \dot{q}_k(t_1')\Delta t_1' = 0, \\ \Delta h(t_1) &= \delta h(t_1) + \dot{h}(t_1)\Delta t_1 = 0, \\ \Delta h(t_1') &= \delta h(t_1') + \dot{h}(t_1')\Delta t_1' = 0 \end{aligned}\right\} (2N+2) \text{ equations} \tag{19}$$

Introduction of (18) into (19), and since $h = h(c,t)$, yields

$$\begin{aligned} &\left(\frac{\partial q_k}{\partial c_l}\right)_1 \delta c_l + \left(\frac{\partial q_k}{\partial t}\right)_1 \Delta t_1 + (0)\Delta t_1' = 0, \\ &\left(\frac{\partial q_k}{\partial c_l}\right)_1' \delta c_l + (0)\Delta t_1 + \left(\frac{\partial q_k}{\partial t}\right)_1' \Delta t_1' = 0, \\ &\left(\frac{\partial h}{\partial c_l}\right)_1 \delta c_l + \left(\frac{\partial h}{\partial t}\right)_1 \Delta t_1 + (0)\Delta t_1' = 0, \\ &\left(\frac{\partial h}{\partial c_l}\right)_1' \delta c_l + (0)\Delta t_1 + \left(\frac{\partial h}{\partial t}\right)_1' \Delta t_1' = 0. \end{aligned} \tag{20}$$

This is a homogeneous $(2N+2) \times (2N+2)$ system for the $\{\delta c_l\}$s, *and* Δt_1 and $\Delta t_1'$. The vanishing of its coefficient determinant (for nontrivial solutions) i.e.,

$$\Delta_w(t_1,t_1') = \begin{vmatrix} (\partial q_k/\partial c_l)_1 & (\partial q_k/\partial t)_1 & 0 \\ (\partial q_k/\partial c_l)_1' & 0 & (\partial q_k/\partial t)_1' \\ (\partial h/\partial c_l)_1 & (\partial h/\partial t)_1 & 0 \\ (\partial h/\partial c_l)_1' & 0 & (\partial h/\partial t)_1' \end{vmatrix} = 0, \quad (k = 1,2, \ldots N;\ l = 1,2, \ldots, 2N) \tag{21}$$

yields the locations of the NNKF; the subdeterminant inside Δ_w indicated by solid lines is the *Mayer's* determinant whose zeros yield the HKF[3].

The stability/instability criterion can now be formulated as follows: starting from an initial configuration $C_1(t_1)$ on I, one first solves the determinantal equation (21) and finds all its (real) roots to the right of t_1. These roots $\{t_1'\}$ yield all the common points or NNKF $\{q_k(t_1'): C_1'\}$ of I with $I + \Delta(I)$, after C_1. Now, the more (less) such roots I has, and the more (less) densely these roots are distributed on it, the more (less) orbitally stable I will be; when the number of $\{t_1'\}$ is finite, the largest of them indicates the maximum duration of stability of I, starting from C_1.

The next step should be to generalize these ideas to the case of non-Lagrangean possessing systems, i.e., when $Q_k = Q_k(q, \dot{q}, t)$.

The author would like to thank the unknown reviewer for his helpful criticism and suggestions.

Acknowledgment

The support of the U.S. National Science Foundation (Grant MEA-8303663) is gratefully acknowledged.

References

1 Papastavridis, J. G., "On a Lagrangean Action-based Kinetic Instability Theorem of Kelvin and Tait," to appear in *Int. J. Engr. Sc.* during second half of 1985.

2 Papastavridis, J. G., "Toward an Extremum Characterization of Kinetic Stability," *Journal of Sound and Vibration*, Vol. 87, 1983, pp. 573-587.

3 Poincaré, H., *Les methodes nouvelles de la mecanique celeste*, Vol. 3, Dover, N.Y. (originally appeared in 1899).

4 Lur'é, *Mecanique Analytique*, Vol. 2, Librairie Universitaire, Louvain, Belgium, 1968 (original in Russian, 1961).

5 Whittaker, E. T., *A Treatise on the Analytical Dynamics of Particles and Rigid Bodies*, Cambridge U.P., Cambridge, 4th edition, 1937; Dover, N.Y., 1944.

6 Gantmacher, F., *Lectures in Analytical Mechanics*, Mir Publishers, Moscow, 1970.

7 Bliss, G. A., "The Problem of Bolza in the Calculus of Variations," *Annals of Mathematics*, Vol. 33, 1932, pp. 261-273.

Steady-State Response of an Internally Damped Cylindrical Shell Translationally or Rotationally Driven at an Edge

T. Irie[4] and Y. Kobayashi[4]

Introduction

This Brief Note presents an analysis of the steady-state response of internally damped circular cylindrical shells translationally or rotationally driven at an edge. The vibration theory has great importance in many engineering applications such as in the design of tanks, casings, etc. Although a number of papers are available on the free vibration of circular cylindrical shells, the forced response of the shells has been presented in only a few papers cited in a recent one by Irie et al. (1984). There have been also many papers available on the earthquake response of deformable liquid storage tanks (cylindrical shells), including the recent studies of Haroun and Housner (1981) and Haroun (1983). However, no papers have been presented for the dynamic response of the shells reported here.

For this purpose, the equations of vibration of an internally

[3]The above procedure, i.e., equations (19) – (21), is clearly *necessary* for equation (15) to hold; for its *sufficiency* see e.g. [7].

[4]Department of Mechanical Engineering, Faculty of Engineering, Hokkaido University, Sapporo, 060 Japan.

Manuscript received by ASME Applied Mechanics Division, October, 1984; final revision, February, 1985.

Copyright © 1985 by ASME
Downloaded 02 May 2010 to 171.66.16.54. Redistribution subject to ASME license or copyright; see http://www.asme.org/terms/Terms_Use.cfm

damped circular cylindrical shell are written in a matrix differential equation of the first order in terms of the state vector of the shell. The vector is obtained conveniently by numerical integration of the matrix equation, and the steady-state response of the shell is determined together with the natural frequencies under any combination of the boundary conditions.

By the application of the method, the dynamic responses of the shells subjected to a sinusoidally varying axial or transverse deflection, or angular rotation at an edge, are calculated numerically together with the resonant frequencies (the dimensionless frequency parameters) and the mode shapes.

Transfer Matrix Analysis

The Goldenveizer-Novozhilov (1961 and 1964, respectively) equations of vibration of a circular cylindrical shell are written in the matrix differential equation

$$\frac{d}{d\xi}\{z(\xi)\} = l[U]\{z(\xi)\} \quad (0 \le \xi \le 1) \tag{1}$$

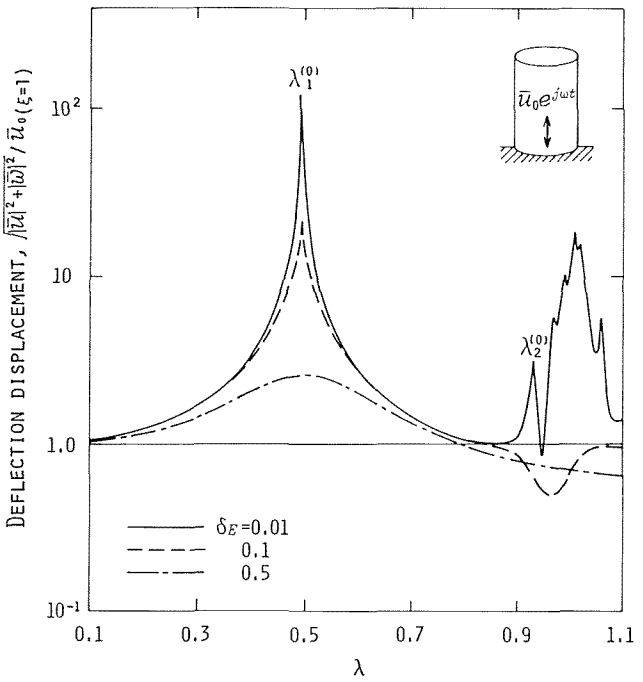

Fig. 1 Deflection displacements of the edge $\xi = 1$ of internally damped shells axially driven by $\bar{u}_0 e^{j\omega t}$ at the edge $\xi = 0$: $l = 3$, $h = 0.02$, $\nu = 0.3$

by use of the state vector $\{\mathbf{z}(\xi) = \{\bar{u}\ \bar{v}\ \bar{w}\ \bar{\psi}\ \bar{M}_x\ \bar{S}_x\ \bar{R}_x\ -\bar{N}_x\}^T$, which was conveniently employed by Irie et al. (1984). Here, u, v and w are the displacements in the axial, circumferential, and radial directions: ψ is the bending slope; M_x and N_x are the components of the moment and membrane force, and S_x and R_x are the Kelvin-Kirchhoff shearing force and membrane force, respectively. The overscored quantities $\bar{u}$, $\bar{v}$, . . . are the respective dimensionless variables. For simplicity of the analysis, the following dimensionless parameters are also introduced

$$\xi = \frac{x}{L},\ (l,h) = \frac{1}{a}(L,H),\ \lambda^2 = \frac{\rho H a^2 \omega^2}{D} \tag{2}$$

where x is the axial coordinate, L is the axial length, a is the radius of the neutral surface, and H is the wall thickness. The parameter λ is the frequency parameter expressed in terms of the mass density ρ, the wall thickness H, the radius of curvature a, the radian frequency ω, and the extensional rigidity $D = EH/(1-\nu^2)$ (ν: Poisson's ratio). The Young's modulus of internally damped shells is considered appropriately to be complex quantity: $E^* = E(1 + j\delta_E)$, where E is the real part of E^*, and δ_E is a damping constant representing the ratio of the imaginary to the real part at any frequency. This assumption has been justified by the results of experimental measurement by Kerlin and Snowdon (1970).

The state vector $\{z(\xi)\}$ can be expressed as

$$\{z(\xi)/ = [T(\xi)]\{z(\mathbf{0})\} \tag{3}$$

by using the transfer matrix $[T(\xi)]$ of the shell in the axial direction. The substitution of (3) into (1) yields

$$\frac{d}{d\xi}[T(\xi)] = l[U][T(\xi)] \quad (0 \le \xi \le 1) \tag{4}$$

The matrix $[T(\xi)]$ is obtained by integrating (4) numerically with the starting value $[T(0)] = [I]$, which is given by taking $\xi = 0$ in (3). In the numerical calculation, the elements of the transfer matrix are conveniently determined by using the Runge-Kutta-Gill integration method. Numerical difficulty arises in the calculation of the matrix if the axial length of the shell is too large, or the wall thickness is too small. However, it can be overcome by subdividing the shell into several segments and calculating the transfer matrix for each segment. The entire structure matrix is obtained by assembling the matrices of these segments.

Dynamic Responses, Resonant Frequencies and Mode Shapes

In this section, by the application of the transfer matrix

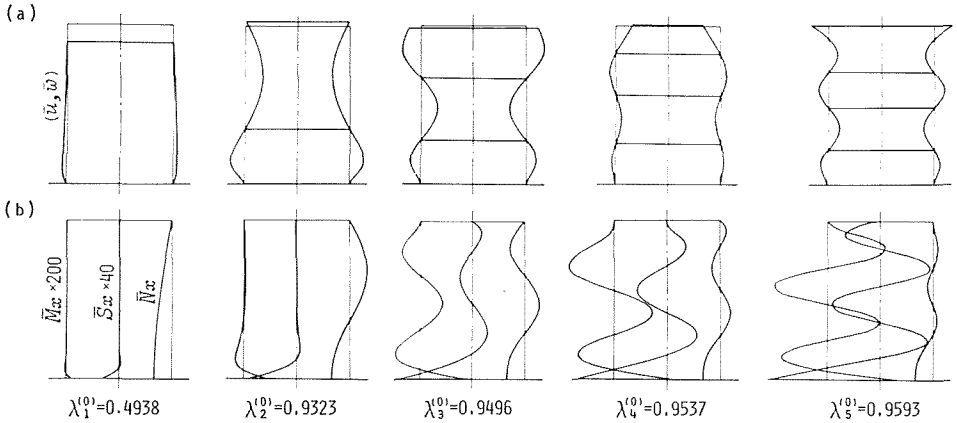

Fig. 2 Axisymmetrical mode shapes, and meridional force and moment distributions of a free-clamped undamped shell: $l = 3$, $h = 0.02$, $\nu = 0.3$, $n = 0$

Downloaded 02 May 2010 to 171.66.16.54. Redistribution subject to ASME license or copyright; see http://www.asme.org/terms/Terms_Use.cfm

analysis method, the dynamic response is calculated numerically together with the resonant frequencies and the mode shapes for circular cylindrical shells in which an edge is free and the other is driven translationally or rotationally. In general, the boundary conditions at the free edge are expressed as

$$\bar{M}_x = \bar{S}_x = \bar{R}_x = \bar{N}_x = 0 \quad \text{at} \quad \xi = 1 \tag{5}$$

Case 1: A Shell Axially Driven at an Edge. Consider a shell driven by an axial displacement $\bar{u}_o e^{j\omega t}$ with uniform amplitude $\bar{u}_o = u_o/H$ at the edge $\xi = 0$. In this case, only axisymmetrical vibration of circumferential wavenumber $n = 0$ arises in the shell, and hence the elements $\bar{v}$ and $\bar{R}_x$ of the vector $\{z(\xi)\}$ vanish. The boundary conditions at the driving edge are given by

$$\bar{u} = \bar{u}_o, \qquad \bar{w} = \bar{\psi} = 0 \quad \text{at} \quad \xi = 0 \tag{6}$$

The substitution of (3) into (5) and (6) yields a set of simultaneous linear equations with unknown coefficients $\{\bar{M}_x \ \bar{S}_x \ -\bar{N}_x\}^T_{(0)}$ at the driving edge. The dynamic response of the shell is determined from (3) by calculating these coefficients.

Figure 1 shows the axisymmetrical response curves (the deflection displacements of the free edge) of the axially driven damped shell. Within the frequency range of this figure, some resonant peaks appear at the resonant frequencies $\lambda_1^{(0)}$, $\lambda_2^{(0)}$, . . . (the natural frequencies of a free-clamped shell). In the axisymmetrical vibration of $n = 0$, many resonant frequencies appear closing up together within the range of $\lambda = 0.9$–1. With an increase of the internal damping factor δ_E, the distinguished resonant behaviors vanish.

Figures 2(*a*) and (*b*), respectively, show the axisymmetrical resonant mode shapes, and the meridional force and moment distributions together with the resonant frequencies for a free-clamped undamped shell. The resonant frequencies of undamped shell ($\delta_E = 0$) are determined by calculating the eigenvalues λ of the frequency equation obtained by taking $\bar{u}_o = 0$ in the simultaneous equations, and the mode shapes of vibration are determined by calculating the eigenvectors corresponding to the eigenvalues. The thick lines in Fig. 2(*a*) show the composition of the axial and radial displacements, where the maximum values of the displacements are taken to have unit value at the free edge or at the loop causing the maximum displacements. The thick lines inside the shells show the nodal lines where the radial deflections are zero. In Fig. 2(*b*), the ordinates of the moment $\bar{M}_x$ and the shearing force $\bar{S}_x$ are taken 200 and 40 times, respectively, as large as that of the membrane force $\bar{N}_x$ in scale, since the magnitude of these values is considerably smaller than that of the membrane force. The first mode vibration is an extensional vibration in which the axial displacement is much larger than the radial one. The meridional variation of the force and moment distributions is more remarkable in higher modes.

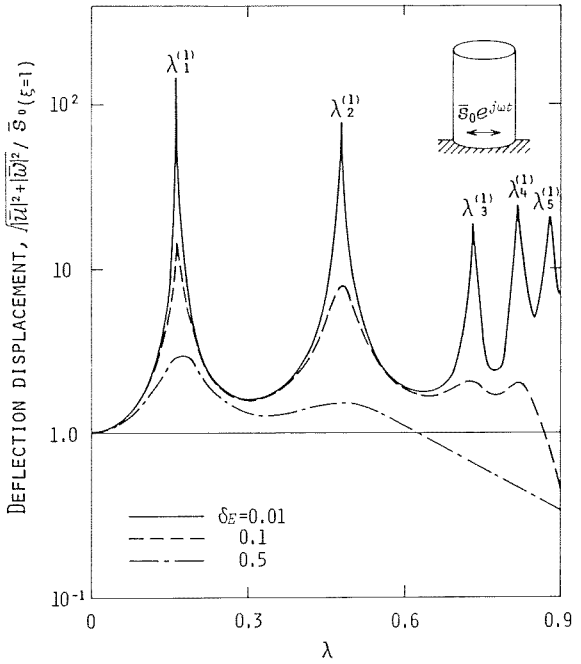

Fig. 3 Deflection displacements of the edge $\xi = 1$ of internally damped shells transversely driven by $\bar{s}_0 e^{j\omega t}$ at the edge $\xi = 0$: $l = 3$, $h = 0.02$, $\xi = 0.3$

Case 2: A Shell Transversely Driven at an Edge. When a shell is driven by a transverse deflection $\bar{s}_o e^{j\omega t}$ with uniform amplitude $\bar{s}_o = s_o/H$ at the edge $\xi = 0$, only the vibration of $n = 1$ arises in the shell. The boundary conditions at the driving edge are written as

$$\bar{u} = 0, \ \bar{v} = \bar{w} = \bar{s}_o, \ \bar{\psi} = 0 \quad \text{at} \quad \xi = 0 \tag{7}$$

The dynamic response and the resonant frequencies are determined in the same procedure as in the preceding case.

Figure 3 shows the response curves of the free edge for the transversely driven shell, in which the resonant peaks appear at the first five frequencies of $n = 1$.

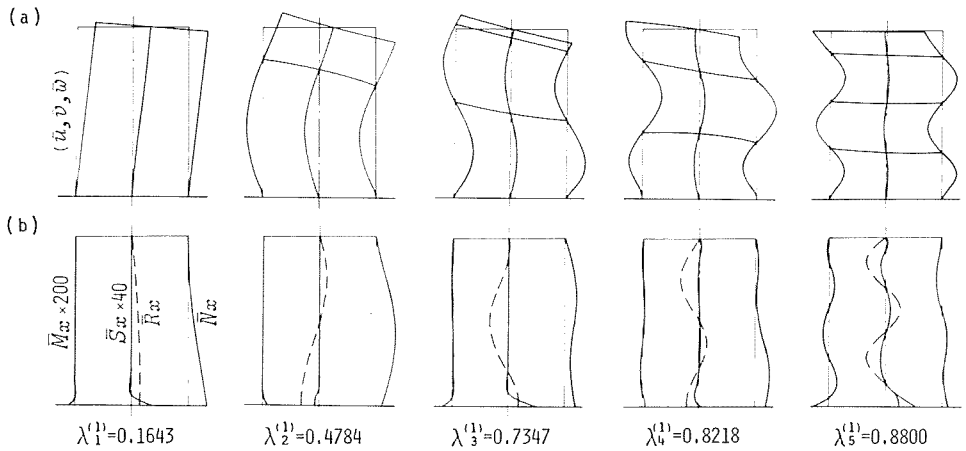

Fig. 4 Asymmetrical mode shapes, and meridional force and moment distributions of a free-clamped undamped shell: $l = 3$, $h = 0.02$, $\nu = 0.3$, $n = 1$

Downloaded 02 May 2010 to 171.66.16.54. Redistribution subject to ASME license or copyright; see http://www.asme.org/terms/Terms_Use.cfm

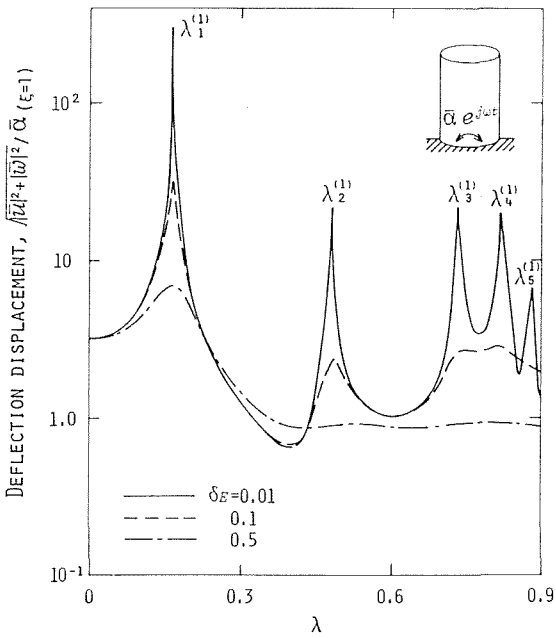

Fig. 5 Deflection displacements of the edge $\xi = 1$ of internally damped shells rotationally driven by $\bar{\alpha}e^{j\omega t}$ around a diameter of the edge $\xi = 0$: $l = 3, h = 0.02, \nu = 0.3$

Figures 4(*a*) and (*b*), respectively, show the mode shapes and the meridional force and moment distributions of a free-clamped undamped shell in the case of $n = 1$. The thick lines in Fig. 4(*a*) show the composition of the axial, circumferential and radial displacements, and the lines inside the shells show the nodal lines. The magnitude of the force and moment distributions is smaller than that of $n = 0$ given in Fig. 2(*b*).

Case 3: A Shell Rotationally Driven Around a Diameter of an Edge. Only the vibration of $n = 1$ arises in a shell rotationally driven by $\bar{\alpha}e^{j\omega t}$ ($\bar{\alpha} = \alpha/h$) around a diameter of an edge, and the boundary conditions at the driving edge are written as

$$\bar{u} = \bar{\alpha}, \bar{v} = \bar{w} = 0, \quad \bar{\psi} = \bar{\alpha} \text{ at } \xi = 0 \tag{8}$$

Figure 5 shows the response curves of the free edge for the rotationally driven shell. The curves are similar to those of the transversely driven shell in which several resonant peaks appear at the resonant frequencies of $n = 1$ given in Figs. 4.

The numerical computations presented here were carried out on a HITAC M-280H computer of the Hokkaido University Computing Center.

References

Irie, T., Yamada, G., and Muramoto, Y., 1984, "The Axisymmetrical Response of a Circular Cylindrical Double Shell System with Internal Damping," *Journal of Sound and Vibration*, Vol. 92, pp. 107–115.

Haroun, M. A., and Housner, G. W., 1981, "Earthquake Response of Deformable Liquid Storage Tanks," ASME JOURNAL OF APPLIED MECHANICS, Vol. 48, pp. 411–418.

Haroun, M. A., 1983, "Vibration Studies and Tests of Liquid Storage Tanks," *Earthquake Engineering and Structural Dynamics*, Vol. 11, pp. 179–206.

Goldenveizer, A. L., 1961, *Theory of Thin Shells*, Pergamon Press, New York.

Novozhilov, V. V., 1964, *The Theory of Thin Elastic Shells*, P. Noordhoff Ltd., Groningen, The Netherlands.

Kerlin, R. L., and Snowdon, J. C., 1970, "Driving-Point Impedances of Cantilever Beams—Comparison of Measurement and Theory," *Journal of the Acoustical Society of America*, Vol. 47, pp. 220–228.

Downloaded 02 May 2010 to 171.66.16.54. Redistribution subject to ASME license or copyright; see http://www.asme.org/terms/Terms_Use.cfm

Journal of Applied Mechanics

Discussion

Liapunov's Direct Method Applied to the Buckling of Rotating Beams[1]

B. L. Ly[2]. The stability boundaries obtained by the authors approach from above the widely accepted stability boundary given by White et al. [1]. Strictly speaking, the boundaries the authors obtained by using a finite number of coordinate functions are sufficient conditions for instability, rather than stability as the authors claimed. If the point (α, λ_c') is above such boundaries, the beam is unstable. However, the beam is not necessarily stable if the point (α, λ_c') is below such boundaries. From a practical point of view, it is more desirable to have a sufficient condition for stability than to have one for instability. It is shown here that a sufficient condition for stability may be given by the expression

$$\alpha = \frac{\sigma_{cr}}{\lambda} \tag{1}$$

where $\alpha = R/L$, $\lambda = m\omega^2 L^4/EI$, and σ_{cr} is the smallest buckling load of the column

$$f^{IV} + \sigma[(1-z)f']' = 0, \quad z = x/L. \tag{2}$$

Expression (1) is derived as follows. It is noted that the beam is self-adjoint. It loses its stability by divergence. The nontrivial equilibrium position is governed by

$$f^{IV} - \lambda[(p_1 - \alpha p_2)f']' - \lambda f = 0 \tag{3}$$

where $p_1(z) = \frac{1}{2}(1-z^2)$ and $p_2(z) = 1-z$. Equation (3) is obtained by substituting $v(z,t) = f(z)\exp(i\Omega t)$ into the equation of motion, then by letting Ω equal to zero. Multiply equation (3) by f and integrate the product by parts to obtain

$$\alpha = \frac{\frac{1}{\lambda}\int_0^1 (f'')^2 dz}{\int_0^1 p_2(f')^2 dz} + \frac{\int_0^1 p_1(f')^2 dz - \int_0^1 f^2 dz}{\int_0^1 p_2(f')^2 dz}$$

$$\geq \text{min.}\ \frac{\frac{1}{\lambda}\int_0^1 (f'')^2 dz}{\int_0^1 p_2(f')^2 dz} + \text{min.}\ \frac{\int_0^1 p_1(f')^2 dz - \int^1 f^2 dz}{\int_0^1 p_2(f')^2 dz}$$

$$= \frac{1}{\lambda}\,\text{min.}\ \frac{\int^1 (f'')^2 dz}{\int_0^1 p_2(f')^2 dz} = \frac{\sigma_{cr}}{\lambda}. \tag{4}$$

Hence, a boundary sufficient to ensure stability is given by the expression in equation (1). To obtain the preceding result, it is necessary to show that min. $\psi = 0$, where $\psi = \int_0^1 [p_1(f')^2 - f^2]dz$, because $\int_0^1 p_2(f')^2 dz$ is positive-definite. From $\delta\psi = 0$, an Euler equation is obtained

$$(1-z^2)f'' - 2zf' + 2f = 0. \tag{2}$$

It is recognized that equation (5) is a Legendre differential equation, the solution of which, in the present case, is a Legendre polynomial $P_1(z) = z$. Upon substitution of $f = P_1(z)$ into ψ, it follows that $\psi = 0$. For other admissible functions, ψ is positive. The exact value of δ_{cr} is 7.84. Hence, $\alpha = 7.84/(\lambda_c')^2$ is a boundary sufficient to ensure the stability of the rotating beam.

Reference

1 White, W. F., Kvaternik, R. G., and Kasa, K. R. V., "Buckling of Rotating Beams," *International Journal of Mechanical Sciences*, Vol. 21, 1979, pp. 739–745.

Authors' Closure

The authors wish to thank B. Ly for his interest in their paper. Ly is correct in stating that the conditions derived in the paper are not sufficient for stability. In most cases, Liapunov's direct method results in conditions which are sufficient for stability; however in the present case, the derived stability conditions approach the actual buckling curve from the unstable side as more terms are added to the assumed solution. This results in conditions which are sufficient for instability.

However, the purpose of the paper was to present a rapidly converging method which is capable of predicting the limiting boundary curve with relatively few terms. As a practical matter, a designer would stay safely clear of the predicted boundary curve. A safe margin can be determined by looking at the convergence properties of the derived buckling curve as successive approximations are made. A three-term expansion in admissible functions using the author's Liapunov technique yields a buckling curve which essentially falls on top of the curve derived by White et al. [1], for values of $\alpha > .3$. The boundary derived by Ly is sufficient for stability, but it does not give a good approximation of the true buckling curve [1]

[1] By D. C. Kammer and A. L. Schlack, Jr., and published in the December 1984 issue of ASME Journal of Applied Mechanics, Vol. 51, pp. 941–942.

[2] Equipment and Seismic Branch, Atomic Energy of Canada Limited, Sheridan Park Research Community, Mississauga, Ontario L5K1B2 Canada.

Copyright © 1985 by ASME
Downloaded 02 May 2010 to 171.66.16.54. Redistribution subject to ASME license or copyright; see http://www.asme.org/terms/Terms_Use.cfm

from below. However, Ly's boundary is a valuable addition to the methods set forth by the authors. A designer could use both methods to bracket the actual buckling curve.

In conclusion, the method presented by the authors is a general technique which can be easily applied to a large class of problems including both inplane and out-of-plane buckling with alternate boundary conditions. In addition, the method easily accommodates nonuniform physical beam properties. Ly's method is not so easily applied to this type of problem due to the increased complexity of equation (5).

Downloaded 02 May 2010 to 171.66.16.54. Redistribution subject to ASME license or copyright; see http://www.asme.org/terms/Terms_Use.cfm

Journal of Applied Mechanics

Book Reviews

The Mechanical Behavior of Electomagnetic Solid Continuua. Edited by G. A. Maugin. (Proceedings, IUTAM-IUPAP Symposium, Paris, July, 1983.) Elsevier, The Netherlands and New York, 1984. 428 Pages. Price $50.00.

REVIEWED BY R. D. JAMES[1]

This collection of papers on deformable electomagnetic solid is drawn from the IUTAM-IUPAP symposium on *The Mechanical Behavior of Electomagnetic Solid Continuua.* The aim of the symposium was to stimulate the exchange of ideas among mechanicians, applied mathematicians, solid state physicists, and electrical engineers on electomechanical problems. The 55 papers are arranged under the 10 categories: acoustoelectricity of piezoelectric dielectric crystals (10), acoustooptics and photoelasticity (2), acoustoelectricity of deformable semiconductors (4), elastic ferroelectrics and ceramics (4), piezoelectric powders (2), models and problems of electroelasticity (7), magnetoelasticity of paramagnets (2), magnetoelasticity of magnetically ordered bodies (9), magnetoelasticity of conductors (5), magnetoelasticity of structures and buckling (10). Nearly half of the papers in the volume are devoted to aspects of wave propagation in piezoelectrics, semiconductors, ferroelectrics, piezoelectric powers, paramagnets, memory alloys, ferromagnetics, and magnetoelastic conductors. Magnetoelastic buckling of magnets producting large fields is well covered, and several papers with abundant reference lists of the fomulation of the basic laws of motion and consitutive equations for deformable electromagnetic materials serve to indicate how this complex subject is currently understood. Fracture of dielectrics, transducers, and filters, electrostatic effects on cell membances, damping in memory alloys and ferromagnets, electrothermodiffusion, optical activity, the converse elastooptic effect (stimulated Brillouin scattering), molecular theory of crystals, and defects are treated briefly. The collection does not emphasize experimental techniques, with two papers on the measurement of elastic moduli and their dpependence on electromagnetic field and one on domain pattern visualization.

While a few interesting topics in this broad field are missing from the volume, those that appear are presented clearly and concisely and are well referenced. The book will be of interest to both solid mechanicians and solid state physicists, expecially those interested in wave propagation.

[1]Asisstant Professor, Division of Engineering, Brown University, Providence, R.I. 02912.

Numerical Methods for Nonlinear Variational Problems. By Roland Glowinski, Springer-Verlag, New York, 1984. 493 Pages. Price $62.00.

REVIEWED BY J. T. ODEN[2]

This is an excellent book, written in a somewhat compact mathematical style, but filled with important results and algorithms which should be of great interest to mechanicians, practicing engineers, and particulary students and scholars in the field of computational mechanics. As Glowinski says in his preface, "To those who might think our approach is too mathematical for a book published in a collections oriented toward computational physics, we would like to say that many of the methods discussed here are used by engineers in industry for solving practical problems, and that, in our opinion, mastery of most of the tools of functional analysis used here is not too difficult for anyone with a reasonable background in applied mathematics. In fact, most of the time the choice of the functional spaces used for the formulation in the solution of the given problem are not artificial, but is based on well-known physical principal, such as energy conservation, the virtual work principal, and others." He goes on to say that "from a computational point of view, a proper choice of the functional spaces used to formulate a problem will suggest, for example, what would be the good finite element spaces to approximate it and also the good preconditioning techniques for the iterative solution of the corresponding approximate problems." The book, therefore attempts to provide a rather complete presentation of the analysis of a wide range of variational problems that occur in mechanics and physics. The variational problem is provided and the correct mathematical setting, often in the form of a variational inequality of one kind or another, and then a finite element or finite difference approximation of it is constructed in appropriate subspaces. But the presentation goes beyond this rather formal apparatus of functional analysis into detailed discussion of specific numerical algorithms for solving the problem, their mathematical and convergence properties, and finally their application to concrete physical examples.

The book begins with some general properties of elliptic variational inequalities and their approximation, primarily aimed at finite element methods. In Chapter 2 the application of finite element methods to the approximation of second-order elliptic variational inequalities is taken up. Applications include problems with friction, contact problems, flow of viscous fluids through pipes, etc. Parabolic variational inequalities are taken up in Chapter 3, subsonic flow problems in

[2]Professor, Department of Aerospace Engineering and Engineering Mechanics, University of Texas, Austin, Texas 78712.

Copyright © 1985 by ASME
Downloaded 02 May 2010 to 171.66.16.54. Redistribution subject to ASME license or copyright; see http://www.asme.org/terms/Terms_Use.cfm

Chapter 4, and relaxation methods and applications in Chapter 5. There we find a detailed discussion of block relaxation methods, some result of convex analysis, and optimization techniques for quadratic functionals. In Chapter 6 the augment Lagrange method are introduced, a favorite of Glowinski and a subject on which he has written many papers. Lee's square approximations to nonlinear problems are discussed in Chapter 7 with applications to fluid dynamics. There some impressive transonic flow calculations are discussed which are handled by Lee square and finite element methods. Three appendices are provided, one on an introduction to linear variational problems, another on finite element methods with upwinding for second-order problems with convective terms, and a third on Navier-Stokes equations and their numerical treatment.

Again, this is a precise, carefully written book and a very welcome addition to the literature on nonlinear computational mechanics.

Nonlinear Elastic Deformations. By R. W. Ogden. John Wiley & Sons, New York, 1984. 532 pages. price: $95.00

REVIEWED BY E. STERNBERG[3]

The revival of interest in the nonlinear theory of elasticity around the middle of this century was prompted in part by a concern with rubber elasticity and partly impelled by issues in the area of elastic instability. While these motivations are evident also in the present treatise, the latter attests as well to the influence of the contemporary axiomatic school of continuum mechanics that has provided an additional impetus for a reconsideration of finite elasticity theory in more recent years.

Professor Ogden's treatment of his subject comprises a mathematical exposition of the purely mechanical nonlinear theory, with primary focus on elastostatics. What sets this book apart from most related treatises, and lends it particular interest as a research monograph, is the emphasis on applications and the inclusion of topics not covered elsewhere, such as a chapter on experimental aspects of large-deformation elasticity. The occasionally unconventional selection of material discussed reflects the author's own research preoccupations. This bias is natural and indeed welcome in view of his significant contributions to the field of investigation at hand.

Chapter 1 is devoted to mathematical preliminaries from the algebra and calculus of tensors. Although the chief concentration here is on vectors and second-order tensors, some—if somewhat cursory—attention is given to higher-order Cartesian tensors and to general tensors. The author's decision to switch back and forth freely between an invariant and a coordinate-based development of these topics is apt to cause discomfort only among puristically inclined readers.

The kinematics of continuous media is taken up in Chapter 2. This chapter opens with a section on the role of "observers" and reference framings, in which the concepts of a body and of configuration maps, deformations, and motions of bodies are introduced. There follows a detailed analysis of deformations, strains, and strain-rates. The chapter ends with a section pertaining to objective tensor fields.

Chapter 3 is devoted to the balance laws of mass, momentum, and energy, the analysis of actual and nominal stress, as well as the Eulerian and Lagrangian versions of the field equations of motion. A closing section on "conjugate stress analysis" contains material not accessible in the previous expository literature.

Relevant topics of constitutive theory are covered in Chapter 4. After a few introductory remarks on "simple materials," the author turns to a farily comprehensive treatment of the constitutive laws associated with elastic and hyperelastic bodies. In this context material symmetry and isotropy, along with the constitutive implications of internal constraints, are discussed.

Chapter 5 deals largely with applications of the nonlinear theory to specific problems. It starts with general comments on displacement and traction boundary conditions, including some observations on the role of "dead loadings—a topic that would appear to remain in need of further exploration. Following a proof of Ericksen's theorem on deformations sustainable by *all* compressible, isotropic hyperelastic materials, a number of particular problems for such material are analyzed. The strain-energy density employed in this connection is a variant of that appropriate to the "harmonic material" introduced by Fritz John. This portion of Chapter 5 concludes with a section on the use of complex variables in plane-strain problems for harmonic materials. The remainder of the chapter is concerned with familiar universal solutions for *incompressible* hyperelastic solids, but for a final section on variational principles and conservation laws in the finite theory of elasticity.

The subject matter of Chapter 6, which occupies over 150 pages, is closely related to some of the author's own work. The chief objective of this chapter is the theory of incremental deformations superposed on a finite deformation. Here the structure of the ensuing linearized boundary-value problems is studied. Further, the foregoing theory is applied in deriving higher-order amendments of the classical linear theory and to the treatment of allied uniqueness, stability, and bifurcation issues. In this setting of the role of various constitutive inequalities, such as the strong-ellipticity postulate, is examined.

Chapter 7, the last chapter, and one that also benefits from the author's research experience, deals with available test results for highly deformable hyperelastic materials and with attempts to match such observed behavior within the framework of the nonlinear theory.

Throughout the book a sizable number of helpful exercises complement the text. Further, a useful—although somewhat haphazard—list of references to the pertinent literature is appended to each chapter.

Professor Ogden's exposition is evidently addressed to a mathematically rather erudite audience. Indeed, readers with an engineering background might at times find his concern with elaborate mathematical detail (e.g., the definition of a "regular surface" on p. 67) out of place in a treatise of this kind. On the other hand, the author's aspiration toward mathematical precision notwithstanding, there are conspicuous occasional lapses in care. The following examples will suffice to illustrate this point.

The assertion on p. 26 that "the eigenvectors [of a symmetric tensor] are mutually orthogonal and the eigenvalues are real" does not convey the intended meaning. Actually, since the underlying space is assumed on p. 1 to be a *real* Euclidean vector space, complex eigenvalues are automatically excluded, as is reaffirmed on p. 24 by the requirement that eigenvalues be "scalars." Accordingly, the argument in support of the spectral theorem sketched on pp. 26, 27, however commonly employed, is open to objection. Next, the field hypotheses in the statement of the generalized divergence theorem on p. 70 are inadequate and do not even assure the existence of the volume integral in (1.5.66). Further, on p. 77 a "configuration" of a body B is defined as a one-to-one mapping of B into the Euclidean reference space.

[3]Professor of Mechanics, Division of Engineering and Applied Science, California Institute of Technology, Pasadena, Calif. 91125

Copyright © 1985 by ASME
Downloaded 02 May 2010 to 171.66.16.54. Redistribution subject to ASME license or copyright; see http://www.asme.org/terms/Terms_Use.cfm

Since no metric or topology is assigned directly to the abstract set of "particles" B, the meaning of the differentiability assumptions imposed on configuration maps is left unclear. Finally, the inequalities cited in the footnote on p. 191 are merely necessary, but not sufficient, in order that I_1, I_2, I_3 be the principal scalar invariants of a symmetric positive-definite tensor, and thus the domain of definition of the function Φ remains unspecified.

Such minor criticisms cannot, and are not intended to, detract from the value of this worthwhile contribution to the literature on an important subject of growing current interest.

Computational Techniques for Differential Equations. Edited by John Noye. North-Holland, The Netherlands, 1984. 680 Pages. Price $74.50.

REVIEWED BY G. MAJDA[4]

The textbook *Computational Techniques for Differential Equations*, edited by J. Noye, is a very valuable addition to the list of textbooks on computational methods in engineering and applied science. It introduces researchers to five different areas of numerical methods:

(1) the numerical solution of ordinary differential equations,
(2) finite difference techniques for partial differential equations,
(3) the Galerkin method,
(4) the finite element method,
(5) the boundary element method.

The text also contains two chapters on direct and iterative methods for the solution of systems of linear algebraic equations.

Each chapter is written by an expert in the particular field. All techniques are illustrated with model problems rather than with complex problems which often occur in applications. As an example, Poisson's equation is used to illustrate the basic properties of the finite element and the boundary element method. However, practical applications are not ignored. Some applications are presented in the text and generous references to the literature appear throughout the book. The theory behind the numerical methods is either given a heuristic motivation or it is briefly sketched. Again, generous references to the literuatre are given where theoretical results can be studied in detail.

The primary contribution of this book is that it covers a broad set of important topics in an expository fashion. All chapter start in a way that assumes that the reader has no previous experience with the material. Noye's text can be used either as a textbook for a graduate class on the numerical solution of differential equations or as a reference for scientists using numerical methods in their research. It has the special feature of including, in one textbook and in a very readable manner, material that usually appears in five or six different books. It should serve as a useful guide for students and researchers who want to get a good overview of most methods that are typically used in the numerical solution of differential equations.

My primary criticism of this book is that despite its breadth, important topics or references to these topics are omitted. The numerical solution of two-point boundary value problems is never mentioned. The numerical solution of systems of hyperbolic conservation laws is given only a one-paragraph discussion and the only reference to the literuatre on this important topic is a 1967 reference to the method of shock fitting. Very little discussion appears on appropriate methods for imposing the extra boundary conditions that are often required for finite difference approximations of initial-boundary value problems for parabolic and hyperbolic partial differential equations.

Atmospheric Dispersion of Heavy Gases and Small Particles. (A Symposium at Delft, August 29–September 2, 1983, under the sponsorship of the International Union of Theoretical and Applied Mechanics.) Edited by G. Ooms and H. Tennekes. Springer-Verlag, New York, 1984. 440 Pages. Price $38.50.

REVIEWED BY R. A. DOBBINS[5]

This conference consisted of four review articles and over two dozen research papers from contributors based in Europe and the United States. The topics include: gravity spreading of dense gases; dense gas dispersion; turbulence models and dispersion of dense gas clouds; laboratory and large-scale experiments of heavy gas dispersion; liquified gas spills on the sea; and many related topics. The substantial number of papers and the numerous references in the review and research papers provides an excellent summary of the status of heavy gas dispersion in 1983. All viewpoints, from rigorous theoretical understanding to practical calculation techniques, seem to be represented. There is frequent reference to works in progress which will be reported at future meetings. Thus, this conference not only summarizes the past results but provides at least a limited view on the nature of the works to be reported in the future. A noteworthy editorial defect does emerge from casual examination of the conference proceedings. In one article there is reference to the now unavailable original paper as the source of the equations from which the quoted graphical results originate.

An early motivation for the study of heavy gas dispersion was and remains the inadvertent release of liquified natural gas. News of a catastrophic release of methyl isocyanate at Bhopal, India and similar types of episodes serve as a reminder that heavy gas dispersion is potentially a factor in a variety of accidents in industrial plants. This volume provides a status report of the knowledge of this topic as of September, 1983.

[4]Assistant Professor, Division of Applied Mathematics, Brown University, Providence, R.I. 02912.

[5]Professor and Chairman, Division of Engineering, Brown University, Providence, R.I. 02912.

Downloaded 02 May 2010 to 171.66.16.54. Redistribution subject to ASME license or copyright; see http://www.asme.org/terms/Terms_Use.cfm

Since no metric or topology is assigned directly to the abstract set of "particles" B, the meaning of the differentiability assumptions imposed on configuration maps is left unclear. Finally, the inequalities cited in the footnote on p. 191 are merely necessary, but not sufficient, in order that I_1, I_2, I_3 be the principal scalar invariants of a symmetric positive-definite tensor, and thus the domain of definition of the function Φ remains unspecified.

Such minor criticisms cannot, and are not intended to, detract from the value of this worthwhile contribution to the literature on an important subject of growing current interest.

Computational Techniques for Differential Equations. Edited by John Noye. North-Holland, The Netherlands, 1984. 680 Pages. Price $74.50.

REVIEWED BY G. MAJDA[4]

The textbook *Computational Techniques for Differential Equations*, edited by J. Noye, is a very valuable addition to the list of textbooks on computational methods in engineering and applied science. It introduces researchers to five different areas of numerical methods:

(1) the numerical solution of ordinary differential equations,
(2) finite difference techniques for partial differential equations,
(3) the Galerkin method,
(4) the finite element method,
(5) the boundary element method.

The text also contains two chapters on direct and iterative methods for the solution of systems of linear algebraic equations.

Each chapter is written by an expert in the particular field. All techniques are illustrated with model problems rather than with complex problems which often occur in applications. As an example, Poisson's equation is used to illustrate the basic properties of the finite element and the boundary element method. However, practical applications are not ignored. Some applications are presented in the text and generous references to the literature appear throughout the book. The theory behind the numerical methods is either given a heuristic motivation or it is briefly sketched. Again, generous references to the literuatre are given where theoretical results can be studied in detail.

The primary contribution of this book is that it covers a broad set of important topics in an expository fashion. All chapter start in a way that assumes that the reader has no previous experience with the material. Noye's text can be used either as a textbook for a graduate class on the numerical solution of differential equations or as a reference for scientists using numerical methods in their research. It has the special feature of including, in one textbook and in a very readable manner, material that usually appears in five or six different books. It should serve as a useful guide for students and researchers who want to get a good overview of most methods that are typically used in the numerical solution of differential equations.

My primary criticism of this book is that despite its breadth, important topics or references to these topics are omitted. The numerical solution of two-point boundary value problems is never mentioned. The numerical solution of systems of hyperbolic conservation laws is given only a one-paragraph discussion and the only reference to the literuatre on this important topic is a 1967 reference to the method of shock fitting. Very little discussion appears on appropriate methods for imposing the extra boundary conditions that are often required for finite difference approximations of initial-boundary value problems for parabolic and hyperbolic partial differential equations.

Atmospheric Dispersion of Heavy Gases and Small Particles. (A Symposium at Delft, August 29–September 2, 1983, under the sponsorship of the International Union of Theoretical and Applied Mechanics.) Edited by G. Ooms and H. Tennekes. Springer-Verlag, New York, 1984. 440 Pages. Price $38.50.

REVIEWED BY R. A. DOBBINS[5]

This conference consisted of four review articles and over two dozen research papers from contributors based in Europe and the United States. The topics include: gravity spreading of dense gases; dense gas dispersion; turbulence models and dispersion of dense gas clouds; laboratory and large-scale experiments of heavy gas dispersion; liquified gas spills on the sea; and many related topics. The substantial number of papers and the numerous references in the review and research papers provides an excellent summary of the status of heavy gas dispersion in 1983. All viewpoints, from rigorous theoretical understanding to practical calculation techniques, seem to be represented. There is frequent reference to works in progress which will be reported at future meetings. Thus, this conference not only summarizes the past results but provides at least a limited view on the nature of the works to be reported in the future. A noteworthy editorial defect does emerge from casual examination of the conference proceedings. In one article there is reference to the now unavailable original paper as the source of the equations from which the quoted graphical results originate.

An early motivation for the study of heavy gas dispersion was and remains the inadvertent release of liquified natural gas. News of a catastrophic release of methyl isocyanate at Bhopal, India and similar types of episodes serve as a reminder that heavy gas dispersion is potentially a factor in a variety of accidents in industrial plants. This volume provides a status report of the knowledge of this topic as of September, 1983.

[4]Assistant Professor, Division of Applied Mathematics, Brown University, Providence, R.I. 02912.

[5]Professor and Chairman, Division of Engineering, Brown University, Providence, R.I. 02912.

Copyright © 1985 by ASME
Downloaded 02 May 2010 to 171.66.16.54. Redistribution subject to ASME license or copyright; see http://www.asme.org/terms/Terms_Use.cfm